

# MTE 2010

21<sup>st</sup> Micromechanics and  
Micro systems Europe Workshop

## Abstracts



Proceedings of the 21<sup>st</sup> Micromechanics and Micro systems Europe Workshop,  
Enschede, The Netherlands, 26-29 September 2010  
Edited by Leon Abelman, Hans Groenland, Joost van Honschoten, and Hein Verputten  
ISBN 978 90 816737 1 6

## Programme

### Sunday September 26 2010

18:00 – 20:00: Registration, buffet  
20:00 – 00:00: Concert in Atak

### Monday September 27 2010

8:30 – 9:00 : Registration  
9:00 – 9:15 : Welcome  
9:15 – 10:00: Invited Speaker 1

#### Understanding and eliminating nanoscale wear

M.A. Lantz

IBM Research Division, Zurich Research Laboratory, Switzerland

10:00 – 11:00: Flash Presentations [Session A](#) (25 x 2 min)  
11:00 – 12:30: Poster [Session A](#)  
12:30 – 14:15: Lunch  
14:15 – 15:00: Invited Speaker 2

#### Optical sensors and actuators enabled by photonic crystals

O. Solgaard

Stanford University, E.L. Ginzton Laboratory, CA, USA

15:00 – 16:00: Flash Presentations [Session B](#) (25 x 2 min)  
16:00 – 18:00: Poster [Session B](#)

19:00 – 20:00: Reception and Grolsch Veste tour  
20:00 – 23:00: Conference Dinner

### Tuesday September 28 2010

8:30 – 9:00 : Registration  
9:00 – 9:45 : Invited Speaker 3

#### Programmed self-assembly and dynamics of DNA nanostructures

K.V. Gothelf

Aarhus University, Denmark

9:45 – 10:45: Flash Presentations [Session C](#) (25 x 2 min)  
10:45 – 12:15: Poster [Session C](#)  
12:15 – 14:00: Lunch  
14:00 – 14:45: Invited Speaker 4

#### Glass-based lab-on-a-chip products

R. van 't Oever

Micronit, Enschede, the Netherlands

14:45 – 15:45: Flash Presentations [Session D](#) (25 x 2 min)  
15:45 – 17:15: Poster [Session D](#)  
17:15 – 17:45: MME2011, poster award and closing remarks

19:30 – ? : Science Cafe and excursion in Enschede

### Wednesday September 29 2010

9:00 – 12:30: MESA+ NanoLab tours

Session A  
(Monday 10:00 – 12:30)

A01

**Silicon carbide thin-film encapsulation of planar thermo- electric infrared (IR) detectors - for an IR microspectrometer**

V. Rajaraman, G. de Graaf, P.J. French and K.A.A. Makinwa

Delft University of Technology (TU Delft), Dept. of Microelectronics, EI Lab - DIMES, the Netherlands

A02

**Design, fabrication and characterization of an in-plane AFM probe with ultra-sharp silicon nitride tip**

E. Sarajlic<sup>1</sup>, J. Geerlings<sup>2</sup>, J.W. Berenschot<sup>2</sup>, M.H. Siekman<sup>1,2</sup>, N.R. Tas<sup>2</sup> and L. Abelmann<sup>2</sup>

<sup>1</sup>SmartTip, Enschede, the Netherlands <sup>2</sup>MESA+ Research Institute, University of Twente, the Netherlands

A03

**A silicon micromachined triaxial accelerometer using the MultiMEMS MPW process with additional deep reactive ion etching as post-processing**

P. Ohlckers, L. Petricca and C. Grinde

Vestfold University College, Institute for Micro- and nano System Technologies, Norway

A04

**Integrated Lab-On-A-Chip silicon nanowire biosensing platform**

A. De, S. Chen, J. van Nieuwkasteele, W. Sparreboom, E.T. Carlen and A. van den Berg

BIOS Lab on a Chip Group, MESA+ Institute for Nanotechnology, University of Twente, the Netherlands

A05

**Surface modification of silicon by 3D etching processes and subsequent layer deposition**

Z. Fekete, D. Gubán, É. Vázsonyi, A. Pongrácz, G. Battistig and P. Fürjes

Research Institute of Technical Physics & Materials Science, Hungarian Academy of Science, Hungary

A06

**Material selection for impedance spectroscopy on an eletrowetting based Lab-On-A-Chip**

T. Lederer, S. Clara, B. Jakoby and W. Hilber

Institute for Microelectronics and Microsensors, Johannes Kepler University, Austria



A07

**Stiction reduction in electrostatic poly-SiGe micromirrors by applying a self-assembled monolayer film**

L. Fangzhou<sup>1,2</sup>, J. De Coster<sup>1</sup>, R. Beernaert<sup>3</sup>, W.-Y. Lin<sup>1,2</sup>, J.-P. Celis and I. De Wolf

<sup>1</sup>IMEC, Belgium <sup>2</sup>Dept MTM, KU Leuven, Belgium <sup>3</sup>CMST, Ghent University, Belgium

A08

**A bridge-connected isolated silicon islands post-processing method for fine-grain-integrated 10V-operating CMOS-MEMS by standard 5V CMOS process technology**

S. Morishita<sup>1</sup>, M. Kubota<sup>1</sup>, K. Asada<sup>1</sup>, I. Mori<sup>1</sup>, F. Marty<sup>2</sup> and Y. Mita<sup>1</sup>

<sup>1</sup>The University of Tokyo, Japan <sup>2</sup>ESIEE, Université Paris Est, France

A09

**Single-mask thermal displacement sensor in MEMS**

B. Krijnen<sup>1,2</sup>, R.P. Hogervorst<sup>1</sup>, J.B.C. Engelen<sup>3</sup>, J.W. van Dijk<sup>1,2</sup>, D.M. Brouwer<sup>1,2</sup> and L. Abelman<sup>3</sup>

<sup>1</sup>DEMCON Advanced Mechatronics, the Netherlands <sup>2</sup>Mechanical Automation, IM-PACT, University of Twente, the Netherlands <sup>3</sup>Transducer Science and Technology, MESA+, University of Twente, the Netherlands

A10

**AlGaIn/GaN C-HEMT for piezoelectric MEMS stress sensor applications**

M. Vallo<sup>1</sup>, T. Lalinský<sup>1</sup>, G. Vanko<sup>1</sup>, M. Držík<sup>2</sup>, S. Hascik<sup>1</sup>, I. Rýger<sup>1</sup> and I. Kostic<sup>3</sup>

<sup>1</sup>Institute of Electrical Engineering of the Slovak Academy of Sciences, Slovakia  
<sup>2</sup>International Laser Center, Slovakia <sup>3</sup>Institute of Informatics, Slovak Academy of Sciences, Slovakia

A11

**A capacitive humidity sensor using a positive photosensitive polymer**

N. P. Pham, V. Cherman, F.F.C. Duval, D.S. Tezcan, R. Jansen and H.A.C. Tilmans  
IMEC, Belgium

A12

**Silicon/glass microchip with a monolithically integrated electrospray ionization tip for mass spectrometry**

L. Sainiemi<sup>1</sup>, T. Nissilä<sup>2,3</sup>, V. Saarela<sup>4</sup>, R.A. Ketola<sup>3</sup> and S. Franssila<sup>1</sup>

<sup>1</sup>Aalto University, Department of Materials Science and Engineering, Finland  
<sup>2</sup>University of Helsinki, Division of Pharmaceutical Chemistry, Finland <sup>3</sup>University of Helsinki, Centre for Drug Research (CDR), Finland <sup>4</sup>Aalto University, Department of Micro and Nanosciences, Finland

A13

**Improving the efficiency of thermoelectric generators by using solar heat concentrators**

M.T. de Leon, P. Taatizadeh and M. Kraft

University of Southampton, School of Electronics and Computer Science, United Kingdom

A14

**Gas sensing micromachined structure based on gallium arsenide**

I. Hotovy<sup>1</sup>, D. Tengeri<sup>1</sup>, V. Rehacek<sup>1</sup>, S. Hascik<sup>2</sup> and T. Lalinský<sup>1</sup>

<sup>1</sup>Microelectronics Department, Slovak University of Technology, Slovakia <sup>2</sup>Institute of Electrical Engineering, Slovak Academy of Sciences, Slovakia

A15

**Structuring techniques of aluminum nitride masks for deep reactive ion etching (DRIE) of silicon**

S. Leopold<sup>1</sup>, T. Polster<sup>1</sup>, T. Geiling<sup>1</sup>, D. Pätz<sup>2</sup>, F. Knöbber<sup>4</sup>, A. Albrecht<sup>3</sup>, O. Ambacher<sup>4</sup>, S. Sinzinger<sup>2</sup> and M. Hoffmann<sup>1</sup>

<sup>1</sup>Ilmenau University of Technology, IMN MacroNano, Germany, Department for Micromechanical Systems <sup>2</sup>Department for Optical Engineering <sup>3</sup>Centre for Micro- and Nanotechnology <sup>4</sup>Fraunhofer Institute for Applied Solid State Physics, Germany

A16

**Design and evaluation of an active cooling concept for functional ceramic circuits**

T. Haas<sup>1</sup>, C. Zeilmann<sup>1</sup>, A. Backes<sup>2</sup>, A. Bittner<sup>3</sup> and U. Schmid<sup>3</sup>

<sup>1</sup>Engineering Substrate, Micro Systems Engineering GmbH, Germany <sup>2</sup>Chair of Micromechanics, Microfluidics/Microactuators, Saarland University, Germany <sup>3</sup>Department for Microsystems Technology, Institute of Sensor and Actuator Systems, Vienna University of Technology, Austria

A17

**Determination of mechanical and swelling properties of epoclad negative photoresist.**

K. Wouters<sup>1</sup>, P. Gijsenbergh<sup>1</sup>, K. Vanstreels<sup>2</sup> and R. Puers<sup>1</sup>

<sup>1</sup>KULeuven, ESAT-MICAS, Belgium <sup>2</sup>IMEC, Belgium

A18

**Graphene for nano-electro-mechanical systems**

Z. Moktadir, S. Boden, H. Mizuta and H. Rutt

University of Southampton, School of Electronics and Computer Science, UK

A19

**Inductive-coupling system for abdominal aortic aneurysms monitoring based on pressure sensing**

A.T. Sepúlveda<sup>1</sup>, A. Moreira<sup>2</sup>, F. Fachin<sup>3</sup>, B.L. Wardle<sup>3</sup>, J.M. Silva<sup>4</sup>, A.J. Pontes<sup>1</sup>, J.C. Viana<sup>1</sup> and L.A. Rocha<sup>1</sup>

<sup>1</sup>I3N/IPC-Institute for Nanostructures, Nanomodelling and Nanofabrication, University of Minho, Portugal <sup>2</sup>University of Porto Faculty of Engineering, Portugal <sup>3</sup>Department of Aeronautics and Astronautics, Massachusetts Institute of Technology, USA <sup>4</sup>INESC Porto, University of Porto Faculty of Engineering, Portugal

Session B  
(Monday 15:00 – 18:00)

B01

**Design and modeling of a three-mass, decoupled, tunable SOI-MEMS gyroscope with sense frame architecture**

I. Sabageh<sup>1</sup>, V. Rajaraman<sup>1</sup>, E. Cretu<sup>2</sup> and P.J. French<sup>1</sup>

<sup>1</sup>Delft University of Technology, Department of Microelectronics, EI Lab- DIMES, the Netherlands <sup>2</sup>University of British Columbia, Department of Electrical and Computer Engineering, Canada

B02

**Robust MEMS for space applications**

A. Delahunty and W.T. Pike

Imperial College London, UK

B03

**Linear variable optical filter with silver metallic layers**

A. Emadi, V.R.S.S. Mokkapati, H. Wu, G. de Graaf and R.F. Wolffenbuttel

Faculty EEMCS, Department ME/EI, Delft University of Technology, the Netherlands

B04

**Fractal-based dual-band small antenna for 2.45 and 5.8 GHz**

S. Ahmed<sup>1</sup>, P. Enoksson<sup>1</sup>, M.V. Rusu<sup>2</sup> and C. Rusu<sup>3</sup>

<sup>1</sup>Chalmers University of Technology, Micro and Nanosystems group, Sweden

<sup>2</sup>Faculty of Physics, Bucharest University, Romania <sup>3</sup>Imego AB, Sweden

B05

**Measuring thermal properties of small volumes of liquid using a robust and flexible sensor**

J.J. Atherton, M.C. Rosamond, S. Johnstone and D.A. Zeze

Durham University, School of Engineering and Computing Sciences, United Kingdom

B06

**Small antenna based on a MEMS magnetic field sensor that uses a piezoelectric polymer as translation mechanism**

R. Lameiro<sup>1</sup>, F.J.O. Rodrigues<sup>1</sup>, L.M. Gonçalves<sup>1</sup>, S. Lanceros-Mendez<sup>2</sup>, J.H. Correia<sup>1</sup> and P.M. Mendes<sup>1</sup>

<sup>1</sup>Algoritmi, UM, Campus de Azurém, Portugal <sup>1</sup>Center/Department of Physics, University of Minho, Portugal

B07

**Fabrication of integrated bimorphs with self aligned tips for optical switching in 2-D photonic crystal waveguides**

S.M. Chakkalakal Abdulla<sup>1</sup>, L.J. Kauppine<sup>2</sup>, M. Dijkstra<sup>2</sup>, M.J. de Boer<sup>1</sup>, E. Berenschot<sup>1</sup>, R.M. de Ridder<sup>2</sup> and G.J.M. Krijnen<sup>1</sup>

<sup>1</sup>Transducers Science and Technology, MESA+ Research Institute, University of Twente, the Netherlands <sup>2</sup>Integrated Optical Microsystems Groups, MESA+ Research Institute, University of Twente, the Netherlands

B08

**High-throughput on-chip DNA fragmentation**

L. Shui, M. Jin, J.G. Bomer, E.T. Carlen and A. van den Berg

BIOS/Lab-on-Chip Group, MESA+ Institute for Nanotechnology, University of Twente, the Netherlands

B09

**Performance metrics for MEMS tunable capacitors**

M. Hill<sup>1</sup>, Y. Kubarappa<sup>1</sup> and C. O'Mahony<sup>2</sup>

<sup>1</sup>Adaptive Wireless Systems Group, Cork Institute of Technology, Ireland <sup>2</sup>Tyndall National Institute, University College Cork, Ireland

B10

**Ultrasoft finemet thin films for magneto-impedance microsensors**

J. Moulin<sup>1</sup>, I. Shahosseini<sup>1</sup>, F. Alves<sup>2</sup> and F. Mazaleyrat<sup>3</sup>

<sup>1</sup>IEF, UMR 8622, Univ Paris Sud, France <sup>2</sup>LGEP, UMR 8507, Supelec, France <sup>3</sup>SATIE, UMR 8029, ENS Cachan, France

B11

**3-dimensional etching of silicon substrates using a modified deep reactive ion etching technique**

S. Azimi, J. Naghsh-Nilchi, A. Amini, A. Vali, M. Mehran and S. Mohajerzadeh

School of Electrical and Computer Eng, Thin Film and NanoElectronic Lab, University of Tehran, Iran

B12

**Microshutters for space physics time of flight applications**

K. Brinkfeldt<sup>1</sup>, P. Enoksson<sup>2</sup>, B. Front<sup>2</sup>, M. Wieser<sup>3</sup>, M. Emanuelsson<sup>3</sup> and S. Barabash<sup>3</sup>

<sup>1</sup>Swerea IVF, Sweden <sup>2</sup>Chalmers University of Technology, Dept. Microtechnology and Nanoscience, Sweden <sup>3</sup>Swedish Institute of Space Physics, Sweden

B13

**Study of injection molded surface features in terms of light reflection, wettability and durability**

S. Kuhn, A. Burr, M. Kübler, M. Deckert and C. Bleesen

Heilbronn University, Mechatronics and Micro System Engineering, PIK, Germany

B14

**Simulation studies of parametric amplification in bio-inspired flow sensors**

H. Droogendijk and G.J.M. Krijnen

University of Twente, MESA+ Research Institute, the Netherlands

B15

**Adsorption studies of DNA origami on silicon dioxide**

B. Albrecht<sup>1,2</sup>, D.S. Hautzinger<sup>1,3,4</sup>, M. Krüger<sup>2</sup>, M. Elwenspoek<sup>4,5</sup>, K.M. Müller<sup>3,5</sup> and J.G. Korvink<sup>1,4</sup>

<sup>1</sup>Laboratory for Simulation, Dep. of Microsystems Engineering (IMTEK),

<sup>2</sup>Laboratory for Sensors, Dep. of Microsystems Engineering (IMTEK), <sup>3</sup>Laboratory for Synthetic Biosystems, Institute of Biology III, <sup>4</sup>FRIAS, <sup>5</sup>Centre for Biological Signaling Studies (bioss), <sup>1-5</sup>University of Freiburg, Germany

B16

**3D lithography based fabrication of neural stimulator electrode arrays**

F. Ceyssens<sup>1</sup>, J. Verstraete<sup>1</sup>, B. Volckaerts<sup>2</sup> and R. Puers<sup>1</sup>

<sup>1</sup>KULeuven dept. ESAT-MICAS, Belgium. <sup>2</sup>Cochlear Technology Center, Belgium.

B17

**A micro fuel cell stack without interconnect overhead - macro world-like stacks in MEMS**

G. Scotti<sup>1,3</sup>, P. Kanninen<sup>2</sup>, T. Kallio<sup>2</sup> and S. Franssila<sup>3</sup>

<sup>1</sup>Department of Micro and Nanosciences, Aalto University School of Science and Technology, Finland <sup>2</sup>Department of Chemistry, Aalto University School of Science and Technology, Finland <sup>3</sup>Department of Materials Science and Engineering, Aalto University School of Science and Technology, Finland

B18

**Fabrication technique of a compressible biocompatible interconnect using a thin film transfer process**

A.A.A. Aarts<sup>1,2,3</sup>, O. Srivannavit<sup>3</sup>, K.D. Wise<sup>3</sup>, E. Yoon<sup>3</sup>, H.P. Neves<sup>1</sup>, R. Puers<sup>1,2</sup> and C. van Hoof<sup>1,2</sup>

<sup>1</sup>Technology Unit, IMEC, Belgium <sup>2</sup>ESAT-Micas, KU Leuven, Belgium <sup>3</sup>EECS, University of Michigan, USA

B19

**Interference filter based absorber for thermopile detector array by surface micromachining**

H. Wu, A. Emadi, G. de Graaf and R. Wolffenbuttel

Delft University of Technology, Faculty of EEMCS, Department of ME/EI, the Netherlands

B20

**Thermal analysis, fabrication and signal processing of surface micromachined thermal conductivity based gas sensors**

G. de Graaf, H. Wu and R.F. Wolffenbuttel

Delft University of Technology, Faculty EEMCS, Dept. for Micro-Electronics, the Netherlands



Session C  
(Tuesday 9:45 – 12:15)

C01

**High aspect ratio hydrogenation-assisted lateral etching of (100) silicon**

M. Kayyalha, J. Naghsh Nilchi, A. Ebrahimi and S. Mohajerzadeh

University of Tehran, Nano-Electronics and Thin Film Lab., Iran

C02

**AFM-based mechanical characterization of fbar cantilevers as first step towards developing of force sensors**

C.J. Camargo, H. Campanella, J. Montserrat and J. Esteve

Instituto de Microelectrónica de Barcelona IMB-CNM (CSIC), Spain

C03

**Post-processing of linear variable optical filter on CMOS chip at die-level**

A. Emadi, H. Wu, G. de Graaf and R. F. Wolffenbuttel

Faculty EEMCS, Department ME/EI, Delft University of Technology, the Netherlands

C04

**MEMS based gravimeters and gravity gradiometers**

R. Cuperus<sup>1</sup>, F.F. Flokstra<sup>1</sup>, R.J. Wiegerink<sup>2</sup> and J. Flokstra<sup>1</sup>

<sup>1</sup>University of Twente, Interfaces and Correlated Electron systems, the Netherlands

<sup>2</sup>University of Twente, Transducers Science and Technology, the Netherlands

C05

**A musical instrument in MEMS**

J.B.C. Engelen, H. de Boer, J.G. Beekman, A.J. Been, G.A. Folkertsma, L. Fortgens, D. de Graaf, S. Vocke, L.A. Woldering and L. Abelmann

Transducer Science and Technology, MESA+ Institute for Nanotechnology, University of Twente, Enschede, the Netherlands

C06

**Microfluidic chip development for an autonomous field deployable water quality analyser**

D. Maher<sup>1</sup>, J. Healy<sup>1</sup>, J. Cleary<sup>1</sup>, G. Carroll<sup>2</sup> and D. Diamond<sup>1</sup>

<sup>1</sup>CLARITY: Centre for Web Sensing Technologies, Dublin City University, Ireland

<sup>2</sup>EpiSensor Ltd., Ireland

C07

**A novel multisite silicon probe for laminar neural recordings with improved electrode impedance**

A. Pongrácz<sup>1</sup>, G. Márton<sup>1</sup>, L. Grand<sup>2,3</sup>, É. Vázsonyi<sup>1</sup>, I. Ulbert<sup>2,3</sup>, G. Karmos<sup>2,3</sup>, S. Wiebe<sup>4</sup> and G. Battistig<sup>1</sup>

<sup>1</sup>Research Institute for Technical Physics and Materials Science, Hungarian Academy of Sciences, Hungary <sup>2</sup>Peter Pazmany Catholic University, Faculty of Information Technology, Hungary <sup>3</sup>Institute for Psychology of the Hungarian Academy of Sciences, Hungary <sup>4</sup>Plexon Inc., USA

C08

**Large deflection actuator for variable-ratio RF MEMS power divider application**

Y. Li<sup>1</sup>, S. Kühne<sup>1</sup>, D. Psychogiou<sup>2</sup>, J. Hesselbarth<sup>2</sup> and C. Hierold<sup>1</sup>

<sup>1</sup>Micro- and Nanosystems, Department of Mechanical and Process Engineering, ETH Zurich, Switzerland <sup>2</sup>Laboratory for Electromagnetic Fields and Microwave Electronics, Department of Information Technology and Electrical Engineering, ETH Zurich, Switzerland

C09

**PVDF micro heat exchanger manufactured by ultrasonic hot embossing and welding**

K. Burlage, C. Gerhardy and W.K. Schomburg

RWTH Aachen University, Konstruktion und Entwicklung von Mikrosystemen (KEmikro), Germany

C11

**A comb based in-plane SiGe capacitive accelerometer for above-IC integration**

L. Wen<sup>1</sup>, K. Wouters<sup>1</sup>, L. Haspeslagh<sup>2</sup>, A. Witvrouw<sup>2</sup> and R. Puers<sup>1</sup>

<sup>1</sup>ESAT-MICAS, Katholieke Universiteit Leuven, Belgium <sup>2</sup>IMEC, Belgium

C12

**Surface-micromachined gas sensor using thermopiles for carbon dioxide detection**

S. Chen, H. Wu, G. de Graaf and R. F. Wolffenbuttel

Delft University of Technology, Faculty of EEMCS, Department of ME/EI, the Netherlands

C13

**Subwavelength nanopylamids for surface enhanced Raman scattering**

M. Jin<sup>1</sup>, V. Pully<sup>2</sup>, C. Otto<sup>2</sup>, A. van den Berg<sup>1</sup> and E.T. Carlen<sup>1</sup>

<sup>1</sup>BIOS/Lab-on-a-Chip Group, <sup>2</sup>Medical Cell Biophysics Group <sup>1,2</sup>MESA+ Institute for Nanotechnology, <sup>2</sup>MIRA Institute for Biomedical Technology and Technical Medicine, University of Twente, the Netherlands

C14

**A microneedle-based miniature syringe for transdermal drug delivery**

C. O'Mahony, J. Scully, A. Blake and J. O'Brien

Tyndall National Institute, University College Cork, Ireland

C15

**On the processing aspects of high performance hybrid backside illuminated CMOS imagers**

J. De Vos, K. De Munck, K. Minoglou, P. Ramachandra Rao, M.A. Erismis, P. De Moor and D.S. Tezcan

IMEC, Belgium

C16

**Fabrication and characterization of carbon nanotube composites for strain sensor applications**

F. Ceyssens<sup>1</sup>, M. De Volder<sup>2</sup>, G. Keulemans<sup>1</sup>, J.W. Seo<sup>3</sup> and R. Puers<sup>1</sup>

<sup>1</sup>KULeuven, dept. ESAT-MICAS, Belgium. <sup>2</sup>KULeuven, dept. Mech. 2Eng, Belgium <sup>3</sup>KULeuven, dept. MTM, Belgium

C17

**Fluidic variable inductor using SU8 channel**

I. El Gmati<sup>1,3</sup>, P. Calmon<sup>1,2</sup>, R. Fulcran<sup>1</sup>, S. Pinon<sup>1</sup>, A. Boukabache<sup>1,2</sup>, P. Pons<sup>1,2</sup> and A. Kallala<sup>3</sup>

<sup>1</sup>LAAS-CNRS, France <sup>2</sup>Université de Toulouse, UPS, INSA, INP, ISAE, LAAS, France <sup>3</sup>Laboratoire instrumentations Monastir, Tunisie

C18

**Low-cost bevel-shaped sharp tipped hollow polymer-based microneedles for transdermal drug delivery**

B.P. Chaudhri<sup>1,2</sup>, F. Ceyssens<sup>1</sup>, P. De Moor<sup>2</sup>, C. Van Hoof<sup>1,2</sup> and R. Puers<sup>1,2</sup>

<sup>1</sup>ESAT, Department of Electrical Engineering, Katholieke Universiteit Leuven, Belgium <sup>2</sup>IMEC, Belgium

C19

**Non-invasive dry electrodes for EEG**

M.F. Silva, N.S. Dias, A.F. Silva, J.F. Ribeiro, L.M. Gonçalves, J.P. Carmo, P.M. Mendes and J.H. Correia

University of Minho, Dept. Industrial Electronics, Portugal

Session D  
(Tuesday 14:45 – 17:15)

D01

**Application of silicon micro-needles in liquid-based sensors and vapor transport**

Z. Sanaee and S. Mohajerzadeh

University of Tehran, School of Electrical and Computer Eng, Nano-electronic Center of Excellence, Thin Film and Nano-Electronic Lab, Iran

D02

**Metallic layer for em pressure sensor sensitivity improvement**

S. Bouaziz<sup>1,2</sup>, M. Mehdi Jatlaoui<sup>1</sup>, D. Mingli<sup>1</sup>, P. Pons<sup>1</sup> and H. Aubert<sup>1,2</sup>

<sup>1</sup>CNRS, LAAS, Toulouse, France <sup>2</sup>Université de Toulouse, INP, LAAS, France

D03

**Microfabrication and caracterization of thin-films solid-state rechargeable lithium battery**

J.F. Ribeiro<sup>1</sup>, M.F. Silva<sup>1</sup>, L.M. Gonçalves<sup>1</sup>, M.M. Silva<sup>2</sup> and J.H. Correia<sup>1</sup>

<sup>1</sup>University of Minho, Algoritmi Centre, Portugal <sup>2</sup>University of Minho, Chemistry Centre, Portugal

D04

**Determination of young's modulus of PZT- influence of cantilever orientation**

H. Nazeer<sup>1</sup>, L.A. Woldering<sup>1</sup>, L. Abelman<sup>1</sup> and M.C. Elwenspoek<sup>1,2</sup>

<sup>1</sup>MESA+ institute for nanotechnology, University of Twente, the Netherlands

<sup>2</sup>Freiburg institute for Advanced Studies, Albert-Ludwigs-Universitat Freiburg, Germany

D05

**Tungsten-siliconnitride medium for mega- to gigayear data storage**

J. de Vries<sup>1</sup>, L. Abelman<sup>1</sup>, A. Manz<sup>2</sup> and M. Elwenspoek<sup>1,2</sup>

<sup>1</sup>MESA+ institute for nanotechnology, University of Twente, the Netherlands

<sup>2</sup>Freiburg institute for Advanced Studies, Albert-Ludwigs-Universitat Freiburg, Germany

D06

**Controlled increase and stabilisation of the tuning range of RF-MEMS capacitors with an active lid electrode**

J. Love<sup>1</sup>, M. Hill<sup>1</sup> and C. O'Mahony<sup>2</sup>

<sup>1</sup>Adaptive Wireless Systems Group, Cork Institute of Technology, Ireland <sup>2</sup>Tyndall National Institute, University College Cork, Ireland

D07

**Two-degree-of-freedom capacitive MEMS velocity sensor: initial test measurements**

A. Alshehri<sup>1</sup>, M. Kraft<sup>1</sup> and P. Gardonio<sup>2</sup>

<sup>1</sup>EDS, University of Southampton, UK <sup>2</sup>DIEGM, Università degli Studi di Udine, Italy

D08

**Computational analysis of microparticle separation in straight channels**

H. Kizil<sup>1</sup>, L. Trabzon<sup>2</sup>, L. Yobas<sup>3</sup>, M. Yilmaz<sup>1</sup> and A. Ozbey<sup>2</sup>

<sup>1</sup>Department of Materials and Metallurgical Engineering, Istanbul Technical University, Turkey <sup>2</sup>Department of Mechanical Engineering, Istanbul Technical University, Turkey <sup>3</sup>Department of Electronic and Computer Engineering, Hong Kong University of Science and Technology, Hong Kong

D09

**Fabrication of cantilever arrays with tips for parallel optical readout**

W.W. Koelmans<sup>1</sup>, T. Peters<sup>1</sup>, L. Abelman<sup>1</sup> and M.C. Elwenspoek<sup>1,2</sup>

<sup>1</sup>MESA+ and IMPACT Research Institutes, University of Twente, the Netherlands

<sup>2</sup>Freiburg institute for Advanced Studies, Albert-Ludwigs-Universitat Freiburg, Germany

D10

**Morphological characterisation of micromachined film bulk acoustic resonator structures manufactured on GaN/Si**

A. Cismaru<sup>1</sup>, A. Stavrinidis<sup>2</sup>, A. Stefanescu<sup>1</sup>, D. Neculoiu<sup>1</sup>, G. Konstantinidis<sup>2</sup> and A. Müller<sup>1</sup>

<sup>1</sup>IMT-Bucharest, Romania <sup>2</sup>FORTH-IESL-MRG Heraklion, Greece

D11

**Static crack growth and fatigue modeling for silicon MEMS**

W.M. van Spengen

TU Delft, 3mE-PME, the Netherlands

D12

**Development of a novel micromirror with high static rotation angle for measurement applications**

S. Weinberger, O. Jakovlev, C.H. Winkelmann, E. Markweg and M. Hoffmann

Ilmenau University of Technology, IMN MacroNano, Department of Micromechanical Systems, Germany

D13

**Applications of all-(111) surface silicon nanowires**

M. N. Masood, S. Chen, E. T. Carlen and A. van den Berg

BIOS Lab on a Chip, MESA+ Institute for Nanotechnology, University of Twente, the Netherlands

D14

**A micromirror for optical projection displays**

R.A. Brookhuis<sup>1</sup>, M.J. de Boer<sup>1</sup>, M. Dijkstra<sup>1</sup>, A.A. Kuijpers<sup>2</sup>, D. van Lierop<sup>2</sup> and R.J. Wiegerink<sup>1</sup>

<sup>1</sup>MESA+ institute for nanotechnology, University of Twente, the Netherlands

<sup>2</sup>Philips Applied Technologies, Eindhoven, the Netherlands



D15

**Frequency shift of MEMS electromechanical resonators induced by process variation**

F. Casset<sup>1</sup>, J. Arcamone<sup>1</sup>, A. Niel<sup>1</sup>, E. Lorent<sup>1</sup>, Y. Civet<sup>1</sup>, E. Ollier<sup>3</sup>, P. Renaux<sup>1</sup>, P. Ancey<sup>1</sup> and P. Robert<sup>1</sup>

<sup>1</sup>CEA, LETI, MINATEC, France <sup>2</sup>STMicroelectronics, France <sup>3</sup>TIMA, CNRS, Grenoble INP, France

D16

**Wet etching optimization for arbitrarily shaped planar electrode structures**

H. Rattanasonti<sup>1</sup>, R.C. Sterling<sup>2</sup>, P. Srinivasan<sup>1</sup>, W.K. Hensinger<sup>2</sup> and M. Kraft<sup>1</sup>

<sup>1</sup>School of Electronics and Computer Science, University of Southampton, UK

<sup>2</sup>Department of Physics and Astronomy, University of Sussex, UK

D17

**Thermal behaviour of three dimensional single crystalline force sensors**

G. Battistig<sup>1</sup>, T. Weidisch<sup>2</sup>, T. Retkes<sup>2</sup>, M. Ádám<sup>1</sup>, I. Bársony<sup>1</sup> and T. Mohácsy<sup>1</sup>

<sup>1</sup>Research Institute for Technical Physics and Materials Science - MFA, Hungarian Academy of Sciences, Hungary <sup>2</sup>Department of Electron Devices of the Budapest University of Technology and Economics, Hungary

D18

**Incorporation of in-plane electrical interconnects to the reflow bonding**

B. Mogulkoc<sup>1</sup>, H.V. Jansen<sup>1</sup>, H.J.M. ter Brake<sup>1</sup> and M.C. Elwenspoek<sup>1,2</sup>

<sup>1</sup>MESA+ and IMPACT Research Institutes, University of Twente, the Netherlands

<sup>2</sup>Freiburg institute for Advanced Studies, Albert-Ludwigs-Universitat Freiburg, Germany

D19

**Piezoelectric power harvesting device with multiple resonant frequencies**

Z. Chew and L. Li

Swansea University, School of Engineering, UK

D20

**Reliability modelling of MEMS cantilever switches under variable actuation stress levels**

P. Fitzgerald<sup>1</sup> and M. Hill<sup>2</sup>

<sup>1</sup>Cork Institute of Technology, Ireland and Analog Devices <sup>2</sup>Cork Institute of Technology, Cork, Ireland



## UNDERSTANDING AND MITIGATING NANOSCALE WEAR

Mark Lantz

*IBM Research Division, Zurich Research Laboratory, Switzerland*

Tip endurance requirements in emerging probe technologies, such as probe based data storage and lithography, are extremely demanding and have been viewed as one of the major roadblocks for the development of such technologies. In this contribution, this issue is introduced with a discussion of tip wear endurance requirements for a probe based data storage device. Following this, recent experiments to quantify wear of nm-scale sharp silicon tips sliding in contact with a polymer surface with sliding distances up to 1000m are presented [1]. This interface is technically relevant for scanned-probe storage and scanned-probe lithography. The observed deviations from Archard's wear law can be explained using a new analytic model that captures the crucial aspects of wear physics in a quantitative way. The data and model predict that the wear rates found for sliding silicon tips are prohibitively large.

In the second part of this contribution, strategies for overcoming the wear problem are presented. First the use of alternative tip materials is investigated, namely: monolithic silicon containing diamond like carbon tips (Si-DLC) [2] and silicon carbide (SiC) terminated silicon tips (see figure 1). Wear tests showing 4-5 order of magnitude improvement in tip life time relative to silicon tips will be presented. Both of these techniques

appear very promising for reducing tip wear, but do not address the reciprocal problem of sample wear. Previously, it has been shown that friction can be controlled by high frequency modulation of the tip-surface force. We have investigated the impact of this technique on tip-wear and media-wear of sliding tips on polymer surfaces [3]. We have demonstrated sliding distances of more than 700m without detectable tip-wear for a sharp tip using high frequency modulation. Force modulation appears to be a viable solution for meeting the challenging lifetime requirements to enable scanning probe lithography and data storage. Moreover, the technique can potentially be used with Si-DLC or SiC tips to further enhance tip robustness.

### References

- [1] B. Gotsmann, M. A. Lantz, Phys. Rev. Lett. 101, 125501, (2008).
- [2] H. Bhaskaran et al., Nature Nanotechnology, Published Online 31 Jan
- [3] M. A. Lantz et al., Nature Nanotechnology 4, 586 - 591 (2009)

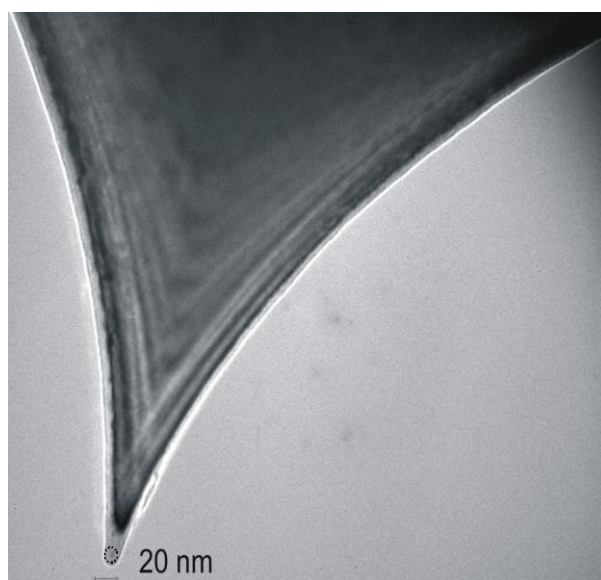
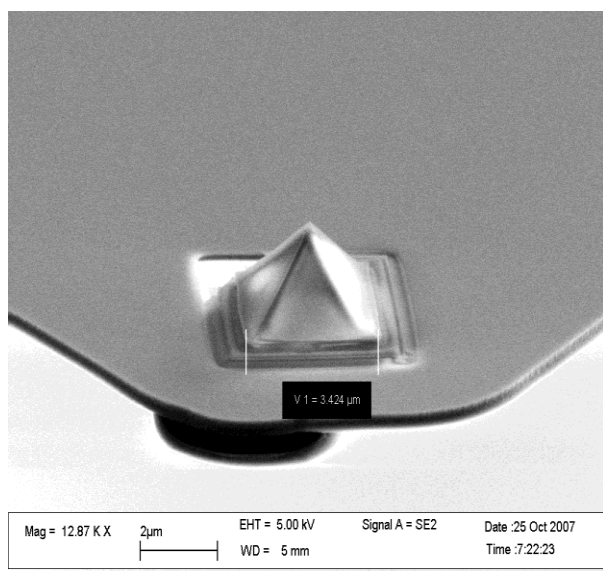


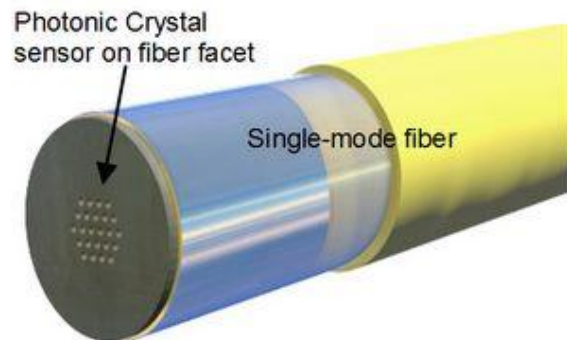
Figure 1. Left panel: monolithic tip made from silicon containing diamond-like carbon (Si-DLC) using a molding process. Right panel: Silicon carbide terminated silicon tip fabricated using carbon implantation into a silicon tip followed by annealing

## OPTICAL SENSORS AND ACTUATORS ENABLED BY PHOTONIC CRYSTALS

Olav Solgaard

*Stanford University, CA, E.L. Ginzton Laboratory, USA*

Photonic Crystals allow miniaturization of free space optics and enable new device concepts, new system architectures, and new applications of Optical Microsystems. In this talk we describe the basics of optical filtering and sensing in two-dimensional photonic crystals, and show how these structures can be combined with MicroElectroMechanical Systems (MEMS) to create miniaturized, low-cost platforms for optical integration and packaging. Practical device designs, including fiber-optic sensors and optical scanners for high-temperature operation, will be presented.



## DNA NANOARCHITECTURES AND MECHANICAL DEVICES

Kurt V. Gothelf

*Centre for DNA Nanotechnology (CDNA); iNANO and Department of Chemistry; Aarhus University  
8000 Århus C, Denmark, [kvg@chem.au.dk](mailto:kvg@chem.au.dk)*

The idea behind our research is to use DNA as a programmable tool for directing the self-assembly of molecules and materials. The unique specificity of DNA interactions, our ability to code specific DNA sequences and to chemically functionalize DNA, makes it the ideal material for controlling self-assembly of components attached to DNA sequences. We have developed some new approaches in this area such as the use of DNA for self-assembly of organic molecules,<sup>1-2</sup> and for electrochemical sensors.<sup>3</sup>

The DNA origami method was first reported by Rothemund in 2006,<sup>4</sup> and in its relatively short lifetime several reports have demonstrated that it is an excellent tool to program self-assembly of DNA nanostructures. For the design of DNA origami we have recently developed a software package that semi-automates the design process allowing the user to focus on optimization and modification of the design.<sup>5</sup> DNA origami provides a unique platform for the assembly of other materials, since the >200 staple strands used to assemble the M13mp18 genome can, in principle, be extended and each may provide a unique recognition sequence at the surface of origami structures. In this presentation it is demonstrated how DNA origami can be used to assemble organic molecules, study chemical reactions with single molecule resolution,<sup>7</sup> and position dendri-

mers and other materials. After initial 2D designs we made a 3D DNA origami box which was characterized by AFM, Cryo-EM, SAXS. The box also worked as a nanomechanical device with a lid that could be controlled and the lid motion was monitored by FRET.<sup>6</sup>

Recently, we have designed a new type of DNA actuator that has a sliding gauge type of motion. It can be positioned in 11 discrete positions and be shifted between the positions. The motion was followed by FRET and by performing chemical reactions that are only geometrically possible in certain states of the actuator.

### References

- [1] Andersen, C. S.; Yan, H.; Gothelf, K. V. *Angew. Chem. Int. Ed.* 2008, **47**, 5569-5572.
- [2] Hansen, M. H. *et al. J. Am. Chem. Soc.* 2009, **131**, 1322-1327.
- [3] Ferapontova, E. E.; Olsen, E. M.; Gothelf, K. V. *J. Am. Chem. Soc.* 2008, **130**, 4256-4258
- [4] Rothemund, P. W. K. *Nature* 2006, **440**, 297.
- [5] Andersen, E. S. *et al. ACS Nano*, 2008, **2**, 1213.
- [6] Voigt, N. V. *et al. Nature Nanotech.* 2010, **5**, 200.
- [7] Andersen, E. S. *et al. Nature* 2009, **459**, 73.



# SILICON CARBIDE THIN-FILM ENCAPSULATION OF PLANAR THERMOELECTRIC INFRARED (IR) DETECTORS – FOR AN IR MICROSPECTROMETER

V. Rajaraman, G. de Graaf, P.J. French, K.A.A. Makinwa, and R.F. Wolffenbuttel

*Delft University of Technology (TU Delft), Dept. of Microelectronics, EI Lab - DIMES, Delft, Netherlands*  
e-mail: v.rajaraman@tudelft.nl, ger.degraaf@tudelft.nl, r.f.wolffenbuttel@tudelft.nl

**Abstract** – In this paper we present the first results of silicon carbide encapsulation technology that has been applied for low pressure encapsulation of planar infrared thermoelectric detector arrays, and thermal conductivity based sensors. The optical property of the silicon carbide encapsulation material, in the wavelength range of 300nm-1600nm, was performed using a variable angle spectroscopic ellipsometer and the results are reported. The optimised microfabrication scheme involving high topography processing is presented together with preliminary results. The reported microencapsulation technology has wide application in the packaging of MOEMS and MEMS devices, including an IR microspectrometer.

**Keywords:** Thin Film Encapsulation, Packaging, Silicon Carbide, Thermoelectric (TE) Detector, Thermopile, Thermal Vacuum Sensor, Infrared (IR) Detector, Microspectrometer, Surface Micromachining

## I – INTRODUCTION

CMOS-compatible microfabrication of thermoelectric (TE) infrared (IR) detectors enables realisation of cost-effective on-chip integration of the sensing elements together with readout circuitry to form an integrated IR microspectrometer. Such devices have a wide selection of applications in different fields ranging from the industry, science and agriculture to biology [1]. Benefits of CMOS-compatible implementation include – smaller weight and size, shorter response time, measurement of smaller sample volumes, and integrated on-chip signal conditioning circuitry [1]. The above arguments are equally valid, where appropriate, for other types of IR detectors and thermal sensors like MEMS-based uncooled IR bolometer arrays that have applications in low cost imaging systems [2], and thermal conductivity-based sensors that are applied in vacuum (pressure) monitoring, process control and gas chromatography [3].

However, the performance of TE IR detectors degrades due to thermal loss mechanisms in air [2, 4] such as convective losses resulting from the thermal conduction of air, substrate (heat sink) leakage and thermal cross-talk between the neighbouring successive sensing elements. Hence, operating these devices in vacuum is a practical solution to improve the device performance. In this paper, an enabling CMOS-compatible encapsulation technology using PECVD Silicon Carbide [5] is intro-

duced for low pressure encapsulation of IR TE detectors, realised by surface micromachining. Further, other devices fabricated using the same surface micromachined process such as thermal conductivity vacuum sensors can also benefit from the vacuum encapsulation. Besides, when left unsealed, the thin-film encapsulation serves as a microdiffusion chamber for thermal conductivity based gas sensors for reducing the effects of gas convection and hence improves device sensitivity [3].

## II – SiC $\mu$ -PACKAGING OF IR DETECTORS

Packaging of MEMS devices provides various benefits such as good mechanical protection, stable and controlled gas environment, hermetic cavity, protection against contamination and harsh environments, etc. [5]. Besides, for some MEMS-based optical sensors the package must also provide good transmission in the wavelength range of interest. In the case of MEMS based TE IR detectors, thermal conductivity based sensors and uncooled bolometers, vacuum packaging is an important requirement for obtaining best device performance [2, 4]. The three fundamental thermal loss mechanisms occurring in thermal sensors, and hence TE IR detectors, are conduction, convection and radiation losses. While at low temperatures, the radiation effects become negligible, the other two effects cannot be ignored. Gas conductivity and hence the thermal conductivity of air is a pressure dependent parameter which becomes negligible at pressures below 1 mbar. For a TE IR detector, at higher pressure levels, the thermal conductance of air,  $G_{air}$ , could be approximated as follows:

$$G_{air} \propto \frac{k_{air} \cdot A}{f(d_{sub}, d_{pitch})} \quad (1)$$

where,  $k_{air}$  is thermal conductivity of air,  $A$  is the area of IR TE detector,  $d_{sub}$  is the gap between the TE detector to the substrate and  $d_{pitch}$  is the inter-TE detector gap. Therefore, the thermal conductance of air  $G_{air}$  due to  $d_{sub}$  and  $d_{pitch}$  act in parallel and could be modelled as such electrically. Thus the gaseous thermal conduction depends on the gaps located between successive neighbouring IR TE detector elements (pitch) and the gap between the TE detector elements and the substrate (sink).

Recently, the need for vacuum packaging of a CMOS-compatible surface micromachined planar IR microspectrometer was emphasised due to design-

associated thermal cross-talk when operated in air [4]. Here, it was shown through simulations that the initial 10% cross-talk, measured at atmospheric pressure and room temperature, dropped to a negligible 0.4% when operated in a low pressure (vacuum) environment of around 1 mbar. Silicon carbide was chosen in this work as the encapsulation material of choice as it provides good mechanical stability, harsh environment capability, low pressure sealing that is allowed by the process pressure of around 1 mbar, and most importantly due to its suitable optical properties for IR sensing that is reported in the literature [6].

### III – FABRICATION

The fabrication of the IR TE detector arrays [4] and the thin film encapsulation layer was done at the DIMES Technology Centre of TU Delft. A simplified resultant device cross-section of an IR TE detector fabricated on a silicon wafer is depicted in *Figure 1a*. The device consisted of polysilicon thermopile arrays built on top of a thermally isolating LPCVD SiN mechanical support layer in the form of a bridge. An array of 26 TE elements on a bridge structure of  $650\mu\text{m} \times 36\mu\text{m}$  has been fabricated [4]. The designed pitch between two successive bridges was  $10\mu\text{m}$ . The bridge is located on top of a densified PECVD TEOS first sacrificial layer. An IR absorber stack made of poly-Si and SiN layers was also included to improve the IR absorbance in the  $1.5\mu\text{m}$ - $5\mu\text{m}$  wavelength range.

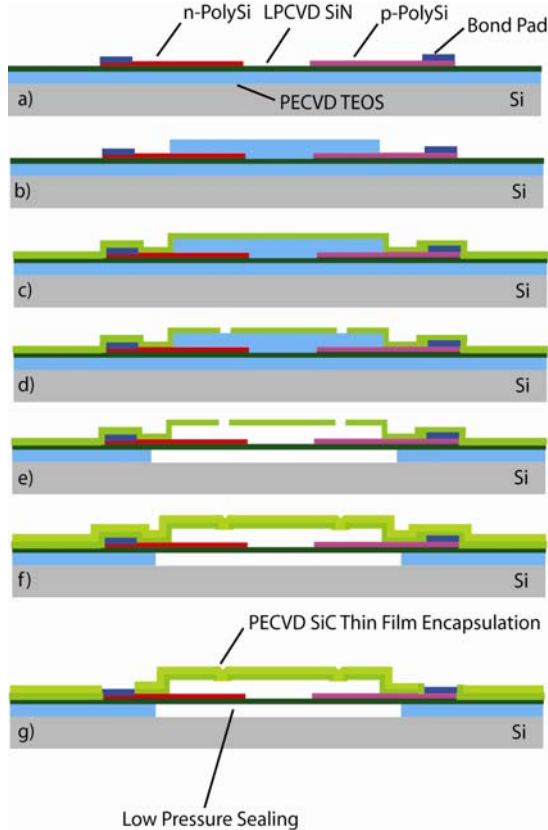


*Figure 1:* Fabrication scheme for thin film encapsulated IR TE detectors and thermal sensors for an IR microspectrometer.

The fabrication scheme for achieving silicon carbide encapsulation of the above device is presented in *Figure 1*. The fabrication required high topography processing that has been optimized. *Table 1* summarizes the various thicknesses of the functional layers used in the high topography fabrication process for manufacturing thin film encapsulated IR TE detectors.

*Table 1:* Different functional layers used in the high topography microfabrication of thin film encapsulated IR TE detectors

Functional Layers/Materials	Thickness
PECVD TEOS 1 <sup>st</sup> and 2 <sup>nd</sup> Sacrificial Layers (nm)	4000
SiN Bridge for Thermal Isolation and Mechanical Support (nm)	700
n- & p- type Poly-Si Thermopiles (nm)	300
Al (1% Si) Metal (nm)	675
PECVD SiC Encapsulation (nm)	3000
PECVD SiC Encapsulation (nm)	3000
Silicon Substrate ( $\mu\text{m}$ )	525

After device fabrication mentioned above, the encapsulation process started with the deposition and lithographic patterning of a PECVD TEOS second sacrificial layer on top of the poly-Si TE detector arrays, as shown in *Figure 1b*. Now a stress optimized encapsulation layer of PECVD silicon carbide is deposited on top of the second sacrificial layer with good step coverage, see *Figure 1c*. Then the etch holes are carefully patterned and RI etched on the silicon carbide encapsulation layer, refer *Figure 1d*. Later, these etch holes are used for removing the first and second sacrificial TEOS layers. The sacrificial etching is done using 73% HF as it offers the highest selectivity between the oxide etching and the aluminium metallisation [5]. For releasing the devices located on the SiN bridge, an etch time of about 22 minutes was sufficient. In order to avoid stiction of the suspended bridge to either the substrate at the bottom or the encapsulation at the top, sublimation drying was performed using Cyclohexane. Then the encapsulation is sealed with another layer of silicon carbide at low pressure, *Figure 1f*. In our case, the sealing pressure was determined by the process chamber pressure that was about 1 mbar. Finally the bond pads are opened for performing electrical measurements, as shown in *Figure 1g*, completing the fabrication.

### IV – RESULTS AND DISCUSSION

PECVD SiC has been used as the encapsulation material of choice due to its harsh environment capability that allowed it to survive the 73% HF etching without disintegration or peeling-off and also due to its preferred optical property. For verification, an experimental evaluation of the optical quality of the deposited PECVD SiC layer was performed by determining the refractive index ( $n$ ) and extinction coefficient ( $k$ ) using a variable angle spectroscopic ellipsometer. The measured spectral range was between 300nm - 1600nm at two

different angles of incidence,  $65^\circ$  and  $75^\circ$ . The ellipsometric data was analysed using the optical models of silicon carbide and silicon from the standard material library. Later the thickness of PECVD SiC and  $n$  were determined using the Cauchy dispersive model. The results of optical property measurements are presented in Figure 2. The  $n$  and  $k$  values ranged between 2.35-2.8 and 2-2.5, respectively.

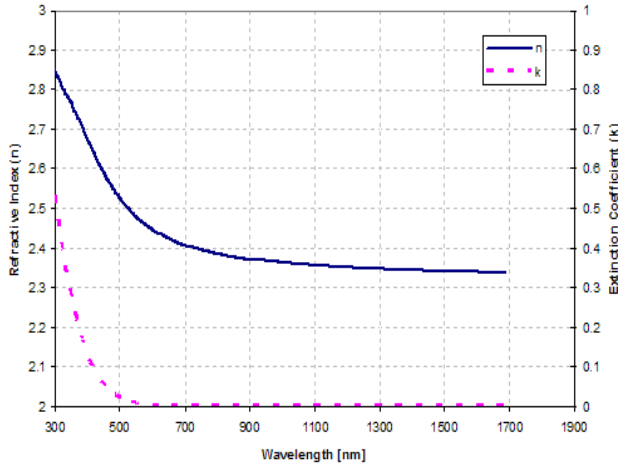


Figure 2: Measured spectral dependence of refractive index and extinction coefficient of PECVD SiC encapsulation layer

Figure 3 shows various microfabricated square and rectangular shaped infrared IR thermoelectric detectors that were considered for silicon carbide thin film encapsulation. The sizes of those devices ranged from about  $900\mu\text{m} \times 100\mu\text{m}$  to  $1250\mu\text{m} \times 650\mu\text{m}$ . Among these some thermal conductivity based gas sensors were also included.

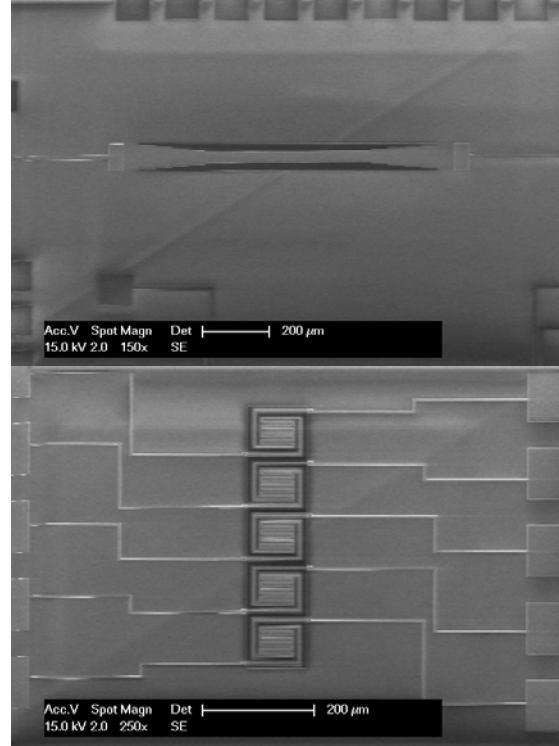
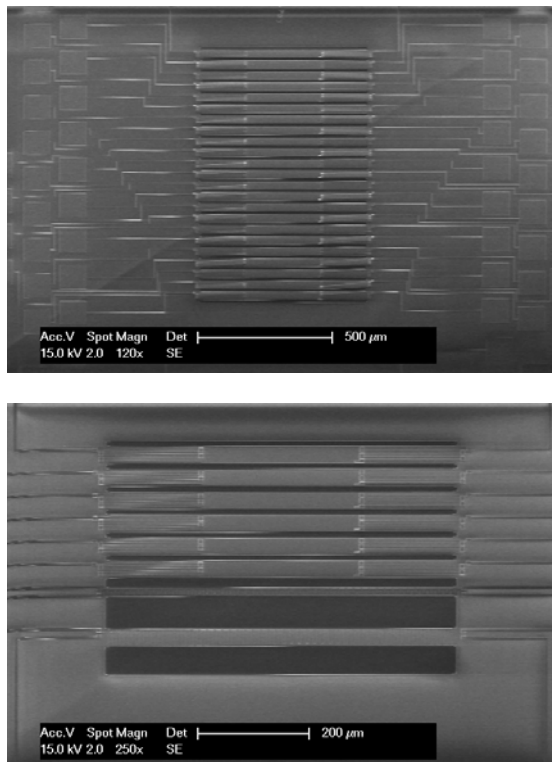


Figure 3: SEM images of four different TE detectors for IR and thermal conductivity measurement before their encapsulation

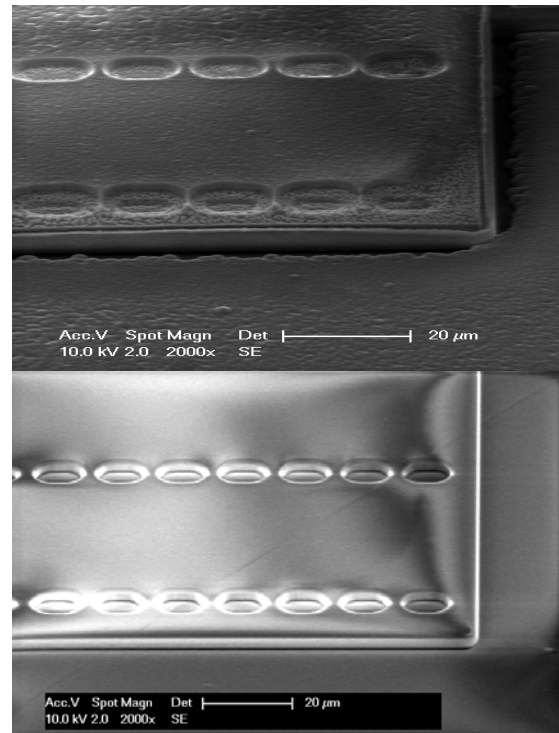


Figure 4: SEM images showing the high topography encapsulation process and release holes etching. The top image shows a failed process while the bottom image shows a successful encapsulation obtained by process optimization.

It could be observed that these devices include slits in the SiN support layer that is situated on top of the first sacrificial PECVD TEOS layer that is  $4\mu\text{m}$  thick. Later



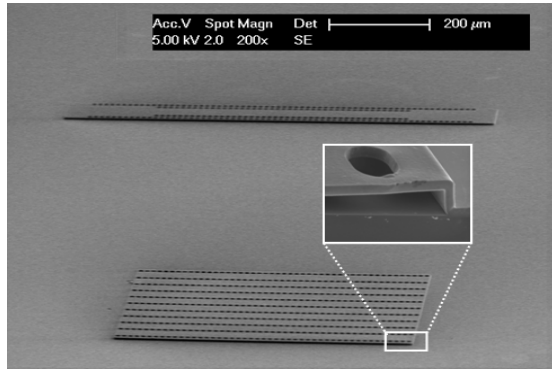


Figure 5: SEM image of fully released encapsulation structures, the inset shows a close-up cross-sectional view.

a second 4μm thick sacrificial PECVD TEOS layer is deposited, which introduces some notable topography requiring thick resist processing. This topography is further increased when the second sacrificial layer of PECVD TEOS is deposited. Now a 3μm thick stress optimized PECVD silicon carbide encapsulation layer is applied over the second sacrificial layer and release holes are RIE patterned on this high topography structure. A number of issues were confronted during micro-fabrication such as the one shown in Figure 4 which required conformal spray coated resist processing.

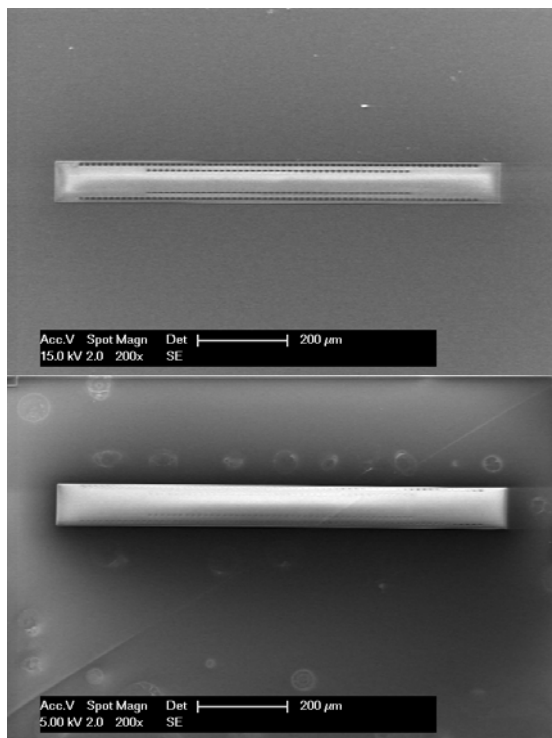


Figure 6: SEM images show a thin film encapsulated device. The top image shows a released encapsulation layer, while the bottom image shows a sealed device.

Figure 5 shows fully released encapsulation layers of two different sizes (devices), done by wet HF etching without any stiction problems. Figure 6 shows an encapsulated device before sealing layer deposition and after sealing layer deposition. The sealing was performed inside the PECVD process chamber that trans-

lates to a pressure of about 1.33 mbar at atmospheric environment. Currently, this process is being developed further and the vacuum level inside the encapsulation is being investigated using the thermal cross-talk performance of the encapsulated IR TE detectors and some thermal conductivity based vacuum sensors. Thus this technology enables the realization of a true IR microspectrometer. Furthermore, in the case of thermal conductivity based gas sensors [3], the encapsulation can be left unsealed (Figure 1e) to form a diffusion microchamber (microcage) that shall stabilise the gas flow over the sensing area avoiding gas turbulence, thereby reducing effects of gas convection and improving the device sensitivity [3].

#### IV – CONCLUSIONS

A CMOS-compatible technology for encapsulation of IR thermoelectric devices that is compatible with device microfabrication was presented. This technology has been realized using PECVD silicon carbide encapsulation, whose optical properties have been measured,  $n = 2.35\text{--}2.8$  and  $k = 2\text{--}2.5$ , to be transparent for IR. In all, the demonstrated technology allows for device operation in a low pressure environment determined by the process during sealing. Currently, the process is being optimized further and the vacuum level is also being investigated and will be reported in the extended paper. Thus the reported silicon carbide microencapsulation technology enables realization of an IR microspectrometer and has wide application potential in the packaging of optical MEMS (MOEMS) devices and also traditional MEMS devices.

#### ACKNOWLEDGEMENTS

The authors, RFW and GdG, wish to thank the Dutch Technology Foundation (STW) for their support in this work, while the authors – VR, KAAAM & PJF, wish to thank NXP Semiconductors, Nijmegen, The Netherlands, for their support. Thanks also to the staff of DIMES (Delft Institute of Microsystems and Nanoelectronics) Technology Centre, TU Delft, for their technical support. Our special thanks are due to Mr. H. Wu for help with the mask layout and the interesting discussions, Mr. W. van der Vlist for device fabrication, Dr. G. Pandraud for help with ellipsometric data analysis, and Prof. Dr. P.M. Sarro for helpful discussions.

#### REFERENCES

- [1] R.F. Wolffenbuttel, MEMS-based optical mini- and microspectrometers for the visible and infrared spectral range, *J. Micro-mech. Microeng.*, 15, pp. S145-S152, 2005.
- [2] F. Niklaus *et al*, MEMS-based uncooled infrared bolometer arrays – a review, *Proc. SPIE*, Vol. 6836, 68360D, 2007.
- [3] G. de Graaf *et al*, Thermal analysis, fabrication and signal processing of surface micromachined thermal conductivity based gas sensors, *Proc. The 21<sup>st</sup> Micromechanics and Microsystems Europe Workshop (MME), The Netherlands*, 2010. (Submitted)
- [4] H. Wu *et al*, Thin film encapsulated 1D thermoelectric detector in an IR microspectrometer, *Proc. SPIE*, Vol. 7726, 772612, 2010.
- [5] V. Rajaraman *et al*, Robust wafer-level thin-film encapsulation of microstructures using low stress PECVD silicon carbide, *Proc. The 22<sup>nd</sup> IEEE Int. Conf. on Micro Electro Mechanical System (MEMS 2009)*, Sorrento, Italy, pp. 140-143, 2009.
- [6] G. Pandraud *et al*, PECVD SiC optical waveguide mode and loss characteristics, *Optics and Laser Technology*, 3 (39), pp. 532-536, 2007.

# DESIGN, FABRICATION AND CHARACTERIZATION OF AN IN-PLANE AFM PROBE WITH ULTRA-SHARP SILICON NITRIDE TIP

E. Sarajlic<sup>1</sup>, J. Geerlings<sup>2</sup>, J.W. Berenschot<sup>2</sup>, M.H. Siekman<sup>1,2</sup>, N.R. Tas<sup>2</sup> and L. Abelmann<sup>2</sup>

<sup>1</sup>*SmartTip, Enschede, The Netherlands*

<sup>2</sup>*MESA<sup>+</sup> Research Institute, University of Twente, PO Box 217, 7500 AE Enschede, The Netherlands*

**Abstract** — Scanning rates of the atomic force microscope (AFM) could be significantly increased by integrating the force sensing probe with microelectromechanical systems (MEMS). We present a micromachining method for batch fabrication of in-plane AFM probes that consist of an ultra-sharp silicon nitride tip on a single crystal silicon cantilever. Our fabrication method is fully compatible with the silicon-on-insulator (SOI) micromachining allowing a straightforward monolithic integration of the AFM probes with high-aspect-ratio monocrystalline silicon MEMS. Scanning probes with a sharp tip having diameter of less than 10 nm are successfully realized and tested in a commercial AFM set-up demonstrating feasibility and the large innovation potential of this method.

**Keywords:** Atomic Force Microscopy, Probes, KOH etching, Video-rate AFM

## I – Introduction

In atomic force microscopy (AFM) a strong drive exists towards video-rate imaging. In addition to convenience, the video rate AFM will enable observation of many real time dynamic processes that are currently impossible to study e.g. diffusion of individual atoms, atom clusters or molecules, film growth or catalytic reactions [1].

In a conventional AFM system the motion in the vertical z-direction is fastest and requires the highest frequency components. Therefore, the mechanical resonance frequencies of a cantilever force-sensor [2] and the driving piezoelectric element [3] are the main speed limiting factors in the conventional AFM systems. In order to obtain higher scanning rates, the external piezoelectric actuation can be substitute with a micromechanical actuator having an integrated force-sensing element [4]. Small dimensions and extremely small mass of the microactuators will improve vibration isolation and enable higher scanning rates.

In this paper we present a novel micromachining method for bulk fabrication of AFM probes with an ultra-sharp tip. This method, which is fully compatible with silicon-on-insulator (SOI) micromachining, allows for easy integration of the scanning probes with high-aspect-ratio monocrystalline silicon microactuators. Distinguishing characteristics of our process are as follows: (i) It allows fabrication of the AFM cantilevers with an in-plane tip (see Figure 1). In the

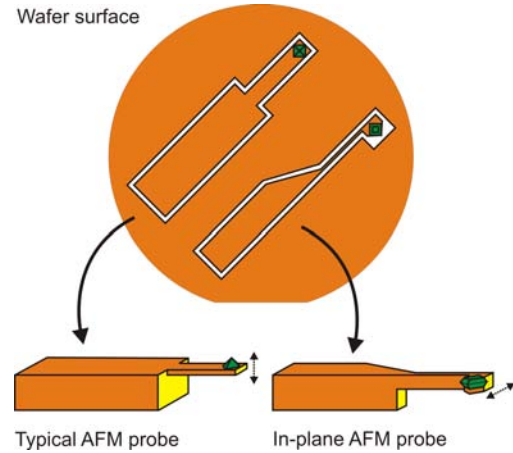


Figure 1: Typical AFM probe with out-of-plane tip and lateral cantilever with in-plane tip.

in-plane configuration, the oscillation direction of the cantilever is parallel to the wafer plane and coincides with the preferable motion direction of different electrostatic microactuators (e.g. parallel plate actuators or comb drives) allowing their straightforward integration. Furthermore, the resonance frequency of the in-plane cantilever probes can be more precisely controlled because both length and thickness are controlled by lithography. Therefore the resonance frequency is less dependent on the process parameters. (ii) The process results in a monocrystalline silicon cantilever. Superior mechanical properties of single crystal silicon such as practically no stress and low intrinsic damping [5] will lead to improved probe performance. (iii) An important innovative aspect of our method is the use of silicon moulds obtained by KOH etching to form in-plane silicon nitride tips. Silicon nitride, which is a wear resistant material will result in the improved life time of the probes. (iv) The in-plane tips are ultra-sharp allowing for high resolution imaging because the resolution of an AFM set-up is mainly determined by the tip sharpness of the probe.

Outline of this paper is as follows. In Section II we describe the basic steps of the microfabrication process and present two different methods for the fabrication of in-plane tips. In Section III we give details on the design of the first probe prototype. The fabrication results and experimental characterization of the probes is presented in Section IV. Conclusions are drawn in the last section.

## II – In-plane AFM probe

### A. Microfabrication process

The fabrication process, schematically shown in Figure 2, is based on an SOI wafer with a (100) top silicon layer.

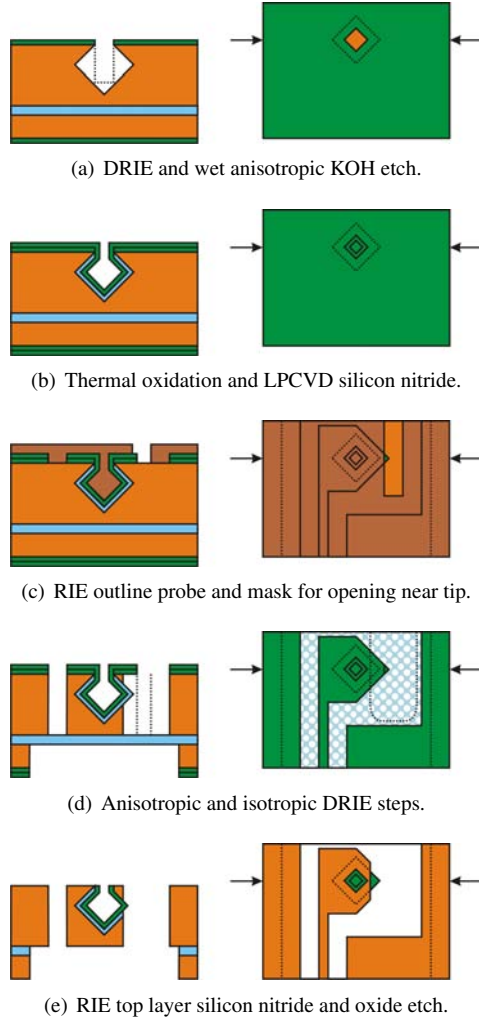


Figure 2: SOI compatible fabrication process of in-plane AFM probes.

In the top layer, a cavity is etched by combination of deep reactive ion etching (DRIE) and wet anisotropic etching in KOH (a). After etching of the cavity, thermal oxidation is performed followed by LPCVD deposition of silicon nitride (b). Next, the outline of the scanning probe is defined in the silicon nitride/silicon oxide stack by reactive ion etching (RIE). Subsequently, an opening near the probe tip is lithographically defined in a photoresist layer (c) and the tip is partially released by combination of anisotropic and isotropic dry silicon etching in a DRIE plasma system. After the tip release, the photoresist mask is removed and the probe layout is etched by DRIE using the silicon nitride/silicon oxide stack as the etching mask. Subsequently, a back etch is preformed (d). Next, the top silicon nitride layer is

removed by a blanket RIE step. Finally, the probe is released by etching of silicon oxide (e). The process results in a monocrystalline silicon scanning probe with an in-plane silicon nitride tip.

### B. Tip formation

In our process, the probe tip is formed by refilling a silicon mould with a silicon nitride layer. The sharpness of the probe tip is defined by the profile of the mould. In this paper, we devised and tested two innovative methods to obtain sharp in-plane tips.

In the first method, which is shown in Figure 3, an octahedron is used as a mould. The silicon octahedron is formed by directional plasma etching followed by wet anisotropic etching in aqueous KOH solution. The in-plane tip is formed in one of the corners of the octahedron, which are sharpened by thermal oxidation prior to silicon nitride deposition. This method results in a plane-symmetrical tip with four faces defined by  $\langle 111 \rangle$  crystallographic planes of the silicon octahedron. In order to obtain a single sharp tip a perfect symmetrical octahedron is required.

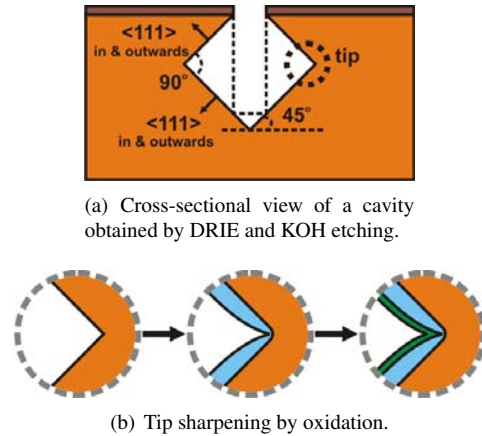


Figure 3: Four-face tip formation.

In the second method, illustrated in Figure 4, a pyramidal silicon mould is formed using an L-shaped mask opening. Silicon oxide is used as the masking layer. The tip formed in the top corner of the mould is bounded by two  $\langle 111 \rangle$  planes of the silicon pyramid and the top plane of silicon oxide. As the three planes always intersect in a single point, we expect that this design will result in an ultra-sharp tip.

## III – Design

To demonstrate the new fabrication method two different types of probes were designed. AFM probes with four-face nitride tips and probes with three-face nitride tips. The layout of silicon cantilever and holder block are the same for both type of probes.

When the tips are formed (as described in the previous section), the next step is the formation of the block

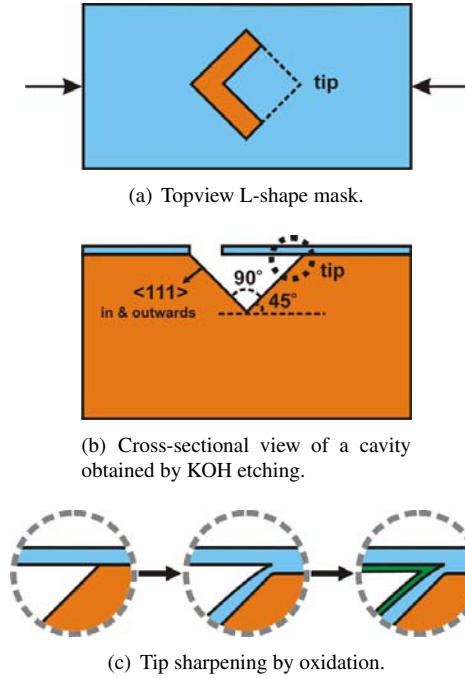


Figure 4: Three-face tip formation.

and cantilever that holds the tip (see right side of Figure 1). Because (100) wafers are used, the octahedron (after KOH) is aligned to the flat of the wafer. However, the tip of the octahedron must be perpendicular to the cantilever. Because oblique lines are difficult to obtain (as mask writers have a limited step resolution) the wafer must be rotated 45 degrees clockwise during the lithography steps needed to form the cantilever and holder block.

Initially the cantilever width is equal to the thickness of the wafer. To reduce the width of the cantilever, a backside etch step is applied. The depth of the backside etch therefore determines the width of the cantilever. When a SOI wafer is used, the oxide layer serves as etch stop layer. In this design a width of 40-50  $\mu\text{m}$  was aimed for. The thickness of the cantilever is chosen equal to the minimal accurate thickness that can be obtained, which is 3  $\mu\text{m}$  in this case. Length of the cantilever is calculated from the desired resonance frequency. For AFM tapping mode the resonance frequency must be between 100 and 300 kHz and for contact mode between 5 and 10 kHz. Table 1 summarizes the chosen cantilever dimensions and calculated approximate resonance frequencies. Definitions of the dimension variables are shown in Figure 5.

Because the resonance frequency does not depend on the width of the cantilever, the back etch step is not critical for the resonance frequency. The cantilever is connected to a block with length of 3000  $\mu\text{m}$ , thickness 450  $\mu\text{m}$  and width determined by the thickness of the wafer (380  $\mu\text{m}$  in this case). This block is necessary for handling the probe and placing it in the AFM machine.

Table 1: Probe dimensions and calculated resonance frequencies of the cantilever.

	Probe 01	Probe 02	Probe 03	Probe 04
<i>Cantilever</i>				
Length ( $L_C$ )	200 $\mu\text{m}$	300 $\mu\text{m}$	400 $\mu\text{m}$	500 $\mu\text{m}$
Thickness ( $T_C$ )	3 $\mu\text{m}$	3 $\mu\text{m}$	3 $\mu\text{m}$	3 $\mu\text{m}$
Width ( $W_C$ )	50 $\mu\text{m}$	50 $\mu\text{m}$	50 $\mu\text{m}$	50 $\mu\text{m}$
Resonance ( $f_0$ )	108 kHz	48 kHz	27 kHz	17 kHz
<i>Holder block</i>				
Length ( $L_B$ )	3000 $\mu\text{m}$	3000 $\mu\text{m}$	3000 $\mu\text{m}$	3000 $\mu\text{m}$
Thickness ( $T_B$ )	450 $\mu\text{m}$	450 $\mu\text{m}$	450 $\mu\text{m}$	450 $\mu\text{m}$
Width ( $W_B$ )	380 $\mu\text{m}$	380 $\mu\text{m}$	380 $\mu\text{m}$	380 $\mu\text{m}$

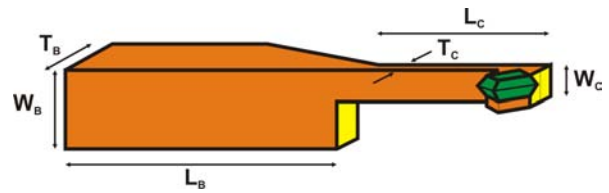


Figure 5: In-plane probe with definition of variables.

The holder block with cantilever is connected to the wafer by means of a breakout beam.

## IV – Results and Discussion

### A. Four-face tip design

Figure 6 shows SEM images of the fabricated in-plane AFM probe with four-face tip.

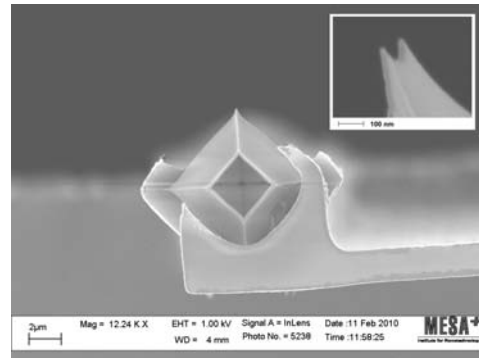


Figure 6: SEM pictures of the silicon nitride in-plane AFM tip (four-face) on a mono crystalline cantilever. Tip diameter (see inset) is 24 nm (left part of the double tip).

Clearly visible is the double tip in Figure 6 which indicates that during KOH etching a ridge was formed in the tip corner, instead of a single sharp tip. This invalidates the initial assumption that the four faces of the octahedron (which bound the tip) always intersect in one point, regardless of the shape of the starting cavity. The role of the starting cylinder on the final cavity was studied by KOH simulations in simulation program ACES [6].



Both graphical analysis and simulations of the octahedron formation showed that a misalignment between bottom plane and top plane of the starting cylinder causes the four planes not to intersect in one point. This is also the case when the bottom plane is not completely flat. Because DRIE etching is not perfectly uniform, a perfect cylinder can not be obtained. The four faces of the octahedron will therefore always lead to a ridge instead of a tip. This was practically confirmed during inspection of the fabricated tips in the SEM (shown in Figure 6).

### B. Three-face tip design

Because three non-parallel planes always intersect in one single point, this design will result in probes with single tips. In Figure 7 the fabrication results of the three-face tip design is shown. Ultra-sharp single tips were indeed observed during SEM inspection of the probes (see Figure 7).

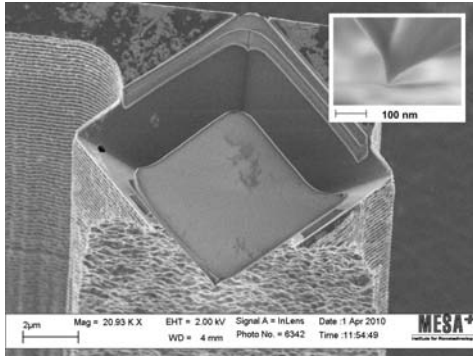


Figure 7: SEM pictures of the nitride in-plane AFM tip (three-face) on a mono crystalline cantilever. Tip diameter (see inset) is 9 nm.

On several cantilevers a reflection coating was deposited by evaporation. This coating consisted of a 5 nm Cr layer and a 15 nm Au layer. These probes were mounted in a Nanoscope Dimension 3100 [7] to obtain AFM images. An AFM image (in tapping mode) of a silicon wafer (with native oxide) is shown in Figure 8. A three-face probe was used for this image. Features less than 10 nm can be observed, indicating the tip sharpness.

### V – Conclusions

A new batch manufacturing process for in-plane AFM probes was presented. By using a silicon mould ultra-sharp durable nitride tips can be constructed on a monocrystalline silicon cantilever. This fabrication method was successfully demonstrated for two different probe designs. The design using an octahedron mould lead to a double tip, however, the design with a pyramidal mould (partially covered with oxide) lead to a single ultra-sharp tip. These probes were successfully mounted in a commercial AFM set-up. AFM images

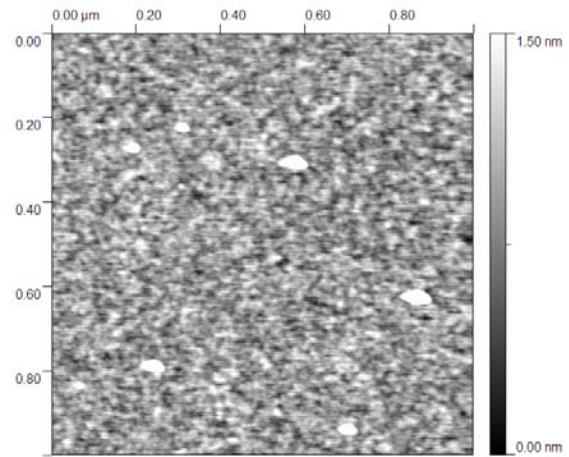


Figure 8: AFM image of a silicon wafer obtained with a three-face tip probe in tapping mode at 34 kHz.

with a resolution less than 10 nm were obtained. The fabrication method is fully SOI compatible which allows for easy integration of an (electrostatic) MEMS actuator. This enables a higher frequency in the z-direction and makes video-rate AFM feasible.

### VI – Acknowledgments

The authors would like to thank Mark Smithers for taking the SEM images.

### References

- [1] M.J. Rost, G.J.C. van Baarle, A.J. Katan, W.M. van Spengen, P. Schakel, W.A. van Loo, T.H. Oosterkamp, and J.W.M. Frenken. *Asian Journal of Control*, 11(2):110–129, 2009.
- [2] G.E. Fantner, G. Schitter, J.H. Kindt, T. Ivanov, K. Ivanova, R. Patel, N. Holten-Andersen, J. Adams, P.J. Thurner, I.W. Rangelow, and P.K. Hansma. *Ultramicroscopy*, 106(8-9):881–887, 2006.
- [3] S.R. Manalis, S.C. Minne, and C.F. Quate. *Applied Physics Letters*, 68(6):871–873, 1996.
- [4] F. Levent Degertekin. In *Lasers and Electro-Optics Society, 2007. LEOS 2007. The 20th Annual Meeting of the IEEE*, pages 832–833, 21-25 2007.
- [5] K.E. Petersen. *Proceedings of the IEEE*, 70(5):420–457, may 1982.
- [6] Z. Zhu and C. Liu. *Journal of Microelectromechanical Systems*, 9(2):252–261, 2000.
- [7] Veeco Instruments. <http://www.veeco.com/>, 2010.

# A SILICON MICROMACHINED TRIAXIAL ACCELEROMETER USING THE MULTIMEMS MPW PROCESS WITH ADDITIONAL DEEP REACTIVE ION ETCHING AS POST-PROCESSING

Per Ohlckers<sup>1</sup>, Luca Petricca<sup>1</sup>, Christopher Grinde<sup>1</sup>

<sup>1</sup>Vestfold University College, Institute for Micro- and nano System Technologies, Norway

## Abstract

We present the design, fabrication and preliminary evaluation of a miniaturized micro-machined silicon triaxial piezoresistive accelerometer using the MultiMEMS MPW foundry process. Together with an additional deep reactive ion etch step, it is possible to etch through wafers with backside topography. The accelerometer is designed to be catheter mounted and applied *in vivo* in a system for postoperative monitoring of heart wall motion following open heart surgery. The final size of the accelerometer including hermetic sealing is 4.2x2x1.5 mm<sup>3</sup>, small enough to allow the removal of the sensor system through the chest wall of the patient without major surgery. The processing was successful, and the prototypes are now being tested and evaluated.

**Keywords:** *Triaxial, MEMS, accelerometer, piezoresistive, deep reactive ion etch (DRIE)*

## I- Introduction

A known complication associated with coronary artery bypass graft (CABG) surgery is that of early graft occlusion resulting in ischemia and possibly infarction. It has been demonstrated that an implantable triaxial accelerometer can provide a means of continuously measuring heart wall motion and analysis of this data can provide a means of early detection of this complication [1]. To do this, the sensor is sutured directly to the epicardium of the heart in the anterior apical region, below the bypass graft. The sensor simultaneously measures the circumferential, longitudinal and radial motion of the heart and any occlusion causes a change in the motion of the heart which is detectable using the sensor. Following surgery, the accelerometer is left attached to the heart for a few days and is then removed by pulling the system free from its stitches and out of the patient's chest using the catheter cable through which collected data is transferred. This application requires that the sensor dimensions, including connector assembly and biocompatible packaging, be no larger than 5 mm in length and 2.5 mm in diameter. Although highly miniaturized accelerometers are currently commercially available, down to sizes 2x2x0.9 mm<sup>3</sup> [2], their shape, number of connectors or requirement for external infrastructure make them unattractive for the application. Effort using a custom designed

process has been undertaken [3]. These designs have been based on silicon-on-insulator (SOI) wafers, piezoresistive transducers and deep reactive etching (DRIE) through the full wafer thickness. This process step has been used to provide accelerometers with equal mechanical sensitivities to accelerations in each of the axes. In addition, cross-axis sensitivity is minimized by aligning the in-plane centre of gravity of the masses with the end of the supporting beams thus minimizing the bending moments due to out-of-plane accelerations.

We have chosen to base our design presented here on the same principles but using a multi-project wafer (MPW) service [4] with the addition of some extra post-processing steps, including a novel process allowing DRIE through already structured wafers. The design has earlier been published [5]

## II- Fabrication process

The fabrication of the sensor has been carried out using the MultiMEMS MPW service [4] from Sensoror Technologies AS (hereafter referred to as Sensoror). This service offers a bulk micromachining process based on the mature Sensoror foundry process that is used for the mass production of tyre pressure sensors. The process offers two types of piezoresistors for the transduction of acceleration to electrical signals, hermetic wafer-level packaging (WLP) using anodic bonding to form a glass-silicon-glass stack, two highly reproducible thicknesses of membrane (3 and 23 microns), under glass electrical feed through and a 10 micron deep front side DRIE recess etch that also allows making freely moving structures such as accelerometers [4]. A typical cross section of a fabricated device using this process is exemplified with the pressure sensor and out-of-plane accelerometer shown in Figure 1.

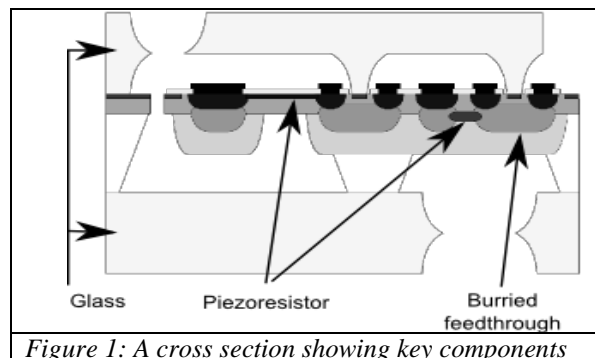


Figure 1: A cross section showing key components

from the MultiMEMS foundry MPW process.

However, with only 10 microns DRIE, proof masses thicker than 23 microns are not possible to fabricate in the offered process, and hence, triaxial accelerometers lacking in sensitivity to in-plane accelerations and with comparable sensitivities in all directions are difficult to achieve. A post processing step offered by the MicroBUILDER project [6] offers a novel process enabling etch through of the whole wafer thickness with local termination. The process is outlined for half a mass-beam system of the accelerometer described in this paper in Figure's 2 through to 5 where the dashed line indicates the centre of the supporting beam and symmetry line of the accelerometer proof mass. After processing in the MPW service but before the packaging by anodic bonding, aluminium is sputtered onto the backside of the wafer to act as an etch-stop. Photoresist is then patterned on the front side of the wafer and is followed by the DRIE process step. The DRIE terminates against the aluminium as illustrated in Figure 4. Finally, the aluminium and resist is stripped and the wafers are returned to the MPW service provider for anodic bonding. The feasibility of this processing approach has previously been proven with the fabrication of a microphone [7].

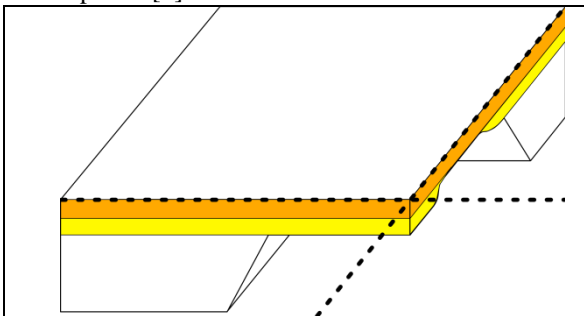


Figure 2: After processing in the Sensoror Multi-MEMS MPW service, the wafers have membranes with 3 and 23 micron thicknesses as well as full wafer thickness. The dashed line indicates the centre line of the beam to be fabricated.

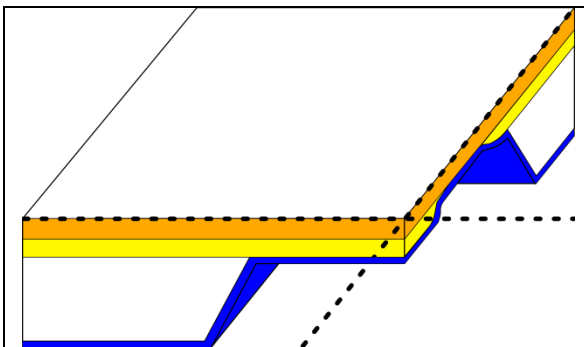


Figure 3: Aluminium is sputtered onto the backside of the wafer.

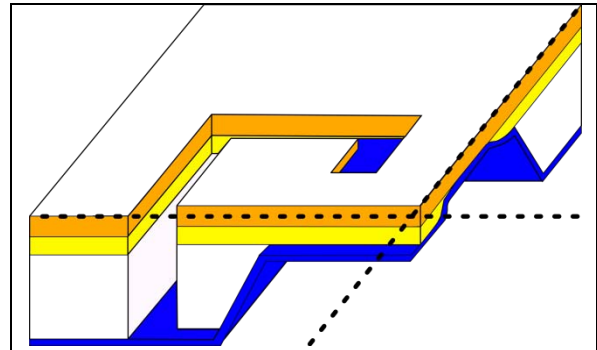


Figure 4: Resist (not shown) is used for masking when DRIE is used to etch until termination against the aluminium on the backside of the wafer.

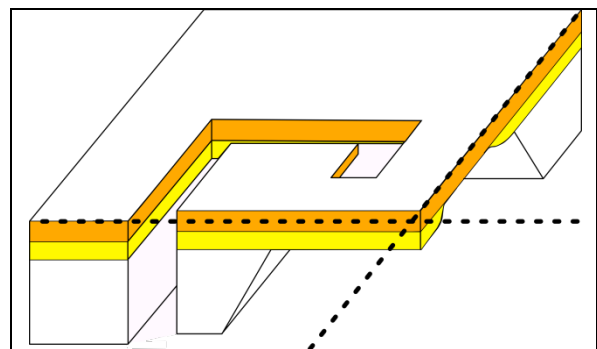


Figure 5: Resist and aluminium is removed before the wafers are sent back to the MPW service for anodic bonding.

### I- Accelerometer design

The accelerometer design can be thought of as a pair of dual-axis accelerometers rotated 90 degrees with respect to each other as illustrated in Figure 6.

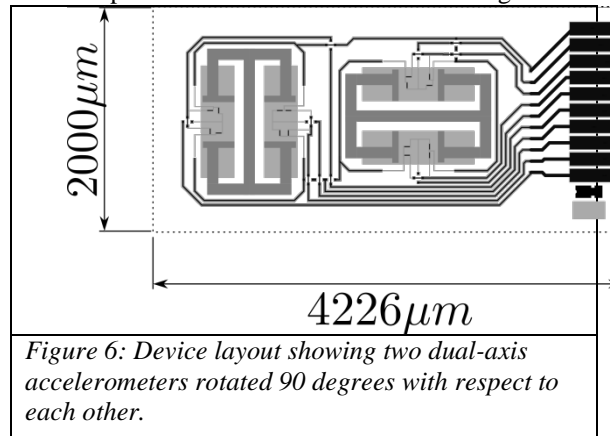


Figure 6: Device layout showing two dual-axis accelerometers rotated 90 degrees with respect to each other.

Each accelerometer consists of two seismic masses, each suspended by one beam at the centre of the side. At the base of each beam there are piezoresistors for acceleration to electrical signal transduction, implanted into the surface of each of the thin stress-sensitive beams near to the fixed-end. The piezoresistors are configured in full Wheatstone bridges with the resistors distributed and aligned such that each bridge provides accel-

eration data for one direction only. This scheme was first used for a two axis accelerometer presented in [8]. Due to the MPW fabrication process described above, the effective beam lengths are defined by a soft transition region between the 23 micron thickness and the 3 micron thickness regions. When using this transition region rather than the anisotropic etch stop to define the start and end of the beams, the reproducibility of the designs is increased. The non-uniform thickness of the beam, as illustrated in Figures 7 and 8, gives well defined regions of stress due to the cubic dependency the second area moment of inertia has to the thickness.

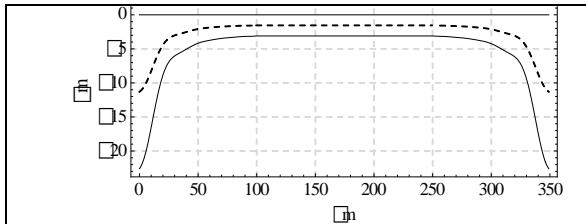


Figure 7: An illustration of the cross section of the beam along its centre (not to scale). At each end the transition between the 3 and 23 micron thick region defines the start and end of the beam. Dashed line indicates centre line

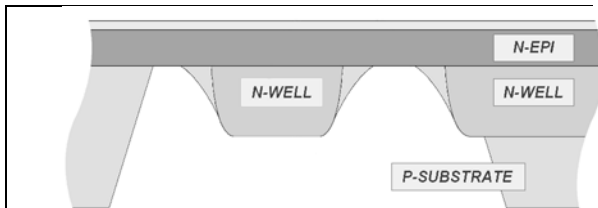


Figure 8: Cross section illustrating the transition regions between 2 and 23 micron regions.

When etching the backside of the wafer as described above, the lateral offset from the exposed (111) plane corresponds to about 250 microns for a wafer of 400 microns thickness. A limitation of the MPW service requires that two such etched trenches to be 200 microns apart in order to guarantee separation. To minimize the accelerometer size, only one backside trench is used for each dual-mass system. This results in a proof mass shape as illustrated in the half symmetry illustration of Figure 5.

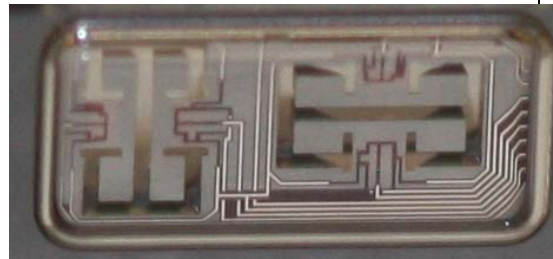
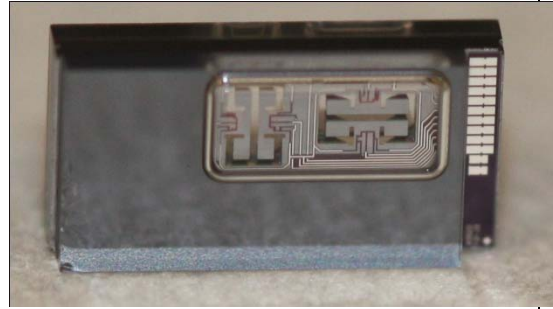


Figure 9: A picture of the front side and the back side of a prototype fabricated in the MPW service with no post-processing. The last picture shows details of the micromachined structures with the 4 suspended inertial masses. Die size defined by the MPW service is 6x3 mm<sup>2</sup>. Used area, including necessary areas for anodic bonding is 2x4.3 mm<sup>2</sup>.

The DRIE process was evaluated during processing to ensure the cavities were properly etched. A cross section SEM picture of a DRIE cavity is shown in Fig 9. As can be seen and was expected, some deviations from the idealised vertical etch pit is observed. However, designed functionality was achieved; to release the inertial masses and spring elements without compromising the piezoresistor network.

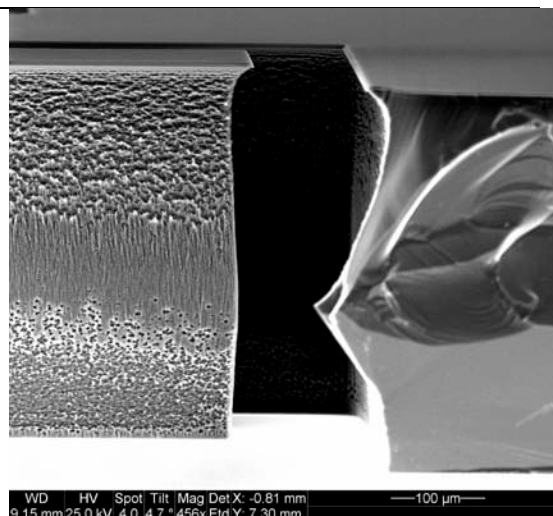


Figure 10: A cross section SEM picture of a DRIE cavity.



### III- Testing and evaluation

20 prototypes have been mounted in transistor headers for functionality testing as triaxial accelerometers on a vibration table. Thereafter, we intend to mount prototypes on a heart monitoring catheter for in vivo testing. Test and evaluation results to be published.

### IV- Discussions

The design and fabrication of a triaxial accelerometer presented in this paper show that the MultiMEMS MPW service with DRIE post processing can be used to make miniaturized micro-machined silicon triaxial piezoresistive accelerometers suitable for heart monitoring. The results of design and fabrication are promising, but we need test and evaluate the fabricated prototypes to assess the performance and functionality of the devices.

### V- Conclusion

The design and fabrication of a triaxial accelerometer has been presented in this paper. The sensor utilizes the piezoresistive effect as a sensing principle. The regular MPW process run has been finalized and the post-processing is expected to be finalized by August 1. The resulting die measures  $6 \times 3 \times 1.5 \text{ mm}^3$  (Figure 9) where only 4.3 mm in length, 2 mm in width and 1.5 mm in thickness are needed for the actual sensor. The design is optimized for minimizing the sensor size given the requirements of the MPW service using a novel process to obtain through wafer etching of wafers with multiple thicknesses. The resulting accelerometer consists of two dual-axis accelerometers with novel proof masses.

The sensor has been designed as a solution to *in vivo* monitoring of heart wall motion. In doing this, an assessment of coronary artery bypass graft patency is possible. A graft occlusion can result in myocardial ischemia leading onto infarction and it has been demonstrated that such a sensor solution can provide a continuous, user-independent method for detecting such complications.

### VI- Acknowledgements

We thank G.U. Jensen and M.M. Mielnik at Sintef MiNaLab for their work with the DRIE post processing, and D. Lapadatu at Sensoron Technologies for organising the MPW processing.

### References

- [1] Halvorsen, P.S. et al (2008), "Feasibility of a three-axis epicardial accelerometer in detecting myocardial ischemia in cardiac surgical patients", J Thorac. Cardio. Sur., Vol. 136, No. 6, pp. 1496-1502.
- [2] Kionix, <http://www.kionix.com>, accessed May 29, 2009.
- [3] Lowrie, C. et al (2009), "MEMS Three-Axis Accelerometer: Design, Fabrication and Application of Measuring Heart Wall Motion", in Procs. DTIP, Tima Labs, Rome, 2009, pp. 229-234.
- [4] MultiMEMS MPW Service, available at <http://www.multimems.com> (accessed 29 May 2009). Design handbook version 4.2.
- [5] Grinde, C., Lowrie, C., Ohlckers, P: "Fabrication of a MEMS Triaxial Accelerometer Using Novel Post-Processing of an MPW Process" Proceedings of MME2009, Toulouse, France, 20.-22. September 2009.
- [6] MicroBUILDER, available at <http://www.microbuilder.org> (accessed 29 May 2009).
- [7] Grinde, C. et al (2010), "Two Clover Shaped Silicon Piezoresistive Microphone for Photoacoustic Gas Sensors", in Journal of Micro-mechanics and Microengineering 2010
- [8] Velten T. et al (1997), "Dynamic behaviour of a new two-axis accelerometer," Solid State Sensors and Actuators, Chicago, IL, pp. 1217-1220.

# INTEGRATED LAB-ON-A-CHIP SILICON NANOWIRE BIOSENSING PLATFORM

A. De, S. Chen, J. van Nieuwkastele, W. Sparreboom, E.T. Carlen, A. van den Berg

BIOS Lab on a Chip Group, MESA+ Institute for Nanotechnology, University of Twente, The Netherlands

**Abstract** — We present an integrated lab-on-a-chip (LOC) label-free biosensing platform that consists of a scalable silicon nanowire (Si-NW) fabrication technology integrated with microfluidic channels for small volume sample transport. The integrated miniaturized biosensing platform is sealed with a novel stand-alone sample holder that combines spring-loaded electrical connecting pins that preclude the need for wire bonding and low dead volume fluidic interconnects. The functional biosensing platform is demonstrated with pH sensing experiments.

**Keywords :** Silicon nanowires, Lab-on-a-chip, Integrated label-free biosensor

## I – Introduction

Lab-on-a-chip (LOC) systems for the detection of biomolecules at very low concentrations are becoming increasingly important for applications requiring high-throughput biomolecular analyses, such as protein assays for basic molecular biology research, disease marker identification, and pharmaceutical drug screening [1]. Currently, fluorescence detection of target-receptor binding is the most frequently used technique, but although very sensitive, this method suffers from the need of target-labeling and possible alterations in target-receptor interactions caused by conformational changes or steric hindrance induced by the label [2]. For this reason, there is considerable effort to investigate alternatives for fluorescent detection. Surface plasmon resonance (SPR) sensing [3] is one well-established label-free technique, but requires sophisticated optical instrumentation and is not easily made suitable for large sensor arrays. Another promising technique relies on electrochemical sensing, and here we will evaluate a recent variant of this, electrochemical sensing using nanowires.

There has been a steady increase in reports of ultra-sensitive sensors over the past few years based on nanoscale structures and devices such as nanowires (NW) [4], carbon nanotubes (CT) [5], nanoparticles [6], and nanocantilever beams [7]. One-dimensional electronic structures such as NW and CT are particularly compelling due to their potential for biosensing applications, suitability for large-scale high-density integration [8], and all-electrical readout capability. NW devices are advantageous compared to CT devices because NW devices can be fabricated from materials, such as Si, with a vast existing knowledge base of material proper-

ties, mature fabrication technologies and techniques for surface passivation and modification. Si-NW sensors have recently attracted a large amount of attention due largely to the reported high label-free detection sensitivities of biomolecules in aqueous phase and claims of ultimately detecting single molecules electrically in real-time.

In this paper we present an integrated LOC / Si-NW biosensing platform. The work is significant because it employs a high-yield top-down Si-NW fabrication technology combined with well-established small sample volume LOC technology thus forming a highly reliable and manufacturable platform for label-free biosensing with all-electrical signal readout. This potential platform can be used for the electrical detection of biomolecules, such as proteins [9] and DNA [10].

## II - Experimental Details

### A. Integrated microfluidic platform

The integrated biosensing platform consists of a Si-NW biosensing chip, microfluidic LOC for sample delivery, and a novel chip holder that seals the Si-NW and LOC chips together and provides electrical and fluidic interconnects in a stand-alone assembly. Figure 1 shows a schematic drawing of the integrated LOC/Si-NW biosensing platform.

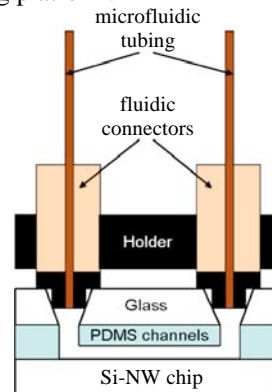


Figure 1: Integrated LOC/Si-NW biosensing platform with microfluidic tubing, sample inlet and outlet fluidic connectors, and three-layer integrated chip sealed with a custom-made chip holder.

### B. Silicon nanowires

We have developed a top-down fabrication method to realize sub-50 nm Si-NWs for sensor applications, which is based on a method consisting of conventional microlithography, wet etching and size reduction [11]. The advantage of our technique is that moderately dense

arrays of Si-NWs, with precisely controlled dimensions and atomically smooth surfaces, are directly fabricated with thicker microscale electrical contact regions from a continuous layer of single crystal silicon. The thick silicon contact regions result in reduced contact resistance compared to ultrathin silicon layers. Additionally, fabrication techniques compatible with conventional semiconductor manufacturing, such as ion implantation and optical lithography, can be used resulting in high wafer-scale device yield. Briefly, silicon microwires are first fabricated from silicon-on-insulator (100) wafers with a patterned silicon nitride mask layer using anisotropic wet etching (5% tetramethyl ammonium hydroxide) of the silicon device layer. Exposed (111) facets of the microwire edges are then thermally oxidized resulting in local oxidation of silicon at the silicon/nitride interface. The oxide layer is used as an etch mask for the second anisotropic wet etch that results in Si-NWs with triangular cross-sections. Finally, size reduction anisotropic wet etching of the remaining silicon (111) surfaces produces Si-NWs with precisely controlled height  $h$  and width  $w \approx 2h/\tan(54.7^\circ)$ . Using this method, we have fabricated electrically functional Si-NWs with heights ranging from 200 nm to ~50 nm and lengths up to 100 microns. The electrical contact regions are highly doped for ohmic contacts and  $H_2/N_2$  annealing has been performed to reduce interface charge and reduce metal-silicon contact resistance. The Si-NW channel doping concentration has been selectively varied over 3 orders of magnitude  $10^{16}$ - $10^{18} \text{ cm}^{-3}$ . Figure 1 shows a brief fabrication process.

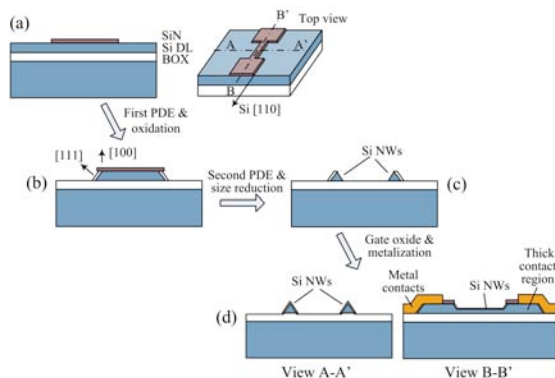


Figure 2: Top-down Si-NW microfabrication procedure. (a) first lithography and etch steps for SiN layer patterning (BOX: buried oxide layer and Si DL: silicon device layer of the SOI substrate) (b) silicon device layer PDE and local oxidation (c) second PDE and size reduction (d) gate oxidation and contact metallization.

Figure 2 shows high resolution scanning electron (HRSEM) and high resolution transmission electron (HRTEM) microscopy images representative of Si-NWs fabricated with this technology. This fabrication technology is capable of producing high-density Si-NW arrays with device diameters down to 10-20 nm and

itches ~50-60 nm with the use of high resolution patterning methods to define the initial SiN masking layer (Figs. 1a).

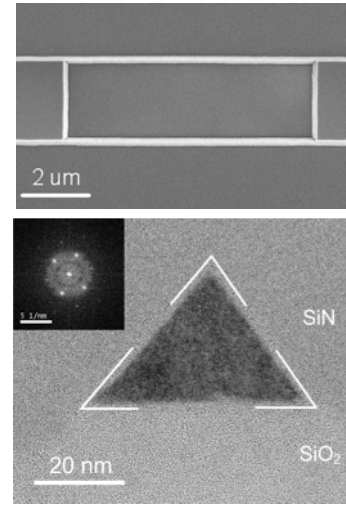


Figure 3: Microscopy images of fabricated Si-NWs (a) HRSEM image (b) HRTEM image.

### C. LOC microfluidics

The LOC microfluidic chip consists of a top glass layer, a center polymer microfluidic layer made of a molded polydimethylsiloxane (PDMS) elastomer and the bottom Si-NW chip. The chip layers are shown in Fig 4. The top glass (Borofloat) layer provides a solid

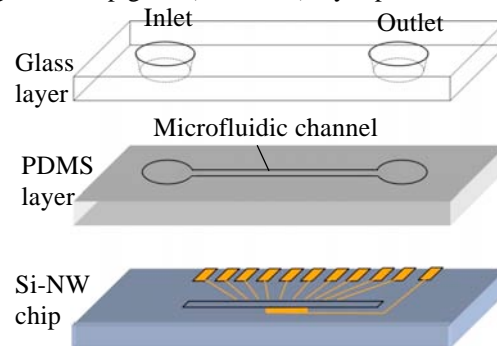


Figure 4: NW device chip assembled with PDMS and glass slide.

support for attachment of the fluidic connections, and therefore, through-wafer holes are required to form the inlet and outlet ports. The through-wafer holes (1 mm top diameter) were formed by powder blasting with 30 μm diameter alumina particles. The center microfluidic layer is formed with a molded PDMS material. The PDMS layer was prepared from a silicon mold with the specified channel dimensions. The PDMS layer was 1 mm in thickness and made from a 10:1 mix of silicone to curing agent and cured at 70 °C. The microchannel dimensions in the PDMS layer are width=50 μm, height=50 μm, and length=10 mm. The inlet and outlet holes have 1 mm diameters. The PDMS and glass layers were bonded together following an O<sub>2</sub> plasma treatment on both surfaces. The glass/PDMS chip dimensions is



width=5 mm and length=20 mm. Next, the glass/PDMS assembly was aligned to the Si-NW chip using a custom alignment tool. Briefly the alignment tool consists of

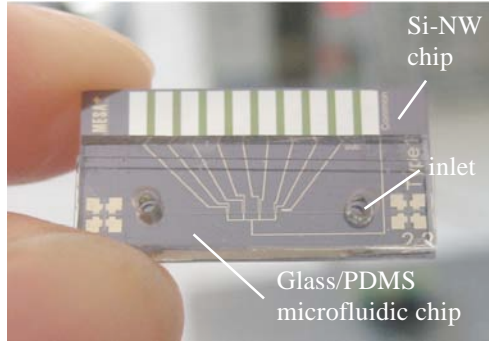


Figure 5: Integrated LOC / Si-NW biosensor chip.

two movable stages under a microscope. The Si-NW chip is placed on a x-y-z stage. The Si-NW and glass/PDMS chips were assembled by aligning the channel with the nanowires sensors on the Si-NW chips and pressed together and clamped into a custom chip holder. Figure 5 shows an example of an integrated LOC/Si-NW biosensing chip prior to assembly into the custom chip holder.

### III - Results and Discussion

#### A. Integrated LOC/Si-NW biosensing platform

The integrated LOC/Si-NW biosensing chip is clamped into the custom-made chip holder, which provides a leak-tight seal between the PDMS and Si-NW chip surfaces. The chip holder has two parts: top and bottom. Figure 6 shows different views of the chip holder. The top part of the chip holder has a printed circuit board (PCB) connected with a spring-loaded pin assembly (Fig. 6b) that contacts directly to the metal pads on the Si-NW chip to provide the electrical connection to the sensors. Coaxial connectors and cables are used for external electrical connections. The bottom part of the chip holder has a groove for holding the Si-NW chip assembly in place (Fig. 6c). The top part goes on top of the chip assembly and it is screwed to the bottom of the holder with screws. The LOC/Si-NW chip is then placed between the two parts and subsequently screwed together to hold the chip in place (Fig. 6d). The top part has holes tapped to fit conventional tubing holders (Nanoport, Upchurch), which was placed on the bottom part of the chip holder was screwed together. Commercially available PEEK (polyetheretherketone) tubing with 360  $\mu\text{m}$  OD is directly connected to the Nanoport fitting at the inlet and outlet ports (Fig. 6d). The PEEK tubing at the inlet port is connected directly to a commercially available pressure controller (MFCS-8C, Fluigent) and pressurized sample cuvettes. The MFCS pressure based flow system provides an efficient pulse

free pumping of solution through the microfluidic assembly, which is important for real-time biosensing

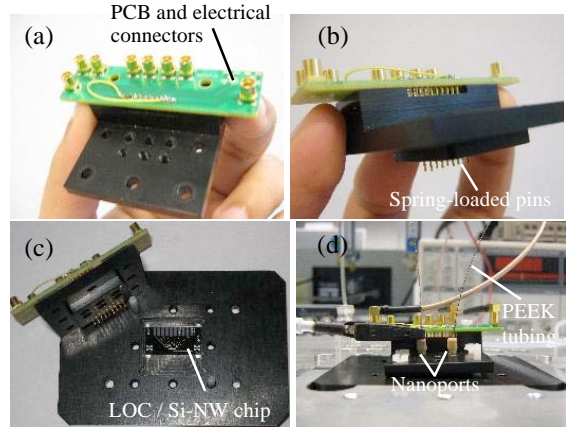


Figure 6: Chip holder (a-b) top (c) bottom and (d) assembled system.

and the extraction of binding thermodynamic parameters. The flow through the channel has a short response time and is stable over long duration of time. The PEEK tubing is flexible and can be easily bent to reduce the solution flow path from the reservoir to the channel. The PEEK tubing is specially chosen as it is biocompatible, chemically inert and hence suitable for biological sample flow. The PEEK tubing connected to the outlet port is connected directly to a waste reservoir.

#### B. Si-NW solution gating

The Si-NWs were characterized in solution before they were used in the integrated biosensing system. For solution measurements, a reference electrode was used as a front gate to bias the Si-NWs for all surface charge related measurements. Front gate biasing affects the depletion region differently than back-gate biasing as presented previously and we expect higher surface charge sensitivity for biosensing applications with this configuration [12]. Front gate conductivity modulation with a reference electrode (Ag/AgCl) in an electrolyte (100 mM NaCl) and corresponding transconductance

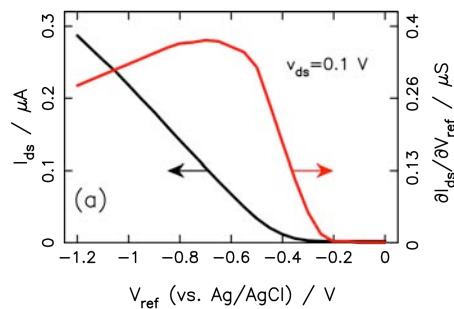


Figure 7: Measured Si-NW front gate biasing characteristic in solution.

$(\partial I_{ds}/\partial V_{ref}, \text{ constant } v_{ds})$  illustrate the transition from depletion mode to depletion/accumulation mode operation as  $V_{ref}$  is scanned negative (Fig. 4). The decrease in

transconductance for increasing  $V_{ref}$  is due to a decrease in field-dependent effective mobility and charge screening. For biosensing applications, the devices can be biased in the region with highest transconductance and linear  $i_{ds}$  range [12].

### C. pH sensing with integrated LOC/Si-NW platform

The integrated LOC/Si-NW biosensing chip was mounted in the chip holder and clamped into position with set-screws. The PEEK tubing attached to the inlet port was connected directly to the pressurized sample cuvettes (Fluwell, Fluigent). The cuvette was filled with 2 ml of sample buffers with varying pH. The buffer solution was pumped using the pressure control system. Additional PEEK tubing was connected from the outlet port to a waste reservoir. The output PEEK tubing was sputter coated with a 1  $\mu\text{m}$  thick Pt layer to serve as a pseudo-reference electrode to ensure a solution potential and to set the Si-NW bias point. Coaxial connectors and cables were used to connect the AC drain-source voltage source  $v_{ds}$  and low frequency current measurement (SR 830, Stanford Research Systems). The DC backgate voltage  $V_{bg}$  (2400 Series, Keithley) is connected to a common ground that includes the Pt electrode.

The pH sensing was done using the integrated LOC/Si-NW chip with a low frequency  $v_{ds} = 500$  mV and DC  $V_{bg} = -7.5$  V with respect to the Pt electrode. First, a pH 4 buffer solution was transported through the microchannel for 5 min at a flow rate of 0.5  $\mu\text{l}/\text{min}$  followed by a buffer solution with pH 10 for 5 minutes and the same flow rate. The Si-NWs are p-type, and therefore, a change from pH 4 to pH 10 results in a

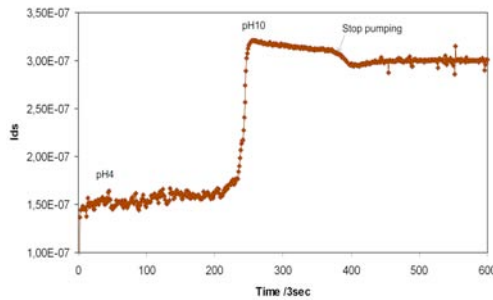


Figure 8: pH measurement with integrated LOC/Si-NW biosensing platform.

negative surface potential change  $-\Delta\phi_o$ , where  $\Delta\phi_o = \phi_o(\text{pH } 10) - \phi_o(\text{pH } 4)$ , which results in a reduced depletion region of the depletion-mode Si-NW devices, and therefore, an increase in the Si-NW current  $i_{ds}$ . Figure 8 shows an example measurement of conductance increase as the pH is changed from 4 to 10 in the integrated sensor system.

## IV - Conclusion

We have realized a scalable Si-NW fabrication technology and have integrated the Si-NWs with well-developed LOC technology to form a label-free biosensing platform with all-electrical signal readout that is ideal for biosensing applications. The advantage of this new fabrication technique is that moderately dense arrays of Si-NWs, with precisely controlled dimensions and atomically smooth surfaces, can be directly fabricated and are compatible with conventional semiconductor manufacturing and LOC manufacturing technology. The integrated LOC/Si-NW biosensing platform offers several advantages for solution-based measurements. The new integrated sensing platform eliminates the requirement for wire bonding for electrical interconnects and sensor encapsulation for electrical isolation. The chip holder with the clamped LOC/Si-NW approach makes for a systematic, stable and leak free system for simultaneous electrical measurements with small volume transport.

## References

- [1] P. Bertone and M. Snyder, *FEBS Journal*, 272, 5400, 2005.
- [2] N. Ramachandran, D. N. Larson, P. R. H. Stark, E. Hainsworth, and J. LaBaer, *FEBS Journal*, 272, 5412, 2005.
- [3] J. Homola, S. S. Yee, and G. Gauglitz, *Sensors and Actuators B-Chemical*, 54, 3, 1999.
- [4] Y. Cui, Q. Q. Wei, H. K. Park, and C. M. Lieber, *Science*, 293, 1289, 2001.
- [5] S.J. Tans, M. H. Devoret, H. J. Dai, A. Thess, R. E. Smalley, L. J. Geerligs, and C. Dekker, *Nature*, 386, 474, 1997.
- [6] L. Brus, *Applied Physics A-Mater*, 53, 465, 1991.
- [7] J. Fritz, M. K. Baller, H. P. Lang, H. Rothuizen, P. Vettiger, E. Meyer, H. -J. Güntherodt, Ch. Gerber, J. K. Gimzewski, *Science*, 288, 316, 2000.
- [8] R. Beckman, E. Johnston-Halperin, Y. Luo, J. E. Green, and J. R. Heath, *Science*, 310, 465, 2005.
- [9] G. Zheng, F. Patolsky, Y. Cui, W. U. Wang and C. M. Lieber, *Nature Biotechnology*, 23, 1924, 2005.
- [10] J. Hahm, and C. M. Lieber: *Nano Letters*, 4, 51, 2004.
- [11] S. Chen, J. G. Bomer, W. G. van der Wiel, E.T. Carlen, A. van den Berg, *ACS Nano*, 3, 3485, 2009.
- [12] H. D. Tong, S. Chen, W. G. van der Wiel, E.T. Carlen, A. van den Berg, *Nano Letters*, 9, 1015, 2009.

# SURFACE MODIFICATION OF SILICON BY 3D ETCHING PROCESSES AND SUBSEQUENT LAYER DEPOSITION

Z. Fekete<sup>1</sup>, D. Gubán<sup>1</sup>, É. Vázsonyi<sup>1</sup>, A. Pongrácz<sup>1</sup>, G. Battistig<sup>1</sup>, P. Fürjes<sup>1</sup>

<sup>1</sup>*Research Institute of Technical Physics & Materials Science, Hungarian Academy of Science  
H-1525 Budapest, P.O. Box 49, Hungary*

**Abstract** — MEMS compatible processes, as two-step wet chemical etching and Deep Reactive Ion Etching are elaborated, applied and characterised for modification of surface properties of silicon combined with subsequently deposited dielectric layers (Hexamethyl-disilazane - HMDS or plasma-polymerised fluorocarbon). The feasibility of the combined technique is demonstrated by the analysis of the wetting behaviour of the realised structures applying contact angle measurements. The developed micro- and nanoscale surface topographies by wet and dry etching techniques are characterised by AFM and SEM, detailed discussion on geometric design and fabrication techniques are also included.

**Keywords :** surface modification, 3D alkaline etching, DRIE, self-assembled monolayers, superhydrophobicity

## I - Introduction

Recently there was a significant progress in the development of water-repellent surfaces regarding biomimetics [1] or ElectroWetting on Dielectric (EWOD) for digital microfluidics [2]. Bioinspired surface topographies are of key importance, therefore a range of micromachining concepts have been demonstrated [3, 4]. The fabrication of superhydrophobic surfaces has involved a wide variety of techniques including surface preparation, micromachining and the application of several surfactants. In spite of the rapid development of dry etching techniques, like deep reactive ion etching (DRIE), there is still room for further investigation as regards the combination of less expensive wet etching techniques [5].

The functionality of the micro- or nanofluidic structures is significantly influenced by the surface properties of the applied structural materials. The fluidic behaviour can be modified by micro- and nanoscale surface structuring and deposition of additional coatings. In this paper the effects of 3D surface topography, nanoscale roughness and additive chemical layers are discussed.

## II - Experimental Details

During the fabrication of microstructured silicon surfaces, the wet etching processes inevitably modify both the micro- and nanoscale topography of the

surface. In this work, a two-component alkaline etching (NaOH, NaOCl) in case of different substrate orientation and subsequent polishing (HF : HNO<sub>3</sub> : H<sub>3</sub>PO<sub>4</sub>) with varied mol-ratio (see Table 1) was investigated. The proposed alkaline etching is successfully applicable for the formation of high aspect ratio microstructures, shown in Figure 1.a.-b. To evaluate the feasibility of the technique microstructures of similar patterns were also produced by DRIE (Figure 1.c.).

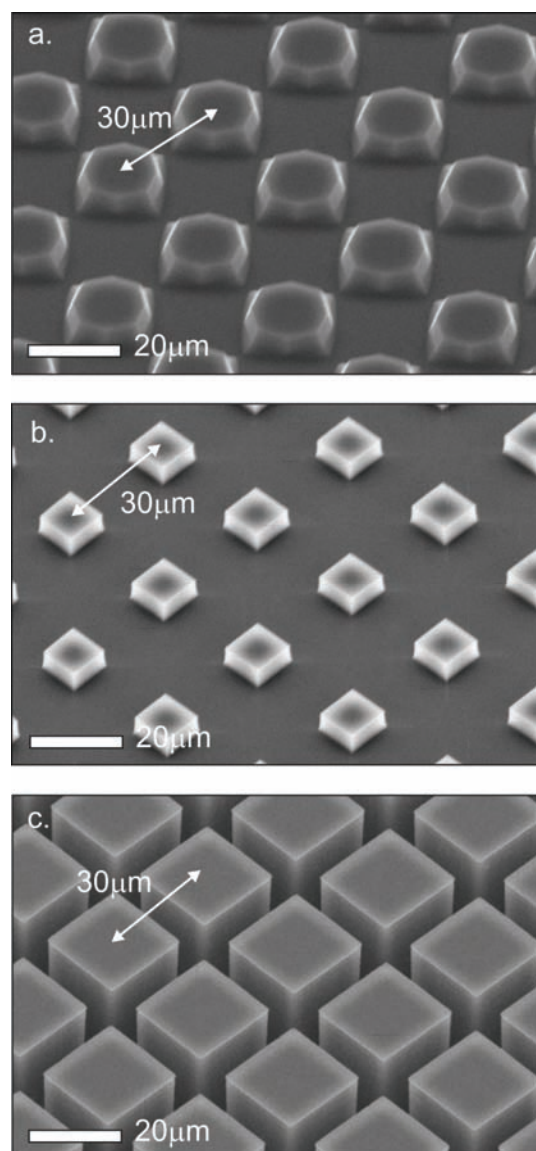
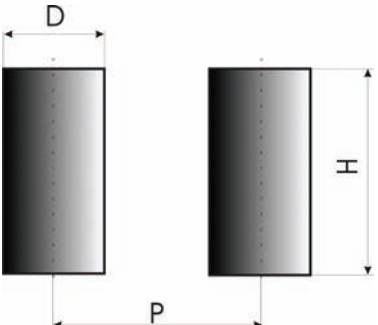


Figure 1: 3D silicon microstructure array formed by two component alkaline etching (a., b.) and deep reactive ion etching (c.)



Distances between columnar structures (pitch) and solid-air surface ratio was varied in order to achieve superhydrophobic patterns and to investigate structural dependence of water-repellent surfaces.

Table 1: Structural parameters of the applied structures for alkaline etching



<b>H</b>	NaOH etched with both orientation: 10μm DRIE etched: 25μm					
<b>D</b>	NaOH etched with 0° orientation: 20μm NaOH etched with 45° orientation: 5μm DRIE etched: 25μm					
<b>P</b>	30	40	50	60	70	80

The secondary geometry of the designed structures was developed by subsequent chemical polishing, as apparently presented in Figure 2. The compositions and silicon etching rates of the applied polishing solutions are detailed in Table 2. Effects of nano-roughness on the hydrophobic behaviour was analysed by AFM.

Table 2: Chemical compositions ( $HF : HNO_3 : H_3PO_4$ ) and the calculated etching rates of the applied polishing solutions

<b>0,7:1:0,3</b> 6.9μm/min	<b>0,7:1:0,4</b> 6.1μm/min	<b>0,7:1:0,5</b> 5.4μm/min	<b>0,7:1:0,6</b> 2.9μm/min	
<b>1:1:0,3</b> 10.7μm/min	<b>1:1:0,4</b> 10μm/min	<b>1:1:0,5</b> 5.2μm/min		
<b>1,2:1:0,3</b> 12.2μm/min	<b>1,2:1:0,4</b> 12.8μm/min	<b>1,2:1:0,5</b> 8.5μm/min	<b>1,2:1:0,6</b> 6.6μm/min	<b>1,2:1:0,7</b> 5.7μm/min
<b>1,4:1:0,3</b> 13.7μm/min	<b>1,4:1:0,4</b> 9.8μm/min	<b>1,4:1:0,5</b> 9.5μm/min	<b>1,4:1:0,6</b> 7.1μm/min	<b>1,4:1:0,7</b> 6.1μm/min
<b>1,6:1:0,3</b> 15.3μm/min		<b>1,6:1:0,5</b> 8.6μm/min		<b>1,6:1:0,7</b> 5.1μm/min
<b>1,8:1:0,3</b> 26.9μm/min		<b>1,8:1:0,5</b> 12.1μm/min		<b>1,8:1:0,7</b> 7μm/min
<b>2:1:0,3</b> 22.7μm/min		<b>2:1:0,5</b> 11.4μm/min		<b>2:1:0,7</b> 8.4μm/min

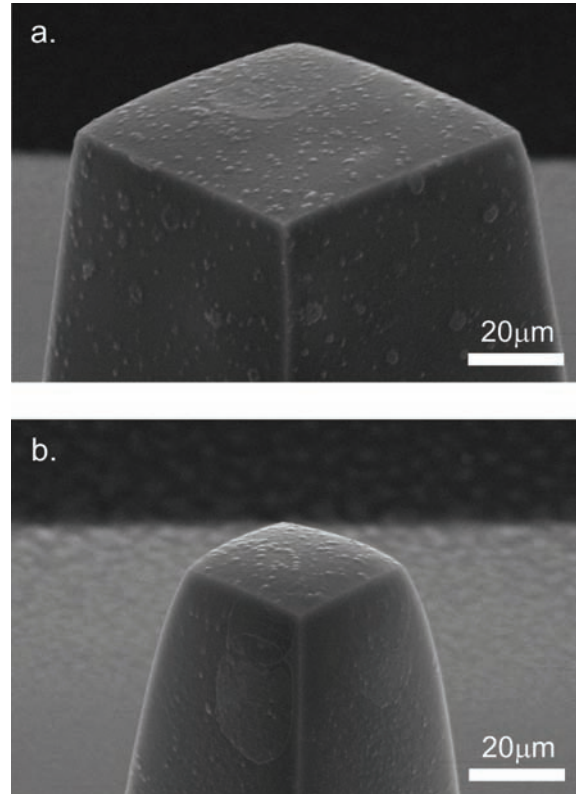


Figure 2: Secondary geometry developed by subsequent chemical polishing using different  $HF : HNO_3 : H_3PO_4$  concentrations (a: 0.7:1:0.3, b: 1.8:1:0.3 mol-ratio respectively, 1min. etching time both)

The surface properties of the processed silicon samples were also modified by subsequent layer deposition. Further improvement in hydrophobic behaviour was achieved by gas phase deposition of Hexa-methyl-disilane (HMDS) and plasma-polymerisation of fluorocarbon layer in the passivation phase of the Bosch-type deep reactive ion etching process.

### III - Results and Discussion

The surface modification effects of the detailed 3D structuring methods and subsequent layer deposition techniques were characterised by analysing the wetting behaviour of the resulted surfaces. The combination of the two surface modification steps was applied for realisation water-repellent surfaces.

The nanoscale surface topography was characterised by AFM. A typical surface morphology of a chemically polished silicon surface is presented in Figure 3. Although nanoscale roughness significantly modifies the optical parameters of the surface, causing dimming of mirror-like silicon regarding its wetting behaviour only a slight effect was observed.

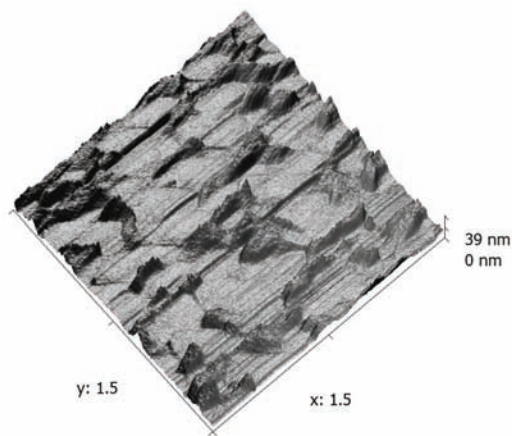


Figure 3: Representative AFM topography of a chemically polished silicon surface applying  $\text{HF} : \text{HNO}_3 : \text{H}_3\text{PO}_4$  etchant with the concentration of 0.7:1:0.3

In contrast to the nanoscale morphology the deposited chemical layers caused a visible change in contact angles representing the modified surface behaviour. The hydrophobic properties of different layers were preliminary characterised on plain silicon surfaces as shown in Figure 4.

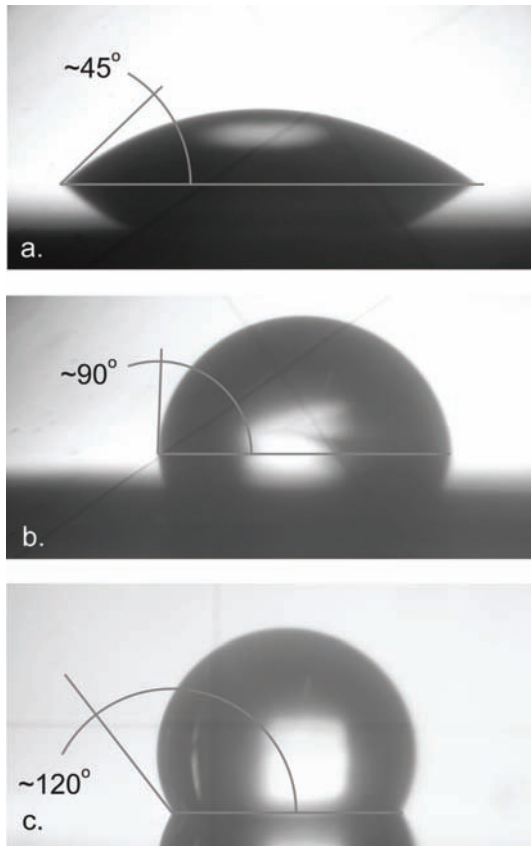


Figure 4: Hydrophobic characteristics of the uncoated (a.), HMDS coated (b.) and poly-fluoro-carbon coated (c.) silicon surfaces, respectively. (The estimated contact angles are indicated.)

The combination of the 3D bulk micromachining and the subsequent chemical layer deposition steps is expected to modify the surface behaviour of the silicon radically. The microstructured silicon surfaces coated by plasma-polymerised poly-fluoro-carbon represented excellent hydrophobicity (see Figure 5). The HMDS coated structures resulted moderate change in the wettability.

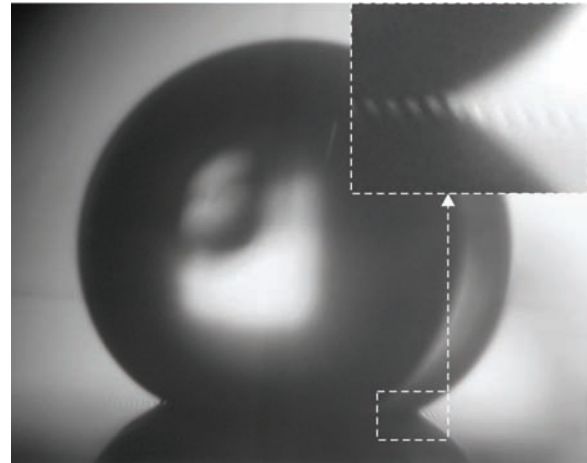


Figure 5: Superhydrophobic behaviour demonstrated on solid-air composite surface fabricated by two-component alkaline etching and subsequent plasma-polymerisation of poly-fluoro-carbon layer. Air cushions are clearly shown in enlarged area.

Contact angle measurements in case of the different structures (geometric parameters are listed in Table 1.) coated by poly-fluoro-carbon deposited by DRIE proved the feasibility of the fabrication process. Results in case of two-component alkaline etching solution (at the orientation of  $45^\circ$ ) are illustrated on Figure 6.

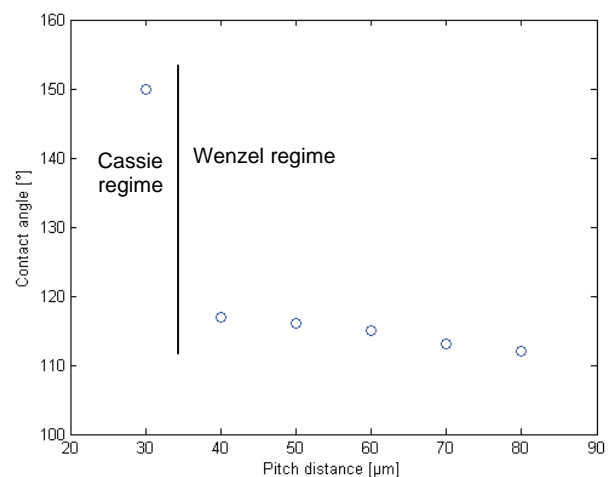


Figure 1: Measured contact angles at different pitch distances in case of chips fabricated by alkaline etching. Cassie-Wenzel transition is apparently noticeable on the figure.

#### IV - Conclusion

The applicability of the combined wet etching processes for realisation periodic high aspect ratio 3D silicon microstructures was demonstrated and compared to the DRIE. The additional surface modification of these primary structures is of key importance regarding fluidic behaviour of the final device considering the adequate sample manipulation in microfluidic systems or on highly hydrophobic surfaces.

#### Acknowledgements

The support of the European Commission, the Seventh Framework Programme via P3SENS project (project no.: 248304), the ENIAC JTI and the Hungarian National Office for Research and Technology (NKTH) via CAJAL4EU project and the János Bolyai fellowship of the Hungarian Academy of Sciences (recipients: Péter Fürjes) is gratefully acknowledged.

#### References

- [1] Ai Lin Chun, *Nature Nanotechnology*, 2009 10.1038/nnano.2009.230
- [2] F. Mugele, J. Baret, *Condensed Matter* vol. 17 pp. 705–R774, 2005
- [3] Y. C. Jung, B. Bhushan, *Scripta Materialia* vol. 57 pp. 1057–1060, 2007
- [4] P. Roach, N. J. Shirtcliffe, M. I. Newton, *Soft Matter*, vol. 4 pp. 224–240, 2008
- [5] É. Vázsonyi, Cs. Dücső and Á. Pekker, *J. Micromech. Microeng.*, vol. 17 pp. 1916, 2007



# MATERIAL SELECTION FOR IMPEDANCE SPECTROSCOPY ON AN ELECTROWETTING BASED LAB-ON-A-CHIP

T. Lederer, S. Clara, B. Jakoby, W. Hilber

All: Institute for Microelectronics and Microsensors; Johannes Kepler University Linz; Austria

**Abstract** — In this paper we discuss the question if and under which conditions a lab-on-a-chip platform can be realized utilizing electrowetting on dielectrics as an actuation principle and impedance spectroscopy as a sensor principle. In order to examine the different isolation layers used for electro wetting, we measured the impedance function over a range from 40Hz to 110 MHz. As a result we found an impedance signal with characteristic properties measured through thin isolation layers with high capacitance. With increasing thickness and additional layers the impedance signal got dominated by the lower capacitance. Thus, materials with higher permittivity and hydrophobic layers consisting of self assembled monolayers are suggested.

**Keywords:** Impedance spectroscopy, electro wetting, PTFE, Ta2O5, ZrO, SAM

## I - Introduction

Microfluidics which deals with fluids of sub nl-volume is a fast developing research area and is promising to significantly reduce production and operating costs and time of chemical and biochemical assays. To handle single droplets in a modular grid, which is referred to as digital microfluidics, rather than a continuous flow in defined channels, allows to perform multiple different processes on the same platform. An actuation principle which allows for droplet manipulations, e.g. creation, transport, mixing and divisions of droplets [1], is called electro wetting on dielectrics (EWOD). The shape of a droplet laying on a hydrophobic surface surrounded by an ambient fluid (liquid or gas) is predetermined through the balance of forces, i.e. surface tensions, gravitation as well as electrostatic forces. For small droplets with a high surface to volume ratio gravitation can be neglected. Thus the shape can be approximated by a sphere which is cut off by the underlying surface. At the contact point of the underlying surface, the droplet and the ambient fluid a contact angle can be defined. An applied voltage lowers the effective surface energy of the solid/liquid interface and thus the contact angle is lowered, see Fig. 1.

Structuring an electrode pattern allows for applying an inhomogeneous electric field and therefore inhomogeneous surface tension which results in droplet motion. This electrical actuation allows for programmable sequences of droplet actuations, see Fig. 2. Different processes for chemical or biological analysis can be

performed on one chip just by changing the program [2], [3].

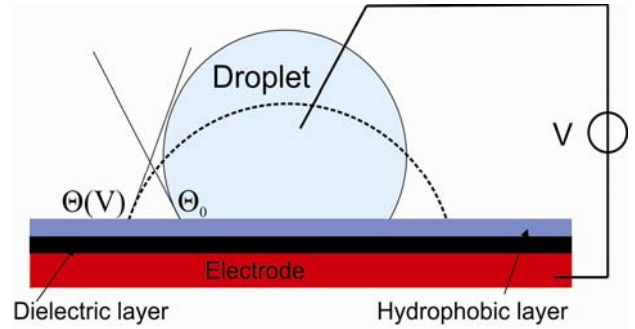


Figure 1: Scheme of a droplet resting on top of an electrode isolated by a combination of a dielectric and a hydrophobic layer. Applying a voltage between the droplet and the electrode lowers the effective surface energy and pulls the droplet down to the surface.

For the development of an electro wetting platform a hydrophobic surface is most critical. The contact angle  $\theta_0$  between the substrate surface and the liquid/gas contact line is defined via Young's law:

$$\gamma_{LG}(\cos \theta) = \gamma_{SG} - \gamma_{SL} \quad (1)$$

$\gamma$  denotes the surface energy of the material interfaces between the solid substrate  $S$ , the liquid  $L$  and the ambient fluid  $G$  to each other. Therefore it is a good measure for the work of adhesion  $W_a$  which is given in the Young-Dupré Equation:

$$W_a = \gamma(1 + \cos \theta) \quad (2)$$

Electro-wetting lowers the surface energy of solid to liquid interface and therefore the contact angle  $\theta$  proportional to the specific capacitance  $c$  and the square of voltage  $V$  according to derivations of the Lippmann-Young equation:

$$\gamma_{SL}(V) = \gamma_{SL} - \frac{cV^2}{2} \quad (3)$$

$$(\cos \theta) = \cos(\theta_0) + \frac{cV^2}{2\gamma_{LG}} \quad (4)$$

Beside the contact angle the so called hysteresis angle  $\alpha$  is an important parameter [5]. It represents the fact that a droplet with an increasing volume shows a higher contact angle on the same substrate than a droplet with decreasing volume, where  $\alpha$  is the difference. One can think of it as a "pinning" of the contact line up to a certain unbalance of the surface tensions.

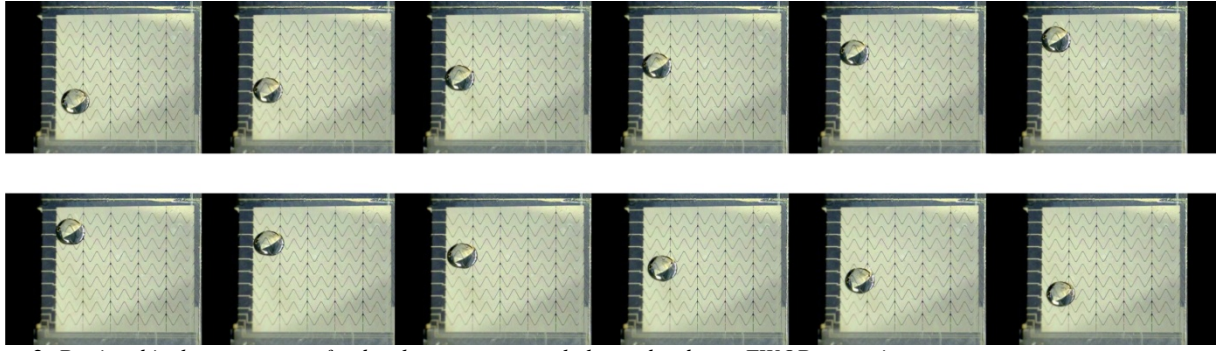


Figure 2: Depicted is the movement of a droplet across several electrodes due to EWOD actuation.

Impedance spectroscopy is used as a sensor principle to characterize the composition of fluids due to the frequency dependent electric impedance  $Z(\omega)$ .

$$Z(\omega) = Z'(\omega) + jZ''(\omega) \quad (5)$$

The real part of the impedance consists of the dissipative effects of the measured cell and the imaginary part is the energy storage of the system like capacitors and inductances.

IS holds the advantages of a relative simple electrical measurement which can provide information about physical and chemical properties of tested materials. A comprehensive overview about theoretical background and technical realizations can be found in [4]

The combination of EWOD with impedance spectroscopy is favorable because of the common electric nature of both sensor and actuator principle. Necessary electrodes for IS and EWOD can be structured in one lithography step and a hydrophobic coating can be deposited homogeneously on top of electrode pattern.

In our contribution we focus on the combined realization of impedance spectroscopy and electro wetting on dielectrics which implies measurements through hydrophobic isolation layer. Special attention is given to the applied/implemented materials.

## II - Experimental details

### A. Electrode design and isolation layers

For reliable EWOD actuation it is essential that the droplet resting at an arbitrary position can be reached by an inhomogeneous electric field. This is secured by a jagged electrode design. A round shaped droplet with a diameter larger than the width of one electrode plus the width of the separation gap is always affected by at least two electrode lines. EWOD actuation is typically performed on a hydrophobic surface with low hysteresis angle. The electrodes have to be isolated from the droplet in order to prevent electric currents through the droplet when voltages are applied. Both requirements are typically met by a material combination of a dielectric layer, e.g. ceramic materials like  $\text{Al}_2\text{O}_3$  or  $\text{SiO}_2$  or a polymer like PTEE and a hydrophobic layer, typically PTFE. Recently isolation layers were described in literature which allow for low actuation voltages as low as 15V, consisting of high permittivity materials like

$\text{Ta}_2\text{O}_5$  and an additional hydrophobic layer of thin (20nm) PTFE [5].

The impedance is measured between two parallel electrodes at different frequencies. Separation width, length and broadness of the electrode were varied to determine the geometric dependences of the system. The impedance electrodes can be integrated into the EWOD electrodes and can be used for actuation if set to a common voltage with the surrounding actuation electrodes. EWOD electrodes as well as IS electrodes are separated from the fluid by a combination of dielectric and hydrophobic layers. The applied combinations are denoted in Table 1.

Table 1: Layer structure above the impedance electrodes

Layer number	Dielectric layer	Hydrophobic layer	Specific Capacitance [ $\text{Fm}^{-2}$ ]
1	-	-	-
2	$\text{Al}_2\text{O}_3$ 100nm	-	$7,9 \cdot 10^{-4}$
3	$\text{Al}_2\text{O}_3$ 150nm	PTFE 40nm	$3,0 \cdot 10^{-4}$
4	$\text{Al}_2\text{O}_3$ 150nm	PTFE 800nm	$2,4 \cdot 10^{-5}$
5	$\text{Ta}_2\text{O}_5$ 100nm	-	$2,1 \cdot 10^{-3}$
6	$\text{Ta}_2\text{O}_5$ 100nm	PTFE 40nm	$4,0 \cdot 10^{-4}$
7	$\text{Ta}_2\text{O}_5$ 100nm	FTP 3nm	$1,6 \cdot 10^{-3}$

### B. Fluids

The electrodes underneath the different layer combinations were used to measure the frequency dependent impedance of different fluids of constant volume, height and temperature 25°C: a) Ambient air; b) DI Water  $1,2 \cdot 10^{-7} \text{ S/m}$ ; c) 0,9% NaCl in  $\text{H}_2\text{O}$

To ensure constant height and volume a fluid chamber was built which sealed a defined space above the impedance electrodes. Therefore different contact angles of pure and NaCl enriched DI water did not lead to changes in height.

### C. Impedance measurements

The frequency dependent impedance was determined by an AGILENT 4294 A Precision Impedance Analyzer. In order to get a constant capacitance and resistance from the connection between analyzer and electrodes a fix adapter was constructed. This constant additional impedance was calibrated out of the measurements.

Over the measurement range from 40Hz to 110MHz which is the maximal width of the available Impedance Analyzer 801 data points ( $|Z|$  and phase  $\theta$ ) were taken.

### III - Results and Discussion

The interpretation of the measurement data is a sensible task because the physical realization of the hydrophobic and dielectric layer influences the contact area to the fluid. Multiple chemo-physical mechanisms are contributing to the impedance of the system.

The excess charges between an electrolyte and the isolation layer form a diffuse double layer screening the electrochemical potential at the boundary. An inner (Stern) layer of hydrated ions and a diffuse outer (Gouy-Chapman) layer can be seen as two capacitors in series. Due to the bigger radius of the hydrated ions the dielectric constant of these two layers is significantly lower than that of pure water.

An equivalent circuit for the charge transition between the electrode and the electrolyte is known as Randles cell [6], which is depicted in Fig. 3

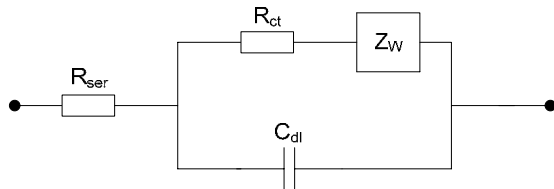


Figure 3: The Randles cell consists of a serial resistance  $R_{ser}$ , a charge transfer resistance  $R_{ct}$ , the capacitance of the double layer and the Warburg impedance  $Z_W$  [7].

Out of the measured impedance spectra the properties of the fluid can be extracted by data fitting. This has to be done by cautiously selecting the proper equivalent circuit, representing the measured fluid, the electrode to fluid transition as well as the fluid camber and substrates. Depending on the composition of the fluid the properties of the double layer are defined; i.e. the thickness of the double layer, distance of the inner layer to the electrode as well as the electro-chemical potential. Furthermore, if biological cells are present in the fluid, some of them will stick to the surface and change resistance, capacitance and equivalent circuit as well.

To show how the impedance function is affected by the applied isolation layer we measured the impedance signal of Air, DI Water and different NaCl concentrations in DI water trough different isolation layers and determined the relation between the impedance of the fluid filled setup and the non filled setup as an indication whether the isolation layer is compatible to impedance spectroscopy or not. The measurement was performed in the range from 40Hz to 110 MHz. A series of measurements up to 1.8 GHz was performed to rule out additional kinks in the transfer function. The pure capacitive progression confirmed the validity of the used equivalent circuit.

The actual capacitance of the double layer does not only depend on the ions of the electrolyte but also on the geometry of the electrodes. The distance between

the impedance electrodes affects the resistance and the capacitance. This can be used to change the absolute level of the measured impedance functions and to shift the Warburg impedance and double layer capacitance in the measurable frequency range.

In Fig. 4 the measured impedance spectra of deionised water and of 0,9% NaCl concentration in deionised water through different isolation layers are shown. In both parts of Fig. 4 the same mechanism can be seen: The impedance function of DI water in direct contact with the gold electrode (blue curve) is most sensitive and with decreasing capacitance of the isolation layer the transfer function loses its characteristics; see green, red and turquoise curve.

To conserve the original properties of the impedance function, the overall capacitance of the isolation layer has to be increased by the use of high permittivity materials and hydrophobic layers as thin as possible. Examples for high permittivity materials can be Tantal-pentoxide  $Ta_2O_5$  or Zirconium oxide  $ZrO$ . Thin hydrophobic layers can be implemented by using hydrophobic self assembled monolayers (SAM) or mixtures of nanoparticles of high permittivity materials with hydrophobic fluorinated polymers. The calculated specific capacitance of layers structured to that specification is two orders of magnitude higher than the conventional aluminium oxide ( $Al_2O_3$ ) plus Teflon PTFE layer; compare with Table 1.

### V - Conclusion

Combining impedance spectroscopy as a sensor principle with electro wetting on dielectrics as an actuator for lab-on-a-chip applications is advantageous because of the common electric nature of both.

The standard isolation layers used in EWOD setups show capacitances which are dominating the transfer function. To improve the sensitivity of the measured transfer function through an isolating layer the capacitance has to be increased. Measurements on various material combinations have to be performed to validate the feasibility of significant impedance measurements in an EWOD actuated system. Achieving this, the IS electrodes can be integrated in an EWOD electrode array covered by a common isolation layer. Thus, a cost effective sensor element for various lab-on-a-chip applications can be realized.

### Acknowledgment

This work was financed by the Austrian Science Fund FWF under contract no. L442-N14 and partially supported from the Austrian Center of Competence in Mechatronics ACCM.



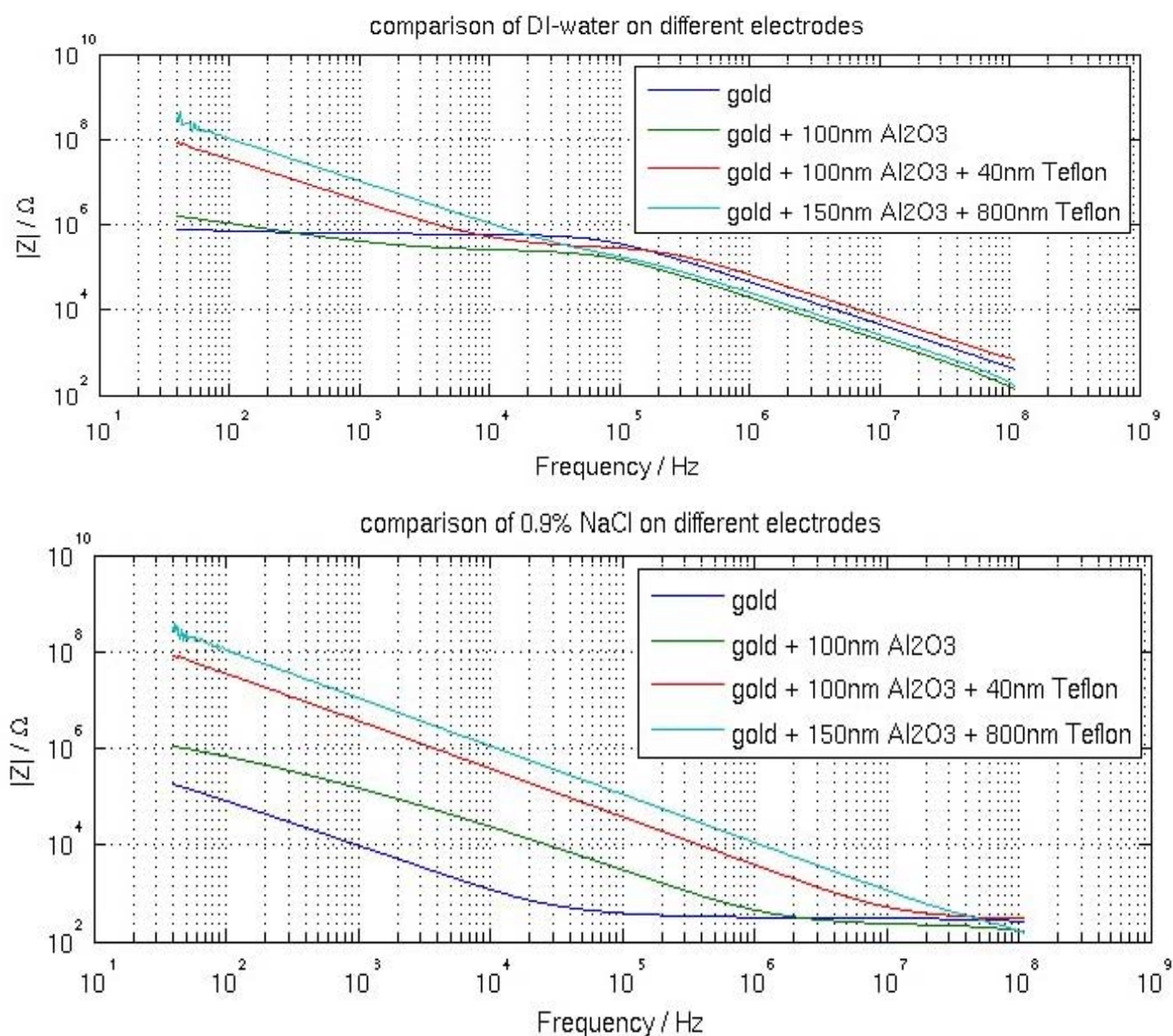


Figure 4: Impedance measurements on a 5  $\mu$ l DI water droplet (upper figure) and a droplet of a 0.9% NaCl solution (lower figure) resting on different surfaces. With increased thickness and breakdown strength of the isolating layers the characteristics of the impedance spectrum is getting dominated by the systems decreased capacitance.

## References

- [1] S.K. Cho, H. Moon and C.-J. Kim; *Journal of Microelectromechanical systems*, Vol. 12, No.1; (2003)
- [2] V. Srinivasan, V.K. Pamula and R. B. Fair; *Miniaturisation for Chemistry, Biology & Bioengineering*, 2004
- [3] M.G. Pollack, *PhD thesis, Duke University*, 2001
- [4] E. Barsoukov and J.R. Macdonald, *Impedance spectroscopy*, second edition, *Wiley Inter-science*, 2005
- [5] Y. Li, W. Parkes, Les I. Haworth, A. W. S. Ross, J. T. M. Stevenson, and A. J. Walton, *Journal of Microelectromechanical systems*, vol. 17, no. 6, December, 2008
- [6] J.E.B. Randles, *Disc. Faraday Soc. No 1*, 11-19, 147
- [7] E. Warburg, *Ann. Phys. Chem.* 67, 493-499, 1899

# STICTION REDUCTION IN ELECTROSTATIC POLY-SiGe MICROMIRRORS BY APPLYING A SELF-ASSEMBLED MONOLAYER FILM

Fangzhou Ling<sup>1,2</sup>, De Coster Jeroen<sup>1</sup>, Roel Beernaert<sup>3</sup>, Wan-yu Lin<sup>1,2</sup>, Celis.Jean Pierre<sup>1,2</sup>, De Wolf Ingrid<sup>1,2</sup>

<sup>1</sup>imec, Kapeldreef 75, 3001 Heverlee, Belgium

<sup>2</sup>Dept MTM, KULeuven, Katseelpark Arenberg 44, 3001 Leuven, Belgium

<sup>3</sup>CMST, Ghent University, Belgium

**Abstract** — This paper discusses for the first a study on stiction of poly-SiGe micromirrors and the effect of a SAM layer. This investigation mainly focuses on analyzing the hysteresis in the displacement-versus-voltage characteristic of these electrostatic devices. The width of the ‘pull-in window’ is used as an indication of the amount of mirror-to-surface stiction. Differences in the pull-out voltage of mirrors within an array indicate varying levels of stiction from mirror to mirror. A reduction of stiction is realized by applying a FDTS SAM layer which is deposited by vapor-phase deposition. In addition, the effect of different electrode configurations and hinge length is evaluated.

**Keywords:** MEMS, MicroMirror, Stiction, SAMs

## I - Introduction

The large surface-area-to-volume ratios of Micro Electro Mechanical Systems (MEMS) bring the role of stiction into the foreground [1]. As a fundamental catastrophic failure mechanism for most micromechanical systems, a thorough investigation should be carried out on stiction. Stiction is the term used in the MEMS field to describe undesired adhesion, which can be divided into two categories [2]: release-related stiction and in-use stiction. Release-related stiction is present during the release process when the surface tension of the draining rinse liquid draws the microstructure into contact with the underlying substrate due to capillary forces. In-use stiction occurs when the components of the device intentionally or accidentally come into contact and remain into contact for a longer period than specified for. This strongly affects the reliability and long-term durability of MEMS devices, and is a serious problem in fabrication and application of MEMS devices.

Poly-Silicon MEMS stiction has been widely studied and reported in recent years. Many experimental techniques have been developed specifically to examine the surface-surface interaction involved in silicon microstructures. Several chemical modification methods are proposed to reduce stiction [1-3].

Polycrystalline silicon germanium (poly-SiGe) is being studied as a promising material for MEMS monolithic integration because of its excellent mechanical properties and ability to be integrated together with signal processing electronics on the same CMOS

substrate. However, no studies exist that investigate stiction in SiGe MEMS on device level [4].

The main purposes of the present paper are using a poly-SiGe electrostatically-actuated torsion micromirror array as a test vehicle to study the stiction sensitivity of SiGe MEMS and also trying to reduce stiction by applying a self-assembled monolayer (SAM) through vapor phase deposition.

## II - Experimental Details

### A. Poly-SiGe micromirror array

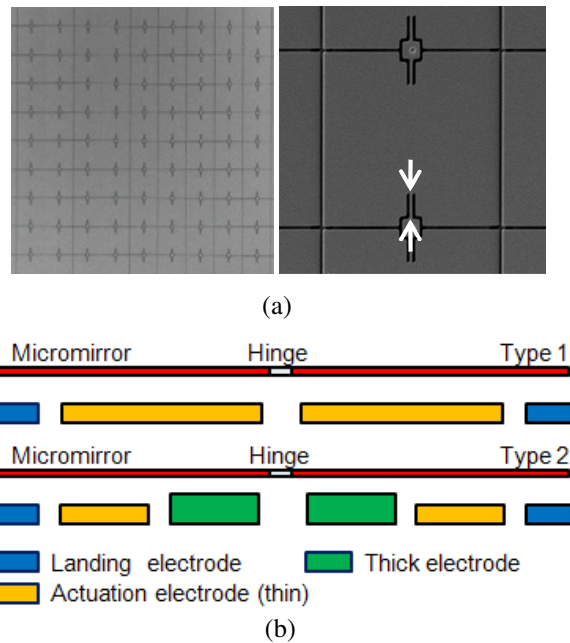


Figure 1: (a) Top-view SEM picture of micromirror array. Arrows indicate hinge length (b) Cross-section schematic picture of a single micromirror.

Table 1: Parameters of micromirror arrays

Sample	Width	Hinge length	Electrodes configuration
A1	15 $\mu\text{m}$	3 $\mu\text{m}$	Type 1: Thin electrodes
A2	20 $\mu\text{m}$	3 $\mu\text{m}$	
B1	20 $\mu\text{m}$	2 $\mu\text{m}$	Type2: Thin and thick electrodes
B2	20 $\mu\text{m}$	3 $\mu\text{m}$	
B3	20 $\mu\text{m}$	4 $\mu\text{m}$	

The devices investigated in this study are electrostatically actuated micromirror arrays made of poly-SiGe

for optical imaging applications [4, 5], see Fig. 1. The micromirror arrays are fabricated by a CMOS compatible SiGe platform and are laid out in arrays of either 22x22 or 16x16 mirrors. Arrays with two different mirror sizes (15 $\mu\text{m}$  and 20 $\mu\text{m}$ ) have been used. In addition, the hinge length (indicated by the arrows in Fig. 1) varied between 3 $\mu\text{m}$  and 4 $\mu\text{m}$ . Moreover, two different designs of the electrodes below the micromirrors were compared. Arrays A1, A2 have two actuation electrodes and two landing electrodes, both of which have a height 0.4  $\mu\text{m}$ . However, arrays B1, B2, B3 have a more complicated electrode configuration, which has two thin electrodes, landing electrodes and two 0.6  $\mu\text{m}$  thick electrodes. The main difference among samples B1, B2, B3 is the length of the hinge. The detailed parameters are listed in Table 1.

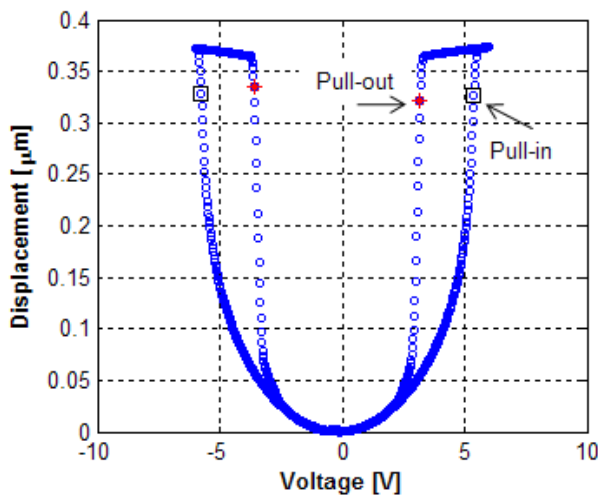


Figure 2: Typical electrostatically actuated device voltage displacement characteristic

When electrostatically actuated, the micromirrors tilt and the angle of rotation depends on the actuation voltage applied between the micromirror and bottom electrodes. The mechanical restoring force is a linear function of the displacement yet the electrostatic force is a quadratic function of the same displacement. In static equilibrium state, the electrostatic force and the mechanical restoring force between the micromirror and the electrode underneath are equal. As the applied voltage increases, the micromirror is electrostatically attracted towards the electrode and at a certain value the electrostatic force beats the mechanical restoring force and the micromirror pulls into the most extreme point near to the attracting electrode. The corresponding voltage value is called pull-in voltage. The micromirror pulls into the most extreme position at which a dedicated object landing electrode leads to obstruction. Once the micromirror and landing electrode come into contact, another factor, namely the adhesion force, may have a large impact on the operational characteristic. When the applied voltage decreases, at a certain value the mechanical restoring force beats the electrostatic and adhesion forces, and the mirror releases. This occurs at a voltage which is called pull-out voltage [6]. One such typical characteristic is shown in Fig. 2.

## B. Experimental setup

A schematic overview of the experimental setup is presented in Fig. 3. The experiment was performed in ambient atmosphere at room temperature. A low frequency (1kHz) bipolar triangular waveform generated by a waveform generator is amplified twenty times and applied to one of the thin actuation electrodes, which results in the displacement of the micromirrors. The out-of-plane movements are recorded by a Polytec laser-Doppler vibrometer (LDV) as a function of time. The laser is focused and measures at points near the edges of mirrors, which show the longest displacement. From these optical measurements, the pull-in voltage and release or pull-out voltage were determined. This information could not be obtained electrically because the capacitance change due to pull-in or pull-out is too small to be measured.

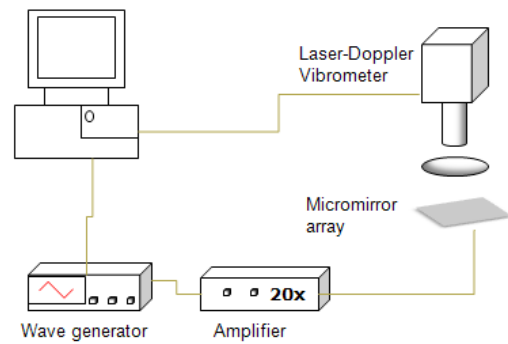


Figure 3: Experimental setup for tracking and recording device displacement

## C. Vapor-phase SAM deposition

Surfaces coated with a SAM are exceedingly hydrophobic. SAM also is molecularly thin (FDTS is about 1.4nm), which means it will not have substantial influence on the bulk materials properties. In this study, the chlorosilane based precursor 1H, 1H, 2H, 2H-perfluorodecyltrichlorosilane (FDTS) was used to produce SAM on the micromirror arrays. A pretreatment procedure is needed before starting the SAM deposition process. The samples firstly should be treated in Ultraviolet-Ozone for 30 minutes to clean and reoxid-

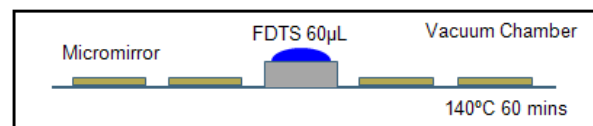


Figure 4: Vapor phase SAM deposition

ize the surface for SAM formation to occur. Then the samples were immediately loaded into the process chamber together with FDTS precursor. Afterwards, the chamber was heated up to 140 °C with a reduction of the pressure to 0.2 mbar. As a result, the FDTS precursor evaporates and creates a saturated atmosphere consisting of film molecules which react on the surface



and form the FDTD SAM. After 60 minutes, the samples were taken out and examined by contact angle measurement.

### III - Results and Discussion

#### A. Contact angle measurement

There are few articles discussing the surface energy of SiGe in the literature, so contact angle measurements were performed on blank SiGe films as a quick method to investigate the effect of applying a self-assembled monolayer. Like silicon, there is also a very thin native oxide layer existing on top of a SiGe film, which induces a high surface energy. As shown in Fig. 5, the water contact angle on a blank SiGe film is about  $16^\circ$ . After depositing SAM FDTD, the surface becomes hydrophobic, the water contact angle dramatically increases to  $125^\circ$ , which suggests FDTD is successfully deposited on the surface and lowers the surface energy.

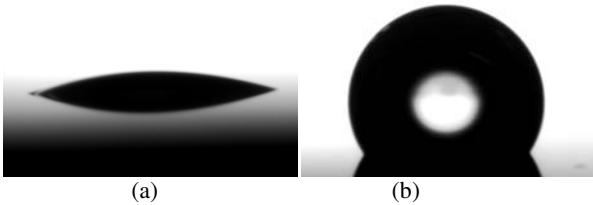


Figure 5: Water contact angles on (a) blank poly-SiGe and (b) a FDTD-coated poly-SiGe surface

#### B. Micromirror Array without FDTD SAM Test Results

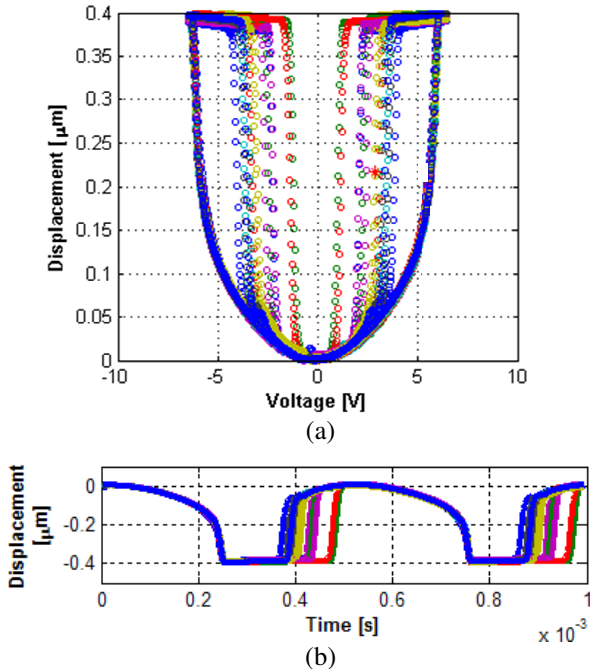


Figure 6: (a) Measured pull-in and pull-out voltage curve of mirrors from array B3 without FDTD top layer (b) Displacement of the mirrors of array B3 as a function of time when a triangular actuation voltage waveform is applied.

In a second type of experiment, the functional parameters of a micromirror array were measured before and after deposition of the SAM.

First, measurements were performed on the micromirror arrays without FDTD deposition. As shown in Fig. 6, the displacement is plotted as a function of the applied voltage for a micromirror array of type B3. It is observed that all mirrors in the array pull in at a consistent voltage which has a small standard deviation of 0.03V. However, the pull-out voltage of the mirrors on the same array exhibits a significantly larger variation and the standard deviation is 0.61V.

The low spread on the pull-in voltage of mirrors implies that the mechanical properties of different mirrors are identical. The pull-in voltage is primarily dominated by the elastic restoring force of the torsion hinges and the electrostatic force generated by the field between the bottom electrode and the mirror. The pull-out voltage on the other hand is also influenced by the adhesion force between the mirror and the landing electrode. Consequently, the remarkably high spread of the pull-out voltage can be attributed to differences in adhesion between the landing electrodes and the micromirrors. The mirrors do not stick permanently, but are clearly affected by adhesion forces.

The principal adhesion force between two surfaces in standard atmospheric conditions is the capillary force. Due to their high surface energy, the existence of hydrophilic native oxides on the surfaces makes them extremely sensitive to moisture which could increase the capillary force.

A detailed summary of results from the other arrays is presented in Table 2. For all kinds of mirror arrays, the spread on the pull-out voltage is one order of magnitude larger than the variation of the pull-in voltage. Furthermore, according to the dimension of the micromirrors, with the same electrodes configuration, the longer the hinge length, the larger the variation of the pull-out voltage shift. This can be explained by the stiffness of the torsion hinge decreasing with increasing length. This makes the elastic restoring force smaller compared to the adhesion force and thus makes the mirrors more sensitive to adhesion.

#### C. Micromirror Array with FDTD SAM Test Results

The performance of the micromirror arrays is clearly improved after FDTD SAM deposition. As presented in Table 2, there is a marginal increase of the pull-in voltages while the pull-out voltages of all the micromirrors increase significantly. While without SAM, the absolute value of the pull-out voltages for array B3 ranged between about 1 and 4 V (see Fig. 6), now this spread is much smaller and centered around about 4 V (Fig. 7). This is a clear signal of the reduction of stiction. The pull-out is with SAM mainly determined by the elastic restoring force of the mirrors. As an example again, Fig. 7 presents the operating characteristic of the same mirror array B3 after FDTD SAM deposition. Compared to operating curves of untreated mirrors, the variation of the pull-out voltage of mirrors with FDTD SAM is obviously reduced. The remaining spread is probably due to fabrication variations, roughness and

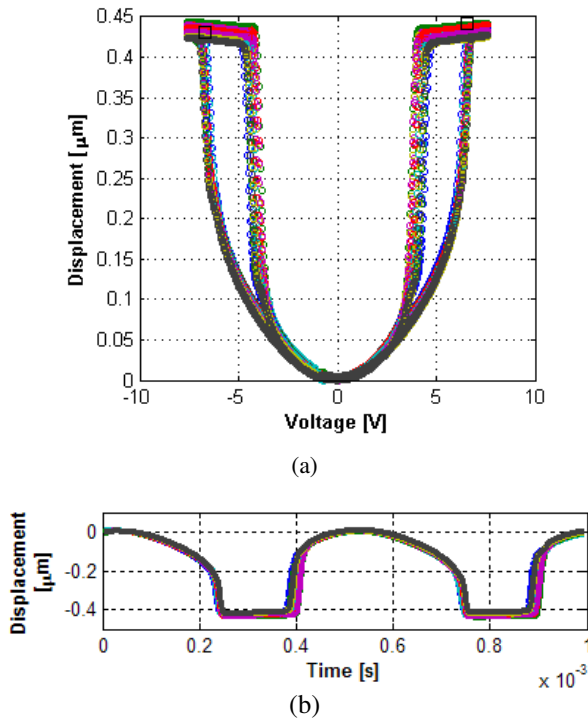


Figure 7: (a) Measured pull-in and pull-out voltage curve of mirrors from array B3 without FDTS deposition (b) Displacement of the mirrors of array B3 as a function of time when a triangular actuation voltage waveform is applied.

Table 2: Detailed results of tested samples and standard deviation

Samples	Pull-in ( $\pm$ ) [V]		Pull-out ( $\pm$ ) [V]	
	$\mu$	$\sigma$	$\mu$	$\sigma$
<b>Without SAM</b>				
A1	13.515	0.96%	8.4	8%
A2	7.39	0.81%	4.22	13%
B1	7.34	0.67%	4.85	8%
B2	6.4	0.59%	3.8	12%
B3	4.96	0.60%	2.82	22%
<b>With FDTS SAM</b>				
A1	13.53	0.96%	9.37	3%
A2	7.73	0.78%	5.1	5%
B1	7.56	0.66%	5.49	4%
B2	6.59	0.61%	4.55	5%
B3	5.29	0.57%	3.65	5%

other weak adhesion forces such as Van der Waals forces, chemical bonding, etc. Additionally, Fig. 8 presents the comparison of the coefficient of variation (ratio of standard deviation to mean value) of the pull-out voltage after SAM deposition which clearly indicates the relation between hinge length, mirror size and variation of pull-out voltage. For the mirrors (A1, A2) with the same hinge length, the stiction mainly depends on the size of the micromirror, the larger size mirror has a higher possibility to have stiction. However, for the mirrors (B1, B2, B3) with same size, the one with the

lower stiffness is more sensitive to the stiction, as can be expected.

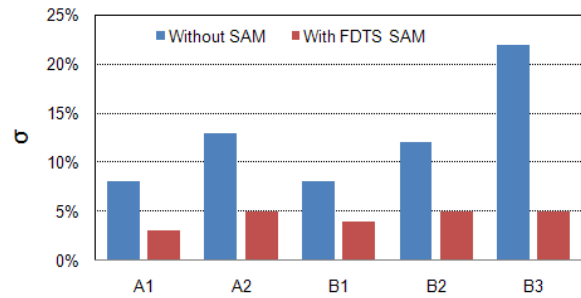


Figure 8: Comparison of coefficient of variation of pull-out voltage

#### IV - Conclusion

In this paper, micromirror arrays made using poly-SiGe as a structural material are used as a test vehicle to study stiction in SiGe MEMS. The micromirrors are different in size, hinge length and electrode configuration. FDTS SAM was successfully deposited by vapor-phase deposition. Contact angle measurements showed that the SAM layer modified the surface properties and reduced the surface energy. Untreated micromirror arrays showed a large variation of the pull-out voltage indicating a non-neglectable effect of adhesion forces. However, micromirror arrays with SAM layer exhibited a much reduced spread of pull-out voltage.

#### Acknowledgments

The authors acknowledge the contribution of many imec colleagues. The SBO project 'GEMINI' is also greatly acknowledged.

#### References

- [1] R.Maboudia and R.T.Howe, "Critical review: Adhesion in surface micromechanical structures," J.Vac.Sci.Technol. B, 15, 1-20, 1997
- [2] Kim BH, et al. A new organic modifier for anti-stiction. J Microelectromech Syst, 10 (1): 33-40, 2001
- [3] Roya Maboudian, Self-assembled monolayers as anti-stiction coatings for MEMS: characteristics and recent developments, Sensors and Actuators A: Physical, 82 (1-3), 219-233, 2000
- [4] Ann witvrouw, CMOS-MEMS integration today and tomorrow, Scripta. Mater, 59, 945-949, 2008
- [5] Roel Beernaert, Novel micromirror design with variable pull-in voltage, Microelectron. Eng, 87, 1248-1252, 2010
- [6] J. De Coster, Design and characterisation of RF-MEMS components, PhD thesis, KULeuven, 35-38, 2006

# A BRIDGE-CONNECTED ISOLATED SILICON ISLANDS POST-PROCESSING METHOD FOR FINE-GRAIN-INTEGRATED $\pm 10\text{V}$ -OPERATING CMOS-MEMS BY STANDARD 5V CMOS PROCESS TECHNOLOGY

Satoshi Morishita<sup>1</sup>, Masanori Kubota<sup>1</sup>, Kunihiro Asada<sup>1</sup>, Isao Mori<sup>1</sup>, Frédéric Marty<sup>2</sup>, and Yoshio Mita<sup>1</sup>

<sup>1</sup>The University of Tokyo, Japan. [mems@if.t.u-tokyo.ac.jp](mailto:mems@if.t.u-tokyo.ac.jp)

<sup>2</sup>ESIEE, Université Paris Est, France.

**Abstract** — A fine-grain integrated monolithic CMOS MEMS post-processing method is proposed. One simple two-mask Deep Reactive Ion Etching (DRIE) on an SOI wafer produces isolated silicon islands of electrical circuits and deep MEMS structures in one batch. Careful combination of anisotropic and isotropic DRIE made it possible to produce suspended fine electrical feed-through bridges to connect isolated silicon islands each other. The method is to be applied at the end of the process sequences, so that no special process tuning is required for CMOS fabrication (one may simply substitute bulk silicon with SOI). Another novelty is that the method can provide individual transistors whose substrates are separated one from another, thus opening a large opportunity to electrical circuits that have been suffered from the “connected substrate” of standard Integrated Circuits. In the paper the fabrication example of 4 to 20  $\mu\text{m}$ -wide, 50 to 400  $\mu\text{m}$ -long  $\text{SiO}_2$  bridges is reported. Also, a method to realize high-voltage (0-to-10V) MEMS driver circuit out of substrate-isolated 5-V standard CMOS transistors is proposed and demonstrated.

**Keywords:** VLSI, CMOS-MEMS, post-process, bridge feedthrough, isolated substrates, high voltage switch

## I – Introduction

VLSI and MEMS integration or CMOS-MEMS technologies exist since long time. Two major issues of the CMOS-MEMS were process compatibility and high working voltage. A number of process integration technologies as well as high-voltage devices have been proposed; however almost all these technologies required modification of process recipe and or process sequences, so that each technology is in principle dedicated to, or only available at, the company where the process was developed. Therefore it is fair to say that the impact of the proposed processes to the community have been limited. Foundry service exist since decades, but standardization have been the big issue due to the nature of MEMS is diversity; each MEMS may require his own device structures such as device thickness.

The authors propose to solve all above-mentioned issues by an universal method that may make use of an existing CMOS fabrication process for high voltage CMOS-MEMS. The method applies to the Silicon-On-Insulator (SOI) CMOS-MEMS fabrication as shown

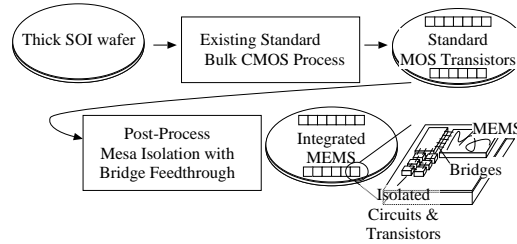


Figure 1: *Proposed Universal CMOS-MEMS Scheme. A Bulk CMOS Transistor Circuits are made on Thick SOI wafer. The Post-Process Makes Isolated Islands of Transistors, Circuits, and MEMS.*

in Figure 1. The idea is to fabricate standard CMOS circuits on a thick SOI wafer without any modifications of process sequences nor recipes. The fabricated SOI wafer is then post-processed to isolate circuits and MEMS part. Individual circuit blocks are connected by electrical feedthrough wires that have been fabricated in the standard CMOS process. The SOI silicon under the feedthrough is removed by post-process to realize air-suspended micro bridges.

The clear advantages of the proposed method are listed below:

1. **Fast CMOS Process Development:** The idea is to simply replace a bulk Si wafer with a thick SOI wafer. Many VLSI-MEMS integration methods such as [1] require processing of deep trench isolation prior to CMOS fabrication, and not so many foundries can accept pre-processed wafers.
2. **Isolated Transistor Substrates:** Bridge Forming process is highly controllable process; Thickness of remaining SOI silicon can be controlled from a couple of microns down to zero micron (i.e. only wiring materials will be suspended.). So each SOI islands are electrically isolated one from another. This is the critical advantage over standard Integrated Circuit, on which back gates of transistors are connected through substrate. By isolating individual transistor, one can set backgate bias to any voltage needed, thus enabling high-voltage switching by means of series of standard 5V transistors.

In the following sections, the post-processing method of the suspended micro-bridges and 10-V switching by 5V transistors simulation are presented.

## II – Suspended Bridge Feedthrough Fabrication

The process chart is shown in the Figure 2. The process intelligently combine passivation and isotropic etching to etch-out underlying silicon below the bridge feedthrough. The bridge releasing process is a variant of SCREAM process [2][3]: Etching the bottom of DRIE MEMS structure by long isotropic etching. New discovery in the authors' proposed method is that the remaining silicon thickness is controllable by initial DRIE depth, passivation thickness and isotropic etching time. Another suspended-bridge formation process using two equipments of  $\text{XeF}_2$  silicon etcher and deep RIE is found in the literature[4]. Although the one-batch DRIE process is much simpler than  $\text{XeF}_2$  process, these two are the identical in principle.

In the CMOS LSI circuit design, bridge feedthrough is drawn. The isolated part can be connected either or both by poly-silicon and metal wiring layer. MEMS part is left blank; only  $\text{SiO}_2$  layer on bare SOI silicon layer is laid as-delivery.

All lithography must be done before any deep etching process to avoid practical difficulties. This principle is known as “Delay-Mask” or “embedded-masking-method” [5]. Firstly, the MEMS structure as well as bridges are patterned on the  $\text{SiO}_2$  part. Then the isotropic etching window is patterned with thick (2.6  $\mu\text{m}$  was used) resist over the hard-mask pattern. Using the resist mask layer, a Deep-RIE is performed at first, then the process recipe is switched to  $\text{SF}_6$ -only isotropic etching. Then the soft-mask is removed by plasma- $\text{O}_2$  ashing and the MEMS structure is etched by deep RIE using embedded hard mask.

### A. Bridge Feedthrough Fabrication Results

The authors used a 4-inch Silicon wafer for the first prototyping device. For the rapid prototyping, the patterns were exposed by high-throughput Electron Beam Writer. The  $\text{SiO}_2$  was etched by high density (ICP) plasma etcher. After the second exposure, the wafer was etched by Deep-RIE apparatus to form undercut isolation and subsequently MEMS devices.

Fabricated Feed-Through test structure is shown in Figure 3. The widths of fabricated bridges were from 4 to 20  $\mu\text{m}$ , and lengths were from 50 to 400  $\mu\text{m}$ . Undercut as well as remaining bridge height can be controlled in proportion to the isotropic etching time. The longer the  $\text{SF}_6$  time is, the thinner the silicon becomes, and finally will be etched out from the bottom and side directions. The long isotropic etching ends up with  $\text{SiO}_2$  suspended bridges as shown in the Figure 4.

### B. Application to Other Types of Structures

By using the same process recipe, it is possible to fabricate different types of structures that may be useful for applications such as micro chemical systems. 200  $\mu\text{m}$ -long cantilevers (Figure 5) was fabricated as the demonstration of post-release etching. As shown in Figure 6, the third etching can be performed as well, to

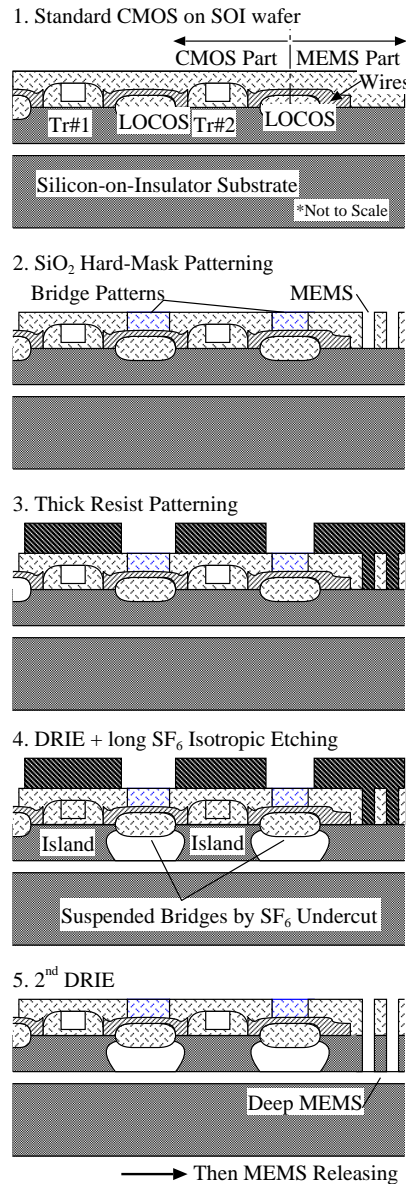


Figure 2: Two-mask One-batch DRIE makes MEMS, isolated MOS devices, and suspended bridges feedthrough.

form three-step multiple height.

## III – Zero-to-10V MEMS driving switch out of 5V transistor islands

The latter half of the important feature enabled by the bridge-feedthrough method is that transistors in the islands are electrically isolated each other. Which means that the circuit designer can treat transistors as if they are “discrete” components bought at an electronic shop. Substrates are isolated so that the voltage can be independently defined to any value by the circuit designer. In the standard CMOS Integrated Circuit on the other hand, substrates are connected so that dynamic range of the substrate (or well) potential has been limited. To demonstrate the benefit of isolated substrate



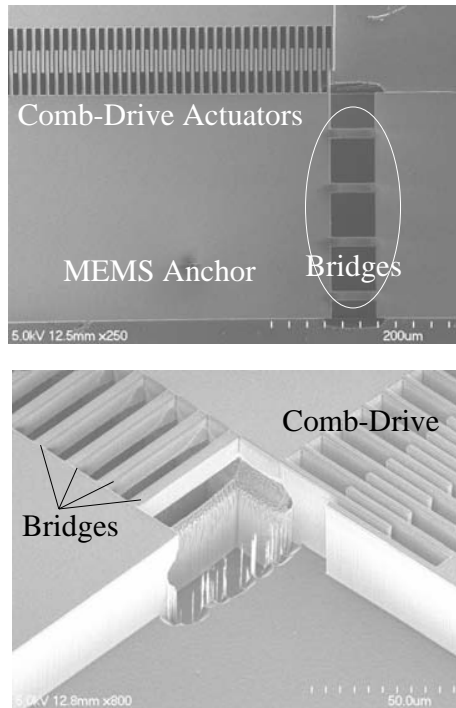


Figure 3: Fabricated Silicon Bridge Structure co-fabricated with comb-drive actuators

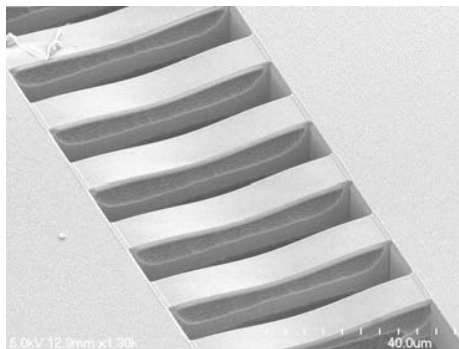


Figure 4: Longer Isotropic Etching etches out the underlying silicon. The bridge is only with SiO<sub>2</sub> in the SEM view.

biasing, a 0-to-10V MEMS driving switch is fabricated. Each transistors are working on 0-to-5V and the total circuit outputs 0-to-10V.

#### A. Working principle and prototyping

As shown in the Figure 7, the idea of high-voltage switch is to share voltage by series of transistors. To support 10V for example, two transistors NMOS1 and NMOS2 are connected in series; NMOS1 and NMOS2 take parts of 0V-5V and 5V-10V respectively. The isolated island transistors can sustain such configuration by tying substrate of NMOS2 to 5V (Source of NMOS2). The same principle is not realizable by the standard CMOS, in which both substrates must be tied to ground level so that NMOS2 suffers from threshold voltage

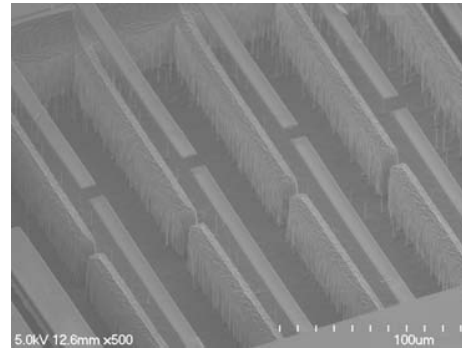


Figure 5: Demonstration of Silicon Cantilever. Bridge was cut in the middle by DRIE.

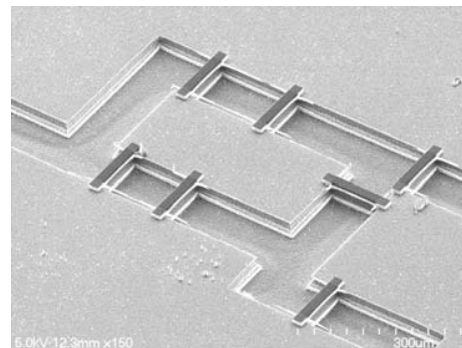


Figure 6: Demonstration of Triple heights etching (Known as Königsberg's Bridges)

alternation by back gate bias.

Following the successful simulation of  $2 \times V_{DD}$  switching inverter, the authors have fabricated a prototype using discrete enhancement-type CMOS transistors (2SK982 and 2SJ148, Toshiba.  $V_{th}$ : 2.5V). Figure 8 shows prototype circuit schematic and oscilloscope waveform. Operating frequency is 3kHz. The waveform clearly shows that individual transistors are working under 5V (plus some overshoot), and total circuit gives 10V.

#### B. MEMS actuator driving demonstration

Because capacitance is used as the level shifter for high-side transistor (PMOS1), the 10V driving circuit cannot handle static (or low-frequency) command. For static oscillate - non-oscillate operation of MEMS devices differential or bipolar driving technique can be applied as shown in Figure 9. When phases A and B are in the same phase (Figure 8(b)), there is no voltage difference so microactuator does not move, and in case of the anti-phase (Figure 8(a)) there are  $\pm 10V$  in between actuator electrodes. The principle has been successfully confirmed using stroboscopic microscope with rotational comb-drive microactuator having resonant frequency of 3kHz: Actuator moved at anti-phase driving and stood still at in-phase signals.



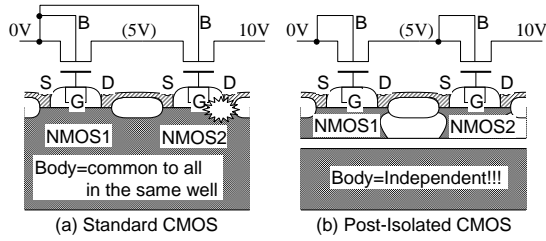


Figure 7: Isolated transistors chain can support higher voltage than the breakdown voltage.

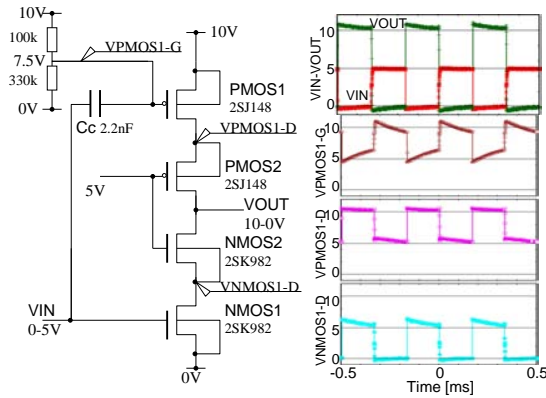


Figure 8: Measurement result of 0-to-10V MEMS driving switch prototype.

#### IV – Conclusions

A post-process method to fabricate isolate substrates with bridge feedthrough is demonstrated. Fabricated minimum bridge width have been  $4 \mu\text{m} \times 50 \mu\text{m}$  though not limited to. Application structures such as suspended long cantilevers and three-height bridge-islands are demonstrated. As one of the most critical advantages that have not been claimed for CMOS-MEMS field to the authors' knowledge, use of substrate-separated transistors is discussed. High-voltage switch out of standard-transistors was designed and prototyping is successful. The first SOI IC using standard CMOS recipe, on which HV circuits are to be fabricated is underway through VLSI Design and Education Center's Multi-chip project.

#### References

- [1] K. Takahashi et. al., *Int. Conf. on Solid-State Sensors, Actuators and Microsystems (Transducers 05)*, pp. 417–420.
- [2] K. A. Shaw et. al., *Sensors and Actuators A*, **40**, pp. 63-70.
- [3] E. Sarajilc et. al., *J. Micromech. Microeng.*, **14**, pp. S70-S75.
- [4] H. Takao et. al., *Int. Conf. on Micro Electro Mechanical Systems (MEMS2008)*, pp. 359–362.
- [5] M. Mita et. al., *IEEE Trans. on Sensors and Micromachines*, **120-E**, No.11, pp. 493–497.

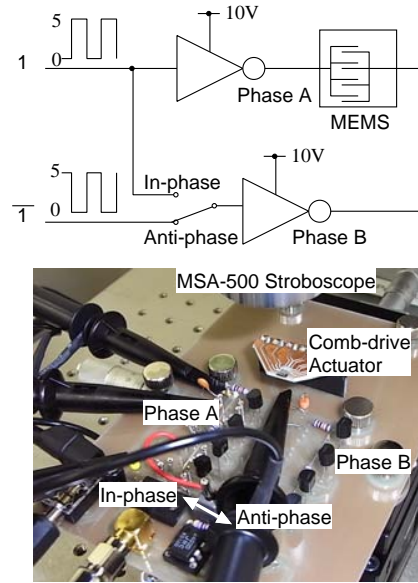


Figure 9: MEMS actuator operating experimental setup.

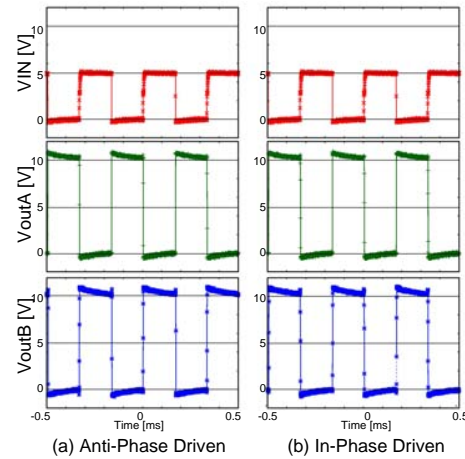


Figure 10: Measured driving voltage waveforms. Actuator worked only for anti-phase driving.

#### V – Acknowledgments

The CAD patterns used in this work were designed with Cadence Virtuoso that is accessible through the University of Tokyo, VLSI Design and Education Center (VDEC)'s academic program and directly patterned on a SOI wafer by using the VDEC's 8-inch EB writer F5112+VD01 donated by ADVANTEST Corporation. Alcatel ICP-RIE MS-100 is proprietary of 21<sup>st</sup> century Center of Excellence programs and maintained by Takeda Sentanchi Device Laboratory (AIMD: Advanced Intellectual Materials and Devices Laboratories). Toyotsu Electronics VAN partners is acknowledged by its FESEM Hitachi S-4700. Mr. Takemasa Komori helped for SPICE simulation. The work is partially supported by MEXT Nanotechnology Network Project and Global COE projects of the University of Tokyo "Secure-life Electronics" and "Mechanical Systems Innovation", Japan Society of Promotion of Science (JSPS) Grant-in-aid: 20686024, New Energy Development Organization BEANS project

# SINGLE-MASK THERMAL DISPLACEMENT SENSOR IN MEMS

B. Krijnen<sup>1,2</sup>, R.P. Hogervorst<sup>1</sup>, J.B.C. Engelen<sup>3</sup>, J.W. van Dijk<sup>1,2</sup>, D.M. Brouwer<sup>1,2</sup>, L. Abelmann<sup>3</sup>

<sup>1</sup>DEMCON Advanced Mechatronics, Oldenzaal, the Netherlands

<sup>2</sup>Mechanical Automation, IMPACT, University of Twente, the Netherlands

<sup>3</sup>Transducer Science and Technology, MESA<sup>+</sup>, University of Twente, the Netherlands

**Abstract** — In this work we describe a one degree-of-freedom microelectromechanical thermal displacement sensor integrated with an actuated stage. The system was fabricated in the device layer of a silicon-on-insulator wafer using a single-mask process. The sensor is based on the temperature dependent electrical resistivity of silicon and the heat transfer by conduction through a thin layer of air. On a measurement range of 50  $\mu\text{m}$  and using a measurement bandwidth of 30 Hz, the 1-sigma noise corresponds to 3.47 nm. The power consumption of the sensor is 209 mW, almost completely independent of stage position. The drift of the sensor over a measurement period of 32 hours was 32 nm.

**Keywords :** MEMS, thermal displacement sensor, silicon resistivity, lumped model, SOI, manipulator, precision stage

## I - Introduction

The trend towards smaller and more accurate systems stimulates the use of MEMS applications with integrated actuators and sensors. An electrostatic comb-drive actuator is often used for the actuation of an elastically straight-guided stage. Position sensing in MEMS is often based on the varying capacitance between the fixed world and an actuated stage [1]. Some alternative position sensors use integrated optical waveguides [2], the piezoresistive effect [3], or varying thermal conductance [4, 5, 6]. Lantz et al. [4] demonstrate a thermal displacement sensor achieving nanometer resolution over a 100  $\mu\text{m}$  range. However a multi-mask production process and manual assembly were needed to fabricate this displacement sensor together with a stage. In this work we present the design, fabrication and experimental validation of a thermal displacement sensor integrated with an actuated stage in a single-mask production process.

The thermal displacement sensor consists of two U-shaped resistive heaters in a differential configuration, as schematically shown in figure 1. A differential sensor configuration is chosen to make the sensor less sensitive to changes common to both heaters, like ambient temperature and air humidity. The temperature distribution over the heaters depends on the stage position, because an increased overlap of the heater with the stage causes increased cooling of the heater towards the stage. Heat transfer to the stage is dominated by thermal conductance through air. The electrical resistivity of silicon is highly dependent on temperature and therefore the electrical resistance of the heater is a measure for the stage position. Applying a constant voltage to both

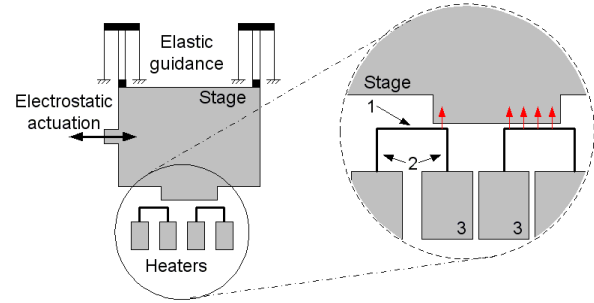


Figure 1: Schematic design of the integrated thermal displacement sensor. Each heater structure consists of a sensing part (1), two legs (2) and two bondpads for mechanical and electrical connection (3). The heat flow from the heaters to the stage is dependent on stage position.

heaters, the stage displacement is measured by the difference in current through the heaters. The temperature dependent electrical resistivity of highly p-doped silicon ( $\approx 2 \cdot 10^{18} \text{ cm}^{-3}$ ) is given by [7] and is shown in figure 2.

## II - Modelling and design

A lumped-element model of the thermal sensor is created in 20-sim [8] in order to obtain a dynamic multi-physics model. The model elements, shown in figure 3, include among others the non-linear temperature dependent electrical resistivity of silicon, the temperature dependent thermal conductivity of silicon and the temperature dependent thermal conductivity of air. The elements of the model consist of a heat capacity coupled to an electrical resistance. The temperature of the heat capacity ( $^{\circ}\text{C}$ ) determines the electrical resistance ( $^{\circ}\Omega$ ) which in turn determines the dissipated power in the heater element. The model is used for the determination of several design parameters with respect to the sensor

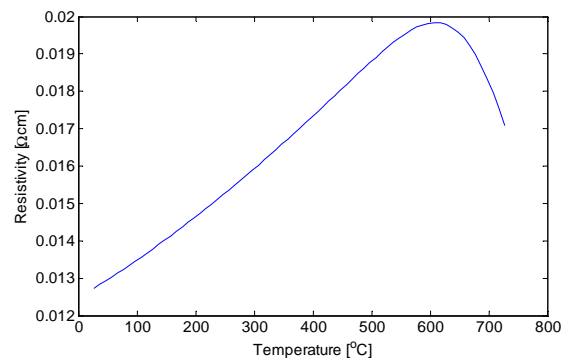


Figure 2: Resistivity of highly p-doped silicon ( $\approx 2 \cdot 10^{18} \text{ cm}^{-3}$ ) as a function of the temperature.

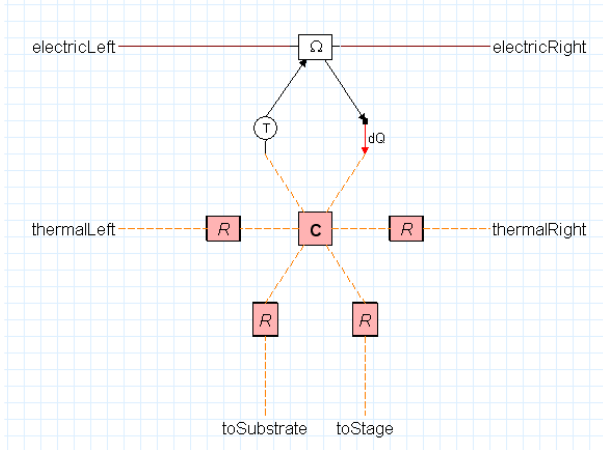


Figure 3: Lumped model element of the thermal sensor. The top of the diagram shows the electrical resistance ( $\Omega$ ). The thermal capacity ( $C$ ) is connected with multiple thermal conductivities ( $R$ ). Interaction between the electrical and thermal domain is included in the element ( $T$  and  $dQ$ ).

sensitivity, power balance and temperature profile over the heaters. The lumped element model has been verified by finite element modelling in COMSOL Multiphysics [9].

The heater dimensions are chosen such as to maximize the power flow towards the stage with respect to the input power and the heater resistance. The length of the heater legs influences the thermal conductance and therefore the power flow towards the bondpads and directly towards the substrate. The heater legs have a length of 100  $\mu\text{m}$  and the sensing part has a length of 60  $\mu\text{m}$ , which limits the measurement range of the sensor. Minimum feature size and minimum trench width are both 3  $\mu\text{m}$ , dictated by the DRIE process. The heater width and air-gap between the heaters and the stage therefore are 3  $\mu\text{m}$ . The height of all structures is 25  $\mu\text{m}$ , defined by the SOI device layer thickness.

Table 1: Power balance for the differential sensor configuration at maximum deflected position for a fixed heater voltage of 7.7 V. In maximum deflected position of the stage, one of the heaters has no overlap with the stage and the other heater has full overlap with the stage.

	Heater 1: No overlap (mW)	Heater 2: Full overlap (mW)
Stage	0.56	6.29
Bondpads	78.93	77.92
Substrate	21.75	19.60
Radiation	0.09	0.07
<b>Total</b>	<b>101.33</b>	<b>103.88</b>

At an operating voltage of the heaters of 7.7 V and at maximum deflection of the stage, heater 1 at no overlap and heater 2 at full overlap, the power flow from heater 1 to the stage is 0.56 mW and the power flow from heater 2 to the stage is 6.29 mW. The power balance of the differential sensor configuration is shown in table 1. It shows that most of the power supplied to the sensor will be lost towards the bondpads and di-

rectly towards the substrate. Heat transfer due to radiation is negligible in this configuration.

Using the 20-sim lumped-element model, the temperature profile over the heater is modelled, figure 4. From no overlap to full overlap it is clear that the heat flow towards the stage increases and therefore the temperature of the heater decreases. At no overlap the maximum temperature is 712 K and at full overlap the maximum temperature is 664 K. As a result the resistance of a single heater drops from 585.1  $\Omega$  to 570.7  $\Omega$  for the given temperature profiles at no and full overlap respectively. This roughly corresponds to a sensitivity of 0.58  $\Omega/\mu\text{m}$  at 7.7 V heater voltage for the differential configuration.

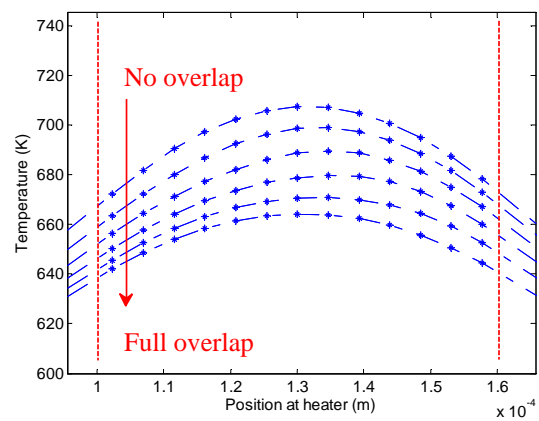


Figure 4: Temperature profile over the heaters as a function of stage overlap. The sensing part of the heater is located in between the vertical lines. The heater voltage is 7.7 V and the overlap ranges from 5  $\mu\text{m}$  (no overlap) to 55  $\mu\text{m}$  (full overlap).

The differential sensor is integrated in the system design. The stage is actuated using electrostatic comb-drives [10]. The stage uses four double folded flexures as a straight guidance mechanism to ensure parallel movement with respect to the heaters. The straight guidance also prevents the complete stage from snap-in due to electrostatic forces perpendicular to the direction of motion of the stage.

### III - Fabrication

The designed sensor was micromachined in a SOI wafer with a highly boron-doped ( $\approx 2 \cdot 10^{18} \text{ cm}^{-3}$ ) device layer of 25  $\mu\text{m}$  thickness and a buried oxide layer of 1  $\mu\text{m}$ . Aspect-ratio controlled deep-reactive-ion etching (DRIE) was used to etch through the full device layer of the wafer. The directional etching and resulting high aspect ratios are particularly useful for good mechanical behaviour of the leafsprings used for straight guiding the stage, resulting in low driving stiffness and high transversal and out-of-plane stiffness. A minimum trench width of 3  $\mu\text{m}$  is used, restricted by the used DRIE process. A maximum trench width of 50  $\mu\text{m}$  is used to prevent large variations in etch loading. Etch loading effects influence the etch rate and the subsur-

face profile development [11]. For this reason several etch compensation structures are included in the design.

After reactive ion etching, the structures were released from the substrate by isotropic etching of the buried oxide with vapour-HF. Thin structures ( $<10\text{ }\mu\text{m}$ ) and perforated bodies are released from the substrate in this way. Large structures will stay mechanically fixed to the substrate, while being electrically isolated from the substrate due to the oxide layer. The resulting design is shown in figure 5. The fabricated devices are glued and wire bonded with thin aluminium wires to a PCB for measurement.

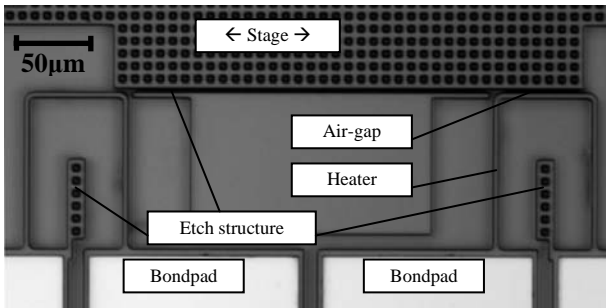


Figure 5: Top view, optical microscope image of the fabricated sensor with the stage in its rightmost position. 'Etch structures' are incorporated to increase the DRIE quality.

#### IV - Experimental results

A constant voltage is applied across both heaters. Due to varying stage overlap, the heater resistances and the resulting heater currents will change. The two heater currents are amplified using two equal current-to-voltage amplifiers. The second amplifier stage consists of a differential voltage amplifier in combination with a low-pass filter to reduce common noise. The stage deflection as a function of actuation voltage is measured by stroboscopic video microscopy measurements, performed with a Polytec MSA400 and its Planar Motion Analyzer software. Interpolation of the measurement data provides accurate information about the actual stage position at a specified actuation voltage. For a deflection of  $25\text{ }\mu\text{m}$  an actuation voltage of around  $80\text{ V}$  is required.

At a heater voltage of  $9\text{ V}$  the displacement versus sensor amplifier output voltage was quasi-statically measured, shown in figure 6 (top). The sensor output varies between  $-0.776\text{ V}$  and  $4.316\text{ V}$ , with an offset of  $1.770\text{ V}$  due to an initial resistance mismatch of the two heaters. The resistance variation of a single heater over the measurement range of  $48\text{ }\mu\text{m}$  is determined to be  $25.3\text{ }\Omega$ . In a differential configuration this results in a sensitivity of  $1.056\text{ }\Omega/\mu\text{m}$ .

Figure 6 also shows the nonlinearity of the measurement signal with respect to stage displacement. Considering the non-linear effects in the electrical resistivity of silicon as a function of the temperature and the fairly large temperature fluctuation over the sensing part of the heater, the differential sensor is surprisingly linear. A non-linearity of the sensor of approximately

$\pm 40\text{ mV}$  ( $\pm 400\text{ nm}$ ) was measured. Using a polynomial fit of the amplifier output voltage with respect to stage displacement and subtracting the fit from the measurement signal, the resulting noise signal has an approximate Gaussian distribution with a 1-sigma value of  $3.47\text{ nm}$ . This data was measured using a low-pass filter with a bandwidth of  $30\text{ Hz}$ . Due to the fairly large temperature fluctuation over the sensing part of the heaters, the sensitivity of the sensor decreases slightly towards the outer boundaries of the measurement range, at large deflections of the stage.

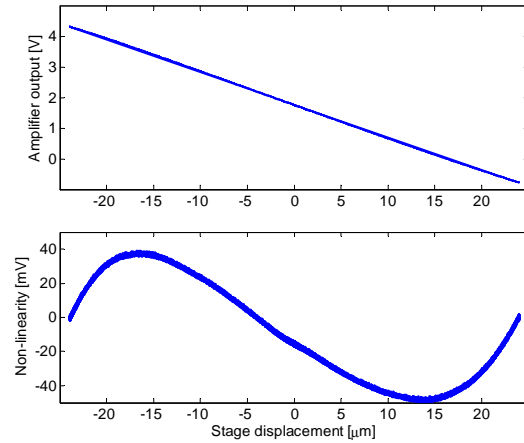


Figure 6: Quasi-static measurement of the amplifier output voltage as a function of stage displacement at a heater voltage of  $9\text{ V}$  (top). The bottom figure shows the deviation from a linear fit ( $106\text{ mV}/\mu\text{m}$ ) of the amplifier output voltage with respect to the stage displacement.

Figure 7 shows that the measured sensitivity is highly dependent on the heater voltage. A maximum sensitivity was reached at a heater voltage of  $10\text{ V}$ ,  $1.247\text{ }\Omega/\mu\text{m}$ . The measured sensitivity curve is related to the resistivity curve of silicon as a function of temperature (figure 2) in two ways: a) the power flow from heater to stage and b) the resulting change in electrical resistance. The power flow from heater to stage (a) is determined by the temperature difference between heater and stage and therefore the temperature 'setpoint' on the resistivity curve. The change in electrical resistance (b) as a result of the power flow from heater to stage is dependent on the slope of the resistivity curve at the temperature setpoint.

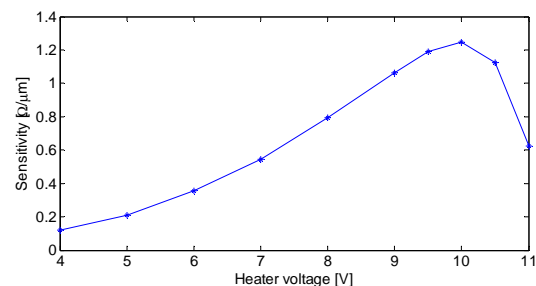


Figure 7: The measured sensor sensitivity as a function of the applied heater voltage.



Figure 8 shows the resistance of a single heater when a step voltage is applied from 0 V to 5 V. A change in resistance from 435.3  $\Omega$  to 474.9  $\Omega$  was measured. A first order exponential was used to make an approximation of the thermal time constant of the heater. The behavior of the sensor matches really well with a first order fit with a time constant of 165  $\mu$ s. A second time constant of 30 ms was measured, most likely caused by local heating of the substrate underneath the heater. Constant usage of the sensor prevents this time constant from showing up in the measurements. A startup time of around 200 s is necessary for the complete system to reach a thermal equilibrium. Since the power dissipation of the differential sensor configuration is nearly independent on stage position, the thermal steady state situation of the complete system will not be affected and will therefore not have any influence on the measurement.

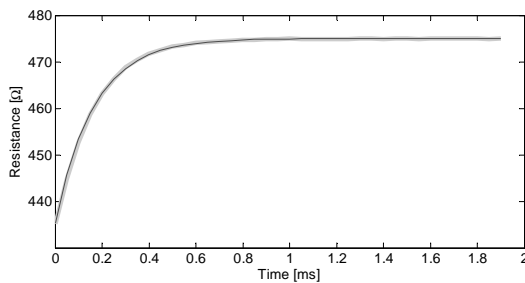


Figure 8: The thermal time constant of a single heater is 165  $\mu$ s: measured (light grey) and exponential fit (dark grey).

A drift measurement was performed with the differential sensor. Without the control of ambient temperature and air humidity, the drift of the sensor was determined to be 32 nm over a measurement period of 32 hours. A run-in time of several days was required to remove long-term drift. For example thermal oxidation [7] and thermal activation of oxygen [12] are effects that can change the thermal and electrical properties of the silicon material. Both effects will stabilize in a time period of multiple days.

## V - Conclusion

We have designed, fabricated and validated a thermal displacement sensor in MEMS. The sensor principle is based on the temperature-dependent electrical resistivity of silicon and the heat transfer by conduction through a thin layer of air. The sensitivity of the sensor is highly dependent on the applied heater voltage: sensitivities up to 1.247  $\Omega/\mu\text{m}$  were measured. The sensitivity of the sensor is determined by the power flow towards the stage, due to the temperature difference between heater and stage, in combination with the slope of the resistivity curve of silicon. The 1-sigma noise of the measurement signal corresponds to 3.47 nm at a measurement bandwidth of 30 Hz and with a power dissipation of 209 mW. The time response of the heater structures was determined to be 165  $\mu$ s, allowing a higher measurement bandwidth. The major advantage of

the presented thermal displacement sensor is that it can be easily integrated in the device layer of a SOI-wafer together with, for example, an elastically guided stage and electrostatic comb-drive actuation.

## References

- [1] A.A. Kuijpers, et al., *A micromachined capacitive incremental position sensor: Part I. Analysis and simulations*, Journal of Micromechanics and Microengineering, vol. 16, pp. S116-S124, 2006.
- [2] Y. Bellouard, et al., *High accuracy micro-displacement sensor with integrated optics-based detection means*, IEEE 2005 International Conference on Robotics and Automation, ICRA 2005.
- [3] N. Maluf, K. Williams, *An introduction to Microelectromechanical Systems Engineering*, Artech House, Boston, 2<sup>nd</sup> edition (2004)
- [4] M.A. Lantz, et al., *A micromechanical thermal displacement sensor with nanometre resolution*, Nanotechnology 16 p1089-1094 (2005).
- [5] Dauderstädt, et al., *Silicon accelerometer based on thermopiles*, Sensors and actuators A: physical, vol. 46, pp 201-204 (1995).
- [6] Petropoulos, et al., *A Novel Thermal Position Sensor Integrated on a Plastic Substrate*, Microelectronics Journal, vol. 40, pp. 1387-1392 (2009).
- [7] S.M. Sze, *Physics of semiconductor devices*, New York, Wiley, 3<sup>rd</sup> edition (2006).
- [8] Controllab Products B.V., *20-sim*, <http://www.20sim.com/>.
- [9] COMSOL, *COMSOL Multiphysics* <http://www.comsol.com/>.
- [10] R. Legtenberg, et al., *Comb-drive actuators for large displacements*, Journal of Micromechanics and Microengineering, vol. 6, pp. 320-329, 1996.
- [11] H.V. Jansen, *Black silicon method X: a review on high speed and selective plasma etching of silicon with profile control: an in-depth comparison between Bosch and cryostat DRIE processes as a roadmap to next generation equipment*, Journal of Micromechanics and Microengineering, vol. 19, pp. 1-41, 2009.
- [12] V. Cazcarra, P. Zunino, *Influence of oxygen on silicon resistivity*, Journal of applied physics, vol. 51, pp. 4206-4211, 1980



# ALGAN/GAN C-HEMT FOR PIEZOELECTRIC MEMS STRESS SENSOR APPLICATIONS

M. Vallo<sup>1</sup>, T. Lalinský<sup>1</sup>, G. Vanko<sup>1</sup>, M. Držík<sup>2</sup>, Š. Haščák<sup>1</sup>, I. Rýger<sup>1</sup> and I. Kostić<sup>3</sup>

<sup>1</sup>*Institute of Electrical Engineering of the Slovak Academy of Sciences, Bratislava, Slovakia*

<sup>2</sup>*International Laser Center, Bratislava, Slovakia*

<sup>3</sup>*Institute of Informatics, Slovak Academy of Sciences, Bratislava, Slovakia*

**Abstract** — In this paper we present for the first time a systematic investigation of the piezoelectric response of AlGaIn/GaN C-HEMT sensing device to be potentially applied for design of circular membrane based MEMS stress sensors. The measured C-HEMT sensor devices exhibit good linearity in the piezoelectric response under dynamic stress conditions. The measurements revealed excellent stress detection sensitivity that is independent on the measured frequency range. The sensitivity of the C-HEMT sensing devices can be easily increased by increase of the area of the Schottky gate ring electrode. The further increase of the sensitivity can be tuned by an optimal selection of the DC drain and gate bias.

**Keywords:** Stress sensor, AlGaIn/GaN, HEMT, piezoelectric response, cantilever structure, SiC

## I - Introduction

Group III-Nitrides (III-N) are very attractive for pressure and strain sensor applications due to their excellent piezoelectric properties [1]. In addition, comparing to other common used piezoelectric materials, they have some important advantages: (1) a direct compatibility with high electron mobility transistors (HEMTs) and high biocompatibility; (2) high mechanical stability of epitaxial films and therefore a possibility to integrate into micro(nano)-electro-mechanical system - M(N)EMS mechanical sensors; (3) possibility to operate at high temperatures due to their ability to preserve their piezoelectric properties in wide temperature range. Commonly, AlGaIn/GaN based devices exploit a fact that the piezoelectric polarization in the nitride layer can be changed by external forces. This change causes the corresponding change in the density of the 2DEG confined at the AlGaIn/GaN interface. As a result, we can obtain the gauge factor of the sensor, which means the relative resistance change,  $\Delta R/R$  subjected to the strain. Therefore, HEMTs but also Schottky diodes and resistors based on AlGaIn/GaN heterostructures could be very useful as sensing devices, especially for application in harsh environment or at high temperatures (e.g. the wings of an aircraft, in combustion engine, exhaust etc.) [2].

To investigate piezo-response of these devices the following approaches were currently reported: (a) a bulk device approach; (b) devices integrated on a bulk substrate cantilevers; (c) devices integrated on membrane structures.

The first approach (a) does not require the realization of suspended microstructures. The function is based on the action of hydrostatic pressure which alters Ni/AlGaIn Schottky barrier height, the internal fields in GaN/AlGaIn/GaN heterostructures and the polarization in AlGaIn/GaN heterostructure [3]. These effects are relatively small compared to the strain sensors exposed to bending. Thus, the realized sensor is sensitive to high pressure and the high mechanical stability of this structure favors such applications.

In the second approach (b) AlGaIn/GaN HEMT process technology is performed on a bulk sapphire substrate. The substrate with the integrated HEMT as a strain sensor is then cut out into a bulk cantilever structure. This structure is then exposed to bending [4, 5]. The resulting channel resistivity is measured in dependence on applied strain. It can be concluded from the obtained results that the interaction between piezoelectric and piezoresistive properties improves the sensitivity of pressure sensors by using AlGaIn/GaN heterostructures with confined 2DEG.

In contrast to SiC, the potential of group of III-nitrides for pressure sensors based on membrane structures (c) is much less evaluated. The difficulty to fabricate suspended AlGaIn/GaN heterostructure arises from the high chemical stability of group III-nitrides, which complicates the necessary undercutting techniques. A promising approach is the deposition of AlGaIn/GaN heterostructure on Si or SiC. Despite the high prospects of the 2DEG for mechanical sensors with internal amplification, only a few reports on membrane test structures are available [1, 6].

It should also be noted that in these studies the conventional devices such as HEMT, Schottky diode and 2DEG resistor were used to sense the external stress changes.

The main objective of this work is to evaluate for the first time the piezoelectric response of the circular HEMT (C-HEMT) as new device to be potentially applied for design of circular membrane based MEMS stress sensors. The process technology and methodology of the piezoelectric response investigation of the C-HEMT sensing device are presented.

## II - Experimental Details

We have proposed for the first time a circular HEMT device for external pressure and stress sensing. There are some advantages of this structure comparing to that of the conventional rectangular HEMT. First of all there is no "MESA"- etching step needed to define

C-HEMT, so the continuity of the top AlGaIn barrier layer is not broken and therefore, no partial relaxation of the applied bending stress is there observed. Likewise the ring gate of variable area can be easily patterned and gate leakage currents significantly suppressed due to absence of the gate edge tunneling effects. Finally, the circular symmetry of 2DEG channel is fully compatible with the circular AlGaIn/GaN membrane structure preferentially used for MEMS pressure sensors design. Undoped AlGaIn/GaN heterostructure grown by metal-organic chemical vapor-phase deposition (MOCVD) on SiC substrate was used to define C-HEMT device as schematically shown in Figure 1.

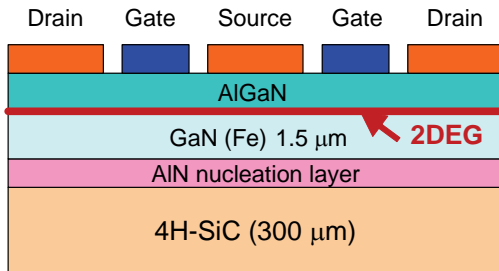


Figure 1: Schematic cross-section through C-HEMT sensing device.

The thicknesses of AlGaIn and GaN layers were 25 nm and 1.5  $\mu\text{m}$ , respectively. The aluminum mole fraction of the AlGaIn layer was nominally 0.25. The simple C-HEMT process technology consisted of circular source/drain ohmic contacts formed in the first step using Nb/Ti/Al/Au metallic system alloyed at 850  $^{\circ}\text{C}$  for 35 s. Ni/Au electron beam evaporation and lift-off were carried out subsequently to form the ring gate contacts of variable area in the second step. Finally, Ti/Au metallic layer was patterned on the top of alloyed ohmic contacts to improve device bonding.

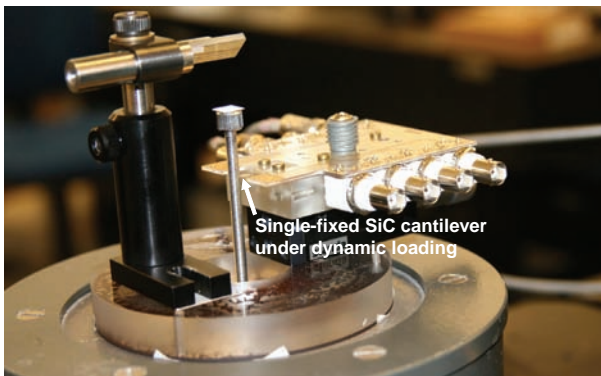


Figure 2: Experimental set-up used for measurement of C-HEMT piezoelectric response.

To investigate piezoelectric response of the C-HEMT device we have used an approach based on a bulk substrate cantilever structure. A rectangular SiC substrate cantilevers of the wide and length of 3 mm and 20 mm, respectively were sawed from the wafer and then fixed into the lucite block. The measured C-

HEMTs on the single-fixed SiC cantilever were then dynamically stressed with a certain frequency and amplitude of the deflection. These parameters of deflection were measured by using a laser vibrometer system. Both forcing and induced signals were displayed on the display of an oscilloscope. The experimental set-up used for measurement of C-HEMT piezoelectric response is shown in Figure 2.

Here it should be mentioned that the measured C-HEMT devices placed on the top of a bulk SiC cantilevers closely to the clamped point are under uniaxial loading that is not optimal in regard to the radial symmetry of these sensor devices.

### III - Results and Discussion

Previous research on strain detection using Al-GaN/GaN heterostructures has focused on exploiting their piezoresistive properties. The piezo-response was investigated under static strain loading [5], so a dominant piezoresistive effect was detected. A little effort has been directed toward the study of piezo-response that uses directly the piezoelectric transduction mechanism. The piezo-response with a dominant piezoelectric effect has been studied using the Schottky diode sensing structures for the first time in [7]. However, the sensing diodes were prepared on n-GaN epitaxial layer, so they did not include 2DEG channel based on AlGaIn/GaN. Therefore, in this chapter a dominant piezoelectric response of the C-HEMT sensing devices is investigated.

#### A. Piezo-response of Unbiased Ring Schottky Diode

The piezoelectric response of unbiased ring-type Schottky diode was measured as a function of the amplitude of the deflection with various excitation frequencies. There are analytical expressions in order to obtain the value of the external stress at point of the Schottky electrode derived from the amplitude of deflection.

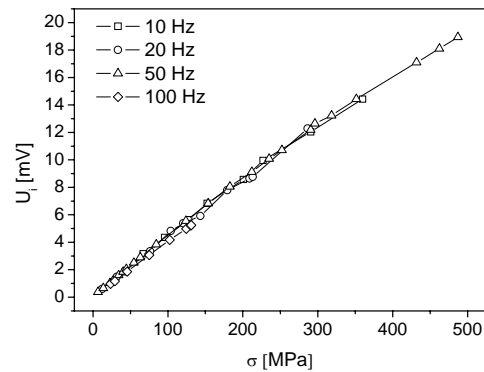


Figure 3: Induced voltage as a function of external stress at various frequencies.

Piezoelectric charge induced in the diode ring electrode was captured by a charge amplifier and evaluated on the display of the oscilloscope as an induced voltage. Figure 3 shows the induced voltage as a function of the external stress at various excitation frequencies. As we can see that unbiased Schottky diode exhibits a good linearity in the induced voltage. Moreover, the piezoelectric response does not depend on the frequency of the external stress. In order to obtain the maximum detection sensitivity of the sensor diode, the impact of the gate ring area was also investigated. Figure 4 reveals that the sensitivity increased with the increase of the diode ring gate area.

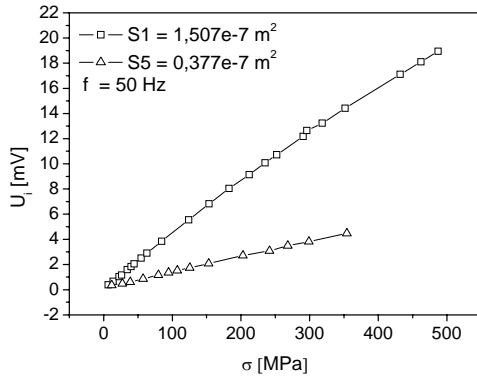


Figure 4: Induced voltage as a function of external stress at two different ring gate areas.

### B. Piezo-response of Circular Resistor

In order to obtain the stress dependent resistance of a circular resistor (C-resistor), the C-HEMT structure without ring gate electrode was employed. In practice that works as a stress dependent 2-DEG resistor. The distance between two ohmic contacts was 180  $\mu\text{m}$ . The C-resistor was placed near to the clamping point and the cantilever was dynamically strained at the free end with a frequency of 20 Hz. The current between ohmic contacts as a response to the deflection under different biasing conditions in the linear region (constant voltage 1V, 0,5V and 0,25V) as well as in the saturation region (constant voltage 8V and 6V) were measured.

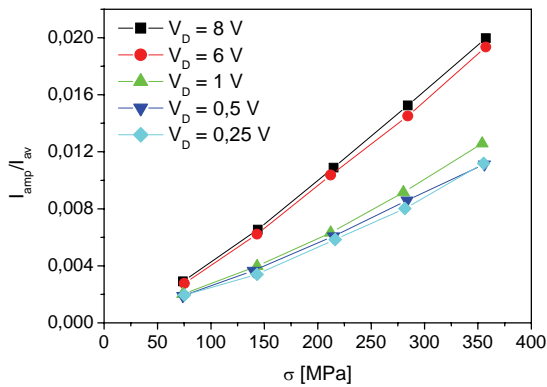


Figure 5: Relative change in induced current as a function of external stress at different voltages between ohmic contacts.

In Figure 5 the relative change (the amplitude in proportion to the average value) of the obtained current in response to the uniaxial stress is shown. The sensitivity of the C-resistor was increased with increasing the biasing voltage in the linear region of the resistor. We can achieve higher piezo-response of the measured resistor by biasing it to the saturation region but further increase of the biasing voltage does not affect the increase of the sensitivity to the external stress but the increase of the self-heating effect which is an unwanted case.

### C. Piezo-response of Circular HEMT

Finally, we investigated the piezo-response of the whole C-HEMT structure under the dynamic stress conditions. The source-drain voltage was kept constant ( $V_{DS} = 6\text{V}$ ) and the gate voltage was decreased with the constant step ( $V_G = 0, -1, -2, -3\text{V}$ ). This way we were able to ensure the well-defined and also well-controlled conditions in the HEMT channel and to monitor the changes of the drain current as a response to the applied stress. The same analysis as in the case of circular resistor was evaluated and it is shown in Figure 6.

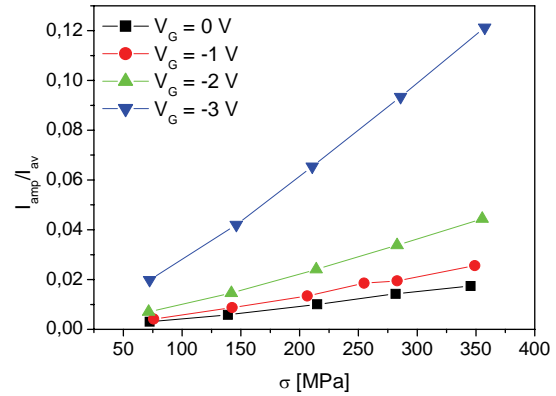


Figure 6: Relative change in induced current as a function of external stress at different gate voltages.

We found that decreasing gate voltage (which in practically means the decrease of the carrier concentration in the channel) causes the increasing sensitivity of the sensor device. The relative change in current response near the pinch off is approximately 6 times higher than at  $V_G = 0\text{V}$ .

## IV - Conclusion

In our work, we have investigated the possibility of dynamic stress detection using AlGaIn/GaN based circular high electron mobility transistors (C-HEMTs). In our knowledge, stress sensors in that account are introduced for the first time.

The piezo-response of three different C-HEMT deduced sensing structures such as unbiased ring Schottky diode, circular resistor and ring gate HEMT was evaluated. Unbiased ring Schottky diodes exhibit good

linearity in the piezoelectric response under dynamic stress conditions. The measurements revealed excellent stress detection sensitivity that is independent on the measured frequency range. The detection sensitivity of the diode can be easily improved by an increase of the area of the Schottky gate ring electrode.

Circular resistor showed good linearity in the measured range of the external stress values dependent on the voltage applied between ohmic contacts. It indicated the necessary to find optimal bias conditions to maximize the sensor signal and to avoid self-heating of the device.

Ring gate HEMT devices yielded the improved sensitivity to the external stress by decreasing the gate bias. The relative change in current response near the pinch off is approximately 6 times higher comparing to that at  $V_G = 0V$ .

In conclusion, it should also be mentioned that the piezo-response of C-HEMT sensing structures was investigated under uniaxial dynamic loading that is not optimal in regard to the radial symmetry of these sensor devices. Therefore, higher detection sensitivity of these devices could be expected by their integration directly on the AlGaIn/GaN circular membrane of the piezoelectric MEMS pressure sensors that are recently in progress.

## Acknowledgement

This work was supported in part by the following projects: - Slovak Research and Development Agency under the contracts APVV-0655-07, APVV-VVCE-0049-07, SK-FR-0041-09 and VEGA project 2/0163/09.

## References

- [1] V. Cimalla, J. Petzoldt and O. Ambacher, *J. Phys. D: Appl. Phys.* vol. 40, pp. 6386-6434, 2007.
- [2] S. J. Pearton, B.S. Kang, S. Kim, F. Rena, B. P. Gila, C. R. Abernathy, *J. Phys.: Condens. Matter* vol. 16, pp. 961-994, 2004.
- [3] Liu Y., Ruden P. P., Xie J., Morkoc H. and Son K. A., *Appl. Phys. Lett.* vol. 88, 013505, 2006.
- [4] Chia-Ta Chang, Shih-Kuang Hsiao, Edward Yi Chang, Chung-Yu Lu, Jui-Chien Huang, and Ching-Ting Lee, *IEEE Electron Device Lett.* vol. 30, pp. 213-215, 2009.
- [5] B. S. Kang, S. Kim, J. Kim, F. Rena, K. Baik, S. J. Pearton, B. P. Gila, C. R. Abernathy, C.-C. Pan, G.-T. Chen, J.-I. Chyi, V. Chandrasekaran, M. Sheplak, T. Nishida, S. N. G. Chu, *Appl. Phys. Lett.* vol. 83, pp. 4845-4847, 2003.
- [6] Zimmermann T., Neuburger M., Benkart P., Hernandez-Guillen F. J., Pietzka C., Kunze M., Dammiller I., Dadgar A., Krost A. and Kohn E., *IEEE Electron Device Lett.* vol. 27, pp. 309-312, 2006.
- [7] R.P. Strittmatter, R. A. Beach, J. Brooke, E. J. Preisler, G. S. Picus, and T. C. McGill, *J. Appl. Phys.*, vol. 93, pp. 5675-5681, 2003.

# A CAPACITIVE HUMIDITY SENSOR USING A POSITIVE PHOTSENSITIVE POLYMER

Nga P. Pham, Vladimir Cherman, Fabrice F.C. Duval, Deniz S.Tezcan, R. Jansen  
and Harrie A.C. Tilmans

*Imec, Kapeldreef 75, B-3001 Leuven, Belgium*

**Abstract**—This paper presents the fabrication and characterization of a capacitive humidity sensor using a polymer (CRC-8900) from Sumitomo Bakelite. One of the attractive features of this polymer is that it is photo-sensitive with positive tone and further that standard alkaline aqueous development is used. Furthermore, its low dielectric constant (3.2) and low cure temperature (250°C) makes it suitable for use in a CMOS compatible process. Characterization of the humidity sensor shows linear variation of relative capacitance change with relative humidity (RH) in the whole measurement range from 5% to 90% RH. The sensor's sensitivity is close to 160ppm/1%RH. The presented design of CRC-based planar humidity sensor defines a cheap and reliable alternative for humidity monitoring for zero- and first-level MEMS packages.

**Keywords :** Humidity sensor, positive photosensitive polymer, CRC-8900, CMOS compatible process.

## I - Introduction

With the growing of advanced technology, humidity sensors can find a lot of applications in our daily life. It is used in various industrial, agricultural and medical applications. Large production volume, high performance and small form factor of microsensors is demanded. It would be a great advantage if the microsensor can be fabricated in a CMOS compatible process. In this paper, we present the results of a capacitive humidity sensor development using a positive tone photosensitive polymer from Sumitomo, i.e., CRC-8900. There have been several works on humidity sensor using polymer, but most of them are based on polyimide, either non-photosensitive or photosensitive with a negative tone [1-3]. Positive tone has the advantage of aqueous development, which makes it easier to pattern with a very good resolution up to an aspect ratio of 1:2 and which directly compatible with standard photoresist processing. CRC further has the advantage of a low cure temperature (250°C) as compared to polyimide (which requires curing at 400°C). This makes it suitable for use in combination with wafer bonding and debonding (for 3D integration purposes).

## II - Experimental Details

### A. Humidity sensor fabrication

The humidity sensor is integrated as a post-CMOS process. After the completion of other devices, the

humidity sensor is integrated on top of a Cu Damascene CMOS back-end as the last processing on this wafer. A schematic drawing of the cross-section of humidity sensor on top of Cu back-end is illustrated in Figure 1.

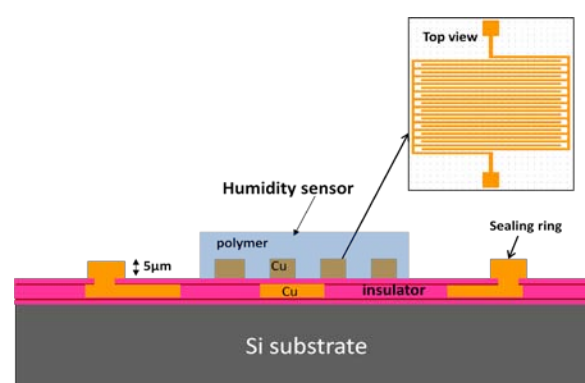


Figure 1: Schematic view of a humidity sensor integrated on top of Cu CMOS backend.

The capacitive sensor is designed in the form of interdigitated Cu electrodes with various lines and spacing. The Cu lines are 5µm thick. In this paper we have tested 2 types of interdigitated electrodes with lines and spacing of 15µm (so called humidity sensor H1) and with lines and spacings of 10µm (so called humidity sensor H2), as shown in Figure 2. The sensitive area of the sensor is about 780x780µm for H1 sensor and 530x570µm for H2 sensor.

The length of the interdigitated electrodes and the number of fingers are respectively, 700µm and 25 for the sensor H1 and 470µm and 27 for the sensor H2. The fabrication of the humidity sensor starts with a photolithography step of a thick resist (7µm) to define a mould for Cu plating of the electrode. Next, the Cu electroplating is used to form the 5µm thick Cu electrodes. After removing of the photoresist mould layer, a humidity sensitive layer is spincoated and patterned on top of the Cu interdigitated electrodes.



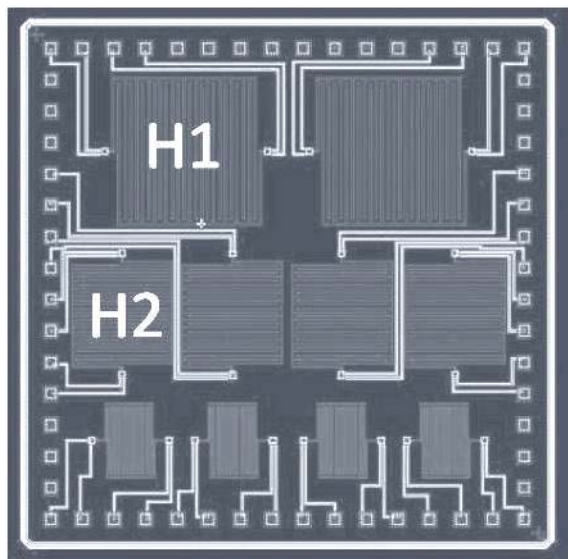


Figure 2: Image of a die containing humidity sensors of type H1 and H2 integrated on top of a Cu back-end.

#### B. Positive photosensitive polymer for humidity sensor

A positive photosensitive polymer from Sumitomo Bakelite (CRC-8900) is used as the moisture sensitive layer for the development of this humidity sensor. CRC-8900 is a positive tone photosensitive material with polybenzoxazoles (PBO) as a base resin (Fig. 3).

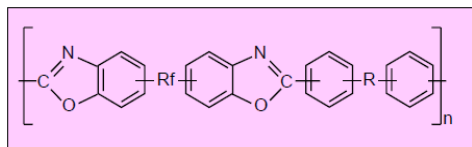


Figure 3: Based polymer of CRC-8900 with Rf: free fluorine group. (Courtesy from Sumitomo).

The material has some unique characteristics, which are more favorable than other commonly used polymers such as its low cure temperature (250°C), low dielectric constant (3.2), high lithographic resolution, and it is aqueous developable. For example, CRC has a lower cure temperature (250°C) compared to polyimide (400°C) due to a high cyclization rate with no cross linkage agent. This CRC material can coat a film thickness from 3-15µm depending on the spin speed.

For the fabrication of our humidity sensor, the CRC is applied after Cu plating of the electrodes. The CRC is first spun on the wafer and then is patterned using contact printing with I-line (365nm) UV energy. As coated, before curing, the thickness of the CRC layer is 9µm. The wafer is next cured at 250°C for 90min in an N<sub>2</sub> ambient. The thickness after cure is ~7µm. To measure the sensitivity of a humidity sensor, both sample with CRC cured and CRC non-cured are used. Figure 4 shows the SEM picture of a humidity sensor H1 from top view (of a design with 15µm lines and 15µm spacings).



Figure 4: Top view SEM picture (tilted) of fabricated humidity sensor.

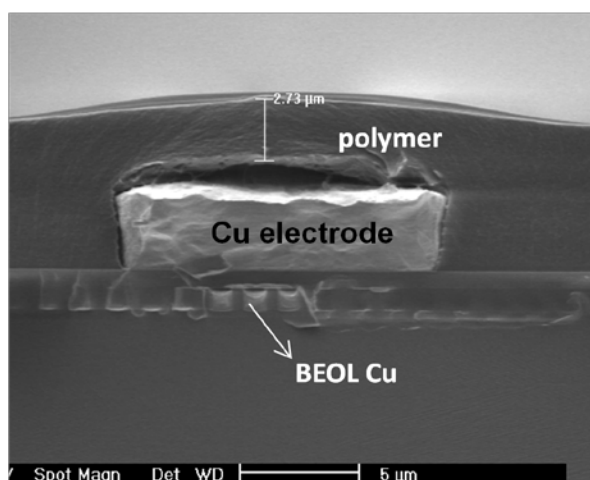


Figure 5: Cross-sectional view of the humidity sensor with Cu electrode and polymer on top. The CMOS Cu BEOL (back-end of line) is also visible (the delamination of polymer on Cu surface is due to the cleaving of sample for crosssection).

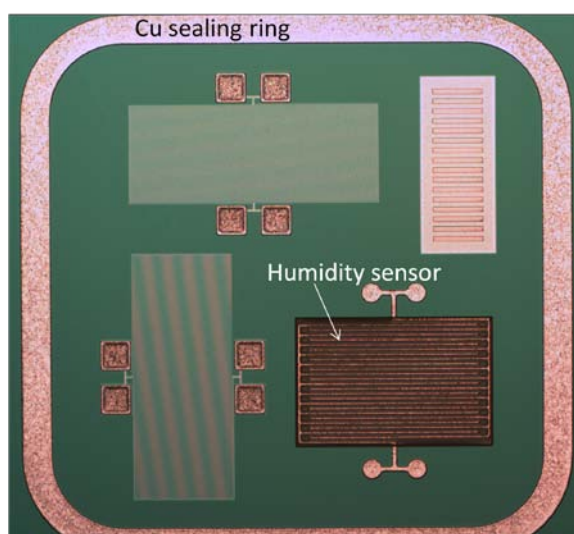


Figure 6: Optical picture of a humidity sensor inside a 0-level MEMS package.

Figure 5 shows a cross-sectional view of the polymer covering the Cu electrode, which is integrated on top of a wafer with Cu back end.

This humidity sensor was actually designed as a test vehicle for a MEMS 0-level package and allows testing of the hermeticity against humidity of micropackages. An optical image of such a micropackage before bonding, containing the humidity sensor integrated inside is illustrated in Figure 6. The sealing ring of the micropackage in Figure 6 is made by Cu being electroplated in the same processing step as the Cu electrode of the humidity sensor. Bonding of a capping chip will complete this micropackage.

### C. Electrical measurements

The wafers were diced and next the sensor chips were mounted in ceramic DIL-40 packages and placed inside a VGI2000M humidity chamber for test and characterization. Capacitance measurements were done using an Agilent E4980 precision LCR meter. The capacitance of the devices was monitored as a function of frequency of an ac carrier signal being swept between 500Hz and 1MHz and as function of relative humidity (RH). All the measurements were performed at a temperature of +23°C and at an amplitude of the ac signal of 10mV. Both cured sensors (at 250°C, 7µm thick) as well as non-cured (9µm thick) sensors H1 and H2 (as in Figure 2) were investigated. In addition, the capacitance measurements were carried out on sensors H1 without the CRC film and with the CRC non-cured films thinned down by dry etch. The dry etching is done in an oxygen plasma with a small amount of SF<sub>6</sub> for 3 minutes. The thickness of etched polymer was lowered down to 6µm. The effect of thickness of a (non-cured) CRC polymer film onto the sensor sensitivity is illustrated in Figure 7, where the relative capacitance change as a function of relative humidity of the sensor H1 is shown. The comparison is done between the humidity sensor with the full-thickness polymer (9µm), the one having partly etched CRC film (6µm) and the one without the polymer. The time between measurements at two different humidity levels was set to 10 minutes to minimize capacitance drifts and hysteresis effects. As was expected, it is clearly seen from Figure 7 that the capacitor having no polymer film is not sensitive to humidity variations. It is also seen that the thicker the polymer layer on top of the interdigitated electrodes, the higher the sensitivity of the sensor. This trend with increasing thickness is expected to hold true up to thicknesses of the polymer comparable to the spacing between the planar electrodes and their line width. However, the response time of the sensor to humidity change will also increase with the film thickness, thus a tradeoff between sensor sensitivity and the response time will have to be made.

The relative capacitance changes as functions of relative humidity for sensors H1 and H2 with cured polymer at 250°C and with non-cured polymer film are compared in Figure 8.

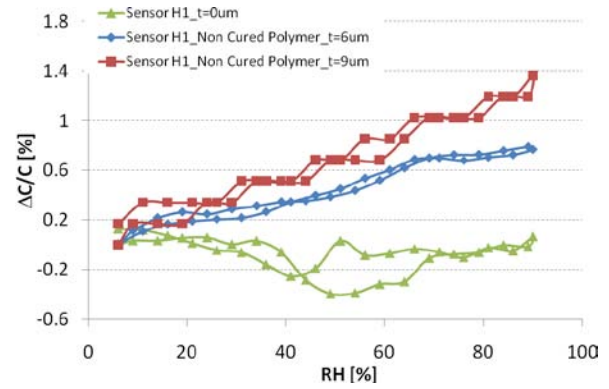


Figure 7: Relative capacitance change as function of relative humidity for sensors H1 (lines & spacings 15µm) with different thickness of the CRC polymer film. The measurements were done at a carrier ac frequency of 10kHz.

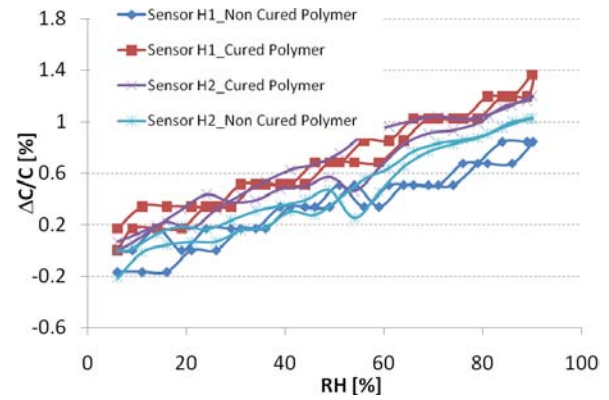


Figure 8: Relative capacitance change of sensors H1 and H2 as function of humidity. The measurements were done at a carrier ac frequency of 10kHz.

The sensors H1 and H2 having different electrode widths and spacings show similar capacitance versus humidity dependence. This dependence is linear in the whole humidity range between 5% RH and 90% RH and it can be translated to a sensor's sensitivity of close to 160 ppm/1% RH. This sensitivity was calculated using the following equation:

$$Sensitivity = \frac{C(90\% RH) - C(5\% RH)}{C(5\% RH)} \cdot \frac{1}{\Delta RH} \cdot 10^6 \left[ \frac{ppm}{1\% RH} \right]$$

where C(90% RH) and C(5% RH) are the capacitance values measured at 90% RH and 5% RH, respectively, and ΔRH=85% RH. A noticeable effect of curing on the sensitivity of the investigated humidity sensors was not observed.

The relatively small sensitivity (an order of magnitude smaller from what is published elsewhere [1], [4-5]) can be explained by a redistribution of the electric field between the sensitive polymer layer deposited on top and between the interdigitated electrodes, the SiO<sub>2</sub> layer under the electrodes, and the air above the polymer. This conclusion can also be confirmed by compar-

ing the capacitance values of sensors with and without the polymer presented as functions of frequency in Figure 9.

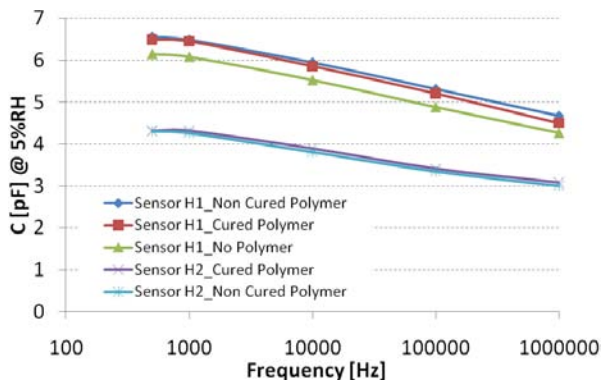


Figure 9: Capacitance of investigated humidity sensors measured as a function of frequency at a relative humidity fixed at 5%RH and at a temperature of +23°C.

It is seen, that the contribution of the CRC polymer film into the total capacitance of H1 capacitor is only 500fF (or 10% from the total capacitance of the sensor). From Figure 8, it is also seen that the change of the capacitance of the sensor is less than 0.7fF per 1%RH. These numbers and the measured sensitivity of the capacitor can be used to calculate the sensitivity of the CRC polymer film, which is an order of magnitude higher than the sensitivity of the sensor and equals 1600 ppm/1%RH. This value agrees well with experiments reported elsewhere [1], [4-5], where same order of magnitude sensitivity (1500-2600) ppm/1%RH is reported for humidity sensors in which the humidity sensitive dielectric material is sandwiched between metal plates [4], [5] or were similar planar interdigitated configuration is used but additional thick dielectric layer under metal electrodes is deposited to improve sensitivity [1].

The frequency dispersion of the capacitance observed even at very low humidity levels (<5%RH) and reported in Figure 9 can be explained by the significant contribution of the Si substrate to the total capacitance of the sensor. Minimizing the effect of the substrate will help in reducing the frequency dispersion and also in improving the sensitivity. However, it would require an increase of the thickness of the SiO<sub>2</sub> dielectric and/or replacing the substrate material which may make the sensor non-CMOS compatible and thus not acceptable from an integration point of view.

#### IV – Conclusions

The photosensitive positive tone polymer CRC-8900 is used for humidity sensing application for the first time. Fully CMOS compatible CRC based capacitive humidity sensors have been fabricated and characterized. The sensitivity of the sensors to humidity was measured to be 160 ppm/1%RH. Based on the experimental results it is theoretically shown that the sensitivity

of the CRC polymer film itself is much higher and equals 1600 ppm/1%RH, which is comparable with that of other materials (like polyimide) traditionally used in humidity sensors. However, its low curing temperature (250°C) and the possibility to avoid the curing step all together, makes the CRC-8900 a very attractive material for humidity sensors designed for 0-level MEMS packages and 3D integrated circuits where a low-temperature bonding process is utilized. The presented design of CRC-based planar humidity sensor is fully CMOS-compatible and does not require extra metal deposition steps on top of the polymer film.

#### References

- [1] J.Laconté, V.Wilmart, J.-P.Raskin, D.Flandre, "Capacitive humidity sensor using a polyimide sensing film", proc. DTIP of MEMS/MOEMS (2003), pp. 223-228, 2003.
- [2] C.Laville, C.Pellet, "Comparison of three humidity sensors for a pulmonary function diagnosis micro-system", IEEE Sensors Journal, vol. 2(2), pp. 96-101, 2002.
- [3] M.Matsuguchi, T.Kuroiwa, T.Miyagishi, S.Suzuki, T.Ogura, Y.Sakai, "Stability and reliability of capacitive-type relative humidity sensors using cross-linked polyimide films", Sensors and Actuators B, vol. 34, pp. 343-237, 1996.
- [4] A.K. Sen, J.Darabi "Modeling and Optimization of a Microscale Capacitive Humidity Sensor for HVAC Applications", IEEE Sensors Journal, vol. 8(4), pp. 333-340, 2008.
- [5] Ji-Hong Kim, Sung-Min Hong, Jang-Sub Lee, Byung-Moo Moon, and Kunyun Kim, "High Sensitivity Capacitive Humidity Sensor with a Novel Polyimide Design Fabricated by MEMS", Proc. Of the 2009 4<sup>th</sup> IEEE Int. Conf. on Nano/Micro Eng. And Molecular Systems, January 5-8, 2009, Shenzhen, China. pp. 703-706, 2009.

#### Acknowledgement

The authors wish to thank Geraldine Jamieson, Goele Potoms (imec) for helping with the polymer etching and XSEM, Philippe Soussan (imec) for his support for this project. This work was financially supported by the EC FP7 project MEMSPACK ([www.memspack.eu](http://www.memspack.eu)), under grant agreement nr. 223882, a collaboration between IMEC, VTT, FhG-ISiT, Univ. Perugia, FBK institute, CNRS-IEMN, and MEMS TC. The help and support given by the other partners of the project are greatly acknowledged.



# SILICON/GLASS MICROCHIP WITH A MONOLITHICALLY INTEGRATED ELECTROSPRAY IONIZATION TIP FOR MASS SPECTROMETRY

L. Sainiemi<sup>1</sup>, T. Nissilä<sup>2,3</sup>, V. Saarela<sup>4</sup>, R. A. Ketola<sup>3</sup> and S. Franssila<sup>1</sup>

<sup>1</sup>*Aalto University, Department of Materials Science and Engineering, FI-00076 Aalto, Finland*

<sup>2</sup>*University of Helsinki, Division of Pharmaceutical Chemistry, FI-00014 Helsinki, Finland*

<sup>3</sup>*University of Helsinki, Centre for Drug Research (CDR), FI-00014 Helsinki, Finland*

<sup>4</sup>*Aalto University, Department of Micro and Nanosciences, FI-00076 Aalto, Finland*

**Abstract** — In this paper we present the first miniaturized silicon/glass electrospray ionization (ESI) chip for mass spectrometry (MS). The microchips are made by bonding a silicon wafer, which has deep reactive ion etched micropillar-filled channels, together with a glass lid. Both the silicon channel and the glass lid have through-wafer etched sharp tips that enable stable electrospray without nebulizer gas or acids. The fabrication process utilizes only the standard microfabrication techniques and circumvents manual gluing of ESI tips. The sample transportation in the channel relies on pumping. The chips were coupled to a mass spectrometer and electrospray ionization performance of the chips was analyzed. We found out that the chips produce a stable electrospray at flow rate range of 100–5000 nl/min. The capability to analyze drugs with good sensitivity was demonstrated with mass spectrometric measurements.

**Keywords :** Microfabrication, Microfluidics, Electrospray ionization, Mass spectrometry

## I – Introduction

Electrospray ionization mass spectrometry (ESI-MS) is a technique where a liquid sample is ionized and sprayed into a mass spectrometer for analysis. ESI-MS is a widely used technique in chemical analysis because it enables analysis of wide variety of different kinds of molecules with high sensitivity and specificity [1–3]. Especially, capability to analyze large biomolecules without fragmentation has made a great impact and the discovery was also honored with the Nobel Prize in Chemistry in 2002 [4].

Traditionally ESI needles were pulled fused silica capillaries [5]. A need to integrate functions before the ionization led to the integration of an electrospray tip to a microfluidic device. This way other procedures such as chemical reactions and separation of different substances can be done prior the ESI-MS [6, 7]. These kinds of multifunctional analytical microchips are also known as micro total analysis systems ( $\mu$ TAS) or lab-on-chips [8].

A wide variety of different microfluidic ESI chip designs has already been published [1–3]. The first ESI chips were made of glass [9]. Since that also several silicon [10] and polymer [6, 7] chips have been published. Glass microfabrication methods are cumbersome

compared to silicon and polymer microfabrication and therefore realization of a sharp ESI tip is difficult [11] and it is typical that an external ESI tip has to be connected to the chip manually [12]. On the other hand silicon does not support electroosmotic flow but pumps or capillary action has to be employed for sample transportation. Therefore most of the recent ESI chips have been made of polymers [1]. Limitations of polymers include poorer chemical inertness, opacity, and a more limited thermal range.

We have earlier published a simple lidless ESI chip design where the sample transportation is based purely on the spontaneous flow of liquid in a micropillar channel due to capillarity. The chip has a sharp tip at the end of the micropillar channel, where electrospray ionization takes place. When the microchip is coupled to a mass spectrometer drugs and biomolecules can be analyzed with good sensitivity [13]. The chip can be made of silicon [10] or SU-8 epoxy polymer [6] and a microreactor can be integrated on chip, which allows studying of enzymatic reactions before the MS analysis [6]. Here we demonstrate an ESI chip, which has a micropillar channel deep reactive ion etched (DRIE) into a silicon wafer and a glass lid. Both the silicon channel wafer and the glass lid wafer are thru-etched in order to form sharp ESI tips. To our knowledge this is the first silicon/glass ESI chip ever published. The chips have three-dimensionally sharp monolithically integrated ESI tips and the fabrication process does not require manual attachment of external ESI tips.

## II - Experimental Details

### A. Microchip design

A schematic illustration and a photograph of the microchip are shown in Figure 1. The initial channel is 256  $\mu\text{m}$  wide and 15  $\mu\text{m}$  deep. It also has a 100  $\mu\text{m}$  wide circular thru-etched inlet. The initial channel is gradually divided to 128 individual 2  $\mu\text{m}$  wide channels in the manner shown in the Figure 1a. All 128 channels are finally connected to a 1024  $\mu\text{m}$  wide and 3 cm long pillar channel, which has a hexagonally packed pillar array of circular micropillars with the diameters of 6  $\mu\text{m}$ . At the end of the pillar-channel the flow is divided back to 128 individual 2  $\mu\text{m}$  channels that are gradually merged to a single 256  $\mu\text{m}$  wide channel which ends to a sharp thru-etched ESI tip. A thru-etched glass lid has only the sharp ESI tip.

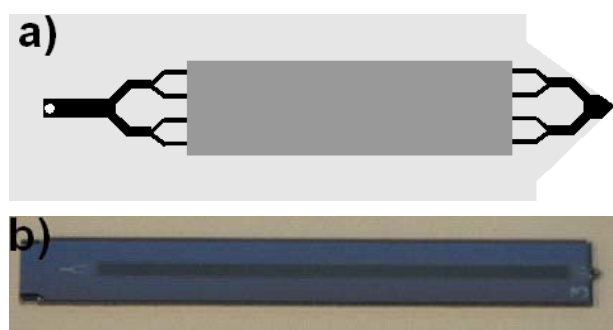


Figure 1: a) A schematic illustration of a silicon/glass ESI chip. Black area is microchannel without pillars, dark gray area a pillar-filled channel, light gray area non-etched silicon and white area is thru-wafer etched. b) A photograph of a fabricated microchip.

### B. Microchip fabrication

The microchips are fabricated by bonding silicon and glass wafers together. The silicon wafer has the channels, the inlets, and the sharp tips, while the glass wafer has only the sharp thru-etched tips.

The silicon microfabrication started with a 300  $\mu\text{m}$  thick oxidized  $\langle 100 \rangle$  wafer. The thickness of the thermal oxide was 622 nm. The patterns of the flow channels were etched into the oxide layer using lithography and  $\text{CHF}_3/\text{Ar}$  based RIE (Plasmalab System 80, Oxford Instruments), respectively. From the backside of the wafer the oxide was removed using a similar RIE process. The photoresist was removed in acetone and 200 nm thick layer of aluminum was sputtered (Plasmalab System 400, Oxford Instruments) on top of the patterned  $\text{SiO}_2$  layer. The patterns that define the inlets and the electrospray ionization tips were defined to the aluminum and underlying silicon dioxide layers with the second lithography, followed by phosphoric acid etching and  $\text{CHF}_3/\text{Ar}$  based RIE, respectively. After photoresist removal, the silicon wafer was thru-etched using cryogenic DRIE (Plasmalab System 100, Oxford Instruments) with  $\text{SF}_6/\text{O}_2$  plasma. Then, the aluminum mask was removed in phosphoric acid to expose more silicon and the patterned silicon dioxide mask. The following cryogenic DRIE step also utilized  $\text{SF}_6/\text{O}_2$  chemistry and it formed the flow channels. The  $\text{SiO}_2$  mask was removed in buffered hydrofluoric acid (BHF) and finally the wafer was treated in oxygen plasma to make the channels hydrophilic. Fabrication process of similar silicon chips has been described in more detailed manner elsewhere [10].

The glass microfabrication started with low pressure chemical vapor deposition (LPCVD) of 400 nm thick amorphous silicon layer on a 500  $\mu\text{m}$  thick borosilicate glass (Borofloat 33) wafer. The patterns of electrospray ionization tips were defined to the amorphous silicon layer on the wafer topside by photolithography and  $\text{SF}_6$  based RIE process, respectively. The amorphous silicon layers acted as etch masks during the isotropic thru-wafer etching in 10:1  $\text{HF-HCl}$  solution. After the glass

etching the photoresist was removed in acetone and the amorphous silicon layers in 25% tetramethylammonium hydroxide (TMAH) solution at the temperature of 80°C.

After the silicon and glass microfabrication the wafers were anodically bonded together at the temperature of 360°C (AWB-04, AML). The applied voltage was 600 V. Finally, the bonded wafers were diced using a dicing saw.

### C. Electrospray ionization and mass spectrometry

The microchip was coupled to a Micromass/Waters QTOF Micro time-of-flight mass spectrometer (Manchester, UK). The voltage of 5 kV was applied between the mass spectrometer and the chip to form the electrospray. A syringe pump (Harvard apparatus PhD 2000 infusion) was used to provide a stable flow of liquid sample to the chip. A 1/32 in. o.d. polyetheretherketone (PEEK) capillary was connected between a 10-ml glass syringe and the chip using a custom made copper-aluminum chip holder with flat bottom fluidic connectors (Super Flangeless, Upchurch scientific, Oak Harbor, WA). A similar chip holder has also been used elsewhere [14]. The chip was positioned in front of the mass spectrometer. The distance between the tip of the chip and the first lens of the mass spectrometer was set to 5 mm. The setup and the chip under operation are shown in Figure 2. The scanning rate of the MS used was approximately 1 Hz for the mass range of  $m/z$  80 to 800. The extracted ion chromatogram for protonated verapamil ( $m/z$  455.3  $\pm$  0.1) was followed. The concentration of the verapamil sample was 1  $\mu\text{M}$ . Methanol-water 1:1 was used as solvent. Two minutes of data was recorded for flow rates of 100 nl/min, 250 nl/min, 500 nl/min, 1  $\mu\text{l}/\text{min}$  and 5  $\mu\text{l}/\text{min}$  and the relative standard deviations of the signal intensity were calculated for each flow rate. A mass spectrum was recorded at the flow rate of 100 nl/min.



Figure 2: The microchip coupled to the mass spectrometer. A strong electrospray is seen at the very end of the tip of the chip.



### III - Results and Discussion

#### A. Microchip fabrication

Fabricating complex structures in silicon is fairly straightforward, but fabrication of sharp electrospray ionization tips out of glass has been more problematic due to limited capabilities of DRIE of glass. Instead of DRIE, our approach is based on isotropic wet etching of glass which results in a 3-dimensionally sharp electrospray ionization tip like shown in the scanning electron microscopy (SEM) images in Figure 3.

The mask openings for both the silicon and the glass ESI tips were identical, although silicon was etched using anisotropic DRIE, and glass using isotropic wet etching. The etch rate of HF-HCl etching solution at room temperature was measured to be approximately  $7.8 \mu\text{m}/\text{min}$ . Timing the glass etching process accurately is important, because overetching moves the edges of the thru-hole further at the rate of  $7.8 \mu\text{m}/\text{min}$ . Etching through a  $500 \mu\text{m}$  thick wafer takes 64 minutes. Still, we used total etch time of 66 minutes, because we wanted to make sure that the coverlid does not exceed the edge of the silicon tip. Producing a stable electrospray is difficult if the coverlid fully covers the micro-channel.

Due to isotropic nature of the HF-HCl etching of glass, the ESI tip is three-dimensionally sharp as clearly shown in Figures 3c and d. The sharpness of the tip is crucial for the performance of the chip. It creates the electrospray to a predetermined location and thus eases the operation of the chip. The sharpness of the tip also reduces the voltage required for the electrospray formation. Three-dimensional sharpness also reduces the spreading of the liquids along the edges of the tip during operation [1].

The main strengths of our fabrication process flow are its simplicity and scalability. All the process steps are standard microfabrication processes and the ESI tip is monolithically integrated to the chip. This circumvents manual and cumbersome chip level insertion of fused capillary tips. An obvious limitation of our microchip design is that the bottom part is made of silicon. Therefore, an electroosmotic flow cannot be used for sample transportation and the use of electrophoresis for sample separation before ESI is impossible.

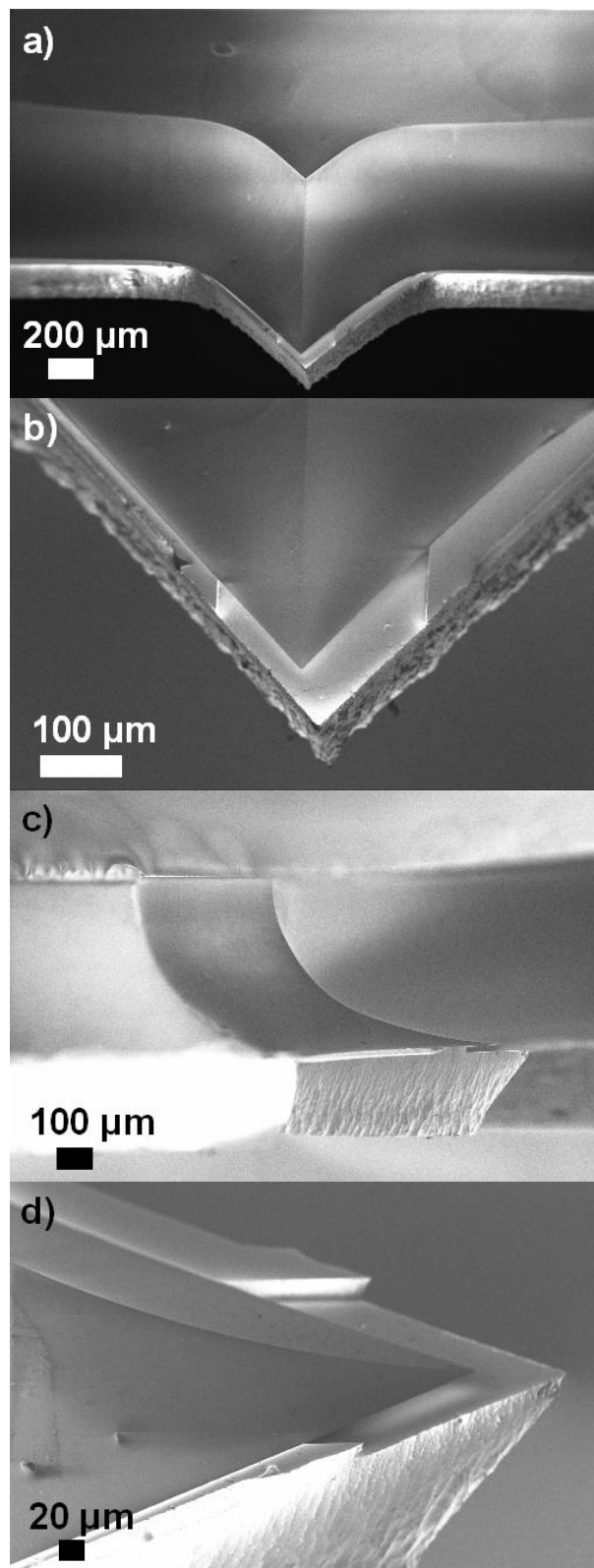


Figure 3: SEM images of the ESI tip of a fabricated chip. The images a and b show the front of the ESI tip while the images c and d show the side view of the tip.

### B. Electrospray ionization and mass spectrometry

The mass spectrum of verapamil, showing a protonated molecule at  $m/z$  455.3 (Figure 4), demonstrates the analytical capability of our microchip, when it is coupled to a mass spectrometer. The measurement shown in Figure 4 was done using the flow rate of 100 nL/min, while the electrospray process was measured to be stable for a flow rate range of 100 nL/min to 5  $\mu$ L/min. The relative standard deviations of signal intensities were calculated for five different flow rates from 2 minute-long measurements. The results are presented in Table 1. Standard deviations at flow rates of 500 nL/min and higher are fairly low and therefore the microchip would be well-suited for making liquid chromatographic separations prior to mass spectrometric analysis. At the flow rates below 500 nL/min the standard deviation is higher due to dilute sample concentration.

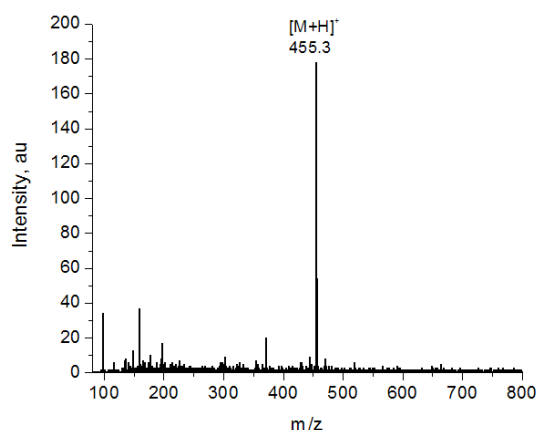


Figure 4: A mass spectrum of protonated verapamil collected with 100 nL/min flow rate when the microchip was coupled to the mass spectrometer.

Table 1: Relative standard deviations of signal intensities calculated for the different flow rates of sample.

Flow Rate [nL/min]	Relative standard deviation [%]
100	57
250	41
500	29
1000	12
5000	6.9

### IV - Conclusion

We have demonstrated the first ever truly microfabricated silicon/glass electrospray ionization source. The chip has a monolithically integrated three-dimensionally sharp ESI tip which produces a stable electrospray when coupled to a mass spectrometer without a help of nebulizer gas. When the microchip is coupled with mass spectrometry it can be used for the

analysis drugs and other polar compounds. The usable flow rate range is between 100 nL/min and 5  $\mu$ L/min. In future the possibility to do chromatographic separations prior to the MS analysis will be studied.

### References

- [1] S. Koster and E. Verpoorte, *Lab Chip*, 7, pp. 1394–1412, 2007.
- [2] G. T. T. Gibson, S. M. Mugo and R. D. Oleschuk, *Mass Spectrom. Rev.*, 28, pp. 918–936, 2009.
- [3] T. Sikanen, S. Franssila, T. J. Kauppila, R. Kostiaainen, T. Kotiaho and R. A. Ketola, *Mass Spectrom. Rev.*, 29, pp. 351–391, 2010.
- [4] J. Fenn, M. Mann, C. Meng, S. Wong and C. Whitehouse, *Science*, 246, pp. 67–71, 1989.
- [5] G. A. Valaskovic, N. L. Kelleher, D. P. Little, D. J. Aaserud and F. W. McLafferty, *Anal. Chem.*, 67, pp. 3082–3085, 1995.
- [6] T. Nissilä, L. Sainiemi, S. Franssila and R. A. Ketola, *Sens. Actuators B, Chem.*, 143, pp. 414–420, 2009.
- [7] T. Sikanen, S. Tuomikoski, R. A. Ketola, R. Kostiaainen, S. Franssila and T. Kotiaho, *Anal. Chem.*, 79, pp. 9135–9144, 2007.
- [8] A. Arora, G. Simone, G. B. Salieb-Beugelaar, J. T. Kim, A. Manz, *Anal. Chem.*, published online, 2010.
- [9] R. S. Ramsey and J. M. Ramsey, *Anal. Chem.*, 69, pp. 1174–1178, 1997.
- [10] L. Sainiemi, T. Nissilä, V. Jokinen, T. Sikanen, T. Kotiaho, R. Kostiaainen, R. A. Ketola and S. Franssila, *Sens. Actuators B, Chem.*, 132, 380–387, 2008.
- [11] P. Hoffmann, U. Häusig, P. Schulze and D. Belder, *Angew. Chem. Int. Ed.*, 46, pp. 4913–1916, 2007.
- [12] N. H. Bings, C. Wang, C. D. Scinner, C. L. Colyer, P. Thibault and D. J. Harrison, *Anal. Chem.*, 71, pp. 3292–3296, 1999.
- [13] T. Nissilä, L. Sainiemi, T. Sikanen, T. Kotiaho, S. Franssila, R. Kostiaainen and R. A. Ketola, *Rapid Commun. Mass Spectrom.*, 22, pp. 3677–3682, 2007.
- [14] M. Haapala, V. Saarela, J. Pöl, K. Kolari, T. Kotiaho, S. Franssila and R. Kostiaainen, *Anal. Chim. Acta*, 662, pp. 163–169, 2010.

# IMPROVING THE EFFICIENCY OF THERMOELECTRIC GENERATORS BY USING SOLAR HEAT CONCENTRATORS

M. T. de Leon, P. Taatizadeh, and M. Kraft

*University of Southampton; School of Electronics and Computer Science, United Kingdom*

**Abstract** — In this paper, we propose a method of improving the efficiency of thermoelectric generators (TEGs) by using a lens to concentrate heat on the heat source of a TEG. Initial experiments performed using discrete components show about 60mV increase in the amount of voltage generated when using a magnifying lens. Simulation results on the proposed TEG configuration exhibit up to 16% efficiency when the input heat flux is increased to 500 times that of the sun's heat flux. The effects of varying the thermoelement length, width, and membrane diameter on the TEG's performance are also characterized. Lastly, plans to fabricate the device on a SOI wafer in the future are presented.

**Keywords :** Thermoelectric generator, Solar heat concentrator, Carnot efficiency

## I - Introduction

The global energy crisis has paved the way for researchers to explore alternative means of generating power. One approach to providing electrical energy is by direct conversion of heat to electrical power with the use of thermoelectric generators (TEGs). It is attractive to use TEGs because they have no mechanical parts; hence resulting in an alternative power system that is silent, stable, reliable, environment-friendly, and possess virtually unlimited lifetime [1, 2].

The basic principle behind the operation of a TEG is the Seebeck effect. The Seebeck effect produces voltage when a temperature difference is applied between the junctions of two different materials. For a TEG to supply a significant amount of power, several thermocouples are connected electrically in series and thermally in parallel. Unfortunately, TEGs typically have low Carnot efficiency described by the equation below,

$$\eta_c = (T_h - T_c)/T_h \quad (1)$$

where  $T_h$  and  $T_c$  are the temperatures at the hot and cold sides, respectively. A typical Peltier device exhibits only about 5-8% efficiency.

By utilizing a solar heat concentrator in conjunction with a TEG, the temperature difference across the thermoelements can be increased; subsequently improving the TEG's efficiency. Figure 1 illustrates this innovation with the lens concentrating solar heat at the center of the TEG's membrane. A similar concept of focusing light onto a lens to provide the required actuation energy in powering up a micro-actuator using photo-thermal-mechanical energy transformation was proposed in [3] but their design was not fabricated.

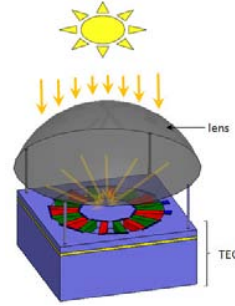


Figure 1: Illustration of proposed TEG with solar heat concentrator system.

Suppose the sun uniformly irradiates an energy density  $q_s$  onto the lens and that the lens has a convex surface area  $A_L$ , then the heat power density  $q_h$  of the incoming heat flux to the TEG's membrane is given by:

$$q_h = \frac{A_L}{A_h} q_s \quad (2)$$

where  $A_h$  is the area of the heated surface at the TEG's membrane. With this approach, we can generate an input heat flux in the order of hundreds of kW/m<sup>2</sup>. Based on the general heat transfer equation [4], an increase in the input heat flux would translate to a corresponding increase in the temperature difference across the thermoelements; also resulting in an effective increase in its output voltage given by:

$$V_o = N(\alpha_p - \alpha_n)\Delta T \quad (3)$$

where  $N$  is the number of thermocouples and  $\alpha_p$  and  $\alpha_n$  are the Seebeck coefficients of the p- and n-type thermoelements, respectively.

The main objective of this work then is to present the feasibility of the proposed system by first conducting experiments using commercially-available lenses and a TEG module. Heat transfer simulations of the proposed system are also performed to validate the improvement in the efficiency of the TEG. Plans to fabricate an integrated lens and TEG system for future work are also presented. This microscale system has promising applications in on-board power sources, sensor networks, and autonomous microsystems.

## II – Preliminary Experiment and Results

As proof of concept, we first verified the functionality of using a magnifying lens as the solar heat concentrator of a commercially-available TEG unit. To perform the experiment, a Farnell MCPE1-12707AC-S Peltier TEG unit is placed over the center of a Farnell 395-1AB heat sink. A 5x magnifying lens is then

positioned over the TEG keeping a distance equivalent to its focal length to give the best solar heat concentration ratio. To monitor the temperature changes, one thermocouple wire is glued to the middle of the TEG unit and another wire is glued 1cm away. The output terminals of the TEG are connected to a digital multimeter that displays the value of the generated voltage.

Figure 2 shows a plot of the system's output voltage with and without the use of a magnifying lens. Two magnifying lenses having diameters of 6cm and 10cm are used. As expected, higher voltage is generated when a lens is used which can only be attributed to a greater temperature difference across the thermocouple junctions of the TEG. Moreover, using the lens with a larger surface area resulted in a higher output voltage. Unfortunately, the thermocouple wires placed on the surface of the TEG unit only gives us an idea of how heat is distributed across the device but not the actual temperature difference across the thermocouple junctions. Nevertheless, the increase in the amount of voltage generated is sufficient to show that the efficiency can be increased by using a heat concentrator.

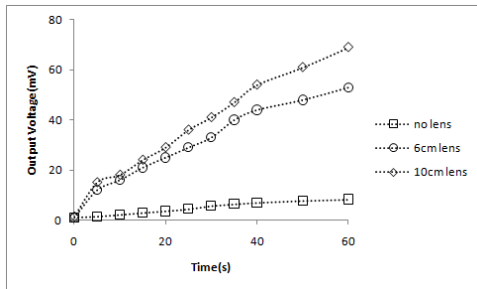


Figure 2: Open circuit output voltage measured with the experiment set-up with and without a magnifying lens.

### III – TEG Design and Simulations

After verifying that the proposed system can be an effective way of improving the efficiency of thermoelectric generators using discrete components, its application at the micro level is investigated. Micro-thermoelectric generators are classified based on the direction of heat flow through the device and on the layout orientation of the thermocouples during fabrication [5]. We chose to focus on the lateral/lateral type of TEGs because it is the simplest to fabricate and has the most potential for CMOS integration.

The configuration of the proposed TEG, shown in figure 3, is similar to the one proposed in [6] where the SOI wafer's device layer is utilized for the suspended membrane and thermoelements. The membrane acts as the heat source of the TEG while the substrate acts as the heat sink. The suspended membrane is circular in geometry to insure optimum transfer of heat from the center of the membrane to the tip of the thermoelements. The oxide and substrate layers below the membrane and the thermoelements are to be etched away to provide better thermal isolation and to optimize the heat

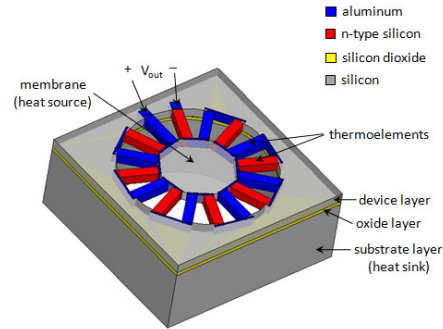


Figure 3: Conceptual design of the TEG device.

flux path so as to obtain the largest temperature difference across the device.

The thermocouple materials are heavily-doped n-type silicon and aluminum. Heavily-doped silicon is seen to be a viable choice for thermoelement material since it has high Seebeck coefficients at doping levels between  $3.5 \times 10^{19} \text{ cm}^{-3}$  to  $1.6 \times 10^{20} \text{ cm}^{-3}$  [7, 8]. A high doping level is also preferred because the electrical resistivity of silicon decreases with increasing dopant concentration; thus providing a smaller series resistance to the TEG device. It is preferred that both thermoelements use doped silicon but to minimize the number of masks needed during fabrication, aluminum is selected for the second thermoelement instead. The electrical and thermal properties of the two thermocouple materials are listed in table 1. The assumed dopant concentration of the n-type silicon thermoelement is  $5 \times 10^{19} \text{ cm}^{-3}$ .

Table 1: Electrical and thermal properties of n-type silicon and aluminum.

Property	n-type silicon	aluminum	references
Seebeck coefficient (V/K)	-400	-1.8	[7,9]
Electrical resistivity ( $\Omega\text{-cm}$ )	$2 \times 10^{-3}$	$2.65 \times 10^{-6}$	[6,10]
Thermal conductivity (W/mK)	122	237	[6,11]

Heat transfer simulations of the proposed TEG device are performed using COMSOL. The SOI wafer used in the simulations has the following thicknesses: 500  $\mu\text{m}$  for the substrate layer, 5  $\mu\text{m}$  for the oxide layer, and 50  $\mu\text{m}$  for the device layer. Although a thinner device layer is preferred to obtain a larger temperature drop across the thermocouple, a 50  $\mu\text{m}$  device layer is selected to ensure mechanical stability of the TEG. Each thermoelectric leg is set to have a length of 500  $\mu\text{m}$  and a width of 20  $\mu\text{m}$ . Heat transfer by convection is modeled by setting the top and bottom surfaces of the membrane, top surface of the rim, and bottom surface of the substrate to have heat transfer coefficients corresponding to natural external convection with air. The ambient temperature is set to 20°C. The membrane to be heated located in the middle of the device has a diame-



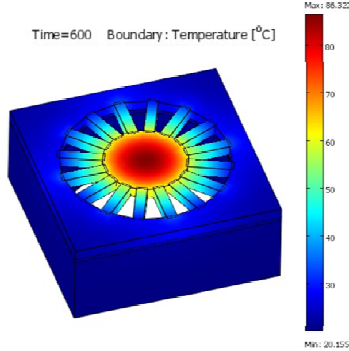


Figure 4: Temperature distribution after 10min for a 1mm x 1mm device with 8 thermocouples. Input heat flux is 20kW/m<sup>2</sup>.

ter of 5mm. The above-mentioned dimensions allow 300 thermocouples to be placed uniformly along the circumference of the membrane with at least 6 m distance between thermoelements. The temperature distribution of a smaller TEG device (1mm x 1mm) is shown in figure 4 to illustrate the heat transfer simulations performed.

For the 10mm x 10mm device simulations, only 16 thermocouples are distributed uniformly along the circumference of the membrane so as to minimize simulation time. We expect that having more thermocouples would decrease the temperature difference across each thermocouple as there is an increase in the area of the heat flux path from the membrane to the rim of the device layer. However, trends in efficiency improvement indicated by changes in  $\Delta T$  should still hold.

To demonstrate the effect of using a heat concentrator, a constant heat flux occupying 1mm<sup>2</sup> is applied at the center of the membrane. The value of the input heat flux is varied from 50kW/m<sup>2</sup> to 500kW/m<sup>2</sup>. With the solar heat flux equivalent to 1 kW/m<sup>2</sup> [12] and based on equation 2, the surface area of the lens is effectively varied from 50mm<sup>2</sup> to 500mm<sup>2</sup>. The results obtained, listed in table 2, clearly shows that the efficiency of the TEG improves with increasing input heat flux. This means that by using a convex lens, the temperature difference across a thermocouple can be increased; resulting in an increase on the TEG's efficiency.

Table 2: Temperature difference and efficiency of 10mm x 10mm TEG with 16 thermocouples for varying input heat flux  $Q$ . Lens surface area is equivalent to  $Q/1000 \text{ mm}^2$ .

$Q \text{ (kW/m}^2\text{)}$	$T_c \text{ (K)}$	$T_h \text{ (K)}$	$\Delta T \text{ (K)}$	$\epsilon \text{ (%)}$
50	321.482	330.838	9.356	2.828
100	342.356	360.926	18.570	5.145
150	361.222	388.947	27.725	7.128
200	378.943	415.789	36.846	8.862
250	395.894	441.835	45.941	10.398
300	412.279	467.297	55.018	11.774
350	428.227	492.308	64.081	13.016
400	443.823	516.957	73.134	14.147
450	459.132	541.309	82.177	15.181
500	474.199	565.413	91.214	16.132

Simulations are also performed with variations on the dimensions of the thermocouple and on the diameter of the membrane. Higher efficiencies can be achieved by using TEGs with longer lengths and narrower widths. However, the mechanical stability of the TEG after etching out the oxide and substrate layers must also be considered. It is targeted to fabricate different geometries of the device to explore this tradeoff. Characterizations of these variations are exhibited in figures 5-7.

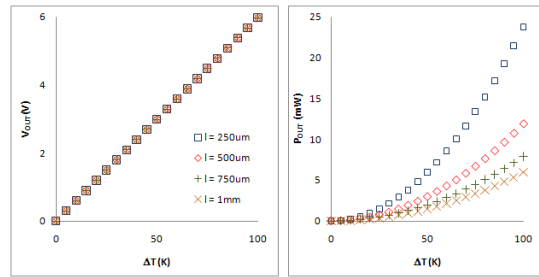


Figure 5: Open circuit output voltage and output power to a matched load for different thermoelement (TE) lengths. TE width is 20  $\mu\text{m}$  and membrane diameter is 5mm.

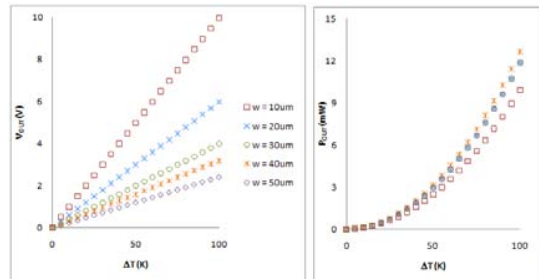


Figure 6: Open circuit output voltage and output power to a matched load for different thermoelement (TE) widths. TE length is 500  $\mu\text{m}$  and membrane diameter is 5mm.

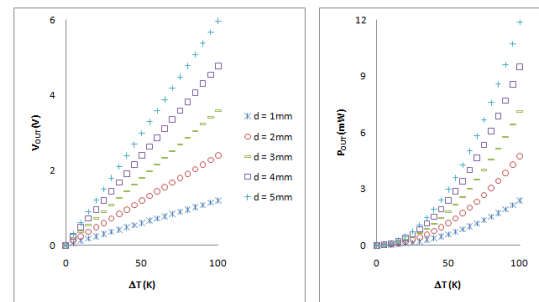


Figure 7: Open circuit output voltage and output power to a matched load for different membrane diameters. Thermoelement length is 500  $\mu\text{m}$  and width is 20  $\mu\text{m}$ .

Figure 5 shows that the open circuit output voltage versus temperature plot does not change with thermoelement length. It should be noted, though, that the change in temperature increases with the thermoelement length so a longer thermocouple would have a larger temperature difference across it, resulting in a higher output voltage. Meanwhile, a longer thermocouple



results in a higher series resistance, which translates to a lower output power under matched load conditions.

Variations in the thermoelement width shown in figure 6 also imply variations in the number of thermocouples. A wider thermoelement would have lesser number of thermocouples around the 5mm-diameter membrane. Hence, wider thermoelements result in a drop in the output voltage. The supposed reduction in output power due to the drop in the output voltage is offset by the lower series resistance of wider thermoelements, showing minimal variations of the output power to a matched load at different thermoelement widths especially at  $\Delta T$  less than 50K.

Similarly, changing the membrane diameter also means a change in the number of thermocouples of the device. A smaller membrane diameter implies lesser number of thermocouples. Figure 7 shows that a larger membrane diameter results in a higher output voltage and output power. The only limiting factor for the membrane diameter is the structural stability of the device, which is better for smaller membrane diameters.

#### IV – Fabrication

Several 10mm x 10mm TEGs are to be fabricated at the Southampton Nanofabrication Center. The device layer of the SOI wafer should have resistivity in the order of a few k $\Omega$ -cm to avoid parasitic resistive coupling between adjacent thermocouples. The fabrication begins by RCA cleaning of the SOI wafer. The next step is doping of the n-type thermoelements by diffusion. Then, the silicon areas of the device layer to be occupied by aluminum as the second thermoelement and for electrical contacts are to be patterned using a negative photoresist and removed by deep reactive ion etching (DRIE). Next, deposition through e-beam evaporation and liftoff of aluminum follow to form the aluminum thermoelements and the electrical connections of the thermocouples. After which, patterning and removal of silicon between thermoelements must be performed by DRIE, forming the gaps between thermoelements. In this step, holes on the membrane are also etched out in preparation of oxide etching. The last step of the TEG fabrication process involves back etching of the substrate and oxide etching by HF vapor phase to release the membrane and the thermoelements.

For the solar heat concentrator, a potential technique for the fabrication of spherical convex lens molds using isotropic wet etching of silicon is presented in [13]. These molds can be subsequently used to fabricate the lenses using hot embossing or UV-molding processes. The lenses to be fabricated are estimated to have a diameter of about 10-15mm to maximize the lens area to heated surface area ratio.

It is also envisioned that an array of these TEGs may be connected in series to boost the open circuit output voltage. Inter-TEG connections in this case may be done internally by including inter-TEG routing in the mask design for aluminum or externally using bond wires. With a TEG array, accurate design of an array of

lenses is also critical for proper heat concentration on each TEG's membrane.

#### V - Conclusions

This work proposes a method of improving the efficiency of thermoelectric generators with the use of solar heat concentrators. Experiments consisting of commercially-available magnifying lenses and a thermoelectric module proved that the use of a heat concentrator generates higher output voltage. Simulation results of a 10mmx10mm TEG device with increasing input heat flux demonstrate an increase in the device's Carnot efficiency. Characterization plots of the output voltage and output power for different thermoelement lengths, widths, and membrane diameters are also discussed as a guide in determining the geometry of several TEGs for fabrication. Fabrication processes under investigation for both TEG and convex lens are also presented.

#### VI - Acknowledgements

M. T. de Leon is supported by the University of the Philippines and the Department of Science and Technology, Philippines.

#### References

- [1] Y. Deng and J. Liu, *Journal of Renewable and Sustainable Energy* 1, 052701, 2009.
- [2] M. Strasser, R. Aigner, C. Lauterbach, T.F. Sturm, M. Franosch and G. Wachutka, *Sensors and Actuators A* 114, pp. 362-370, 2004.
- [3] S. Baglio, S. Castorina, L. Fortuna, and N. Savalli, *Sensors and Actuators A* 101, pp. 185-193, 2002.
- [4] A. Bejan and A. Kraus (editors), *Heat Transfer Handbook*, John Wiley & Sons, 2003.
- [5] W. Glatz, E. Schwyter, L. Durrer, and C. Hierold, *Journal of Microelectromechanical Systems*, vol. 18 no.3, pp. 763-772, 2009.
- [6] R. Egbert, M. Harvey, and B. Otis, *5<sup>th</sup> European Conference on Thermoelectrics*, Ukraine, pp.219-221, 2007.
- [7] F. Salleh, K. Asai, A. Ishida, and H. Ikeda, *Applied Physics Express* 2, 071203, 2009.
- [8] H. Ikeda and F. Salleh, *Applied Physics Letters* 96, 012106, 2010.
- [9] S. Kasap, *Thermoelectric Effects in Metals: Thermocouples*, Web-Materials, pp. 3, 2001.
- [10] *The Physics Hypertextbook*, <http://physics.info>, Accessed last May 2010.
- [11] J. Shackelford and W. Alexander, *CRC Materials Science and Engineering Handbook*, CRC Press, pp. 270-274, 2001.
- [12] R. Amatya and R. Ram, *J. of Electronic Materials* (DOI:10.1007/s11664-010-1190-8), 2010.
- [13] J. Alberio, L. Nieradko, C. Gorecki, H. Ottevaere, V. Gomez, H. Thienpont, J. Pietarinen, B. Paivanranta, and N. Passilly, *Optics Express*, vol. 17 no. 8, pp. 6283-6292, 2009.

# GAS SENSING MICROMACHINED STRUCTURE BASED ON GALLIUM ARSENIDE

I. Hotovy<sup>1</sup>, D. Tengeri<sup>1</sup>, V. Rehacek<sup>1</sup>, S. Hascik<sup>2</sup>, T. Lalinsky<sup>2</sup>

<sup>1</sup>*Microelectronics Department, Slovak University of Technology, Ilkovicova 3, 812 19 Bratislava, Slovakia*

<sup>2</sup>*Institute of Electrical Engineering, Slovak Academy of Sciences, Bratislava, Slovakia*

**Abstract** — In this paper we present the fabrication, electro-thermal characterization and sensing properties of a NiO gas sensor prepared on GaAs micromachined structure. Combination of surface and bulk micromachining techniques in two steps was used to obtain a low power consumption microheater on suspended GaAs membrane. Development and characterization of a GaAs micromachined gas sensing element is described. The double spiral type microhotplate is situated on a thermal isolated  $150 \times 150 \mu\text{m}^2$  suspended membrane using four microbridges. It can be operated at temperatures up to  $270^\circ\text{C}$  and the heating power consumption does not exceed 35 mW. The thermal time constant of the microheater is lower than 5 ms measured at  $180^\circ\text{C}$ . Gas sensing properties of device are presented on detection of low concentration of ethanol, where NiO sensing layer was used. The response of the gas sensing element rose with rising operating temperature as well as with ethanol concentration.

**Keywords :** GaAs suspended membrane; bulk and surface micromachining, gas sensor; NiO sensitive layer, ethanol

## I - Introduction

Gas sensors based on semiconducting metal oxides are actually one of the most investigated groups of gas sensors. Sensory properties of these devices are based on change in resistance of metal oxide layer upon exposure to specific gas, where oxidation/reduction properties play a role. Resistance is measured usually by electrode structure lying below sensing layer. In spite of fact that there are many approaches [1,2] and a lot of work has been reported in this field, one can see the united effort in development of systems and microsystems compatible with the semiconductor technology used in production of integrated circuits, by means of producing microsensors and electronic circuitry on the same chip. Such circuitry can include parts for signal amplification and signal evaluation [3] and thus cost reduction can be achieved in this way. As it is well known, metal oxide gas sensors generally work in a high temperature mode to accelerate the chemical reactions between molecules of the specified gas and the surface of sensing layer [4]. However, for stable operation of integrated gas sensor system is required to keep part of substrate with electronic circuitry, except of active gas sensing area, at low temperature

Gallium arsenide-based micro-electro-mechanical system (MEMS) devices are an attractive alternative to

the well-developed silicon-based MEMS. They can provide the best solutions for micro-optoelectronic applications with a number of material-related and technological advantages over silicon [5]. GaAs-based MEMS are being developed for microsensors and microactuators, such as accelerometers and tunable optoelectronic devices [6]. For optical telecommunication applications, GaAs-based optical MEMS require selective deep etching to create microstructures, such as membranes and via holes [7]. GaAs micromachining is also very interesting for the RF-MEMS field thanks to its potential for easy monolithic integration of micro-machined passive circuit elements with active devices manufactured on the same chip [8]. A GaAs suspended microheater for MEMS metal oxide gas sensors can bring a substantial reduction of thermal losses due to removal of the substrate. However, GaAs micro-machined structure for MEMS gas sensors have not been developed yet.

In our contribution we have demonstrated a new approach to developing of a low-power consumption micromachined structure based on a GaAs suspended membrane with a thickness of  $2 \mu\text{m}$ . The surface and bulk micromachining processes were developed and optimized with usage of SRIE in  $\text{CCl}_2\text{F}_2$  plasma. The microheater was of double spiral type and it was situated on a thermally isolated  $150 \times 150 \mu\text{m}^2$  suspended membrane using four microbridges. To complete the characterization of the developed of gas sensor, its gas sensing behavior towards ethanol was measured. The selected dynamic responses were determined and they rose with raising temperature.

## II - Experimental Details

In the fabrication of the suspended microheater, the basic steps are to surface and bulk micromachining of GaAs. The GaAs/AlGaAs heterostructure layer system grown by MBE on the GaAs substrate was designed to be used for micromechanical structure fabrication. Figure 1 shows the process sequence of the preparation of the GaAs suspended membranes. In the first step, double-side aligned photolithography was carried out to define the etching masks on both sides of the substrate. After this, highly selective reactive ion etching (SRIE) based on  $\text{CCl}_2\text{F}_2$  plasma chemistry of GaAs from the front side defined the lateral dimension of the structure. Resist AZ 5214 was used for masking (see Fig. 1a-c).

The bulk micromachining process started by preparing a Ni mask for backside etching using the lift-off technique. The vertical dimension was defined by deep

back side RIE through a 300  $\mu\text{m}$  thick GaAs substrate to the AlGaAs etch-stop layer, hence the structure thickness is precisely determined by the thickness of MBE grown GaAs layer over this etch stop layer. We used again  $\text{CCl}_2\text{F}_2$  as a process gas (Fig. 1d). Finally, the resist and the etch stop layer are removed (Fig. 1e).

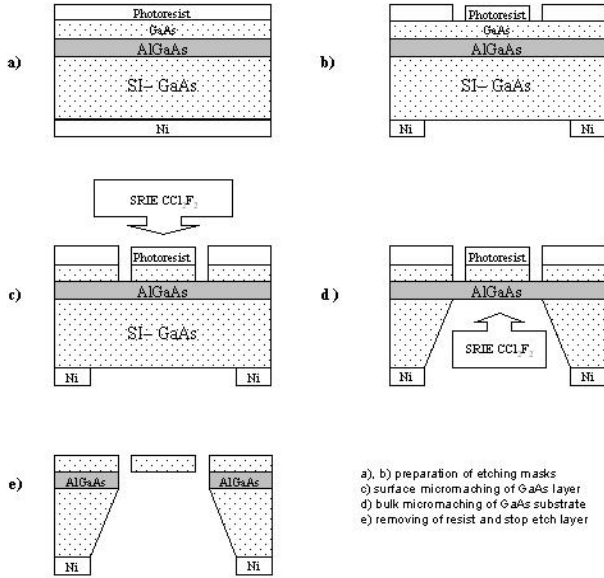


Figure 1: The fabrication process flow.

The heater structure was of double spiral type and it was situated on a thermally isolated  $150 \times 150 \mu\text{m}^2$  suspended membrane using four microbridges. A 20 nm thick TiN adhesion layer followed by 200 nm of Pt was deposited by magnetron sputtering and lift-off technique. The resulting resistance of the heater was in the range from 63 to 71  $\Omega$ . After annealing at 400°C, stabilization of the electrodes was achieved. After this process, the micromachined substrate was diced, the chips were mounted on TO package and four wire bonds (two for the microheater contacts and two for the temperature sensor contacts) were realized. The fabricated structure is shown in Fig. 2. The cavity under the microheater structure through GaAs substrate was  $400 \times 400 \mu\text{m}^2$ . The SEM micrograph (Fig. 3) shows the bulk etching of back GaAs wafer through the Ni mask.

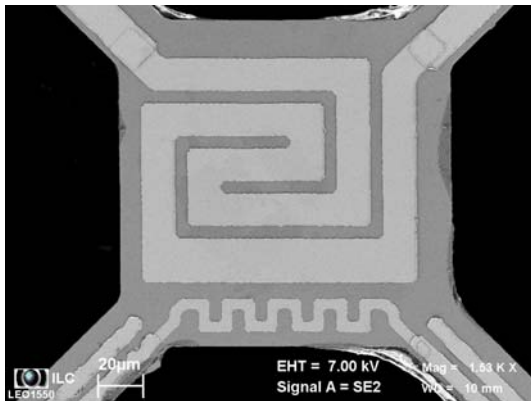


Figure 2: SEM image of a suspended TiN/Pt microheater.

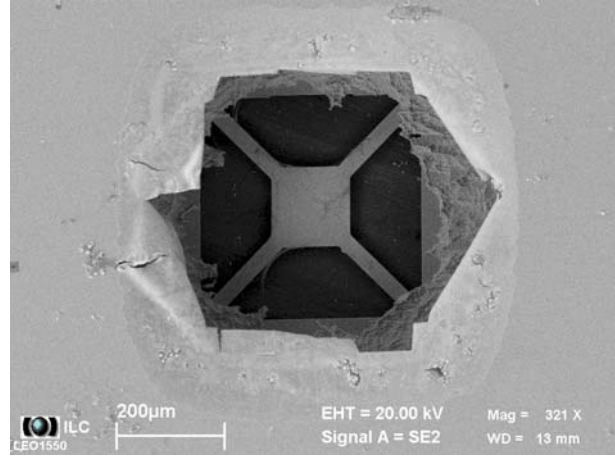


Figure 3: SEM view of bulk etched GaAs window  $400 \times 400 \mu\text{m}^2$ .

In our experiments, the optimal etching conditions were found for preparing 2  $\mu\text{m}$  thick suspended membranes for the MEMS sensor arrays. The etch rate was about  $2 \mu\text{m min}^{-1}$ , the selectivity to the sputtered Ni etch mask better than 2000 and to the AlGaAs stop-etch layer better than 1000 when using a pressure of 18 Pa and rf power 150 W.

### III - Results and Discussion

#### A. Microheater Electro-Thermal Analysis

For testing purposes, the microheater was powered up with a variable voltage of 0-3 V source using a probing system. I-V measurements were performed using an automatic measurement system consists of AgilentVee Software environment and KEITHLEY 237 and 238 Source Measure Units. The temperature sensitivity of TiN/Pt thin film temperature sensor was investigated in the first stage. I-V characteristic of the temperature sensor at constant current biasing was used to convert the temperature into voltage. Fig. 4 shows the measured voltage response to the temperature at constant current biasing of 3 mA. As expected there is very good linearity in the sensor voltage response observed.

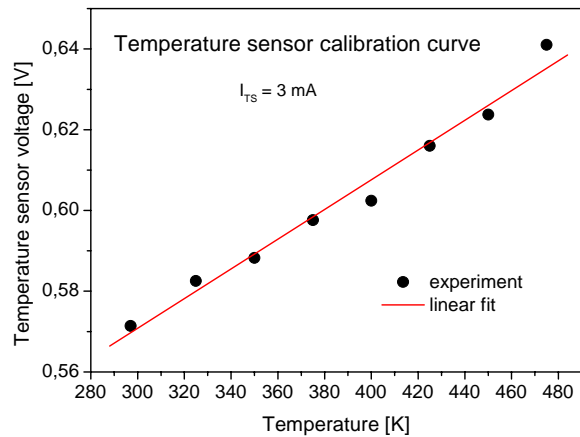


Figure 4: Temperature sensor calibration curve.

After temperature calibration of the temperature sensor (Fig. 5), it is possible to evaluate the electro-thermal conversion efficiency of the microheater that fulfils the role of so called thermal converter device. We changed the power dissipated in the microheater as a product of voltage and current. The temperature sensor was operating at the constant current biasing ( $I_{TS} = 3$  mA), so the temperature sensor voltage response to the power dissipation was measured immediately. Figure 6 shows typical behavior of the measured power to temperature sensor voltage (P-V) conversion characteristic.

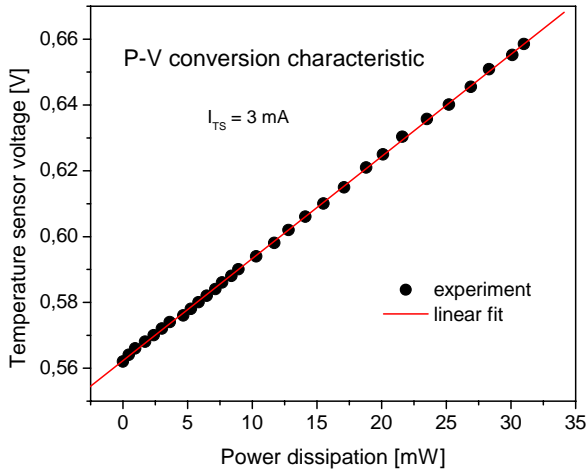


Figure 5: Dissipated power vs. the variation of the temperature sensor voltage.

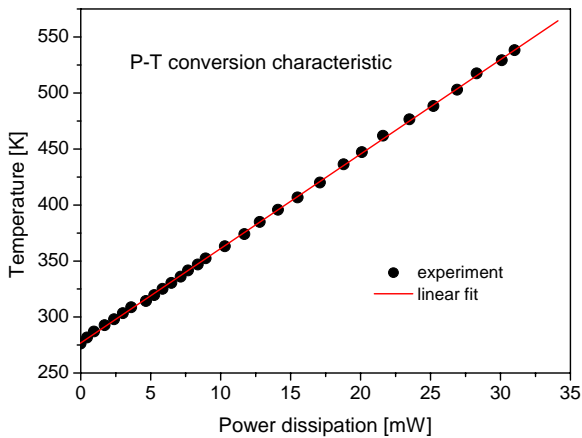


Figure 6: Dissipated power vs. the variation of the microheater temperature.

The linear fit performed on the temperature sensor calibration curve in Fig. 6 allows make transfer of the temperature sensor voltage directly to the temperature. Finally, Fig. 8 shows so called power to temperature (P-T) conversion characteristic that can be used to evaluate the conversion efficiency of the device. As we can see there is also very good linearity in the P-T conversion observed. After fitting the measured data by a linear regression ( $T = 276.878 + 8.4346 P$ ) it is clear that thermal resistance  $R_{TH}$  defined as  $\partial T / \partial P$  is practically constant in the range of applied power dissipation (measured temperature range).  $R_{TH}$  achieves the value

of 8.43 K/mW. So, the temperature increase in the sensor active area on the level of 550 K (predicted operating temperature of gas sensor) can be achieved by the power dissipation about 30 mW.

### B. Thermal Time Constant Measurement

To minimize power consumption of heater, AC temperature modulation is promising way of how to achieve it [1]. Furthermore, Vegara et al [10] pointed to new opportunities of using temperature-modulated micro-hotplate gas sensor for quantitative gas mixture analysis. To use low frequency temperature modulating signal, it is necessary to determine maximum modulating frequency by measuring thermal time constant (TTC) of investigated device. In our study it was used constant current source Keithley 238 to power-up the heater and Tektronix TDS305B oscilloscope to measure voltage across the heater. This voltage variation is directly linked to the change in the resistance of the heating element. The circuit was switched on by two-positional switch and oscilloscope was set-up to sense rising edge of the signal. Measured characteristics at different current flow through heater element (and so at different temperature) are shown in Fig. 7.

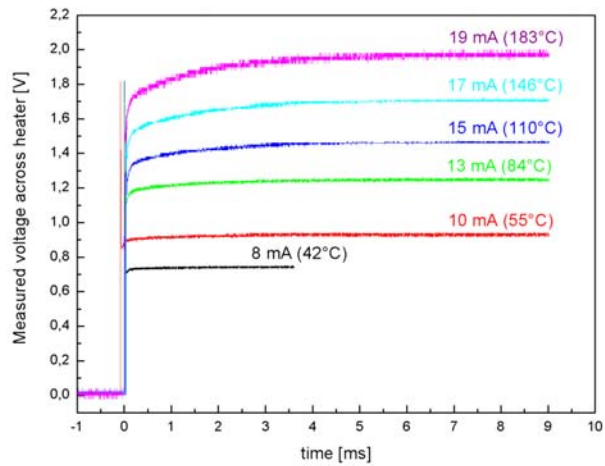


Figure 7: Measurement of voltage variation in time as function of current-flow through the heater.

The TTC corresponds to the time required to reach the 99% of the steady-state voltage and was determined to be 4.2 ms when reaching the temperature of 183°C. The TTC dependence on microheater's temperature is shown in Fig. 8. One can see the rising tendency of TTC on increasing temperature. However, the higher is the temperature, and the lower is change of TTC. This effect is probably because the ratio of the thermal conductivity to heat capacity of the GaAs membrane increases with increasing temperature. We assume that the whole thermal losses are influenced not only by heat conduction over the membrane, but also by radiation and convection, which also arises with temperature and thus the TTC has rising tendency with rising temperature.



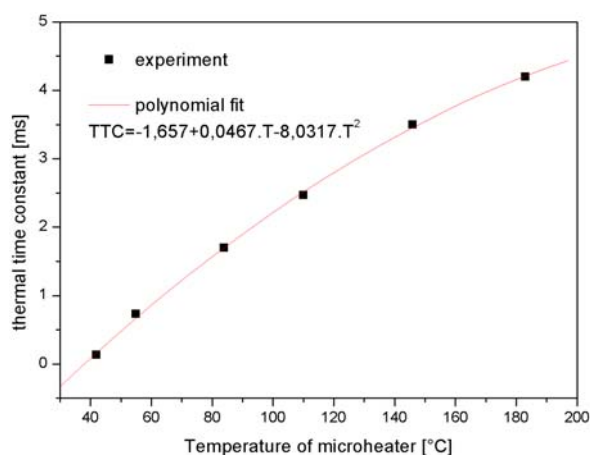


Figure 8: Thermal time constant dependence on microheater's temperature.

### C. Gas Sensing Tests Towards Ethanol

Gas sensing properties of model device with complete sensor structure was tested under exposure towards ethanol. All tests were performed in real conditions and measured relative air humidity was in range of 40-50%. Sensor was exposed in every measurement to ethanol vapor for 30 min and afterwards to air for 30 min and its response was measured through change in resistance of NiO sensing layer. Temperature of the sensor was regulated by known temperature-resistance dependence of the heater, setting resistance to desired value by powering from voltage source. Over the one cycle of measurement, operating temperature was kept on constant value. FLUKE 45 multimeter measured resistance of sensing layer. Ethanol was evaporated from liquid phase in amount from 4 to 20  $\mu\text{l}$  which corresponds to concentrations in range from 2400 ppm to 9600 ppm. Operating temperature of gas sensor was varied from 160°C to 208°C. Device was warmed up one hour before measurement to reach steady-state value of NiO resistance. This warming up process was necessary to repeat every time the operating temperature of sensor was changed. To check the measurement reproducibility, sensor response was measured three times at ethanol concentration of 4667 ppm at three different temperatures (165°C, 184°C, 208°C). These characteristics are shown in Fig. 9. Relative humidity (RH) of air during measurement was 41%.

### IV - Conclusion

In this paper, a TiN/Pt microheater prepared on a GaAs micromechanical structure has been fabricated and characterized as a prospective device for MEMS gas sensor array. Both the suspended membrane (150 x 150  $\mu\text{m}^2$ ) and the four microbridges were made of a 2  $\mu\text{m}$  of GaAs and the heater element and temperature sensor were made of platinum. The properties of micromechanical structure were verified using electro-thermal analysis. It was found that the temperature of heater on GaAs membrane could be raised to 550 K at

very low power consumption about 30 mW. To complete the characterization of developed model device of gas sensor, its gas sensing behavior towards ethanol vapor was measured.

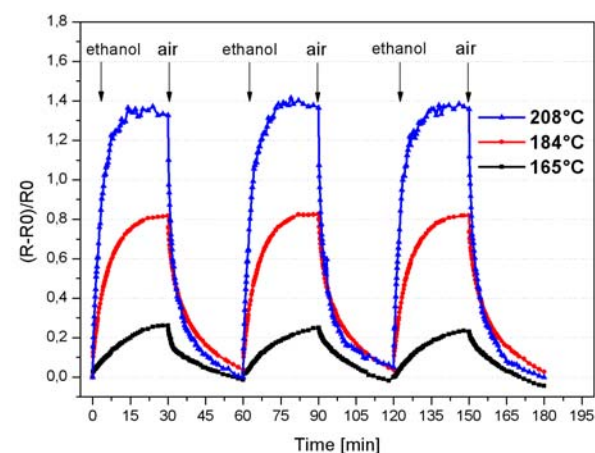


Figure 9: Response towards 4667 ppm of ethanol in air with relative humidity 41% at three temperatures.

### References

- [1] I. Simon et al., *Sensors and Actuators B* **73**, 1-26, 2001.
- [2] N. Barsan, D. Koziej, U. Weimar, *Sensors and Actuators B* **121**, 18-35, 2007.
- [3] C. Hagleitner et. al, *Nature* **414**, 293-296, (15 November 2001)
- [4] P. T. Moseley, B.C. Tofield (Eds.), *Solid State Gas Sensors*. IOP Publishing Ltd., Bristol, UK: Adam Hilger 1987.
- [5] H.L. Hartnagel, K. Mutamba, J. Pfeiffer, R. Rieamentschneider, J. Peerlings, *57th Annual Device Research Conference Digest*, Santa Barbara, 112-115, 1999.
- [6] Y. M. Chiang, J. Lau, M. Bachman, G.P. Li, H.K. Kim, Y. Ra, K. Ketola, *Mat. Res. Soc. Symp. Proc.*, Vol. 729, Materials Research Society: U3.1.1-U3.1.6, 2002.
- [7] R.J. Shul, M.L. Lovejoy, J.C. Word, A.J. Howard, D.J. Rieger, et al, *J. Vac Sci Technol B*, **15**, 657-664, 1997.
- [8] A. Pantazis, D. Neculoiu, Z. Hatzopoulos, D. Vasilache, M. Lagadas, M. Dragoman, et al, *J. Micro-mech. Microeng.* **15**, 853-859, 2005.
- [9] A. Vegara, et al., *Sensors and Actuators B* **123** 1002-1004, 2007.

### Acknowledgement

The work was supported by Scientific Grant Agency of Ministry of Education of Slovak Republic and Slovak Academy of Sciences, No. 1/0553/09, by Science and Technology Assistance Agency under contract No. VVCE-0049-07 and No. APVV-0655-07.



# STRUCTURING TECHNIQUES OF ALUMINUM NITRIDE MASKS FOR DEEP REACTIVE ION ETCHING (DRIE) OF SILICON

S. Leopold<sup>1</sup>, T. Polster<sup>1</sup>, T. Geiling<sup>1</sup>, D. Pätz<sup>2</sup>, F. Knöbber<sup>4</sup>, A. Albrecht<sup>3</sup>, O. Ambacher<sup>4</sup>, S. Sinzinger<sup>2</sup> and M. Hoffmann<sup>1</sup>

<sup>1</sup>Ilmenau University of Technology, IMN MacroNano®, PF 100565, 98694 Ilmenau, Germany,

Department for Micromechanical Systems,

<sup>2</sup>Department for Optical Engineering,

<sup>3</sup>Centre for Micro- and Nanotechnology,

<sup>4</sup>Fraunhofer Institute for Applied Solid State Physics, Tullastr. 72, 79108 Freiburg, Germany

**Abstract** — In this paper we present structuring techniques for Aluminum Nitride (AlN). Therefore, etch profile and surface roughness for etching with potassium hydroxide (KOH) and plasma etching are investigated. For KOH etching of AlN a gold / chromium mask is used. Silicon is found to be an etch stop. For plasma etching, a photoresist mask is used. The roughness evolution, the etch rate and selectivity are measured and the resulting profile is analyzed. In addition, an optimized etching process based on chlorine (Cl<sub>2</sub>), boron trichloride (BCl<sub>3</sub>) and argon (Ar) is investigated. Low roughness is desired and a mask of silicon dioxide (SiO<sub>2</sub>) is used on chip level. Finally, the potential of AlN mask during deep reactive ion etching (DRIE) of silicon is investigated.

**Keywords** : aluminum nitride (AlN), wet etching, plasma etching, potassium hydroxide (KOH), chlorine (Cl<sub>2</sub>), boron trichloride (BCl<sub>3</sub>), silicon dioxide (SiO<sub>2</sub>), photoresist, needle, columnar

## I - Introduction

During the last years sputtered and epitaxially grown aluminum nitride (AlN) has intensively been investigated for microelectromechanical systems (MEMS), since it offers unique properties. Previous research primarily concentrated on the piezoelectric and dielectric parameters. Piezoelectrically driven resonators made of AlN are used for communication devices [1] or mass sensing. [2,3]. Furthermore, the piezoelectric properties offer opportunities for energy harvesting [4] and pressure sensing, such as microphone/micro speaker applications [5]. In addition to that, AlN also promises to be mechanically, chemically and thermally stable in a wide range of MEMS-applications. These versatile properties provide many opportunities for advanced MEMS.

The scope of this investigation is on wet and plasma assisted structuring techniques for reactively sputtered AlN layers on Si-based materials. The presented processes are essential for the fabrication of complex MEMS devices. On one hand, structuring AlN layers with rather big feature sizes using wet etching with potassium hydroxide (KOH) and gold as mask material is investigated. On the other hand, structuring AlN elements with small feature sizes is established utilizing a chlorine (Cl<sub>2</sub>), boron trichloride (BCl<sub>3</sub>) an argon (Ar) based plasma etch process.

For both techniques the resulting profiles are analyzed considering roughness and profile angle. In addition, the etch rates are measured and the selectivity against mask materials are determined. In case of plasma etching of sensitive and small AlN structures, silicon dioxide (SiO<sub>2</sub>) and photoresist are used as mask materials. Both materials can be removed with vapor or plasma etching, respectively. Hence, wet etching, which may destroy sensitive structures, is not needed.

Furthermore, the utilization of AlN masks for deep reactive ion etching (DRIE) of silicon is investigated. The mechanical and chemical stability of AlN promises a good resistance against the physical and chemical etching in DRIE processes.

## II - Experimental

### A. AlN Preparation

Double-side polished silicon wafers (100) with a diameter of 100 mm and a thickness of 300 µm are used. The silicon has a resistivity of 1 - 20 Ω cm. The 500 nm thick AlN layer is deposited by reactive sputtering in a Nordiko 2000 system. The sputter process parameters are shown in table 1.

Table 1: AlN deposition process parameters

Process parameter	Unit	Value
Sputter power	W	1000
Substrate temperature	°C	300
Process pressure	Pa	0.4
Nitrogen (N <sub>2</sub> ) flow	sccm	18
Argon (Ar) flow	sccm	12
Process duration	min	50

### B Wet etching of AlN

During the KOH etch tests, a metal mask consisting of 10 nm chromium and 120 nm gold is used. The bi-layer is sputter deposited in a Von Ardenne LS250 ES system. Both layers are structured using lift-off technique. The AlN layer is etched in a 25 wt.-% KOH solution at room temperature. After the AlN layer is completely etched, the gold mask is removed with a potassium iodide / iodine solution (KI/I<sub>2</sub>). Chromium is etched with CR-Etch 3144 (Honeywell).

### C Dry etching of AlN

In order to establish an AlN plasma etch process on chip level, the prepared Si wafer is coated with silicon dioxide (SiO<sub>2</sub>). The SiO<sub>2</sub>, which serves as mask material, is deposited with plasma enhanced chemical vapor

deposition (PECVD) in an inductively coupled plasma system (Oxford PlasmalabSystem 100). The SiO<sub>2</sub> mask is structured with reactive ion etching (RIE) in an Oxford PlasmalabSystem 100, while using photoresist AZ 1518 as mask. After removing the resist, AlN is structured in a chlorine-based ICP RIE system (Surface Technology Systems plc). In order to achieve smooth etch profiles, different ratios of Cl<sub>2</sub> and BCl<sub>3</sub> are investigated. After plasma etching of AlN the SiO<sub>2</sub> mask is removed with buffered oxide etch.

The chosen AlN plasma etch regime is transferred to wafer level using a plasma-stable photoresist mask (AZ 6612). For all wafers, roughness and height of etch steps are measured with profilometry (Veeco Dektak 150). The remaining layer thickness of the etched AlN is measured with ellipsometry (Sentech SE500). The resulting etch profiles are analyzed with scanning electron microscopy (SEM, Hitachi S4800).

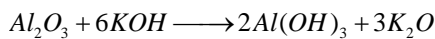
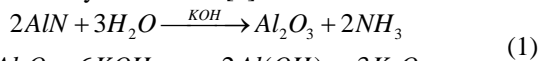
#### D. Deep Silicon Etching using AlN mask

The mechanical and chemical stability of AlN implies good selectivity in fluorine-based DRIE etching of silicon. In order to show its suitability as mask material, a 1.500 µm thick silicon wafer with a diameter of 100 mm is coated with a 600 nm thick AlN layer. To achieve a higher deposition rate, the sputter parameters are slightly different (15 sccm N<sub>2</sub> and 15 sccm Ar flow). For structuring the AlN mask, nickel (Ni) is deposited and structured via “lift off”. Afterwards AlN is etched in a Cl<sub>2</sub> and Ar based plasma. When the AlN layer is structured, Ni is removed with Ammonium persulfate (NH<sub>4</sub>)<sub>2</sub>S<sub>2</sub>O<sub>8</sub> and Iron(III)chloride (FeCl<sub>3</sub>). The following DRIE process for deep silicon etching consists of an alternating sequence of passivation (c-C<sub>4</sub>F<sub>8</sub> plasma) and etching (SF<sub>6</sub> and O<sub>2</sub> plasma) as well-known for deep silicon etching.

### III - Results and Discussion

#### A. AlN Structuring Techniques

Wet etching of AlN with KOH containing fluids is firstly presented by Miliham et al. [6]. Further investigations concerning the etching mechanism (eq. 1) are presented by Chen et al. [7]:



In figure 1 the AlN etch profile after KOH etching is shown. One can see the rough sidewall and an anisotropic under etch of approximately 190 nm while etching the 500 nm thick AlN layer. We assume, that if one grain of the nano-crystalline film is damaged, crystallographic faces are opened, which are etched rapidly. After the grain is removed completely, etching slows down until the next grain is opened. Hence the former grain boundaries form the sidewall, resulting in a rough etch profile and an anisotropic etch progress. In addition to the AlN etch profile, the smooth and unetched silicon surface and the gold / chromium mask can be seen in figure 1. As the KOH is used at room temperature, the etch rate for silicon is rather low. The mask shows the characteristic “lift off” edge geometry.

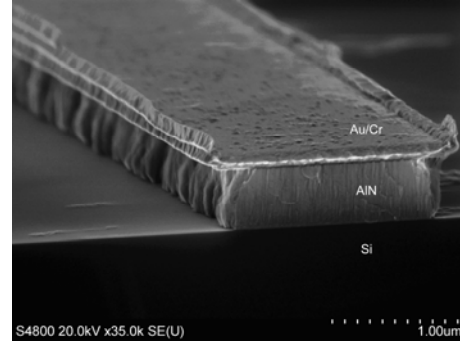


Figure 1: AlN profile after 18 minutes KOH etching.

The roughness development during AlN wet etching is shown in figure 2. We observe an increasing Ra for etch times up to 12 minutes. The solid AlN layer is etched completely after 12 minutes, which corresponds to an etch rate of approximately 42 nm/min. Residues of AlN remain on silicon surface forming the maximum roughness of approximately 28,1 nm (R<sub>a</sub>). Further etching decreases the roughness, which indicates, that the residues are etched while silicon remains unetched. This is supported by figure 1, where no significant silicon etching can be observed. Hence for AlN etching with a KOH solution (25 %) at room temperature, silicon can be used as etch stop, in order to achieve smooth surfaces.

For plasma etching of AlN grown by molecular-beam epitaxy, Zhu et al. [8] present a Cl<sub>2</sub>/ Ar based regime. They observe a significant roughness development during the process. In order to reduce the surface roughness, Xu et al. [9] present a BCl<sub>3</sub> pretreatment.

A similar process, containing Cl<sub>2</sub>, BCl<sub>3</sub> and Ar, for etching poly-crystalline AlN is presented by Kahn et al. [10]. In order to find optimal process conditions, we investigate the influence of the gas composition (Cl<sub>2</sub>, BCl<sub>3</sub> and Ar) on etch rate and roughness. Therefore, the Cl<sub>2</sub> / BCl<sub>3</sub> ratio is varied, while the Ar flow rate is kept constant, starting with a pure Cl<sub>2</sub> / Ar plasma. The resulting etch profile after 5 minutes is shown in figure 3. On the right side one can see the textured and nano-crystalline structure of AlN on silicon surface. On top of AlN the SiO<sub>2</sub> mask is shown. During etching, needle like AlN structures are formed. There are two possible mechanisms of needle generation. On the one

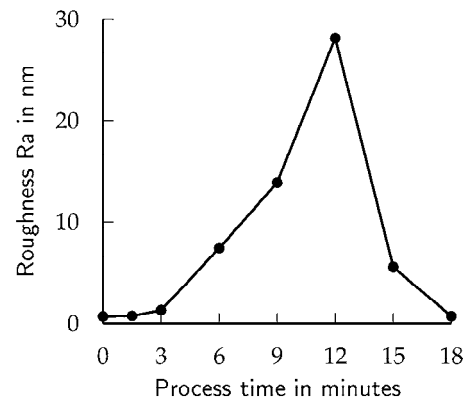


Figure 2: Roughness evolution of the etched surface during KOH etching

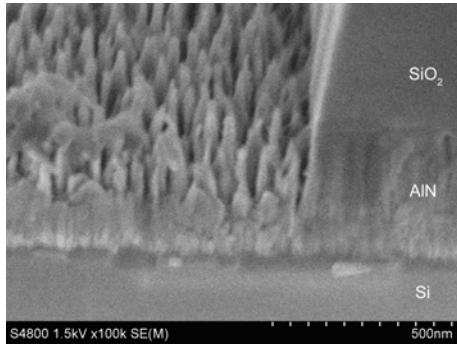


Figure 3: Needle-like surface structure, occurring after 5 minutes etching of AlN in pure  $\text{Cl}_2/\text{Ar}$  plasma, using a  $\text{SiO}_2$  mask.

hand, textured grains could form the columnar structures during etching. On the other hand, oxygen containing chemical compounds such as  $\text{Al}_2\text{O}_3$  may act as micro mask. Since they are etched slower, they cover the underlying AlN and inhibit etching locally and temporarily. The oxygen containing compounds may be formed due to native oxidation under ambient conditions or during plasma etching. In latter case the  $\text{SiO}_2$  mask may be sputtered and oxygen is redeposited on AlN surface.

In order to avoid needle-like AlN structures,  $\text{BCl}_3$  is added according to Xu et al. Different  $\text{Cl}_2/\text{BCl}_3$ -flow ratios (10:10, 15:5 and 17:3) are investigated, while keeping the total gas flow constant. All samples are etched 5 minutes and the roughness as well as the etch rates of AlN and  $\text{SiO}_2$  are measured. The results are shown in figure 4.

Both, AlN and  $\text{SiO}_2$  etch rate, decrease with increasing  $\text{BCl}_3$  percentage. The roughness of the AlN surface strongly depends on  $\text{Cl}_2/\text{BCl}_3$  ratio. While forming needle-like structures without  $\text{BCl}_3$ , the average roughness ( $R_a$ ) decreases to 0.7 nm for a 10:10 ratio. The measured roughness is in line with the results presented by Xu et al. A ratio of 15:5 is found to be optimal, considering high etch rate and smooth etch profiles.

In table 2 the chosen process parameters are summarized. The achieved etch profile is shown in figure 5. Again the textured structure of AlN on silicon surface and the  $\text{SiO}_2$  mask can be seen. A smooth, vertical sidewall and a grainy roughness on the etched surface are visible. In contrast to KOH etching, the sidewall profile of plasma etched structures is determined by the

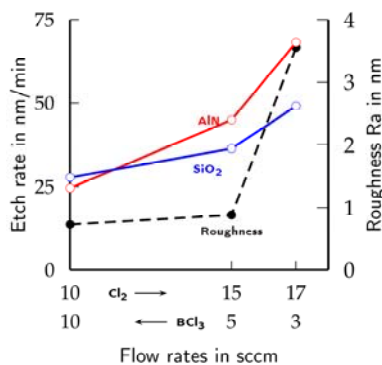


Figure 4: AlN and  $\text{SiO}_2$  etch rates and roughness of the etched surface for different gas mixtures

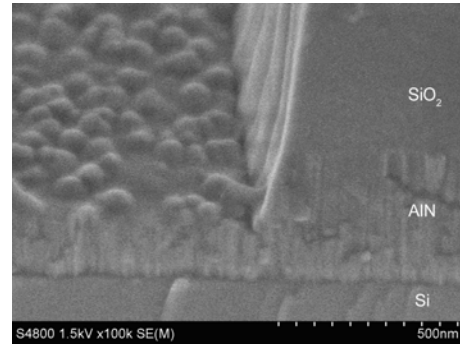


Figure 5: Profile after 5 minutes of plasma etching at optimal conditions, using a  $\text{SiO}_2$  mask.

Table 2: Optimal process parameters for AlN plasma etching

Process parameter	Unit	Value
Coil Power	W	500
Platen Power	W	25
Chlorine ( $\text{Cl}_2$ ) Flow	sccm	15
Boron Trichloride ( $\text{BCl}_3$ ) Flow	sccm	5
Argon (Ar) Flow	sccm	5

mask profile. The nano-crystalline structure of AlN seems to have no significant influence.

The process, which is found to be optimal, is transferred to wafer level. Here, photoresist (AZ 6612) is used as mask material. Using photoresist is possible since the process works at a low platen power of 25 W and thus low ion bombardment. For etching AlN on wafer level with resist mask, the etch rates and roughness is measured time-resolved. The results are displayed in figure 6. The etch rates of AlN and resist are found to be constant during etching, while the resist is removed approximately twice as fast as AlN. The roughness increases during the process up to a value of  $R_a=10$  nm. Although the platen power is comparably low, the resist is sputtered. If the resist is redeposited on the etched surface, it may mask locally, which explains the increased roughness, compared to a  $\text{SiO}_2$  mask.

In addition to that, the transfer on wafer level, and therefore the different thermal conditions, change sputtering and redeposition properties, which also may be responsible for the increased roughness.

The achieved etch profile is shown in figure 7. The etch process is interrupted after 6 minutes, hence the AlN layer is not completely etched. One can see smooth sidewalls and a high angle between the sidewall and the surface, which is determined by the profile of the photoresist AZ 6612. In the upper left part of figure 7

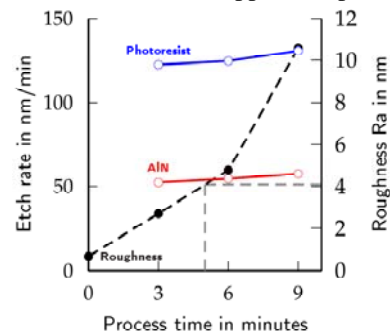


Figure 6: Etch rates and roughness evolution during plasma etching of AlN with photoresist mask



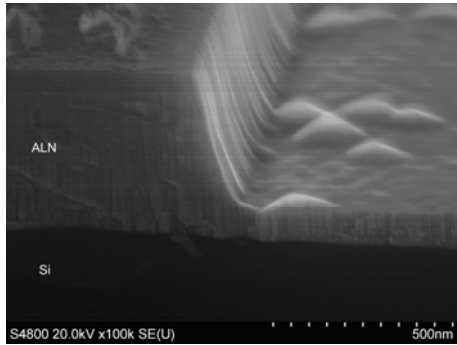


Figure 7: Etch profile of the AlN structuring process on wafer level interrupted after 6 minutes

one can see residues left on the AlN layer after removal of the photoresist in oxygen ( $O_2$ ) plasma. Since the AlN layer itself takes part as mask material in subsequent processes, the residue-free removal of photoresist is not necessary. However, the plasma ashing is introduced to reduce micro masking effects due to redeposition in subsequent processes.

#### B. Silicon Structuring Technique

The manufactured structure after DRIE is shown in figure 8. With a 600 nm thick AlN mask, 1000  $\mu\text{m}$  deep trenches are etched. The selectivity is measured to be 1:10,000. This very high selectivity due to its mechanical and chemical stability shows the potential of AlN masks. In future the presented plasma etching techniques of AlN will help to manufacture accurate features with very high aspect ratios in silicon. In addition to that, AlN is a suitable mask for plasma etching process with a strong physical compound (high bias voltages). For example deep oxide etching for manufacturing optical elements will be one application area.

#### IV - Summary

We present three AlN structuring techniques with different properties and fields of application. The first is KOH etching for rather big AlN features, where sidewall roughness is less important. A etch rate of 42 nm/min, while structuring 500 nm thick AlN with an underetch of 190 nm, is achieved. Silicon is not significantly etched and hence, smooth surfaces are possible. During etching we observed a maximum roughness of the etched surface of 30 nm (Ra). After etching AlN completely, including the residues, the roughness decreases to 0.7 nm.

The 2nd established process structures AlN in a plasma process using photoresist mask. The smallest feature sizes are determined by the lithographic resolution. Smooth sidewalls and high dimensional accuracy can be achieved. During the process, photoresist has a selectivity of 0.4 and no underetch occurred. The etched surfaces have a roughness of up to 10 nm. After structuring AlN, the resist is stripped in oxygen plasma, where residues on AlN surface are observed. These residues should not have any influence, while using the structured AlN as mask for following plasma processes.

For manufacturing AlN MEMS a third process is presented. In contrast to resist, a mask of  $SiO_2$  can be removed completely (HF vapor etching) after AlN

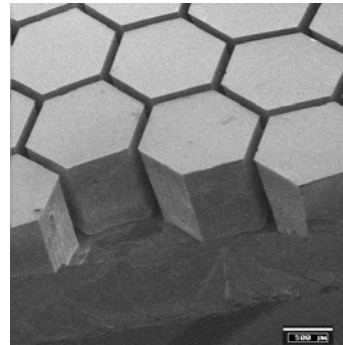


Figure 8: Deep silicon etching with AlN mask

etching. Different gas mixtures of  $Cl_2$ ,  $BCl_3$  and Ar are evaluated. A  $Cl_2/BCl_3$  ratio of 15:5 is found to be optimal, concerning roughness and etch rate. Smooth surfaces with a roughness of less than 1 nm and a good etch profile are achieved. For a pure  $Cl_2$  and Ar plasma a needle like surface structure is observed. Two possible generation mechanisms are presented.

Finally AlN mask is used for DRIE etching of silicon. A selectivity of 1:10,000 is achieved.

#### V - Acknowledgement

The authors acknowledge support from M. Breiter, T. Stauden and F. Niebelschütz. This work was supported by “Deutsche Forschungsgemeinschaft” DFG (grant number HO 2284/1-1)

#### References

- [1] B. Ha, I. Song, Y-K. Park, D-H. Kim, W. Kim, K. Nam and J.J. Pak, *Sensors and Actuators, A* 130-131, pp. 247-253, 2006.
- [2] S. González-Castilla, J. Olivares, M. Clement, E. Iborra, J. Sangrador, J. Malo and J.I. Izpura, *Applied Physics Letters*, vol. 92, pp. 183506, 2008.
- [3] G. Wingqvist, V. Yantchev and I. Katardjiev, *Sensors and Actuators, A* 148, pp. 88-95, 2008.
- [4] J. Elfrink, T.M. Kamel, M. Goedbloed, S. Matova, D. Hohlfeld, Y. van An del and R. van Schaijk, *Journal of Micromechanics and Microengineering*, vol. 19, pp. 094005, 2009.
- [5] H.C. Cho, S.C. Ur, M.S. Yoon and S.H. Yi, *IEEE 3rd Int. Conf. on Nano/Micro Engineered and Molecular Systems*, Sanya, pp. 637-640, 2008.
- [6] J. R. Mileham, S. J. Pearton, C. R. Abernathy, J. D. MacKenzie, R. J. Shul and S. P. Kilcoyne, *Applied Physics Letters*, vol. 67, pp. 1119-1121, 1995.
- [7] D. Chen, D. Xu, J. Wang and Y. Zhang, *Journal of physics D: Applied Physics*, vol. 41, pp. 235303, 2008.
- [8] K. Zhu, V. Kuryatkov, B. Borisov, J. Yun, G. Kipshidze, S. A. Nikishin, H. Temkin, D. Aurongzeb and M. Holtz, *Journal of Applied Physics*, vol. 95, pp. 4635-4641, 2004.
- [9] X. Xu, V. Kuryatkov, B. Borisov, M. Pandikunta, S. A. Nikishin and M. Holtz, *Materials Research Society Symposium Proceedings*, vol. 1108, pp. 181-186, 2009.
- [10] F. A. Khan, L. Zhou, V. Kumar, I. Adesida and R. Okojie, *Materials Science and Engineering*, vol. 95, pp. 51-54, 2002.



## Design and Evaluation of an Active Cooling Concept For Functional Ceramic Circuits

**T. Haas<sup>1</sup>, C. Zeilmann<sup>1</sup>, A. Backes<sup>2</sup>, A. Bittner<sup>3</sup>, U. Schmid<sup>3</sup>**

<sup>1</sup>Engineering Substrate, Micro Systems Engineering GmbH, Berg, Schlegelweg 17, 95180 Berg, Germany.

<sup>2</sup>Chair of Micromechanics, Microfluidics/Microactuators, Saarland University, 66123 Saarbrücken, Germany.

<sup>3</sup>Department for Microsystems Technology, Institute of Sensor and Actuator Systems, Vienna University of Technology, Floragasse 7, 1040 Vienna, Austria.

thomas.haas@mse-microelectronics.de

**Abstract** - In this study, an innovative cooling concept is proposed for LTCC (low temperature co-fired ceramics)-based printed circuit boards. Micromachined channels are integrated into the glass-ceramic body which are streamed with water as cooling medium to enhance the heat transfer from surface mounted components, such as MMICs or laser diodes compared to conventional thermal vias made of silver. Coupled thermo-fluidic finite element analyses are performed to optimize important parameters such as the channel geometry and the flow condition in the channel. Next, test structures are fabricated simulating the dissipated power losses of active devices by a thick film resistor which was heated up to a maximum temperature of 92°C with an electrical power of 0.3 W. Under these conditions, the temperature can be decreased to about 47°C when forcing water with a pressure of 0.3 MPa through the micro channel (width: 240 µm, height: 130 µm). In general, the results with respect to the reduction in temperature as a function of flow velocities are in good agreement with those gained from numerical calculations.

**Keywords:** *LTCC technology, micromachined channels, active cooling, finite element analyses, turbulent flow.*

LTCC ceramic, which is  $3\text{--}4\text{ W}\cdot\text{m}^{-1}\cdot\text{K}^{-1}$  [4] is disadvantageous and insufficient for an efficient thermal management especially for such high power application scenarios.

State-of-the art solutions use passive concepts with thermal vias, heat spreaders and heat sinks to improve the integral value of the thermal conductivity and to achieve adequate system cooling [5]. This approach, however, is limited due to a very specific design for each application as well as the poor efficiency [6], as the range of via geometries and their position within the layout are fixed. This is due to the limitations set by the design rules which, in turn, are based on manufacturability and system reliability (e.g. hermeticity) aspects. Therefore, active cooling concepts have to be investigated to combine all benefits of functional ceramic boards together with the required demand for high system reliability.

It is the objective of this study to design with FEA (finite element analysis) an integrated, miniaturized cooling system for LTCC ceramics using water as cooling medium. For verification purposes, test devices are fabricated comprising besides the micromachined channels a resistor element placed on top so that the efficiency in heat transfer and the overall thermal performance can be investigated experimentally and evaluated with the theoretically predicted results.

## I INTRODUCTION

Basically, LTCC (low temperature co-fired ceramics) circuits are widely used as functional ceramics in microwave applications due to a high reliability, the enhanced RF characteristics of the ceramic system itself as well as the excellent physical properties of the gold and silver conductors providing a low resistivity [1]. Furthermore, this technology offers the possibility to integrate passive components into the ceramic body, such as resistors, capacitors and inductors [2], what makes this technology advantageous to meet the increasing requirements in circuit miniaturization and performance by a continuous increase in the packing density of active and passive devices. However, this miniaturization trend leads also to higher power losses per unit area. Depending on the geometrical dimensions of the bare die, application specific values with respect to the dissipated heat can range up to some 100 W for RF components as well as power SSL (solid-state lighting) modules [3]. In addition, the poor thermal conductivity of the

## II EXPERIMENTAL DETAILS

The test substrates consisting of 6 layers are fabricated applying a conventional LTCC manufacturing process which is described in detail elsewhere [7]. As substrate material a commercially available LTCC tape from DuPont (DP 951) is used. For the realization of the microfluidic components (i.e. inlet/outlet, main channel) punching was chosen as well-established technique for the patterning of individual LTCC layers. Next, the layers are stacked and laminated at a pressure of about 16.5 MPa and a temperature of 70°C. The complete laminate is fired at a peak temperature of about 900°C. After firing a thick film resistor acting as heat source is applied onto the substrate surface. The realization of this component consists of two steps. First, contact lines and pads are printed with a 5734 Ag paste. After this post-firing step gold forming the resistor element is applied using a 50 Ω/square resistor paste. Both paste materials were purchased from DuPont.

A constant power of 0.3 W is applied to the resistor with an area of 0.078 mm<sup>2</sup>, resulting in a maximum resistor temperature of 92°C without cooling. As cooling medium a pressure driven water flow at 24°C is used. The driving pressure  $\Delta p$  can be varied between -0.3 and 0.3 MPa, so that a flow in both directions through the LTCC device is possible. The resistor temperature as a function of electrical heating power is measured with an infrared imaging system T200 from FLIR.

### III RESULTS AND DISCUSSION

The channel design being compatible to the standard production flow for LTCC devices is investigated by means of numerical simulation using the software tool ANSYS Fluent Version 12.0.16.

The cooling channel has a rectangular profile with a height of 130  $\mu\text{m}$  and a width of 240  $\mu\text{m}$ . The channel is connected to two service pipes, i.e. the channel inlet with a radial cross-section of 83  $\mu\text{m}$  diameter and the outlet with a rectangular cross-section having the same dimensions as the main channel (see Fig. 1a). In Fig. 1b, the corresponding hardware realization is presented, showing the arrangement of the different components in top view.

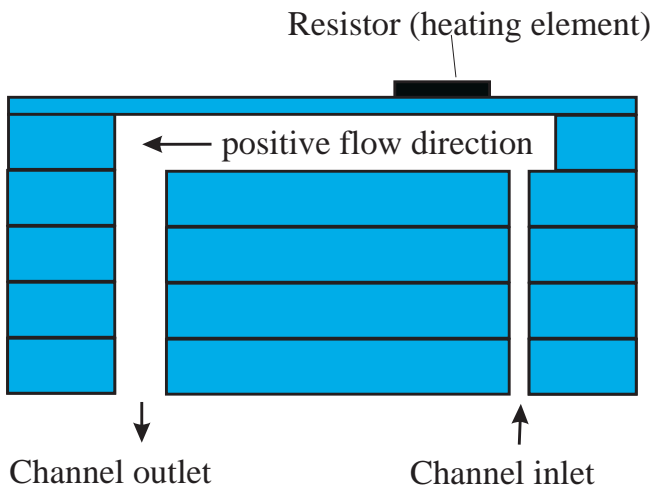


**Figure 1a:** Schematic, cross-sectional view on the test device.

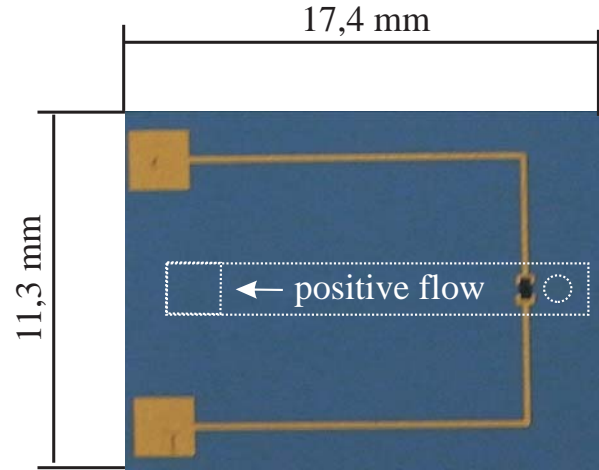


**Figure 1b:** Optical micrograph of the LTCC test substrate with integrated microchannels (dashed area), thick film heater (black) and contact lines (gold).

When forcing a water flow through the channel a cooling effect can be achieved. Besides laminar flow conditions typically expected in micrometer sized channels the geometry causes an enhanced degree of turbulence being, however, only induced when the water flow is injected from the inlet channel into the main channel. Doing so, two areas with corkscrew-type vortices are generated.

If the water flow is varied in negative and positive direction, Figs. 2a and b show the corresponding flux vectors gained from numerical simulations. The color refers to the flow velocity at the given position.

In Fig. 2a a laminar flow is displayed which is generated when forcing the water flow from the outlet via the main channel to the inlet which refers to a negative pressure difference ( $\Delta p < 0$ ) in this nomenclature. As expected, the flux propagates predominantly parallel to the channel axis.

In contrast, Fig. 2b illustrates the situation inside the channel when applying the water flow in opposite direction ( $\Delta p > 0$ ) through the LTCC device. Corkscrew-type vortices are formed in the area of the injection point due to the change in flow direction of 90° and hence, forcing the water flux to impinge on the top LTCC coverage layer. The artificially generated eddies are reflected back and follow the cooling channel with decreasing intensity (see Fig. 2b).

Besides the flow vector being predominantly parallel to the channel axis under laminar conditions, velocity components occur in the case of the induced turbulence which substantially deviate from this direction. As a consequence of the generated vortices, the velocity along the channel is decreased so that the mean duration time of the cooling liquid in the system is enhanced. This is demonstrated by a maximum velocity component of rotation reaching up to 5 m·s<sup>-1</sup>, which is about twice the value of the velocity in the laminar regions of the channel.

Another important advantage of the corkscrew motion in the cooling liquid is the local velocity distribution across the channel. Under ideal laminar flow conditions the velocity decreases parabolically from the maximum located in the middle of the channel to 0 m·s<sup>-1</sup> at the walls. The corkscrew-type vortices, however, shift the regions of maximum

velocity closer to the walls due to a more rectangular velocity profile, thus resulting in enhanced heat transfer from the hot spot. Based on this effect, the temperature of the heater  $T_h$  is lowered in comparison to laminar flow conditions. Comparable results of an enhanced heat transfer based on non-laminar flows conditions are well-known and reported in literature [8].

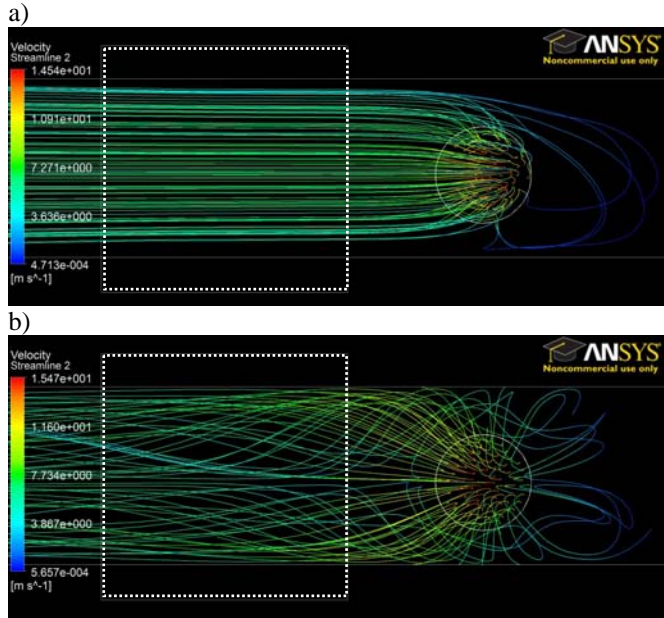


**Figure 2:** Top view on the area of the heater element. a) Streamlines indicating a laminar flow at negative driving pressure ( $\Delta p = -0.3$  MPa). b) Streamlines indicating two domains having corkscrew-type vortices which are generated at a positive driving pressure ( $\Delta p = 0.3$  MPa). In both figures the dashed lines mark the heating elements.

As an indicator of the corkscrew-type degree of turbulence, the helicity  $H$  of the flow field is calculated according to

$$H = \mathbf{v} \cdot \text{rot}(\mathbf{v}) \quad (1)$$

with  $\mathbf{v}$  as the velocity vector [9]. At a driving pressure of  $\Delta p = 0.3$  MPa the helicity reaches values up to about  $H = 2 \cdot 10^5 \text{ s}^2$ , whereas for negative flow directions this quantity is decreased to  $H = 2 \cdot 10^3 \text{ s}^2$ .

To achieve the highest cooling efficiency, the heater is placed right on top of this region with the highest helicity in the channel. To validate the simulated results, the calculated temperature levels are compared to experimental data measured with an infrared imaging system. Fig. 3 shows  $T_h$  as a function of  $\Delta p$  indicating the higher cooling effect with increasing pressure difference (i.e. water flow velocity).

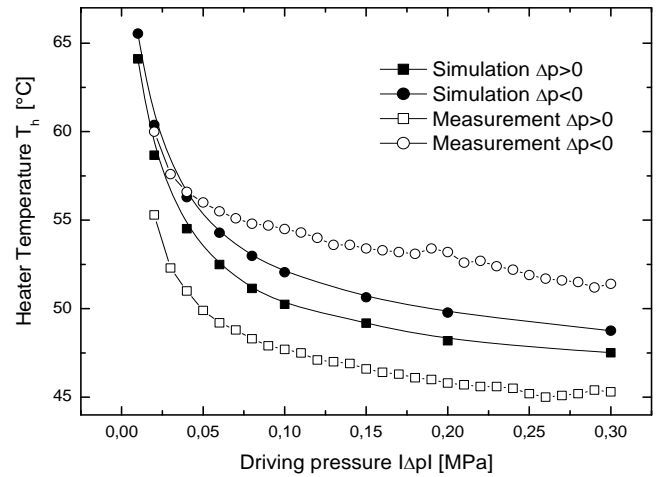


**Figure 3:** Temperature at the heating element as a function of pressure difference (i.e. positive and negative flow direction).

Independent of the absolute value of the pressure difference, an enhanced cooling effect is determined when the water flows in positive direction through the channel due to the induced vortices.

Furthermore, this effect is in principal theoretically predicted by the numerical calculations, although the FE analyses overestimate the heat transfer under laminar flow conditions and underestimate this quantity when a turbulent water flux is present. This may be in principal due to the roughness of the channel walls which is expected to be at least in the  $1\text{-}2 \mu\text{m}$  range as this value is measured on top of “as fired” LTCC substrates [10]. Therefore, this quantity is relatively large compared to the width and the height of the channel. For pre-evaluation purposes, however, this impact was not included in the FE analyses. Under laminar flow conditions, it is reasonable to assume that the velocity gradient near the walls is increased when using a perfectly smooth wall characteristic as approximation, so that an enhanced heat transfer results. In the case, however, where the water flux is impinging on the LTCC top coverage generating the corkscrew-type vortices along the channel axis, the convective heat transfer may be dominated by a larger active surface resulting in a more effective cooling in the real device.

## IV SUMMARY AND OUTLOOK

In this study, a LTCC substrate with integrated micro channels is proposed to enable an active cooling of surface mounted high power devices, such as laser diodes. For these pre-evaluation purposes, a heating element made in thick film technology was applied on top of the micro channel, providing a power density up to  $300 \text{ W}\cdot\text{cm}^{-2}$  which corresponds to a maximum temperature of  $92^\circ\text{C}$ . Water was used as cooling medium.

Depending on the water flow direction in the channel either laminar or turbulent conditions can be generated locally. In the latter case, an enhanced heat transfer is predicted by numerical simulations and by infrared imaging investigations in the region of the inlet channel due to an impinging water flux on the LTCC top coverage layer. So this area is preferred to apply the high power devices. Systematic deviations in the temperature of the heating device between the FEA and the experimental data as a function driving pressure are attributed to the roughness of the channel walls which are not included in the numerical calculations. Under maximum driving pressure and the generated vortices, the device temperature can be reduced from  $92^\circ\text{C}$  to values below  $50^\circ\text{C}$ , what is sufficient for most high power applications.

All in all, it can be summarized that the possibility to actively manage the dissipated heat on LTCC substrates within a wide range widens their fields of application substantially and paves the way for advanced high frequency and high power application scenarios. In the near future, further investigations have to concentrate on the long-term stability of such channels using glass-ceramic materials, as it is known that massive corrosive effects occur in copper-based approaches.

## REFERENCES

- [1] H. Jantune, T. Kangasvieri, J. Vöhökangas, S. Leppävuori: *Design aspects of microwave components with LTCC technique*, J. Europ. Ceram. Soc., Vol. 13 (14), pp. 2541-2548, 2003.
- [2] R. Körber, V. Ziegler, U. Schmid; *Imaging millimeter wave radar with phased array antenna*, Proc. 12<sup>th</sup> AMAA-conference, Springer Press, ISBN: 978-3-540-77979-7, pp. 167-180, Berlin, 2008.
- [3] Ryan Feeler, Jeremy Junghans, Edward Stephens, Greg Kemner, Fred Barlow, Jared Wood, Aicha Elshabini: *Advanced laser diode cooling concepts*, Mater. Res. Soc. Symp. Proc. Vol. 1076, 2008, Material Research Society.
- [4] T. Zawada: *Simultaneous estimation of heat transfer coefficient and thermal conductivity with application to microelectronic materials*, Microelectronics Journal, Vol. 37 (4), pp. 340-352, 2006.
- [5] J. Müller, M. Mach, H. Turst, C. Kluge, D. Schwanke; *Thermal design considerations for LTCC microwave packages*, Proc. EMPS-conference, pp. 159-164, Terme Catez, Slovenia, 2006.
- [6] M. A. Zampino, H. Adluru, Y. Liu, W. K. Jones: *LTCC substrates with internal cooling channel and heat exchanger*, International Symp. on Microelectronics; pp. 505-510, Boston, 2003.
- [7] L.J. Golonka: *Technology and application of low temperature cofired ceramic (LTCC) based sensors and microsystems*, Bull. Polish Academy of Science, Vol 54 (2), pp. 221-231, 2006.
- [8] Frank Kreith and David Margolis: *Heat transfer and friction in turbulent vortex flow*, Appl. Sci. Res Section A, Vol8, pp. 457-473, 1959.
- [9] H.K. Moffatt: *Helicity in laminar and turbulent flow*. Annu. Rev. Fluid Mech. Vol 24, pp. 281-312, 1992.
- [10] U. Schmid, G. Krötz, D. Schmitt-Landsiedel: *A volumetric flow sensor for automotive injection systems* J. Micromech. Microeng. Vol. 18, pp. 045006, 2008.



# DETERMINATION OF MECHANICAL AND SWELLING PROPERTIES OF EPOCLAD NEGATIVE PHOTORESIST.

Kristof Wouters<sup>1</sup>, Pieter Gijzenbergh<sup>1</sup>, Kris Vanstreels<sup>2</sup> and Robert Puers<sup>1</sup>

<sup>1</sup>KULeuven, ESAT-MICAS, Kasteelpark Arenberg 10, 3001 Leuven, Belgium.

<sup>2</sup>IMEC, Kapeldreef 75, 3001 Leuven, Belgium

**Abstract**—In this paper, the internal stress and the Young modulus of Epoclad are investigated using different methods. The swelling behavior, when submerged in common processing liquids, is also measured and reported, according to the authors knowledge, for the first time. Different on-wafer MEM structures were used together with nano-indentation measurement. The experimental results yield an internal stress that is strongly dependent on the ambient or submersion liquid and a Young's modulus of approximately 4.4GPa.

**Keywords:** Epoclad, internal stress, nano-indentation, polymer MEMS, Young's modulus

## I. Introduction

EPOCLAD is a relatively new, negative tone photoresist produced by micro resist technology GmbH [1]. Prior investigations have shown that the mechanical properties of Epoclad resemble those of the commonly used SU-8, also an epoxy based resin [2]. Over the last decade, SU-8 has emerged as a popular structural material for polymer MEMS, in high aspect ratio applications, such as microfluidics [3], in optical waveguides [4] and mechanical springs [5]. In this study Epoclad is characterized, as a polymer that can be used for the fabrication of polymer MEMS. The use of polymers has the potential to decrease the cost of the MEM system or enables the use of the versatile properties polymers can offer, compared to the traditionally used silicon and metal [6].

Epoclad is a photo definable epoxy. This means that the high crosslinked polymer network of Epoclad provides a very stable polymer, mechanically and chemically. In order to use this material as an active mechanical structure, a detailed study of the mechanical properties is mandatory.

The internal stress of the Epoclad polymer is measured using on-wafer stress indicator structures and nano-indentation on chariot wheel structures [7]. The stress indicator structures were also used for the swelling behavior tests. This is in more detail a measurement of the volume change of the polymer depending on the ambient. When the Epoclad is submerged in a liquid, the liquid can be absorbed by the polymer network. The absorbed material will take up space in the Epoclad layer and induces a compressive stress. This change of stress can then be recorded by the stress indicator structures. Although it is known that negative photoresists swell during development or in other circumstances, a more quantitative study of this behavior will yield more insight in the properties and behavior of the polymer and is mandatory when used as a permanent layer in MEMS.

Also, the Young modulus is measured using standard CSM (continuous stiffness measurement) nano-indentation on thick Epoclad films and nano-indentation on chariot wheel structures. These results are compared with data from a standard macroscopic tensile test [2].

In the first section of this report, a short overview of the modeling of the on-wafer test structures and the fabrication is given. The second part describes the testing and results of the indicator structures in different ambients and the nano-indentation experiments.

## II. Devices Modeling And Manufacture

### A. Stress Indicator Structures

The stress indicator structures used are an adaption of the design proposed by Goosen et al [8]. It produces a measureable displacement depending on the stress in the testbeams, present before the structure is released during the fabrication process, see Figure 1. Devices with testbeam lengths of 250 $\mu$ m and 100 $\mu$ m were used for the measurements, [9].

When the freestanding testbeams will relax their built-in tensile stress, they will shrink and produce a measureable displacement that can be accurately recoded using the Vernier grating.

When the structures are submerged in a liquid and the Epoclad polymer absorbs the submersion liquid, an additional stress component is induced that will shrink or expand the testbeam more. Hence, the stress in an Epoclad layer can be recorded depending on the ambient of the layer.

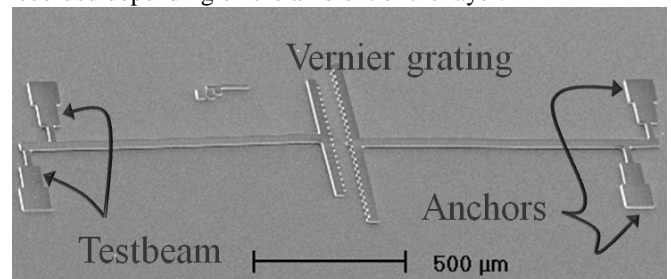


Figure 1: A SEM image of a stress indicator structure with 100 $\mu$ m test beams and a Vernier grating at the end of the amplification beams.

Using finite element simulations the relationship between measured displacement and internal stress was obtained. Models of the structures were created and a deviation-to-stress conversion factor was derived. For these models, material

characteristics were chosen to be 2.2GPa for the Young modulus  $E$ , as determined by a standard strain test during prior research [2], the internal stresses were swept around 10MPa and a value of 0.26 for the Poisson ratio, a typical value for polymers, was used.

### B. Chariot Wheels

In this section, an analytical model of the wheel structures that was used in the derivation of the Young modulus and the internal stress of Epoclad is described, see Figure 2. The outer part of each chariot wheel is connected to the substrate. Each of the four spokes are suspended approximately  $3\mu\text{m}$  above the surface. Spoke widths ( $W$ ) are  $40\mu\text{m}$  or  $20\mu\text{m}$ . Spoke lengths ( $L$ ) vary between  $900\mu\text{m}$  and  $200\mu\text{m}$ . The wheels were fabricated in two thicknesses ( $H$ ):  $17\mu\text{m}$  and  $19\mu\text{m}$ .

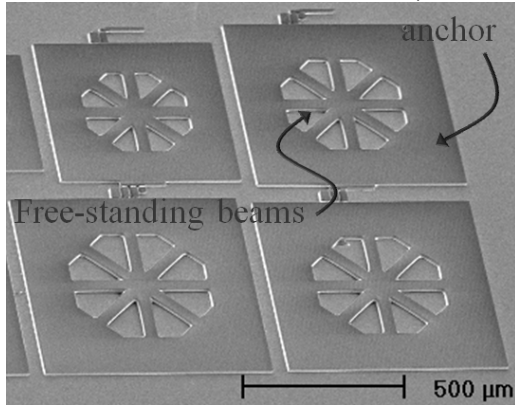


Figure 2: A SEM image showing four fabricated chariot wheel structures as part of a larger array with different beam lengths. Structural thickness is  $19\mu\text{m}$ , spoke width is  $40\mu\text{m}$ . Spoke lengths in this picture are between  $350\mu\text{m}$  and  $450\mu\text{m}$ .

The model is an adaption from a more thorough discussion by Senturia [10]. For a double-clamped beam, the stiffness,  $k$ , can be written in terms of beam dimensions  $W$ ,  $H$  and  $L$ , the internal stress  $\sigma_0$  and the elastic modulus  $E$  of the beam material. This is done by means of an energy optimization technique. The shape of the deformed beam is approximated by an arbitrary parameterized deformation function. The parameters in this function are determined so that the elastic energy of the beam and the work done for the deformation is minimal. As an example: when a vertical load is applied to the center (at  $x = 0$ ) of the beam with length  $L$ , (1) is a suitable deformation function,  $w(x)$ . It automatically fulfills the boundary conditions of ideal mechanical clamping at  $x = \pm L/2$ .

$$w(x) = \frac{c}{2} \left[ 1 + \cos\left(\frac{2\pi x}{L}\right) \right] \quad (1)$$

Using this test function with  $c$  as the parameter to be optimized, via the basis for the energy method, will result in

$$F = \left[ A \left( \frac{\sigma_0 W H}{L} \right) + B \left( \frac{E W H^3}{L^3} \right) \right] \cdot c \quad (2)$$

with  $F$  the central applied force and  $c$  the center displacement. Higher order terms of the center displacement were discarded. The values of the dimensionless parameters  $A$

and  $B$  in (2) are  $\pi^2/2$  and  $\pi^4/6$ , respectively and are dependent on the choice of the initial deformation function (1).

With finite element simulation several beams with different lengths were modeled. From the simulation data, the values of  $A$  and  $B$  were determined to be 3.551 and 16.13 respectively, which is only slightly different from the theoretical values above. These values were used for all further calculations.

Since the wheels are basically constructed out of four double-clamped beams, it is possible to use the stiffness of one such beam to define the stiffness of the entire wheel. An additional stiffness multiplier  $\alpha$  is needed and (2) is changed to:

$$F = k_{wheel} \cdot c = \alpha \cdot k_{beam} \cdot c \quad (3)$$

With  $k_{wheel}$  and  $k_{beam}$ , the stiffness coefficients of the chariot wheel and the individual beam respectively. Combining (2) and (3) finally results in:

$$k_{wheel} \cdot L = \alpha A H W \sigma_0 + \alpha \frac{B H^3 W}{L^2} E \quad (4)$$

To determine the stiffness multiplier, finite element simulations of the chariot wheel structures with different beam lengths were made. The stiffness of each wheel was simulated and compared to the stiffness of the corresponding single beam. For each length  $L$ , a value for the stiffness multiplier  $\alpha$  was found. As can be seen from Figure 3.

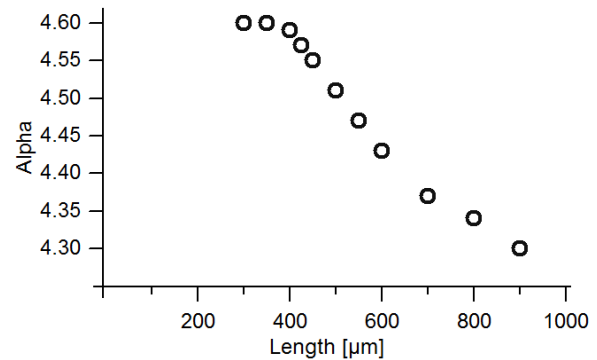


Figure 3: Graph of the stiffness multiplier  $\alpha$  in function of the spoke length. For very short or very long beams,  $\alpha$  converges to a fixed value.

The value of  $\alpha$  converges to 4 for increasing beam length, the number of beams that make up a single chariot wheel. For ever shorter beams, the center of the wheel behaves more like a membrane and  $\alpha$  also converges to a fixed value.

### C. Fabrication

To start the processing of the structures, a silicon substrate was prepared by removing any organic residue in piranha etch (sulfuric acid and hydrogen peroxide). Although adhesion between the substrate and Epoclad was expected to be high enough, a chrome layer was sputtered onto the dehydrated substrate to improve it even further.

A  $3\mu\text{m}$  sacrificial polyimide layer was coated and patterned with a conventional photolithography step. The Epoclad was spincoated for a thickness of approximately  $18\mu\text{m}$ . The film was softbaked on a conventional hotplate. Temperatures were

as recommended by the manufacture datasheet, except the times were increased in order to avoid stiction during exposure. The UV illumination had an intensity of  $5\text{mW}/\text{cm}^2$  around the g-line of the spectrum. A post exposure and hardbake were performed under  $\text{N}_2$  atmosphere in a conventional oven at respectively  $110^\circ\text{C}$  and  $150^\circ\text{C}$ . After the Epoclad structure was patterned and cured, the sacrificial layer was etched in an alkaline solution. A  $\text{CO}_2$  critical point drying (CPD) step was used to obtain a stictionless release. During CPD, a residual thin film had formed on top of the structures. This residue was removed by means of a two-minute reactive ion etching (RIE) in an oxygen plasma.

### III. Experimental Details And Results

#### A. Stress indicator Structures

After RIE, the dried indicator structures were inspected by means of an optical microscope. Photographs were taken and the deviation of the Vernier gratings was recorded. The dry structures were also submerged in several liquids to determine the swelling behavior. The internal stress was recorded in PGMEA (Propylene Glycol Methyl Ether Acetate), IPA (IsoPropyl Alcohol) because of their importance in the processing and in water, because it has a high influence on the internal stress and it is always present in the form of humidity in the ambient air.

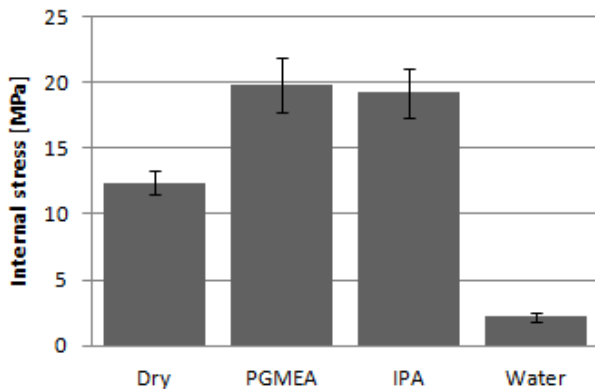


Figure 4: Comparison of the internal stress in dry structures and structures submerged in various liquids.

Figure 4 represents the results of the swelling tests. The internal stress increases when the Epoclad structures are submerged in PGMEA or IPA, to just below 20MPa. An additional, internal, compressive stress caused by the absorbed water molecules brings the total stress down to 2MPa.

The solvents possibly dehydrate the moisture absorbed before the experiment, present in the ambient air and thus increase the internal stress relative to the dry situation. When submersed in water, it is absorbed by the polymer and causes it to swell. Or in other words, the absorbed water induces an extra compressive stress in the Epoclad together with the built tensile stress. The net result is a stress of the film close to zero relative to the dry situation. All recorded values were averaged and standard deviations were calculated.

#### B. Nano Indentation Measurement On Epoclad

A conventional nano-indentation experiment was done using a nano-indenter XP system from MTS Systems Corporation with a dynamic contact module and a CSM option under constant strain rate condition ( $0.05\text{ s}^{-1}$ ). A standard three-sided pyramid diamond indertip (Berkovich) was pushed into a layer of Epoclad. [11]. While indenting, a small 75Hz oscillating signal was superimposed on the downward movement of the indertip.

The CSM was executed on thirty different locations. The Young modulus was calculated from the gathered data. It should be noted that Epoclad is a visco-elastic polymer, which means that the stiffness of the material is a function of the indentation speed and of the frequency of the superimposed signal. Briscoe [12] noted some other possible issues concerning the indentation of polymeric surfaces such as creep and relaxation [2].

The indentations performed on the chariot wheel structures were different from the ones performed on the Epoclad layer. Instead of a Berkovich geometry, a conical flat ended tip with a diameter of  $10\mu\text{m}$  was used to apply a monotonically increasing load of  $0.005\text{mN/s}$ . On every wheel, 15 consecutive indentations were performed. Applied loads and center displacements were recorded and used to calculate an average stiffness per wheel. This data was used to produce a graph representation of the  $kL$  versus  $1/L^2$  relationship per set of wheels (same width and height). Using a linear fit and correlating this with (4) the Young modulus and the internal stress of Epoclad can be calculated, as shown in Figure 5.

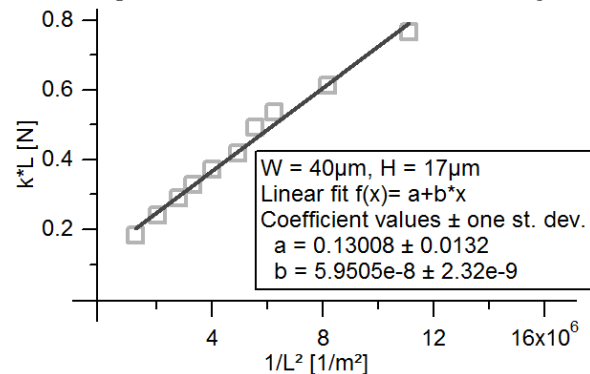


Figure 5: Linear fit through the indentation data of ten wheels with a thickness of  $17\mu\text{m}$  and a width of  $40\mu\text{m}$ . The line equation combined with (4) and values of  $a$  result in values for internal stress and modulus of elasticity.

Three sets of wheels were tested. Results over all wheels in a set were averaged and a standard deviation was calculated.

Figure 6 presents the measured values for the residual stress in dry Epoclad. Three sets of indicator structures were analyzed and three sets of chariot wheels were indented. Most of the results show an internal stress of 12MPa in the Epoclad, which is consistent with earlier work published in [9]. The thicker chariot wheels show a significantly lower internal stress. Testing conditions, such as relative humidity of the air, may have a large influence on these results.

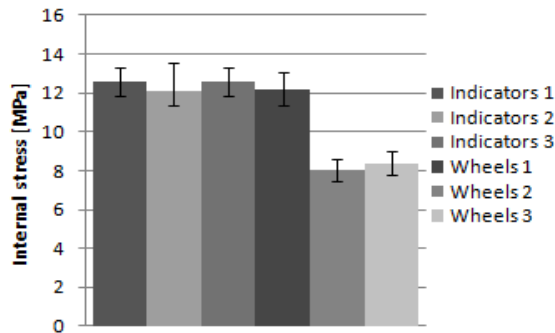


Figure 6: Results for the internal stress measurements. The indicators in set 1 were 17 $\mu$ m thick with 250 $\mu$ m test beams. Indicatorsets 2 and 3 were 19 $\mu$ m thick with respectively 250 $\mu$ m and 100 $\mu$ m test beams. Wheelset 1 was 17 $\mu$ m thick with spoke width 40 $\mu$ m. Wheelsets 2 and 3 were 19 $\mu$ m thick with respectively 40 $\mu$ m and 20 $\mu$ m spoke width.

In Figure 7, the Young modulus shows very constant results for all executed tests. Both the indentation of the plane via CSM and the nano-indentation of different sets of chariot wheels return a value of 4.4GPa. A prior macroscopic tensile strain test on Epoclad revealed a modulus of elasticity of 2.2GPa. This difference can be explained by several arguments. First of all, Epoclad is a visco-elastic polymer which makes it hard to determine one fixed elastic constant. The difference of test method can also have an influence. The nano-indentation is a compressive test, or has a large compressive load component in the case of the wheels. The strain test, however, applies a tensile load. Also the built-in stress, which can change depending on the air humidity, can affect the measurement of the Young modulus.

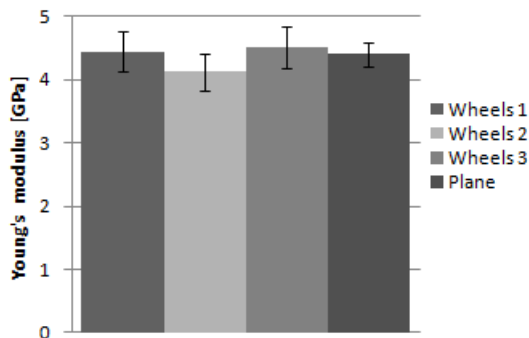


Figure 7: Results for the modulus of elasticity measurements. For the chariot wheels, the legend is the same as in Fig. 5. The Epoclad plane was 17 $\mu$ m thick.

#### IV. Conclusion

This paper presented the fabrication process, the testing methods and a theoretical background to determine important material characteristics for micromachined polymers, applied

to Epoclad negative tone photoresist, using on-wafer test structures. The internal stress was found to be approximately 12MPa in dry and room temperature conditions (RH 45% and 21°C). Internal tensile stress reached a maximum of 20MPa in PGMEA and similar values were recorded in IPA. Water absorption relieved the stress to just 2MPa. According to the authors knowledge this is the first published quantitative swelling behavior result of Epoclad. It should be noted that the fabrication of the stress indicator structure is relatively simple. Thus, the swelling test for other liquids can be performed when needed.

The Young modulus was measured to be 4.4GPa using standard CSM nano-indentation and using indentation on chariot wheels made of Epoclad.

#### Acknowledgment

This work has been carried out in the frame of SBO-program project 060046, Gemini, sponsored by the "Instituut voor de aanmoediging van Innovatie door Wetenschap en Technologie in Vlaanderen" (IWT), Belgium.

Supported by the Hercules initiative for large equipment (AKUL034), cluster for micro and nanolithography

#### References

- [1] EpoClad/EpoCore Negativ Tone photoresist series, datasheet online at [http://home.snafu.de/microresist/products/negative\\_photoresists/epocore\\_clad\\_en.htm](http://home.snafu.de/microresist/products/negative_photoresists/epocore_clad_en.htm)
- [2] K. Wouters and R. Puers, "Determining the Young's modulus and creep effects in three different photo definable epoxies for MEMS applications," *Sens. Actuators A: Phys.*, 2009.
- [3] F. E. H. Tay, J. A. van Kan, F. Watt and W. O. Choong, "A novel micro-machining method for the fabrication of thick film SU-8 embedded micro-channels," *Journal of Micromechanics and Microengineering* 11, pp. 27-32, 2001.
- [4] K. K. Tung, W. H. Wong and E. Y. B. Pun, "Polymeric optical waveguides using direct ultraviolet photolithography process," *Appl. Phys. A* 80, pp. 621-626, 2005.
- [5] D. Bachmann, B. Schoberle, S. Kuhne, Y. Leiner and C. Hierold, "Fabrication and characterization of folded SU-8 suspensions for MEMS applications," *Sens. Actuators A: Phys.* 130-131, pp. 379-386, 2009.
- [6] Chang Liu, "Recent developments in polymer mems", *Advanced materials*, 2007 vol:19, pp: 3783
- [7] G. Van Barel et al, "determination of the Young's modulus of poly-SiGe micromachined structures using novel mechanical actuation test techniques", *Proceedings XX Eurosensors*, :Leuven Belgium 2006, 282-283
- [8] J. F. L. Goosen, B. P. van Driehhuizen, P. J. French and R. F. Wolffenbuttel, "Stress measurement structures for micromachined sensors," *Tech. Dig. 7<sup>th</sup> Int. Conf. On Solid State Sensors and Actuators, Transducers* 93, pp. 783-786, 1993.
- [9] K. Wouters and R. Puers, "Design and measurement of stress indicator structures for the characterization of Epoclad negative resist". *J. Micromech. Microeng.* 19, 2009, 074019-8pp
- [10] S. Senturia, *Microsystem design*. KAP, 2001.
- [11] J. Mencik, "Determination of mechanical properties by instrumented indentation," *Meccanica* 42, pp. 19-29, 2007.
- [12] B. J. Briscoe, L. Fiori and E. Pellilo, "Nano-indentation of polymeric surfaces," *J. Phys. D: Appl. Phys.* 31, pp. 2395-2405, 1998.



# GRAPHENE FOR NANO-ELECTRO-MECHANICAL SYSTEMS

Z. Moktadir, S. Boden, H. Mizuta and H. Rutt,

University of Southampton, School of Electronics and Computer Science, Highfields,  
SO17 1BJ, Southampton UK

**Abstract** — We discuss the prospect of graphene as a material for nano-electro-mechanical-systems. A comparison between SOI silicon and graphene fabrication technologies is presented as well new ideas for integrated new electromechanical devices combining novel electronic and mechanical properties of graphene. We also present new results of graphene nanostructuring with the helium ion microscope as an emerging technology for fabrication of electromechanical devices..

**Keywords** : Graphene, Helium ion microscope, NEMS, MEMS

## I - Introduction

Recent years have seen a growing interest in graphene material. This material, has attracted such interest thanks to its remarkable electrical properties. Graphene is only one to a few atomic layers thick and yet it is the strongest known material. Electrons in graphene exhibit very high mobility, with zero effective mass and mean free path of a few micrometers, even at room temperature [1]. It can sustain current densities five order of magnitude larger than ordinary metals, and exhibits very large thermal conductivity [2] and strength [3]. It also exhibits large negative thermal expansion coefficient which is up to 10 times that of graphite [4].

To date, only electronic properties of graphene are widely explored. These studies revealed novel electronic properties by fabricating structures such as p-n junctions [5], nano-ribbons [6], quantum point contact [7], single electron transistors [8], and quantum dots [9], etc. Research progress in this direction will make graphene a "neo-silicon" material of choice for future electronic components.

Other graphene attributes such as mechanical or thermal properties have not been so widely investigated. A few studies reported values of room-temperature thermal conductivity of  $\sim 5000 \text{ W m}^{-1} \text{ K}^{-1}$  [2] and breaking strength of 42 N/m [3]. Values of Young's modulus were reported to be close to 1 TPa [3]. Studies also showed that graphene is a very flexible material and impermeable to gases making it ideal for many applications in life science [10].

Despite the significant amount of work on graphene electronic devices such as the field effect transistor, its use in sensors, actuators or micro and nano-electro-mechanical systems (MEMS/NEMS) in general, is as yet little explored. Bunch et al. have demonstrated graphene electromechanical resonators exhibiting charge sensitivities down to  $8 \times 10^{-4}$  electrons per root Hz at room temperature, highlighting the potential of

graphene for NEMS applications [11]. By combining graphene's electronic and mechanical properties, monolithic sensors can be developed with superior sensitivity.

Despite the fact that silicon technology remains dominant in NEMS and MEMS areas, the growing interest in graphene is slowly building up, which could pave the way to new devices. For example mono or bilayer graphene has been tipped as a new channel material of choice for transistors to compete with the latest silicon innovations such as the development of extremely thin silicon SOI material with only a few atomic layers of silicon [12]. In spite of the enhanced carrier mobility of ultrathin SOI MOSFET (i.e. in channel thicknesses of around 3~4 nm, the mobility enhancement is due to subband energy modulation), mono and bilayer graphene show even higher values of the carries mobility, which can exceed  $15,000 \text{ cm}^2 \text{ V}^{-1} \text{ s}^{-1}$  [13], enabling fast electronics as demonstrated by IBM on their 100 GHz graphene FET [14].

From the mechanical point of view, graphene is one of the strongest materials ever discovered with a breaking strength of over 200 times that of steel [3]. It is thus logical to consider thick graphene\* as a material for micro and nano mechanical devices, e.g. accelerometers, pressure sensors, membranes, resonators, etc. Recent progress in epitaxial growth of graphene led to the development of very high quality "thick graphene" made of a stack of single atomic layers [15], on a wafer scale, by Fujitsu Ltd. The mechanical properties of this high quality material remain to be investigated. This development will open possibilities for the development of new technologies based on thick graphene.

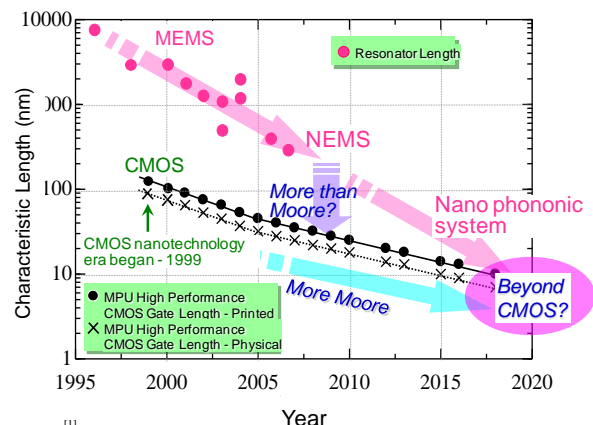


Figure 1: Graphic representation of NEMS down-scaling trend.

[1] A tunable carbon nanotube electromechanical oscillator

Nature, 431, p284-287 (2004)

[2] Sensitive detection of nanomechanical motion using piezoresistive signal downmixing

Appl.Phys.Lett. 86, 133109 (2004?)

Si/Si doped Bolon cantilever

Length 2-3  $\mu\text{m}$ , Width 700nm, Thickness Si 80nm + Si(B) 30nm

[3] Feedback controlled nanomechanical device

Appl.Phys.Lett. 85, 681 (2003?)

\* Here we mean by "thick graphene" more than 3

atomic layers

[4] Nanomechanical systems: Nanodevice motion at microwave frequencies

Nature, 421, p496 (2003)

Double clamped 3C-SiC beam

Length 1.1  $\mu\text{m}$ , Width 120nm, Thickness 75nm

[5] Nanowire-based very-high-frequency electromechanical resonator

Appl.Phys.Lett. 83, 1240 (2002)

Double clamped Pt nanowire

Length 1.3  $\mu\text{m}$ , Diameter 43nm

[6] Parametric frequency tuning of phase-locked nanoelectromechanical resonator

Appl.Phys.Lett. 79, 3521 (2001)

Double clamped Si covered Au?

Material	Young Modulus TPa	Mobility $\text{cm}^2\text{V}^{-1}\text{s}^{-1}$ (300°K)	Thermal conductivity $\text{Wm}^{-1}\text{K}^{-1}$	Poisson ratio
Graphene(mono-bilayer)	~ 1 [3]	>15000 [1]	~ 5000 [2]	0.165 [3]
silicon	~0.13[16]	$\leq 1400$ [17]	~1500[18]	~0.28 [18]

Table 1: Materials properties of graphene and bulk silicon.

One can envisage a hybrid thin-thick graphene structures, using thin graphene (less than 4 atomic monolayers) for electronics and thick graphene for mechanical structures.

In figure 1 we show the silicon NEMS downscaling trend. Graphene NEMS (GNEMS) would join the trend later on during the -SiNEMS era. One foresees two possibilities; graphene for more Moore or graphene for more than Moore by combining GNEMS with graphene transistor.

## II – Material properties and technology

NEMS technology has recently emerged as a viable route towards the production of novel, high speed devices, offering high density integration and devices with low power consumption. These devices are a result of a hybrid approach, combining NEMS with conventional CMOS electronics ("More than Moore"). Such hybrid devices find applications in logic [19], non-volatile memory [20] and ultrasensitive mass detectors [21]. An example of a non-volatile memory NEMS device is the suspended gate field effect transistor (SGFET) [22], consisting of a moveable beam (the gate) and a MOS channel. This device exhibits a higher switching speed compared to the conventional silicon MOSFET. The remarkable mechanical and electronic properties of graphene, suggest that it is possible to develop such hybrid structures using this material instead of silicon. However, to manufacture reliable graphene NEMS/MEMS, will require the maturity of graphene growth technologies on the wafer scale and low cost production. Such technologies are still in their infancy despite recent development by research groups and industries [15].

Thin body SOI has been the material of choice to develop integrated NEMS. in which mechanical as well as electronic structures can be fabricated, allowing low power and high frequency operation. The technologies used here are mature MEMS and IC manufacturing processes combining material deposition, dry and wet etching technologies, etc. To be able to manufacture (GNEMS) devices, various technologies need to be developed including wet and dry etching of graphene as well as selectivity with regard to various mask materials e.g. photoresist, silicon oxide, silicon nitride, etc.

It is useful to draw a comparison between silicon and graphene although bulk properties of silicon may differ from thin SOI silicon, but good approximations can be made with the available data. Table 1 shows different material parameters for graphene and bulk silicon.

One notices for instance, graphene's higher value of the Young modulus compared to that of silicon. This higher value will allow the fabrication of high frequency resonators from graphene. For example a nano-beam made of multilayer graphene would have a resonant frequency roughly three times larger than a beam of silicon having the same dimensions based on the values in Table 1. The remarkably higher thermal conductivity and high current carrying capacity will allow the use of graphene as interconnects in electronic 'chips' as a replacement for copper. The high values of graphene mobility will provide a good material to be used as a channel in MOSFETs.

Thin body SOI production is performed by successive thermal dry oxidation and wet chemical etching of an initial SOI wafer, until the desired silicon thickness is reached. This method has achieved thicknesses of three to four atomic layers [12]. To produce graphene, three methods are used in general: mechanical exfoliation of graphite [25], epitaxial growth on SiC [23] and chemical vapor deposition (CVD) onto metallic surfaces [15]. Thin graphitic layers can be epitaxially grown on 4H-SiC substrate, by the thermal decomposition of either Si-or C-terminated surface [23]. Epitaxial graphene on silicon carbide can be patterned using standard micro-electronics processes allowing large integrated electronics on SiC [24]. Exfoliation of graphene sheets remains the only method that produces high quality graphene flakes which are obtained by micromechanical cleavage of bulk graphite [25].

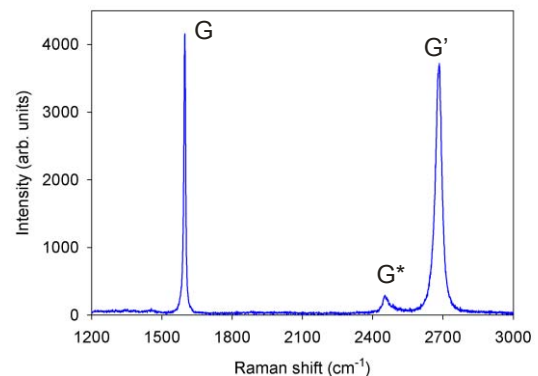


Figure 2: Raman spectra taking on a monolayer graphene showing the G-band peak position at 1600  $\text{cm}^{-1}$  and G' band of monolayer graphene at. 2685  $\text{cm}^{-1}$

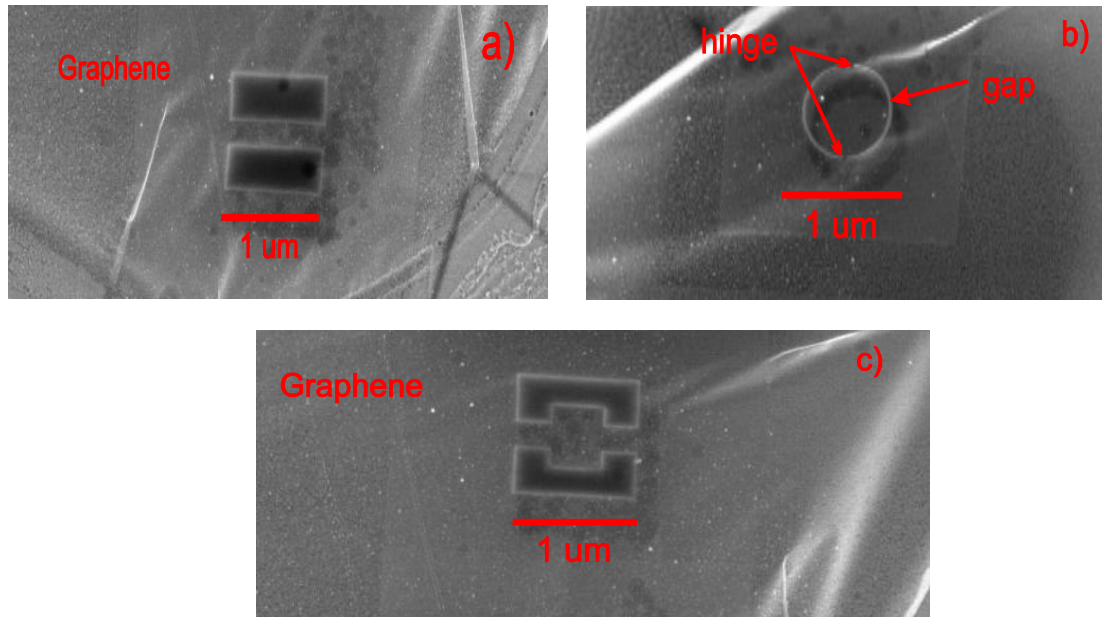


Figure 3. Helium ion patterning of nanostructures on bilayer graphene: a) a nano-beam having a length of 1  $\mu\text{m}$ , a width of 200 nm; b) a wine glass disk graphene resonator and c) a resonant torque structure.

### III – Graphene nano-patterning with the helium ion microscope

Here we present results on nano-patterning of exfoliated graphene using a new tool: the helium ion microscope (HIM)[26]. This tool is a new imaging technology based on a scanning helium ion beam instead of an electron beam. The HIM provides a helium ion probe with a size smaller than 0.7 nm which can be scanned across a sample in a pre-defined pattern to selectively remove areas by direct sputtering of the graphene material [27]. The He ion beam also exhibits low proximity effect compared to Ebeam lithography. This allows a highly localized writing on materials as we will show here. Our tool integrates pattern generator software which offers a user interface allowing the exposure parameters to be adjusted such as the dose, dwell time, writing resolution, etc., as well as the definition of the pattern to be written, either as predefined geometries or a bitmap file. Here, graphene samples are obtained using the exfoliation procedure resulting in monolayer, bilayer and multilayer graphene. The number of atomic layers was determined by Raman spectroscopy. Figure 1 shows an example of a Raman spectrum taking on a monolayer region of the flakes. The characteristic G ( $\sim 1600\text{ cm}^{-1}$ ) and  $G'$  ( $\sim 2685\text{ cm}^{-1}$ ) peaks are clearly visible and the absence of the D peak at  $1345\text{ cm}^{-1}$ , the presence of which is associated with disorder in  $\text{sp}^2$ -hybridized carbon systems, indicates the high quality, defect-free nature of the flake [28].

The sample was loaded into the HIM and the writing was performed under a vacuum of  $\sim 5 \times 10^{-7}$  Torr. Prior to writing, the HIM chamber was cleaned overnight by an embedded plasma system to avoid contamination of

the sample during the writing operation.

Figure 2-a, 2-b and 2-c show a nano-beam, a wine glass disk resonator nanostructure and a resonant torque nanostructure respectively. These structures were patterned with a resolution of 1 nm/pixel. After patterning, the structures were released by vapor HF etching of the underlying oxide (300 nm thick). One notices the fine edges of these structures thanks to the very small spot of the beam. This level of accuracy is very hard to achieve with e-beam lithography which is widely used for graphene patterning. The nano-beam has a length of 1  $\mu\text{m}$  and the width of about 200 nm, while the resonator has a diameter of 1  $\mu\text{m}$  and a gap of less than 30 nm. Gaps less than 10 nm can be achieved. These structures are very familiar MEMS and NEMS structures which are used as sensors or resonators. For instance, as the Young modulus of graphene is close to 1 TPa, very high-frequency resonators (Lame' mode resonators) can be fabricated. The graphene patterning with HIM can achieve a variety of other devices with extremely small dimensions. We are actively working on the functionalisation of these structures by patterning metal electrodes on the structures to allow sensing applications using an integrated gas injection system (GIS) which provides a local metal deposition. This system is used in combination with the He beam to deposit thin metal films and metallic nano-structures by means of chemical vapor deposition (CVD). By taking advantage of graphene enhanced electronic properties, it is possible to develop monolithic schemes for graphene devices which combine movable structures, such as those fabricated here, and a graphene field effect transistor (GFET). Sensing can be achieved through capacitive coupling between the channel of the GFET and the moving graphene structure. One can also take advantage of the fact that

graphene is easily gated (i.e. the resistivity is modulated by the back gate voltage) and in combination of mechanical structures to develop tunable grapheme sensors and actuators.

#### IV – Conclusion

We have shown that graphene can be used as a material for nano-electro-mechanical-systems. Owing its extraordinary electrical and mechanical properties, enhanced performance devices can be achieved. However, real progress can only be made with the availability of graphene on the wafer scale and the development of new fabrication technologies for graphene. This will allow design and patterning using standard MEMS/NEMS and IC technologies. We have demonstrated the feasibility of graphene nano-patterning using the helium ion microscope. Very fine structures can be obtained thanks to the small beam size and the milling capabilities of the helium ion beam. Future work will focus of the functionalisation of such devices by electrodes deposition on the structures using a gas injection system embedded in the helium ion microscope.

#### References

- [1] Novoselov, K. S. et al. Nature 438, pp. 197–200 (2005)
- [2] Balandin, A. A. et al, Nano Letters 8 (3): pp. 902–907 (2008).
- [3] Lee, C. et al. Science 321 (5887): pp. 385–388 (2008).
- [4] Bao, W. et al., Nature Nanotechnol. 4, p. 562 (2009).
- [5] J. R. Williams, L. DiCarlo, C. M. Marcus, Science 317, 638 (2007)
- [6] Z. Chen et al., preprint available at <http://arXiv.org/abs/cond-mat/0701599>.
- [7] Barbaros Özyilmaz et al. Appl. Phys. Lett. 91, p. 192107 (2007)
- [8] C. Stampfer et al. Nano Lett. 8 (8), pp 2378–2383(2008).
- [9] A. K. Geim, K. S. Novoselov, Nat. Mater. 6, p. 183 (2007).
- [10] Bunch, J. S. et al. Nano Letters 8 (8), pp. 2458–2462 (2008).
- [11] Bunch, J. S. et al. Science 315, p. 490 (2007).
- [12] K. Uchida, et al. IEDM Tech. Dig. pp. 47–50, (2002).
- [13] Novoselov, K. S. et al. Nature 438, p. 197(2005).
- [14] Yu-Ming Lin et al. Nano Lett. 9, pp. 422–426 (2009).
- [15] Daiyu Kondo et al. Apply. Phys. Exp. 3 p. 025102(2010)
- [16] Petersen K. E. and Guarnieri J. Appl. Phys. 50, p. 6761, (1979).
- [17] <http://www.ioffe.rssi.ru/SVA/NSM/Semicond/Si/electric.html>
- [18] M. Gad-el-Hak edit., *MEMS Handbook*, CRC press (2002).
- [19] Pruvost, B et al. IEEE trans. Nanotech. In press (2010)
- [20] Nagami, T. et al, Jpn. J. Appl. Phys., 49 , p. 044304 (2010).
- [21] Hassani, F. A. et al, In: 2009 International Conference on Solid State Devices and Materials (SSDM 2009), 7–9 October, Sendai-Japan.
- [22] Garcia Ramirez, M. et al. Microelec. Eng. 87 p. 1284 (2009).
- [23] C. Berger, et al. , Science 312, p. 1191 (2006).
- [24] Berger, C. et al. J. Phy. Chem. B 108, p. 19912 (2004)
- [25] K.S. Novoselov, et al. Science 306, p. 666 (2004).
- [26] [www.smt.zeiss.com](http://www.smt.zeiss.com)
- [27] Bell, D. C. et al. Nanotechnology 20, 455301 (2009).
- [28] Dresselhaus, M. S. et al. Nano Letters 10 (3) pp.751– 758 (2010).



# INDUCTIVE-COUPPLING SYSTEM FOR ABDOMINAL AORTIC ANEURYSMS MONITORING BASED ON PRESSURE SENSING

A.T. Sepúlveda<sup>1,3</sup>, A. Moreira<sup>2</sup>, F. Fachin<sup>3</sup>, B.L. Wardle<sup>3</sup>, J.M. Silva<sup>4</sup>, A.J. Pontes<sup>1</sup>, J.C. Viana<sup>1</sup> and L.A. Rocha<sup>1</sup>

<sup>1</sup>*13N/IPC-Institute for Nanostructures, Nanomodelling and Nanofabrication, University of Minho, Portugal*

<sup>2</sup>*University of Porto – Faculty of Engineering, Porto, Portugal*

<sup>3</sup>*Department of Aeronautics and Astronautics, Massachusetts Institute of Technology, Cambridge, MA, USA*

<sup>4</sup>*INESC Porto, University of Porto – Faculty of Engineering, Porto, Portugal*

**Abstract** — Permanently implanted sensors with continuous monitoring of pressure for cardiovascular applications are particularly attractive as they provide additional opportunities for better therapies and enhanced quality of life. In Abdominal Aortic Aneurysms (AAAs), where stent-grafts are frequently used for treatment, are exemplary applications for this type of device. This paper introduces a new carbon nanotube (CNT)-based flexible capacitive sensor along with two different reading systems based on inductive-coupling. The fabrication process for the flexible sensor and the main characteristics of the reading systems are presented, as well as simulation results and preliminary experimental results of CNT-PDMS elements. Electrical conductivity of PDMS membranes with embedded aligned CNTs is 10 S/m, in the direction perpendicular to the CNT axis.

**Keywords:** *Inductive-Coupling, Stent-Graft, Pressure Sensor, Carbon Nanotube.*

## I - Introduction

Abdominal aortic aneurysms (AAAs) are a common vascular disease affecting 12 per 100 000 persons-year [1] and are expected to increase with the rise in life's expectancy. Nowadays, two treatments are available: conventional surgical repair (open surgery) and endovascular aneurysm repair (EVAR). EVAR is a minimally invasive procedure in which a stent-graft is guided from the femoral artery to the affected artery segment in order to prevent wall rupture, thereby shielding the aneurysm from the blood pressure (BP). This treatment requires regular surveillance in order to detect and prevent complications such as graft migration, stent fracture, endoleaks, enlargement of the aneurysm sac, and AAA rupture. Despite the advances in EVAR in recent years, reintervention is still needed in ~10 % of patients [2]. Therefore, procedures for monitoring and supervising are crucial in detecting future problems and improving overall efficacy of AAS repair.

The sensing methods used in today's procedures require a long time to complete, causing discomfort to the patients while exposing them to carcinogenic risks [2-4] due to ionization radiation (e. g. computed tomography). Moreover, the results are not always accurate in the detection, leading in some cases to false-positive findings [4].

This work proposes a new method to monitor AAAs after the EVAR procedure. The monitoring system uses inductive-coupling to deliver energy and to communi-

cate with a flexible capacitive sensor that is placed inside the aortic aneurysm sac, prefabricated and attached to the stent-graft. The proposed solution does not require any additional surgical intervention, and is passive except when read. The system should be able to incorporate multiple sensors (figure 1) rather than a single sensor to increase both the efficiency of the monitoring system, provide important information about the evolution of the aneurysm, as well as effectively eliminate false positives by providing statistical information as a function of spatial placement of the multiple sensors.

Each sensor comprises an LC resonant circuit, with a different oscillation frequency. The monitoring system is based on the deviation of the sensors' oscillation frequency by means of a capacitive pressure transducer. This paper focuses mainly on the telemetry reader system, the most critical block of the entire reading circuit, and on the fabrication technology of the pressure sensor, given requirements that the sensor be foldable, extremely flexible and characterized by a very small profile (in line with the minimally-invasive procedure used for endoprosthesis deployment).

This paper is divided in four major sections. Section II describes the two alternative circuits being developed for the communication with the sensors. Section III provides the details of the flexible sensor fabrication process. Section IV shows some of the preliminary results obtained and finally, section V highlights the conclusions and points out future work.

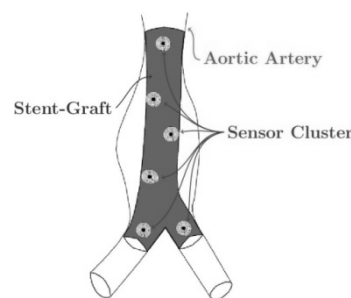


Figure 1: Abdominal aorta aneurysm after EVAR, featuring the sensor cluster attached to the stent-graft.

## II - Reader/Sensors Communication

The system oscillation frequency was chosen to operate in the frequency band from 12.5 MHz to 20.0 MHz allocated specifically for medical applications. This frequency band was also selected because, unlike the low frequencies of operation, it does not require inductors and capacitors with large dimensions that would affect the overall sensors' area. Additionally, this

band guarantees some protection against biological effects and interferences generated by other electronic equipment. The frequency band from 30.0 MHz to 37.5 MHz can also be adopted (the same rationale discussed before also applies).

Next, two different circuit methodologies under study to read the signals from the sensors are discussed.

#### A. Reader Based on an Impulse Response

The first method is based on the sensors' impulse response. Figure 2 shows the schematic of the system including both the reader and sensor circuits. The  $R_p$  and  $R_{tp}$  resistors are the parasitic resistances values from the inductors  $L_p$  and  $L_{tp}$ .

In order to read the sensors response, a square wave  $v_{vs}$  is sent through the inductor  $L_p$  that in turn activates the sensor by generating a magnetic field. Once the sensor is activated, the output  $v_o$  superimposes the signal sent by the reader (the input) plus the sensors' response.

The duplication of the circuit marked as "twin" is necessary for the successful reconstruction of the sensors' signal. The use of a square wave to activate the sensors has the drawback of producing a high number of harmonics in the reader's output preventing the recognition of the true signal sent by the sensors. To detect the sensors' signal, the "twin" circuit enables the elimination of the unwanted harmonics  $v_{to}$  by subtraction ( $v_o - v_{to}$ ).

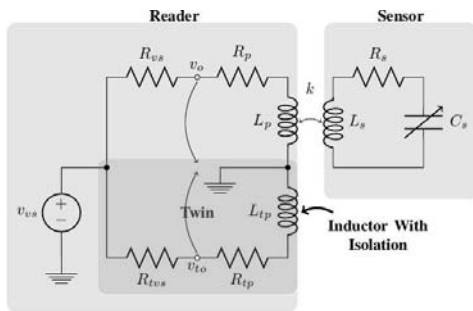


Figure 2: Reader's circuit based on an impulse input.

#### B. Reader Based on Power Transmission

The second method is similar to the operation of a network analyzer, where sine waves with different frequencies are sent to the network to characterize the transmitted power. Since each sensor has an unique impedance at the oscillation frequency, this is reflected in the power transmitted when the sine wave frequency matches the sensors' oscillation frequency.

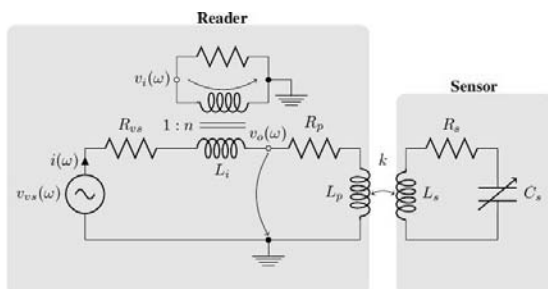


Figure 3: Reader's circuit based on the power transmission.

Figure 3 shows the schematic of the described system. The transformer captures the current  $i(\omega)$  that is being drawn and converts the current to a proportional voltage  $v_i(\omega)$  that is used to calculate the proportional transmitted power as described in equation 1:

$$\bar{P} = \frac{1}{n} \cdot \sum_{j=0}^n P_j(\omega) \equiv \frac{1}{n} \cdot \sum_{j=0}^n v_{ij}(\omega) v_{oj}(\omega) \quad (1)$$

### III - Sensors' Fabrication and Specifications

Given the characteristics of the application (the sensor will be attached to the stent-graft), the capacitive sensor must be foldable, extremely flexible and characterized by a very small profile. In addition, the technology should be simple and biocompatible. Silicon based microtechnologies are widely used in implantable medical devices [5], but due to the application specifications, a new fabrication process is introduced.

The proposed fabrication process uses carbon nanotubes (CNTs) to build the conductive elements, namely the inductor and the capacitor electrodes. The CNTs are embedded in a flexible substrate of polydimethylsiloxane (PDMS), a transparent, nontoxic and biocompatible silicone elastomer.

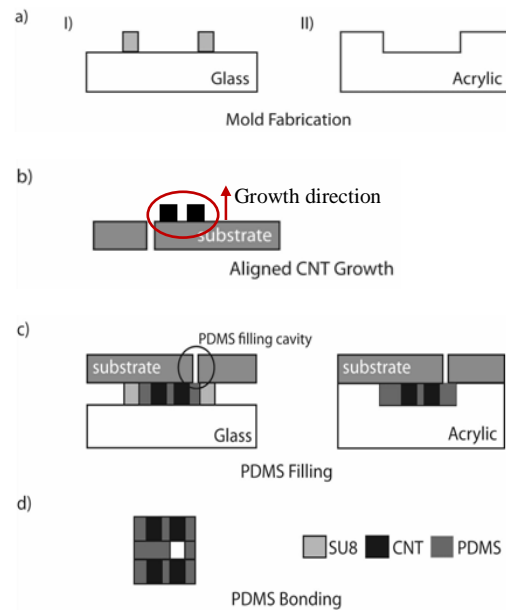


Figure 4: Fabrication process flow for the development of a flexible pressure sensor.

The fabrication process flow for the development of the flexible pressure sensor is schematically presented in figure 4. Two different approaches are being pursued to manufacture the flexible CNTs embedded PDMS films (figure 4). On one side, molds are fabricated using SU-8, a photoresist resin with excellent lithographic and optical characteristics (figure 4a-I). The high structural ratio of SU-8 allows obtaining structures with high dimensional control, an essential property to enable accurate control of the PDMS membrane thickness. On the other side, acrylic molds are produced by CNC milling (figure 4a-II). This technique presents some advantages relatively to SU-8 molding, such as lower

costs and faster production times, but it is associated with poorer dimensional control.

The electric components (capacitor electrodes and inductor) are based on continuous aligned CNTs, as shown in figure 4b. Chemical vapor deposition (CVD) is used to grow forests or “carpets” of vertically-aligned CNTs (VACNTs) [6]. A SC silicon substrate with patterned with 1/10nm Fe/Al<sub>2</sub>O<sub>3</sub> catalyst and placed in a horizontal quartz tube furnace at atmospheric pressure at 750 °C [7] for the CNT growth. This method has the advantage of allowing the growth of high purity, high yield and vertically aligned continuous CNTs. Figure 5 shows two different experimental structures obtained using this method. The CNTs are nominally 8 nm in dia., contain 2-3 walls, and spaced ~80 nm apart giving a bulk volume fraction of ~1%.

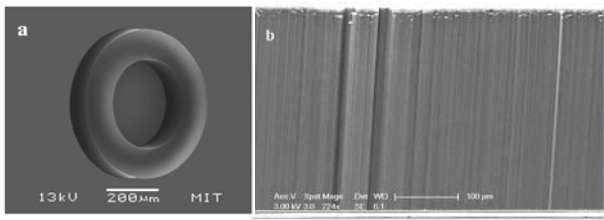


Figure 5: SEM images of two different CNT-based structures: a) “zero” shape and b) forest (no shape) of CNTs.

Next, the CNTs are embedded into the polymer matrix (PDMS). This step is schematically represented in Figure 4c, for both SU-8 and acrylic molds. The substrate is placed against the molds, and the PDMS is introduced in the cavities through a hole, followed by the curing of the elastomer. This follows similar procedures demonstrated for SU-8 and several epoxies [7, 8, 9 and 10] that utilize the CNT alignment to enhance capillary action of drawing the polymer into the aligned CNT network.

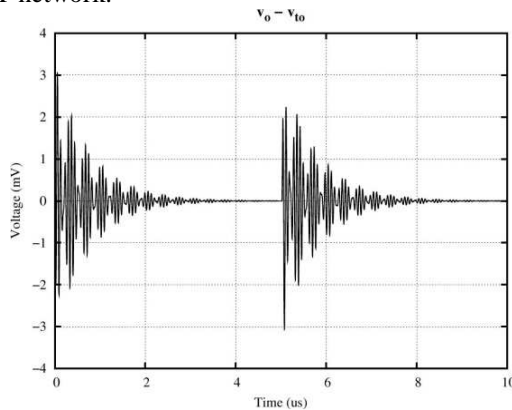


Figure 6: Agilent ADS transient simulation of the reader's circuit due to an impulse input.

The flexible pressure sensor is composed of three thin layers, with the top and bottom layers defining the inductor and the electrodes, and the middle one defining the dielectric (air). This configuration requires bonding of PDMS membranes. In [11], five different bonding techniques were tested and the highest reported bond strength was obtained for both partial curing and uncured PDMS adhesive techniques. The latter approach

has proven successful in our work as well, and will be used for future experimentation (figure 4d).

Regarding the main specifications for the transduction element (pressure sensor), namely dynamic range, resolution and accuracy, they can be retrieved from the maximum values of blood pressure within the human body and required accuracy and maximum errors admitted by the legislation for pressure measurement devices [12]. For aortic aneurysm pressure measurement the sensor should have a dynamic range between 20mmHg and 250mmHg, a 1mmHg resolution and an absolute accuracy below 5mmHg [13].

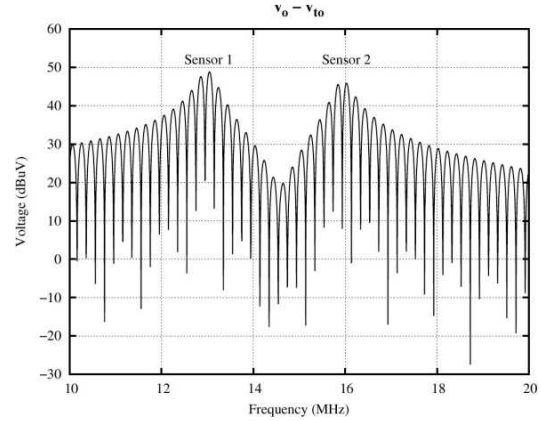


Figure 7: Agilent ADS Fourier analysis of the reader's circuit based on the impulse response.

## IV - Results

### A. Reader

The simulation results of the circuits described earlier are presented in this section. Figure 7 shows the response ( $V_0 - V_{i0}$ ) of two different sensors ( $L_{S1}=10\mu H$ ,  $C_{S1}=14pF$  and  $L_{S2}=10\mu H$ ,  $C_{S2}=10pF$  and  $k_{s1}=0.06$ ,  $k_{s2}=0.06$ ,  $k_{s12}=0.01$ ) when a square wave is applied to the reader. Figure 7 shows the Fourier transform of the response signal of Figure 6. These simulations consider ideal components and therefore the output shows no distortion. Small asymmetries in the real case will cause deviations in the circuits that fail to completely eliminate the harmonics in the output signal, contributing to distortion after the subtraction operation. Moreover, the differential amplifiers used have finite values of common mode rejection ratio (CMRR) and therefore the subtraction operation is also not ideal.

The simulation results from the 2<sup>nd</sup> approach, the circuit based on the power transmission, are presented in Figure 8. This circuit presents some advantages relatively to the impulse response based reader since it does not require subtraction and consequently has a lower output distortion. On the negative side, this circuit is more complex due to the sine wave frequency sweeping and requires more time to acquire the complete data.

### B. Sensors' Process Fabrication Characterization

The key step of the fabrication process is the CNT's impregnation by PDMS, and respective mechanical and electrical properties (required for the sensor design). Both acrylic and SU8 molds have been fabricated

(Figure 9), and are being used to build the PDMS flexible membranes with embedded aligned CNTs (Figure 10).

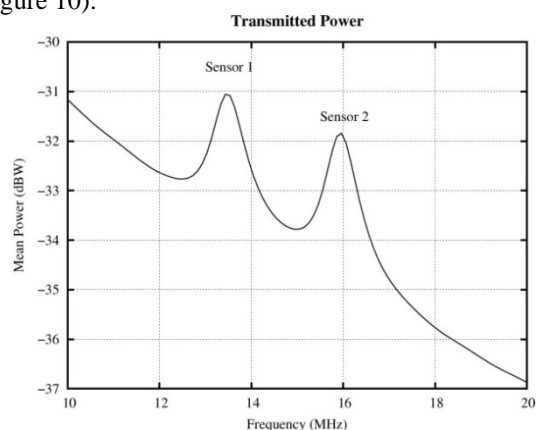


Figure 8: Agilent ADS simulation of the reader's circuit based on the transmitted power.

First measurements to a series of samples (PDMS membranes with embedded CNTs) indicate an electrical conductivity of 11,43 S/m with standard deviation of 13,37 S/m in the direction perpendicular to the CNT axis. Recent work has shown that conductivity in the direction parallel to CNTs for polymer-nanocomposites containing aligned CNTs is 10-100X that in the direction perpendicular to the CNT axis [14] (as found herein for PDMS).

a)



b)

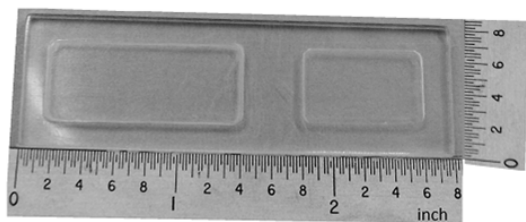


Figure 9: Fabricated a) SU-8 and b) acrylic molds for the production of PDMS membranes.

## V - Conclusions

This paper presented two different solutions for wireless monitoring of AAA based on implantable flexible pressure sensors. The first solution (impulse response) does not require high circuit complexity while the second solution, based on power transmission, is more complex with regard to the sinusoidal source controllability, but enables an improved and more information-rich output signal to be captured.

The flexible pressure sensors will be based on flexible PDMS membranes with embedded CNTs. The process is under mechanical and electrical characterization and first functional pressure sensors are expected

soon. Prototypes of the telemetric reading system are also under development and will provide more data to access which of the two solutions will perform better.

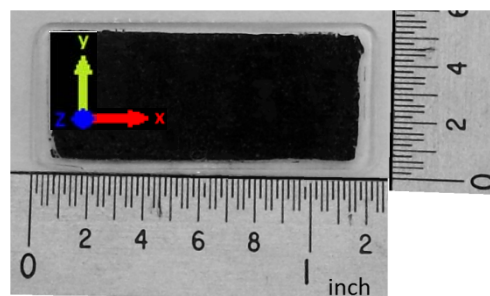


Figure 10: PDMS membrane with embedded CNTs (the "z" axis corresponds to the direction of CNTs).

## Acknowledgments

The first author wishes to thank FCT - Fundação para a Ciência e Tecnologia, Portugal, for the financial support provided by the grant SFRH/BD/42922/2008. This work is supported by FCT under the project MIT-Pt/EDAM-EMD/0007/2008.

## References

- [1] Ricotta II, J. J., R. D. Malgor, et al. (2009), *Annals of Vascular Surgery* 23 (6): 799-812
- [2] Lukla Biasi, Tahir Ali, Robert Hinchliffe, Rob Morgan, Ian Loftus, and Matt Thompson, *Cardiovasc. Intervent. Radiology*, 32(3):535-538, 2009.
- [3] I.M. Nordon, A. Karthikesalingam, R.J. Hinchliffe, P.J. Holt, I.M. Loftus, and M.M. Thompson, *European Journal of Vascular and Endovascular Surgery*, In Press, 2009.
- [4] Brian J. Manning, Sean M. O'Neill, Syed N. Haider, Mary P. Colgan, Prakash Madhavan, and Dermot J. Moore, *Journal of Vascular Surgery*, 49(1):60- 65, 2009.
- [5] R. A. M. Receveur, F. W. Lindemans and N. F. de Rooij, *J. Micromech. Microeng.* 17 (2007) R50-R80.
- [6] Garcia, E.J., Hart, J., and B.L. Wardle, *AIAA Journal*, 46(6), 2008, pp.1405-1412.
- [7] Hart, J., Slocum, A.H., *Journal of Physical Chemistry B*, 110 (2006) p. 8250-8257.
- [8] Garcia, E.J., Wardle, B.L., Hart, A.J., and N. Yamamoto, *Composites Science & Technology*, 68(9), 2008, pp. 2034-2041.
- [9] Garcia, E.J., Hart, J., Wardle, B.L. and A. Slocum, *Nanotechnology*, 18(16), April 2007, pages 165602 (11pp).
- [10] Garcia, E.J., Hart, J., Wardle, B.L. and A. Slocum, "Fabrication and Nanocompression Testing of Aligned CNT/Polymer Nanocomposites," *Advanced Materials*, Vol. 19, 2007, pp. 2151-2156.
- [11] Eddings, M.A., Johnson, M.A., Gale, B.K., *J. Micromech. Microeng.* 18 (2008).
- [12] U.S. Department of Health and Human Services, Blood pressure measurement devices (sphygmomanometers)—accuracy. Report # CPG 7124.23 (2005, Feb. 18)
- [13] Joseph A. Potkay, *Biomed. Microdevices* (2008) 10, 379-392.
- [14] Cebeci, H., Guzmán de Villoria, R., Hart, A.J., and B.L. Wardle, *Composites Science and Technology*, 69 (2009), pp. 2649-2656.



# DESIGN AND MODELING OF A THREE-MASS, DECOUPLED, TUNABLE SOI-MEMS GYROSCOPE WITH SENSE FRAME ARCHITECTURE

Ikpemi Sabageh<sup>1</sup>, Vijay Rajaraman<sup>1</sup>, Edmond Cretu<sup>2</sup> and Patrick J. French<sup>1</sup>

<sup>1</sup>Delft University of Technology, Department of Microelectronics, EI Lab- DIMES, Delft, Netherlands

<sup>2</sup>University of British Columbia, Department of Electrical and Computer Engineering, Vancouver, Canada

Phone: +31-15-2781602, Fax: +31-15-2785755, E-mail: v.rajaraman@tudelft.nl

**Abstract** – The design and modeling of a three-mass doubly-decoupled SOI-MEMS yaw rate gyroscope with a tunable bandwidth, and quadrature error compensation is presented. The three-frame structure of the gyroscope, with an outer sensing frame, leads to an improved electrical sensitivity over the conventional architectures. It also leads to a full decoupling between the sense and drive modes, thus eliminating the cross axis sensitivity that usually limits the angular rate sensing performance. Both COMSOL finite element simulations and macro models implemented in Agilent ADS have been used to validate the structure. The drive and sense mode resonance frequencies are 2500Hz and 2830Hz respectively, with an input angular rate bandwidth tunable between 40Hz and 330Hz. The device achieves a theoretical maximum resolution of 0.14 °/s/sqrt(Hz) at 50 Hz and 0.359 °/s/sqrt(Hz) at 330 Hz and a maximum sensitivity of 1.244 fF/°/s.

**Keywords:** Gyroscope, angular rate sensor, quadrature error, SOI-MEMS, modes decoupling

## I – INTRODUCTION

A MEMS vibratory gyroscope is an active sensor that uses Coriolis force to measure the angular rate relative to an inertial reference frame. Its operation relies on the transfer of energy between two orthogonal vibration modes, transfer modulated by the external angular rate. There is usually a compromise between sensitivity and bandwidth, as the maximum sensitivity corresponds to matched resonant frequencies for drive and sense vibration modes, which leads to a minimum angular rate sensing bandwidth [1]. Single mass, two-modes vibratory gyroscopes are implemented with relatively simple mechanical structures, but the large quadrature errors and other cross-axis effects limit the achievable resolutions and bandwidth. Decoupled two-mass (double frame) gyroscopes [2, 3] are a step forward in reducing these deterministic errors, but the sense mass has a 2 degrees-of-freedom motion (DOF) that does not completely decouple it from the cross-axis influence. The architecture leads nevertheless to higher sensitivity, tunable bandwidth angular rate sensing.

In this paper, a three-mass doubly-decoupled yaw-rate (z-axis) MEMS gyroscope with tunable bandwidth and quadrature error compensation is introduced. In the double decoupled design a third 2-DOF coupling mass is introduced in between the 1-DOF drive and sense

masses. The proposed design leads to improved performances in terms of resolution, sensitivity and tunability. The use of a custom developed high-aspect ratio SOI-MEMS fabrication technology contributes as well to the increase of the mechanical sensitivity.

Target applications of this device, which exploit the tunable bandwidth and sensitivity, include: medical instrumentation (e.g. in active tremor compensation for handheld surgical tools and micro-surgical navigation), inertial navigation, stabilization and path prediction in automotive and consumer applications.

## II – THREE-MASS GYROSCOPE DESIGN

### A. Design Concept and Operation

The operation principle of the doubly-decoupled MEMS gyroscope is illustrated in *Figure 1*. Masses  $m_2$  and  $m_3$  are driven in the drive (y) direction with a resulting electrostatic force that is given by [1]:

$$F_{drive-mode} = \frac{\omega_{dm}^2 Y_{dm} (m_2 + m_3)}{Q_{dm}} \sin(\omega_{dm} t) \quad (1)$$

where  $\omega_{dm}$  is the drive-mode resonance frequency,  $Y_{dm}$  is the drive-mode amplitude and  $Q_{dm}$  is the drive-mode quality factor.

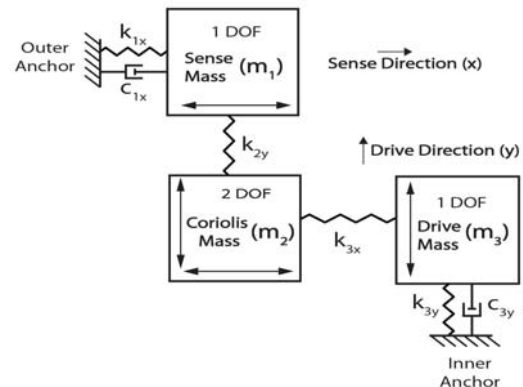


Figure 1: Operation principle of the doubly-decoupled MEMS Gyroscope

The presence of an external angular rate about the z-axis,  $\Omega_z$ , will induce a supplementary Coriolis force that is exerted on mass  $m_2$  (the only one with 2 DOF) along the x direction. This force is expressed as [1]:

$$F_C = -2m_2\Omega_z Y_{dm} \omega_{dm} \cos(\omega_{dm} t + \phi_{dm}) \quad (2)$$

where  $\phi_{dm}$  is a phase mismatch relative to the AC driving force.

The Coriolis force causes  $m_1$  to move as well in the sense (x) direction, motion transferred to  $m_1$  through its elastic coupling to  $m_2$ . The resultant Coriolis displacement is given by [1]:

$$X_{sm} = \Omega_z \frac{m_2 \omega_{dm}}{(m_1 + m_2) \omega_{sm}^2} \frac{2Y_{dm}}{\sqrt{\left[1 - \left(\frac{\omega_{dm}}{\omega_{sm}}\right)^2\right]^2 + \left[\frac{\omega_{dm}}{Q_{sm} \omega_{sm}}\right]^2}} \quad (3)$$

where  $\omega_{sm}$  is the sense-mode resonance frequency and  $Q_{sm}$  is the sense-mode quality factor.

The Coriolis displacement induces a change in the sense capacitance formed by comb fingers attached to the sense mass and the fixed fingers anchored to the substrate. The readout capacitance variation  $\Delta C$ , is given by:

$$\Delta C(t) = C_0 \frac{X_{sm}(t)}{g_{s_0} - X_{sm}(t)}, C_0 = N_s \frac{\epsilon_0 A}{g_{s_0}} \quad (4)$$

where  $N_s$  is the number of sense comb fingers per side,  $\epsilon_0$  is the free space permittivity,  $A$  is the overlap area of the sense combs,  $g_{s_0}$  is the initial gap between the sense combs and  $X_{sm}(t)$  is the time varying Coriolis displacement.

The amplitude of this capacitance change is a direct measure of the external angular rate. The rotation resolution of the gyroscope can be written as [1]:

$$\Omega_N = \sqrt{\frac{k_B T \omega_{\Delta} \omega_{sm}}{(m_1 + m_2) Q_{sm} \omega_{dm}^2 Y_{dm}^2}} \quad (5)$$

where  $k_B$  is the Boltzmann constant,  $T$  is the temperature and  $\omega_{\Delta}$  is the bandwidth of the gyroscope.

### B. Design Architecture

The proposed mechanical architecture is a three-frame implementation of a doubly-decoupled gyroscope and is shown in Figure 2. The outer sensing frame ensures a larger value of its associated variable capacitance capacitors and thus improves the gyroscope's electrical sensitivity [1, 3].

The architecture features three masses namely  $m_1$  (sense mass),  $m_2$  (Coriolis mass) and  $m_3$  (drive mass). The drive-mode of the gyroscope is formed by the masses  $m_2$  and  $m_3$ , while the sense-mode of the gyroscope is

formed by masses  $m_1$  and  $m_2$ . Bandwidth tunability and quadrature error compensation in this design is achieved by electrostatic DC actuation applied on four dedicated comb fingers attached symmetrically to the sense mass.

A common-mode applied DC voltage causes an equivalent electrostatic negative spring effect that will induce a voltage-controlled mismatch between the resonant frequencies of the vibration modes, controlling the equivalent bandwidth of the mechanical transfer function.

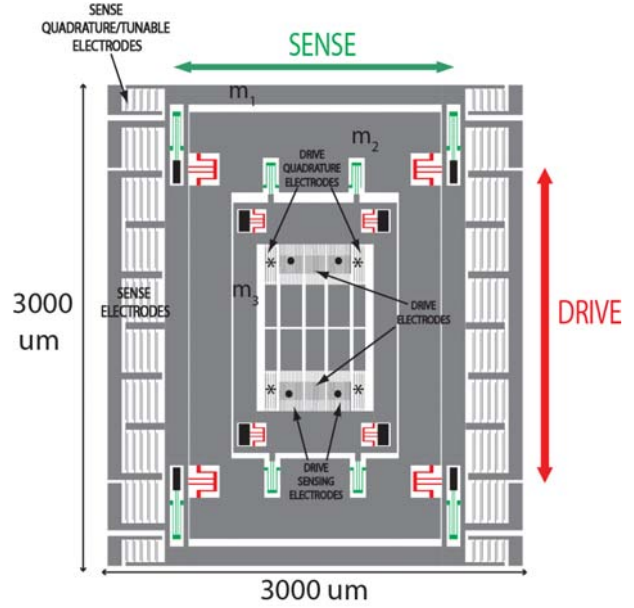


Figure 2: Schematic of the gyroscope architecture

The relationship between the DC tuning voltage and the equivalent sense-mode spring constant can be expressed as [3]:

$$V_{tune} = \sqrt{\frac{-\omega_{sm}^2 (m_1 + m_2) + k_{sm}}{27 N_Q \epsilon_0 h l_{q_0}}} 2 g_{q_0}^3 \quad (6)$$

where  $k_{sm}$  is the sense-mode spring constant,  $g_{q_0}$  is the initial gap between the quadrature combs,  $N_Q$  is the total number of quadrature combs and  $l_{q_0}$  is the overlap length between the quadrature combs.

Fabrication imperfections typically result in quadrature errors, given by the geometric coupling of the driven y motion into the sensing x motion and are independent of the external angular rate. The quadrature error is minimized by applying a differential DC voltage between the pairs of quadrature combs, such that the orientation of the sense axis is tuned relative to the drive axis.

### C. Technological Implementation

The above design is being implemented using a custom developed high aspect ratio SOI-MEMS technology [4]. A cross-section through a typical structure is shown in

Figure 3, while the SEM image of a fabricated structure is presented in Figure 4. The large thickness ( $>50 \mu\text{m}$ ) of the structural layer leads to higher values of the inertial proof masses and large spring constants in  $z$  direction; the direct consequence is an increase in the mechanical sensitivity, while reducing the influence of external  $a_z$  accelerations. The low-temperature technology enables CMOS-compatible fabrication of MEMS by post-processing.

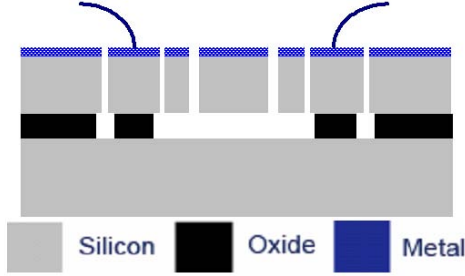


Figure 3: Thick SOI-MEMS Technology

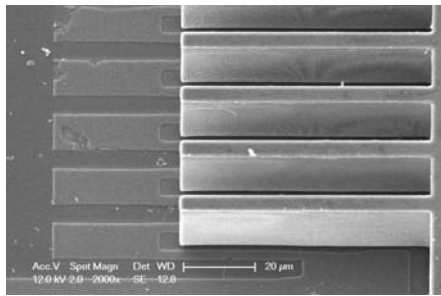


Figure 4: High Aspect Ratio SOI-MEMS Comb Structures

### III – RESULTS AND DISCUSSIONS

The design phase of the gyroscope structure started from desired specifications and a first order analytical estimation. Then, using these equations, equivalent circuit macromodels implemented in Agilent ADS have been used to further validate and optimize the structure. The results have been refined afterward through finite element simulations in COMSOL Multiphysics. Table 1 summarizes the electrical and mechanical parameters of the designed gyroscope, while Table 2 shows the mechanical modeling parameters and their electrical equivalents [5].

Table 1: Electrical and mechanical parameters of the gyroscope

Parameter	Value
Overall Size	3000 $\mu\text{m}$ x 3000 $\mu\text{m}$
Structural Thickness	50 $\mu\text{m}$
Bandwidth	40 - 330 Hz
Drive Mode Resonance Frequency	2500 Hz
Sense Mode Resonance Frequency	2830 Hz
Nominal sense	5.147 pF

capacitance per side, $C_0$	
Sense capacitance change per side, $\Delta C$	0.6223 pF
Mechanical Resolution	0.14 $^{\circ}/\sqrt{\text{Hz}}$ @ 50 Hz 0.359 $^{\circ}/\sqrt{\text{Hz}}$ @ 330 Hz
Sensitivity	1.244 fF/ $^{\circ}/\text{s}$
Dynamic Range	99.3 dB
Pull-in Voltage	86.7 V
Tuning Voltage	5 V

Table 2: The mechanical modeling parameters and their electrical equivalents

Mechanical Parameter	Electrical Analog
Mass – $m$	Capacitance – $C$
Damping Coefficient – $b$	Inverse of Resistance – $1/R$
Spring Constant – $k$	Inverse of Inductance – $1/L$
Displacement – $x$	Electronic Charge – $Q$
Velocity – $v$	Voltage – $V$
Force – $F$	Current – $I$

Figure 5 shows the equivalent (small signal) circuit model of the gyroscope, with forces represented as generalized through variables. It can be seen that the Coriolis mass is present in both drive and sense modes: the drive-mode mass consists of the individual drive and Coriolis-drive masses, while the sense-mode mass consists of the individual sense and Coriolis-sense masses.

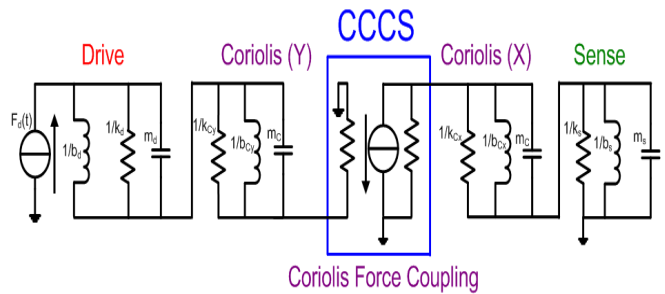


Figure 5: Equivalent circuit model for the drive, Coriolis and sense masses of the gyroscope

The equivalent Bode amplitude plots obtained from the above macromodel are presented in Figure 6 that are in good agreement with the analytical calculations and numerical simulations.

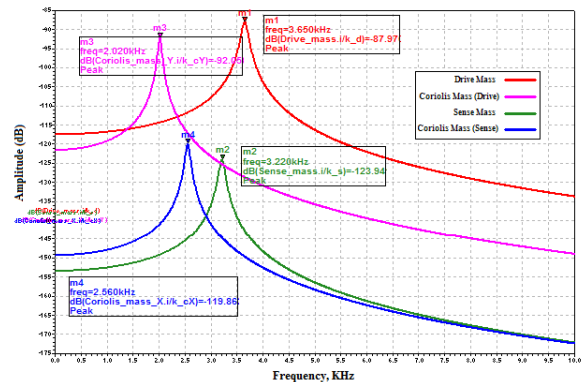


Figure 6: Resonance characteristics of the drive, Coriolis (in drive and sense directions) and sense masses of the gyroscope

Figure 7 shows an equivalent circuit model of the gyroscope, reduced to the drive and sense modes. The corresponding resonant modes characteristics are presented in Figure 8.

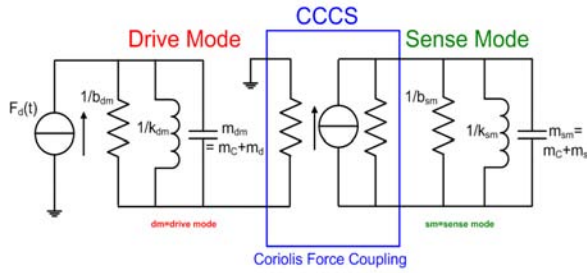


Figure 7: Equivalent circuit model for the drive and sense modes of the gyroscope

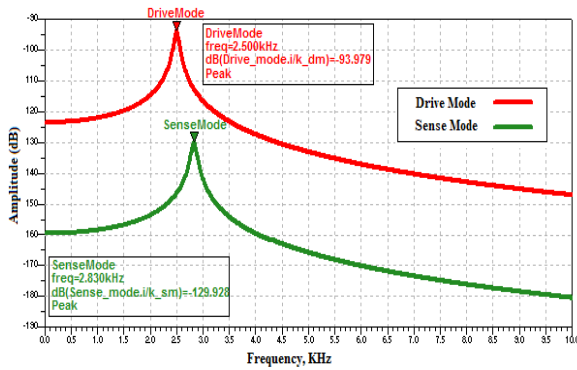


Figure 8: Resonance characteristics of the drive and sense modes of the gyroscope

The final step consists in refined optimizations of the design using finite element analysis. The layout of the MEMS device has been imported in COMSOL Multiphysics [6], and more time-consuming analyses have been performed on the generated 3D microstructure. Figures 9 and 10 show the vibration modes corresponding to the drive and sense resonances.

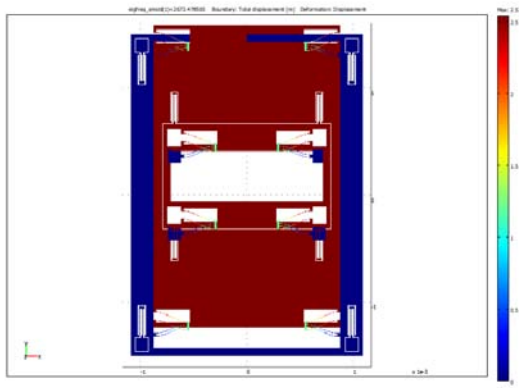


Figure 9: FEA drive-mode resonant frequency (2673 Hz)

It can be observed that the results from the analytical modeling (Table 1) and of the finite element analysis are in good agreement, with a deviation of 6.5% between the calculated and simulated drive-mode resonant frequency and 3.38% mismatch between the calculated and simulated sense-mode resonant frequency.

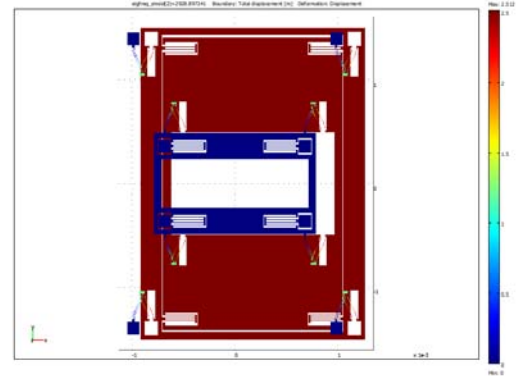


Figure 10: FEA sense-mode resonant frequency (2929 Hz)

## IV – SUMMARY

A MEMS yaw-rate (z-axis) doubly-decoupled gyroscope with outer sense frame architecture was presented. The structure offers electrostatic tuning of the equivalent bandwidth and compensation of the quadrature errors. The design is currently being optimized for implementation in a high aspect ratio SOI-MEMS technology. Target applications for the presented gyroscope include medical instrumentation (tremor compensation, micro-surgical tool navigation, etc.), in automotive (path prediction) and consumer applications.

## ACKNOWLEDGEMENTS

The authors - VR and PJF - gratefully acknowledge the financial support of NXP Semiconductors, Nijmegen, The Netherlands, in this work under the framework of the project contract #NL614500184543. Our thanks are due to Prof. Dr. Kofi A.A. Makinwa (TU Delft), Dr. Henk Boezen (NXP) and Dr. Jan-Jaap Koning (TU Eindhoven) for their support.

## REFERENCES

- [1] C. Acar and A.M. Shkel, MEMS Vibratory Gyroscopes: Structural Approaches to Improve Robustness, *Springer*, 2009, ISBN: 978-0-387-09535-6.
- [2] C. Acar and A.M. Shkel. An approach for increasing drive-mode bandwidth of MEMS vibratory gyroscopes, *J. Microelectromechanical Systems*, vol.14, no. 3, pp. 520-528, 2005.
- [3] S.E. Alper, Y. Temiz and T. Akin, A Compact Angular Rate Sensor System Using a Fully Decoupled Silicon-on-Glass MEMS Gyroscope, *J. Microelectromechanical Systems*, vol.17, no. 6, pp. 1418-1429, 2008.
- [4] V. Rajaraman, P.J. French, et al., DRIE Assisted HAR MEMS Processing of Inertial Sensors and Actuators, *Proc. The 18<sup>th</sup> Micromechanics and Microsystems Europe Workshop (MME 2007)*, Guimarães, Portugal, 2007.
- [5] E. Cretu, Inertial MEMS Devices – Modeling, Design and Applications, *PhD Dissertation*, Delft University of Technology, The Netherlands, 2003.
- [6] COMSOL Multiphysics FEA Software (Internet: [www.comsol.com](http://www.comsol.com))



# ROBUST MEMS FOR SPACE APPLICATIONS

A. Delahunty<sup>1</sup>, W.T. Pike<sup>1</sup>.

<sup>1</sup>Imperial College London

**Abstract** —In this paper we present a new concept for the shock protection of MEMS using solder armouring on protective bumpers. Upon impact the more ductile solder armour absorbs the kinetic energy of the collision thereby protecting silicon structures from brittle fracture. A model suspension system has been designed, fabricated and tested to verify this approach. The devices were fabricated using through-wafer deep reactive-ion etching (DRIE) and were shock tested using a drop testing rig at estimated levels of up to 14,000g. Although the solder suffered severe damage about half the silicon suspensions survived these very high shocks.

**Keywords :** MEMS, Shock Protection, Collision.

## I - Introduction

Micro-electrical-mechanical systems (MEMS) due to their very low mass and volume, tight integration with electronics and low power consumption are becoming increasingly popular for space applications. They allow the size and mass of spacecraft to be reduced without forgoing functionality and they can allow for significant savings in money with launch costs of approximately \$10,000 to place one kilogram in low Earth orbit [1-3].

However for MEMS to be used in space exploration they need to withstand significant shock and vibration levels during both the launch phase as well as during entry, descent and landing. Vibration levels will depend on the launcher, but the MEMS on board could potentially be subjected to a sine vibration from 6 Hz to 100 Hz and from 3 to 20G and a shock of 500G at stage and fairing separation [2]. Furthermore if they are to be used in penetrator-based space missions the level of shock which they must cope with significantly increases again, meaning that the microstructures will need to be modified in order for them to survive the impact phase [3, 4].

There are two directions one can take when shock-hardening MEMS, external protection or permitting collision and dealing with it. External protection measures include mechanical latching [5], electrostatic clamping [6] and electromagnetic clamping [7] of the central proof mass. Electrostatic and electromagnetic clamping both require an external power source during the shock event, often difficult to achieve. They also along with mechanical latching methods only provide limited clamping forces. Hopf *et al* [4] demonstrate an effective external passive shock isolator where the structures are encapsulated in a waxy solid that sublimates in vacuum conditions in order to restore the instrument back to normal operation; however issues

regarding how the MEMS are exposed to the vacuum upon landing and where the wax resolidifies would need to be addressed in any mission scenario.

Where collisions are permitted and dealt with, the traditional method of shock hardening devices in order to minimise fracture is to optimise the dimensions of the structure in question so that the stresses do not exceed the fracture strength [8]. However device performance including sensitivity will suffer as a result of this protection and it is only applicable to cases where the shock requirement is known [9]. Yoon *et al* [9] investigate using non-linear springs and soft coatings as methods of shock protecting MEMS, but the former affects the Q-factor of the entire system and the latter is not compatible with DRIE. Younis *et al* [10] explore using squeeze-film damping as a method of mitigating the effects of shock, but as space is a vacuum squeeze-film damping is not an option. Yoon *et al* [11] present a method of shock protection which uses a microgranular bed to protect micromachined electronic devices (MEDs) for use in high-g military applications, but the micro glass beads prevent movement and thus cannot be used with moving structures. Hard shock stops have been investigated [9] but were found to be limited in their protection as they themselves can generate secondary sources of shock; and fluid-damping shock isolators which dissipate energy through heat and acoustic energy were found to be too bulky for use in MEMS and not suitable for harsh environments [11].

## II - Experimental Details

The microseismometer in figure 1 below is an example of a MEMS device that incorporates fragile moving parts in its suspension.

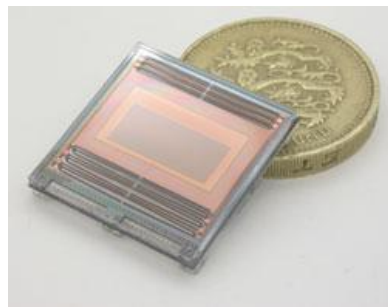


Figure 1 – Silicon Microseismometer

Within the microseismometer there are ‘bumpers’ located on either side of the proof mass which prevent the silicon suspensions being compressed and destroyed by limiting travel when a force is applied, see figure 2. While these bumpers protect the springs, they themselves are still made from brittle silicon and are thus

very susceptible to fracture. If a direct silicon-silicon collision could be avoided, fracture could theoretically be minimised.

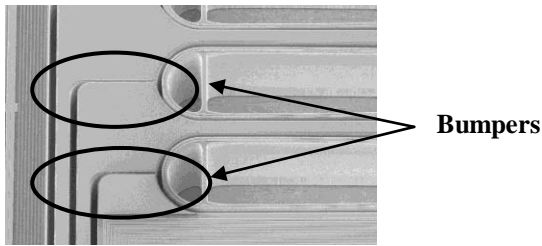


Figure 2- SEM Image of the 'bumpers' being compressed and protecting the springs.

The solution which was investigated involves creating a geometry whereby solder hits solder so avoiding direct silicon-on-silicon impact. Solder is a ductile metal alloy that should be able to absorb large amounts of energy upon impact. By reflowing solder on metal pads located at the edge of the silicon bumpers it is possible to create new solder structures that extend beyond the silicon, thus creating the desired effect.

For experimental purposes new model structures were designed to incorporate suspensions and solder-armoured buffers. In order to maximise the number of test structures per silicon wafer each 20 x 20mm die has four structures. The advantage of this is two-fold, not only is there four times as many samples being tested per die but also it provides a means for direct comparison. The suspension dimensions are based on the suspensions of the original microseismometer. The model structures incorporate a pair of folded cantilevers either side of the proof mass and a central bumper provides a single point of contact.

Surface Evolver [12], an interactive program that can model liquid surfaces shaped by surface tension and other energies was used to simulate the reflow shapes of the solder and to determine the overall heights, impact points and the solder cushions (the amount of solder protruding beyond the silicon). Various shapes and sizes were investigated before the U-Shaped 'channel buffer' and oval 'ball-buffer' were chosen (figure 3).

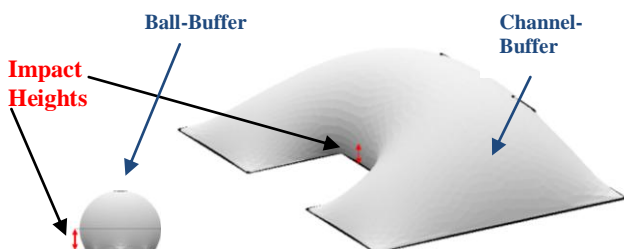


Figure 3 – Surface Evolver simulation

The geometry of the central bumper is shown in figure 4.

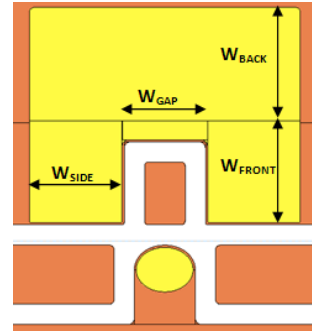


Figure 4 – Ball and Channel-buffers on the central bumper.

Figure 5 below shows the mask design for one set of four model structures.

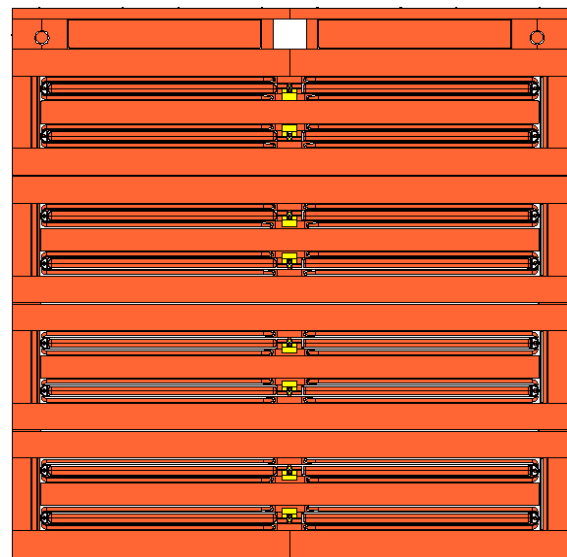
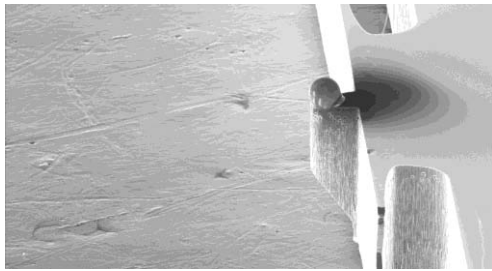


Figure 5 – Mask Design for 20 x 20mm die with four model structures, (Orange: DRIE, Yellow: Gold).

### III - Results and Discussion

The results presented below were obtained from prototype devices fabricated using low-resolution masks. The purpose of these prototypes was to determine proof of concept, whether the solder reflowed as expected and whether the solder armour succeeds in protecting the suspension. They were also used to determine the failure modes of the solder. It is very difficult to predict the failure mode of a solder joint as joint reliability under shock loads such as drop impacts depends on a number of different factors such as solder alloy, pad finishing, reflow profile, package geometry, ball layout, high temperature storage, drop impact loading etc, and as such it needs to be determined experimentally [13].

Using a drop-testing rig the model structures were subjected to estimated shocks of 7,000, 10,000 and 14,000g. Following these tests various failure modes were observed. In about half the cases the fragile suspensions fractured and failed. Figure 6 shows a surviving ball buffer from one such case.



*Figure 6 – Ball-buffer post shock.*

Looking at a closer view of the surviving ball buffer (figure 7) it is possible to see that the damage incurred is not ductile deformation as expected but rather looks like brittle fracturing.

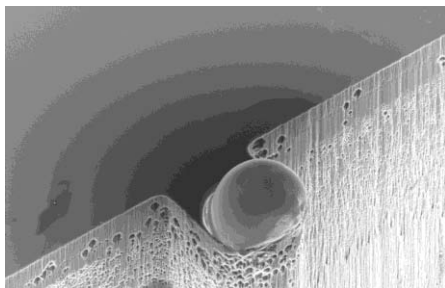


*Figure 7 – Ball-buffer post shock.*

This image also clearly shows the pitting which can occur in the silicon below the solder pad making the silicon weak in this area.

In the cases where the solder armour was successful in protecting the silicon suspensions the ball buffers in every case failed. The severity of the failure depended on the alignment of the structures during the drop test. The ball-buffers on the lower side of the proof mass which absorbed the initial impact in each case, ruptured the silicon when the pads lifted off (figure 8), while the ball-buffers on the upper sides which absorbed the rebound force after impact lifted the pad alone (figure 9). The hole which can be observed in figure 9 underneath where the ball-buffer once stood is not part of the damage, it is a shallow etch which had the purpose of aiding the placement of the 100 $\mu$ m diameter solder balls during fabrication.

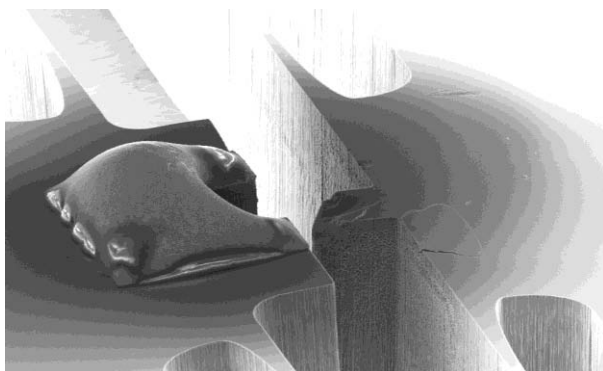


*Figure 8 – Channel and Ball-buffers post shock (lower side).*

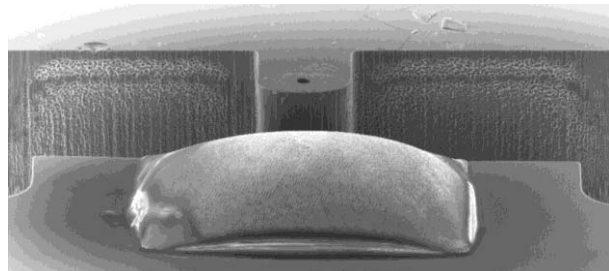


*Figure 9 – Channel and Ball-buffers post shock (upper side).*

Looking at figure 8 it is possible to see that there is a fracture on the left hand side of the ball-buffer support where most likely the edge of the channel-buffer collided during a rebound after the solder pad had already lifted off. Looking at a closer view of this area in figure 10 below it can be seen that the fracture occurs along the pitted areas. With a high-resolution mask there would be less pitting and thus more resilience against fractures such as the one below and rupturing of the base during pad lift as seen in figure 8.

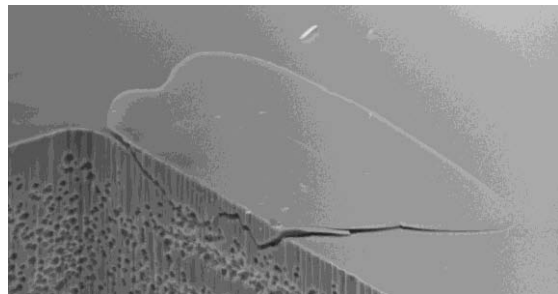


*Figure 10 – Side fracture.*

A very unexpected result was the lack of damage in all cases to the channel-buffers. It was predicted that the solder would absorb the kinetic energy of the collision and being an extremely soft metal alloy it would deform, as both bodies have curved surfaces Hertzian contact stresses were used to estimate the deformation expected, however below in figure 11 it can be seen that in fact no deformation has occurred.

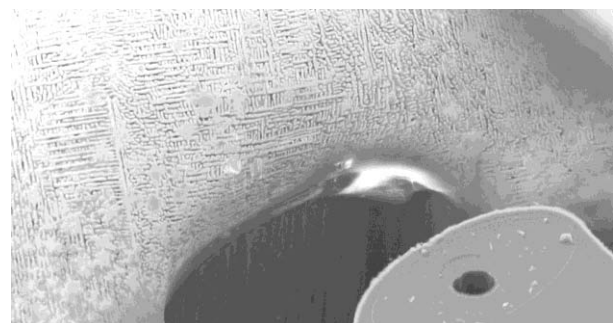


*Figure 11 – Undamaged channel-buffer post shock.*

#### **IV – Future Work**

Low-resolution masks are relatively cheap and have a very quick turn round time, and as such were suitable for the purpose of proof of concept. However they come



with the inevitable compromise of poor quality silicon suspensions.

Four sets of model structures have been designed to investigate changes in: 1) The impact height above the wafer surface, 2) The channel width ( $W_{\text{GAP}}$ ) see figure 4, 3) The channel depth ( $W_{\text{BACK}}$ ) and 4) Gold Metallisation (figures 12a and 12b).



Figure 12a – Gold-plated structure.

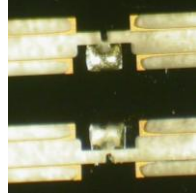


Figure 12b – Gold-plated springs.

On each set of structures the first structure is identical thus allowing for direct comparisons between the different sets. In this first structure the ball buffer has the lowest possible impact height whilst still maintaining an adequate solder cushion and the height of the channel buffer was matched so that the force is perpendicular to the wafer surface normal, surface evolver was used to estimate these impact heights.

Using high-resolution masks for future fabrication it will be possible to create high quality silicon suspensions. These new devices will be used to calculate the exact shock forces that the suspensions can survive and to compare the different sets of model structures in order to determine the merits of the varying geometries. Further investigation into the lack of deformation of the channel-buffer will also be undertaken.

## V – Conclusion

The initial proof of concept tests presented proved to be successful, the solder reflowed exactly as expected and in many cases the springs survived the drop tests they were subjected to. Even though the 30 $\mu\text{m}$  springs were of poor quality, the solder armour managed to protect them during estimated shocks of up to 14,000g with an overall survival rate of 47%. However in every case the ball-buffers failed and severely failed in the case of all the lower-side ball-buffers. Modifications to strengthen the ball-buffers possibly by increasing the surface area of the solder pad, before ordering high-resolution masks are presently being considered. The authors would like to mention that the complete analysis for these future results along with detailed analysis regarding the shock forces that the model structures can survive as well as the relative performance of the model structures in comparison to each other will be presented in the final paper.

## Acknowledgements

The authors would like to thank Dr Werner Karl and Robert Hergert for providing fabrication support.

## References

- [1] H. Shea. In *Photonics West 2006: Reliability, Packaging, Testing, and Characterization of MEMS/MOEMS V*. San Jose, CA, USA, 2006.
- [2] H. Shea. In *Photonics West, MOEMS and Miniaturized Systems VIII*: San Jose, CA, USA, 2009.
- [3] B. Stark. *MEMS Reliability Assurance Guidelines for Space Applications*, Jet Propulsion Laboratory: Pasadena, California, 1999.
- [4] T. Hopf, S. Kumar, W.J. Karl and W.T. Pike. *Advances in Space Research*. 45(3): p. 460-467. 2009.
- [5] R. Buser. *Sensors and actuators. B, Chemical*. 21(1): p. 323, 1990.
- [6] F.T. Hartley. In *SPIE Conference on Electronics and Structures for MEMS*. Qld, Australia, 1999.
- [7] K. Ikuta, S. Aritomi, and T. Kabashima. In *Micro Electro Mechanical Systems, MEMS '92, Proceedings. An Investigation of Micro Structures, Sensors, Actuators, Machines and Robot. IEEE*. 1992.
- [8] D.M. Tanner, J.A. Walraven, K. Helgesen, L.W. Irwin, F. Brown, N.F. Smith and N. Masters. In *Reliability Physics Symposium, Proceedings. 38th Annual 2000 IEEE International*, 2000.
- [9] S.W. Yoon, N. Yazdi, N.C. Perkins and K. Najafi. *Sensors and Actuators A: Physical*. 130-131: p. 166-175, 2006.
- [10] M.I. Younis, D. Jordy, and J.M. Pitarresi. *Journal of Microelectromechanical Systems*. 16(3): p. 628-638, 2007.
- [11] S.H. Yoon, J.E. Roh and K.L. Kim. *Journal of physics. D, Applied physics*. 42(3): p. 035501, 2009.
- [12] K. Brakke. *Surface Evolver*, Susquehanna University. 2008.
- [13] L. Jing-en, T. Tong Yan, Z. Xueren, E. Hussa, W. Jason, C. Ford and K.C. Jend. In *Electronic Packaging Technology Conference. EPTC 2005. Proceedings of 7th*. 2005.



## LINEAR VARIABLE OPTICAL FILTER WITH SILVER METALIC LAYERS

A. Emadi, V.R.S.S. Mokkapati, H. Wu, G. de Graaf and R. F. Wolffenbuttel

Faculty EEMCS, Department ME/EI, Delft University of Technology, Mekelweg 4, 2628 CD, Delft, The Netherlands

**Abstract** — In this paper the design, fabrication and characterization of a Linear Variable Optical Filter (LVOF) with Silver mirrors is presented. The advantage of using a metal film for the reflectors of the Fabry-Perot (FP) LVOF is the wide spectral operating bandwidth, while silver offers superior optical performance as compared to other IC-compatible metals. A LVOF has been designed and fabricated to cover the entire visible spectral range of 400 nm – 700 nm. A process based on resist reflow and etching is used to fabricate a tapered cavity layer for the FP LVOF. This filter is highly suitable for implementation in a microspectrometer with wide spectral operating range.

**Keywords :** metallic Fabry-Perot, microspectrometer, Linear Variable Filter, Silver

### I - Introduction

Single-chip optical micro-spectrometers have huge potential in many applications, such as identification of bio-molecules, gas detection and in chemical analysis, because of their properties such as low-cost and low sample volume [1]. A small Linear Variable Optical Filter (LVOF) integrated with an array of optical detectors is a very suitable candidate for a microspectrometer that should feature both low unit cost and high resolving power [2]-[3]. A Fabry-Perot (FP) device consists of two mirrors separated by a cavity. The length of the cavity determines the wavelength that can pass through the filter. A LVOF is in principle a FP filter in which the cavity layer is tapered and its thickness varies linearly along the filter.

The applications of microspectrometers can be classified in two modes of operation: (1) narrow spectral range with maximum resolving power (for instance for use around an absorption line in air) or (2) wide spectral range with moderate requirements on resolving power and throughput (when used as a general-purpose micro-instrument). In the first mode of operation light absorption in the mirrors of the LVOF should be minimum to ensure high throughput. This is the reason for the emphasis in FP designs on dielectric mirrors. Light absorption in metallic layers is generally significant. However, Silver shows an acceptable performance in terms of reflection and absorption of light in the visible spectral range and is, therefore, suitable in the second mode of operation. A compromise between resolving power is possible using Silver with 20 % throughput in the visible spectral range and 5 nm spectral resolution.

Previous reported work by authors on LVOF-based microspectrometers was based on fabrication using dielectric mirrors on a glass substrate and mounted on commercial CMOS cameras for characterization and

spectral measurements [4]-[6]. When using the microspectrometer as a universal micro-instrument, LVOFs with silver reflectors are highly suitable. Design, fabrication and characterization results are presented here.

### II – Principle of operation and design

Figure 1 shows the principle of operation of a LVOF when dielectric mirrors used as reflectors.

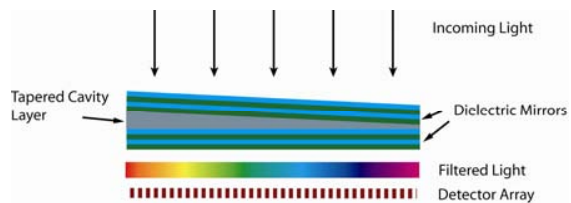


Figure 1: Principle of operation of a Linear Variable Optical Filter (LVOF).

The LVOF is basically a one-dimensional array of many Fabry-Perot (FP)-type of optical resonators. Rather than a huge number of discrete devices, the LVOF has a center layer (the resonator cavity) in the shape of a strip and a thickness that changes over its length. Reflective layers are on either side. The spectral resolution of a Fabry-Perot interferometer is determined by surface flatness, parallelism between the two mirror surfaces and mirror reflectivity. The possibility to have high number of spectral channels in a LVOF spectrometer theoretically makes it possible to have spectral resolution better than 0.2 nm in the visible spectrum range using signal processing techniques. For a Fabry-Perot type of LVOF, the thickness variation of the cavity layer has to be in order of quarter of the wavelength and very well controlled, which makes fabrication of miniature LVOFs a technological challenge. The theoretical limit for the spectral resolving power of the LVOF-based spectrometer is the spectral bandwidth divided by the number of channels in the detector array. However, this is difficult to achieve when considering the Signal to Noise Ratio. This simple geometric optimum is only approached in case of a high SNR.

Figure 2 shows reflection from different metallic layers. [7]-[8]

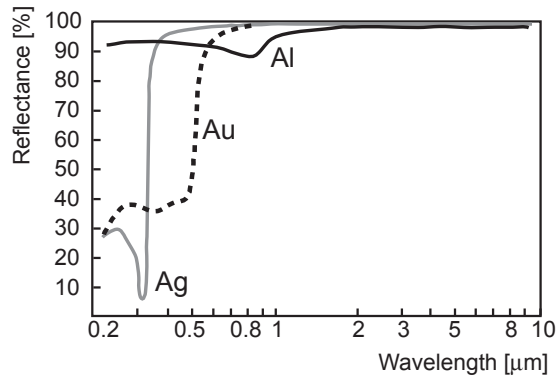


Figure 2: Optical reflectance of Au, Ag and Al.

From the Figure can be noted that Ag has over 90 % reflection in the visible spectral range of 400 nm – 700 nm.

Table 1 shows the optimized thicknesses of the layers for the LVOF.

Table 1: Layer structure of the Linear Variable Filter

Layer Material	Layer thickness
Silver	45 nm
SiO <sub>2</sub>	90 nm – 190 nm
Silver	45 nm
SiO <sub>2</sub>	220 nm

The LVOF has two 45 nm thick Silver reflectors. The simulated reflection, absorption and transmittance of a 45 nm Silver layer are shown in Figure 3a (using TFCalc 3.3). As it can be seen from the figure a 45 nm silver layer results in over 90 % reflection in the visible spectral range, while absorption and transmission are in the same order of magnitude. In order to show the advantage of Silver to Aluminum a comparison between the two metals needs to be drawn. The minimum thickness of an Aluminum layer that gives the same reflectance as a 45 nm Silver layer is 35 nm. Figure 3b shows the simulated reflection, absorption and transmittance for a 35 nm Aluminum layer.

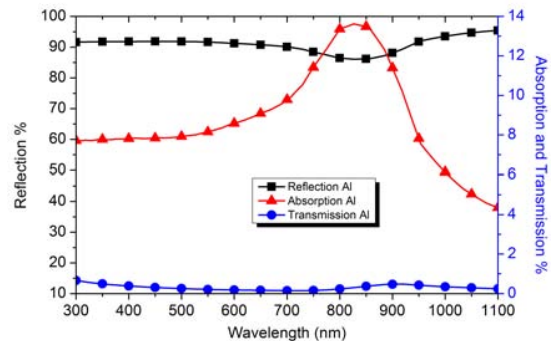
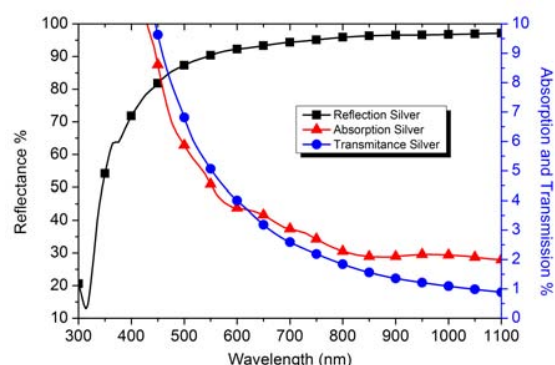


Figure 3: Reflectance, Transmission and absorption of a) 45 nm Silver and b) 35 nm Aluminum

The figure demonstrates that for Aluminum most of the non-reflected light is absorbed and not much is transmitted through the layer. Hence, a resonance filter with Aluminum has a very low throughput and is not practical. This conclusion drawn from the comparison of the two figures can be supported by theory on optical resonance.

The spectral response of the Silver-based LVOF with layers defined in Table 1 has been simulated and shown in Figure 4.

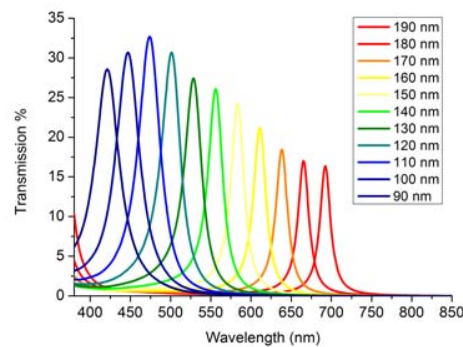


Figure 4: Transmission through the LVOF at different thicknesses of the cavity.

The LVOF has a throughput of 15 % - 30 %, covers the entire visible spectral range with blocking of the infrared. The cavity layer thickness should vary from 90 nm to 190 nm along the length of the LVOF. Producing such a small variation in thickness is the challenging part of the fabrication. The purpose of the top 220 nm of SiO<sub>2</sub> layer is twofold: (1) increase of the reflection at the top mirror and (2) protection of the underlying Silver layer from oxidation.

### III – Fabrication of the LVOF

Figure 5 shows the process flow for the fabrication of the Silver-based LVOF. LVOF fabrication starts by deposition of 45 nm of Silver and 350 nm of SiO<sub>2</sub> on a

glass substrate. Both depositions are done in a Leybold L560 evaporation deposition tool without breaking the vacuum to avoid Silver being exposed to air (tarnishing). Tapered layer fabrication is based on reflow of a specially patterned layer of resist. Photoresist is spin-coated and lithography is applied to define the strip-like structure in the resist layer to be reflowed. A series of trenches of constant width and with variable spatial frequency or trenches of variable width and constant pitch are etched over the length of the strip of resist to vary the effective amount of resist per unit area. The mask for such lithography is design based on a simple geometrical model and further optimized by FEM modeling. The subsequent reflow transfers this gradient volume of resist into a smooth tapered resist layer [9]. The topography of the tapered resist layer is transformed into the thick oxide cavity layer by an appropriate plasma etching process. The dry etching process has to be optimized to result in minimum roughness on the surface of the oxide. For this reason the process is done at the minimum possible pressure of 8 mBar, 50 W power, 25 sccm CHF<sub>3</sub> and 25 sccm of Ar. Performing the dry etching at the minimum possible pressure avoids Nano-masking and makes the process very slow [10]. The etch rate of resist is measured to be 14-15 nm/min and etch rate of SiO<sub>2</sub> is 20 nm/min.

The fabrication process is completed by deposition of the top Silver mirror and additional SiO<sub>2</sub> layer. This prototype of the LVOF was fabricated on a glass substrate. IC-compatible fabrication of the LVOF allows the LVOF to be directly integrated to a CMOS detector array [11].

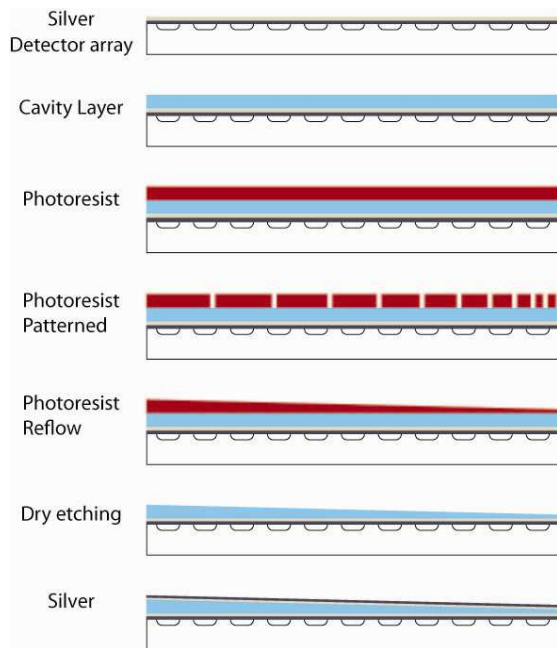


Figure 5 Process flow for fabrication of a Linear Variable Optical Filter (LVOF).

Figure 6 shows a photograph of the fabricated LVOF. Since the etch rates were not fully calibrated parts of the structures at the two side have been etched away and removed. This may be due variations of the etch rates in time. Improved in-situ etching monitoring should be applied by measuring reflection from a laser source in future fabrication.

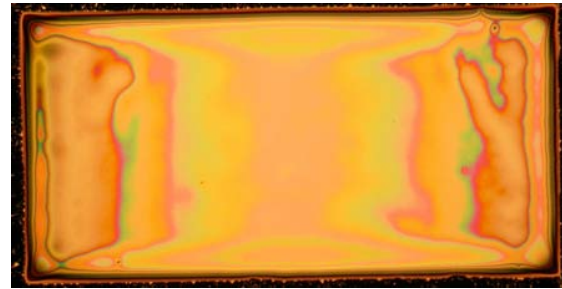


Figure 6 Photograph of a Linear Variable Optical Filter (LVOF).

#### IV – Characterization of the LVOF

The LVOF is placed in front of a CMOS camera and collimated monochromatic light is projected on the Camera. The wavelength is swept from 400 nm to 740 nm with 5 nm steps. At each wavelength only the part of the camera is illuminated for which the LVOF transmits the light. Figure 8 shows the plot of recorded intensity of pixels at 500 nm – 695 nm wavelength range with 15 nm steps. Due to over etching of the structure one third of the structure is removed and thus the LVOF does not operate in 400 – 500 nm wavelength range.

The peak of the recorded intensity changes 1.5 - 2.5 pixels/nm. Therefore it is expected that using such a filter can provide a 5 nm spectral resolution when signal processing is applied.

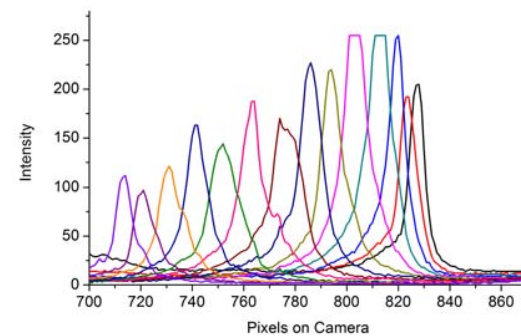


Figure 7 Intensity on Camera pixels at 500 nm – 695 nm with 15 nm wavelength steps.

Figure 8 shows the images recorded by the camera at 600 nm and 650 nm wavelengths. The two outer lines in each image show the area of the LVOF structure and the two illuminated lines in the middle move apart along the structure as the wavelength is changed. The image shows that the lines are not perfectly parallel, which is

due to thickness non-uniformity. This problem can be solved in an improved deposition control.

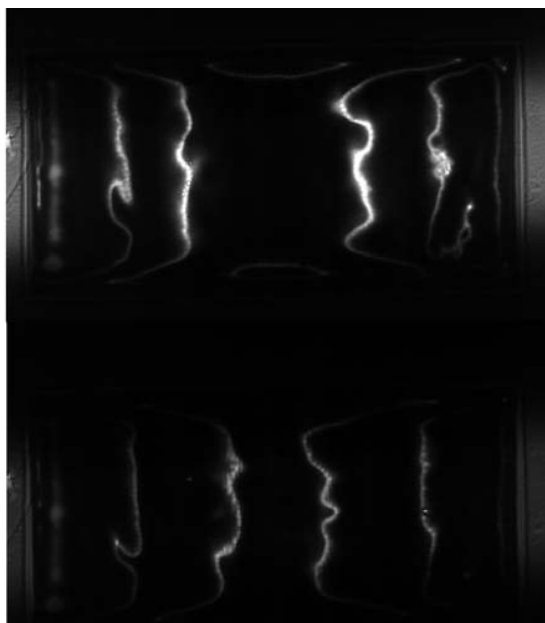


Figure 8 Image recorded at 600 nm and 650 nm using a CMOS camera.

#### IV - Conclusion

LVOFs with Silver reflectors has been designed and fabricated. The LVOF has a throughput of 15 % - 30 % and covers the entire visible spectral range and blocks the infra-red. The advantage of using Silver in comparison to Aluminum has been discussed. The LVOF has been mounted on a commercial CMOS camera for characterization. Characterization proves the concept. It is expected that a spectral resolution of 5 nm can be achieved in such a LVOF over the visible spectral range of 400 nm – 700 nm. IC-compatible fabrication of the LVOF provides the possibility of integration of the LVOF to a CMOS chip as a post-process.

#### Acknowledgement

This work has been supported in part by the Dutch technology Foundation STW under grant DET.6667.

#### References

- [1] G. Minas, R. F. Wolffenbuttel and J. H. Correia. An array of highly selective Fabry–Perot optical channels for biological fluid analysis by optical absorption using a white light source for illumination, *Journal of Optics A: Pure and Applied Optics*, IOP Publisher, 8, pp.272-278.
- [2] R. McLeod, T. Honda. Improving the spectral resolution of wedged etalons and linear variable filters with incidence angle, *Optics Letters*, Vol. 30, No. 19 (2005), pp 2647-2649.

- [3] S.F. Pellicori, US Patent 4957371 - Wedge-filter spectrometer
- [4] Arvin Emadi, Huaiwen Wu, Ger de Graaf, and Reinoud F. Wolffenbuttel, “CMOS-compatible LVOF-based visible microspectrometer”, *Proc. SPIE* 7680, 76800W (2010)
- [5] Arvin Emadi, Semen Grabarnik, Huaiwen Wu, Ger de Graaf, Karin Hedsten, Peter Enoksson, Jose Higinio Correia, and Reinoud F. Wolffenbuttel, “Spectral measurement using IC-compatible linear variable optical filter”, *Proc. SPIE* 7716, 77162G (2010)
- [6] Arvin Emadi, H. Wu, S. Grabarnik, G. De Graaf, K. Hedsten, P. Enoksson, J.H. Correia, R.F. Wolffenbuttel, Fabrication and characterization of IC-compatible linear variable optical filters with application in a micro-spectrometer, *Sensors and Actuators A: Physical*, In Press, Accepted Manuscript, Available online 7 May 2010
- [7] D Rossberg, *S&A A54*, 1996, pp. 793
- [8] J. H. Correia, M. Bartek, R. F. Wolffenbuttel, Bulk-micromachined tunable Fabry-Perot micointerferometer for the visible spectral range, *Journal Sensors and Actuators A*, 76, pp. 191-196, 1999
- [9] A Emadi *et al* 2009,” Vertically tapered layers for optical applications fabricated using resist reflow” *J. Micromech. Microeng.* **19** 074014
- [10] K. Mohamed, M.M. Alkaisi, Three-dimensional pattern transfer on quartz substrates, *Microelectronic Engineering*, Volume 87, Issues 5-8, The 35th International Conference on Micro- and Nano-Engineering (MNE), May-August 2010, Pages 1463-1466
- [11] Chi Liu, Arvin Emadi, Huaiwen Wu, Ger de Graaf, and Reinoud F. Wolffenbuttel, “A CMOS 128-APS linear array integrated with a LVOF for high sensitivity and high-resolution micro-spectrophotometry”, *Proc. SPIE* 7726, 772616 (2010)



# FRACTAL-BASED DUAL-BAND SMALL ANTENNA FOR 2.45 AND 5.8 GHZ

Sultan Ahmed<sup>1</sup>, Peter Enoksson<sup>1</sup>, Mircea V. Rusu<sup>2</sup>, Cristina Rusu<sup>3</sup>

<sup>1</sup>Chalmers University of Technology, Micro and Nanosystems group,; SE-412 96 Gothenburg, Sweden

<sup>2</sup>Faculty of Physics, Bucharest University, MG-11, Bucharest-Magurele, Romania

<sup>3</sup>Imego AB, SE-400 14 Gothenburg, Sweden

peter.enoksson@chalmers.se

**Abstract** — *Small antennas are becoming important and required for many domestic and commercial wireless applications. New design and first experimental results confirming the simulations of multi-band patch antenna optimized for the 2.45 GHz and 5.8 GHz bands are presented. This design is based on the practical considerations found for our Minkowski-based fractal antenna that predict the influence of geometry modifications on the frequency of operation.*

**Keywords:** RFID tag, patch antenna, fractal geometry, 2.45 GHz, 5.8 GHz, wireless applications

## I - Introduction

Within mobile communications and other commercial devices like RFID tags there is an increased interest for small antenna. Comparing the geometrical size of the antenna with the wavelength makes small-size antenna to be considered ‘small antennas’ from the radiation point of view. Their work is inherently at the limit of low efficiency and radiation power. Moreover, they have to be thin and eventually multiband antennas as well. It is known that the ensemble of requirements make their design complex.

Planar microstrip antenna with fractal geometry is one of possibilities for a RFID tag. Fractal geometry is known for long time [1], but fractal geometry for antennas is used only in the last decade mainly for short-range wireless devices and mobile handsets [2-4]. Fractal antennas have some very special properties attractive for the design of a multi-band antenna:

- broad band operation;
- gain is slowly varying with frequency;
- possible to use one single layout for more than one frequency for different applications;
- can operate efficiently at smaller sizes than ordinary antenna.

However, fractal antenna is difficult to design because there are no formulas or analytical models that make the connection between the antenna characteristics and fractal geometry. This means that each layout must be checked both by simulations and measurements.

Our investigations [5, 6], showed that choosing the correct compromise between the principal characteristics, it is possible to obtain useful workable small antennas with reasonable good results. For example, it is possible to find a geometry that could resonate at both UHF and MW frequency bands [5].

The design procedure, the simulation and measurement results of a Minkowski-based dual-band antenna for non-harmonic frequencies 2.45GHz and 5.8 MHz

are presented in the following paragraphs. This design is intended for passive RFID sensing tags.

## II – Simulations

Multi-band and non-harmonic frequencies are an obvious response for a fractal antenna mainly due to its self-similarity property. Thus 2<sup>nd</sup> and 3<sup>rd</sup> orders of Minkowski-based geometry as loop antenna (Fig. 1) and patch (Fig. 2) have been analyzed. These investigations were necessary for finding the optimum design for 2.45 GHz and 5.8 GHz (frequency bands for RFID applications).

Antenna behaviour has been simulated in Momentum ADS by Agilent Technologies (3D planar electromagnetic simulator based on Method of Moments), where it has been modelled as printed copper wires (20 µm thick, and 0.5 mm wide for the loop antenna) on a 1.2 mm thick Rogers Duroid substrate having loss tangent 0.0012 and with a uniform ground plane on the other side of the substrate (20 µm-thick).

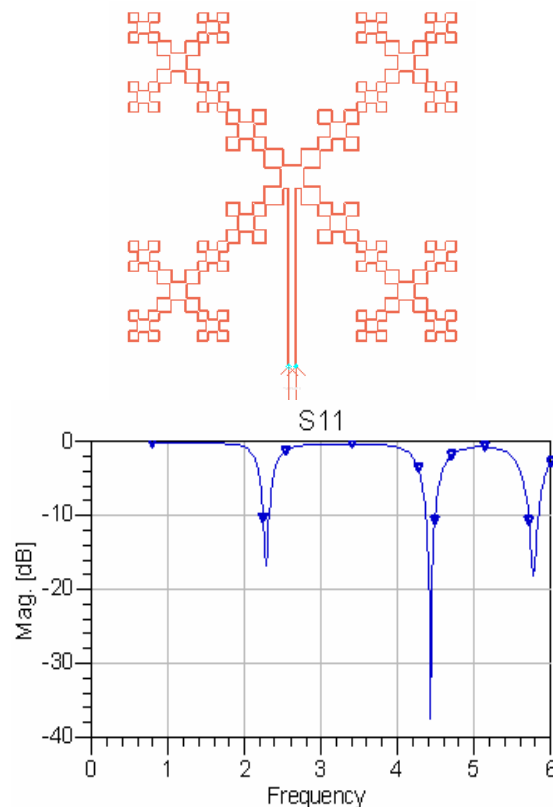


**Figure 1:** Example of a 3<sup>rd</sup> order Minkowski layout for a loop antenna (a) and S11 for this design (b).

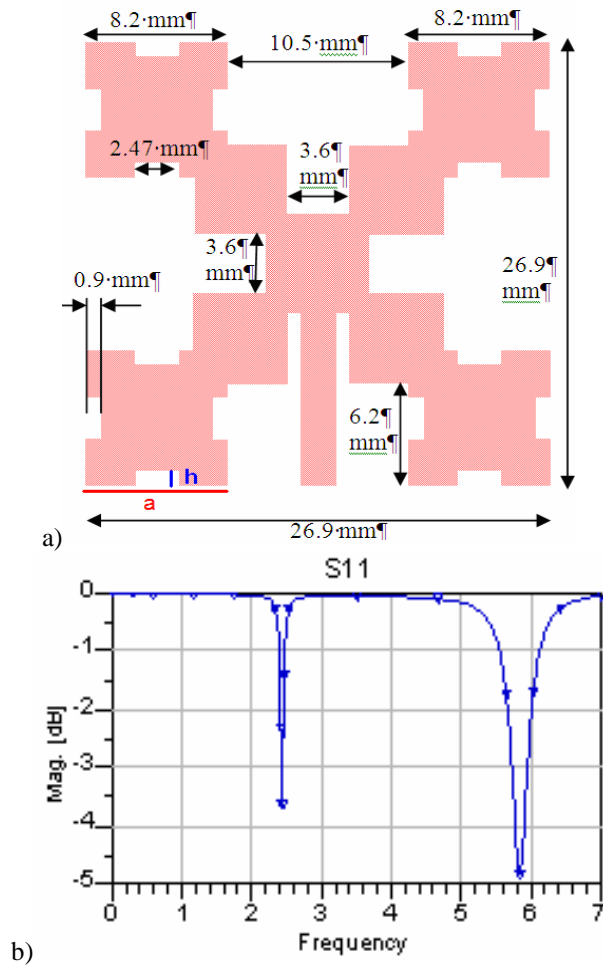


**Figure 2. Simulation of the optimized 2<sup>nd</sup> order Minkowski-based fractal patch antenna; (a) layout showing the corners' indentation height,  $h$ , and initiator,  $a$ ; (b) S11.**

To get response exactly at 2.45 and 5.8 GHz, indentation height,  $h$ , of all four corners (Figure 2a) has been decreased from ' $0.3a$ ' to ' $0.11a$ ' in steps of ' $0.01a$ ' (where  $a$  is the length of the initiator with which a fractal is generated [1]). The response of higher order frequency was slightly changing while the response of lower order frequency has moved more to lower frequency as shown in Figure 3.

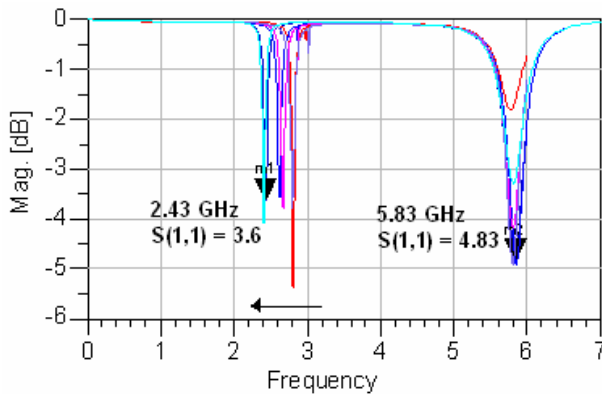


**Figure 3: Change of frequency response with decreasing indentation height,  $h$ .**

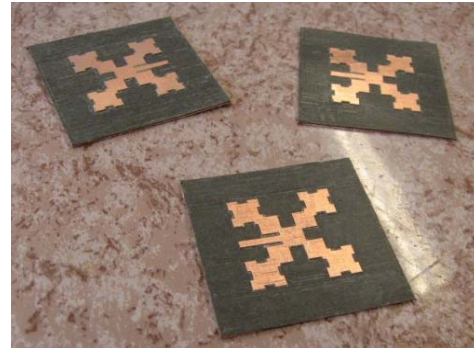


**Figure 5: Manufactured Second order Minkowski Fractal**

Radiation pattern of 2<sup>nd</sup> order patch antenna for 2.45 and 5.8 GHz are shown in figures 4 and 5, respectively. For 2.45 GHz (figure 4), the gain is above 4 dB with HPBW of 90 degree and efficiency is almost 50%. For 5.8 GHz (figure 5), gain is almost 2 dB but for  $\theta$ , -20 to +20 the gain goes down to -11 dB, so for 5.8 GHz the antenna works like a directional antenna. So the designed works more well in 2.45 GHz than 5.8 GHz.

### III –Experimental and Discussions

The antenna was manufactured on Rogers Duroid 5870 substrate as shown in Figure 6. This substrate has slightly different properties as the simulated ones (with simulation values within brackets); permittivity 2.33 (2.212), loss tangent of 0.0005...0.0012 (0.0012), thickness of 0.787 (1.2) mm, copper layer metal with thickness of 35 (20)  $\mu$ m.

The measurements were performed at VTT (Finland) by using a test antenna Huber Suhner (type 1324.19.0002) for lower band and a self-made directive patch antenna for the upper band. The measurements were done in the direction of the maximum radiation at the both bands.

The measured S11 behaviour with frequency is shown in Figure 6. From S11 parameters (Re and Im part), the impedance was calculated and it showed that the antenna feed impedance is differed from 50 Ohm due to substrate's different properties.

The coupling factor for conjugate match at the both resonance frequencies was also calculated for the evaluation of the potential bandwidth of the antenna (showing in table 1). The antenna is not pure resistive at that frequencies so for maximum power transfer the coupling with the measuring device has to be done with a complex conjugate of the antenna impedance. Table 1 shows the results and the bandwidth in this case.

f0 (MHz)	Re(Z) / W	Im(Z) / W	B coupled
2313	10,54	-16,6089	16,9 MHz
5758	147,97	-142,954	111 MHz

**Table 1. Measured Impedance and coupling factor**

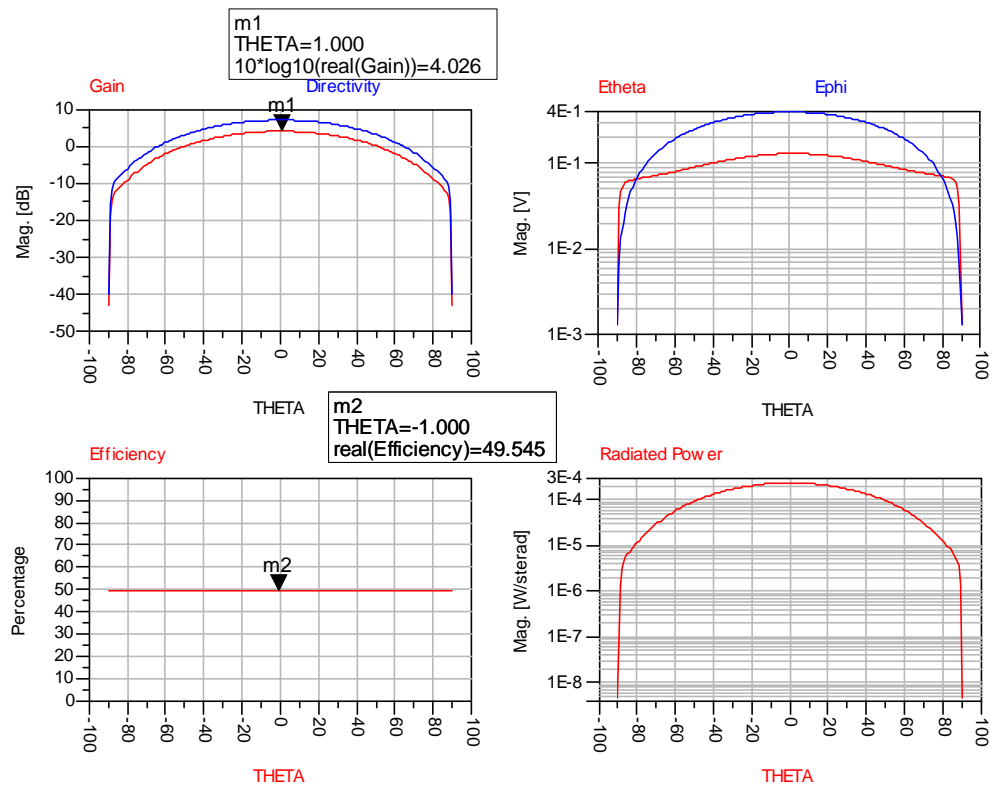


**Figure 4: Radiation pattern for 2.45 GHz**

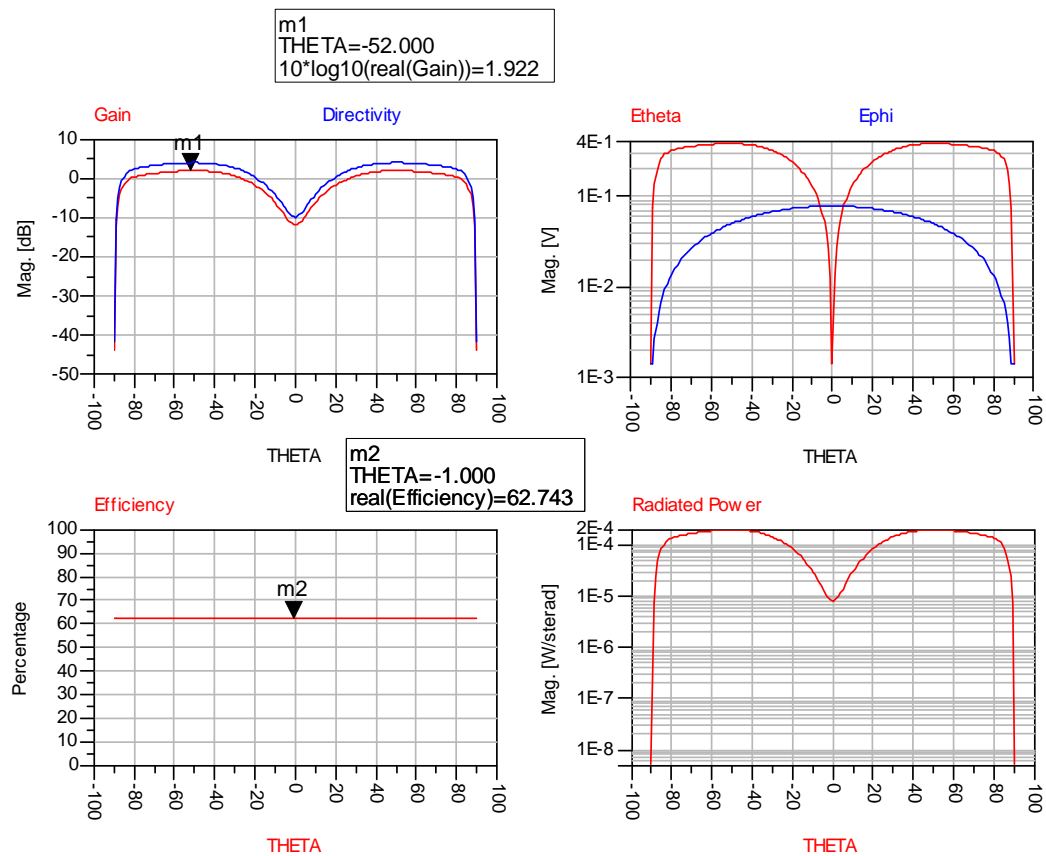


**Figure 4: radiation Pattern for 5.8 GHz**

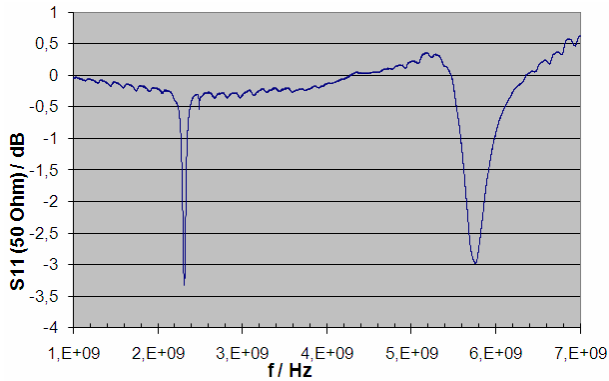


**Figure 6. Measured S11 for the manufactured antenna.**

The radiation measurement data, S21, confirm that the directions of the maximum radiation are as the simulation predicted; that is  $\phi=0$ ,  $\theta=0$  for the lower band and about  $\phi=0$ ,  $\theta=45$  deg for the upper band. The power budgets were also calculated for the both bands which give the antenna gain. By the measurements, the efficiency and directivity cannot be separated as factors of the gain. If we assume the simulation results for the directivity to be right (8 dBi @ 2.45 GHz and 4 dBi @ 5.8 GHz), from the gain measurements we obtain radiation efficiencies of 16 % (lower band) and 29 % (upper band). These values are lower than the simulated ones are understandable since thinner substrate of a microstrip structure practically always increases losses.

#### IV – Conclusion

Generally, comparing the measurement results to the simulations, the antenna's characteristics are close to the intended ones such as frequencies, direction of maximum radiation.

The change of the substrate has influenced the impedances and bandwidths as already the feeding stub on the antenna is now different from 50 Ohms. Nevertheless, these good experimental results confirm the simulations and the possibility of designing a fractal geometry with good antenna characteristics based on empirical methods.

The benefits of the designed fractal antenna are:

- Multiband response at 2.45 and 5.8 GHz;
- Gain is around 3 dB with radiation efficiency of about 50% for both bands (simulated);
- Measured radiation efficiency of 16 % and 29 %, respectively for thinner substrate;
- Antenna dimension 2.69 cm x 2.69 cm.

#### Acknowledgment

This work is done within the Nordic project 'SAFFO RFID' financed by VINNOVA (Sweden). Authors express thanks to Kaarle Jaakkola (VTT, Finland) for the measurements on the antenna.

#### References

- [1] B. Mandelbrot, How long is the coast of Britain? Statistical self-similarity and fractional dimension, *Science* **156**, 636-638, 1967.
- [2] N. Cohen, Fractal antennas and fractal resonators. US6452553, 1995.
- [3] [www.fractenna.com](http://www.fractenna.com)
- [4] [www.fractus.com](http://www.fractus.com)
- [5] H. Rahimi, M.V. Rusu, P. Enoksson, D. Sandström, C. Rusu, Small patch antenna based on fractal design for wireless sensors, *Proc. MME 2007, 18<sup>th</sup> Workshop on Micromachining, Micromechanics, and Microsystems*, 16-18 Sept. 2007, Portugal.
- [6] M.V. Rusu, M. Hirvonen, H. Rahimi, P. Enoksson, C. Rusu, N. Pesonen, O. Vermesan, H. Rustad, Min-kowski Fractal Microstrip Antenna for RFID Tags, *Proc. EuMW2008 Symposium*, Amsterdam, 2008.



# MEASURING THERMAL PROPERTIES OF SMALL VOLUMES OF LIQUID USING A ROBUST AND FLEXIBLE SENSOR

J.J. Atherton<sup>a</sup>, M.C. Rosamond, S. Johnstone and D.A. Zeze

*Durham University, School of Engineering and Computing Sciences, Durham, DH1 3LE, United Kingdom*

<sup>a</sup>*j.j.atherton@durham.ac.uk*

**Abstract** — This report describes a new device which is flexible, robust and capable of measuring the thermal conductivity of samples with dimensions of 10's of microns. The device consists of thin film micro heaters and two thermoelectric junctions fabricated on a thin, flexible polyimide substrate which is also used as an encapsulant. Key advantages include electrical isolation and the ability to measure small volumes (~100  $\mu$ L), e.g. liquid droplets and thin sheets.

Mixtures of glycerin and water are used here to demonstrate the ability of the device to measure the thermal properties of small volumes of liquids. An analytical model is presented to extract thermal conductivity values from experimental data. In addition a numerical model is contrasted against the experimental data.

**Keywords:** Thermal conductivity, polyimide, liquid samples

## I – Introduction

Thermal conductivity ( $k$ ) is an important material property in a wide range of industrial and academic areas since it dictates the flow of heat in materials. Whilst the properties of pure bulk materials are well known, this is not the case for heterogeneous materials (e.g. food [1] or nano-fluids [2]). In such a material it is difficult to estimate the values of the thermal conductivity from a knowledge of its constituent parts [3]. Instead, it is necessary to directly measure the thermal conductivity of a sample. From this data other physical properties can also be derived, such as the composition of a mixture (e.g. the fat content of milk [4]).

Biological samples are likely to be heterogeneous, therefore, their thermal properties can only be ascertained experimentally. Ideally, such measurements should be made using only small volumes, since biological samples are often of limited size. Micro thermal probe devices have been reported, particularly in the microcalorimetry field (e.g. [5]). However, many involve complicated fabrication procedures.

To effectively probe biological or chemically aggressive materials, the sensor must be encapsulated and chemically inert. For example, Kadjo et al. [6] use two parallel tantalum wires to measure the thermal properties of concentrated nitric acid. However, the relatively large size of the probe limits the liquid sample volume to around 2 mL.

There are a number of methods used to measure the thermal properties of materials. The flash method

suggested by Parker et al. [7] is widely used. The basic principle is to apply a high intensity, short duration pulse of heat (e.g. a laser pulse) to one side of a sample while a thermal sensor located on the opposite side of the sample monitors the response. Various sensors are used, such as infra-red sensors [8], pyroelectric crystals [9] or photoacoustic methods [10]. These methods provide good accuracy, at the expense of complexity.

The hot wire method is a popular and simple method based on the measurement of the temperature rise at a defined distance from a linear heat source (hot wire) embedded in the test material (e.g. [1] and [11]). This places the material under test between a heater and thermal sensor. The benefits of these hot wire methods are outlined by [12] as: easy analytical solutions, short measurement times (a few seconds), simple and inexpensive experimental setup, the ability to sense thermal conductivity and heat capacity simultaneously and the fact that they are suitable for solids, liquids and gasses.

The devices proposed here combine many of the benefits mentioned in literature, giving the advantages of simplicity, measurement of small volumes, robustness, electrical isolation, chemical resistance and flexibility as well as biocompatibility.

This report outlines the fabrication of thin film (~190 nm) thermocouples on a 20  $\mu$ m thick polyimide substrate. An analytical model is presented, which allows the thermal conductivity to be calculated from two temperature measurements. Mixtures of water and glycerin are used to allow a comparison of experimental results with a numerical model and literature values to validate the operation of the device.

## Principle of operation

To measure the thermal properties a sample (of unknown thermal conductivity) is brought into contact with the device. A resistive heater patterned on the substrate provides a heat source into the sample under test, while two thin film thermocouples patterned at distances of 75  $\mu$ m and 150  $\mu$ m monitor the variation of temperature caused by the heat flowing through the sample. These temperature changes can be exploited to calculate the thermal conductivity of the sample.

The fact that both the heater and sensor sit in the same plane is beneficial since it simplifies the fabrication of the devices as well as allowing an analytical solution to be derived for thermal conductivity calculations. In addition, the sensing elements are encapsulated using polyimide, which is chemically resistant, biocompatible, robust and flexible. Polyimide is a good elec-

trical insulator, therefore only a thin encapsulation layer is required for electrical and chemical isolation. As polyimide has a thermal conductivity of  $\sim 0.105 \text{ Wm}^{-1}\text{K}^{-1}$  [13], this allows the thicker substrate to act as a good insulator, preventing heat loss through the substrate and isolating the sensing junctions. However, the encapsulation layer is thin by comparison so the sensing junctions are not isolated from the material under test. The encapsulation makes the device chemically inert and electrically isolated, while the size makes the device suitable for measuring small volumes. This will allow the device to measure the thermal conductivity of small droplets of liquid.

The flexibility of the substrate opens a wide range of potential applications, such as measuring the thermal properties of thin sheets (e.g. paper or leaves), while the robustness of a polyimide device should eventually enable the device to be used outside a laboratory setting.

## II – Design & Fabrication

A schematic of the device is shown in Figure 1. Each substrate has two heaters and six sensors patterned on it, of which only one heater and two sensors were required in these experiments. The sensors used were located at distances of  $75 \mu\text{m}$  and  $150 \mu\text{m}$  from the heater. The polyimide substrate is around  $20 \mu\text{m}$  thick, with a  $1.75 \mu\text{m}$  encapsulation layer.

The heaters are formed out of  $125 \text{ nm}$  thick nickel (Ni), while the thermocouples are a combination of  $63 \text{ nm}$  chromium (Cr) and  $125 \text{ nm}$  Ni, with line widths at the sensing junctions of  $17.5 \mu\text{m}$ .

The thermocouple ‘cold’ junctions are located a distance of at least  $10 \text{ mm}$  from the heater to ensure that the sensing junctions measure a temperature relative to ambient. Ni and Cr were chosen because they have the highest bulk Seebeck coefficients of the materials available (Cr:  $21.8 \mu\text{VK}^{-1}$  and Ni:  $-14.5 \mu\text{VK}^{-1}$  [14]). It is also important to note that Cr and Ni have very good adhesion the substrate, therefore do not suffer any damage or delamination during subsequent processing stages.

Many microfabricated thermal sensing devices are formed on a membrane (e.g. silicon nitride [15], or silicon oxide [16] or SU8 [17]) by etching a silicon substrate. However, these introduce a number of complex fabrication stages and produce delicate devices, unlike the polyimide substrate chosen here.

The devices were fabricated using standard photolithographic techniques. In the first stage, polyimide (PI2610, HD Microsystems) was spun on a  $2''$  silicon wafer. A thickness of  $20 \mu\text{m}$  was achieved by spinning at  $800 \text{ rpm}$  for  $60 \text{ s}$  three times, with a  $5 \text{ minute}$ ,  $85^\circ\text{C}$  bake stage between spins. The polyimide was subsequently baked at  $350^\circ\text{C}$  for  $30 \text{ minutes}$  to fully cure it.

The next stage consisted of depositing and patterning the metal layers. This was achieved using a bi-layer lift-off and electron beam thermal evaporation. Due to its superior adhesion properties, the  $63 \text{ nm}$  Cr layer was deposited first, followed by the  $125 \text{ nm}$  Ni layer. A

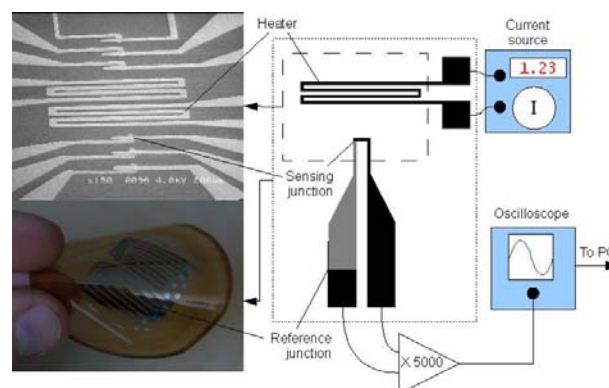


Figure 1- Schematic of the device with a scanning electron microscope image (top left) showing the resistive heaters each with 3 sensing junctions and photograph (bottom left) demonstrating the overall device and its flexibility.

$1.75 \mu\text{m}$  polyimide layer was spun at  $3000 \text{ rpm}$  for  $30 \text{ s}$  and cured to encapsulate the devices. The polyimide was removed over suitable contact pads to allow electrical connections to be made. This was achieved with an oxygen plasma etch (Oxford, Plasma Lab 80+). Finally, the polyimide was peeled from the silicon substrate to release the device.

The devices were tested using a current source (Keithley, 6221) to provide a heat input to the resistive heater, while the thermocouple output voltages were amplified using a custom built amplifier based on an instrumentation amplifier (LT1167, Linear Technologies), with a gain of  $5000$ , set by a single external resistor. Both the input voltage to the heater and the output from the amplifier were monitored and stored using an oscilloscope (Agilent, DSO3102A) and PC.

### Calibration of the device

As a non-standard pair of materials were chosen to form the thermocouples, it was necessary to calibrate the device. To achieve this, the thermocouple output was recorded while the junctions were held at a known temperature. A  $70 \Omega$   $5 \text{ W}$  wire wound resistor was used as a heat source and clamped over the sensing junctions while a standard K-type thermocouple was fastened on one surface of the resistor to monitor its temperature.

The power applied to the resistor was varied, to control the surface temperature. The output of the K-type thermocouple was compared to the voltage produced by the device. The results are shown in Figure 2.

The bulk values of the Seebeck coefficients for Cr and Ni are available [14]; however Zhang et al. [18] suggest that thin films below  $100 \text{ nm}$  do not exhibit bulk values. Despite being formed from thin films (Cr:  $63 \text{ nm}$  and Ni:  $125 \text{ nm}$ ), the device demonstrates a sensitivity of  $0.179 \text{ V}^\circ\text{C}^{-1}$  after amplification, representing  $35.7 \mu\text{VC}^{-1}$ , when taking into account the amplifier gain of  $5000$ . This sensitivity value is close to the  $36.3 \mu\text{VC}^{-1}$  expected for bulk Cr-Ni junctions. Annealing during the  $350^\circ\text{C}$  curing stage for the polyimide encapsulation layer may account for the near bulk values.

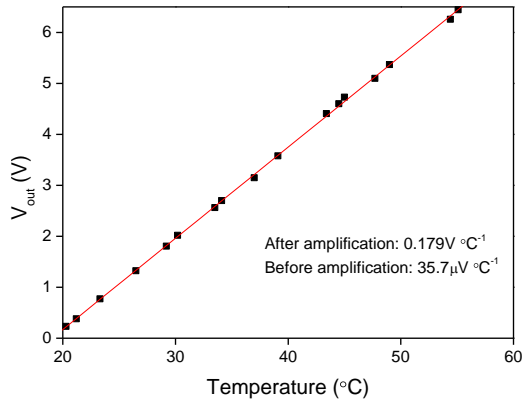


Figure 2- The output voltage from the device, after amplification (with a gain of 5000) is plotted against the surface temperature of a wire wound resistor clamped over the sensing area of the device.

### III - Results

The steady state temperature gradient for a known power input was recorded for several liquid samples. Six samples were prepared, containing a mixture of water and glycerin in different ratios, from pure water to pure glycerin. This gave thermal conductivities ranging from  $0.286 \text{ Wm}^{-1}\text{K}^{-1}$  for pure glycerin [19] to  $0.58 \text{ Wm}^{-1}\text{K}^{-1}$  for pure water [20]. The liquids were contained by gluing a small piece of tubing over the sensing area of the device, giving a total volume of liquid of around  $100 \mu\text{L}$ . A  $5 \text{ mW}$  step input was applied to the resistive heater. Each sample reached 90 % of its steady state value within about 1 s, with the steady state value assumed to be the maximum value achieved after 5.5 s.

A numerical model (COMSOL) was created using nominal values for thermal conductivity taken from [19]. This allows a comparison to be made between the theoretical temperature change expected by conduction alone and the experimental temperature changes measured. The results are shown in Figure 3.

The experimental results show good correlation with the numerical model for the closest junction, however the furthest junction records a temperature around  $1^\circ\text{C}$  lower than the model predicts. This is likely to be due to convective losses, not accounted for within the model.

For the device to be useful, the change in temperature must be related to the thermal conductivity. To achieve this, a simplified one-dimensional, steady state analytical model of conduction, based upon Fourier's law applied to a sphere with constant thermal conductivity, can be used:

$$q_{in} = -kA \frac{dT}{dr} = -k(4\pi r^2) \frac{dT}{dr} \quad (1)$$

Where  $q_{in}$  is the heat transfer rate applied to the area represented by the locus of  $r_1$ . This is assumed to be the same as the power applied to the heater which implies that there is no heat loss through the substrate.  $k$  is the isotropic thermal conductivity,  $A$  is the area through

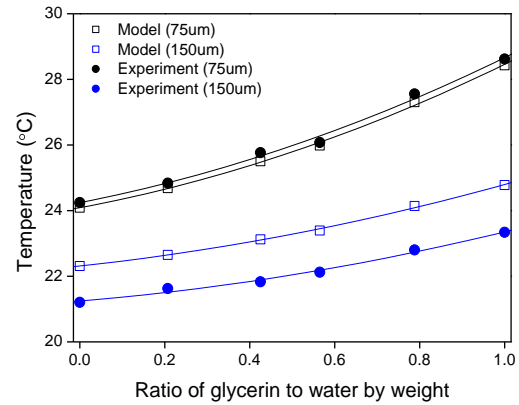


Figure 3- A comparison of the experimental and modeled temperature changed experienced at distances of  $75 \mu\text{m}$  and  $150 \mu\text{m}$  from the heater. The model values were calculated using thermal conductivities extracted from [19].

which the heat flows,  $T$  is the temperature and  $r$  the radius.

Integrating and rearranging:

$$k = \frac{q_{in} \left( \frac{1}{r_1} - \frac{1}{r_2} \right)}{4\pi(T_1 - T_2)} \quad (2)$$

Where  $T_1$  and  $T_2$  are the temperatures at radii of  $r_1$  and  $r_2$  respectively (see Figure 4).

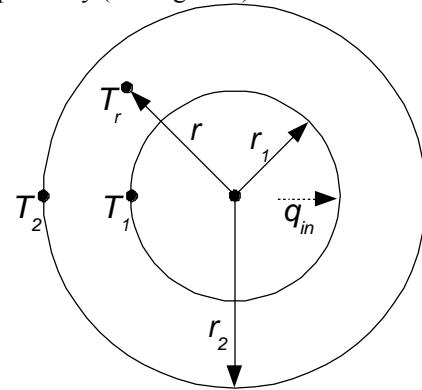


Figure 4- Simplified one-dimensional, steady state analytical model of conduction, based upon Fourier's law applied to a sphere with constant thermal conductivity.

The values obtained using this formula in combination with the experimental and model results are shown in Table 1.

The experimental values give a much larger difference in temperature between the two junctions, leading to thermal conductivity values that are lower than those suggested by [19]. Calibration of the device validates its ability to measure the correct temperature, so the discrepancy in the calculated thermal conductivity values is likely to be due to oversimplification in the models.

Firstly, the models do not account for convection within the fluid, which would cause anisotropic heat flow. This discrepancy would increase with distance,

implying that the 150  $\mu\text{m}$  temperatures would be lower than expected. This is seen in Figure 3. Secondly, the numerical model assumes the polyimide substrate is a perfect insulator, which may not be valid as, it has a thermal conductivity of  $\sim 0.105 \text{ W m}^{-1} \text{ K}^{-1}$  (around half the value for glycerin). Further work is under way to build more complete analytical and numerical models.

*Table 1 - A comparison of the calculated thermal conductivity, using equations 2 with temperature differences taken from experimental results and numerical models.*

Ratio of glycerin to water by weight	Thermal conductivity ( $\text{W m}^{-1} \text{ K}^{-1}$ )		
	Calculated (Analytical model + experimental results)	Numerical model	Literature
0%	0.30	0.52	0.59
21%	0.29	0.46	0.52
43%	0.24	0.39	0.44
57%	0.23	0.36	0.40
79%	0.19	0.29	0.33
100%	0.18	0.25	0.28

#### IV - Conclusions

A simple, robust, chemical resistant and biocompatible device capable of measuring the thermal conductivity of small volumes has been demonstrated by photolithographically defining coplanar heaters and sensors 75  $\mu\text{m}$  apart on a 20  $\mu\text{m}$  thick polyimide substrate.

The planar nature of the device simplifies the fabrication process and requires no external, simplifying the testing procedure.

A 1.75  $\mu\text{m}$  thick encapsulation layer of polyimide ensures that the sensing elements are electrically and chemical protected from the material being tested, without affecting the performance of the device.

This report demonstrates the devices' ability to measure the thermal conductivity of small ( $\sim 100 \mu\text{L}$ ) samples of water and glycerin mixtures. An analytical model is presented, which allows the thermal conductivity of the sample to be calculated from measurement of the temperature gradient produced by the resistive heater, however experimental results and a numerical model suggest that a more complex analytical model is required, to account for convection and heat loss through the substrate.

Future work will investigate the potential of the devices to probe biological materials and thin sheets. Investigation into the transient response could also yield further information on the thermal properties of the material being tested.

#### Acknowledgement

This research is supported by funding from EPSRC and One North East.

#### References

1. Y. Muramatsu, A. Tagawa and T. Kasai. Thermal Conductivity of Several Liquid Foods. *Food Sci. Technol. Res.* 11, 2005, Vol. 3, pp. 288-298.
2. Wongwises, W. Duangthongsuk and S. Measurement of

temperature-dependent thermal conductivity and viscosity of  $\text{TiO}_2$ -water nanofluids. *Experimental Thermal and Fluid Science.* 33, 2009, pp. 706-714.

3. Suleiman, B.M. Effective thermal conduction in composite materials. *Appl. Phys. A.* 2010, pp. 223-228.

4. Gustafsson, M. Gustavsson and S. E. Thermal conductivity as an indicator of fat content in milk. *Thermochimica Acta.* 442, 2006, pp. 1-5.

5. Kima, S. R. Choi and D. Real-time thermal characterization of 12 nl fluid samples in a microchannel. *Review of Scientific Instruments.* 79, 2008.

6. Kadjo, A. Garnier, J.P., Maye, J.P. and Martemianov, S. A New Transient Two-Wire Method for Measuring the Thermal Diffusivity of Electrically Conducting and Highly Corrosive Liquids Using Small Samples. *Int J Thermophys.* 29, 2008, pp. 1267-1277.

7. W.J. Parker, R.J. Jenkins, C.P. Butler and G.L. Abbott. Flash method of determining thermal diffusivity, heat capacity, and thermal conductivity. *J. Appl. Phys.* 1961, Vol. 32, 9, pp. 1679-1684.

8. Blumm, J. Lindemann, A. and Min, S. Thermal characterization of liquids and pastes using the flash technique. *Thermochimica Acta.* 455, 2007, pp. 26-29.

9. J.A.P. Lima, et al. Measurement of the thermal properties of liquid mixtures using a thermal wave interferometer. *Appl. Phys. B.* 73, 2001, pp. 151-155.

10. J. A. Balderas-Lopez, et al. Photoacoustic measurements of transparent liquid samples: thermal effusivity. *Meas. Sci. Technol.* 6, 1995, pp. 1163-1168.

11. H. Xie, H. Gu, M. Fujii and X. Zhang. Short hot wire technique for measuring thermal conductivity and thermal diffusivity of various materials. *Meas. Sci. Technol.* 17, 2006, pp. 208-214.

12. Torchio, V. Giaretto and M. F. Two-Wire Solution for Measurement of the Thermal Conductivity and Specific Heat Capacity of Liquids: Experimental Design. *International Journal of Thermophysics.* 2004, Vol. 25, 3, pp. 679-699.

13. HD MicroSystems. Product Bulletin: PI-2600 Series - Low Stress Polyimides. 2008.

14. S.C. Allison, R.L. Smith, D.W. Howard, C. Gonzalez and S.D. Collins. A bulk micromachined silicon thermopile with high sensitivity. *Sensors and Actuators A.* 2003, Vol. 104, pp. 32-39.

15. H. Wu, S. Grabarnik, A. Emadi, G. de Graaf and R. F. Wolffenbuttel. A thermopile detector array with scaled TE elements for use in an integrated IR microspectrometer. *J. Micromech. Microeng.* 2008, Vol. 18.

16. D. Randjelovic, A. Petropoulos and G. Kaltsas. Multipurpose MEMS thermal sensor based on thermopiles. *Sensors and Actuators A.* 2008, Vol. 141, pp. 404-413.

17. L. Wang, B. Wang and Q. Lin. Demonstration of MEMS-based differential scanning calorimetry for determining thermodynamic properties of biomolecules. *Sensors and Actuators B.* 2008, Vol. 134, pp. 953-958.

18. Zhang, X. Choi, H. Datta, A. and Li, X. Design, fabrication and characterization of metal embedded thin film thermocouples with various film thicknesses and junction sizes. 2006, Vol. 16, pp. 900-905.

19. Company, Dow Chemical. True Coefficient of Glycerine-Water Solutions. [Online] [Cited: 05 07, 2010.] <http://www.dow.com/glycerine/resources/table13.htm>.

20. Lide, D.R., [ed.]. "Thermal Conductivity of Liquids", in *CRC Handbook of Chemistry and Physics.* 89th Edition. s.l. : CRC Press/Taylor and Francis, Boca Raton, FL, 2009.

21. Hashimoto, J. and Morikawaa, T. Thermal diffusivity of aromatic polyimide thin films by temperature wave analysis. 2009, Vol. 105, p. 113506.

22. Greswell, R.B. Riley, M.S. Alves P.F. and Tellam, J.H. A heat perturbation flow meter for application in soft sediments. 2009, Vol. 370, pp. 73-82.

23. R. Buchner, K. Froehner, C. Sosna, W. Benecke and W. Lang. Toward Flexible Thermoelectric Flow Sensors: A Technological Approach. 2008, Vol. 17, pp. 1114-1119.

24. E. Iervolino, A.W. van Herwaarden and P.M. Sarro. Calorimeter chip calibration for thermal characterization of liquid samples. *Thermochimica Acta.* 492, 2009, pp. 95-100.



# SMALL ANTENNA BASED ON A MEMS MAGNETIC FIELD SENSOR THAT USES A PIEZOELECTRIC POLYMER AS TRANSLATION MECHANISM

R. Lameiro<sup>1</sup>, F. J. O. Rodrigues<sup>1</sup>, L. Gonçalves<sup>1</sup>, S. Lanceros-Mendez<sup>2</sup>, J. H. Correia<sup>1</sup>, P. M. Mendes<sup>1</sup>

<sup>1</sup>Algoritmi, UM, Campus de Azurém, 4800-058 Guimarães, Portugal.

<sup>2</sup>Center/Department of Physics, University of Minho, Braga, Portugal.

**Abstract** — This paper shows the proof of concept for an on-chip antenna using a MEMS structure and an electroactive polymer as detection mechanism. On-chip antennas tend to be very inefficient, which becomes worst when designing electrically small antennas. One solution may be the use of different approaches to receive the electromagnetic fields. The detection using magnetic MEMS sensors is a possible approach. The MEMS sensing structure requires a translation mechanism, where polymeric materials with outstanding electroactive properties, like Poly(vinylidene fluoride) (PVDF), may be a solution.

It is shown that the use of  $\beta$ -PVDF layers makes possible the on-chip reception of low-frequency electromagnetic waves, which may contribute for more efficient wireless (bio)microdevices.

**Keywords :** Antenna, MEMS, magnetic sensor.

## I - Introduction

It is expected a high degree of miniaturization and efficiency for wireless microsystems applied to health monitoring [1]. The integration of efficient small antennas on those microdevices for biomedical applications will be a challenge [2]. The techniques used to build micro-antennas based on standard antenna miniaturization must be replaced by the development of new solutions to work with high efficiency, at relatively low frequencies (within the range kHz - MHz) [3], leading to innovative solutions in the medical field. A proposal to overcome such problems is the antenna integration with the remaining microdevice (fig. 1).

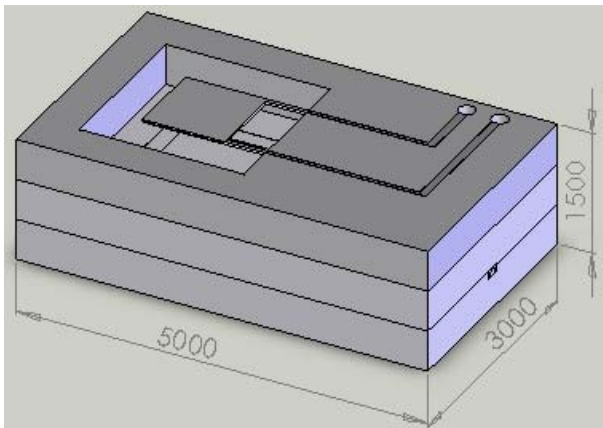


Figure 1: Global artistic view of the wireless biomedical microdevice (All dimensions are in  $\mu\text{m}$ ) [3].

This solution uses wafer level packaging to bond several wafers, where the antenna is placed on the top wafer. This paper will be dealing with a solution to the antenna.

After the work on design, modeling and simulation of the on-chip MEMS antenna [4], it was necessary to fabricate the proposed antenna, measure it, and see how it compares with the developed model.

In this paper, we describe the fabrication of the proposed antenna, which uses the PVDF as a translation mechanism from the mechanical domain to the electric domain. Before obtaining an on-chip antenna, a scaled up model and prototype were obtained to be used for proof of concept. The paper presents the results obtained from the model, the antenna prototype, and the signal obtained with this antenna approach.

## II - Operating principle of the antenna

This antenna operation is based on the Lorentz force that relates the force felt on a current carrying wire, in the presence of a magnetic field. That relation can be written as:

$$\vec{F}_L = (\vec{B} \times \vec{I})L \quad (1)$$

where  $L$  is the length of interaction,  $B$  is the magnetic field and  $I$  is the current [3]. In this work, a cantilever was used as a structure to detect the magnetic field component of an electromagnetic wave.

When the magnetic field acts on the cantilever, which is free to move, it may easily start oscillating when the incoming signal has the same frequency then the cantilever resonant frequency. To extract the information present in the carrier, the oscillation is converted to an electric voltage using the PVDF, an electroactive polymer. Using the PVDF on top of the cantilever, it produces a voltage in response to a deviation, leading to a simple electronic readout and a low operating power.

This type of antenna may become very smaller, since the structure oscillations depend on the dimensions and material properties. This means that higher frequencies require smaller mechanical structures, leading to smaller antennas, as desired.

The piezoelectric polymers are materials with the ability to transform mechanical energy into electrical energy and vice versa. They may be developed from a few nanometers to hundreds of micrometers, making them interesting for many applications in microsystems, as sensors and as actuators. One application is for radio-frequency microdevices, mainly for switching and/or

tuning applications. However, the integration of electroactive polymers in the processing steps of microdevices is still hard to achieve.

#### a) Piezoelectric material (PVDF)

The proposed mechanism of detection is based on a piezoelectric material such as PVDF. In the last decades it has been increasing interest on electroactive polymeric materials technological applications, especially in the electronics engineering domain. Among polymers, Poly(vinylidene fluoride) (PVDF) and (vinylidene fluoride) (VDF) copolymers has remarkable properties leading to electro-optics, electro-mechanical and bio-medical applications. In particular its piezo and pyroelectric properties provide possibilities for many technological applications. The semicrystalline nature of PVDF, combined with the occurrence of at least four crystalline phases ( $\alpha$ ,  $\beta$ ,  $\delta$  and  $\gamma$ ) implies a challenging physical microstructure. The most frequently described and important phase is the  $\beta$  one due to its high piezo and pyro-electric properties, when compared to the other crystalline phases and even compared to other polymeric materials [5].

#### b) Electroactive transduction mechanism

The piezoelectric response is responsible for the sensor and actuator behavior of the polymer. In this sense, larger piezoelectric coefficients will allow larger deformations for a given voltage.

In the thickness mode, piezoelectric actuators increases or decreases its thickness according to the inverse piezoelectric relation:

$$\epsilon_3 = d_{33}E_3, \quad (2)$$

where  $\epsilon_3$  is the strain of the actuator,  $d_{33}$  is the piezoelectric coefficient and  $E_3$  is the applied electric field. In eq. (2) the index 3 of the symbols mean that only the piezoelectric 3 axis is considered. This axis corresponds to the thickness direction of the polymer. For a given application, other piezoelectric coefficients could be more suitable.

The piezoelectric response is determined both by thickness changes and by the variation of the dipole moment of the film at constant thickness [6, 7]. It is proposed that 2/3 of the total piezoelectric response correspond to dimensional variations of the film, whereas the remaining 1/3 is due to the different contributions related to variations of the dipolar moments [7].

Theoretical calculations lead to a value of  $|d_{33}| \sim 25.19 \text{ pC.N}^{-1}$  [8], close to the obtained experimentally for corona poled  $\beta$ -phase PVDF ( $|d_{33}| \cong 28 \text{ pC.N}^{-1}$ ) [9]. The piezoelectric coefficients strongly depends on the processing conditions of the material [10]

### III – Modeling

Based on a previous work [4], a scaled model was

built to predict the behavior of a larger structure. It was necessary to understand if the fields and forces associated to such a scaled model would be in a range that could be easily generated and measured. Fig. 2 shows the options simulated with the model, to understand what would be the best positioning for the MEMS antenna.

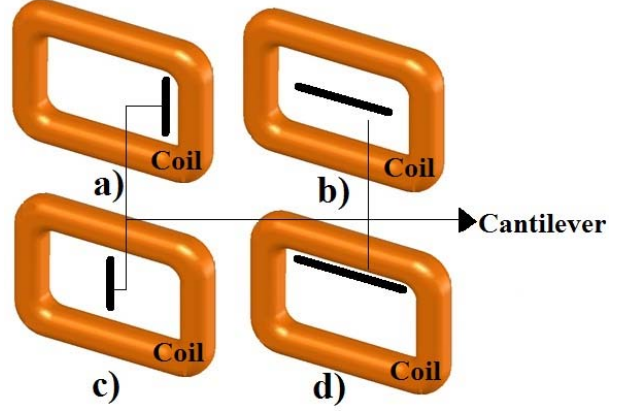


Figure 2: a) Cantilever aligned with the transverse axis parallel to the coil and its smaller segments. b) Cantilever aligned with the longitudinal axis of the reel is parallel to its major segments. c) Cantilever aligned with the transverse axis of the reel. d) Cantilever very close to a larger segment.

The figure shows both the cantilever and the magnetic field generator. A static analysis was used for simulations, and a voltage of 5 V was considered for coil excitation. To obtain the desired magnetic field, the cantilever was placed 2 mm apart from the coil. Table 1 shows a summary for the simulation results.

Table 1: Results for force and displacement, considering different cantilever positions.

Position	$\vec{B}_{total,min}$	$\vec{B}_{total,max}$	$\vec{F}_{mag,max}$	Displacement
a	200 $\mu\text{T}$	119 mT	1.27 $\mu\text{N}$	1,6 mm
b	781 $\mu\text{T}$	139 mT	3.27 $\mu\text{N}$	5 mm
c	618 $\mu\text{T}$	335 mT	3.22 $\mu\text{N}$	4 mm
d	201 $\mu\text{T}$	119 mT	1.27 $\mu\text{N}$	1,6 mm

Results from table indicate position b) as the place for larger force and displacement. The maximum force obtained is precisely when the cantilever is aligned with the longitudinal axis of the coil, leading to a larger displacement. This is the place to use for measurements.

### IV – Antenna Fabrication

The cantilever was obtained by coating a piezoelectric film in both sides using an evaporated aluminum layer, which form the electrodes. The polymeric material is based on the polyvinylidene fluoride (PVDF) polymer in its electroactive ( $\beta$ ) phase. It can be processed in the form of a film by extrusion, injection or from the solution, usually in the non electroactive  $\alpha$

phase. In order to obtain the electroactive  $\beta$  phase, the  $\alpha$  phase films must be submitted to mechanical stretching at temperatures below 100°C and with a reason of stretching (ratio between the final and the initial lengths of the sample) from 4 to 7 [11]. After getting the electroactive  $\beta$  phase, the material must be activated by poling. This is done by subjecting the film to an electric field with amplitude larger than 60 MV/m along the thickness direction.

For the present work, high performance films were used [5]. Unoriented films exclusively in the  $\beta$  phase were obtained from the crystallization of PVDF from solution with N,N-Dimethyl Formamide or Dimethyl Acetamide at temperatures below 70 C. The electromechanical properties of the film were improved by a treatment that consists on pressing, stretching and poling at high temperature. A final step of stretching at a temperature around 80°C results in oriented films, which further increases the material performance. Final film thickness ranged from ~20 to 60  $\mu\text{m}$ .

After that, in order to metalize the PVDF sample, a thin layer of aluminum (Al) (500 nm) was deposited onto both sides of the sample by thermal evaporation. The current was applied in the range of 100-150A at pressures between  $10^{-5}$  to  $10^{-6}$  mbar. The Al layer thickness was obtained by the crystal thickness sensor in gold and thickness controller SyCon STM-100.

Finally, several “U” shapes with different sizes were formed in order to obtain the desired structure. Fig. 3 shows one prototype used for measurements.

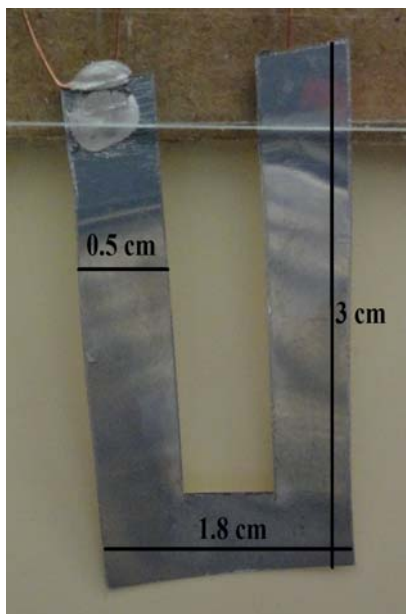


Figure 3: Antenna prototype.

Due to the small thickness of Al layer, the electrical wiring to readout electronics was made using conductive silver ink glue.

### V – Measurements setup

With the antenna structure completed, the readout electronics was connected to the antenna output.

Figure 4 shows the block diagram used. A notch filter tuned to 50 Hz was required since the resonant frequency for the developed structures was in this frequency neighborhood.

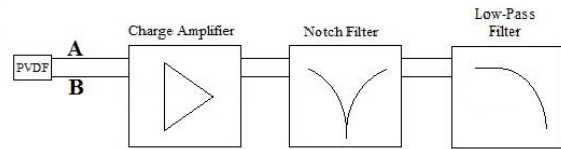


Figure 4: Block diagram to obtain the signal generated by PVDF foil.

It was also required a setup to generate the magnetic field that the MEMS antenna will read. Despite we are trying to develop a device to receive electromagnetic waves, at this point it was enough to generate only the magnetic field that will represent the magnetic component of an electromagnetic wave. Figure 5 shows the setup two main blocks: RF signal source and fabricated receiving antenna.

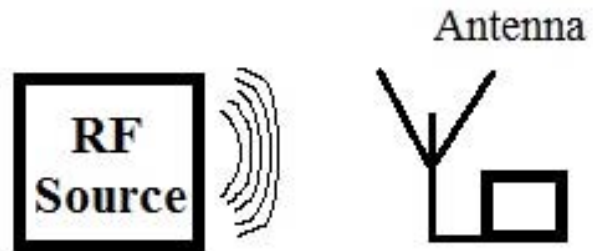


Figure 5: Setup used for measurements.

The RF signal source was obtained from a rectangle coil-shaped, measuring 40x57x8.5 mm<sup>3</sup>. To produce the required magnetic field, the coil has of 200 turns of copper, with 200 micrometers in diameter.

The receiving antenna module was formed by the PVDF antenna connected to the readout electronics. The fabricated and tested PVDF antenna has the dimensions shown in Fig. 3. The cantilever thickness is the result of 110  $\mu\text{m}$  PVDF and 500 nm of Al in both faces. Large dimensions were selected to allow cantilever vibration at low frequencies, so it can be observed with naked eyes.

It is injected in the coil an AC signal, a sinusoid (frequency adjustable) with maximum amplitude of 5V. The frequency of this signal was varied during the experiment until we find the resonant frequency of the cantilever at around 12 Hz. At this frequency the displacement of maximum amplitude of the cantilever was 4 cm.

To move the cantilever, two techniques could be used to have a reacting force to the magnetic field generated by the coil. The first used consists on passing a DC current through the cantilever, and the second uses a permanent magnet placed on the cantilever surface. With the first technique, the cantilever displacements obtained were in the order of  $\mu\text{m}$ , since the current



allowed was very small, due to the thin layer of aluminum. With the second technique, the displacements obtained were in the order of mm. Since it is easier to read, the second technique was chosen for testing for proof of concept.

Figure 6 shows the final setup used for measurements.

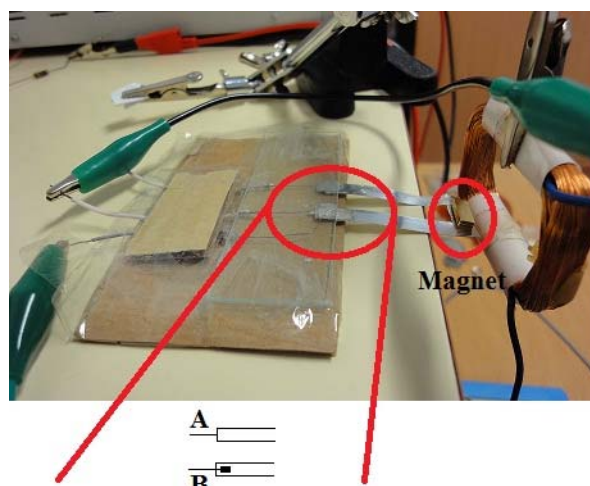


Figure 6: *Experimental setup.*

In the previous figure, magnet position and output leads from the antenna are highlighted.

## V – Results and Discussion

Figure 7 shows the measured results, when a sinusoid with 12 Hz was applied to the source coil.

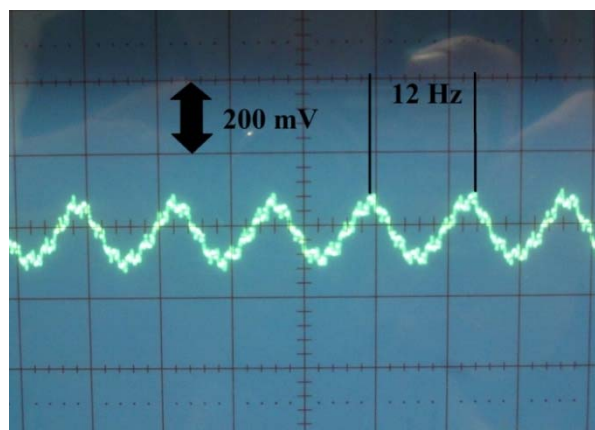


Figure 7: *Signal obtained from the vibrating cantilever, after amplification and filtering.*

The antenna signal that was generated by the deformation of the piezoelectric material was easily amplified up to 200 mV peak to peak. The frequency of this signal is 12 Hz, the structure resonating frequency. That signal was only present when the coil was turned on and for frequencies where the structure was oscillating. That allows to safely concluding this is a viable solution for receiving magnetic fields.

The present results were obtained with the cantilever very close to the source coil, and the received signal

drops very fast when the receiving cantilever moves away from the coil. However, it is not a problem of the receiving antenna. The problem is that the magnetic field also drops because it is not a radiated field. It is expected that for a radiated field, this solution will also work, and will operate in the antenna far field.

It was also possible to verify that the experimental results for displacement agreed with the results obtained from simulations. The values were in the same range of magnitude. Some differences appear to be from the many variables that are difficult to control for the mechanical setup.

## VI – Conclusions

This paper presents a new solution for a small receiving antenna, with increased efficiency. It was possible to demonstrate the operation of a low-frequency telemetric link. It was possible to test the MEMS antenna deformation translation to a voltage.

Next step will be to use the obtained models to design a new antenna for fabrication using the standard microfabrication technologies.

## Acknowledgments

This work is sponsored by POCTI and FEDER, by FCT (PTDC/EEA-TEL/65286/2006), PTDC/CTM/69316/2006 and NANO/NMed-D/0156/2007 projects.

## References

- [1] G. Broek, F. Cavallo, L. Odetti, C. Wehrmann, VDI/VDE-IT, AALIANCE Office, 2009.
- [2] L. A. Rocha, P. M. Mendes, European Microwave Conference 2008, Amsterdam, Netherlands, October 2008, pp. 262-265.
- [3] P. M. Mendes, L. A. Rocha, Biodevices 2008, Funchal, Portugal, January 2008, pp. 202-205.
- [4] F. J. O. Rodrigues, J. H. Correia and P. M. Mendes, MicroMechanics Europe 2009, September 20-22, 2009, Toulouse, France.
- [5] V. Sencadas, R. Gregorio Filho and S. Lanceros-Mendez, J. of Macromolecular Science part B-Physics 48 (3), 514-525 (2009)
- [6] M.G. Broadhurst, G.T. Davis, J.E. McKinney and R.E. Collins, J. Appl. Phys. 49, 4992 (1978).
- [7] M.G. Broadhurst, G.T. Davis, Ferroelectrics, 60, 3 (1984).
- [8] K. Tashiro, M. Kobayashi, H. Tadokoro and E. Fukada, Macromolecules 13, 691 (2002).
- [9] Y. Jiang, Y. Ye, J. Yu, Zh. Wu, W. Li, J. Xu and G. Xie, Polymer Engineering & Science 47, 1344 (2007).
- [10] J. Gomes, J. Serrado Nunes, V. Sencadas and S. Lanceros-Mendez, Smart Mater. Struct. 19 (2010) 065010 (7pp)
- [11] V. Sencadas, R. Gregorio Jr., S. Lanceros-Méndez, Journal of Macromolecular Science, Part B: Physics, 48:514–525, 2009



# FABRICATION OF INTEGRATED BIMORPHS WITH SELF ALIGNED TIPS FOR OPTICAL SWITCHING IN 2-D PHOTONIC CRYSTAL WAVEGUIDES

S.M. Chakkalakal Abdulla<sup>1</sup>, L.J. Kauppinen<sup>2</sup>, M. Dijkstra<sup>2</sup>, M.J. de Boer<sup>1</sup>, E. Berenschot<sup>1</sup>, R.M. de Ridder<sup>2</sup> and G.J.M. Krijnen<sup>1</sup>

<sup>1</sup>Transducers Science and Technology and <sup>2</sup>Integrated Optical Microsystems Groups, MESA+ Research Institute, University of Twente, P.O. Box 217, 7500 AE Enschede, The Netherlands

**Abstract** —This paper presents the fabrication technology for a novel class of photonic devices. This technology integrates silicon 2-D photonic crystal (PhC) waveguides and electrostatically actuated bimorph cantilevers with tips that are self-aligned relative to the holes of the PhC. The bimorph cantilevers modulate the propagation properties of the slab PhC depending on the proximity of the tips to the holes. The integrated devices have been successfully fabricated on wafer scale by surface micromachining techniques. First experiments with these devices have shown 80% throughput modulation using a square wave drive signal of 0 to 8 V at 1 kHz.

**Keywords** : bimorph, opto-mechanical modulation, photonic crystal waveguide, self aligned tips.

## I- Introduction

Photonic crystals are periodic dielectric materials having a photonic band gap; a frequency range for which the light propagation is prohibited [1]. A row of missing holes in the PhC constitutes an optical waveguide, with the possibility to create sharp bends with low optical loss. Having a dynamic control on the PhC waveguide characteristics allows for the realization of modulated optical devices such as switches, attenuators and tunable filters which can form the miniaturized photonic components for integrated optical circuits. Propagation properties of a photonic crystal waveguide (PhC-WG) can be controlled by a variety of methods such as with electro-optics, liquid crystals, charge injection or by perturbation with an AFM tip [2]. Modulation by an integrated micro electrostatic actuator has advantages such as compactness of the device, ease of integration, designable switching speed (trade-off between switching voltage and switching speed) and near zero dissipation in the stationary state [3].

Silicon on Insulator (SOI) based air bridge PhCs have two distinct properties: a high index contrast which enables strong out of plane confinement and a symmetric cladding which promotes symmetry of the TE like and TM like slab modes. Also the air light line is higher than the silica light line, which increases the operating bandwidth of the device. However its geometry makes it difficult for monolithic integration with mechanical or electrical structures. In this paper we describe the fabrication technology for a novel class of devices where electrostatically actuated bimorph cantilevers are monolithically integrated with SOI based 2-D air bridge PhC-WG, on wafer scale, using surface micromachining

techniques. The bimorph cantilevers, equipped with tips, can change the propagation properties of the PhC slab depending on the proximity to the holes. Since in high optical index contrast structures the exponentially decaying evanescent fields extend typically only a few hundred nanometers into the air cladding the required cantilever strokes for switching can be accordingly small. This implies that for fast actuation stiff cantilevers with resonance frequencies in the MHz range can be used. The integrated bimorph discussed here consists of an upper layer, which acts as the electrode and a lower layer that acts as a dielectric. The thermal mismatch between the layers and the deposition-induced stresses make it bend upward in the off-state [4]. The bimorph is actuated by application of a voltage between the upper electrode and the substrate. For the proof of concept, optical modulation of the integrated device is demonstrated.

## II- Design

Figure 1 (A) shows the schematic illustration of the top view of the integrated device and (B) the cross-sectional view of the device in Y-direction. PhC-WGs and their access waveguides are fabricated on SOITEC SOI wafers by the silicon photonics platform ePIXfab [5], established at IMEC, Leuven. The thickness of the silicon device layer is 220 nm and that of the handle wafer is 700  $\mu\text{m}$ . Before integration, the lower cladding is a 2  $\mu\text{m}$  thick thermal oxide (refractive index  $n = 1.45$ ) and the upper and side claddings are air ( $n = 1.0$ ). After the integration lower and upper claddings are air.

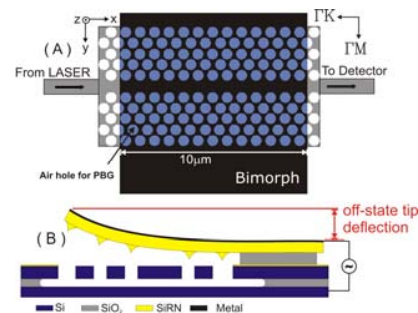


Figure 1: Schematic illustration of the integrated device (A) top view (B) cross-sectional view in the Y-direction.

The PhC-WG, designed to operate in the C-band (1530 – 1565 nm) of the telecommunication wavelengths, has a hole diameter of 270 nm and a periodicity of 440 nm. The waveguide in the PhC is formed by a

line defect caused by removing a single row in the  $\Gamma$ K direction.

### III- Fabrication

Figure 2 shows the fabrication flow for the integrated device. (a) PhC-WGs, are fabricated on an 8 inch SOI wafer by a 193 nm deep-UV lithography process at ePIXfab. This wafer is first diced into four pieces to fit into the 4 inch wafer systems of the MESA<sup>+</sup> clean room. (b) On top of these wafers, first a 43 (standard deviation expressed in  $3\sigma = 2.11$ ) nm thick LPCVD [6] Silicon Rich Nitride (SiRN) layer ( $n = 2.202$ ) is deposited which acts as a protective layer for the access waveguides during sacrificial layer etching (SLE). (c) This layer is etched from the backside of the wafer by reactive ion etching to later have access to the lower silicon electrode. In order to fabricate tips and to reduce losses during optical transmission, the protective nitride has to be removed from the PhC area of the wafer. For this reason, (d) a 93 ( $3\sigma = 1.00$ ) nm thick TEOS (tetra-ethyl-ortho-silicate) layer is deposited as an etch mask layer and (e) a dark mask (Etch mask) is used to define the etch windows in the PhC area. After the lithography, the wafer is first ozone treated to make the TEOS layer hydrophilic and then chemically etched in BHF (1:7) to remove the TEOS from the etch windows. (f) After stripping the photoresist, the protective nitride is removed from the etch window by 85%  $\text{H}_3\text{PO}_4$  at 180°C. The measured selectivity as found from the etch-rates was SiRN : TEOS = 1.83:1. The thickness of the remaining TEOS layer is 49 nm.

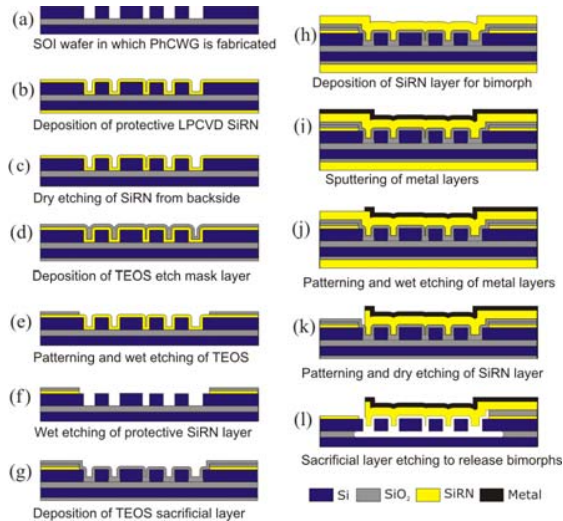


Figure 2: 2-D Fabrication flow

(g) Following this, the SOI wafers are first coated conformally by a 105 ( $3\sigma = 1.48$ ) nm thick TEOS sacrificial layer (SL) and then (h) by a 1061 ( $3\sigma = 41.75$ ) nm thick SiRN layer ( $n = 2.18$ ). (i) A 50-nm thick gold (Au) is chosen as the upper electrode layer. A thin layer of chromium (Cr) is used as an adhesive layer for gold where the thickness of Cr layer is selected to be as low as possible, to reduce the stress in the electrode

layer. The measured total thickness of the electrode layer (Au + Cr) by Dektak-V.8 surface profiler is 62.93 nm.

After the pattern transfer from the masks, (j) Cr and Au layers are etched by wet chemical methods and (k) the SiRN bimorph layer by reactive ion etching. Finally, (l) SLE is done by BHF (1:7) followed by freeze release technology [6]. During SLE the lower cladding of the PhC is also etched through the PhC holes and through the sides of the PhC. This transforms the PhC into a symmetric air bridge membrane, having a larger transmission window. Timed SLE also defines the anchor point for the bond pads which are designed to be  $300\text{ }\mu\text{m} \times 300\text{ }\mu\text{m}$ . We have fabricated bimorphs with lengths varying from  $40\text{ }\mu\text{m}$  to  $100\text{ }\mu\text{m}$  at a fixed width of  $10\text{ }\mu\text{m}$  for all cases.

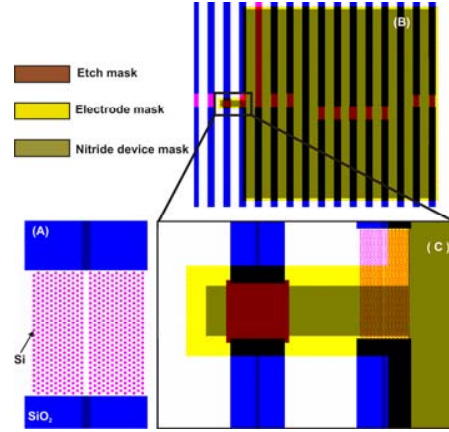


Figure 3: Devices as drawn in the mask: (A) PhC-WG, (B) Bimorph with its bond pad on top of the PhC-WG and (C) zoomed view of the integrated device.

The fabrication is a three-mask process where all the masks use positive photo resist for the UV lithography. The first mask is used to open the SiRN on the PhC-WG areas. The second mask is used for patterning the metal layers and the third mask is used for patterning the SiRN bimorph device layer. Figure 3 shows the different masks drawn for integrating the bimorph cantilevers with the PhC-WGs. Figures 4-7 show HRSEM images of the integrated device.

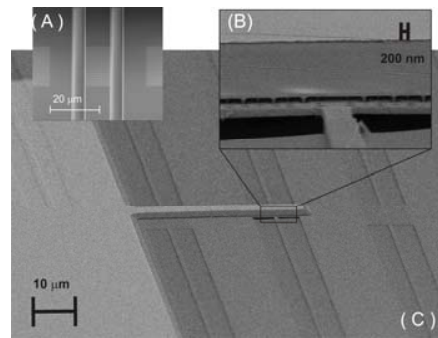


Figure 4: SEM images of (A) grating couplers at the end of the access waveguides, (B) tips self aligned with respect to the holes of the PhCWG and (C) an integrated device.

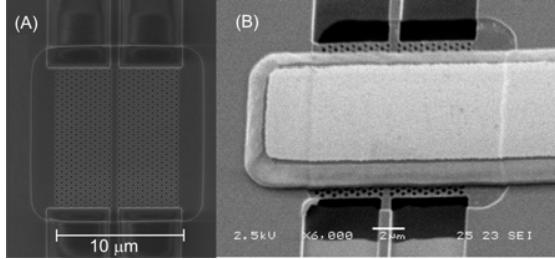


Figure 5: (A) Top view of a PhC-WG after the protective nitride has been removed from the PhC area and (B) oblique view of the final integrated device.

#### IV- Discussions on fabrication

One of the important steps to monitor was to check whether the protective nitride is completely removed from the PhC holes. In order to analyze this, the bimorph is removed from one of the integrated devices. Figure 6(A) shows this device where part of the PhC-WG membrane is broken apart. The top view shows partially etched lower cladding layer and the inset shows SiRN rings at the bottom of the PhC holes.

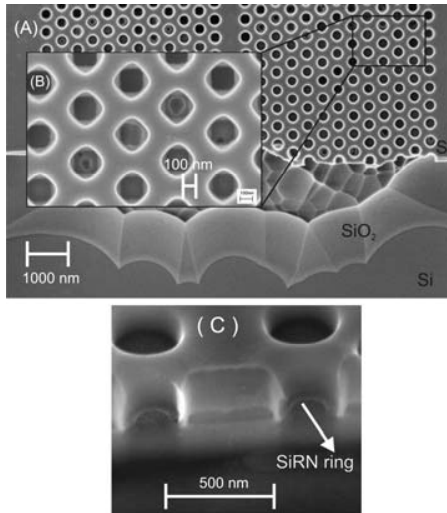


Figure 6: SEM pictures of (A) Top view of PhC holes after freeze drying (B) SiRN rings inside the holes (C) Cross-sectional view after FIB milling.

For a further investigation on the shape of the SiRN rings, we have milled PhC holes with focused ion beam (FIB) as shown in figure 6C. After milling, they were etched for 2 min using 1% HF to make the rings partially release. In order to compare the optical loss introduced by the SiRN rings we have compared the transmission of light through a planar waveguide and the PhC-WG. The losses in both waveguides are approximately the same indicating that the SiRN rings inside the holes do not introduce large optical losses.

From figure 6C, it is clear that the side walls of the PhC holes are not exactly at right angles but at an obtuse angle ( $< 10$  degree). This geometry together with the conformal deposition makes the tips to be in conical shape. The depths of the tips are directly related to the

thickness of the sacrificial TEOS layer. By increasing the thickness of SL greater than 135 nm (half of PhC hole diameter), PhC holes will be completely filled which later results in a flat bimorph having no tips. Hence for fabricating tips, thickness of SL should be less than 135 nm. Decreasing SL thickness further increases the diameter of the tips. Figure 7 shows the fabricated tips self aligned relative to the PhC holes. During SEM imaging bimorph advances close to the PhC-WG due to charging of the SiRN layer.

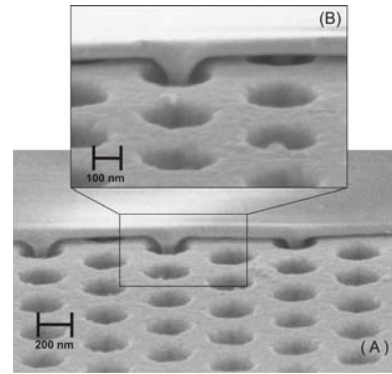


Figure 7: Cross sectional of the self aligned tips.

Another critical step during the fabrication is the selective etch of a thick ( $\approx 1 \mu\text{m}$ ) SiRN layer from a thin ( $\approx 100$  nm) TEOS layer. Non-uniformity in both the layers makes the situation complex and, hence, the uniformity in the deposited TEOS and the SiRN layers are very important to be monitored. The selectivity between SiRN and TEOS layers by reactive ion etching at  $10^\circ\text{C}$ , with 10 mTorr pressure, using  $\text{CHF}_3/\text{O}_2$  gas mixture is  $\text{SiRN} : \text{TEOS} = 1.5:1$ . By carefully checking the thickness and uniformity of both the layers with dummy wafers and by analyzing the loading effect, we could successfully etch  $1 \mu\text{m}$  SiRN layer with a 30 nm over etch into the SL.

Undesired etching of the silicon device layer by BHF with light during SLE was also critical. In order to avoid this, SLE was done in a dark environment.

The actual length of the fabricated bimorph is increased from the design length due to the undercut at the anchor points during SLE. The measured undercut by the optical microscope is  $5.5 \mu\text{m}$ . In general this undercut will present itself as an increase of the effective bimorph length with associated lower resonance frequency and pull-in voltage [4].

Removing the protective SiRN from the PhC area leaves the conformal deposition of bimorph layer with a step (figure 5B). Due to this and by the upward deflection of the bimorph, the gap between the bimorph and the PhC-WG is varying along the length of the beam. The gap near the base of the bimorph is the combined thickness of the protective nitride layer, the remaining TEOS etch mask layer and the sacrificial TEOS layer. But the gap on top of the PhC-WG is only due to the thickness of the sacrificial layer and by the upward deflection of the beam.



## V- Optical measurements

The optical modulation of an integrated device is measured using a set up as shown in figure 8. Infrared light (1530 nm) from a tunable laser of 1 mW output power is coupled to the input access waveguide with the help of a cleaved fiber end and grating coupler (figure 4-A), through a polarization maintaining fiber (PMF). Output light is recoupled from an output grating by another cleaved fiber and is sent to the photodetector through a single mode fiber (SMF).

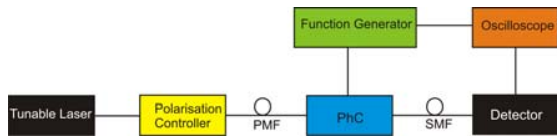


Figure 8: Schematic representation of the optical modulation experimental set up.

We have observed ON-OFF switching of the integrated device by applying a square wave drive signal of 0 to 8 V at 1 kHz (figure 9). The time constant for the signal rise time is 85  $\mu$ s and that for the fall time is 95  $\mu$ s. The time response of the bimorph is also measured by a Laser Doppler Vibrometer (Polytec MSA400). Figure 10 shows both the rise and fall time to be about 2  $\mu$ s. Further investigations have shown that the increased time delay in the optical modulation measurement is caused by the slow response introduced by the photo-detector.

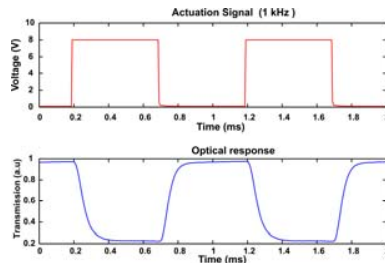


Figure 9: Optical modulation at 1 kHz with a square wave drive signal of 0-8 V.

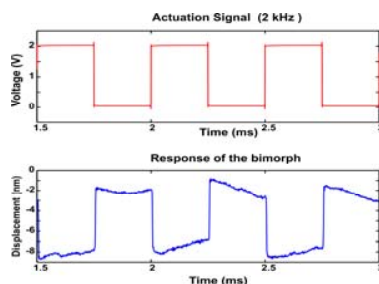


Figure 10: Time response of the bimorph at 2 kHz with a square wave drive signal of 0-2 V measured by a Laser Doppler Vibrometer.

## VI- Conclusion

We have reported a fabrication process that enables the forming of electrostatically driven bimorph cantilevers with sharp tips that are self-aligned with respect to

photonic crystal slab-waveguides (2D photonic crystal). This CMOS compatible wafer-scale technology allows for the fabrication of a new class of devices exploiting modulation of the (exceptional) waveguiding properties of PhC-WGs by changing the proximity of the tips to (and into) the holes of the PhC. As an example a MEMS integrated PhC-WG modulator has been fabricated. Optical modulation of the device at 1 kHz with a square wave drive signal of 0-8 V has been demonstrated.

## Acknowledgements

The authors would like to acknowledge their colleagues in the NanoPhotonics project NOEMS for their stimulating discussions and input to this work. This project is funded by the NanoNED programme of the Dutch Ministry of Economic Affairs.

## References

1. Yablonovitch E. "Inhibited spontaneous emission in solid-state physics and electronics" (1987) Physical Review Letters, 58 (20), pp. 2059-2062
2. Iwamoto S., et al. "Observation of micromechanically controlled tuning of photonic crystal line-defect waveguide" (2006), Applied Physics Letters, 88 (1), pp.0111041-3
3. Hopman, W.C.L, "Light-Flow Characterization and Manipulation in 1 and 2 Dimensional Photonic Crystals" (2007), PhD thesis, University of Twente.
4. Chakkalakkal Abdulla.S.M, et al. "Optimisation study of micro cantilevers for switching of photonic band gap crystals", In Proceedings of the International Conference on Photonics in Switching (2009), Pisa, Italy. pp. 1-2.
5. ePIXfab. Available: <http://www.epixfab.eu/>
6. Gardeniers J.G.E, et al., "LPCVD silicon-rich silicon nitride films for applications in micromechanics, studied with statistical experimental design", (1996) Journal of Vacuum Science and Technology A, Vacuum, Surfaces and Films, vol. 14, pp. 2879-2892.



# HIGH-THROUGHPUT ON-CHIP DNA FRAGMENTATION

L. Shui, M. Jin, J.G. Bomer, Edwin T. Carlen, and A. van den Berg

*BIOS/Lab-on-Chip Group, MESA+ Institute for Nanotechnology, University of Twente, The Netherlands*

**Abstract** — In this paper we report a high throughput clog-free microfluidic deoxyribonucleic acid (DNA) fragmentation chip that is based on hydrodynamic shearing. Genomic DNA has been reproducibly fragmented with 2-10 kbp fragment lengths by applying hydraulic pressure  $\Delta P$  across micromachined constrictions in the microfluidic channels. The utilization of a series of constrictions reduces the variance of the fragmented DNA length distribution; and parallel microfluidic channels design eliminates the device clogging.

**Keywords:** Microfluidics, DNA fragmentation, Hydrodynamic shearing

## I - Introduction

Sample pre-treatment is one of the most important steps in applying lab-on-a-chip (LOC) technology to real world applications. DNA fragmentation is a sample pretreatment step for nucleic acid analysis, which is important for rapid hybridization reaction kinetics and the production of genomic DNA libraries and is often a critical and sometimes rate-limiting step in the DNA sequencing pipeline.

Four methods are commonly used for genomic DNA fragmentation including enzymatic digestion, sonication, nebulization and hydrodynamic shearing [1-10]. Although all of these methods are currently used for DNA fragment generation, each has advantages (+) and disadvantages (-), which are listed in Table 1.

Table 1: Various DNA fragmentation methods with advantages (+) and disadvantages (-).

Method	+	-
Restriction enzyme	Fragmentation in specific location	Denaturation; Fragment bias; Fragmentation non-uniformity
Nebulization	Cheap and fast	Large volumes; Concentrated NA; Difficult LOC integration
Sonication	Fast and simple	Not size specific; NA damage; Difficult LOC integration
Mechanical shearing	Size specific; Narrow size range; Low NA damage (compared to other methods); Amenable to LOC integration	Slow loading in conventional apparatus; conventional systems easily clog

Enzyme digestion can lead to fragment bias and induces a relatively large number of single-chain breaks as

opposed to double-chain scissions. Sonication can result in damage to the fragmented DNA and is difficult to integrate into a LOC platform. Nebulization typically results in a large fragment length distribution and is also not amenable for LOC integration. Fragmentation based on hydrodynamic shearing is reported to be one of the most robust techniques for the generation of small fragment length and low sheared length variation [10, 11], and the fragments result from double-chain scission [12]. However, conventional single orifice hydrodynamic shearing systems are expensive and are prone to clogging.

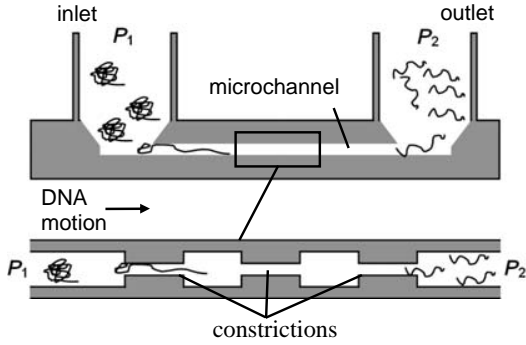
The hydrodynamic shearing method is widely used for shearing genomic DNA [8,10]. The DNA molecules are fragmented by hydrodynamic shear stress when they are forced through a small orifice at high speed. Genomic DNA can be efficiently sheared with high quality fragments [8,10]. The length of the fragments is determined by the flow speed of the sample solution and the diameter of the orifice and has been reported to be independent of the initial DNA length, concentration, and salt concentration of the fragmentation buffer [10]. Although DNA fragmentation instruments based on shearing forces are commercially available [13], they require high pressures, complex interconnections, and are prone to clogging. Implementation of DNA fragmentation in a LOC platform has several advantages: small sample requirements (at least 10× reduction), low dead volume, generating high shear rates at comparatively low flow rates.

In this paper, we present a low cost LOC platform for genomic DNA fragmentation based on the hydrodynamic shearing. The LOC consists of inlet and outlet ports that connect a microfluidic channel with a precisely defined series of constrictions located at the center of the microchannel. Genomic DNA samples are introduced to the inlet port and transported through the constrictions with hydraulic pressure. Assuming a constant volumetric flow rate, as the DNA approaches the constriction, the flow speed increases due to the reduced cross-sectional area of the constriction. Drag forces stretch the DNA molecule until it fragments. The clogging problem has been eliminated by introducing many identical constrictions in parallel, which increases the fragment generation rate without affecting the quality or length of the fragments.

## II - Experimental Details

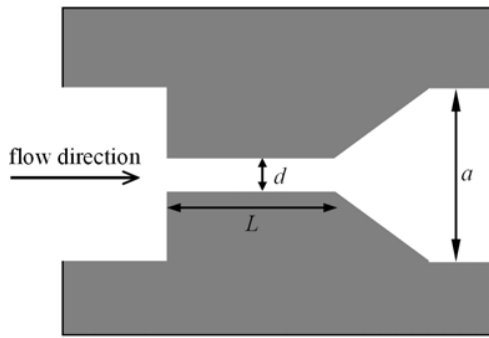
Figure 1 depicts the concept of hydrodynamic shearing-based DNA fragmentation in a microfluidic channel. Long DNA molecules are introduced into left side of the channel (inlet with pressure  $P_1$ ) and transported through the microchannel with a hydraulic pressure

difference ( $\Delta P = P_1 - P_2$ ). As the DNA approaches the constriction, the flow speed increases and the coiled DNA molecules are elongated and then fragmented by drag forces when the DNA is located in the constrictions. The series of constrictions are used to reduce the



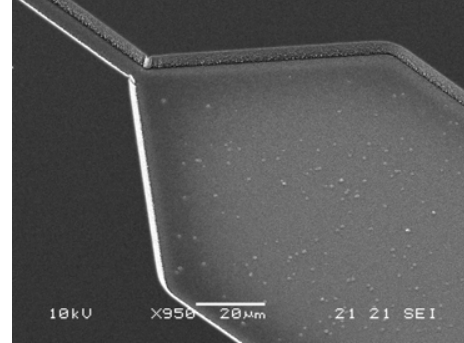
**Figure 1:** Schematic drawing of DNA fragmentation device using hydrodynamic shearing forces.  $\Delta P = P_1 - P_2$ .

variance in the fragment length distribution. Figure 2 shows a top-view of a single constriction with length  $L$  and width  $d$ , and main channel width  $a$ . The angled constriction design reduces bubble entry into the fragmentation stream [11].



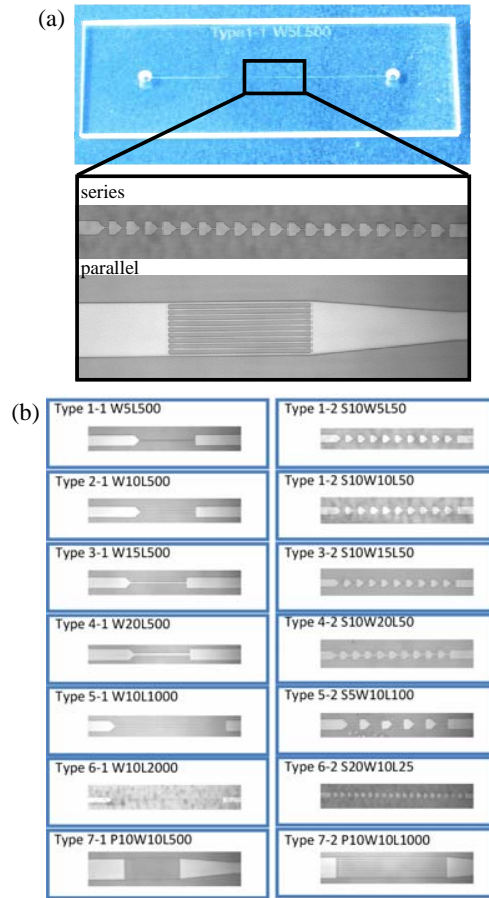
**Figure 2:** Top-view schematic drawing of fragmentation constriction with length  $L$  and width  $d$ .

Two types of device structures have been designed and fabricated: series constrictions and parallel channels. The fragmentation devices are fabricated entirely from glass (Borofloat) substrates. A single lithography mask is used to define the planar channel and constriction structures and etched in the glass substrate using reactive ion etching (Adixen AMS100DE). A second glass capping substrate is then patterned and the inlet and outlet through-wafer holes are created using powder-blasting with 10  $\mu\text{m}$  diameter alumina particles. The glass wafers are then thermally bonded and subsequently diced into  $1 \times 3 \text{ cm}^2$  size chips. Figure 3 shows a scanning electron microscopy (SEM) image of a constriction region. The depth of the channels is 5  $\mu\text{m}$ .



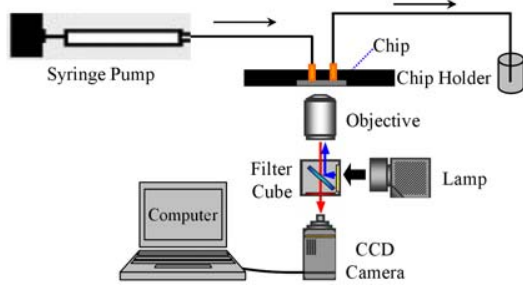
**Figure 3:** SEM image of a fragmentation constriction region.

Figure 4a shows optical microscopy images of completed glass microfluidic chips used for DNA fragmentation. The lower image shows an example a single fragmentation channel with multiple constrictions and multiple channels with constrictions. Figure 4b shows an example of various fragmentation chip designs.



**Figure 4:** (a) Top: A Borofloat glass fragmentation chip ( $1 \times 3 \text{ cm}^2$ ). Bottom: series and parallel fragmentation channels. (b) Fragmentation chips with varying constriction dimensions.

The fragmentation chip was clamped into a custom-made chip-holder and connected to a gas-tight syringe (Hamilton) driven by a syringe pump (Harvard PHD2000) [14]. Sheared DNA samples were collected into a transparent cuvette. A schematic drawing of the DNA fragmentation setup is shown in Figure 5. The samples were then separated and analyzed using a chip-based automated gel electrophoresis system (Experion, Bio-Rad). The fluid flow rate and constriction size determines the final DNA fragment sizes. Passing the DNA through the serial constrictions reduces the variability of the fragmented length and the parallel constriction design prevents clogging.



**Figure 5:** Schematic setup for DNA fragmentation.

### III - Results and Discussion

#### A. Effect of constriction channel structure

Microchannel clogging is a common problem for microfluidic devices. A device with a series of constrictions has been expected to reduce the fragmented DNA size distribution and parallel channels to eliminate clogging [11,15]. In order to study the effect of the constriction channel structure on clogging, we have designed two types: series and parallel channels, as shown in Figure 4a. We have tested the chips with single and serial constriction channels with different channel size and number as show in Figure 4b. All constrictions with single or several serial channels had clogging problems during the experiments. When any constriction in the series channel was clogged, fluid is not able to pass through the channel and experiments had to be terminated.

The parallel constriction channels eliminate the clogging problem (Figure 4a). When a dust particle of organic debris enters the main channel into the constrictions then a single constriction can be clogged, however, fluid could still pass through the unclogged constriction channels to the outlet. In this case it is important to have a large number of parallel constriction channels so that one or two clogged channels does not result in a large change in the pressure drop  $\Delta P$  across the chip. The chip with parallel channel constriction can be used repeatedly without obvious change in performance, which makes this type of chip very important for reliable fragmentation performance. Therefore, the experi-

mental results from the parallel constriction channel design are presented in this paper.

#### B. Effect of fluid flow rates (pressure)

The effect of fluid flow rates has been studied by varying the applied fluid flow rates in the same microfluidic device. A syringe pump was used to pump fluids through the chip. The chip was first flushed by DI water (dH<sub>2</sub>O) for 15 minutes. The DNA sample (50 kbp genomic DNA, 40 ng/μL in dH<sub>2</sub>O) was then pumped through the chip and collected in a transparent cuvette. The DNA sample was then transferred and analyzed using the Experion 12K DNA analysis system. Figure 6 shows representative electropherograms of DNA samples sheared at different flow rates. It indicates a clear shift towards smaller fragment sizes as flow rate is increased.

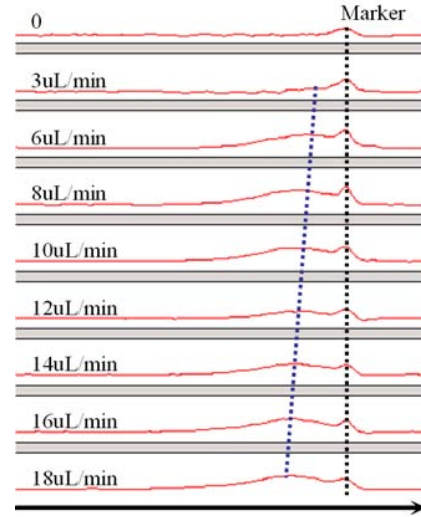


**Figure 6:** Electropherograms of sheared DNA samples at different flow rates. The fragment size decreases with increasing flow rate. The constriction channel depth, width and length are 3.8, 10 and 1000 μm, respectively. The results shown in Figure 7 were obtained using the same device.

In Figure 7, we summarize experimental results of DNA fragment sizes varying with applied pressure using a chip with parallel constrictions (10 parallel constriction channels, channel depth, width and length are  $h=3.8$  μm,  $d=10$  μm and  $L=1000$  μm, respectively) at room temperature. Here, we use pressure instead of fluid flow rates to eliminate the effect of channel dimensions and directly show the pressure requirement for experimental performance. The pressure difference between a microfluidic channel inlet and outlet is calculated using the Hagen-Poiseuille equation:

$$\Delta P = \frac{C\eta LQ}{d^4},$$

where  $C$  is a geometrical constant,  $\eta$  is the fluid dynamic viscosity (Pa s);  $L$  is the channel length (m),  $Q$  is the volumetric sample flow rate ( $\text{m}^3/\text{s}$ ), and  $d$  is the characteristic dimension of the microfluidic device (m). The average fragment length was calculated by dividing the sum of the raw intensity values by the sum of the relative population values. The relative population of each fragment length was calculated by dividing the raw intensity values with their corresponding base pair number.

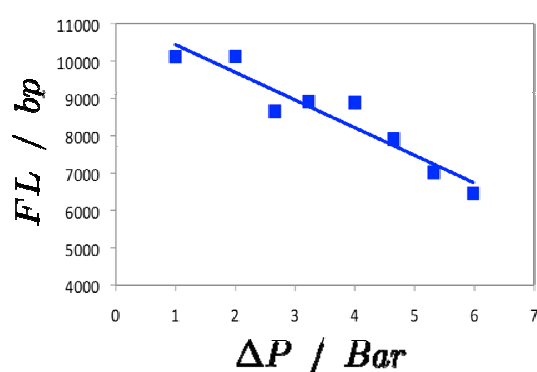


**Figure 7:** DNA fragment length (FL) as a function of  $\Delta P$  at room temperature. The pressure difference along fragmentation channels is calculated using Hagen-Poiseuille equation.

As seen in Figure 7, the fragmented DNA length decreases as the pressure is increased. The DNA sample can be fragmented to 10 kbp-6 kbp in a pressure range of 1-7 Bar using the current device, thus demonstrating that this method is useful for integration with other steps for on-chip sample pre-treatment (e.g. DNA extraction) or post-treatment (e.g. DNA separation and hybridization).

### Acknowledgement

The authors gratefully acknowledge the Framework 7 European Union project TheraEDGE for financial support.

### References

- [1] P. N. Hengen, *Trends in Biochemical Sciences*, 22(7), 273-274, 1997.
- [2] S. Anderson, *Nucleic Acids Research*, 9, 3015-3027, 1981.
- [3] P. M. Slocombe, *Heredity*, 36(Apr), 289-289, 1976.
- [4] P.L. Deininger, *Analytical Biochemistry*, 135, 247-263, 1983.
- [5] B. M. Dancis, *Biophysical Journal*, 24(2), 489-503, 1978.
- [6] C. M. Okpodu, D. Robertson, W. F. Boss, R. K. Togasaki, and S.J. Surzycki, *BioTechniques*, 16, 154-159, 1994.
- [7] M. L. Wu, S. S. Freitas, G. A. Monteiro, D. M. F.

Prazeres and J. A. L. Santos, *Biotechnology and Applied Biochemistry*, 53, 237-246, 2009.

- [8] P.J. Oefner, S.P. Hunicke-Smith, L. Chiang, F. Dietrich, J. Mulligan, and R.W. Davis. *Nucleic Acids Research*, 24, 3879-3886, 1996.
- [9] Y. K. Lentz, L. R. Worden, T. J. Anchordoquy and C. S. Lengsfeld, *Journal of Aerosol Science*, 36(8), 973-990, 2005.
- [10] Y. R. Thorstenson, S. P. Hunicke-Smith, P. J. Oefner and R. W. Davis, *Genome Research*, 8(8), 848-855, 1998.
- [11] J. Lichtenberg, L. Ceriotti, N. A. Lacher, S. M. Lunte, N. F. D. Rooij, and E. Verpoorte. in *mTAS2003*, Squaw Valley, California USA, 172-174, 2003.
- [12] L. F. Cavalieri and B. H. Rosenberg, *Journal of the American Chemical Society*, 81(19), 5136-5139, 1959.
- [13] P. F. Davison, *Proceedings of the National Academy of Sciences of the United States of America*, 45(11), 1560-1568, 1959.
- [14] L. L. Shui, F. Mugele, A. van den Berg and J. C. T. Eijkel, *Applied Physics Letters*, 93(15), 153113, 2008.
- [15] A. Joneja and X. H. Huang, *Biotechniques*, 46(7), 553-556, 2009.



# PERFORMANCE METRICS FOR MEMS TUNABLE CAPACITORS

Martin Hill<sup>1</sup>, Yamuna Kubarappa<sup>1</sup> and Conor O'Mahony<sup>2</sup>

<sup>1</sup>*Adaptive Wireless Systems Group, Cork Institute of Technology, Bishopstown, Cork, Ireland*

<sup>2</sup>*Tyndall National Institute, University College Cork, Ireland*

**Abstract** - The application of Microelectromechanical (MEMS) components for RF applications has generated significant interest and research effort over recent years. The promise of MEMS tunable capacitors with higher quality factors, tuning ranges and linearity for lower cost and size has seen many device configurations demonstrated but none has reached the mass market. Some significant hurdles remain for market adoption and comparison of existing varactor components with emerging MEMS or ferroelectric alternatives for RF designers is still a major problem. In addition to performance metrics common to all device types some additional considerations are required when assessing MEMS technologies. This paper presents two common designs of MEMS tunable capacitors and outlines specific performance metrics which can be used to compare them. The metrics cover the key areas of power handling and device stability for a typical impedance matching application.

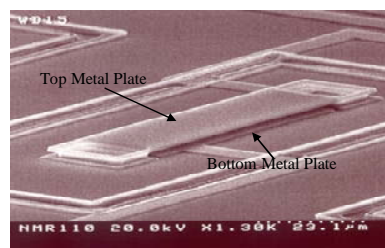
**Keywords :** MEMS, tunable capacitor, power handling, stability.

## I – Introduction

MicroElectroMechanical Systems (MEMS) is rapidly emerging as an enabling technology to yield a new generation of high performance components in wireless communication sub-systems. Among the most promising of these devices are tunable capacitors. These devices can deliver superior RF performance to existing technologies including wider tuning range, higher quality factor and reduced non-linearity [1-2]. However, to realize these benefits device designers must avoid the mechanical pull-in instability observed in electrostatic MEMS devices without compromising increasing device cost or complexity. In this paper the performance of MEMS tunable capacitors is examined and a number of key criteria for comparison of different designs are presented. These criteria are applied to the comparison of two capacitor designs with reference to simulated and measured device performance.

MEMS tunable capacitors are micron scale devices in which the capacitance between two metallic plates is adjusted by moving a mechanical component to alter the separation between the plates. The devices can be fabricated using IC compatible surface micromachining techniques suitable for integration with other passive and/or active elements. A simple fixed-fixed beam structure showing the fixed bottom electrode and movable top electrode is shown in Figure 1.

Figure 1. Fixed-fixed beam tunable capacitor.



In operation, a DC bias voltage is applied between the bottom and top plates causing the top-plate to deflect downwards and thereby increasing the device capacitance. This controlled increase in capacitance is the capacitance tuning which is used in RF applications. Beyond a certain critical 'pull-in' voltage, VPI, the downward electrostatic force is no longer balanced by the elastic restoring force provided by the beam anchors. The structure then becomes mechanically unstable and spontaneously collapses or 'pulls-in' to the ground plane leading to a sharp increase in the capacitance of the system and limiting the tuning range that can be achieved to 50%[3-4]. This paper presents the most common solution to extending the capacitor tuning range, a two-gap capacitor [3-4] and a novel geometric design. A number of performance metrics are introduced and are used to compare the performance of these devices.

## II - MEMS Tunable Capacitor Designs

Two approaches to the design of a MEMS tunable capacitor are considered here and are shown in Figure 2.

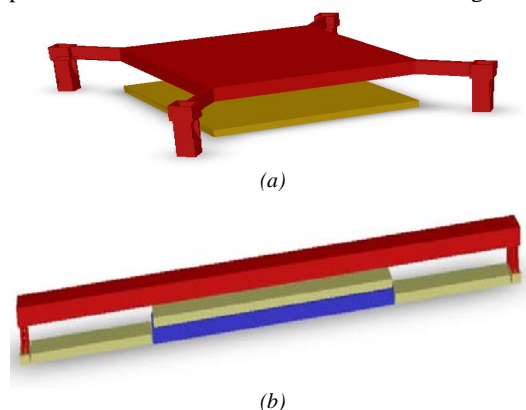


Figure 2 Schematics of (a) a parallel plate and (b) a two-gap MEMS tunable capacitor structure.

The first device, Figure 2(a), is a simple parallel plate design [6,7] which has a theoretical maximum deflection of the movable capacitance electrode of 33% of the initial gap. The second is a two gap structure [8]. The device, shown in schematic Figure 2(b), separates the capacitance and actuation electrodes so that the movable beam

electrode has a larger gap height to the actuation electrodes than to the capacitance electrode. This design extends the maximum deflection of the movable capacitance electrode from 33% of the tuned capacitor gap to 33% of the actuation gap before pull-in occurs.

### III – Performance Metrics

As a potential substitute for varactor diodes in RF circuits it is essential that key performance metrics be comparable across the two technologies. In addition, MEMS devices have some specific operating characteristics which should be used in assessing device performance. Table 1 below outlines a list of key metrics to be considered in comparing MEMS devices. The highlighted metrics are primarily considered in this paper.

TABLE I  
MEMS TUNABLE CAPACITOR METRICS

Metric	Description
Base Capacitance	Capacitance value with zero tuning bias ( $C_b$ )
Tuning range	$TR = \frac{C_{max} - C_b}{C_b} * 100$
Quality Factor	$Q = \frac{\text{Energy Stored}}{\text{Energy Dissipated}}$
Tuning Voltage	Range of voltage required to tune from $C_b$ to $C_{max}$
Linearity	RF linearity ( $IP_3$ )
Power handling	Capacitance variation due to RF power level
C-V characteristic	Analytic/empirical equation of CV curve (e.g. linear)
Stability	Stability margin in voltage for quoted tuning range
Temperature/Stress sensitivity	Capacitance and CV shift with temperature or process stress
MOS compatibility	Ease of wafer scale integration
Process Cost	Number of masks and steps and material costs

### III – Device Comparison

The metrics listed in plain text in Table 1 are commonly applied in RF design to the evaluation of varactor diodes and can be compared directly to the values for MEMS devices. MEMS devices can have comparable base capacitance and tuning ratios and most metal MEMS capacitors have higher quality factor due to low resistance losses. MEMS devices can have higher tuning voltages (5-100V) than varactor diodes but the device mechanical inertia results in much greater linearity.

The metrics highlighted in italics are more specific to MEMS devices. Due to the pull-in instability it is essential that the MEMS tunable capacitor operate at a tuning point where small perturbations which can result from mechanical shock loading or varying RF power do not cause device pull-in. The CV characteristic provides significant information in this regard. As shown in Figure 3 the rate of change of capacitance as a function of tuning voltage near to the maximum tuning ratio is high for both

devices and operation near this point introduces possible instabilities.

In this paper the MEMS specific metrics, power handling and stability, are considered. These performance metrics are essential in the analysis of the suitability of MEMS tunable capacitors in RF applications. An impedance matching circuit using MEMS tunable capacitors is used as a case study example.

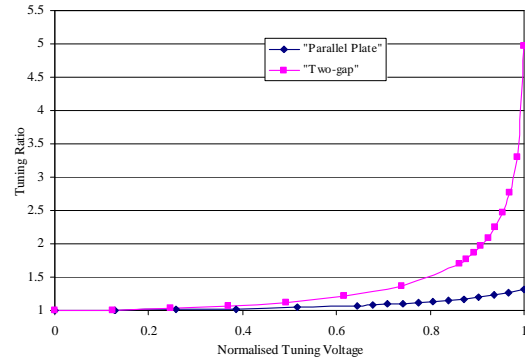


Figure 3 CV curves for devices shown in Figure 2

#### Power Handling

MEMS capacitors change performance with respect to changes in RF power. The RF power in MEMS capacitors causes self-actuation, the attractive force that appears on top beam due to the RF RMS voltage [9]. The self actuation causes the top membrane to actuate in a similar manner to an applied DC bias which changes the tuned capacitance value. To evaluate the effects of different power levels on a MEMS capacitor tuning, a matching network was designed for a Digital Communications System (DCS) with centre frequency of 1.8GHz to match a 6Ω output impedance of power amplifier to 50Ω load at antenna using a Cs–L–CL π-matching network [10,11]. The power amplifier considered is linear with 20dB gain with an input impedance of 50Ω. The optimum values of matching network can be calculated by,

$$X_L = -X_{C_s} = -X_{C_L} = \frac{Z_o}{n} = nZ_s$$

where n is the transformer ratio given by,

$$n = \sqrt{Z_o/Z_s}$$

$X_L$  is the inductive reactance;  $X_{C_s}$  and  $X_{C_L}$  are the capacitive reactances at source and load which can be calculated while  $Z_s$  is the source impedance, (6Ω is considered in this case) and  $Z_o$  is the load impedance (50Ω in this case). The calculated optimum values of  $C_s$  and  $C_L$  are found to be 5pF with an inductance value, 1.53nH for the frequency of 1.8GHz. The impedance matching range can be extended by keeping  $C_1$ ,  $C_6$  and  $L1$  constant and varying the MEMS capacitance ( $C_4$ ,  $C_5$ ,  $C_9$  and  $C_{10}$ ). The simulated circuit is shown in Figure 4. The initial values for the components are given in Table II.

TABLE II  
INITIAL COMPONENT VALUES FOR FIGURE 4

L1	1.53nH
C1=C6	3.6pF
C4, C10 Base capacitance [OFF]	0.1pF
C5, C9 Down state capacitance [ON]	1.3pF

The maximum power handling of the matching circuit can be estimated by measuring the voltage swings across the HZC devices. A small input power can generate fairly large voltage swings across the MEMS capacitors [9,10]. Different power amplifier output levels were simulated and the voltage swing is evaluated at the capacitors C<sub>4</sub> and C<sub>9</sub>. Figure 5 shows the voltage swing across the capacitors C<sub>4</sub> and C<sub>9</sub> for the input of 30dBm power.

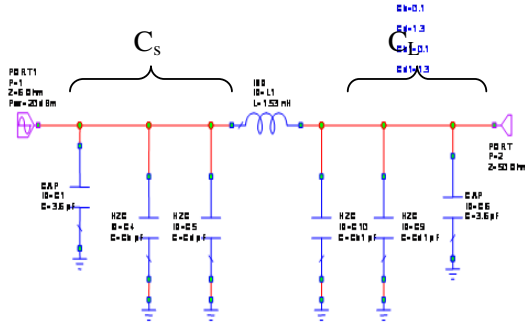


Figure 4 Impedance matching circuit with MEMS tunable capacitors.

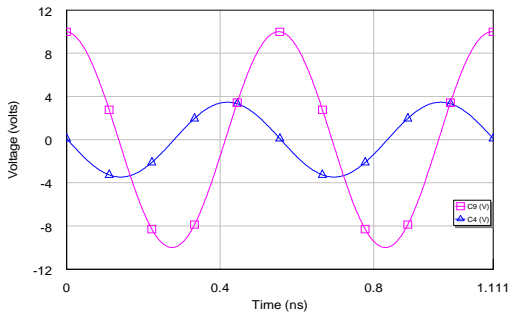


Figure 5 Voltage swing across the capacitor C4 and C9 for 30dBm input power.

TABLE III  
MEMS VOLTAGE DUE TO RF POWER

Pout (dBm)	Voltage at C4 (V)	Vrms at C4 (V)	Voltage at C9 (V)	Vrms at C9 (V)
10	0.34	0.24	0.99	0.70
20	1.09	0.77	3.16	2.23
30	3.46	2.45	9.99	7.06
35	6.16	4.35	17.77	12.56

Table III presents the simulated voltage across the MEMS capacitors with respect to the input power. The values are normalized to the RMS voltage of the load. The maximum voltage swing at C<sub>9</sub> has the maximum RMS voltage on the capacitor at the higher impedance port. From simulations for 35dBm increase in RMS voltage across the capacitor C<sub>9</sub>, with peak RF voltage

values up to 12.56V. This has an RMS voltage level of 8.9V which will significantly alter the tuned capacitance. The effect of these voltage swings on the tuned capacitance of the device depends on the voltage sensitivity of the device which is described below.

#### Stability

The stability of a MEMS capacitor can be interpreted in both open-loop and closed loop operation. In open loop operation the actuated device has a limit to its allowed maximum tuned capacitance before it enters the unstable pull-in regime where the capacitance undergoes a significant step change. In the impedance tuning circuits shown in Figure 4 this would result in an impedance mismatch and a dropped wireless connection. As described above this instability is further complicated by varying RF power levels in the device which causes RF signal actuation superimposed on the DC tuning actuation. To avoid this problem the tuned device must therefore either (a) operate at a safe stability margin from the pull-in stability or (b) operate in a control system which can adapt to the varying RF actuation force. We propose a simple measure of the tuning sensitivity ( $T_s$ ) of the tunable capacitor operation as a function of tuning voltage as:

$$T_s = \frac{dC}{dV} / C_{\max}$$

This measure takes account of the varying sensitivity to voltage of tunable capacitors which can have significantly different tuned capacitance ranges. For devices with separate drive and tuned capacitance electrodes this measure must take account of the instabilities which might occur due to the noise or RF actuation forces on the drive or tuned electrodes and the interaction of these two terms. To take this into account the tuning sensitivity of the two-gap device is specified as a function of the voltage source,  $T_{sd}$  and  $T_{sc}$  for drive and capacitance applied voltages respectively. Drive voltage disturbances result from source noise. Capacitance voltage disturbances arise from noise and RF power induced forces. The influence of these forces are determined by the applied tuning voltage as shown in Figure 6 where the stability is shown for a zero tuning position and a tuning voltage at 50% tuning.

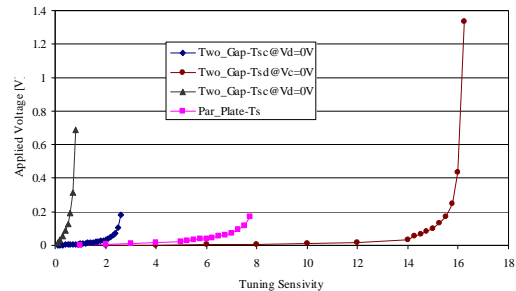


Figure 6 Voltage sensitivity as a measure of stability for different tunable capacitors

#### IV - Conclusions

MEMS offer some significant performance advantages compared to varactor diodes for RF system applications. To evaluate the suitability of different MEMS designs and to compare MEMS devices with other tunable capacitor devices, standard performance metrics are required. These metrics will include some measures common to all device types and some additional measurements specific to MEMS technologies. This paper has presented a list of metrics which need to be considered in evaluating MEMS tunable capacitors. Two specific metrics related to power handling and stability were described in detail. The performance of two different MEMS designs has been compared using these metrics. This paper is a preliminary work which can form the basis for a standard set of metric for MEMS tunable capacitors for RF applications which would contribute to commercial application of suitable MEMS devices.

#### Acknowledgements

The authors would like to acknowledge SFI NAP (National Access Program) and Tyndall National Institute for device fabrication and testing facilities.

#### References

- [1] H. A. C. Tilmans, W. De Raedt and E. Beyne, "MEMS for wireless communications: from RF-MEMS components to RF-MEMS-SiP", J. Micromech. Microeng. 13, pp. S139-S163, 2003.
- [2] G. M. Rebeiz, RF MEMS Theory, Design and Application, New Jersey, John Wiley and Sons, 2003.
- [3] M. Hill, C. O'Mahony, R. Duane and A. Mathewson, "Performance and reliability of post-CMOS metal/oxide MEMS for RF application", Journal of Micromechanics and Microengineering 13 (2003) S131-S138.
- [4] H. A. C. Tilmans and R. Legtenberg, "Electrostatically driven vacuum-encapsulated polysilicon resonators Part II: Theory and performance", Sensors and Actuators A45 (1994) 67-84.
- [5] T. K. K Tsang, M. N. El Gamal, W. S. Best and H. De Los Santos, "Wide tuning range RF-MEMS varactors fabricated using the PolyMUMPS foundry", Microwave Journal (2003) 22-44.
- [6] Dec, A. & Suyama, K., "Micromachined electro-mechanically tunable capacitors and their applications to RF IC's", Microwave Theory and Techniques, IEEE Transactions on 46, pp. 2587-2596, 1998.
- [7] Young, D. J. and Boser, B. E., A micromachined variable capacitor for monolithic low-noise VCO's, Proc. IEEE Int. Conference on solid state sensors and actuators, Hilton Head, pp. 86-89, 2-6th. June 1998.
- [8] J. Zou, C. Liu and J. Schutt-Aine, "Development of a wide tuning range two-parallel-plate tunable capacitor for integrated wireless systems", Int. J. RF Microwave 11 (2001) 322-329.
- [9] J.R.Reid, L.A.Starman, R.T.Webster, "RF actuation of Capacitive MEMS Switches", 2003 MTT-S Digest, Vol.3, pp. 1919-1922, June 2003.
- [9] K. Entesari and G.M. Rebeiz, "RF MEMS, BST and GaAs Varactor System-Level Response in Complex Modulation Systems," International Journal of RF and Microwave Computer Aided Engineering, Jan. 2008, pp. 86-98
- [10] G. M. Rebeiz, "RF MEMS theory, design, and technology," NJ: John Wiley & Sons, 2003
- [11] L. Dussopt and G. M. Rebeiz, "Intermodulation distortion and power handling in RF MEMS switches, varactors, and tunable filters," IEEE Trans. Microwave. Theory Tech., vol. 51, no. 4, pp. 927-930, Apr. 2003.
- [12] Girbau, D. Otegi, N. Pradell, L. Lazaro, A., "A MEMS capacitor with improved RF power handling capability" , Volume 3, European Microwave Conference, 4-6 Oct 2005.
- [13] Leidich, S., Kurth, S., Gessner, T. , "Continuously tunable RF-MEMS varactor for high power applications", IEEE MTT-S International Microwave Symposium digest. Vol.3: Atlanta, GA, 15 - 20 June 2008.



# ULTRASOFT FINEMET THIN FILMS FOR MAGNETO-IMPEDANCE MICROSENSORS

J. Moulin<sup>1</sup>, I. Shahosseini<sup>1</sup>, F. Alves<sup>2</sup>, F. Mazaleyrat<sup>3</sup>

<sup>1</sup>IEF, UMR 8622, Univ Paris Sud, F-91405 Orsay, France

<sup>2</sup>LGEP, UMR 8507, Supelec, F-91192 Gif-Sur-Yvette, France

<sup>3</sup>SATIE, UMR 8029, ENS Cachan, F-94235 Cachan, France

**Abstract** — FeCuNbSiB thin films have been deposited using RF sputtering. Characterizations showed that oxygen contamination and residual stress are mainly responsible for magnetic hardening. The sputtering and annealing conditions have been optimized and films with coercive field as low as 10 A m<sup>-1</sup> (0,125 Oe) have been obtained. In addition, the influence of film thickness on the magnetic properties has been studied. Thus, magnetic field microsensors based on the magneto-impedance effect have been fabricated by stacking up Finemet/copper/Finemet films. The highest sensitivity (4000 V/T/A) is reached for 750 nm thick films and is in the same range as cm-sized macroscopic devices realized using 20 µm thick ribbons.

**Keywords :** Finemet, FeCuNbSiB, Magneto-impedance, ultrasoft thin film, microsensor

## I - Introduction

Since the discovery of the magneto-impedance (MI) effect in amorphous microwires [1] and films [2], magnetic field sensors based on this property have become competitive with other techniques like GMR and fluxgates. The MI effect finds its origin in the variation of the skin depth  $\delta$  with an applied magnetic field  $H_{\text{ext}}$  (through the magnetic permeability) while exciting the conductor using a high frequency current:

$$\delta(H_{\text{ext}}) = \frac{1}{\sqrt{\pi f \sigma \mu_t(H_{\text{ext}})}} \quad (1)$$

with  $f$  the excitation frequency,  $\sigma$  the conductivity and  $\mu_t$  the transversal (or rotational in case of a wire) magnetic permeability.

The impedance of the conductor depends on its geometry:

$$Z = R_{\text{dc}} ka \frac{J_0(ka)}{2J_1(ka)} \quad (2)$$

for a wire [3], with  $J_0$  and  $J_1$  the Bessel function,  $R_{\text{dc}}$  the DC resistance of the wire,  $a$  the wire radius and  $k = (1+j)/\delta$ , or :

$$Z = R_{\text{dc}} ka \coth(ka) \quad (3)$$

for a thin film [4], with  $a$  the film thickness.

For both geometries, the MI variations  $(\Delta Z/Z_{\text{sat}})_{\text{max}}$  are the most sensitive to the external field for  $\delta \approx 2a$ , which corresponds to an optimal excitation frequency for a given geometry. The highest MI ratios are obtained in amorphous Fe-based microwires, in which external and internal stresses are respectively circumferential and axial. This stress orientation corresponds to an optimal magnetic structure. However, collective fabrication, for instance in case of sensors arrays, is much easier while using thin films technique. It has been found that for a planar structure the MI variations can increase strongly by inserting a conductive film between the ferromagnetic layers [5]. In this multilayer structure, the optimal excitation frequency for obtaining  $(\Delta Z/Z_{\text{sat}})_{\text{max}}$  is much lower than for a single film, as the conductivity of common ferromagnetic materials is about 100 times lower than that of a good conductor. Previous calculations using finite elements method on such a structure [6] showed that the highest MI effect is obtained around 10 MHz for a 1 µm thick ferromagnetic film with a thickness ratio of 1/2/1 for the multilayer structure. In addition, if the magnetic domains are oriented perpendicularly to the applied magnetic field, the MI rises because of the increase in transverse permeability in the ferromagnetic layers. That is why the ferromagnetic layers are exposed to a transverse magnetic anisotropy field.

The sensor characteristics, in particular hysteresis and sensitivity, are firmly dependent to the ferromagnetic layer softness. The fig 2 presents numerical calculations using finite elements for a G500 sensor configuration. The MI increases quite linearly with the transverse permeability, what shows the importance of depositing a soft material. Several works

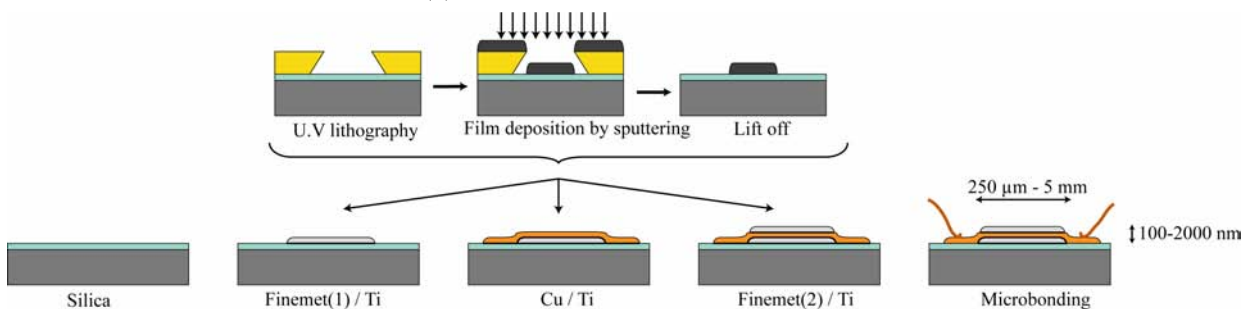


Figure 1: Fabrication process

succeed in integrating Finemet® alloys into thin film MI sensors [7, 8, 9]. Indeed, this material presents ultrasoft properties due to its microstructure: after a heat treatment of the amorphous precursor, ferromagnetic Fe-Si nanograins germinate in a ferromagnetic matrix which remains amorphous. This assures quasi-null magnetostrictive anisotropy by the meaning of negative and positive magnetoelastic effects inside the grains and in the matrix respectively. Moreover, the magnetocrystalline anisotropy in such nanocrystalline materials is decreased following the Random Anisotropy Model proposed by Herzer [10]. The MI results obtained with such a material are promising, despite the fact that the developed sensors present lower MI ratios than those with FeCo-based alloys. However, MI ratio is not the only quality factor for a sensor, variation of the MI with the magnetic field is more relevant. For this purpose, ultra-soft Finemet, which can be obtained by an optimization of the elaboration process, is a good candidate.

## II. Elaboration process

We developed a MI microsensor fabrication process compatible with thicknesses close to 1  $\mu\text{m}$ . Each layer of the sensors was patterned using lift-off technique with a 3  $\mu\text{m}$  thick AZ5214 photoresist (see fig.1). In order to obtain such thick resist, the rotation speed during spin coating was limited to 900 rpm. The lithography exposure dose and development time were also adapted to such a thickness. The materials were deposited using sputtering technique: Finemet® and copper for the ferromagnetic and conductive layers respectively. The Finemet has been deposited on a SiO<sub>2</sub>/Si substrate by RF sputtering in Ar plasma under the following conditions: residual pressure in the range of  $10^{-7}$  mbar, working pressure 40 mbar and RF power 250 W. The copper layer was realized by DC sputtering with a working pressure of 6.5 mbar and a power of 50 W. Before each sputtering, a 10 nm thick layer of titanium was deposited in order to increase adhesion.

The sensors are constituted of rectangular stripes whose dimensions vary from 50 to 430  $\mu\text{m}$  in width and from 1 to 5 mm in length. For our samples, we attempt

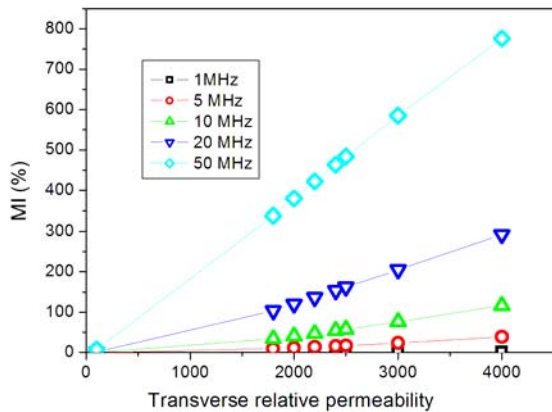


Figure 2: Finite elements calculation of the magneto-impedance as a function of the transverse permeability of the ferromagnetic layer. Dimensions correspond to G500.

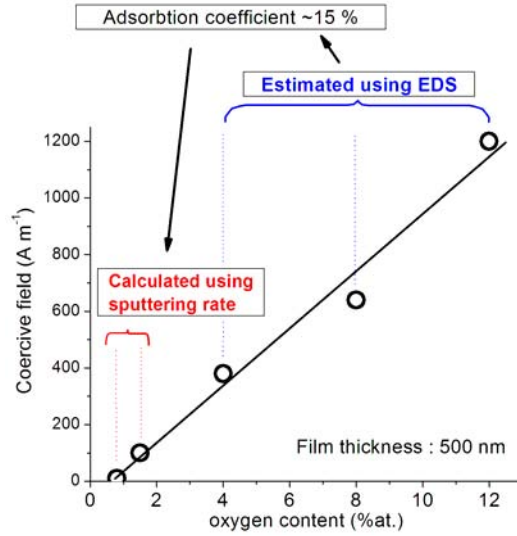


Figure 3: Influence of contamination in oxygen on the coercive field

to obtain a central copper layer totally shielded by ferromagnetic layers, i.e. the Finemet layers are wider than the copper track. However, the latter is longer and is ended by two connection pads for bonding.

In order to obtain the lowest coercivity, the magnetic properties of the Finemet® films have been optimized in terms of elaboration and heat treatment. Former study showed that the coercivity is mainly influenced by the contamination in oxygen (see fig. 3) and the residual stress in the films [11]. Practically, the sample temperature at the beginning of the deposition (sample is not cooled in our equipment) influences strongly on the coercive field of the films (see fig. 4). This phenomenon can be related to the anisotropy induced by magnetoelastic effect. Indeed, the differential thermal expansion between the substrate and the film during the cooling after the deposition is responsible for stress:

$$\sigma_{\text{therm exp}} = (\mu_w - \mu_f) \frac{E_f}{1 - \nu_f} \Delta T = a \Delta T \quad (4)$$

with  $\mu_w$ ,  $\mu_f$ ,  $E_f$ ,  $\nu_f$  and  $\Delta T$  respectively the thermal expansion coefficients of the substrate and the film, Young's modulus and Poisson's ratio of the film and the temperature variation involved in the thermal expansion process. The magnetoelastic anisotropy associated to amorphous material is:

$$E_s = \lambda_s \sigma \quad (5)$$

Former works allowed estimating the coefficient  $a$  close to 0.75 MPa/K while the temperature remains below 200°C. Using the magnetostriction coefficient of such alloys (i.e.  $23 \cdot 10^{-6}$  ppm), one can estimate the increasing of magnetostatic energy due to thermal expansion in the range of 17 J m<sup>3</sup>/K. This corresponds to a variation in the coercive field in the range of 8 to 10 A m<sup>-1</sup>/K. This is coherent with the experimental results that present a slope of 13 A m<sup>-1</sup>/K (see fig 4).

After annealing, the dependence of the coercive field to the initial substrate temperature is reduce to 5 A m<sup>-1</sup>/K. This result is associated to a reduction of  $\lambda_s$  due to a

modification of the microstructure. Indeed, the annealing temperature is higher than the glassy transition.

After optimization of the deposition process (high sputtering rate, addition of a liquid nitrogen trap) and annealing temperature, the coercive field of a 500 nm thick film was as low as  $10 \text{ A m}^{-1}$ .

As reported in other works [12], the device sensitivity is increased after inducing a transverse anisotropy in the ferromagnetic material. This has been performed by annealing in the magnetic field created by a 3 mm thick and 5 cm diameter magnetic circuit containing AlNiCo magnets. The value of the magnetic field in the 7 mm x 14 mm air gap in which samples are disposed is in the range of  $50 \text{ kA m}^{-1}$ . The temperature dependence of the magnetization allows field annealing up to  $500^\circ\text{C}$  in the secondary vacuum of the sputtering chamber. The figure 5 presents hysteresis cycle of 2 mm x 2 mm x 500 nm samples realized by shadow masking and characterized using an AGFM. The anisotropy induced by the field annealing leads to low coercive field, as well as annealing without magnetic field. In addition, the induced energy can be estimated from both cycles measured in the parallel and perpendicular directions of the applied magnetic field. This value, in the range of  $150 \text{ J m}^{-3}$ , is much larger than energies induced in bulk materials by this technique. In addition, the anisotropy field can be estimated close to  $700 \text{ A m}^{-1}$ .

After optimization of the ferromagnetic material properties, sensors with variable size and thickness have been processed. Table 1 resumes their dimensions.

TABLE I  
DIMENSIONS OF THE SENSORS

	Film thickness (nm)	Finemet layer ( $\mu\text{m}$ )	Copper layer ( $\mu\text{m}$ )
G500	500/500/500	4000 x 200	4200 x 50
G750	750/750/750	4000 x 200	4200 x 50
B1000	1000/1000/1000	4000 x 200	4200 x 50

### III. Sensors characteristics

MI measurements have been carried out using a voltage source and a lock-in amplifier in the 1-40 MHz

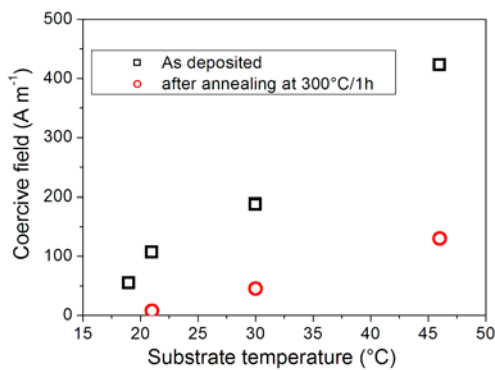


Figure 4: Coercive field of 500 nm thick Finemet films as a function of the substrate temperature at the beginning of the sputtering

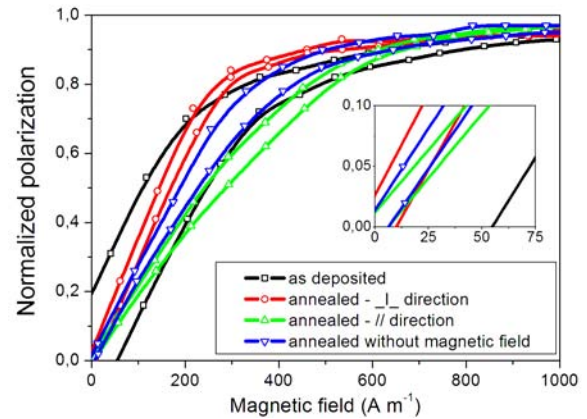


Figure 5: Influence of field annealing on hysteresis cycles of 500 nm thick samples

frequency range. The DC magnetic field measured by the sensor has been created by Helmholtz coils, assuring a 2 cm wide homogeneous zone. The maximal magnetic field applied to the sensor is in the range of  $7000 \text{ A m}^{-1}$ .

The MI ratio variations are weak compared to other type of sensors, in the range of 10 %. Indeed, the resistance value is large (around  $10 \Omega$ ) and varies a little. At the opposite, the inductance variations reach 400 % but inductance value is weak. These measurements highlight magnetic properties like anisotropy field, which is in the range of  $700 \text{ A m}^{-1}$  for sensors G500 and G750. The result is coherent with the value estimated from the hysteresis cycle of the films annealed under magnetic field.

Papers related to MI effect generally compare the materials properties using the MI ratio only. However, this is not a pertinent factor for quantifying a sensor quality. The most important value is either the variation of the MI ratio with the magnetic field (in %/Oe) or the variation of the impedance with the magnetic field (in  $\Omega/\text{T}$  or in  $\text{V}/\text{T}/\text{A}$ ).

Furthermore, measurements at high frequency are strongly sensitive to external perturbations, so the impedance value can not be reliable. To solve this problem, the sensors were characterized by measuring the output voltage as a function of the magnetic field, starting from the saturated state. Then the sensitivity was extracted by numerical derivative.

The characterizations have highlighted a strong dependence of MI properties on the shielding of the central copper track by the ferromagnetic material. Former investigation showed that defects at the edge of the deposited layer appear while the sputtering direction is not vertical enough. This phenomenon is linked to the deposition of the sputtered material on the side of the photoresist for high film thickness and high working pressure. The consequence of this defect on the properties depends on the involved layer: lack of shielding for the central copper track and over-dimensioning of the sensor for the Finemet layers. The former reduces the effect of the induced transversal anisotropy, as the upper Finemet layer is separated in

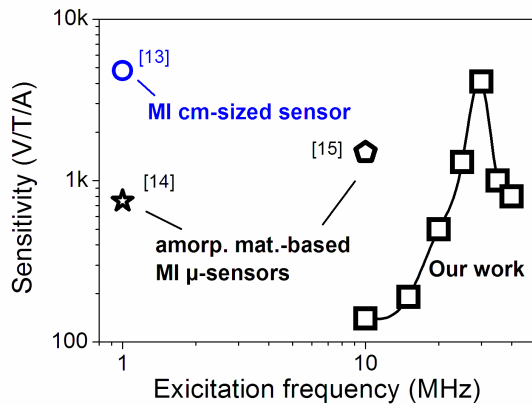


Figure 5: Dependence of the G750 sensor sensitivity (black squares) on the excitation frequency. Comparison with other amorphous material-based MI sensors

three magnetically independent parts. The latter limits the miniaturization of the sensor, thus the spatial resolution also.

The sputtering conditions of the copper have been optimized in order to limit over-deposition at the edge of the central conductive track. Thus the upper Finemet layer is continuous and assures magnetic shielding of the copper. However, the defects at the edge of the finemet layer are not yet eliminated, as deposition conditions are driven by the minimization of the coercivity. Their influence on MI properties is theoretically weak, as calculated by numerical simulation. But these defects act as pinning centers for the magnetic domains displacement and reduce the sensitivity of the device.

Sensors with variable dimensions and thicknesses have been realized (see table 1). Numerical simulations predict, for a given excitation frequency, an increase in the sensitivity with the films thickness. Indeed, experimental characterizations show that the maximal sensitivity increases from 1900 V/T/A for the G500 sensor to 4100 V/T/A for the G750 sensor. Unfortunately, the presence of a defect above the copper track increases with the film thickness. This results in a low sensitivity of the sensor B1000.

Fig. 5 presents the sensitivity of the G750 sensor as a function of the frequency. It reaches a maximum at 30 MHz with a 1.7 mA excitation current. On the same figure, the results are compared to FeCoSiB/Cu/FeCoSiB [14] and FeSiB/Cu/FeSiB [15] MI microsensors. Results are also compared to sensitivity of a macrosensor realized with Finemet and copper ribbons which thicknesses are 20  $\mu\text{m}$  and 40  $\mu\text{m}$  respectively. The total size of the sensor is 5 cm x 1 cm. It is noticeable that there is no drastic decrease of the sensitivity due to scale effect. Indeed, the structures of both the macro-sensor and the present devices are comparable. The maximal sensitivities are in the same range. However, the optimal frequency increases from 100 kHz to 20 MHz for the macro- and microsensors respectively, due to the thickness reduction.

### III. Conclusion

This paper reports a technological process for depositing ultrasoft Finemet thin films using a common technique. In addition, it has been showed that this material can be integrated in MI microsensors. Their sensitivity reach 4100 V/T/A, which is the largest among all published similar structures.

The results highlight a strong dependence of the sensor quality on the presence of a defect above the copper track which stems from the association of lift-off and non directive sputtering of thick films. In future works, strength will be put on the removal of this defect, for instance using a specific lift-off resist dedicated to thick film deposition.

The optimal excitation frequency for the sensor G750 is 30 MHz, which remains high for standard electronic. Thicker films will allow decreasing this frequency to 10 MHz.

### Acknowledgment

This work has been financially supported by the French Agence Nationale pour la Recherche, through the Project IMAGINE ANR-05-NANO-067-01 and by the Conseil Général de l'Essonne through the use of the equipments of the Centrale de Technologie Universitaire IEF-MINERVE.

### References

- [1] L. V. Panina, K. Mohri, K. Bushida, and M. Noda, *J. Appl. Phys.* 76 (1994), 6198
- [2] L.V. Panina, K. mohri, T. Uchiyama, K. Bushida, M. Noda, *IEEE Trans. Mag.* 31 (1995), 1249
- [3] L.D. Landau, E.M. Lifshitz, *Electrodynamics of continuous media*, Pergamon, Oxford, 1975
- [4] C. Kittel, *Phys. Rev.* 70 n°5-6 (1946), 281
- [5] M. Senda, O. Ishii, Y. Koshimoto, T. Toshima, *IEEE Trans. Mag.* 30 n°6 (1994), 4611
- [6] J. Moulin et al., *Sensor Letters* 7 n°3 (2009)
- [7] S.-Q. Xiao et al., *Phys. Rev. B* 61 n°8 (2000), 5734
- [8] J.-A. Chen et al., *Mat. Lett.* 60 (2006), 2554
- [9] M.A. Correa, A.D.C. Viegas, R.B. Da Silva, A. M. H. De Andrade, R. L. Sommer, *J. Appl. Phys.* 101 n°4 (2007), 043905
- [10] G. Herzer, *Physica Scripta* vol. T49 (1993), 307
- [11] J. Moulin, M. Ammar, I. Shah-Hosseini, F. Alves, F. Mazaleyrat, *J. Phys. Conf. Series* 200 n°8 (2010), 082020
- [12] W.-J. Wang et al., *Thin Solid Films* 484 (2005), 299
- [13] F. Alves, J. Moutoussamy, C. Coillot, L. Abirached., *Sens. actuators. A* 145-146 (2008), 241
- [14] Y. Nishibe, H. Yamadera, N. Ohta, K. Tsukada, Y. Nonomura, *Sens. Actuators* 82 (2000), 155
- [15] T. Morikawa, Y. Nishibe, H. Yamadera, Y. Nonomura, M. Takeuchi, Y. Taga, *IEEE Trans. Mag.* 33 n°5 (1997), 4367



### 3-DIMENSIONAL ETCHING OF SILICON SUBSTRATES USING A MODIFIED DEEP REACTIVE ION ETCHING TECHNIQUE

S. Azimi, J. Naghsh-Nilchi, A. Amini, A. Vali, M. Mehran and \*S. Mohajerzadeh

*School of Electrical and Computer Eng, Thin Film and NanoElectronic Lab, University of Tehran, Tehran, Iran*

**Abstract** — We report realization of highly featured three-dimensional structures on silicon substrates with a single masking layer using a hydrogen-assisted deep reactive ion etching process. Three gases of oxygen, hydrogen and SF<sub>6</sub> are used in a sequential passivation and etching process to achieve high aspect ratio features. By controlling the flows of these gases and the power and timing of each subsequence, it is possible to achieve desired deep vertical etching, controlled under-etching and recovery yielding three dimensional features directly on silicon substrates. Etch rates up to 0.75µm/min have been achieved with a low plasma power density of 1W/cm<sup>2</sup>. Also features with a controllable under-etching and recovery with more than 8µm in side-wall recession have been achieved. Furthermore, values of aspect ratio higher than 50 can be obtained.

**Keywords:** Vertical etching, deep reactive ion etching, 3-D structures, curved sidewalls

#### I - Introduction

Three dimensional structures are promising features as they possess promising optical and mechanical properties. Conventionally 3-D structures refer to the structures where the third dimension (height) of the feature is controlled during the etching process. Although these structures can be realized using multiple lithography, a single mask fabrication has also been introduced using deep reactive ion etching combined with gray scale lithography[1]. On the other hand, the evolution of micro-stereo-lithography has shown to be a powerful technique to achieve high-aspect-ratio 3-D structures in which the height remains constant but the structure possesses complex features in the z-direction. In such a technique, a UV laser beam is used to form various slices on a UV-curable polymer according to the desired shape [2]. Nevertheless it can be used as a method to form 3-D features on silicon substrates after a micro-molding step is carried out [3]. Apart from micro-scale features, sub-micro and nanostructures with 3-D features are realized using a glancing low angle deposition and layer engineering technique [4].

A main milestone in the silicon micromachining, as the key step in the realization of many MEMS-devices, has been the advent of deep reactive ion etching, usually referred to as the Bosch process. This technique utilizes a sequential etching and passivation steps to form vertical trenches and walls onto silicon substrates with high aspect ratios [5]. As an alternative approach, a non-sequential cryogenic process has been introduced

which takes advantage of a mixture of oxygen and SF<sub>6</sub> at a cryogenic temperature for the etching of silicon substrate with no need to a polymeric coating step[6].

We have recently reported a high aspect-ratio vertical etching process which neither needs high density plasma nor uses external polymeric coating for the passivation. The vertical removal of silicon substrate is achieved with a sequential etching and passivation sub-cycles as reported elsewhere [7]. The process uses a combination of three gases of hydrogen, oxygen and SF<sub>6</sub> to carry out the vertical etching in a reactive ion etching unit with a RF plasma source. The etching is divided into passivation and etching sub-cycles, where a mixture of H<sub>2</sub>/O<sub>2</sub> gases with a trace of SF<sub>6</sub> constituent is used during the passivation cycle while the next subsequence (etching) is achieved merely with SF<sub>6</sub> as the feed gas. In this paper the creation of highly featured three-dimensional structures with curved sidewalls and directly on silicon with a single masking layer is reported. The etching and passivation sub-sequences are programmed in order to achieve the under-etching and recovery steps to form desired three dimensional features. A potential application of these 3-D silicon structures is in soft lithography in which they can be used as desired molds, suitable for tissue and biocompatible engineering [8, 9].

#### II - Experimental Setup

The fabrication process in this paper is based on a deep reactive etching technique where a sequential etching/passivation procedure is employed [7]. The etching is achieved in a reactive ion etching (RIE) machine operating at 13.56 MHz with an effective area of 20X15cm<sup>2</sup>. The function of every part of this machine is controlled through a computer via customizable software. For this work, p-type 1-5ohm-cm (100) silicon wafers are used. After cleaning the substrates using a RCA #1 solution, they are blow dried and a protective layer of Cr with a thickness of 0.1µm is deposited using an electron-beam evaporation system. The Cr-coated sample is then patterned using standard photolithography to act as the mask for the subsequent etching process and to realize the desired structures.

The etching process is schematically presented in Figure 1, illustrating both the passivation and etching sub-cycles. In the passivation sub-cycle, a mixture of SF<sub>6</sub>, H<sub>2</sub> and O<sub>2</sub> gasses are fed into the chamber. If a vertical etching is required, the underetching is minimized by adjusting the power, gas mixture and duration of the passivation sub-cycle. After each etching sub-

cycle the reactor chamber is evacuated by means of a mechanical pump and the mixture of hydrogen and oxygen gases is fed into the reactor. These two steps are repeated as many times to achieve the desired depth. We believe that during the passivation step the existence of the hydrogen atoms not only assists in the formation of a thin protective layer on the side-walls of the etched pit, it also bombards the bottom of the crater to impart defects to the exposed silicon surface, hence improving the silicon removal in the subsequent etching step. The total etch rate depends on the etching depth during the etching sub-cycle as well as the total duration of a complete cycle. We have achieved a high etch rate of  $0.75\mu\text{m}/\text{min}$  while achieving an aspect ratio of 10 and more. With a reduced rate to  $0.4\mu\text{m}/\text{min}$  a high aspect ratio up to 50 can be obtained.

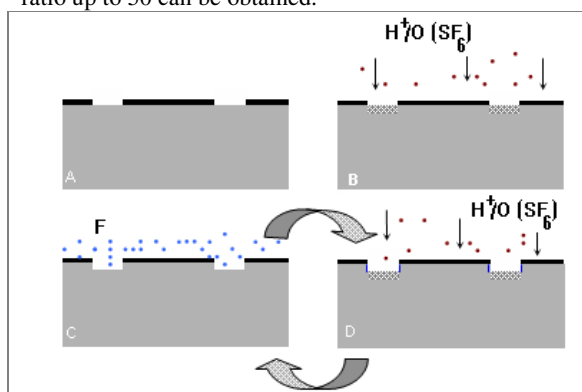


Figure 1: Process steps of deep silicon vertical etching (from A to D). The etching requires a passivation sub-cycle plus an etching sub-cycle to achieve a deep vertical etching.

The etching-passivation sub-cycles are important parameters affecting the whole structure. During the passivation step, all three gases are introduced into the reactor. The plasma power is another important parameter in this sub-cycle and it has a typical value ranging from 150 to 250 W during this sub-cycle. The duration of this sub-cycle can be widely varied ranging from a short treatment of 30 seconds in high speed etching to 120 seconds for high resolution and high aspect ratio etching processes.

The etching sub-cycle is achieved by switching off the  $\text{H}_2/\text{O}_2$  gases and increasing the value of  $\text{SF}_6$  flow rate to 15-20sccm. The duration of this sub-cycle is less and ranges between 10 and 20 seconds with a typical value of 15 seconds and a typical plasma power of 140W. Depending on the desirable structure, the total duration of an etching cycle can be ranging from 55 to 160 seconds. The overall etch rate can be between  $0.25$  to  $0.75\mu\text{m}/\text{min}$ , although a higher etch rate can also be achieved.

### III - Results and Discussion

Figure 2 collects several SEM images for the etching process prepared for this study. The top-right image in this figure corresponds to a high aspect ratio etched thin

rod with a thickness of 150nm and a height of the structure is around  $6\mu\text{m}$ . In addition, an array of silicon rods with high aspect ratio features are presented.

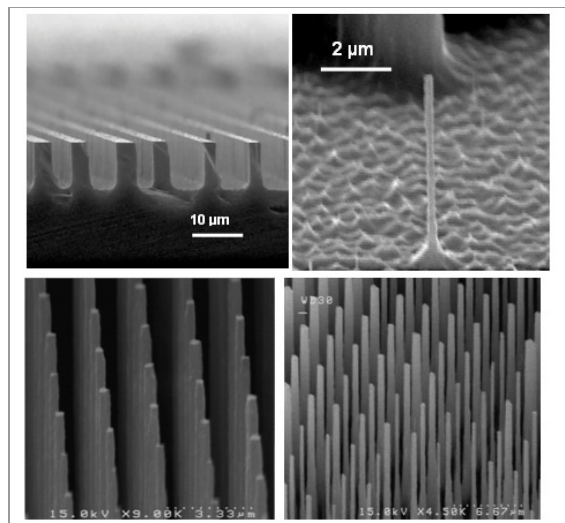


Figure 2: SEM images of various samples processed by silicon vertical etching with various heights and sizes. Arrays of silicon rods with  $20\mu\text{m}$  height and  $0.3\mu\text{m}$  width are obtained.

A maximum etch rate of  $0.65\mu\text{m}/\text{min}$  is obtained for a passivation sub-cycle of 15 sec. The etching sub-cycle has been set at 15 sec. with a plasma power of 150W over an area of  $15\times 20\text{ cm}^2$ . By raising this time to 20 seconds and keeping the passivation time at 30 seconds, it has been possible to obtain a total rate of  $0.75\mu\text{m}/\text{min}$ .

### IV. Three-dimensional etching

Controlling the underetching is an important factor for the formation of highly featured three-dimensional structures. By properly adjusting the  $\text{H}_2/\text{O}_2$  plasma conditions during the passivation sub-cycle, desired 3-D shapes are realized. Interestingly, it is possible to realize a reverse underetching which we refer to as *recovery* by similar controlling tools. Once the gas flows have set back to their optimum values for a vertical etching, sharp walls are obtained.

Figure 3 collects many samples prepared using this underetching/recovery technique. Fig. (3a) shows an unusual reversed glass-like structure where the initial intentional underetching has been fully recovered and a vertical etching has been evolved. For this sample, the initial etching has been carried out with short time and low power passivation steps to minimize the passivation of the side-walls. As observed the sample has undergone an underetching over this period that took “fifteen” etching cycles. After this underetching period, passivation condition turned back to its normal values and the normal etching process has been set. Under such conditions, further progress of underetching has stopped and a recovery is observed. After 15 cycles of normal etching, the original round mask has been recovered and

further progress of the etching results in an almost vertical structure. Other images of this figure belong to the cases where a vertical etching process has been practiced initially followed by a low hydrogen gas flow to ensure moderate underetching over the subsequent cycles. The presence of grass-like features or black-silicon at the very bottom of the sample surface is observed in this figure which could be diminished by a quick exposure to  $\text{SF}_6$  plasma with a low power of 100W. It is worth mentioning that similar shapes can be obtained using a micro-stereo-lithography technique, however a polymeric substance is used for such a 3-D configuration instead of silicon substrates.

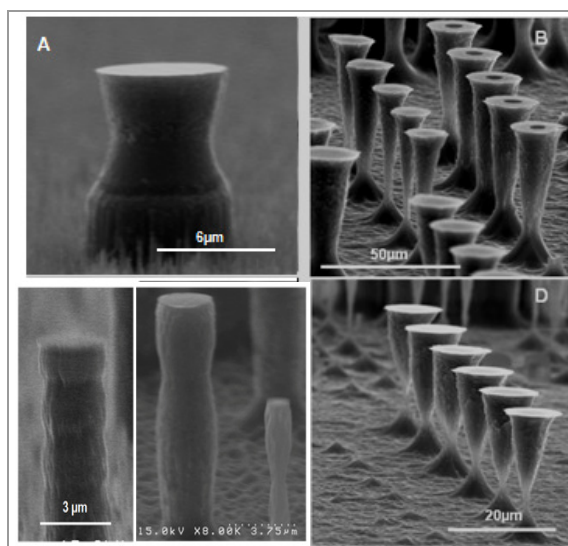


Figure 3: SEM images of some silicon 3-D structures obtained from controlled under-etch/recovery during vertical (anisotropic) etching process.

Figure 4 shows schematically, how complex 3-D structures are realized and repeated. Steps “A” to “F” are needed to form a curved structure. It must be born in mind that the depth of the curved sidewalls can be as much as 20 μm where many etching/passivation cycles are involved. After obtaining the first curved feature, the sample is thermally oxidized in a dry-oxide furnace and the bottom  $\text{SiO}_2$  is removed using direct-current plasma hydrogenation, carried out in a dc-plasma reactor. This step is crucial to remove the oxide layer from the very bottom of the craters and can be obtained by a dc power of  $1\text{W}/\text{cm}^2$  in hydrogen plasma at a pressure of 1-5 torr. Once this oxide layer is partially removed, a quick dip in buffered HF (hydrofluoric acid) ensures the complete removal of the bottom oxide. Care should be taken not to affect the side-oxide to make sure that the subsequent etching would not affect the remaining features of the previous under-etching/recovery stages. At present time we are trying to avoid such an external oxidizing step by better optimization of the etching process.

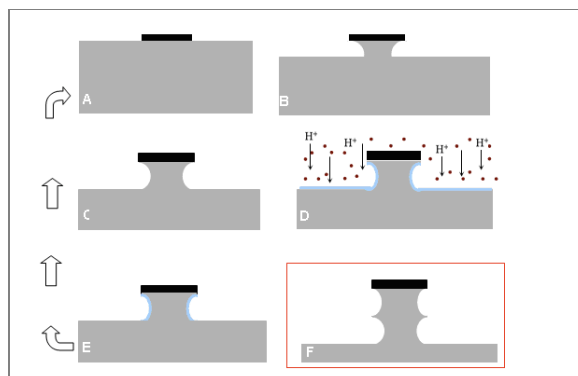


Figure 4: The process steps of a desired 3-D shape silicon etching, starting with mask patterning (A), followed by etching with desired under-etching (B) and recovery (C), oxide passivation (D) and removal from the bottom (E). Final structure depends on the number of times these steps are repeated (F).

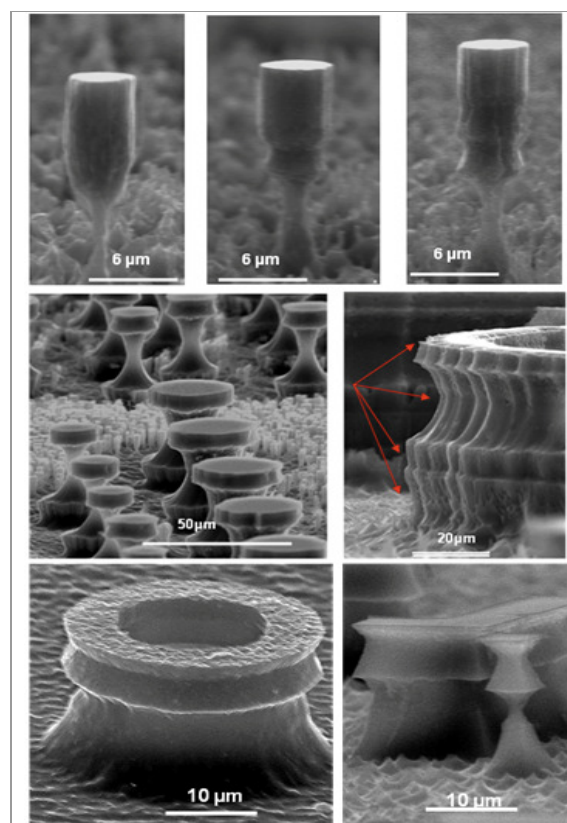


Figure 5: SEM images of desired 3-D shape silicon etching. The under-etching has been as much as 8 μm. By controlling the main gases it has been possible to recover the recessed side-walls and obtain the original mask. The results presented in this figure correspond to one initial step of vertical etching (top) followed with one or two steps of under-etching/recovery. The curved and highly featured edges are evident from this figure.

In Figure 5 we have collected a set of SEM images for several samples which have been prepared with three

sequences to form highly featured structures. As seen from these images, the overall underetching has been as much as  $7\mu\text{m}$  in some of the samples. By controlling the main gases it has been possible to recover the recessed side-walls and obtain the original mask.

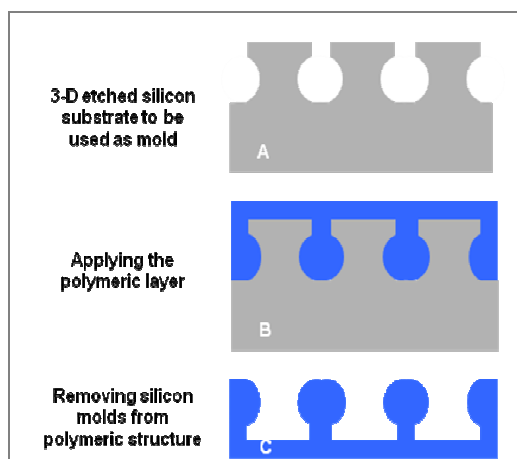


Figure 6: Process steps of polymer molding using 3-D etched silicon substrate as molds.

Such 3D structures can be used for polymeric molding as seen in the Fig. 6. The results of the fabricated structures are presented in Fig 7. As seen from this figure, the round array of polymeric fingers can be arranged to form a hand-like structure. By applying a proper thermal or electrostatic activation it will be possible to gather the fingers together to act as a gripper. Further investigation on the application of such tiny structures as manipulators is being pursued.

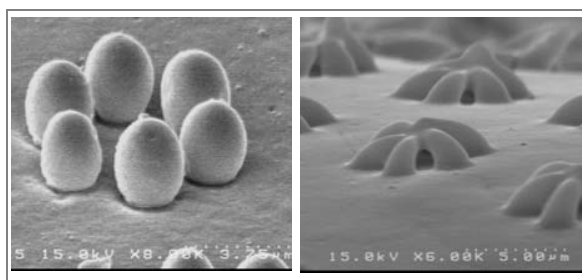


Figure 7: SEM images of round arrays of polymeric fingers obtained from silicon 3-D molds.

## V - Conclusion

We have successfully fabricated three dimensional structures on silicon substrates using a hydrogen assisted deep reactive ion etching technique. This technique allows a moderate rate high aspect ratio vertical etching of silicon substrate with no need to a polymeric coating or high density plasma. In place of using a polymeric coating for the passivation subcycle, a mixture of hydrogen, oxygen and  $\text{SF}_6$  gases is used which not only protect the side wall, it also improves the

verticality by bombarding the exposed surface of the silicon substrate. The use of these gases allows a unique feature which allows the recovery of the underetched side-walls. By controlling the gas flows and plasma conditions during the passivation subcycle, it is possible to achieve desired underetching which can be recovered by proper setting of the gases in subsequent etching steps.

The evolution of highly featured three-dimensional structures can be used in designing photonic crystal arrays of vertical-standing rods where apart from the desired order in the X-Y plane, the order in Z-direction adds up to the filtration capabilities of the array. By combining the polymeric molding and the 3-D features of the fabricated structures, useful structures for tissue engineering can be realized. Realization of a polymeric-based thermal-activated manipulator is being pursued.

## References

- [1] C. M. Waits, A. Modafe and R. Ghodssi, *J. Micro-mech. Microeng.*, vol. 13, pp.170–177, 2003.
- [2] A. Bertsch, S. Jiguet, P. Bernhard, P. Renaud, *Mat. Res. Soc. Symp.*, Vol.758, pp. LL1.1.1–LL1.1.13, 2003.
- [3] Y. Kanamori, J. Sato, T. Shimano, S. Nakamura, K. Hane, *Microsystem Technologies*, vol. 13, no. 8-10, pp. 1411-1416, May 2007.
- [4] K. Rabbie and A. Lakhtakia, *Nature*, vol. 384, pp. 616, Dec 1996.
- [5] W. Ivo and Rangelow, *J. Vac. Sci. Technol. A*, Vol. 21, pp. 1550–1561, Aug. 2003.
- [6] M. J. de Boer, J. G. E. Gardeniers, H. V. Jansen, E. Smulders, M.-J. Gilde, G. Roelofs, J. N. Sasserath, and M. Elwenspoek, *J. Microelectromech. Syst.*, vol. 11, no. 4, pp. 385–401, Aug. 2002.
- [7] A. Samak, S. Azimi, N. Izadi, B. K. Hosseini and S. Mohajerzadeh, *J. Microelectromech. Syst.*, vol. 16, pp. 912, Aug. 2007.
- [8] E. Leclerc, K.S. Furukawa, F. Miyata, Y. Sakai, T. Ushida, T. Fujii, *Biomaterial*, vol. 25, pp.4683-4690, 2004.
- [9] D. Gallego, N. Ferrell, Y. Sun, D. J. Hansford, *Materials Science and Engineering C*, vol. 28, pp. 353-358, 2008.



# MICROSHUTTERS FOR SPACE PHYSICS TIME OF FLIGHT APPLICATIONS

K. Brinkfeldt<sup>1</sup>, P. Enoksson<sup>2</sup>, B. Front<sup>2</sup>, M. Wieser<sup>3</sup>, M. Emanuelsson<sup>3</sup>, S. Barabash<sup>3</sup>

<sup>1</sup> Swerea IVF, Argongatan 30, 431 22 Mölndal, Sweden

<sup>2</sup> Chalmers University of Technology, Dept. Microtechnology and Nanoscience, 412 96 Gothenburg, Sweden

<sup>3</sup> Swedish Institute of Space Physics, Box 812, 981 28 Kiruna, Sweden

\*Corresponding author: Klas Brinkfeldt, +46 (0)31 – 706 60 82 , klas.brinkfeldt@swerea.se

**Abstract:** In present time-of-flight (TOF) mass and energy spectrometers in experimental space plasma physics applications, the resolution is limited by the fact that the particle to be measured loses part of its energy in the generation of the start pulse. To improve the resolution, a fast micromechanical shutter system to generate the start signal has been developed. The microshutter is included in the PRIMA (PRISma Mass Analyzer) ion detector on-board the Swedish PRISMA mission, which will be launched into low Earth orbit on June 15, 2010.

**Keywords:** Shutter, time-of-flight, MEMS

## 1. INTRODUCTION

Micro electro- mechanical systems (MEMS) are predicted to have a large impact in space technology and several groups have started to develop MEMS for different space applications [1]. Among the devices that are either under development or have already been launched into space micronozzles, micropropulsion systems [2], and variable emittance MEMS coatings for thermal control [3] can be mentioned. We intend to use fast MEMS shutters to improve measurements in (atomic) particle mass spectrometers.

Mass spectrometers have been flying on satellites from the beginning of the space era to study the Earth's and the other solar system object's interaction with the solar wind. Since, in the interaction region, the plasma is a mixture of particles of the solar wind (mostly protons) and planetary origin ( $O^+$ ,  $CO_2^+$ ,  $He^+$ ,  $O_2^+$  etc), mass resolving instrumentation is required. Modern space instruments rely on a so called time-of-flight technique (TOF) to measure particle mass or energy (below 1 MeV). The TOF technique measures the time between a START event, for example when electrons emitted as the particle penetrates a thin foil are collected to produce a START signal, and a STOP event when the particle impacts a detector. The velocity of the particle is then calculated and with prior knowledge of the particle energy (or mass), measured in for example an electrostatic analyzer earlier in the instrument, the mass (or energy) of the particle is readily calculated from the velocity.

The problem with TOF measurements today is that the particle velocity is affected in the foil or surface interaction for the START signal generation. This is particularly serious for measuring low energy neutrals, where pre-acceleration of the particles is not possible. To get around this problem a mechanical shutter can be used instead of the foil. Two examples of shutter-based TOF systems are illustrated in Fig. 1.

The basic idea of mechanical velocity filter systems has been tried in space. Experiments with slotted disc velocity filters based on two large

rotating discs with narrow slits cut into them was flown on a sounding rocket experiment in 1975 [4]. However, the system's large size, high power consumption, and high torque it would exert on a spacecraft made it impossible to use on satellites. With MEMS technology, lighter systems can be used and the idea can now work for space applications.

This paper describes the modeling of a MEMS shutter. In Section 2 an analytic model of a shutter element is described, Section 3 describes simulation results that verify the model, Section 4 describes the design and fabrication of the microshutters, and Section 5 describes packaging and integration of the microshutters into the PRIMA instrument.

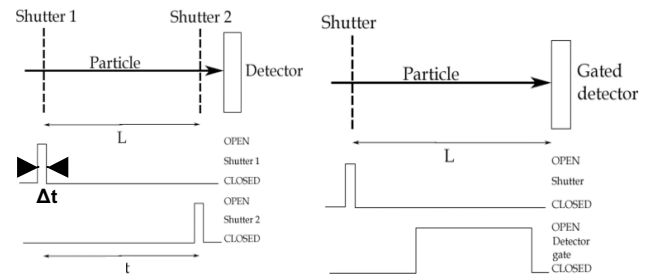


Figure 1: Two examples of using shutters in particle measurements. The sensor to the left operates as a pure velocity filter. Shutter 1 is open for a very short time, admitting particles to propagate across  $L$  to Shutter 2. If the particle has the correct velocity, Shutter 2 is open when it reaches the shutter. If not, the particle will not reach the detector. The example to the right is basically a TOF cell where the START signal comes from the shutter-open time. It uses a detector allowing multiple STOP signals. The shutter opens to let through particles of different velocities and the output is a velocity spectrum of the particles.

## 2. MODEL

The requirements in terms of open time,  $\Delta t$ , driving frequency,  $f$ , and transparency,  $\Omega$  (defined as the ratio of open to closed area times the ratio of open to closed time) of the shutter are listed in Table 1.

Table 1: Shutter timing requirements.

Parameter	Value
Open time, $\Delta t$	25 ns
Closed time, $t$	1700 ns
Driving freq., $f$	300 kHz
Transparency, $\Omega = (A_{\text{open}}/A)(\Delta t/t)$	$> 10^{-5}$

A preliminary design is based on a resonantly vibrating plate of dimensions  $105 \mu\text{m} \times 105 \mu\text{m} \times 10 \mu\text{m}$  attached at a frame via 4 beams. The beams are  $85 \mu\text{m}$  long and  $5 \mu\text{m}$  wide. The plate is perforated with narrow ( $1 \mu\text{m}$ ) slits and it overlays a fixed layer also perforated with narrow slits. As the vibrating plate moves over the fixed plate the shutter will open when the slits are aligned. Since the plate oscillates the closed area between the slits and the amplitude of oscillation defines the open and closed times.

The open and closed times can be determined from the velocity of the plate

$$v = \frac{d}{dt}((2y + s)\sin(2\pi f t)) \quad (1)$$

where  $y$  is the amplitude of the plate movement measured from the edge of the slit, and  $s$  is the slit opening dimension. If the opening occurs at the zero-transition velocity (where the velocity of the moving plate is highest,  $v_{\text{max}}$ ) the open time is calculated from

$$\Delta t = \frac{s}{2 \cdot v_{\text{max}}} \quad (2)$$

and the closed time from

$$t = \frac{1}{2f} - \Delta t \quad (3)$$

The shutter should be actuated electrostatically. For a parallel plate actuator the force generated is

$$F = \epsilon_0 \frac{AV^2}{2d^2} \quad (4)$$

where  $\epsilon_0$  is permittivity of free space,  $A$  is the plate area,  $V$  is the voltage, and  $d$  is the distance between the plates. The maximum displacement of the plate is

$$y = \frac{-Fl^3}{384E \frac{hb^3}{12}} \quad (5)$$

where  $l$  is the combined length of two beams (plate width excluded),  $E$  is Young's modulus,  $h$  is the plate thickness and  $b$  is the width of the beam crosssection. The displacement is assumed to be half that of one beam fixed at both ends with a central

load from [5]. Equation 5 describes the static (non-resonant) displacement. If the system is driven in resonance with low damping the amplitude of the oscillations (i.e. displacement) is multiplied with the Q-factor. Quality factors close to  $Q = 10^5$  has been reported for Si resonant systems at pressures around  $P = 10^{-5}$  torr [6]. Combining equations 4 and 5, an expression for the required voltage,  $V$ , to drive the plate in resonance with total amplitude of  $y_r$  is derived for a model with parallel plate actuation

$$V_{\text{parallel plate}} = \sqrt{\frac{384E \frac{hb^3}{12} \cdot y_r}{\epsilon_0 \frac{A}{2d^2} l^3 Q}} \quad (6)$$

The actuation mechanism can be realized using an electrostatic comb drive. Using comb drive actuation the driving voltage becomes

$$V_{\text{comb drive}} = \sqrt{\frac{384E \frac{hb^3}{12} \cdot y_r}{N_{\text{fingers}} \frac{\epsilon_0 h}{2d'} l^3 Q}} \quad (7)$$

Where  $N_{\text{fingers}}$  are the number of comb fingers and  $d'$  is the distance between the combs.

Using equations 1-3 it is derived that the timing requirements from Table 1 are realized at a frequency of  $f = 300$  kHz if the amplitude  $y_r = 25 \mu\text{m}$ . To achieve this amplitude the theoretical driving voltage should be

$$V_{\text{parallel plate}} = 233 \text{ V}$$

$$V_{1 \text{ finger}} = 178 \text{ V}$$

$$V_{2 \text{ finger}} = 126 \text{ V}$$

$$V_{3 \text{ finger}} = 103 \text{ V}$$

In the next section simulation results that verify the theoretical model are described.

### 3. MODEL VERIFICATION

The plate design has been simulated in COMSOL (v. 3.2) to (1) find the eigenfrequency of the desired oscillation mode and (2) to verify the electrostatic actuation voltages. COMSOL uses finite element calculations to find the mechanical response of a design to various stimuli (force, voltage, temperature, etc.) applied to one or more of its boundaries.

The mechanical response to electrostatic actuation were simulated in 2-D. This is allowed since the stiffness of the plate springs and the electrostatic force between plate and actuation electrodes increase equally with thickness and cancel each other out. Fig. 2 shows the results of electrostatic actuation on the plate for different actuation schemes including a Q-factor of  $Q =$

95 000. Because of the high Q-factor expected in the resonant vibration at low pressure [5] the actuation voltage can be lower than 100 V.

The 3-D eigenfrequency simulation results are shown in Fig. 3. The plate structure simulations included the four different models of actuation used previously. The eigenfrequencies for all models are close to the target 300 kHz, with the fingered comb

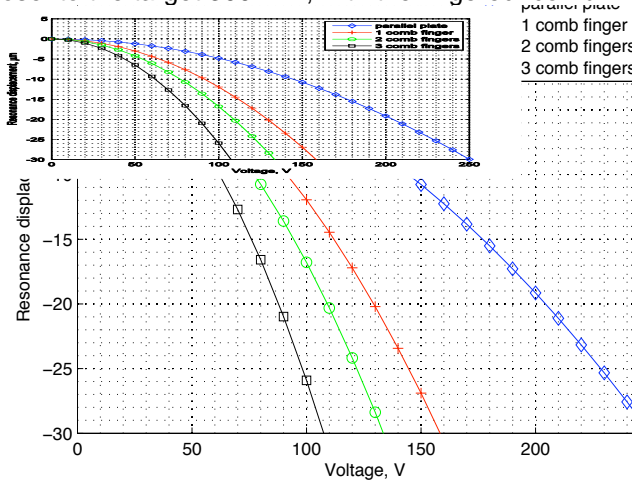


Figure 2: Estimated displacement for different actuation designs at different voltages. Resonance is assumed with a Q-factor of  $Q = 95\,000$ .

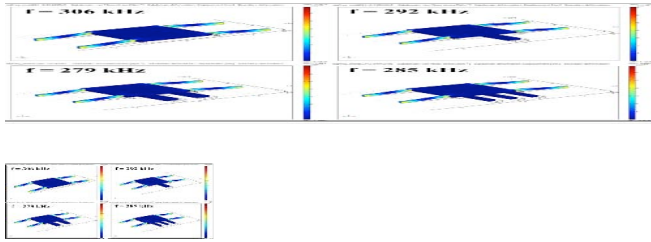


Figure 3: Eigenfrequency simulations of a  $105\,\mu\text{m} \times 105\,\mu\text{m}$  plate structure with different actuation drive. The top left example is actuated via a parallel plate drive, while the others have comb drives of varying size. The resonance frequency for the different models are indicated. In all models the mode shown is the fundamental mode.

drive models slightly lower because of the extra mass added by the finger(s). It should be noted that the 3-fingered model has smaller finger dimensions that actually represents lower added mass than the 2-fingered model, which has also resulted in a higher resonant frequency. It should also be noted that the  $1\,\mu\text{m}$  slits are not included in the simulations. Inclusion of the slits has two effects. It makes the plate structures less stiff, which causes the eigenfrequency to decrease, but the plate mass is also reduced, which causes the eigenfrequency to increase. Simulations of the parallel plate actuated

structure with three  $90\,\mu\text{m} \times 1\,\mu\text{m}$  slits separated by  $30\,\mu\text{m}$  showed that the eigenfrequency increases from 306.1 kHz to 308.6 kHz, which indicates that the latter of the two effects above dominates.

The active area,  $A$ , of one chip is  $2\,\text{mm} \times 8\,\text{mm} = 16\,\text{mm}^2$ . This area is filled with plate structures. The number of plate structures that fit into the active area depends on the actuation design. The parallel plate actuated devices does not require as much area as the comb drive devices, which results in less plate structures (270 compared to 342) within the active area and consequently a smaller open area,  $A_{\text{open}}$ . The transparency of the different designs is

$$\Omega_{\text{parallel plate}} = \frac{A_{\text{open}}}{A} \cdot \frac{\Delta t}{t} = 2.83 \cdot 10^{-5} \quad (8)$$

$$\Omega_{\text{comb drive}} = 2.23 \cdot 10^{-5}$$

provided the timing goals of open time  $\Delta t = 25\,\text{ns}$  and closed time,  $t = 1700\,\text{ns}$  are met. Both designs meet the requirement of  $\Omega > 10^{-5}$  from Table 1.

## 4. DESIGN AND FABRICATION

The microshutters were fabricated in the MC2 Nanofabrication Laboratory at Chalmers University of Technology. The process plan included more than 20 more or less complicated steps and required the use of 9 photolithographic masks. The finished devices consisted of a Silicon-On-Insulator (SOI) wafer with a device thickness of  $13\,\mu\text{m}$ , buried oxide thickness of  $3\,\mu\text{m}$ , and handle thickness of  $300\,\mu\text{m}$ . Fig. 4 is a conceptual view of the different layers in the finished chip.

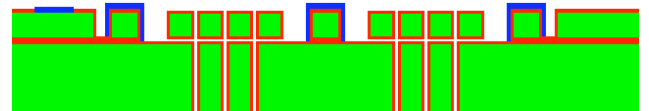


Figure 4: Conceptual view of the fabricated device. The device, buried oxide and handle layers of the fabricated Silicon-On-Insulator (SOI) is shown.

The shutter chip design is complicated by several requirements. The mechanical vibration, temperature range, and radiation tolerance requirements usually associated with space hardware are not of major concern because of the low mass, inherent mechanical properties and small temperature expansion of silicon, and simplicity of the electronics.

## 5. PACKAGING AND INTEGRATION

The chips were glued to a printed circuit board, wirebonded and an aluminium lid was fitted to protect the wirebonds. Holes in the printed circuit board and the aluminium lid allowed for particles to pass through the shutter area.

The microshutter was then integrated in the PRIMA instrument. The microshutter is positioned in

the TOF section behind the electrostatic energy analyzer. On the finished microshutters it was found that the resonance frequency differed between individual shutter elements. The reason was small (nano scale) variations of the dimensions in the structures. This made electrostatic driving of the shutters impossible and in the flight model the microshutters are driven externally by mechanically vibrating the entire chip.

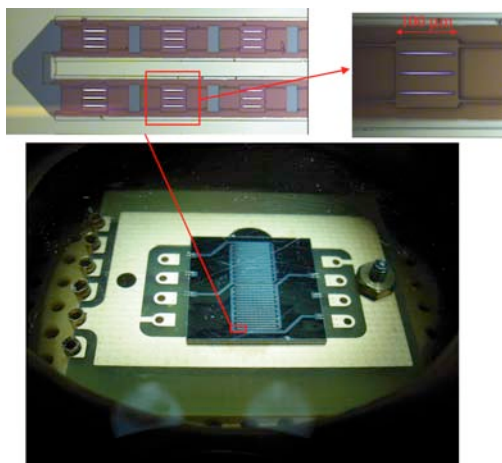


Figure 5: some of the shutter elements in the finished design and the chip mounted on the printed circuit board. The aluminium lid has been removed.

Fig. 5 shows some of the shutter elements and the chip mounted on the printed circuit board.

Fig. 6 shows a conceptual view and Fig. 7 shows a photograph of the integrated microshutter device inside the PRIMA flight model. The PRIMA instrument is scheduled to be launched on-board the Swedish PRISMA mission on June 15, 2010.

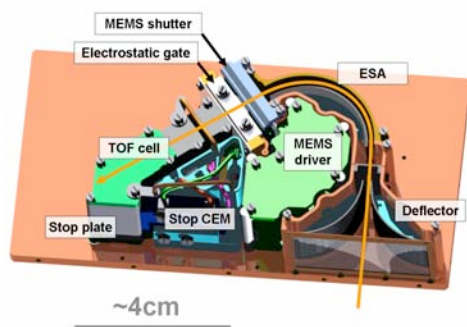


Figure 6: A conceptual view of the PRIMA instrument.



Figure 7: A photograph of the microshutter device integrated into the particle path of the PRIMA instrument.

## 5. CONCLUSIONS

Modelling, fabrication, and integration of a microshutter device into the TOF-based ion detector PRIMA have been described. The detector will be launched on the Swedish PRISMA technological demonstrator mission on June 15, 2010.

## REFERENCES

1. Mehregany M. and S. Roy, in *Microengineering aerospace systems*, Editor H. Helvajian. The Aerospace Press and the American Institute of Aeronautics and Astronautics, Los Angeles, CA 1999, pp. 1-28
2. Köhler J., J. Bejhed, H. Kratz, F. Bruhn, U. Lindberg, K. Hjort and L. Stenmark, *Sensors and Actuators*, A97-98, 2001, pp 587-598.
3. Farrar D., W. Schneider, R. Osiander, J. L. Champion, A. G. Darrin, D. Douglas and T. D. Swanson, *Thermal and Thermomechanical Phenomena in Electronic Systems*, 2002, pp 1020-1024
4. Moore J. H. and C. B. Opal, *Space Sci. Inst.*, 1, 1975, pp 377-386.
5. Young, W. C., in *Roark's formulas for stress and strain*, sixth ed., McGraw-Hill, Singapore, 1989.
6. Legrand B. E. Quevy, B. Stefanelli, D. Collard and L. Buchaillot, *Rev. Sci. Instr.*, 73 (12), 2002, pp 4393-4395



# STUDY OF INJECTION MOLDED SURFACE FEATURES IN TERMS OF LIGHT REFLECTION, WETTABILITY AND DURABILITY

S. Kuhn, A. Burr, M. Kübler, M. Deckert, and C. Bleesen

Heilbronn University, Mechatronics and Micro System Engineering, PIK, D-74177 Heilbronn, Germany

**Abstract** — In this paper we investigate the replication qualities of sub-micron features in the injection molding process. In order to change the surface properties considerably, high-aspect features are molded by using a variothermal mold temperature control system. The molded surface features are characterized with the atomic force microscope and their effects on the macroscopic surface in terms of reflection, wettability and durability are studied. This leads to successful implementation in applications in which the optical appearance in terms of gloss and reflection and the water repellence in terms of drag flow and adhesion is of importance. Furthermore, due to the sensitivity of the surface features molded in the injection molding process their durability is studied by a scratch test with a diamond tip.

**Keywords:** Injection molding, micro-features, variothermal mold temperature control system

## 1 - Introduction

The inclusion of functionalities onto the surface and the scaling down of components is not only a decisive key technology for MEMS devices but also for other consumer products. Especially the effects of injection molded micro surface features on surface properties can be employed in a wide range of possible applications. The self-cleaning surface of the lotus blossom, the non-reflecting cornea of moths' eyes, tribological and hydrodynamic performance of scales on beaked salmon and shark skins are only some examples from nature [1-4]. Depending on the surface effects, the dimensions and shapes of the surface features distinguish significantly.

Surface features can be applied in form of specific functional features e. g. optical gratings, fluidic channels and in form of more general surface topographies to modify optical, repellent and adhesion properties. However, technical barriers in manufacturing processes and the diverse effects of features on the surfaces may limit their use in several applications. The injection molding process is a typical mass production process which involves a replication process where identical devices with high reproducibility are produced with a mold and a master containing the negative of the surface features. However, in order to mold the high-aspect features with lateral sizes below 10  $\mu\text{m}$  completely, a dynamical variothermal mold temperature control system is necessary. In the variothermal injection molding cycle the mold wall temperature is actively changed in the course of a production cycle [5]. The mold wall temperature is increased considerably before

the filling stage starts. To maintain a short cycle time, the mold wall temperature is reduced considerably after the filling stage (see Fig.1). In order to avoid any freezing in the filling stage and to obtain the best filling results of the surface features, the mold temperature during the filling stage should be well above the polymer softening temperature. If the mold wall temperature approaches or even exceeds the glass-transition temperature of amorphous molding materials, the parts might adhere to the tooling surface. Further, the demoldability of the surface features decreases with increasing feature heights (roughness) and steeper feature walls.

The temperature needs to be lowered depending on the molding material, the part geometry and the capacity of the tempering system used (Fig. 1 "mold wall temperature during the ejection stage"). It is essential to aim for the optimal compromise concerning the required part quality and the shortest possible cycle time.

The parts produced with variothermal injection molding have outstanding properties in comparison to those produced with conventional injection molding [5]:

- higher surface quality (e. g. higher crystallinity),
- reduced molecular orientation (for optical elements),
- micro- and nano-surface features with high aspect ratio.

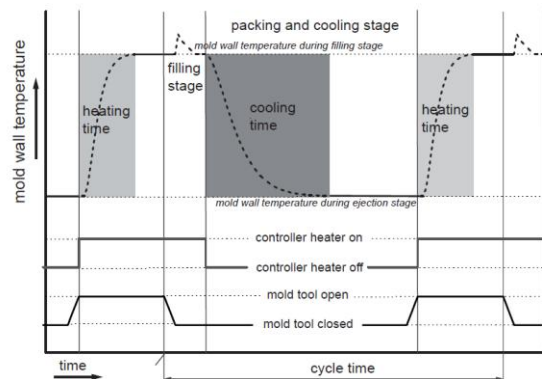


Figure 1: Schematic temperature profile on the mold wall during the variothermal injection molding process

The micro-features molded on the mold wall are investigated in dependence of the mold wall temperature during the filling stage (see Fig. 1). The replication qualities achieved at different micro-features and molding materials are characterized with an atomic force microscope (AFM), a spectrometer and a goniometer. Furthermore, the mechanical resistance of the micro-features molded in different materials has been compared.

## II - Experimental Details

Macroscopic parts including micro-features have been produced in the injection molding process (Fig. 2) and their effects in different molding materials are studied.

Using Microsystems technologies, the negative surface features are first applied to the mold wall by either additive or subtractive structuring processes. Another common process is LIGA (Lithography, Electroplating, and Molding), used for the manufacturing of Digital Versatile Discs (DVD) or Blu-ray Discs. For further details see [6].

In this study, a silicon substrate is used as mold wall with periodic v-groove micro-features. They are produced in a conventional KOH deep-etch process using  $\langle 100 \rangle$  wafers. Another kind of structured mold inserts which is used consists of random features. Titanium aluminum nitride TiAlN or titanium dioxide TiO<sub>2</sub> layers are precipitated on steel inserts using a reactive magnetron sputtering technique. The AFM-topography in Fig. 4 shows faceted surface features which occur due to the given  $\langle 100 \rangle$ -facets of the cubic crystal structure of TiAlN. Alternatively, higher aspect-ratios can be obtained by a tetragonal crystal system as it exists for example in TiO<sub>2</sub> layers. [7]

The masters containing the features are integrated in a molding tool with a form-fitting heating and cooling unit behind them (see Fig. 2a). Minimal heating capacities of the tempering units are intended to enable an economical production of the parts in the variothermal injection molding process. The experimental investigations take place on a 50 tone hydraulic injection molding machine. With the programmable in- and outputs of the machine, the mold wall temperature during the variothermal injection molding process is controlled by the heating and cooling units (Fig. 2a). For a short cooling time the cooling unit is permanently cooling while the heating unit controls the different temperature levels during the variothermal injection molding process (see Fig. 1).

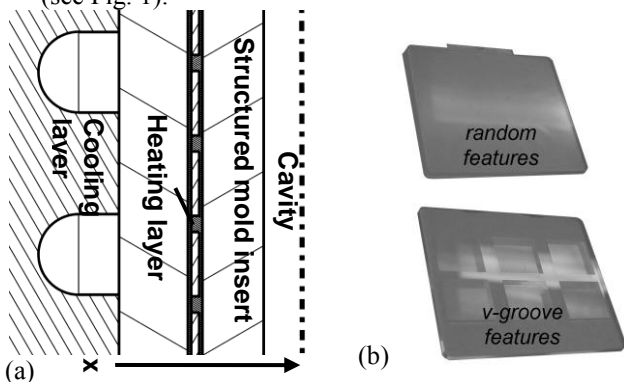


Figure 2: Experimental investigation of the variothermal injection molding process. (a) Cross-sectional view of the mold insert containing the heating and cooling unit (b) picture of the molded parts containing the surface features

The micro-features molded are characterized with an atomic force microscope (AFM). For measuring sub-micron features a high-aspect cantilever is used. All the measurements are performed in ambient air after two

day's storage at room temperature using the SCANControl C from Bruker Nano. The surface topographies are measured on different selected locations on the molded parts and they are compared to the master features.

The materials used for this investigation are polycarbonate (PC Makrolon DP 1265-1) from Bayer, polymethylmethacrylat (PMMA Plexiglas 7N, 8N) from Evonik and polypropylen (PP Hostacom) from LyondellBasell. The first two materials mentioned are amorphous thermoplastic materials; the latter one is a semi-crystalline thermoplastic material.

To investigate the molded surface features in terms of wettability a goniometer is used. An air cushion single-channel pipette (Transferpette S 0,1-10 $\mu$ l) from Brand is used to place a water droplet onto the molded surfaces. The pipette can load aqueous solutions between 0.1-10  $\mu$ l in a precision of  $\pm 1\%$ . Therefore, 1-3  $\mu$ l droplets of deionized water were placed on the structured surface-air side of the samples at ambient conditions. The contact angles of the water droplet with the molded surfaces are measured with a built up goniometer. Furthermore, the optical appearance of the molded surfaces containing features in size below ten micrometers distinguishes significantly in terms of haze and glossy. Therefore, a spectrometer from Avantes (AVS-USB 2000) is used to measure the direct reflection of the molded surfaces. The spectrometer has a detector with a CCD including 2048 pixels. At a spectral range from 200 nm – 1100 nm the resolution is 0.44  $\mu$ m/Pixel. A fiber optic cable with the sensor from OPTO con (FCR-7 VIS-200) is used.

## III – Heat Conduction Model

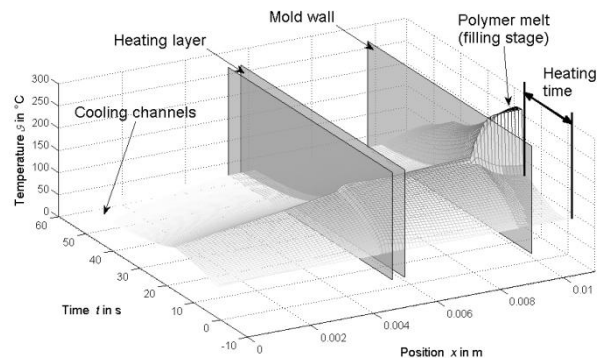


Figure 3: One-dimensional heat conduction model from the cross-sectional view in Fig.2 during the variothermal injection molding cycle (right parting plane: mold wall; left parting planes: heating layer)

The injection molding is only economical for large production quantities. Thus, the cycle time to produce the parts is of great importance. The cycle time depends mainly on the cooling time of the part. The cooling time is determined by the time until the part is below its demolding temperature and can be ejected. Consequently, a transient one-dimensional heat conduction model is used in order to get the temperature profile in the molded part perpendicular to the mold wall (see Fig. 3).

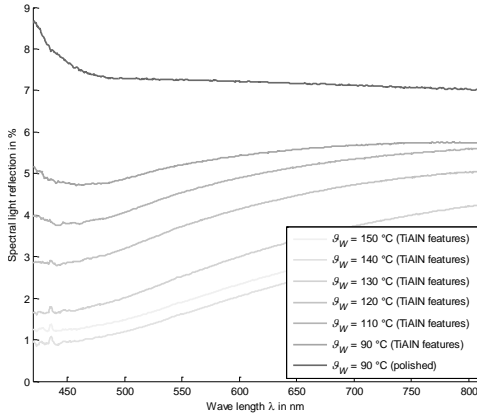


Figure 9: Spectral light reflection on PMMA Plexiglas 8N parts containing TiAlN surface features on both sides

Fig. 9 shows the spectral light reflection of the molded PMMA Plexiglas 8N parts. Due to the light transmission to the backside of the parts both interfaces have been taken into account. Therefore, the TiAlN features are molded on both sides in the injection molding process. In Fig. 10, the mean light reflection in the spectral range from 411-778 nm is plotted for each molding material in dependence of the mold wall temperature. As a result, with increasing surface roughness the light reflection decreases.

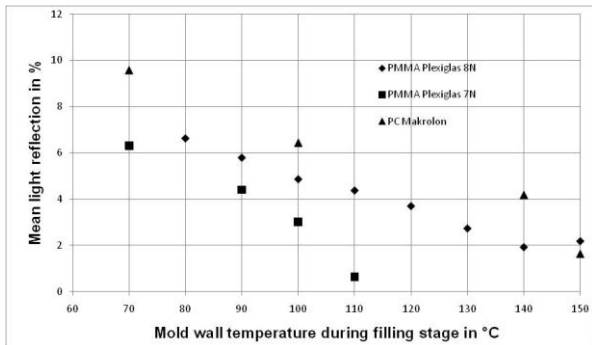


Figure 10: Mean light reflection in the spectral range from 411-778 nm of parts molded in the variothermal injection molding cycle containing TiAlN surface features (see Fig. 2)

In Fig. 11, both the increasing height of the random features and of the v-groove features reduces the direct reflection. However, the v-groove features with 10  $\mu\text{m}$  periodicity reduce both the direct light reflection and the light transmission. Therefore, on surfaces containing v-grooves like in Fig. 4a the visible light is mainly scattered and diffracted.

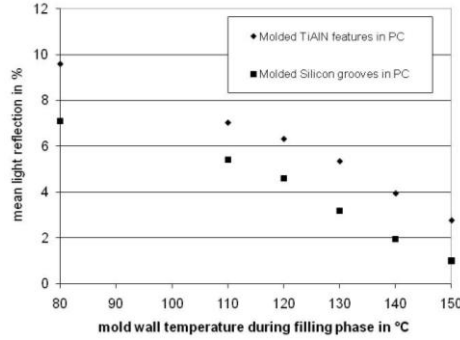


Figure 11: Mean light reflection in the spectral range from 411-778 nm of parts molded in the variothermal injection molding process

A further important property is the wettability of the molded surfaces. It depends on several factors including roughness, preparation and cleanliness of the surface. The static contact angle of a water droplet is used in order to study the wetting of the molded surfaces.

Young's equation determines the contact angle of smooth surfaces:

$$\cos \theta_Y = \frac{\gamma_{sv} - \gamma_{ls}}{\gamma_{lv}} \quad (3)$$

The surfaces tensions at liquid/vapor  $\gamma_{lv}$ , solid/vapor  $\gamma_{sv}$  and liquid/solid  $\gamma_{ls}$  interface results in the contact angle  $\theta_Y$ . The contact angle of a droplet in contact with molded surface features can be determined by Wenzel [15]:

$$\cos \theta_W = r \cos \theta_Y \quad (4)$$

This model implies that smooth hydrophobic (hydrophilic) surfaces become more hydrophobic (hydrophilic) if the features are imparted.  $r$  is the ratio between the actual surface area and the projected surface area. Wenzel's model (Eq. 4) assumes a homogenous interface due to the complete absorbing of a liquid in the structured surface. If the liquid may not penetrate between the surface features molded (resulting trapped air pockets), this leads to a composite solid-liquid-air interface. Cassie and Baxter (1944) extended Wenzel equation for the composite interface [16].

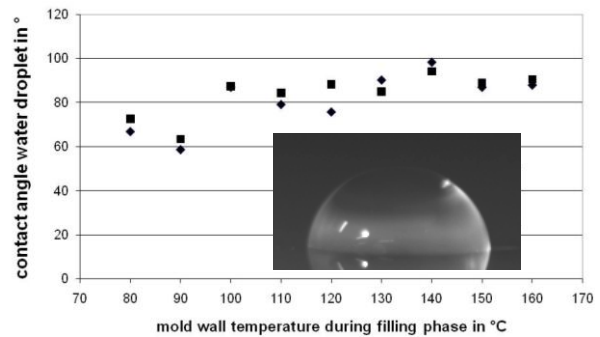


Figure 12: Measured contact angle of a water droplet (3  $\mu\text{l}$ ) on the PMMA Plexiglas 8N parts containing TiAlN features

Fig. 12 shows that the TiAlN features in Fig. 4 do not significantly influence the contact angle of the water droplet. However, the TiAlN surface features molded in PP have a high impact on the contact angle of the water droplet (see Fig. 13).

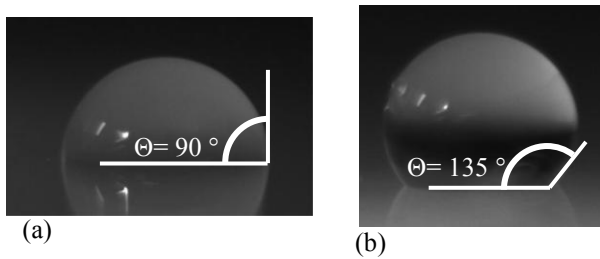


Figure 13: Water droplet (3  $\mu$ l) resisting on a PP part (a) smooth surface (b) TiAlN surface features

The TiAlN features as shown in Fig. 4b increase the contact angle of the water droplets even if it is a hydrophilic material as shown in Fig. 12. This might result from air pockets trapped inside holes.

In contrast, if a droplet resists on PC and PMMA substrates containing one-dimensional oriented periodic v-grooves (Fig. 4a), the droplet spreads in direction of the grooves. Trapped air pockets might be prevented which leads to a homogeneous interface proposed by Wenzel (Eq. 4). The contact angle determined collateral to the grooves is about 60° whereas the contact angle determined perpendicular to the grooves is about 80°. The grooves molded in PP do not significantly affect the contact angle of the water droplet. The contact angle of a water droplet collateral and perpendicular to the grooves is nearly the same as on smooth surfaces (see Fig. 13a). This behavior corresponds to Wenzel's model in Eq. 4, where the roughness factor  $r$  has less influence on materials like PP ( $\Theta_Y = 90^\circ$ ).

#### D. Mechanical resistance of molded surface features

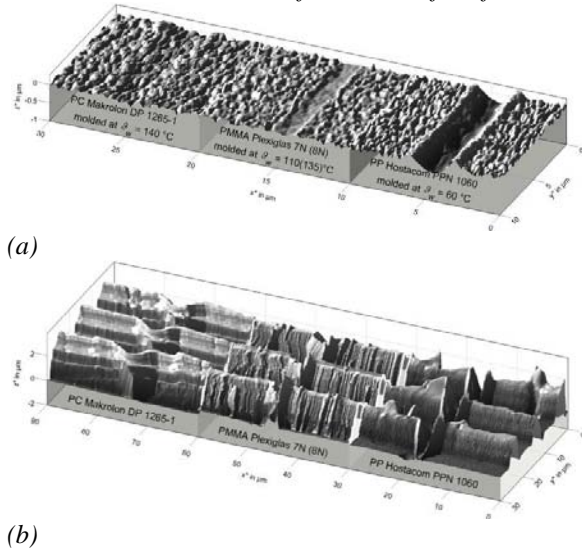


Figure 14: Scratch on the molded surface structures with a diamond tip (load tip  $F_N = 1.2$  mN; velocity tip  $v = 200$   $\mu$ m/sec; tip angle = 90°; tip radius = 1.2  $\mu$ m) at room temperature (a) random features and (b) perpendicular to the molded v-grooves

The mechanical resistance of the molded surface features is investigated with the help of a diamond tip. On the surface of the three molded materials different

behavior can be observed if the same scratch condition is applied (see Fig. 14).

The smooth PP material shows deep scratch marks whereas at both amorphous materials PC and PMMA the scratch on the surface is less marked.

Indeed, PP enables high replication qualities of the surface features at low mold wall temperatures. However, the mechanical resistance of the surface features is weak compared to PC and PMMA. PMMA shows a high durability, no deformation appears on the scratch mark apart from brittle fractures. In PC only deformation of the structures in scratch direction appears.

It has to be considered that the scratch marks were measured after two days with the AFM and in the meantime relaxation processes on the polymer surface have taken place.

#### V - Conclusion

In this study, the filling heights of micro-structures on the mold wall during the injection molding process have been investigated. The mold wall temperature, which is the most important process parameter during the filling and packing stage, was actively changed. On the example of two different surface features below 10  $\mu$ m it could be shown that the replication qualities depend significantly on the glass-transition temperatures and the molecular mass of the amorphous molding materials used. The replication qualities at an optimized variothermal injection molding process are investigated in dependence to the mold wall temperatures during the filling stage for each molding material. The optical appearance of the surface features increases with increasing mold wall temperatures. But the optical effects of the v-grooves features differ compared to the random features. Furthermore, a water droplet which resists on the molded surfaces is significantly influenced by these structures. However, further details like intrinsic surface properties of the molding materials and trapped air pockets have to be taken into account. Finally, the mechanical resistance of the molded surface features has been compared by a mechanical scratch test. As a result, the features can be easily molded at low mold wall temperatures when using PP, but the low surface hardness leads to low durability of the features molded. PP is intrinsically more hydrophobic compared to PC and PMMA. Consequently, the influence of the features molded in PP differ compared to the features molded in PC and PMMA.

#### References

- [1] M. Nosonovsky and B. Bhushan, *Advanced Functional Materials*, vol. 18, pp. 843–855, 2008
- [2] D. Kim, J. Kim, H. C. Park, K. H. Lee and W. Hwang, *Journal of Micromechanics Microengineering*, vol. 18, 015019 (5pp), 2008
- [3] Y. Lee, S. H. Park, K. B. Kim and J. K. Lee, *Advanced Materials*, vol. 19, pp. 2330–2335, 2007
- [4] S. M. Lee, H. S. Lee, D. S. Kim and T. H. Kwon, *Surface and Coatings Technology*, vol. 201, pp.



- 553–559, 2006
- [5] E. Bürkle, A. Burr, A. Müller and M. Kübler, *Kunststoffe International*, vol. 10, pp. 144-148, 2007.
  - [6] M. S. Despa, K. W. Kelly and J. R. Collier, *Microsystem Technologies*, vol. 6, pp. 60-66, 1999
  - [7] F. Burmeister, C. Kohn, R. Kübler, G. Kleer, B. Bläsi and A. Gombert, *Surface and Coatings Technology*, vol. 200, pp. 1555-1559, 2005
  - [8] T. Osswald and J. P. Hernández-Ortiz, *Carl Hanser Verlag*, Munich, 2006
  - [9] W. B. Young WB, *Microsystem Technologies*, vol. 11, pp. 410-415, 2005
  - [10] K. Mönkkönen, J. Hietala, P. Pääkkönen, E. J. Pääkkönen, T. Kaikuranta, T. Pakkanen and T. Jääskeläinen, *Polymer Engineering and Science*, vol. 42, pp. 1600-1608, 2002
  - [11] L. Yu, L. J. Lee and K. W. Koelling, *Polymer Engineering and Science*, vol. 44, pp. 1866-1876, 2004
  - [12] Y. Ono, Y. Kimura, Y. Ohta and N. Nishida, *Applied Optics*, vol. 26, pp. 11142-6, 1987
  - [13] D. H. Raguin and G. M. Morris, *Applied Optics*, vol. 32, pp. 2582-2598, 1993
  - [14] Y. Kanamori, M. Sasaki and K. Hane, *Optics Letters*, vol. 24, pp. 1422-1424, 1999
  - [15] P. G. de Gennes, F. Brochard-Wyart, and D. Quéré, *Capillarity and Wetting Phenomena: Drops, Bubbles, Pearls, Springer*, 2004
  - [16] Y. C. Jung and B. Bhushan, *Nanotechnology*, vol. 17, pp. 4970-498

## SIMULATION STUDIES OF PARAMETRIC AMPLIFICATION IN BIO-INSPIRED FLOW SENSORS

H. Droogendijk<sup>1</sup> and G. J. M. Krijnen<sup>1</sup>

<sup>1</sup>University of Twente, MESA<sup>+</sup> Research Institute; P.O. Box 217, 7500 AE, Enschede, The Netherlands

**Abstract** — In this paper the effect of parametric amplification in MEMS-based air-flow hair-sensors is studied. With an AC-voltage controlled torsional stiffness the rotation of the hair can be influenced. With the appropriate amplitude, phase and frequency, the rotation of the torsional hair system is increased with respect to the case without parametric amplification. Therefore, parametric amplification is identified as a method to improve the performance of MEMS-based hair air flow sensors.

**Keywords:** Cricket hair, Bio-inspired, Flow sensor, Non-linear effects, Parametric amplification

## I – Introduction

Inspired by crickets (figure 1) and their exquisite perception of flow phenomena down to thermal noise levels [1], artificial hair-based flow sensors have been developed successfully in our group [2]. The realization of array structures and improvement of fabrication methodologies have led to better performance, making it possible to measure (illustrated in figure 2) sub-mm/s flow velocities [3]. To further improve the performance of these artificial hair flow sensors, we propose to make use of non-linear effects. In nature a wide range of such effects exist (filtering, parametric amplification, etc.) giving improvements in sensitivity, dynamic range and selectivity.

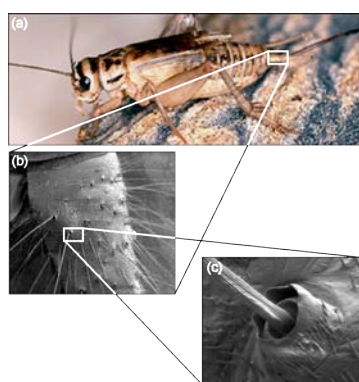


Figure 1: *Flow perception by crickets (SEM pictures courtesy of Jérôme Casas, Université de Tours).*

## II – Parametric amplification

Parametric amplification (PA) is based on a nonlinear response of a material or structure to excitation. Due to this nonlinearity the simultaneous presence of more than one excitation signal will in general lead to a com-

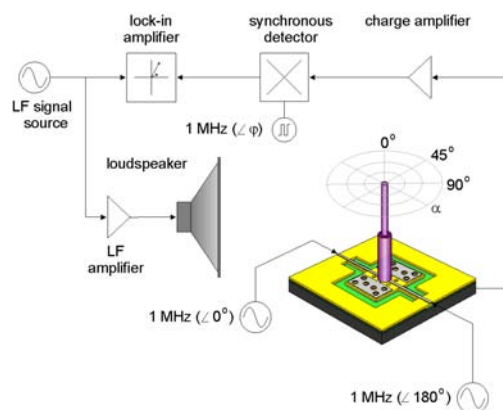


Figure 2: *Performing flow measurements with artificial hair-sensors.*

plex interaction where amplitude, frequency and phase of each of the excitatory signals play important roles in the entanglement of the signals and the overall response. In the case of our capacitive hair-based flow sensors, which are in fact electrostatic transducers, we have the freedom to apply electrostatic torques in addition to the flow driven torques. The former causes the flow-sensing capabilities of the sensor to be modulated and this can be considered as adaptation of the sensor performance. By controlling the mechanical properties of the hair sensory system in time an interesting dynamical system can be obtained. It is shown that with the appropriate choice of parameters the input is amplified by the system compared to the case without parametric amplification [4]. Generally, with a well-defined configuration one can achieve filtering and selective gain of the system.

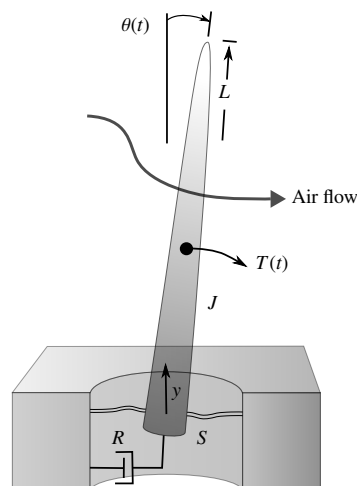


Figure 3: *Model of a flow sensing hair [5].*

To investigate how this principle can be used in our bio-inspired hair sensor (figure 3), we consider the second-order differential equation describing its behavior, where  $J$  is the moment of inertia,  $R$  the torsional resistance,  $S$  the torsional stiffness,  $T$  the drag torque amplitude due to oscillating air flow with angular frequency  $\omega_a$  ( $=2\pi f_a$ ):

$$J \frac{d^2\theta}{dt^2} + R \frac{d\theta}{dt} + S(t)\theta = T_0 \cos(\omega_a t) \quad (1)$$

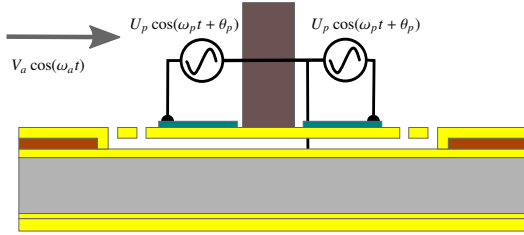


Figure 4: Modulating the torsional spring stiffness in time.

Note that  $J$  and  $R$  may contain contributions due to air flow viscous and inertial effects. Normally the torsional stiffness is given by a spring constant. But it may well be modulated in time applying an AC voltage on the two capacitor plates of the sensors. Assume this signal has amplitude  $U_p$ , frequency  $\omega_p$  ( $=2\pi f_p$ ) and phase  $\phi_p$  (illustrated in figure 4):

$$S(t) = S_0 - \frac{1}{4} U_p^2 \frac{d^2 C}{d\theta^2} - \frac{1}{4} U_p^2 \cos(2\omega_p t + 2\phi_p) \frac{d^2 C}{d\theta^2} \quad (2)$$

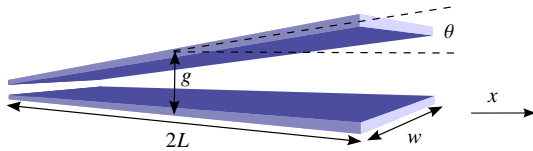


Figure 5: Tilted rectangular capacitor.

The capacitance  $C$  is calculated from the sensor geometry, which is considered as a tilted rectangular plate (figure 5). For this configuration,  $2L$  is the length of the membrane,  $w$  is the width of the membrane,  $g$  is the distance between the (rotational) center of the membrane and the substrate and  $\theta$  is the rotation angle. The capacitance  $C(\theta)$  as function of the rotation angle is:

$$C(\theta) = \int_{-L}^L \frac{\epsilon_0 w \cos(\theta)}{g - x \sin(\theta)} dx \quad (3)$$

Approximation of its solution by a second order Taylor expansion leads to:

$$C(\theta) \approx \frac{\epsilon_0 w 2L}{g} \left( 1 + \frac{1}{6} \left( \frac{2L^2}{g^2} - 1 \right) \theta^2 \right) + O(\theta^4) \quad (4)$$

where the first and third order in  $\theta$  drop because of symmetry of the capacitor geometry. Using this approximation, the value for  $\frac{d^2 C}{d\theta^2}$  in equation 2 can be calculated for small values of the rotation angle  $\theta$ .

An analytical solution for equation 1 with  $S(t)$  given by equation 2 is hard to obtain. According to [6] the solution of this differential equation contains an infinite series of odd harmonics with respect to the pump frequency  $\omega_p$ . Therefore, we use the Runge-Kutta 4 method from MATLAB to solve the differential equation numerically. In order to use this numerical method, the differential equation is converted to a set of linear first-order differential equations in state space:

$$\begin{bmatrix} \dot{\alpha}_1(t) \\ \dot{\alpha}_2(t) \end{bmatrix} = \begin{bmatrix} 0 & 1 \\ -\frac{S(t)}{J} & -\frac{R}{J} \end{bmatrix} \begin{bmatrix} \alpha_1(t) \\ \alpha_2(t) \end{bmatrix} + \begin{bmatrix} 0 \\ \frac{T_0}{J} \end{bmatrix} \mathbf{u}(t) \quad (5)$$

where

$$\theta(t) = \begin{bmatrix} 1 & 0 \end{bmatrix} \begin{bmatrix} \alpha_1(t) \\ \alpha_2(t) \end{bmatrix} \quad \mathbf{u}(t) = \cos(\omega_a t) \quad (6)$$

In these equations,  $\alpha_1(t)$  represents the rotation angle of the hair,  $\alpha_2(t) = \dot{\alpha}_1(t)$  is the angular velocity of the hair,  $\ddot{\alpha}_2(t) = \ddot{\alpha}_1(t)$  is the acceleration of the hair and the output  $\theta(t)$  is the rotation angle of the hair.

To determine the occurrence of parametric amplification experimentally the pump parameters need to be chosen judiciously. The hair sensor is suspended by two silicon nitride beams ideally allowing for torsional movement only. However, in practice the beams also have a vertical compliance due to finite stiffness in that direction, which is illustrated in figure 6.

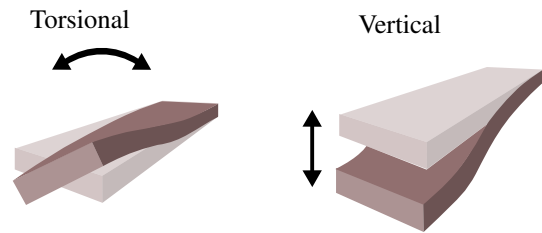


Figure 6: Two types of stiffness.

Since parametric amplification is implemented by applying voltages, leading to vertical forces and torques, the entire membrane structure also moves in the vertical direction. Using the Fourier transform method to determine the effect of parametric amplification on the gain at the flow frequency component  $\omega_a$  in the resulting spectrum, contributions from vertical movement (as a consequence from finite vertical stiffness) are undesired and should be minimized, especially at that frequency component.

### III – Simulation results

To perform the simulations in MATLAB, the data for the MEMS-based hair flow sensor from tabel 1 is used.

Table 1: Properties of a MEMS hair sensor.

Quantity	Symbol	Value	Unit
Torsional stiffness	$S$	$5.2 \cdot 10^{-9}$	N · m/rad
Torsional resistance	$R$	$1.68 \cdot 10^{-12}$	N · m/rad/s
Moment of inertia	$J$	$1.97 \cdot 10^{-16}$	kg · m <sup>2</sup>
Capacitor gap	$g$	600	nm
Capacitor width	$w$	90	μm
Capacitor length	$L$	95	μm

The initial values for the input air flow parameters and the AC voltage (which is denoted "pump") parameters, are listed in table 2. The drag torque calculations for  $T_0$  are based on 40 mm/s flow using Stokes' mechanical impedance for oscillating air flow [5].

Table 2: Simulation parameters.

Quantity	Symbol	Value	Unit
Drag torque amplitude	$T_0$	$4.69 \cdot 10^{-13}$	N · m
Flow frequency	$f_a$	80	Hz
Pump amplitude	$U_p$	1	V
Pump angle	$\phi_p$	0	degree
Pump frequency	$f_p$	80	Hz

The pump frequency  $f_p$  is chosen in such a way that the output signal does not contain a component of vertical movement at the air flow frequency  $f_a$ , using the relationship for the electrically generated force  $F_p$  in the vertical direction  $y$ :

$$F_p = \frac{1}{2} U^2 \frac{dC}{dy} = \frac{U_p^2}{4} \frac{dC}{dy} (1 + \cos(2\omega_p t + 2\phi_p)) \quad (7)$$

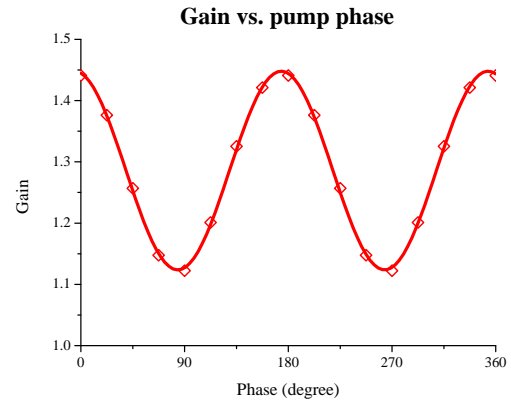
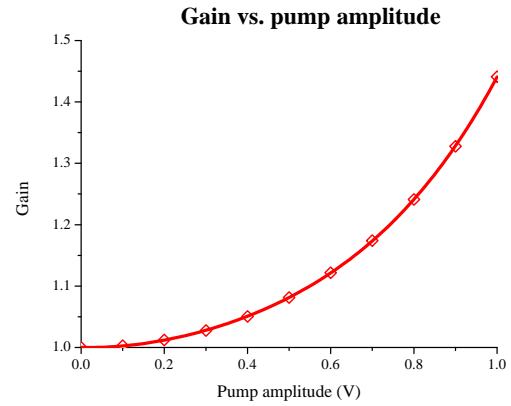
To state the effect of parametric amplification on the sensory system performance, the gain  $G$  is defined as the ratio of the amplitudes of the angular rotation with and without pump:

$$G = \frac{\theta_{0,\text{with pump}}}{\theta_{0,\text{without pump}}} \quad (8)$$

With the simulation parameters given, first the effect of the pump phase  $\phi_p$  with respect to the air flow frequency on the gain  $G$  is determined. The resulting plot is given in figure 7.

The effect of changing the pump phase  $\phi_p$  can be seen clearly, resulting in a gain varying from about 1.12 to 1.44. The sinusoidal shape can be explained as a spring that becomes weaker when the torque is large compared to the case that the spring is weak when the torque is small. Note that the case without parametric amplification has a gain of 1 ( $U_p = 0$ ).

Also, the pump amplitude  $U_p$  affects the strength of parametric amplification, which is also the case when applying electrostatic spring softening by a DC voltage.

Figure 7: Gain vs. pump phase  $\phi_p$ .Figure 8: Gain vs. pump amplitude  $U_p$ .

The relationship between the pump amplitude  $U_p$  and the resulting gain  $G$  is given in figure 8 for  $\phi_p = 0$ .

In this plot a non-linear relation between the pump amplitude  $U_p$  and gain  $G$  is observed, where a gain of about 1.44 is obtained at a pump amplitude of 1 V. The pump amplitude cannot be increased too much, because pull-in occurs when the voltage between the capacitor plates becomes too high.

Parametric amplification can lead to selective gain and thus additional filtering of the system, which is determined by investigating the relationship between the pump frequency  $f_p$  and the resulting gain  $G$  (figure 9).

From this plot we observe that at pumping at half the air flow frequency  $f_a$  the gain is increased a little (from 1.29 to 1.31) with respect to pump frequencies  $f_p$  in the same region, but especially when pumping with the same frequency  $f_p$  as the air flow frequency  $f_a$  (from 1.29 to 1.44, which is about 12%). From equation 2 this means that varying the torsional stiffness  $S(t)$  with twice the frequency of the incoming air flow ( $f_p = f_a$ ) leads to significant gain  $G$ . Other frequencies



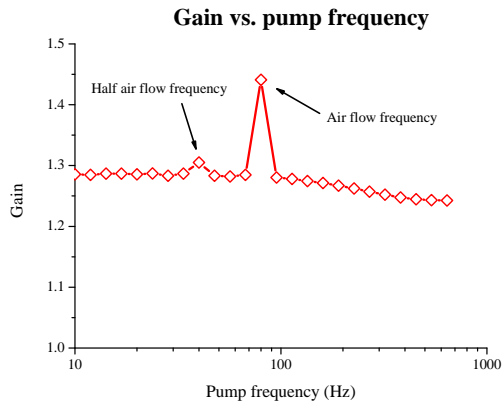


Figure 9: Gain vs. pump frequency  $f_p$ .

also show a gain larger than 1, as a consequence of non-synchronized spring softening and the presence of the DC-component in the voltage squared term (see equation 2).

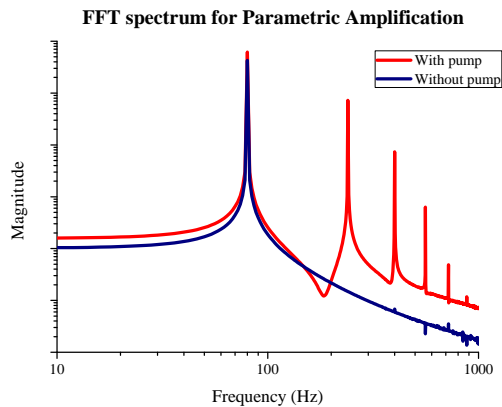


Figure 10: FFT spectrum of the rotation angle with (red curve) and without (blue curve) presence of a pump signal.

By inspection of the angular rotation spectrum in the presence of the pump signal, we observe the occurrence of odd harmonics in the solution (figure 10). Therefore, when performing measurements the gain due to parametric amplification should be determined based on the strength of the flow frequency component by means of a Fourier Transform rather than using the RMS-value for the entire spectrum (also containing undesired vertical movement).

#### IV – Conclusions

By exploiting the non-linearity of our artificial hair sensory system for measuring oscillating air flow, the performance of these sensors can be further improved. Parametric amplification is identified to be a useful

mechanism for improving the flow perception and for allowing filtering by selective gain of the sensor system, using appropriate pump amplitude, phase and frequency.

#### References

- [1] Tateshi Shimozawa, Jun Murakami, and Tsunekazu Kumagai. *Sensors and Sensing in Biology and Engineering*, chapter 10. Cricket Wind Receptors: Thermal Noise for the Highest Sensitivity Known, pages 145–156. Springer, Wien, Austria, 2003.
- [2] M. A. Dijkstra, J. J. J. van Baar, R. J. Wiegerink, T. S. J. Lammerink, J. H. de Boer, and G. J. M. Krijnen. Artificial sensory hairs based on the flow sensitive receptor hairs of crickets. *Journal of micromechanics and microengineering*, 15:S132–S138, July 2005.
- [3] C. M. Bruinink, R. K. Jaganatharaja, M. J. de Boer, J. W. Berenschot, M. L. Kolster, T. S. J. Lammerink, R. J. Wiegerink, and G. J. M. Krijnen. Advancements in technology and design of biomimetic flow-sensor arrays. In *22nd IEEE International Conference on Micro Electro Mechanical Systems (MEMS 2009)*, Sorrento, Italy, number CFP09MEM-USB, pages 152–155, Piscataway, January 2009. IEEE Computer Society Press.
- [4] Dustin W. Carr, Stephane Evoy, Lidija Sekaric, H. G. Craighead, and J. M. Parpia. Parametric amplification in a torsional microresonator. *Applied Physics Letters*, 77(10):1545–1547, September 2000.
- [5] T. Shimozawa, T. Kumagai, and Y. Baba. Structural scaling and functional design of the cercal wind-receptor hairs of cricket. *J. of Comp. Physiol. A*, 183:171–186, 1998.
- [6] G. Floquet. Sur les équations différentielles linéaires à coefficients périodiques. *Annales scientifiques de l'É.N.S.*, 12:47–88, 1883.

## ADSORPTION STUDIES OF DNA ORIGAMI ON SILICON DIOXIDE

Björn Albrecht<sup>1,2</sup>, Daniel S. Hautzinger<sup>1,3,4</sup>, Michael Krüger<sup>2</sup>, Miko Elwenspoek<sup>4,6</sup>, Kristian M. Müller<sup>3,5</sup>, and Jan G. Korvink<sup>1,4</sup>

<sup>1</sup>Laboratory for Simulation, Dep. of Microsystems Engineering (IMTEK),

<sup>2</sup>Laboratory for Sensors, Dep. of Microsystems Engineering (IMTEK),

<sup>3</sup>Laboratory for Synthetic Biosystems, Institute of Biology III,

<sup>4</sup>FRIAS, <sup>5</sup>Centre for Biological Signaling Studies (bioss),

<sup>1-5</sup>University of Freiburg, Germany,

<sup>6</sup>MESA+ research institute for nanotechnology, University of Twente, The Netherlands

**Abstract** — Self-assembled DNA nanostructures promise low-cost ways to create nanoscale shapes. DNA nanostructures can also be used to position particles with nanometer precision. Yet, reliable and low-cost ways of integrating the structures with MEMS technology still have to be developed and innovations are of great interest to the field.

We have examined in detail the adherence of DNA origami tiles on silicon oxide surfaces of wafers in dependence on pH-value and magnesium ion concentration. The results of this work will help to pursue new strategies of positioning DNA nanostructures on SiO<sub>2</sub>. Precise control over the strength of structure-surface adhesion is a prerequisite of reliable processes.

**Keywords** : DNA origami, surface charge density, charge inversion, positioning

### I - Introduction

Employing the DNA origami method [1], it is possible to design and produce arbitrarily shaped two-dimensional DNA nanostructures about 100×100 nm<sup>2</sup> in size by self-assembly. These structures are made of one long (approx. 7000 nucleotides) single stranded DNA molecule of natural origin and around 200 short (24 to 50 nucleotides) tailored synthetic oligonucleotides which determine the final self-assembled shape (Figure 1a, 1b).

As the position in the final nanostructure of every single base of each oligonucleotide is known, non-DNA components can be arranged on the structures with nanometer precision by chemically modifying single oligonucleotides (Figure 1c). Several attachment strategies have been demonstrated [2], and different add-ons at distinct positions of the same structure have been realized [3].

For applications, but also initially for the characterization of e.g. the electronic properties of the produced nano-scale assemblies, integration of the nanostructures with established MEMS technology is of very high interest. However, the standard substrate for the deposition of flat DNA nanostructures, commonly prior to characterization by atomic force microscopy (AFM), is mica. The best conditions with which to use silicon or silicon dioxide as a substrate have yet to be explored.

For self-assembly strategies for the arrangement of the nanostructures on surfaces, good control over the deposition process and adhesion is needed. First progress in the direction of meta-self-assembly has been made by prestructuring hydrophilicity patterns on the surface of silicon wafers.

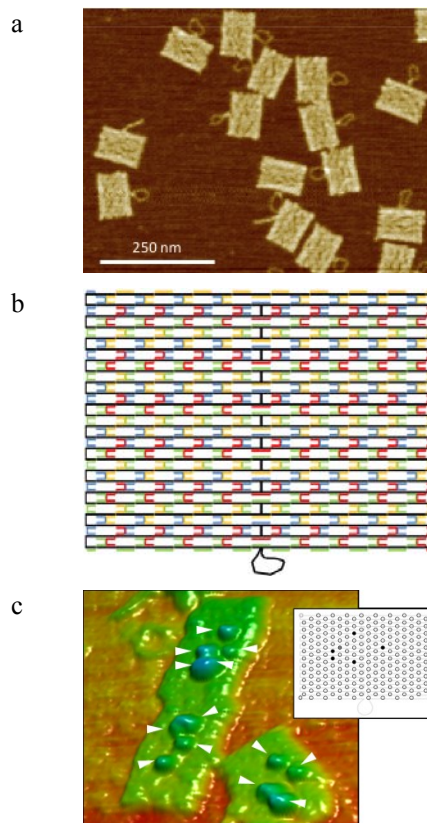


Figure 1: a) 70×90 nm<sup>2</sup> rectangular DNA origami nanostructures deposited on mica and imaged with AFM in air. The DNA loop not used in the rectangle design is clearly visible. b) Schematic of the long single stranded DNA backbone strand (black) held in desired shape after hybridization with specifically designed short oligonucleotides (colored). c) 3D representation of an AFM image of DNA origami of the same size as in a), but containing some oligonucleotides with attached biotin residues to which added streptavidin proteins are bound (white arrowheads). The inset represents the grid of modifiable positions with modifications marked by filled circles.

Kershner et al. [4] managed to deposit triangular DNA origami on specific sites by first modifying the

SiO<sub>2</sub> surface with a hydrophobic tetramethylsilyl (TMS) monolayer and, after electron beam structuring of patterns of similar size as the origami structures, etched through the TMS layer to the SiO<sub>2</sub> surface using oxygen plasma. After stripping of the resist, clean SiO<sub>2</sub> patches in a hydrophobic background remained. As another strategy, Sarveswaran et al. [5] also used e-beam lithography, but realized hydrophilic aminopropyltriethoxysilane (APTES) or trimethyl aminopropyltrimethoxysilyl chloride (TMAC) patches on the SiO<sub>2</sub> surface of a silicon wafer.

We focused on silicon with native oxide on top as substrate, as additional intermediate layers increase the roughness of the surface, which should be kept as low as possible because conventional 2D DNA origami structures are only on diameter of a DNA helix, ca. 2 nm, thick. This strategy also avoids additional parameters such as ratios of APTES and TMAC mixtures used to adjust surface charge density, a parameter that can also be adjusted via magnesium ion concentration when using SiO<sub>2</sub> surfaces.

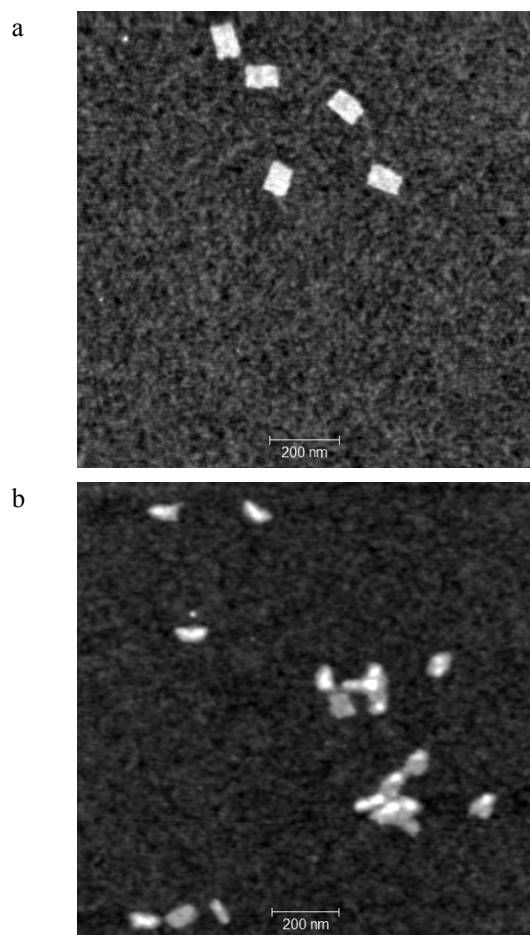


Figure 2: a) AFM image of well attached rectangular DNA origami lying flat on the SiO<sub>2</sub> surface. Deposited from pH 8.3 buffer with 100 mM Mg<sup>2+</sup> ions. B) AFM image of the same type of origami nanostructures as in a), with many structures rolled up. Deposited from pH 7.5 buffer with 100 mM Mg<sup>2+</sup> ions.

The goal of the studies presented here was to obtain a deeper understanding of the interactions between two-dimensional DNA nanostructures and SiO<sub>2</sub> surfaces. Therefore, we acquired quantitative data on the influences of pH and Mg<sup>2+</sup> ion concentration. Since both SiO<sub>2</sub> surface and DNA are negatively charged, the adsorption of DNA nanostructures to the surface is caused by charge inversion [6] [7] that first occurs on the surface due to a dense layer of bivalent Mg<sup>2+</sup> ions. At even higher Mg<sup>2+</sup> ion concentrations, charge inversion can also occur on the DNA structures, leading to repulsion between the SiO<sub>2</sub> surface and the nanostructures and, supposedly, to aggregation of the nanostructures. For correct positioning of DNA nanostructures to certain spots, it is necessary to at first use conditions where the structures adhere but are still mobile, in order to enable the settlement of the structures to reach equilibrium. Afterwards, the conditions may be changed such that the structures stick in place. An adsorption at random first-contact positions is not desirable, neither is non-adsorption followed by drying, in which case the structures would again end up at random positions and in random configurations. Figure 2b shows DNA origami rectangular structures that seem to be rolled up along their length axes, which might arguably be due to either of these unsuitable conditions.

## II - Experimental Details

### A. Assembly of DNA origami nanostructures

DNA origami were assembled as follows. Different mixes of helper strands containing roughly the same concentration of each helper strand were prepared. These pre-mixes were then used with single-stranded M13mp18 phage DNA (M13) and TAE buffer containing Mg<sup>2+</sup> ions, and brought to a final volume of 50  $\mu$ l with DI water (Millipore, 18 M $\Omega$ -cm). Final concentrations were 240 nM per helper strand, 24 nM M13, 40 mM Tris, 20 mM sodium acetate, 1 mM EDTA, and 12.5 mM magnesium acetate (1 $\times$  TAE buffer w/ Mg<sup>2+</sup>). The sample was then heated to 95 $^{\circ}$  C in a thermal cycler (Eppendorf Mastercycler personal) and cooled at a rate of 0.5 $^{\circ}$  C per minute. The produced solution contained self-assembled DNA origami suspended in TAE buffer.

### B. Buffer preparation

A stock solution of 10 $\times$  TAE (all chemicals from VWR) buffer was prepared containing 400 mM Tris, 200 mM sodium acetate, and 10 mM EDTA. Magnesium chloride stock solution was 200 mM in DI water.

To study the effect of Mg<sup>2+</sup> ion concentration, 5 $\times$  TAE buffer with 12.5 mM, 50 mM, and 100 mM Mg<sup>2+</sup> ions and 2.5 $\times$  TAE buffer with 150 mM Mg<sup>2+</sup> ions were prepared. The pH of all solutions was 8.3. The buffer containing 100 mM Mg<sup>2+</sup> ions was used for the studies of the effect of pH to the adsorption. The pH was decreased by titration with hydrochloric acid to 7.1, 7.5, and 7.7.

### C. Sample preparation

For the adsorption of DNA origami to clean or hydrophilic silicon dioxide surfaces, 1 cm<sup>2</sup> pieces of a n-type silicon <100> wafer were cleaned for 20 minutes with acetone and 2-propanol, then rinsed in DI water, assisted by ultrasonic agitation (all chemicals from VWR). Next, the surface was treated with oxygen plasma (FEMTO, Diener Electronic, Germany) to yield a hydrophilic surface, using standard cleaning parameters (50% power and 0.5 mbar chamber pressure for 5 min). A drop of 20  $\mu$ l 5 $\times$  TAE buffer was dispensed onto the cleaned surface. The TAE buffer spreads completely over the cleaned surface. A 1  $\mu$ l drop of DNA origami solution was dispensed on top. The incubation time was 30 minutes in a closed petri dish. After that time the sample was dipped for 5 seconds into a solution of water and ethanol (50:50 v/v), followed by immersion for one hour in a solution of water in ethanol (10:90 v/v) [8]. All steps were done at room temperature. The sample was dried with a nitrogen gas stream before AFM imaging.

### D. AFM measurements

All AFM measurements were done in tapping mode AFM with a scanning speed of 1 Hz (Veeco Multimode AFM, NanoScope III controller). The area of the scans was from 3 $\times$ 3  $\mu$ m<sup>2</sup> up to 8 $\times$ 8  $\mu$ m<sup>2</sup>. The DNA origami per area were counted manually. Additionally, the number of DNA origami adsorbed totally flat on the surface was counted and put in relation to the total amount of DNA origami on the surface.

## III - Results and Discussion

### A. Effect of Mg<sup>2+</sup> ion concentration

Multivalent cations are necessary to mediate the binding between the negatively charged SiO<sub>2</sub> surface and the also negatively charged DNA nanostructures. Our buffer contains monovalent Na<sup>+</sup> ions that compete with divalent Mg<sup>2+</sup> ions for the SiO<sub>2</sub> surface, but do not contribute to overcompensation of the negative surface charge and thus charge inversion of the surface. Therefore, higher Mg<sup>2+</sup> ion concentration should help out-compete Na<sup>+</sup> ions and improve DNA nanostructure adhesion. This is indeed what Figure 3a shows. The number of attached DNA origami nanostructures per area increases at a concentration of 150 mM Mg<sup>2+</sup> ions. We plan to increase the density of data points between 100 mM and 150 mM Mg<sup>2+</sup> ion concentration and up to 400 mM Mg<sup>2+</sup>.

The ratio of rectangular DNA origami structures attached flat on the surface already reaches 90 % at a Mg<sup>2+</sup> ion concentration of 100 mM and does not decrease significantly when 150 mM Mg<sup>2+</sup> are used.

In combination, it can be concluded that the coiled up appearance at lower Mg<sup>2+</sup> ion concentrations is not

due to immediate immobilization of the nanostructures, but rather to insufficient adhesion.

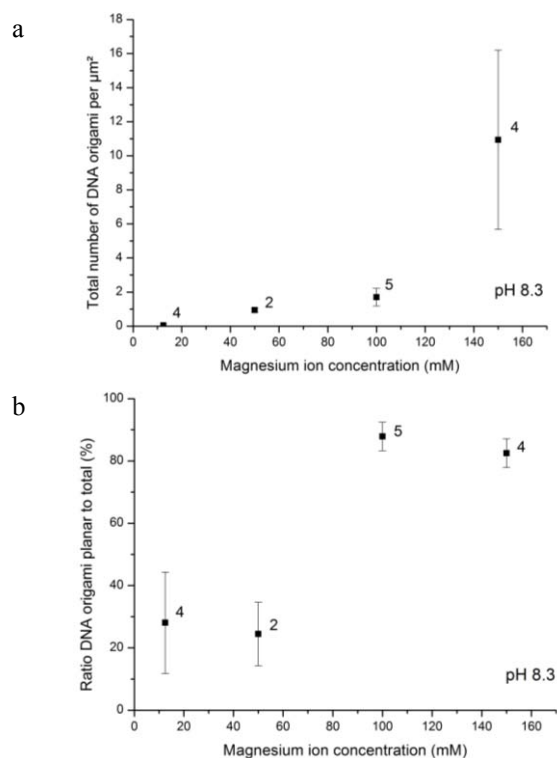


Figure 3: Dependence on Mg<sup>2+</sup> ion concentration in pH 8.3 buffer during deposition. The error bars show the standard deviation. The number of samples is indicated next to each data point. a) Number of DNA origami nanostructures counted per  $\mu$ m<sup>2</sup>. b) Ratio of the number of DNA origami showing desired planar appearance on the substrate over total number of origami counted.

### B. Effect of pH-value

Higher pH increases the density of negative charges because hydroxyl groups on the SiO<sub>2</sub> surface are more likely to be deprotonated. According to theoretical studies of Guldbrand, a critical surface charge density of 2.2 C/m<sup>2</sup> has to be exceeded for charge inversion to occur with divalent ions in the solution [9]. For SiO<sub>2</sub>, this value is reached at about pH 7.5 [7]. In our experiments, the data suggest that out of the pH-values tested, good adsorption is given at pH 7.7 (Figure 4a).

The fraction of structures that are attached flat on the surface, indicating preferred interaction with the surface, clearly increases with pH (Figure 4b). This effect indicates that adsorption is not yet too high, such that the nanostructures would attach in random confirmation at first contact with the surface.



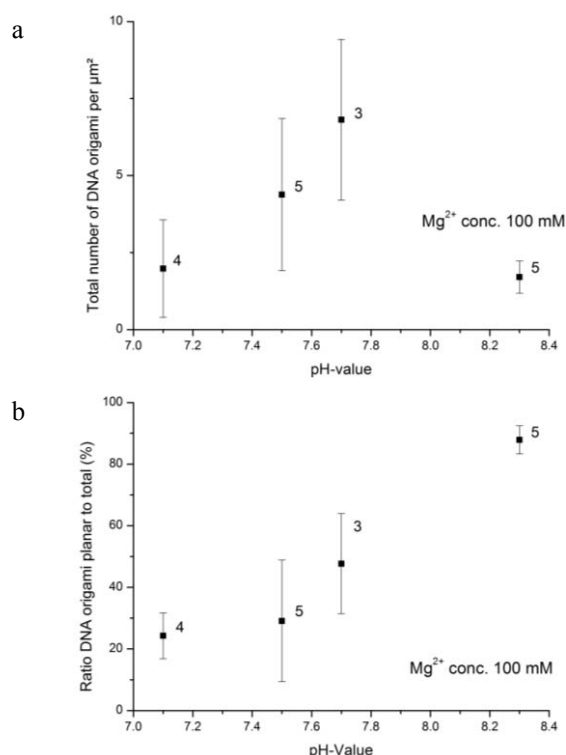


Figure 4: Dependence on the pH-value of the buffer during deposition.  $\text{Mg}^{2+}$  ion concentration was fixed to 100 mM. The error bars show the standard deviation. The number of samples is indicated next to each data point. a) Number of DNA origami nanostructures counted per  $\mu\text{m}^2$ . b) Ratio of the number of DNA origami showing desired planar appearance on the substrate over total number of origami counted.

#### IV - Conclusion

In this work we have shown that the  $\text{Mg}^{2+}$  ion concentration and the pH-value separately influence the adsorption of DNA nanostructures on  $\text{SiO}_2$  surfaces. Charge inversion and the dependence on pH value are well known [7]. It is possible to take advantage of this dependence to control the adhesion of DNA nanomaterial on a silicon dioxide surface. This could be a smart way to arrange DNA material on the surface by changing pH during adsorption. An increased amount of attached DNA origami measured at pH 7.7 shows potential for the control of adsorption of DNA material, but the optimal parameters have yet to be determined.

A rapidly growing dependency of  $\text{Mg}^{2+}$  concentration up to 150 mM indicates the need for further investigation at higher concentrations. In addition, the cross-sensitivity of adsorption on pH and  $\text{Mg}^{2+}$  concentrations of the buffer solution needs to be quantified.

#### References

- [1] Paul W. K. Rothemund, "Folding DNA to create nanoscale shapes and patterns," *Nature*, vol. 440, no. 7082, pp. 297-302, 2006.
- [2] Niels V. Voigt et al., "Single-molecule chemical reactions on DNA origami," *Nature*

*Nanotechnology*, vol. 5, no. 3, pp. 200-203, 2010.

- [3] Baoquan Ding et al., "Gold Nanoparticle Self-Similar Chain Structure Organized by DNA Origami," *Journal of the American Chemical Society*, vol. 132, no. 10, pp. 3248-3249, 2010.
- [4] Ryan J. Kershner et al., "Placement and orientation of individual DNA shapes on lithographically patterned surfaces," *Nature Nanotechnology*, vol. 4, no. 9, pp. 557-561, 2009.
- [5] Koshala Sarveswaran, Wenchuang Hu, Paul W. Huber, Gary H. Bernstein, and Marya Lieberman, "Deposition of DNA rafts on cationic SAMs on silicon [100].," *Langmuir : the ACS journal of surfaces and colloids*, vol. 22, no. 26, pp. 11279-11283, 2006.
- [6] A. Y. Grosberg, T. T. Nguyen, and B. I. Shklovskii, "Colloquium: The physics of charge inversion in chemical and biological systems," *Reviews of Modern Physics*, vol. 74, no. 2, pp. 329-345, 2002.
- [7] Frank H. J. Van der Heyden, Derek Stein, Koen Besteman, Serge G. Lemay, and Cees Dekker, "Charge Inversion at High Ionic Strength Studied by Streaming Currents," *Physical Review Letters*, vol. 96, no. 22, p. 224502+, 2006.
- [8] Albert M. Hung et al., "Large-area spatially ordered arrays of gold nanoparticles directed by lithographically confined DNA origami," *Nature Nanotechnology*, vol. 5, no. 2, pp. 121-126, 2009.
- [9] Lars Guldbrand, Bo Jönsson, Håkan Wennerström, and Per Linse, "Electrical double layer forces. A Monte Carlo study," *The Journal of Chemical Physics*, vol. 80, no. 5, pp. 2221-2228, 1984.
- [10] Jean-Marie Basset, Rinaldo Psaro, Dominique Roberto, and Renato Ugo, *Modern Surface Organometallic Chemistry*, 2009.

# 3D LITHOGRAPHY BASED FABRICATION OF NEURAL STIMULATOR ELECTRODE ARRAYS

F. Ceyssens<sup>1</sup>, J. Verstraete<sup>1</sup>, B. Volckaerts<sup>2</sup> and R. Puers<sup>1</sup>

<sup>1</sup>KULeuven dept. ESAT-MICAS, Kasteelpark Arenberg 10, B-3001 Leuven, Belgium.

<sup>2</sup>Cochlear Technology Center, Schallienhoevedreef, 201, B-2800 Mechelen, Belgium.

**Abstract** — Neural stimulator electrodes such as used in cochlear implants and deep brain stimulators are still largely fabricated using manual, piece-by-piece fabrication techniques. In this paper, a first exploration of a novel fabrication process based on cylinder lithography and molding is presented. This process aims at reducing minimal feature size and fabrication cost and offers the prospect on more automated, batch-scale production, while still allowing the use of industry-proven materials such as Pt, PDMS and Parylene C.

A simple setup and process for cylinder lithography is presented, attaining a minimum resolution of 15  $\mu\text{m}$  on hard surfaces.

Furthermore, a high yield process to create flexible and stretchable PDMS films covered with Pt electrodes and Parylene C dielectric layers is disclosed. A resolution down to 5  $\mu\text{m}$  is obtained.

Combining these processes could yield an industrially applicable fabrication process for neural stimulator electrodes.

**Keywords :** cochlear implants, deep brain stimulation, 3D lithography, laser lithography, PDMS, Platinum

## I - Introduction

Neural stimulator electrode arrays such as used in cochlear implants (figure 1) and deep brain stimulators are still largely fabricated using manual, piece-by-piece fabrication techniques [1].

Worldwide, researchers are seeking to apply thin film and lithography based techniques to the fabrication of such electrode arrays [2-3]. The expected advantages are a higher possible density of electrodes, a lower fabrication cost, a more automated fabrication process and the possibility of integrating electronics.

Most of these designs comprise electrode arrays with a rectangular cross-section. However, in cochlear implants, this implies a larger electrode-nerve distance as the electrode must be inserted in a cochlear channel with a round cross-section. This diminishes the beneficial effects of a higher electrode density.

Therefore, in this work, it is proposed to use 3D lithographic techniques such as cylinder lithography based on direct laser writing to fabricate neural electrode arrays. The aim is to attain both the advantages of a lithographic approach as well as the advantages of the round cross-section achieved with a classic fabrication procedure.

In order to achieve a proof-of-concept, a basic setup for 3D cylinder laser lithography [4-5] was built. This is elaborated in the first part of this paper. In a next part, a thin film based fabrication process is revealed that allows to fabricate electrode arrays consisting of industry-proven materials such as PDMS, platinum and Parylene C on flat substrates.

Combining this fabrication process with the 3D lithography could yield a route to more automated fabrication of complex, high density electrode arrays.



Figure 1: Typical cochlear implant electrode used in current-day implants [6].

## II – Lithography setup

### A. Mechanical design

For this proof-of-concept a simple low cost mechanical setup was constructed, consisting of a linear stage actuated by a stepper engine and a rotational stepper mounted thereon. The setup (figure 2) attains a linear resolution of 1  $\mu\text{m}$  and a rotational resolution of 0.1 degree, equivalent to 1.6  $\mu\text{m}$  for a 0.5 mm diameter substrate.

The linear stage attains a measured accuracy of 14  $\mu\text{m}$  (standard deviation).

### B. Optical design

The optical setup (figure 3) is as follows:

- A low cost diode laser (5 mW, 405 nm center wavelength) used as light source.
- A 300  $\mu\text{m}$  diameter pinhole to clean up the laser beam, leaving a conical beam and taking away some superfluous laser power.
- Lenses to concentrate the light from the pinhole

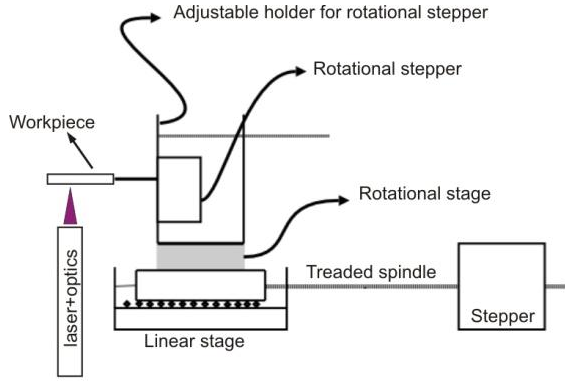


Figure 2: Schematic of mechanical setup.

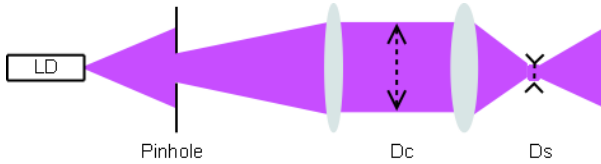


Figure 3: Optical setup

The following equations are used to dimension the optical system [7].

$$\frac{D_s}{2} = 1.220 \frac{f_2 \lambda}{D_c} \quad (1)$$

$$\frac{f_2}{f_1} = \frac{D_s}{D_a} \quad (2)$$

$$DOF = \frac{8\lambda}{\pi} \left( \frac{f_2}{D_c} \right)^2 \quad (3)$$

In these equations,  $D_a$ ,  $D_c$  and  $D_s$  stand for the diameter of the pinhole, the collimated beam and the focal spot respectively and  $f_1$  and  $f_2$  for the focal lengths of the two lenses.

The depth of field (DOF) is the distance over which the radius of the beam is at maximum  $\sqrt{2}$  times the radius at the waist.

A solution that takes the commercial availability of lenses into account is:  $f_1=100$  mm,  $f_2= 3.3$  mm and  $D_c=0.332$  mm. Thus, the pinhole spot is shrunk to over 30 times the original size.

### B. Electronic design

In order to accurately operate the setup, an electronic circuit was built around a PIC 16F2220 microcontroller (figure 4).

It further comprises a laser driver IC, power transistors for driving stepper engines and connections to micro-switches that serve as end-of-range sensors for the stage.

The circuit is connected to a PC by a RS232 serial bus protocol. Thus, it can be controlled through a user

interface written in Matlab, translating higher level commands into lower level routines that move the stepper engine a certain distance, control the pulse width modulation of the laser etc.

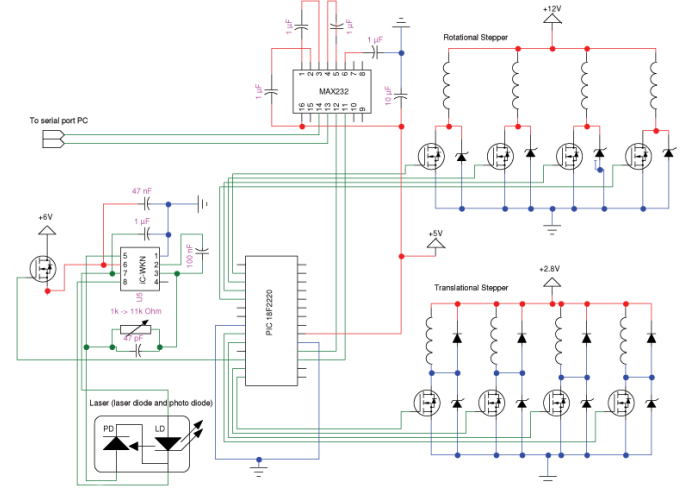


Figure 4: Schematic of control electronics

## III – Cylinder lithography process

### A. Testing of optical system

The profile of the laser beam was measured using a classic moving knife setup (figure 5). The result can be seen on figure 6. The minimum width of the beam is estimated from the graph and is about 13  $\mu\text{m}$ .

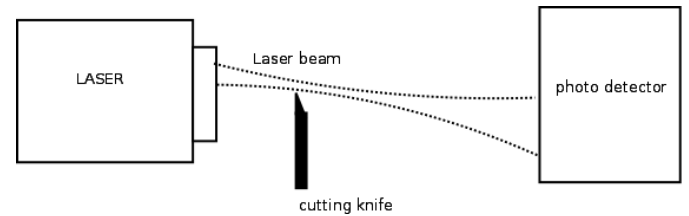


Figure 5: Moving knife setup

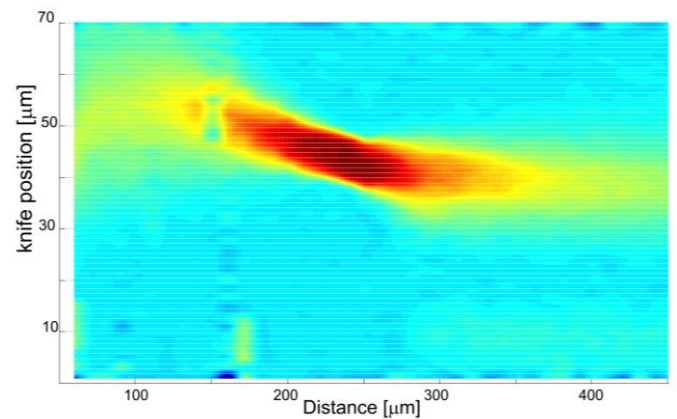


Figure 6: Beam profile measurement

### B. Cylinder lithography

The performance of the cylinder lithography system is now further demonstrated on a polished 1 mm diameter steel cylinder. First of all photoresist has to be applied to the cylinders. The traditional way to apply photoresist is spincoating, but as this is impossible with cylinders, a EVG 101 spraycoater is used. As this spray coater is designed for flat substrates, a holder is used in which the cylinders are positioned vertically. Thus, tens of cylinders can be coated in one run. As a resist Microposit S1818 diluted with methyl ethyl keton and IPA in a 1:3:3 ratio is employed. After spray coating, the cylinders are softbaked for ten minutes at 95 °C.

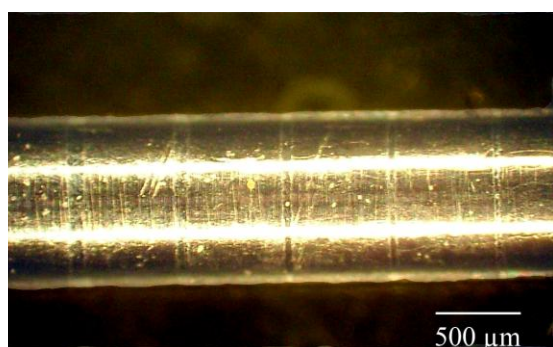


Figure 7: Result of writing on steel cylinder

After exposure by the laser setup, substrates are developed in 3:1 diluted Microposit 351 developer for 1 minute.

Circular (figure 7) and linear test patterns were written. A minimal resolution of 15 μm was obtained. A writing process that would cover an entire 1 mm diameter x 2 cm length cylinder would take about 1 hour using the current setup.

### IV - Pt / PDMS thin film layer transfer process

In order to encourage the adoption of lithography-fabricated implants in practice, it is advisable to use only biocompatible materials already in use in current implants. Thus, the lithography process must allow the fabrication of Pt or Ir metal lines on a PDMS sheet.

In this section, the development of such a process on non-curved substrates is discussed.

Regrettably, patterning metal deposited on PDMS is not straightforward [8]. In our experiments using a liftoff process on a PDMS sheet, microcracks in the lift-off resist leading to short circuits were observed in all cases. This was observed both in flat arrays when using contact printing, as well as on PDMS cylinders when using the laser lithography setup.

Therefore, we have selected a layer transfer process in which PDMS is deposited last.

In the first step of this process (figure 8), a sputtered film stack of titanium and 1 μm thick aluminum is used as sacrificial layer on a temporary glass substrate.

When, in the final step of the process, the sacrificial layer is etched in diluted HCl (6%), the galvanic effect between the noble Ti and the Al speeds up the etching process, allowing several cm of underetching overnight.

In a second process step, a dual LOR10B / S1818 resist layer is deposited on the sacrificial layer. Then, a TiW (1 nm) / Pt (70 nm) / TiW (1 nm) layer is sputtered and a liftoff step is done in NMP solvent.

In a following step, a mixture of a two-component biocompatible PDMS silicone and its crosslinking agent is cast on the temporary substrate.

After thermally induced crosslinking and possible reactive ion etching based patterning of the PDMS, the aluminum sacrificial layer is dissolved and flat electrodes are obtained (figure 9).

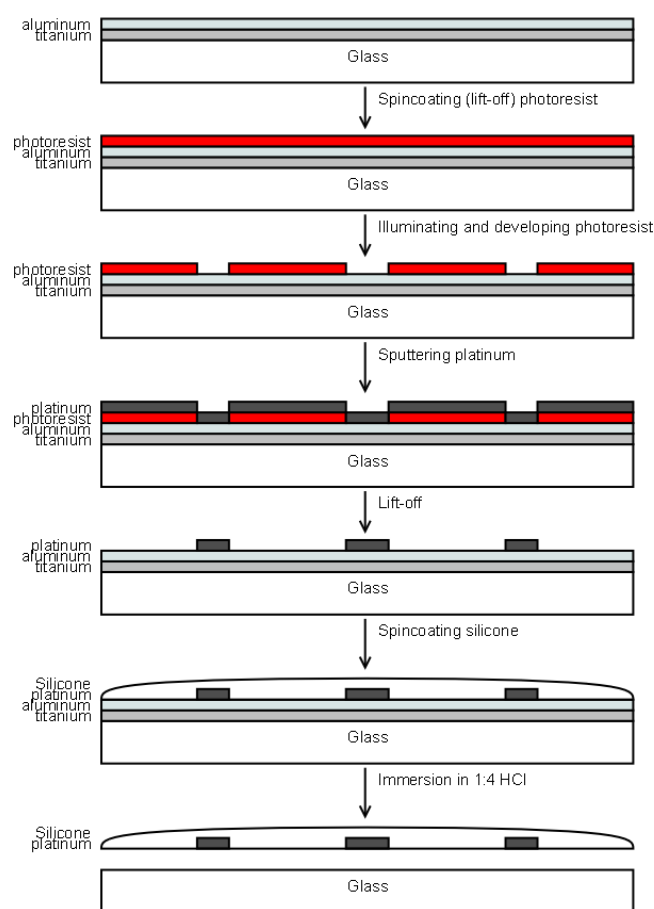


Figure 8: layer transfer process used to fabricate PDMS with Pt electrodes

Using this process, Pt electrodes on PDMS sheets were obtained with very good yield and a resolution down to 5 μm. Also, it was proven possible to deposit the Pt on a patterned Parylene C layer resting on another patterned Pt layer on the temporary substrate, thus allowing an electrode array having long-distance interconnects running under relatively large electrodes (figure 10).



However, with the resistivity of a typical connection in the order of a few k $\Omega$ , for some applications thicker metal layers might be needed. As yield dropped significantly when using longer sputter times, alternative processes based on electroplating or electroless deposition are now being investigated.



Figure 9: strip of 10  $\mu\text{m}$  wide Pt lines on PDMS resulting from the process.

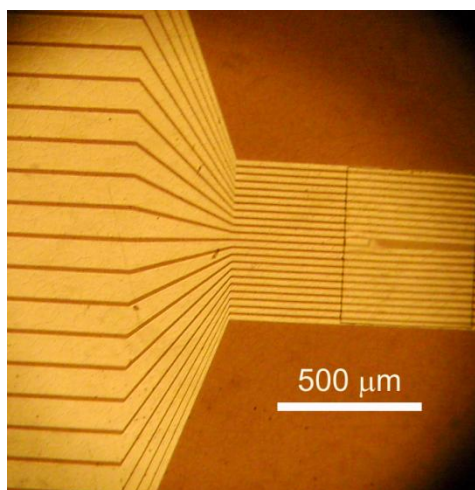


Figure 10: Multilayer Pt / Parylene C structure

In further work, it could be possible to combine the layer transfer process with the laser lithography on hard temporary substrates having hemi cylindrical cavities such as illustrated on figure 11. Alternatively, a more parallel lithographic writing process suitable for high topography surfaces might be employed [9].

The cavities can be lithographically fabricated as well, for examples using an isotropic glass etch process [10]. Thus, a route towards the lithographic fabrication of hemi cylindrical or, if two temporary substrates are combined, cylindrical electrode arrays is opened.

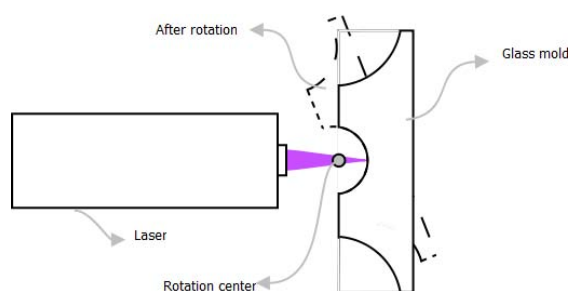


Figure 11: Combining the Pt layer transfer process and the laser lithography setup.

## V - Conclusion

This paper investigates the use of 3D laser lithography as a new route to the fabrication of neural electrode arrays.

We have shown a cylinder laser lithography setup having a positioning accuracy and resolution sufficient for most electrode applications. These results were obtained by applying the laser lithography on hard cylindrical substrates. However, performing lithographic patterning of metal laying on soft PDMS did not prove to be straightforward.

Therefore, a layer transfer process was developed, in which thin films are processed first on a temporary substrate, and then transferred onto PDMS.

Combining these processes could yield an industrially applicable large scale fabrication process for biocompatible non-planar neural stimulator electrodes having superior resolution and lower cost.

## References

- [1] Francis A Spelman, Cochlear electrode arrays: past, present and future, *Audiol. Neurotol.* 11, pp.77-85, 2006.
- [2] P.T. Bhatti and K.D. Wise, High-density cochlear implants with position sensing and control, *IEEE journal of solid-state circuits* 11, pp.2965-2974, 2006.
- [3] Process technology for the fabrication of a chip-in-wire style packaging, M. Vanden Bulcke et al., *Electronic Components and Technology Conference*, pp. 303 -308, 2008.
- [4] G. Lullo, C. Arnone and C. G. Giaconia Technologies for the fabrication of cylindrical fine line devices, *Microelectronic Engineering* 35 pp. 417-420, 1997.
- [5] S. Snow and S. C. Jacobsen, Microfabrication processes on cylindrical substrates Part II: lithography and connection, *Microelectronic Engineering* 84 pp. 11-20, 2009.
- [6] [www.cochlear.com](http://www.cochlear.com)
- [7] K. Iizuka, *Elements of Photonics*. Wiley interscience, 2002.
- [8] J.N. Patel, B Kaminska, B.L. Gray and B.D. Gates, A sacrificial SU-8 mask for direct metallization on PDMS, *Journal of Micromechanics and Microengineering* 19, 2009.
- [9] N.P. Pham et al., Metal patterning on high topography surface for 3D RF devices, *Sensors and Actuators A: Physical* 115, pp.557-562, 2004.
- [10] F Ceyssens and R. Puers, Deep etching of glass wafers using sputtered molybdenum masks, *Journal of Micromechanics and Microengineering* 19, 2009.

# A MICRO FUEL CELL STACK WITHOUT INTERCONNECT OVERHEAD – MACRO WORLD-LIKE STACKS IN MEMS

G. Scotti<sup>1,3</sup>, P. Kanninen<sup>2</sup>, T. Kallio<sup>2</sup> and S. Franssila<sup>3</sup>

<sup>1</sup>*Department of Micro and Nanosciences, Aalto University School of Science and Technology, P.O. Box 13500, 00076 Aalto, Espoo, Finland*

<sup>2</sup>*Department of Chemistry, Aalto University School of Science and Technology, P. O. Box 16100, 00076 Aalto, Espoo, Finland*

<sup>3</sup>*Department of Materials Science and Engineering, Aalto University School of Science and Technology, P. O. Box 16200, 00076 Aalto, Espoo, Finland*

**Abstract** — This paper describes a unique method for vertically stacking microfabricated fuel cells (MFC). Both electrical and fluidic interconnects are reduced to a minimum, and the stacking can be continued without increasing the complexity of the structure. The method allows for a practically unlimited number of elements in the vertical stack. A two-cell stack has been fabricated and the results are reported proving the viability of the design.

**Keywords** : Micro fuel cell, Black silicon, Stacking, Proton electrolyte membrane, Proton exchange.

## I - Introduction

Microfabricated fuel cells (micro fuel cells, MFC) are a promising emerging technology for powering portable electronic devices (mobile phones laptops, camcorders etc.) [1]. The promise lies in the higher energy density of fuel cells, compared to lithium-ion batteries. In this context, a microfabricated power source should, in order to be a good replacement for traditional batteries, have the same or smaller total volume (and/or weight), yet same or higher total energy. This volume includes both the fuel reservoir and the MFC itself. Because micro fuel cell operating temperatures are typically lower than with macro fuel cells, the power density per unit volume in MFCs is usually considerably smaller. To make up for this deficiency, one could take advantage of the miniaturization of MFCs, and simply have more of them in the same package. So if a MFC has a power density of  $1 \text{ mW cm}^{-2}$  but has an overall thickness of 1 mm, then stacking  $n$  of such cells would yield an effective power density of  $n \text{ mW cm}^{-2}$ , within a  $n \text{ mm}$  thick fuel cell stack. The benefit of stacking increases when the thickness of a cell is smaller. We have previously demonstrated a simple, vertically compact MFC [2], which is a good candidate for stacking.

Another advantage of vertical stacking of fuel cells compared to planar stacking is the reduction of total surface to volume ratio, which is a significant factor for thermal confinement of the fuel cells. In [3] a solid oxide MFC is stacked for this purpose: the operating temperatures are in excess of  $500^\circ\text{C}$ , and it is important to both keep them at these levels to further the electrochemical reactions, and to shield the user from

these temperatures. This design, however, does not permit to stack more than two fuel cells vertically, unless an electrical interconnect network is added, increasing assembly costs and total volume, and adversely impacting thermal confinement.

Existing literature on the topic of MFC stacking reveals a conspicuous lack of vertically stacked designs, while a much larger number of publications describe planar stacks such as in [4 – 7]. This is in spite of the fact that planar stacks offer very little in terms of area-to-volume reduction (compared to a single cell), require more overall thermal insulating material and/or structures, and are more restricted by the form-factor of the mobile device that houses them. The reason for such a disproportion in scientific literature lies in the complexities of microfabricating fluidic and electric distribution networks. Planar designs generally eliminate either the need for microfabricating the fluidic or the electrical interconnect network, but not both. On the other hand, in macro fuel cells, the overhead of electrical and fluidic pathways is small, and there the vertically-stacked fuel cells are the norm.

In [3] the issue of fluidic distribution is eliminated by using a single-chamber design, where fuel and oxidant are mixed together, but requires higher operating temperatures. In [8] the problem is somewhat mitigated by sharing a single anode flowfield for two cells. Even in the two-cell setup that is described in the article, there are external fluidic channels, and their number would further increase if more cells were to be added to the stack.

In this paper we present a novel method for the creation of MFC vertical stacks, with virtually no overhead for electrical interconnects nor for fluidic channels, enabling one to add an arbitrary number of cells to the stack, without worrying about the microfabrication of such distribution structures.

## II - Experimental Details

### A. Design and fabrication

The design and fabrication of the device is essentially identical to the one reported earlier [2], apart from the placement of the gas inlet holes (Figure 1) and the requirement for holes in the polymer electrolyte membrane (PEM). These holes, together with a rotationally-symmetric placement of the fuel cell stack

elements, constitutes the main idea of the present work. As can be seen on Figure 1, a cell is constructed by tightening a Nafion® PEM between two electrodes. The fuel and oxidant flow channels and the gas diffusion layer (GDL) have both been fabricated with deep reactive ion etching (DRIE) of silicon; the GDL is made of nanograss (black silicon) created by anisotropic plasma etching under high oxygen flow in  $O_2/SF_6$  etch chemistry. Nanograss increases silicon surface area and the number of triple junction points between electrode, reactant and electrolyte, as reported in [2]. The PEM is coated with carbon-supported platinum nanoparticles on both sides, using a modification of the method developed by Wilson and Gottesfeld [2, 9].

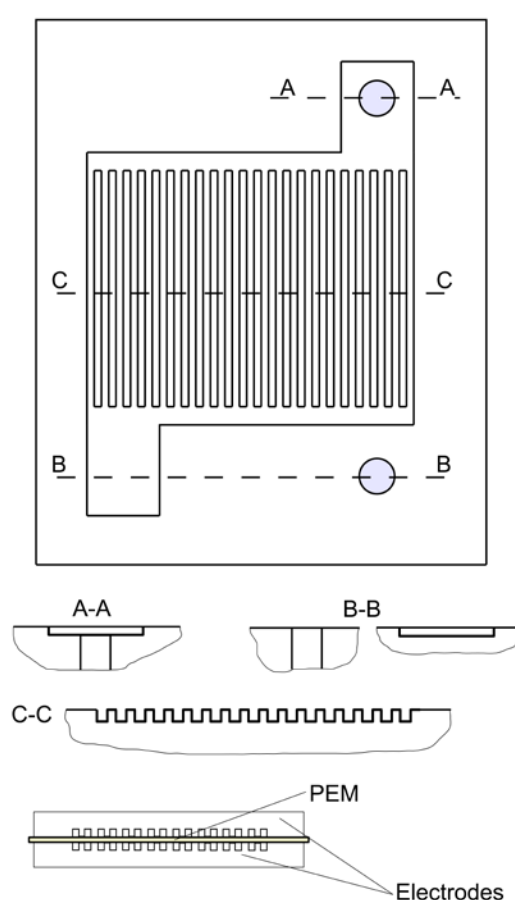


Figure 1: Micro fuel cell electrode and construction.

The gas inlet holes are 1 mm in diameter, while the flowfield area is  $1.5 \cdot 1.5 \text{ cm}^2$ , and the area of the silicon electrode is  $1.9 \cdot 2.8 \text{ cm}^2$ . The overall thickness of a cell is below 0.8 mm (2 wafers 300  $\mu\text{m}$  thick plus Nafion® PEM).

The microfabrication process for the silicon electrodes has been described in much detail in [2], so only a brief overview will be given here. The fuel and oxidant flow channels and the gas diffusion layer (GDL) have both been fabricated with deep reactive ion etching (DRIE) of silicon; the GDL is made of nanograss (black silicon) created by anisotropic plasma etching under

high oxygen flow in  $O_2/SF_6$  etch chemistry. Nanograss increases silicon surface area and the number of triple junction points between electrode, reactant and electrolyte, as reported in [2]. The fabrication steps are (Figure 2): A thermally oxidized, highly doped (0.01  $\Omega \text{ cm}$ ) silicon wafer (Figure 2) is patterned with photolithography and HF etching (2a) to determine the area affected by black silicon etch. Thin resist (AZ1505) is then spinned and patterned (2b) to act as a mask for a deep RIE step (2c) thus bulk-micromachining a 30  $\mu\text{m}$  deep flowfield. To create the gas inlets, aluminum is sputtered on the back side and patterned to form a mask for a deep RIE etch through the wafer (2d). The unprotected top silicon surface is then etched to form the nanograss, which is sputter coated by a thin layer of chromium (2e).

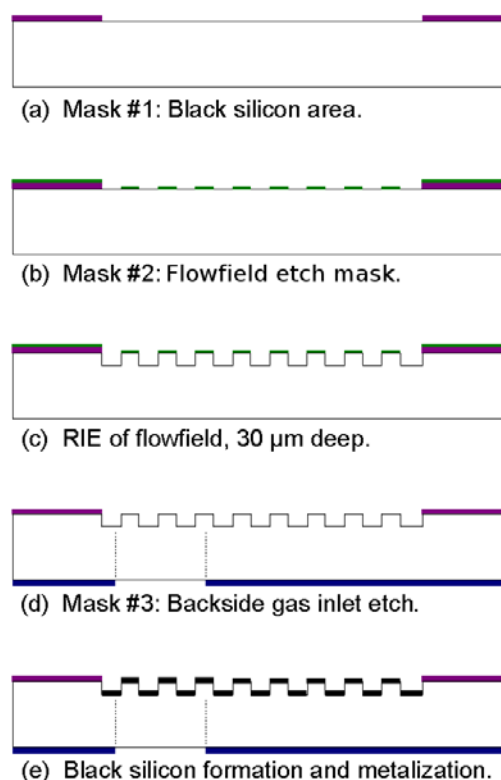


Figure 2: Microfabrication steps of silicon chip.

## B. Stacking

As was mentioned above, the idea for our stackable design centers on the existence and placement of holes in the electrodes and the PEM, and their position with respect to each other. This placement and the resulting fluidic flows are depicted on Figure 3. Note that, with the choice of flow topologies for the fuel and the oxidant as in Figure 3, the upper electrode becomes the anode and the lower the cathode.

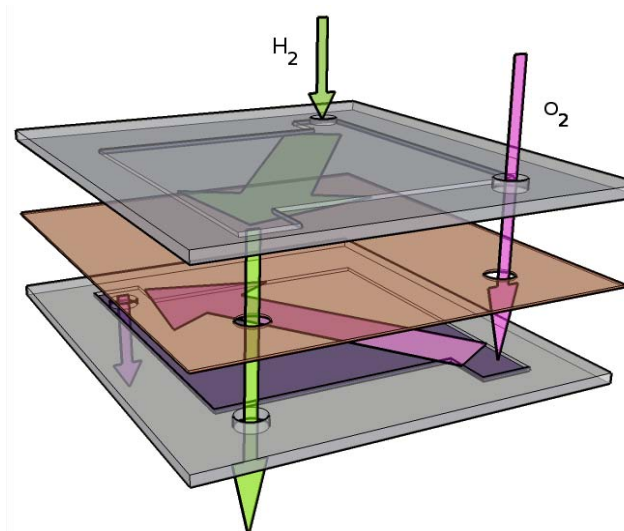


Figure 3: Gas flow through the flowfields of a top and a bottom electrode.

Figure 4 illustrates the principle of operation, in the case of a two-cell stack. It is very beneficial that, using this topology, the cathodes and anodes in a stack always face each other, rendering the addition of an external electrical interconnect network unnecessary. Every cell is rotated 180° with respect to the following and previous cell. By following this pattern, an unlimited number of cells can be added, without increasing the electrical and the fluidic interconnect overhead, because there is no such overhead at all.

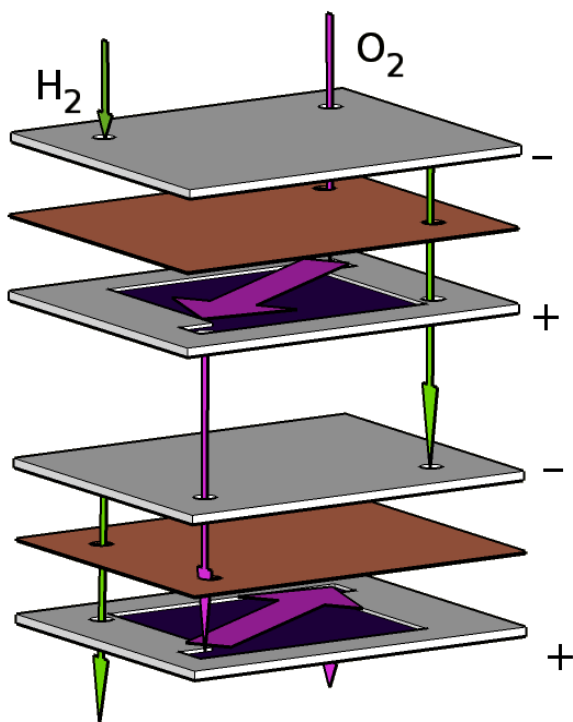


Figure 4: Illustration of a two-cell stack.

### C. Measurements

The stacks were tightened together in a purpose-built jig with gas inlets and electric sockets for the measurement equipment. The fuel and oxidant were humidified, room-temperature hydrogen and oxygen respectively, flowing at a rate of 50 ml min<sup>-1</sup>. The stack is electrically loaded by a computer-controlled potentiostat, and the voltage traverses the interval from open-circuit voltage (OCV) down to 100 mV.

## III - Results and Discussion

An initial result of the measured open-circuit voltage for a two-cell stack was 1.8V, and a maximum current density of 11.8 mA at 100 mV was obtained. The current density is about an order of magnitude smaller than the one obtained for a single cell [2], while the OCV is clearly double that of a single cell. Figure 5 shows a plot of current and power densities for a two-cell stack.

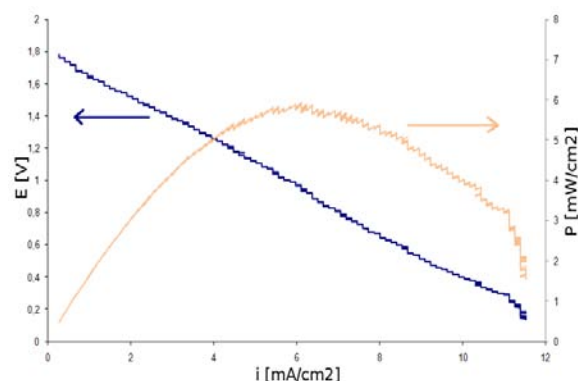


Figure 5: Measurement results of a two-cell stack electrical performance.

The reasons for the lower current density of the stack compared to the single cell design include considerable gas leakage and some ohmic losses in the stack. Both of these were a consequence of insufficient force applied on the stack to keep the elements together. During humidification, the Nafion® membrane would swell and warp irregularly, and the force necessary for eliminating the resulting leaks would cause the silicon chips to fracture.

## IV - Conclusion

Vertically stacking of fuel cells, while simple and commonplace at the large scale, becomes challenging at the microscale. The volume of electric and/or fluidic interconnects becomes comparable to that of the MFCs themselves, and adds to the fabrication cost. Research has, until now, mostly focused on planar stacks, which require more packaging per cell compared to vertical stacks, higher area-to-volume ratio and may be incompatible with some portable device form factors. In this work, we have eliminated the overhead of fluidic



and electrical interconnects. The measurement results are, in spite of lower current density compared to single cells, encouraging. There are several avenues that will lead to increased current density from the proposed design: reduction of the flowfield area will make the electrodes mechanically more robust, which will allow for higher forces to tighten down the stack and reduce the ohmic losses and the gas leakage. Ohmic losses can also be further reduced by patterning both sides of each electrode, making it effectively both a cathode and an anode. This would also further decrease the overall height of a stack. Furthermore, a reduced area fuel cell implies also a Nafion® membrane of smaller area, which leads to lesser warping and again, lesser leakage. Bonding materials will also be tried, which will also reduce or perhaps even eliminate the gas leaks.

The design described here is a promising new tool in the hands of MFC researchers that aim at multi-cell structures while maintaining a simple interconnect and fluidic flow layout, allowing them to concentrate on the improvements of electrochemical and fluidic properties of the fuel cells.

## References

- [1] C. K. Dyer, *Fuel Cells Bulletin*, vol. 2002, pp. 8-9, March 2002.
- [2] G. Scotti, P. Kanninen, T. Kallio and S. Franssila, *Proc. PowerMEMS 2009*, pp. 486-489, 2009
- [3] Z. Shao, S. M. Haile, J. Ahn, P. D. Ronney, Z. Zhan and S. A. Barnett, *Nature*, vol. 435, pp. 795-798, 2005
- [4] K-B. Min, S. Tanaka and M. Esashi, *J. Micromech. Microeng.*, vol. 16, pp. 505-511, 2006.
- [5] S. J. Lee, A. Chang-Chien, S. W. Cha, R. O'Hayre, Y. I. Park, Y. Saito and F. B. Prinz, *J. Power Sources*, vol. 112, pp. 410-418, 2002.
- [6] R. Hahn, S. Wagner, A. Schmitz and H. Reichl, *J. Power Sources*, vol. 131, pp. 73-78, 2004.
- [7] S. D. Pratt, R. J. Kelley, S. Muthuswamy, B. D. Landreth and R. W. Pennisi, *US Patent* 6 127 058, granted on Oct. 3, 2000
- [8] L. Zhong, X. Wang, Y. Jiang, Q. Zhang, X. Qiu, Y. Zhou and L. Liu, *Sens. Actuators A*, vol. 143, pp. 70-76, 2008.
- [9] M. S. Wilson and S. Gottesfeld, *J. Electrochem. Soc.*, vol. 139, L28-L30

# FABRICATION TECHNIQUE OF A COMPRESSIBLE BIOCOMPATIBLE INTERCONNECT USING A THIN FILM TRANSFER PROCESS

A.A.A. Aarts<sup>1,2,3</sup>, O. Srivannavit<sup>3</sup>, K.D. Wise<sup>3</sup>, E. Yoon<sup>3</sup>, H.P. Neves<sup>1</sup>, R. Puers<sup>1,2</sup> and C. Van Hoof<sup>1,2</sup>

<sup>1</sup> Technology Unit, IMEC, Kapeldreef 75, 3001 Leuven, Belgium

<sup>2</sup> ESAT-Micas, KULeuven, Kasteelpark Arenberg 10, 3001 Heverlee, Belgium

<sup>3</sup> EECS, University of Michigan, 1301 Beal Avenue Ann Arbor, MI 48109-2122, USA

**Abstract** — A compressible multifunctional interconnect for out-of-plane MEMS structures has been fabricated using a thin film transfer bonding technique and bio-tolerable materials. The bulk material of the compressible film consists of photo patternable poly-dimethylsiloxane (PDMS) and is fabricated on a carrier substrate. The film is bonded to a slim-base platform. The carrier substrate of the thin film is released using an aluminum anodic dissolution technique. Probe arrays can be assembled perpendicular into a slim base platform. Once the probes are assembled a non-separable electrical connection is made. This interconnect can also facilitate fluidic probes for direct drug delivery applications.

**Keywords** : Stretchable interconnect, Transfer bonding, Anodic dissolution, Photo sensitive PDMS

## I - Introduction

During the past few years there has been a lot of activities in the fabrication of probe arrays. Very successful probe arrays have been demonstrated [1]. However with increasing functionality as CMOS integration (multiplexers, filters, amplifiers, etc.) the base of the probe array becomes taller. Since the available space on the shafts of the probe array is very limited, most of the active components are positioned at the base of the probe arrays. Implantation of such probe arrays requires extra space beyond the implanted area which is not always available. As a result, the probe array can get stuck between the skull and cortical tissue resulting in tissue damage or probe failure. We have demonstrated a slim-base 3D integration technique that can be used in space-limited sites while maintaining the CMOS functionality [2]. The interconnect consists of a gold clip which leads over the edge of the cavity. However, the interconnect has no elastic behavior nor spring effect. This requires a very accurate thickness control of the assembled structures with a very tight thickness specification. Before assembly, the structures often need to be planarised by grinding or polishing techniques to ensure a proper fit.

This paper describes an improved out-of-plane interconnect with stretchable, i.e. compressible, behavior and using significant less process steps. The interconnect consists of a stretchable layer containing several gold clips which are leading over the edge of a cavity, see Figure 1. The cavity acts as a socket for the assem-

bled probe arrays. Several different layouts have been designed and fabricated for the individual gold clips. During the assembly of the probe array, the stretchable interconnect will bend into the cavity and is squeezed against the contact pad of the probe array. The thus compressed layer leading over the edge of the cavity provides a spring effect that presses the overhanging gold contact against the contact pad of the assembled structure. The overhanging compressible contacts enable the assembly of structures containing higher total thickness variation (TTV). The compressible or stretchable film consists of a poly-dimethylsiloxane (PDMS) layer, which can also be used as bonding layer. PDMS is often used in microfluidics and biomedical applications. When assembling fluidic devices the overhanging PDMS layer can be used as sealing ring around the socket. PDMS patterns and structures are often created by casting/molding- or etching techniques. Patterning PDMS using a reactive ion etch (RIE) technique results in underetching of the PDMS layer. This work uses a very low viscosity photosensitive PDMS called WL5150 from DOW Corning. This is a commercially available product [3].

The process flow of the interconnect uses a thin film transfer bonding technique followed by an anodic release. The transferred thin film is fabricated on a temporary carrier substrate. Eventually the thin film is bonded to the slim-base platform and the carrier is released by aluminum anodic dissolution, separating the carrier substrate from the bonded thin film. Test structures have been assembled into the platform to gain information about the contact resistance.

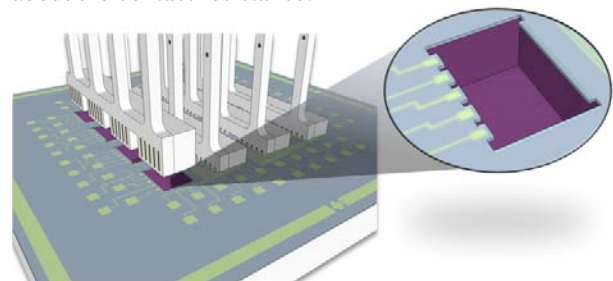


Figure 1: Schematic view of the compressible interconnects showing the gold contact supported by the surrounded PDMS. Probe arrays can be assembled perpendicular into the platform.

## II - Fabrication

The process flow of the compressible interconnect is shown in Figure 2. As explained in the introduction the

thin film containing the gold metallization is fabricated on a carrier wafer while the platform, containing the cavities, is fabricated on another wafer. A die-to-wafer transfer bonding technique is used to bond both structures together. This section is divided in two subsections. Section A describes the fabrication of the thin film, illustrated by Figure 2a-d. Section B describes the thin film transfer bonding technique, illustrated by Figure 2e-g.

#### A. Thin Film Fabrication

The carrier substrate is a standard 4 inch silicon wafer covered with a 200nm thick thermal oxide layer. The backside oxide prevents any gold deposition at the backside of the wafer during the gold electroplating process.

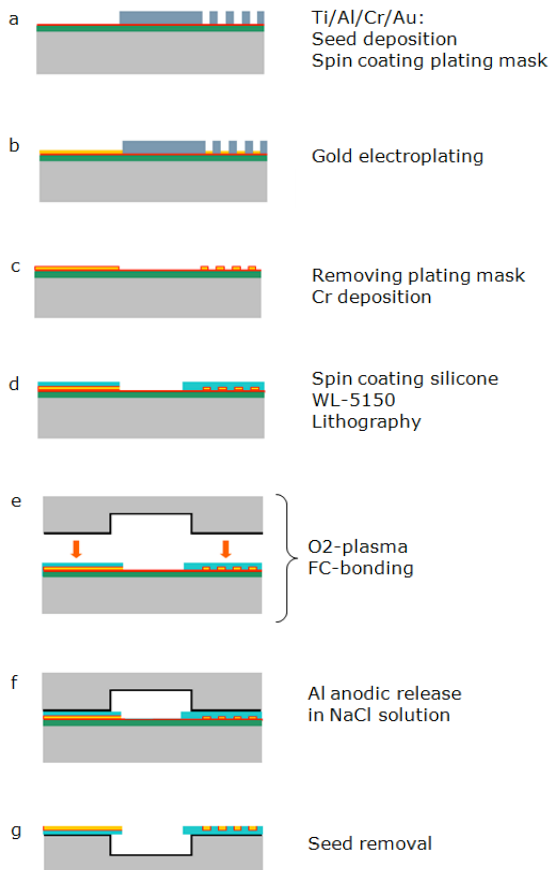
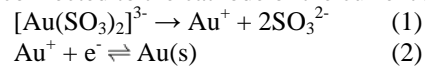


Figure 2: Process flow of the stretchable interconnects.

On top of the silicon oxide layer a Ti/Al/Cr/Au metal layer is deposited using evaporation. The aluminum layer functions as a sacrificial layer during the release process and has a thickness of 500nm. The titanium layer is used as electrical conductive layer during the anodic release process. The gold layer functions as seed layer during the gold electroplating process. The chrome layer in between acts as diffusion barrier preventing the gold to diffuse into the aluminum layer. As shown in Figure 2a, a resist layer is spin coated on top of the gold seed layer and defines the position of the

gold electroplated structures. During the gold electroplating only the exposed gold seed layer will be covered with electroplated gold, see Figure 2b. The gold electroplating rate and morphology is mainly controlled by the current density so it is important to know the total exposed surface area during electroplating. Too high current densities can lead to rough plated structures while too low current densities can result in inhomogeneous structures. The growth rate of the electroplated bath is often dependant of the electroplating setup. The gold plating process is performed in a cyanide free electroplating bath, see Figure 2c. The bath consists of a mixture of BDT-510 plating solution and BDT Brightener, which is commercially available (Enthone-OMI). The electrolyte consists of a gold sulfite solution holding sodium aurosulfite  $\text{Na}_3\text{Au}(\text{SO}_3)_2$  and additional compounds to maintain the conductivity and pH of the bath at a constant level [4]. The salt, sodium aurosulfite, is already dissolved in the plating solution and the aurosulfite ion dissociates in a gold ion (1) which forms solid gold (2) at the surface of the sample which is electrically connected to the cathode of the current source.



Different plated structures with thickness of 1  $\mu\text{m}$  up to 5  $\mu\text{m}$  have been fabricated. Current densities of 1.5 to 2  $\text{mA}/\text{cm}^2$  have been used. Next step is to remove the plating mask with acetone and isopropanol followed by a DI rinse. The gold metallization layer will be encapsulated with PDMS. PDMS has a bad adhesion to gold. Prior spin coating of the PDMS a chrome adhesion layer is deposited by evaporation deposition followed by an oxygen plasma. The  $\text{O}_2$  plasma improves the adhesion of the PDMS and the chrome layer. A 15  $\mu\text{m}$  thick layer of WL5150 is spin coated on top of the chromium layer followed by a soft bake step using a hotplate. During the soft bake all residual solvents are removed however, the PDMS film remains tacky. Spacers were used during alignment and exposure to prevent stiction between the PDMS and mask. UV exposure of WL5150 causes activation of the photosensitive compound. During the post-exposure bake a selective cross-linking process takes place. The non-exposed areas are removed during the development step using a standard negative resist developer like SU-8 Developer. A post exposure bake is required to initiate the cross linking of the PDMS. Without cross-linking the whole film will be removed during the development step. The recommended post exposure bake is at 150°C for 120 seconds. Longer bake times will increase the development time significantly and can leave residues at the bottom corner of the non-exposed areas [5]. A hard bake is used to complete the film curing process. During film curing there is no formation of cure by-products, see Figure 2d. The hard bake is done in a convection oven at 180°C for one hour. After the hard bake a RIE can be used to remove some silicone residues of the developed regions. This plasma etch requires an oxygen/fluorine gas mixture [3]. High plasma densities can damage and crack the

PDMS film. Different interconnect layouts have been fabricated, see Figure 3.

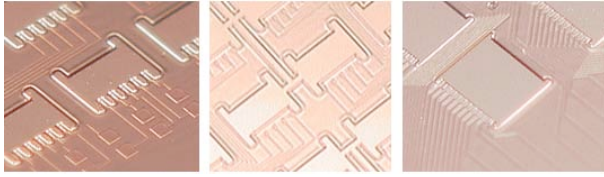


Figure 3: Different PDMS structures containing gold metallization with pitch of 70 μm (left and center) and 35 μm.

### B. Thin Film Transfer Bonding

The edges of the patterned PDMS layer are taller compared to the rest of the film resulting in a local thicker edge around the photo definable structures. The local thickening of the layer (dimple) is mainly caused due to internal stresses in the film [6]. The dimple can be reduced by optimizing the post exposure bake and decreasing the proximity gap during UV exposure [5]. The dimple can cause problems when using too low bonding forces. The dimples can be compressed easily when increasing the bonding temperature. As shown in Figure 2e, the platform is bonded to the carrier substrate holding the thin metallization film. The front side of the platform is covered with a silicon oxide layer which has a good adhesion with the PDMS layer. Prior bonding an oxygen plasma is used to activate the PDMS surface and to make the silicon oxide surface hydrophilic. The PDMS layer consists of repeated groups of  $-O-Si(CH_3)_2-$  which forms a silanol group ( $Si-OH$ ) in place of one methyl group ( $-CH_3$ ) when treated by an oxygen plasma [7]. Silanol groups are polar which results in a hydrophilic surface. Bringing the oxygen treated PDMS in contact with the silicon oxide surface results in a strong  $Si-O-Si$  covalent bond. Too long exposure time of the PDMS in the oxygen plasma as well as too high plasma densities degrades the bonding properties [7]. The alignment and bonding was done using a flip-chip bonder.

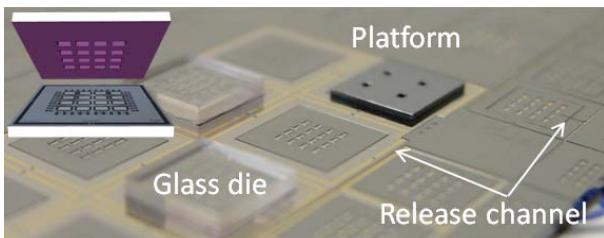
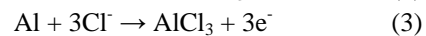
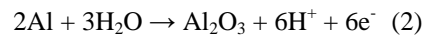


Figure 4: Photograph of bonded structures to the thin film and Schematic view of the alignment and bonding step (upper left).

The release process, see Figure 2f, is done using anodic dissolution. Anodic dissolution of a sacrificial metal can be used to release (complete or partial) thin film structures or other microstructures [8]. It is an electrochemical etch technique which results in a higher etch rate compared to conventional chemical wet etch techniques. Aluminum is used as sacrificial metal and can be selectively (each metal has a different polarization

potential) removed using a neutral sodium chloride solution and applying a small positive potential to the metal layer. The titanium conductive layer under the aluminum is electrically connected to the anode of a voltage source. The cathode is electrically connected to a stainless steel plate. As electrolyte a 2 molar sodium chloride ( $NaCl$ ) solution has been used. The aluminum dissolution is done in a beaker setup. The aluminum layer starts to dissolve at an applied potential of 0.5V. During aluminum dissolution several electrochemical reactions occur [8][9][10]. In addition to the aluminum oxide formation and aluminum reduction:



Aluminum corrodes in water which involves oxidation (1) and reduction. During oxidation the metal loses electrons and dissociates into a free electron and ion resulting in an anodic current. This current will be transported from the metal to the electrolyte solution and is mainly driven by diffusion, potential gradient and convection. This reaction is normally balanced by the reduction reaction where ions capture the free electrons resulting in a cathodic current. Oxidation and reduction happen at distinct sites of the metal surface and without connecting the metal to an external power source these reactions are in equilibrium. Reaction (2) describes the oxide film formation where a spontaneous oxide layer covers the aluminum. The actual dissolution of aluminum under applied potential starts with pitting where ions (often chloride ions) penetrate the oxide film and start to oxidize the aluminum. Aluminum dissolution in a neutral sodium chloride electrolyte involves several species like  $Al^{3+}$ ,  $Cl^-$ ,  $Na^+$ ,  $H_2O$ ,  $OH^-$  and  $H^+$ . The rate of aluminum dissolution involves the depletion layer of the electrolyte species and the solubility of the anodic reaction products (the salt). The dissolved metal near the anode reacts with the anodic reaction products that have to dissolve in the electrolyte. The mass transport is limited by the salt transport mechanism (3).  $AlCl_3$  is the salt that dissolves into the electrolyte. The mass transfer mechanism of the anodic reaction products influences the dissolution rate. The dissolution rate decreases in time because of the increasing underetch paths. The etch rate of the aluminum is about 16 μm per minute. The complete release process of the film takes about 2.5 hours. To speed up the release time and to decrease the underetch path we designed supply channels for the bulk electrolyte in the PDMS layer.

When the carrier substrate is removed the transferred film is flipped with the gold seed layer and chromium adhesion layer facing up, see Figure 2g. The gold seed is removed using a wet etch, based on a potassium io-



dide and iodine chemistry (Gold Etchant TFA, Transene Company). The chromium adhesion layer is etched in diluted chromium etchant (Cr-14, Cyantek Corporation). The interconnect is shown in Figure 5.

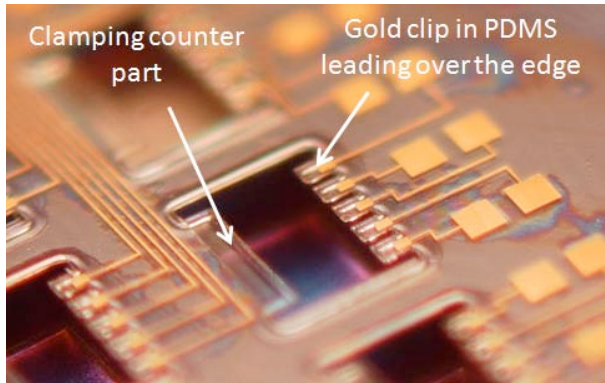


Figure 5: Microscopic picture of the transferred film showing the overhanging electrical contacts.

### III – Results and Conclusion

#### A. Out-of-Plane Assembly

Several test structures have been fabricated to get an idea about the electrical contact resistance. The fabrication of the test structure will not be described in this paper. The test structures are assembled perpendicular into the platform using a flip-chip bonder [2]. The assembly goes smooth and no lubrication, for example methanol, is required to facilitate the assembly [11]. Figure 5 shows the assembled test structure. Preliminary four-point measurements show a contact resistance around  $3.2\Omega$ .

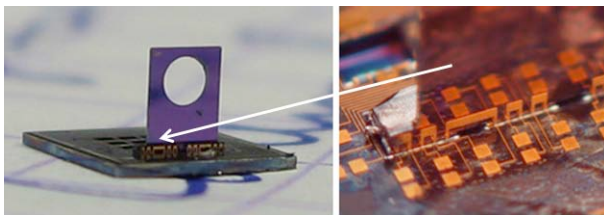


Figure 5: Picture of the out-of-plane assembled structure (left). Macroscopic picture of the compressible interconnects (right).

#### B. Conclusions

A biocompatible compressible interconnect for out of plane structures has been demonstrated. The number of process steps have been pushed to a minimum by using a transfer bonding technique followed by an anodic release process. The interconnect should be fully scalable because all the metallization steps have been done on planar surfaces. Contact resistances of  $3.2\Omega$  have been measured. Future experiments are planned to test the high density interconnect shown in Figure 3.

### IV - Acknowledgements

This work was performed in the Lurie Nanofabrication Facility (LNF) in collaboration with the Wireless Integrated MicroSystems (WIMS) group and the Integrated Microsystems Laboratory of the University of Michigan, Ann Arbor. A.A.A. Aarts would like to thank the staff of the LNF for the technical support and the Research Foundation - Flanders (FWO) together with the agency for Innovation by Science and Technology (IWT) for the financial support.

### References

- [1] Q. Bai, K.D. Wise, and D.J. Anderson, "A high-yield microassembly structure for three-dimensional microelectrode arrays," *IEEE Trans. Biomed. Eng.*, vol. 47, no. 3, pp. 281- 289, March 2000.
- [2] A.A.A. Aarts, H.P. Neves, R.P. Puers and C. Van Hoof, "Interconnect for out-of-plane assembled biomedical probe arrays", *J. Micromech. Microeng.* vol. 18, 064004 (7pp) 2008.
- [3] Product information for WL-5351 and WL-5150, Dow Corning  
<http://www.dowcorning.com/applications/search>
- [4] Kenneth W. Yee, "Gold-Electroplating Technology for X-Ray-Mask", *master thesis department of electrical engineering and computer Science, MIT*, June 1996.
- [5] O. Graudejus, C. Tsay, Z. Yu, B. Morrison, S. P. Lacour, S. Wagner "Advances in Encapsulating Elastically Stretchable Microelectrode Arrays", *Materials Research Society Symposium Proceedings*, Vol. 1009E, U04.2 (2007).
- [6] Salil P. Desai, Brian M. Taff and Joel Voldman, "A Photopatternable Silicone for Biological Applications", *Langmuir* 2008, 24, 575-581.
- [7] S. Bhattacharya, A. Datta, J. M. Berg and S. Gangopadhyay, "Studies on surface wettability of poly(dimethyl) siloxane (PDMS) and glass under oxygen-plasma treatment and correlation with bond strength", *J. Microelectromechanical syst.*, vol 14, NO. 3, June 2005.
- [8] S. Metz, A. Bertsch, and P. Renaud, "Partial release and detachment of microfabricated metal and polymer structures by anodic metal dissolution", *J. Microelectromechanical syst.*, vol. 14, NO. 2, April 2005.
- [9] Vargel, Christian, "The corrosion of Aluminium" *Book: part B. Corrosion of Aluminium* © 2004 Elsevier.
- [10] M. Datta, "Anodic dissolution of metals at high rates", *IBM J. research and Development*, vol. 37, pp.207-226, 1993.
- [11] Y. Tanye Tang et. Al., "Microfluidic Chamber with Active Suction Ports for Localized Chemical Stimulation of Brain Slices," to be presented in MEMS 2010, January 24-28, Hong Kong, China.

# INTERFERENCE FILTER BASED ABSORBER FOR THERMOPILE DETECTOR ARRAY BY SURFACE MICROMACHINING

H. Wu<sup>1</sup>, A. Emadi<sup>1</sup>, G de Graaf<sup>1</sup> and R. Wolffenbuttel<sup>1</sup>

<sup>1</sup>*Delft University of Technology, Faculty of EEMCS, Department of ME/EI, Mekelweg 4, 2628 CD Delft, The Netherlands*

**Abstract** — A thermopile based Infrared (IR) detector array fabricated in a CMOS-compatible MEMS process is used for realization of a microspectrometer. The IR absorption in IC-compatible materials, such as silicon, polysilicon and silicon nitride, is insufficient for realizing an efficient sensitivity in the 1-5  $\mu\text{m}$  spectral range. Interference filter based IR absorbers using titanium/aluminum layers with one silicon carbide cavity layer have been designed, fabricated and validated. Device with thin film stacks as the absorber are suitable for the subsequent processes as compared with one using none IC compatible materials. The interference filter based absorber features a narrow-band absorption, which is an advantage in IR microspectrometers, but a disadvantage in the more conventional wideband IR detectors.

**Keywords :** CMOS-compatible IR detector, Silicon carbide, IR absorber, Thermopile.

## I - Introduction

The requirements for an Infrared (IR) microspectrometer fabricated by IC-compatible MEMS technologies are: small system volume, fast response, small dimensions, weight and integrated circuits for signal pre-processing [1]. A thermal-electric detector array is in principle highly IC compatible. This detector array can be implemented in a microspectrometer based on either a grating [2] or linear variable optical filter (LVOF) as the dispersive element. The dispersed IR spectrum is projected onto a 1-dimensional detector array for the grating based system. Therefore, the position of a spectral component within the IR spectrum is determined by the position of the element in the array. The response in terms of generated heat due to absorbed IR radiation at that particular element is a measure of the optical power within that part of the spectrum. The resulting localized increase in temperature is available as temperature difference relative to ambient temperature, which can conveniently be measured directly using a thermopile between the suspended absorber and the bulk silicon.

The characteristic feature of a thermocouple of measuring temperature difference rather than temperature makes the integrated system insensitive to variations in the temperature of the bulk of the chip. High-sensitivity of an element in the thermopile-based IR detector requires minimum thermal conductance between absorber and heat sink. Micromachining technologies are generally employed for the removal of the

thermal shunt of any bulk silicon or oxide underneath the thermal-electric (TE) detector for maximum sensitivity.

However, the materials used in the IC compatible process, e.g. silicon (Si), polysilicon (PolySi) and silicon nitride (SiN), have very low absorption in the IR range. One of the solutions is to use black gold (Au) as an absorber [3]. The absorption can be achieved to more than 90% in the mid IR range. The disadvantage is that the wafer after sputtering with black Au cannot be further processed, e.g. thin film encapsulation, in high standard clean room due to IC compatibility issue. This paper introduces an interference filter based absorber with good absorption in IR range, while the wafer can still be processed for the elaborate fabrication steps. The idea of thin film IR absorber was first calculated in 1956 by solving the Maxwell equations [4]. The best absorption can be realized by matching the absorber to air interface with  $377 \Omega/\text{sq}$  [5]. This was verified using microwave theory [6]. Recently, the thin films absorber was applied on a bolometer for use in the far-IR spectral range [7].

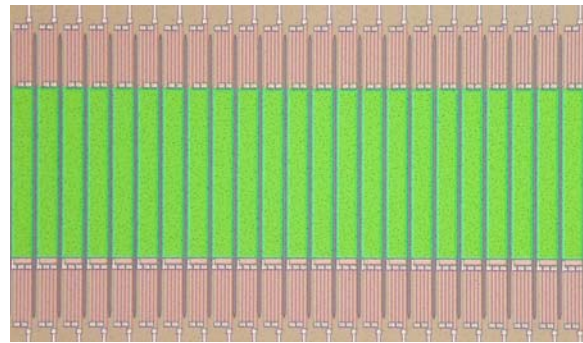


Figure 1: Fabricated detector array with IR absorber.

We present an interference filter based absorber which contains two metallic layers and one resonance cavity on top of TE elements for the mid IR range from 1-5  $\mu\text{m}$ . The dimensions of the detector array are  $7.2 \times 0.76 \text{ mm}^2$ , with an area of each TE element of  $650 \times 36 \mu\text{m}^2$  with a  $45 \mu\text{m}$  pitch, as shown in figure 1. The thin film absorber deposition is CMOS compatible and is followed by surface micromachining. The design of the absorber is presented in section 2. Simulation results shows a high absorption is achieved as compared to the case with no absorber applied. The fabrication and micromachining are described in section 3. The detector array is released by vapor Hydrogen fluoride (HF). The residual after etching has to be removed in a sublimation process at low pressure.

## II – Design of the absorber

The thin-film optical software package TFCalc 3.3 [8] has been used to simulate and design the interference based absorbers. Titanium (Ti) and aluminum (Al) are chosen as the metallic layers of the absorber. The optical properties of Ti are measured using ellipsometry on a test sample. Optical properties were measured up to 1.2  $\mu\text{m}$  wavelength by ellipsometry. Figure 2 shows the refractive index and extinction coefficient of Ti for wavelengths up to 1.2  $\mu\text{m}$ .

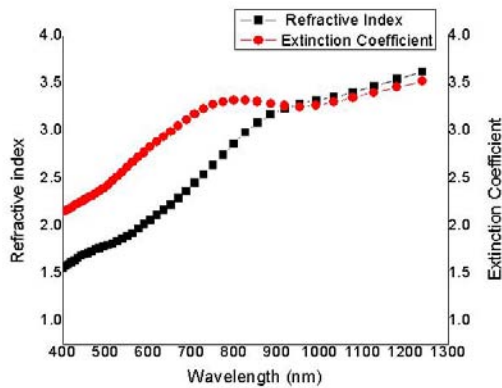


Figure 2: Measured optical properties of sputtered Ti.

The absorber consists of one dielectric centre layer with thin-film Ti layers on either side. PECVD silicon carbide (SiC) has been used as the dielectric spacing layer. SiC is to be preferred because of the high resistance to HF etching. Another advantage of using SiC for the spacing layer is the decreased process complexity, since it is also used for the protective coating. Prior to the design, the optical properties of PECVD SiC have been measured by ellipsometry. Figure 3 shows the measured optical properties of PECVD SiC, which are in agreement with the values reported in literature [9].

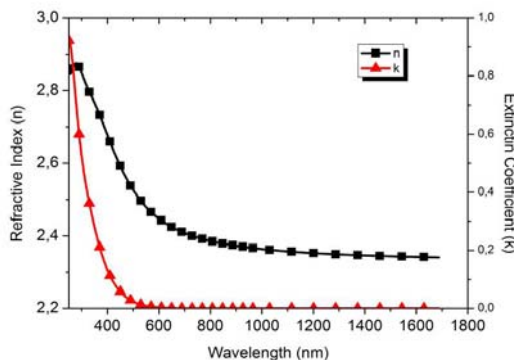


Figure 3: Measured optical properties of PECVD SiC.

The Ti (50 nm)/SiC (200 nm)/Al (300 nm) three layer stack interference absorber with the additional SiC (200 nm) protective layer result a 4-layered SiC/Ti/SiC/Al stack, which is the IR absorber. In an optimization step also the bridge layers are taken into account. The layers on the bridge include 700nm SiN, 300nm PolySi and 100nm 2<sup>nd</sup> SiN. The comparison

between absorber on top of thermopile bridge and bridge only case is shown in figure 4. The relatively high absorptance covers from 1.5  $\mu\text{m}$  to 5  $\mu\text{m}$  wavelength range. This wide spectral range could be applied to some targets for gas spectroscopy application.

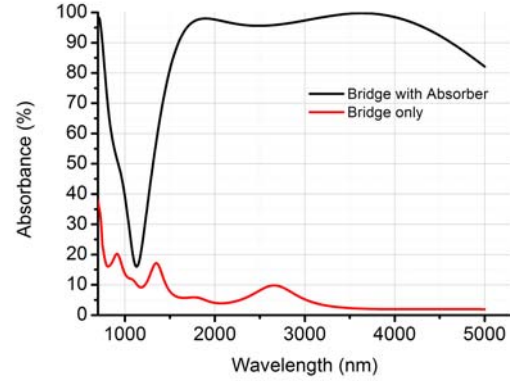


Figure 4: IR absorbance simulation results.

## III - Fabrication of the absorber

The fabrication of thermopile detector array starts with a 4  $\mu\text{m}$  PECVD TEOS as the sacrificial layer. The process used for the fabrication of the uncoated TE elements has been described in detail in previous work [2]. However, surface micromachining is implemented instead of bulk micromachining. This section is focused on the fabrication of absorber and realizing of bridge structure illustrated in figure 5. The CMOS compatible bridge fabrication stops at the second SiN layer of 100 nm thickness and is followed by deposition of the layer stack used for the absorber. The contact hole etching and metallization are completed prior to sacrificial etching. The process steps for the absorber are: The 300 nm Al is sputtered followed by the patterning step to define the thin film in the middle position of the bridge. SiC with 200 nm thickness is deposited with PECVD process. Next, the 50 nm Ti is sputtered and patterned on top of SiC layer. The second 200 nm SiC is deposited on top of these layers to form SiC/Ti/SiC/Al four-layer stacks. The two SiC layers are etched and patterned, followed by reactive ion etching (RIE) in a final step to form the bridges in the detector array out of membrane. The fabricated device before sacrificial release is shown in figure 1. The dimension of the detector array has 7.2×0.76 mm<sup>2</sup>, with an area of each pixel of 650×36  $\mu\text{m}^2$  with a 45  $\mu\text{m}$  pitch. The absorber is deposited in the middle position of bridge with 5 thermocouples at the upper and lower side of bridge. The SEM photo shows the cross section of absorber in figure 6(a). The aluminum layer is not uniform distributed and therefore do apply to the subsequent layers. This is due to the skip of annealing process after the sputter of Al as shown in figure 6(b). Ti and Al layer together with a 200 nm SiC layer forms a sandwich structure that is used as the IR absorber.



### Processing Steps

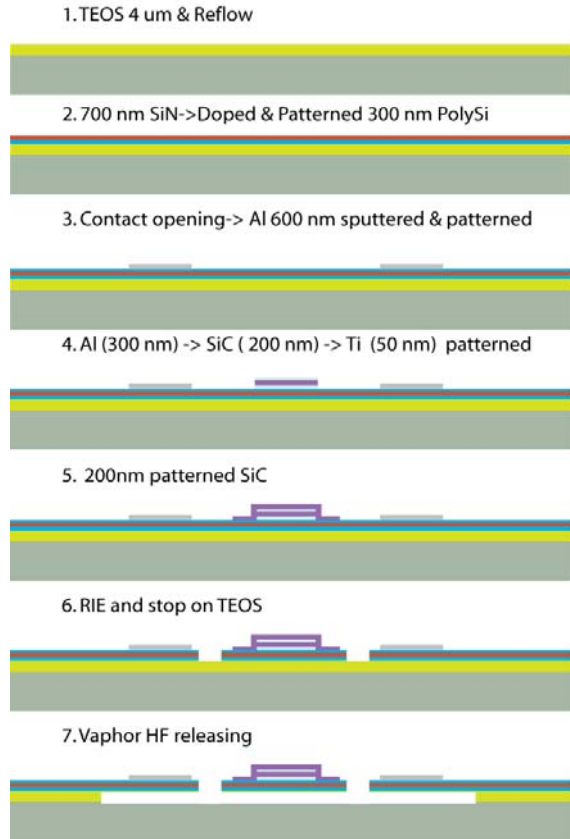
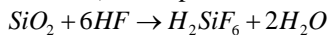


Figure 5: Fabrication steps. (thermopile is not illustrated)

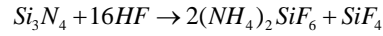
Sacrificial etching is performed to realize structures with reduced thermal diffusion in the direction normal to the plane in which the TE elements are integrated (i.e. vertical). The width of a bridge is  $36\ \mu\text{m}$  with and the spacing between bridges is  $10\ \mu\text{m}$ . HF at 73% was used as the etchant due to the relatively slow etch rate of aluminium. The etch rate was determined by initial tests and was found to be  $1740\ \text{nm}$  per minute. The total etching time is set to 10 min and 30 sec by considering the etching rate and the width of the bridge. After that the die is rinsed in IPA for several times to remove HF. To prepare for freeze drying, the die is immersed in Cyclohexane solution for 10 minutes. Freeze drying is performed to avoid stiction of the released structures. The yield of free-standing structures is better than 90%. However, the insufficient coverage by the protection layer, which is  $200\ \text{nm}$  SiC, is examined at the sidewall. As a result underetching is observed at the rim of the absorber, due to partly removal of the thin Ti layer.

Another effort was aiming on the prevention of the Ti attack by vapor HF etching. A sample was placed above 73% solution with the distance of  $4\ \text{cm}$  in a closed chamber. The device was placed on a heater (at the backside) to evaporate the water during the reaction:



The purpose of removing the generated water is to significantly reduce the etch rate of metal used at the absorbers and the electrical interconnection. The etch rate is  $600\ \text{nm}$  per minute at a temperature of  $30^\circ\text{C}$ . Higher temperatures would decrease the etch rate

dramatically. One of advantages to use vapor HF is to minimize stiction during structural etching. During the vapor HF etching of SiN, residues are created according to equation:



The residue,  $2(\text{NH}_4)_2\text{SiF}_6$ , forms a non-transparent film and cause an apparent increase in film thickness which in extreme cases can lead to a cracking of the structural layer on top as shown in figure 7. The etch rate of SiN in vapor HF is still subject to test.  $2(\text{NH}_4)_2\text{SiF}_6$  can be sublimated with hotplate in the vacuum pressure [10]. The device has been placed into  $180^\circ\text{C}$  hotplate at  $1\ \text{mBar}$  for 40 minutes.

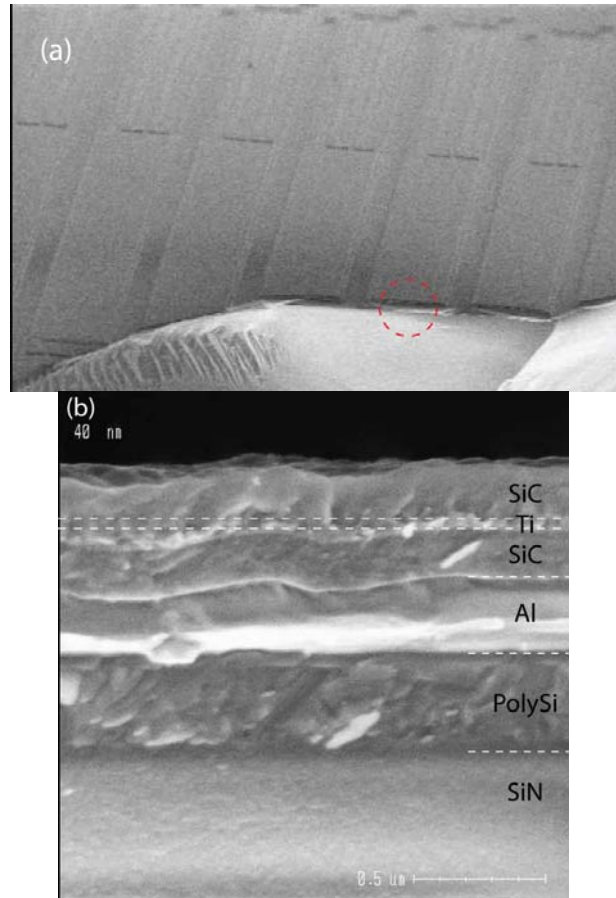


Figure 6: (a) SEM of clipped bridge for cross-section analysis. (b) SEM detail of the cross-section of circle shown in the circle in figure 6(a) before structural release.

### IV – Measurements

The measurement results of the IR absorptance of thermocouple bridge is shown in table 1. Three different wavelength LEDs with different optical power have been used as light source under atmosphere and vacuum pressure. A  $1285\ \text{nm}$  LED is used to illuminate the bridge with and without absorber respectively, meanwhile the static response of thermal Seebeck voltage is recorded. The range of output voltages of bridge with absorber present is up to  $180\ \text{mV}$  while the maximum voltage is only  $55\ \text{mV}$  without absorber. The voltage ratio is calculated to be about 3. The simulation result of



absorptance of bridge with absorber is about 44% between 1280-1290 nm wavelength range, while the absorptance of the bridge without absorber is 14%. As a result, the absorptance ratio is 3.2. The difference between measured and simulated results is only 7%, which adds to the credibility of the simulations. The sensitivity of TE element is low (10.6 V/W) when operated at atmospheric pressure. This is mainly due to most of heat flux from absorber conduct to substrate via 4  $\mu\text{m}$  path instead of bridge. The sensitivity is relatively high (461.5 V/W) in the low-pressure environment when detector is illuminated with a 3400 nm IR LED. The absorptance ratio at 3400 nm wavelength is about 8.6, which is much lower than the simulated result of 39. This deviation can be explained by the following reasons. First, extrapolated data is being used in the simulation tool for wavelength above 1.2  $\mu\text{m}$ . Secondly, the LED source is not perfectly aligned with the targeted bridge when operating in the vacuum chamber. Thirdly, variations in the thickness of the thin film due to fabrication tolerances are not considered. Despite the discrepancy between simulation and measured results, the improved sensitivity of TE element at the vacuum pressure operation is considerable.

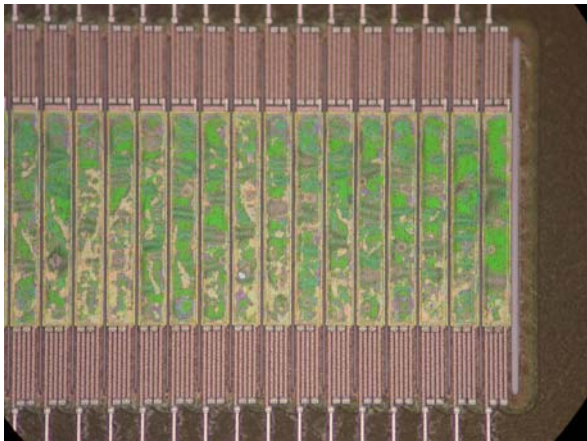


Figure 7: Residues formed after vapor HF release.

Table 1: Measurement results

Source wavelength/ operating pressure	TE with absorber		TE only	
	V	Sen	V	Sen
1285 nm/1016 mBar	180	10.6	55	3.2
3400 nm/0.2 mBar	60	461.5	7	53.8
3400 nm/117 mBar	3	23	0	0
4200 nm/0.2 mBar	3	77	2	51.3
4200 nm/114 mBar	0.3	7.7	0.2	5.1
V: voltage of TE element. Unit: $\mu\text{V}$				
Sen: calculated sensitivity of TE element by reference detector				
Unit: V/W				

## V - Conclusions

The design and fabrication of the CMOS compatible interference filter based absorbers for thermopile detector array is presented. The dimensions of the detector array are  $7.2 \times 0.76 \text{ mm}^2$ , with an area of each pixel of  $650 \times 36 \text{ } \mu\text{m}^2$  with a 45  $\mu\text{m}$  pitch. The approach presented here can be used on the narrowly spaced and thin

micromachined bridges that are typically used in high sensitivity MEMS thermopile detectors. SiC has been used as the spacing layer in the interference filter based absorber, together with Ti and Al to form the sandwich structure. SiC is relatively resistant to HF etching compared to  $\text{SiO}_2$ . However, sidewall and pin holes issues had to be taken into account in the design phase. Although, the measured results have shown higher deviation in the longer wavelength range, the sensitivity of device is promising at vacuum pressures.

## Acknowledgements

This work has been supported in part by the Dutch technology foundation STW under grant DET.6667. Devices have been fabricated at the DIMES (Delft Institute of Microsystems and Nanoelectronics). The authors are indebted to W van der Vlist for his assistance in device fabrication and to P. M. Sarro for helpful discussions on the processing.

## References

- [1] R. F. Wolffenbuttel, *J. Micromech. Microeng.*, 15, pp.145-152, 2005.
- [2] H. Wu, S. Grabarnik, A. Emadi, G. de Graaf and R.F. Wolffenbuttel, *J. Micromech. Microeng.*, 18 064017, 2008.
- [3] M. Hirota, Y. Nakajima, M. Saito and M. Uchiyama, *Sensors and Actuators A*, vol. 135, pp. 146-151, 2007.
- [4] P. A. Silberg, *J. Opt. Soc. Am.*, vol. 47, pp. 575-578, 1957.
- [5] A.D. Parsons, D.J. Pedder, *J. Vac. Sci. Technol. A* 6, pp. 1686, 1987.
- [6] H. Bosman, Y. Y. Lau, and R. M. Gilgenbach, *Appl. Phys. Lett.* 82, pp. 1353, 2003.
- [7] F. Niklaus, C. Jansson, A. Decharat, J. E. Källhammer, H. Pettersson, G. Stemme, *Proceedings of SPIE 6542 Infrared Technology and Applications XXXIII*, pp. 65421M-1–65421M-12, 2007.
- [8] TFCalc™ 3.3, Software Spectra Inc, [www.sspectra.com](http://www.sspectra.com)
- [9] G. Pandraud, H. T. M. Pham, P. J. French, and P. M. Sarro, *Optics and Laser Tech.*, no. 3(39), pp. 532–536, 2007.
- [10] B. Du Bois, G. Vereecke, A. Witvrouw, P. De Moor, C. Van Hoof, A. De Causemaeker and A. Verbist, *Proc. Sensor Technol. Conf. (Leuven, Belgium)*, pp. 131–6, 2001.

# THERMAL ANALYSIS, FABRICATION AND SIGNAL PROCESSING OF SURFACE MICROMACHINED THERMAL CONDUCTIVITY BASED GAS SENSORS

G. de Graaf, H. Wu and R.F. Wolffenbuttel

*Delft University of Technology, Faculty EEMCS, Dept. for Micro-Electronics, Mekelweg 4, 2628 CD Delft, The Netherlands*

**Abstract** — This paper presents the design, analysis, fabrication and readout of surface micro-machined Thermal Conductivity (TCD) gas sensors. The sensors were fabricated on thin SiN bridges. Integrated thermoelectric detectors are used as temperature sensors and polysilicon resistors as heaters. A general thermal analysis of surface micro-machined structures is included for calculating the static and dynamic response of the micro-scale TCD. Based on this analysis, methods for DC and AC readout of the device are discussed and have been implemented. The sensitivity for hydrogen in air is around  $60\mu\text{V}$  per %  $\text{H}_2$  at  $1\text{mW}$  heater dissipation. Preliminary measurements have indicated a good stability and a higher sensitivity than the bulk micro-machined TCD gas sensors currently available.

**Keywords :** Thermal Conductivity Sensor, TCD, Surface micromachining, Thermal Gas Sensor, Dynamic Thermal Analysis.

## I – Introduction

Gas detection based on thermal conductivity is widely used in process control and in gas chromatography [1][2]. The most common technique is the hot-wire sensor [1], which is based on a thin metal wire mostly made of platinum. The wire simultaneously operates as a heater and sensing element. The wire and the surrounding medium under investigation, is heated by applying a transient electrical current. Recording the corresponding temperature response of the wire enables the determination of the thermal conductivity and diffusivity of the surrounding gas. Instead of a wire, other heater geometries such as thin metal sheets have also been utilized [3]. Micro hot-wire sensors have already replaced the traditional hot-wire and hot-strip sensors in many applications [4][5]. Micro-strip TCD's based on thin film platinum wires have been published by several authors and are also commercially available [6][7][8]. Separation of the heater and the temperature sensor enables a more flexible design in a micro-TCD. The recent advances in IC technology enable the fabrication of many types of IC-compatible, small, high sensitivity and low cost thermal sensors and heaters. Additional MEMS post-processing technology enables fabrication of these devices on thermally isolated structures resulting in more new low-power, high-performance thermal conductivity gas sensors [9][10][11]. Most of these devices use bulk micro-machining for thermal isolation of the sensor. The design presented here is based on surface-micromachining technology, since TCD's fabricated in

surface micromachining technology devices can have a higher sensitivity, smaller sample volume and, as a consequence, a shorter response time. In addition this technique is more compatible with current CMOS IC technology.

## II – Micro TCD design and operation

The thermal conductivity sensor has been fabricated using IC compatible techniques on a thin silicon-nitride bridge structure, as shown in the cross-section in figure 1. Gas venting to the bottom of the membrane and the substrate is possible via the bridge sidewalls and the etching holes, as can be seen in figure 1 and 2. The sensor membrane size is typically  $250 \times 330 \mu\text{m}^2$ . Thermocouples, using poly-silicon wires, have been chosen as temperature sensors. Bridge or cantilever structures provide the highest thermal isolation when using thermopiles as temperature sensors. As will be shown in the thermal model, the sensor will be less sensitive to changes in ambient temperature by the use of integrated thermopiles, since these devices inherently measure temperature differences in the device. The heating element is a poly-silicon resistor placed in the middle of the bridge.

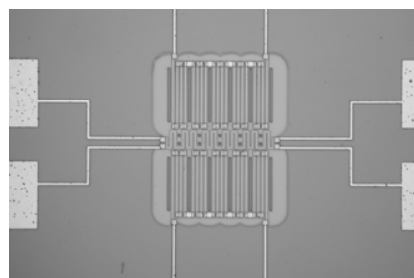


Figure 1: Microphotograph of the fabricated MicroTCD

The membrane is heated by the resistor in the middle of the membrane. The temperature difference between the membrane and ambient is measured by the thermopiles at the top and bottom.

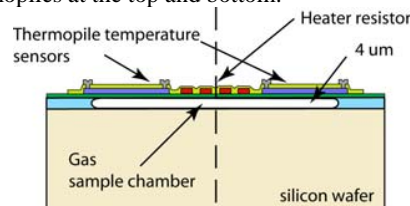


Figure 2: Cross-section of the fabricated MicroTCD

The measurement principle relies on the decrease in effective thermal resistance between the sensitive area

of the sensor (the membrane) and ambient, mainly by the thermal conductance of the gas in the narrow cavity below the membrane, as shown in the cross-section of figure 2. The thin gas layer results in a high sensitivity for the gas thermal conductance.

## II – Thermal model

For reasons of symmetry only a half of the bridge is considered in the analysis. A three-dimensional thermal model of the beam is shown in figure 3. The model has been simplified by assuming a very thin membrane, a heat flow in the x-direction by conduction in the beam and a dominant heat flow through the very thin layer of gas to the substrate in the (-z) direction only.

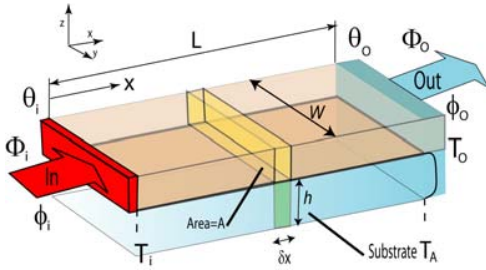


Figure 3: Heat conduction in the TCD membrane.

Based on these assumptions the static heat balance of a slice of the beam equals:

$$\phi(x+dx) = \phi(x) - \left( \frac{\lambda_g W}{h} dx \right) (T - T_A), \quad (1)$$

where the right-hand term represents the conduction of the beam (width=W) through the gas with a thermal conductivity  $\lambda_g$  and a path length  $h$  to the substrate ( $T_s$ ). Due to the low mass of the gas volume in the sample chamber the effect of changes in thermal diffusivity of the gas sample will be around five orders of magnitude lower than the equivalent thermal diffusivity of the bridge structure. As a consequence changes in diffusivity of the gas can be neglected in the thermal model of the device. The dynamic heat equation of the beam can now be written as:

$$\frac{\partial^2 T}{\partial x^2} - \left( \frac{\lambda_g W}{h} \right) (T - T_A(t)) = \frac{1}{\alpha} \frac{\partial T}{\partial t}, \quad (2)$$

where  $\alpha$  is the equivalent thermal diffusivity of the beam. Application of the Laplace transform yields:

$$\frac{\partial^2 \Theta}{\partial x^2} = \left( \frac{p}{\alpha} + \frac{\lambda_g W}{h} \right) (\Theta - \Theta_A(p)) \quad (3),$$

where  $p$  is the Laplace operator and  $\Theta$  and  $\Theta_A(p)$  are the Laplace variables of the temperatures  $T$  and  $T_A(t)$  respectively. Assuming a constant ambient temperature  $T_A(t) = T_A$  above equation can be written as:

$$\frac{\partial^2 \Theta}{\partial x^2} = \left( \frac{p}{\alpha} + \frac{\lambda_g W}{h} \right) (\Theta - \Theta_A), \quad (4)$$

Its solution is:

$$(\Theta_{out} - \Theta_A) = (\Theta_{in} - \Theta_A) e^{\gamma x} \text{ with: } \gamma^2 = \left( \frac{p}{\alpha} + \frac{\lambda_g W}{h} \right) \quad (5)$$

The input heat flow  $\phi_{in}$  is by definition proportional to the temperature gradient across the surface at  $x=0$  and therefore given by:

$$\phi_{in} = -\lambda A \left\{ \frac{\partial T}{\partial x} \right\}_{x=0} \quad (6)$$

with  $\lambda$  the equivalent thermal conductivity of the beam and  $A$  the cross-sectional area of the beam. The Laplace transform of the input heat flow  $\Phi_{in}$  can be found using equation (5) with  $x=0$  as

$$\Phi_{in} = \lambda A \left\{ \frac{\partial \Theta}{\partial x} \right\}_{x=0} = \lambda A \left\{ \frac{\partial ((\Theta - \Theta_A) e^{\gamma x})}{\partial x} \right\}_{x=0},$$

therefore  $\Phi_{in} = \gamma \lambda A (\Theta - \Theta_A)$  (7)

The thermal impedance  $Z_b$  of the beam is now found as:

$$Z_b = \frac{(\Theta - \Theta_A)}{\Phi_{in}} = \frac{1}{\gamma \lambda A} = \frac{1}{\lambda A \sqrt{\frac{p}{\alpha} + \frac{\lambda_g W}{h}}} \quad (8)$$

It should be noted that in this analysis the thermal impedance is proportional to  $p^{-1/2}$  while in the lumped element approach, using  $R_L C_L$  elements, the thermal impedance would be in the form  $Z_{bL} = \frac{R_L}{1 + p R_L C_L}$  so

proportional to  $p^{-1}$ . In both models the beam can be regarded as a thermal low-pass filter. With  $p=j\omega$  equation (8) results in a -3dB corner frequency

$$\omega = 1.73 \frac{\alpha \lambda_g W}{h} \text{ and a slope of -10 dB/dec.}$$

In the steady-state regime ( $p=0$ ) we can write the thermal resistance as:

$$R_b = \frac{1}{\lambda A \sqrt{\frac{\lambda_g W}{h}}} \quad (9)$$

The equivalent thermal conductivity  $\lambda$  of the beam structure can be found by measuring the sensor in vacuum using the  $3\omega$  method [12]. For this reason the temperature coefficient of the polysilicon heater needs to be known also. This value may result from an accurate resistance measurement at different temperatures in an oven.

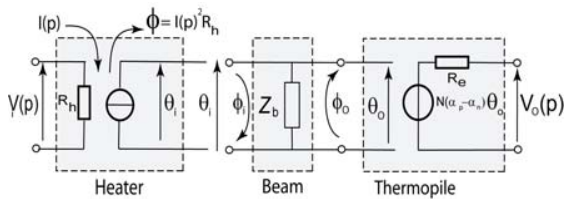


Figure 4: Block diagram of the TCD in the Laplace domain.

The output signal of the thermopile caused by the temperature difference is given by:

$$V_o = N(\alpha_N - \alpha_p)(T - T_A) \quad (8)$$

with  $N$  the number of thermocouple pairs and  $\alpha_N, \alpha_p$  the Seebeck coefficients of the thermopile material pair.

The Seebeck coefficient of the thermopiles in the described process has been measured as  $(\alpha_N - \alpha_P) = 180 \mu\text{V/K}$  [13]. Dynamic or (quasi)static operation is of the micro-TCD is possible, depending on the electrical excitation signal to the heater.

### III – DC operation

If a DC current  $I$  is fed through the heater the relation between the sensor output  $V_o$  and changes in the gas conductivity  $\lambda_G$  can be calculated by combining equations 7 and 8

$$V_o = N(\alpha_N - \alpha_P)\Phi_{in}R_b = \frac{N(\alpha_N - \alpha_P)R_h I^2}{\lambda A \sqrt{\frac{W}{h}}} \frac{1}{\sqrt{\lambda_G}} \quad (8)$$

This equation shows that the thermopile output voltage is proportional to the heater power  $I^2 R_h$  and inversely proportional to the square root of the thermal conductivity of the gas.

### IV – AC operation

Offset, caused by parasitic heat flows in the sensor or by the readout amplifier of the thermopile, can be eliminated by modulation. Basically the amplitude or the phase of the thermopile output voltage with respect to the excitation signal can be detected.

#### A. Square wave modulation

A square wave with an offset equal to the amplitude (on/off signal) is the most straightforward implementation for modulation of the sensor. The main disadvantage is that direct electrical crosstalk, e.g. by ground loops or capacitive coupling via the bonding wires, of the large excitation voltage may introduce synchronous switching spikes that may appear as an offset after demodulation of the thermopile signal.

#### B. Harmonic modulation

A harmonic excitation current  $I(t) = A \sin(\omega t)$  will produce a second harmonic in the thermal signal according to:

$$\begin{aligned} \phi(t) &= R_h I^2 (\sin(\omega t))^2 \\ &= R_h I^2 \left( \frac{1}{2} - \frac{1}{2} \cos(2\omega t) \right) \end{aligned}$$

Demodulation of the cosine (phase shift of  $90^\circ$ ) component at a frequency  $2\omega$  detects the second harmonic only. This method enables detection of the thermal signal only and suppresses DC offset and the electrical crosstalk at the fundamental  $\omega$  in the excitation signal. The relation between the thermal conductivity of the gas  $\lambda_g$  and the thermopile output voltage in the Laplace domain is then given by

$$V_o(p) = \frac{N(\alpha_N - \alpha_P)\Phi_{in}Z_b}{p} = \frac{N(\alpha_N - \alpha_P)R_h}{p\lambda A \sqrt{\frac{p}{\alpha} + \frac{\lambda_g W}{h}}} I^2(p)$$

$$\text{For a sine wave: } V_o(p) = \frac{N(\alpha_N - \alpha_P)R_h}{p\lambda A \sqrt{\frac{p}{\alpha} + \frac{\lambda_g W}{h}}} I_o \left( \frac{\omega^2}{p^2 + 4p\omega^2} \right)$$

After transformation to the time domain above equation shows that the amplitude and phase shift of the thermopile signal at  $2\omega$  depends on the gas conductivity  $\lambda_g$ .

## V – Fabrication of the micro TCD

Fabrication of the TCD sensor was done in DIMES facility of the TU-Delft. The process sequence is shown in figure 5. Wafer processing started with the deposition and reflow of the sacrificial layer of  $4 \mu\text{m}$  TEOS. On top of the oxide layer a  $700 \text{ nm}$  layer of low stress SiN film is deposited. Next, a  $300 \text{ nm}$  low-stress PolySi layer is grown by LPCVD. After this several masked process steps followed for the fabrication of the thermopiles and the heater. Boron is implanted at  $40 \text{ keV}$  and  $5 \times 10^{15} \text{ cm}^{-2}$  to realize p-type PolySi. After a cleaning procedure, n-type PolySi is formed by phosphorous doping ( $40 \text{ keV}$  and  $7.5 \times 10^{15} \text{ cm}^{-2}$ ). In the next step,  $100 \text{ nm}$  SiN is deposited by LPCVD and patterned. A RIE etch, stopping on the sacrificial layer, is applied for defining the MEMS structures. Contacts to the PolySi are patterned and etched in the top SiN layer. Finally aluminium is deposited and patterned on top to define the connections between the PolySi layers and the bonding pads. After this the wafers were tested and diced.

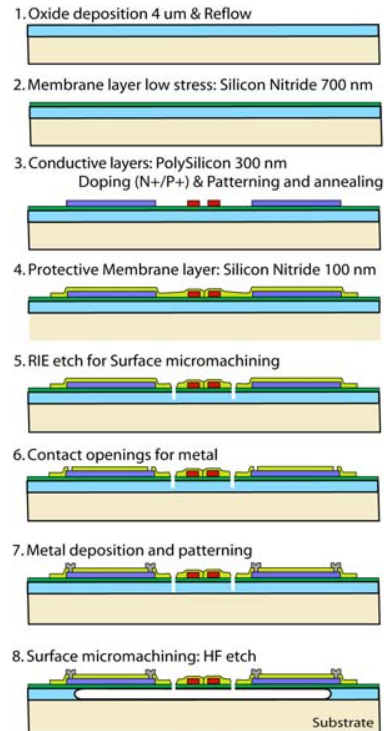


Figure 5: Fabrication steps.

Surface micromachining has been applied as post process at the die level. Several dies were etched simultaneously in a holder using both wet and vapour etching techniques. High concentration (73%) HF has been used, since this does not attack the unprotected aluminium. An etching time of 10min and 30s at an etch rate of  $1.74 \mu\text{m/min}$  was required for the TEOS layer to free all membranes and bridges. After this the dies were thoroughly rinsed several times in IPA to remove the HF. Next the dies were immersed in cyclo-hexane for 10



minutes as a preparation for the final freeze-drying step. Sublimation was achieved at  $-14^{\circ}\text{C}$  for 30 min to finish the process. Another method to free the structures is vapour etching. At  $30^{\circ}\text{C}$  an etch rate of  $0.6\text{ }\mu\text{m}/\text{min}$  has been used for around 28min to free all structures. The wet etching requires a very careful cleaning and freeze-drying procedure to prevent sticking of the structures, while using the vapor etch technique almost no sticking of the bridges has occurred. Figure 1 shows a photo of one of the devices after the surface micromachining step. For complete processing of the device only six masks were needed.

## VII - Measurement results

The first samples have been tested using the DC method as described in section IIIa. For this a Keithley 236 DC current source has been applied to the heater and an Agilent 34420A DC nano-voltmeter has been used for the measurement of the thermopile voltage. Due to safety reasons we used helium instead of hydrogen as a test gas. The thermal conductivity of hydrogen is about 20% higher than helium and therefore the output signals for hydrogen are expected to be a factor  $\sqrt{1.2} = 10\%$  higher than the results presented here. The thermal conductivity of carbon dioxide is a factor 9.7 lower than that of helium and so for pure  $\text{CO}_2$  the signals will be a factor 3 lower. Some measurement results on gas sensing using the micro TCD sensor with helium as a test gas are shown in figure 6.

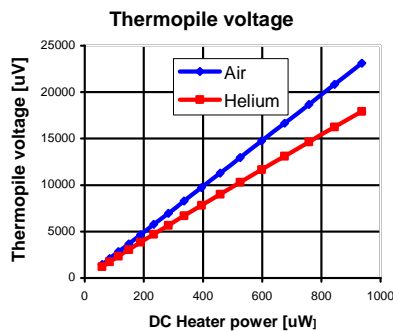


Figure 6: TCD Gas sensor: DC output voltage using He and air (100mBar) at different heater power levels.

The overall sensitivity can be increased by increasing the input current, i.e. heating power. A input power of around 1 mW provided a sufficient temperature difference for the detection of helium at a level of less than 1%. AC measurements have been done using a sine wave at a frequency  $f=20\text{ Hz}$  for modulation. A Stanford Research SR830 lock-in amplifier has been used for measuring the quadrature ( $90^{\circ}$ ) component of the second harmonic  $2f$ . This signal showed a significant less amount of drift and noise as compared to the DC system. More data on measurements is given in the paper by S. Chen.

## VIII - Conclusions

Design, analysis, fabrication, signal processing and first measurement results of a thermal conductivity

(TCD) gas sensor based on surface micromachining technology has been presented in this work. The sensor membrane size is typically  $250 \times 330\text{ }\mu\text{m}^2$ . The sensitivity for hydrogen in air is around  $60\text{ }\mu\text{V}$  per %  $\text{H}_2$  at 1mW heater dissipation. Due to the short thermal path of the sensor via the gas to the substrate, a significantly higher sensitivity than other MEMS TCD's is possible. The sensors have shown a good stability and low hysteresis. More long term measurements on accurate gas mixtures are needed for more quantitative data. Thermal conductivity gas sensors are inherently sensitive to the gas pressure and therefore future work on these devices will be on the integration of a pressure sensor for compensation. Other future research topics are the reduction of the effects of gas convection and on the integration of the electronic circuits for the readout using the AC method.

## Acknowledgments

This work has been supported in part by the Dutch technology foundation STW under grant DET.6667. Devices have been fabricated at the DIMES Institute in Delft. The authors are indebted to S. Chen for measurements, P. M. Sarro for processing advice and especially to W. van der Vlist from DIMES for the main part of the device fabrication.

## References

- [1] H.A. Daynes, Gas Analysis by Measurement of Thermal Conductivity, Cambridge University Press, Cambridge, Great Britain, 1933, pp. 1–302.
- [2] W. Jennings, E. Mittlefehldt and P. Strempel, Analytical Gas Chromatography, Second Edition, Elsevier Inc., ISBN-13: 978-0-12-384357-9, 389 pages, Sep. 1997.
- [3] S.E. Gustafsson, H. Nagai, T. Okutani, Thermal diffusivity measurements of insulating liquids using micro-sized hot-strip probes, Rev. Sci. Instrum. 74 (10) (2003) 4542–4548.
- [4] M. Kimura, J. Manaka, S. Satoh, S. Takano, N. Igarashi and K. Nagai, Application of the Air Bridge Microheater to gas detection. Sensors&Actuators B 24–25 (1995), pp. 857–860.
- [5] R.P. Manginell, J.H. Smith, A.J. Riccio, An overview of micro-machined platforms for thermal sensing and gas detection, Proceedings of SPIE on International Society of Optical Engineering, 1997, pp. 273–284.
- [6] P. Tardy, J. Coulon, C. Lucat, F. Menil, Dynamic thermal conductivity sensor for gas detection, Sensors and Actuators B 98 (2004) 63–68.
- [7] S. van Herwaarden, Thermal Conductivity Gauge TCG-3880 for gas type and vacuum measurement, <http://www.xensor.nl/pdf/files/sheets/tcg3880.pdf>.
- [8] L. Boon-Bretta, J. Bouseka, P. Moretto, Reliability of commercially available hydrogen sensors for detection of hydrogen, Part II, Int. Journal of Hydrogen Energy 34 (2009) 562 – 571.
- [9] G. Pallack-Diener and E. Obermeier, Heat conduction microsensor based on silicon technology, Sensors&Actuators B 13–14 (1993), pp. 345–347.
- [10] I. Simon and M. Arndt, Thermal and gas-sensing properties of micromachined thermal conductivity sensor for the detection of hydrogen in automotive applications. Sensors&Actuators A32-12(2002), pp. 1–5.
- [11] S. Sorge and T. Pechstein, Fully integrated thermal conductivity sensor for gas chromatography without dead volume. Sensors&Actuators A 63 (1997), pp. 191–195.
- [12] D.G. Cahill, Thermal conductivity measurement from 30 to 750 K: the 3x method, Rev. Sci. Instrum. 61 (2) (1990) 802–808.
- [13] H. Wu, A. Emadi, G. de Graaf, and R.F. Wolfenbittel, Encapsulated thermopile detector array for IR microspectrometer, Proc. SPIE, Vol. 7680, 27 April 2010.

# HIGH ASPECT RATIO HYDROGENATION-ASSISTED LATERAL ETCHING OF (100) SILICON

M. Kayyalha<sup>1</sup>, J. Naghsh Nilchi<sup>1</sup>, A. Ebrahimi<sup>1</sup>, S. Mohajerzadeh<sup>1</sup>

<sup>1</sup>University of Tehran; Nano-Electronics and Thin Film Lab.; Tehran, Iran

**Abstract** — In this paper hydrogenation-assisted high aspect ratio lateral etching of (100)-oriented Si wafer is presented. After desired patterning, vertical etching is used to etch the structure to achieve the appropriate height where needed. Afterward, a hydrogenation step is applied to create defects in depth of about 100 nm. Created damaged planes are finally dissolved in Secco etchant, releasing a thin silicon layer. The effect of hydrogen ions in formation of defects at desired depth has been investigated. Process temperature was swept to examine its influence on lateral etching. In addition to scanning electron microscopy, EDX analysis has been performed to prove existence of a silicon layer underneath chromium which served as the protection layer.

**Keywords:** Etching, (100)-silicon, Secco, Hydrogenation

## I - Introduction

Anisotropic dry etching of silicon, especially vertical etching, is one of the most important steps in fabrication of Micro Electro-Mechanical Systems (MEMS), such as accelerometers, microphones, gyroscopes, actuators, etc. There have been many researches focused on vertical micromachining of silicon, such as a process developed by Robert Bosch GmbH [1], hydrogenation-assisted reactive ion etching [2] and a process which relies on cooling the silicon substrates to cryogenic temperatures using liquid nitrogen [1, 3, 4]. However lateral micromachining of silicon is not as mature as its etching in vertical direction.

Intentional underetching is one of the key parameters in different microelectronic areas, e. g. floating of movable proof masses in MEMS structures [5], Silicon on Nothing (SON) devices [6], etc. So far, several techniques have been reported by different research groups. In SON transistors, an epitaxial growth of a SiGe layer followed by epitaxy of silicon is practiced on silicon substrates and finally thin silicon film, which is later served as transistor channel, is floated by lateral etching of SiGe layer [6]. Also, in fabrication of MEMS devices, SOI wafers or successive deposition/isolation/etching of sacrificial layer steps is used to float the structure [5].

In this paper, a novel method of lateral micromachining of (100) Si is introduced to form a thin released silicon layer. Our technique is based on defect creation by use of plasma hydrogenation, followed by delineation of defects by means of wet chemical etching in Secco etchant. Evolution of laterally etched structures

has been depicted in scanning electron microscope (SEM) images. Also EDX analysis has been performed to examine the validity of the obtained results.

## II - Experimental Details

The fabrication procedure for realization of lateral etching is shown in Figure 1. The starting material is p-type (100)-Si wafers with a resistivity of about 10  $\Omega$ -cm. A 140 nm chromium layer, deposited using E-beam evaporator, is used as the protection layer in the following reactive ion etching step. The patterned sample is put into our deep etching reactor to achieve 3-4  $\mu$ m vertically etched structures. This etching step includes a sequential combination of passivation and etching steps. During the passivation step, a combination of three gases, i.e. H<sub>2</sub>, O<sub>2</sub>, and SF<sub>6</sub> is used to passivate sidewalls. In etching step, only SF<sub>6</sub>-plasma is used to etch silicon. Total etch rate of this method is about 0.25  $\mu$ m/min [2].

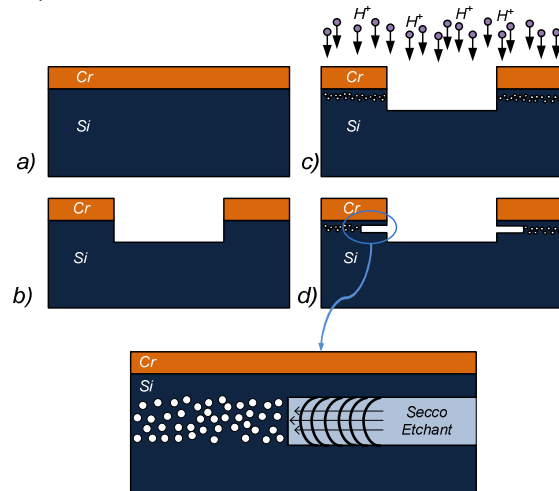


Figure 1: Fabrication procedure of lateral etching. a) Deposition of chromium layer. b) Vertical etching of silicon. c) Hydrogen bombardment. d) Lateral etching with Secco solution.

Once vertical structures are obtained, the sample is placed in a plasma hydrogenating system which its schematic is shown in figure 2. This system has a chamber evacuated up to  $10^{-2}$  Torr and can work in different temperatures as well as different plasma conditions, i.e. different voltage and current conditions.

For defect formation, the above set-up with power of 2.78 W/cm<sup>2</sup> and pressure of 1 Torr is employed to bombard the sample with hydrogen ions. During hydrogen bombardment, the temperature is kept fixed at 550 °C. Direct exposure to plasma introduces damages due to charged particle bombardment [7]. This step leads to

creation of defects in the planes parallel to the surface of the patterned sample [8]. These defects are the main factor responsible for lateral etching of Si. Afterward, etching is carried out in a 0.15-molar Secco solution which consists of hydrofluoric acid and potassium dichromate, and with relative composition as follows: Hydrofluoric acid 67% by volume and 0.15M  $K_2Cr_2O_7$  in  $H_2O$  33% by volume [9]. Although at its preliminary stages, the etch rate of the proposed technique is found to be more than 10 $\mu$ m/min in the wet-etching step, further investigation is needed to arrive at a comprehensive understanding of the etching mechanism and the overall etch-rate.

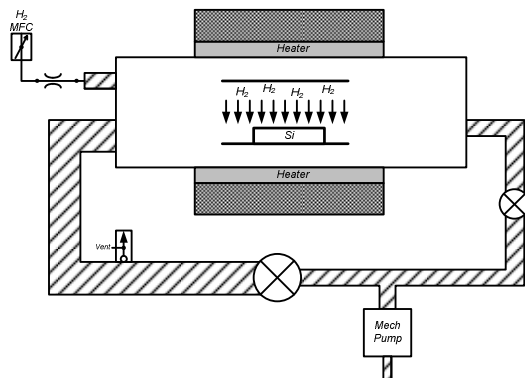


Figure 2: Schematic view of hydrogenating system.

### III - Results and Discussion

SEM images of the sample after vertical etching, with etching depth of about 3 $\mu$ m, are depicted in figure 3. A closer view can be found in the inset. After vertical etching, the sample is put into the designed hydrogenating system and exposed to hydrogen ions by which the defects are created. Finally the sample is placed in 0.15-molar Secco solution which results in lateral etching of Si sample.

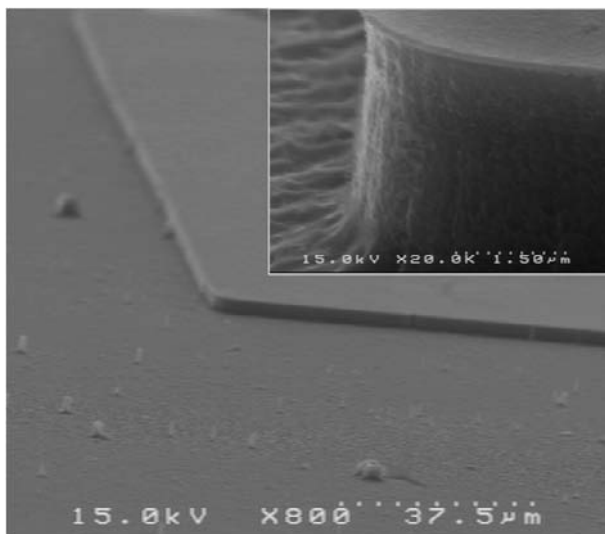


Figure 3: SEM image of sample after vertical etching step. Inset shows its closer view.

Figure 4 shows SEM image of sample at the end of the process. As can be seen from this figure, a thin layer of silicon of about 100-140 nm thickness is separated from silicon substrate. Notice that the top chromium layer of this sample is not removed. The arrow in the figure is to specify the line from where chromium and Si layers are separated.

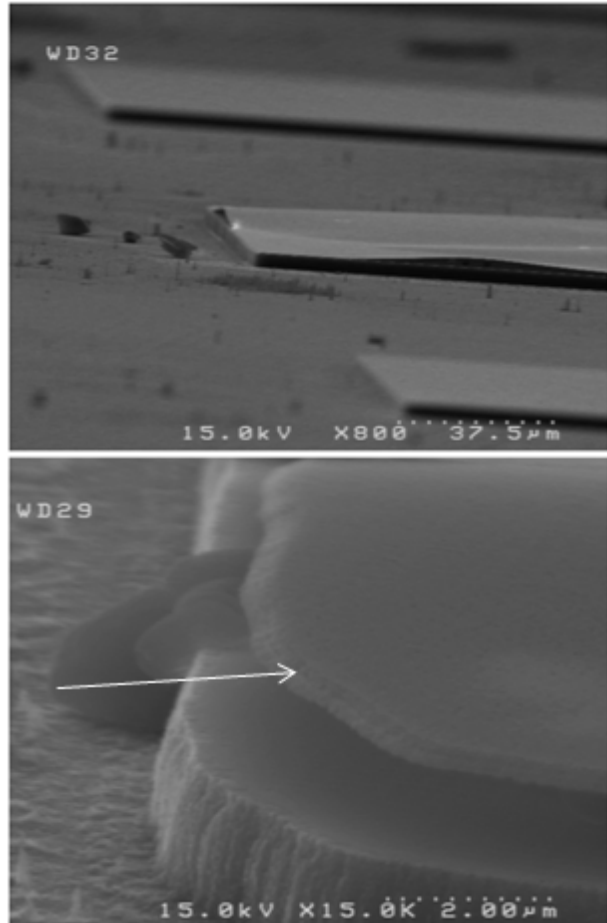


Figure 4: SEM image of sample at the end of process, which is performed in hydrogenating system with power of 2.78 W/cm<sup>2</sup> and pressure of 1 Torr. 0.15-molar Secco was used as the defect-selective etchant. A multi-layer of Si and Cr has been separated from the substrate.

We believe that chromium layer helps the separation of the multilayer sheet from the substrate. In fact, intrinsic stress of Cr layer enhances the split of the top silicon layer from the substrate. Therefore, for two reasons Cr is used as the protecting layer. First, Cr does not easily form silicide at process temperature and second, it resists  $SF_6$  plasma during vertical etching step. Usage of other choices such as silicon nitride may result in requirement of higher energies in hydrogenation step, because electrons do not easily transmit through dielectric layers. Besides,  $Si_3N_4$  does not resist in  $SF_6$  plasma.

Figure 5 shows the comparison of using Secco and KOH solutions to dissolve the defected planes. Since KOH is not defect sensitive and cannot etch the (111) planes, using KOH solution leads to creation of (111) planes which are not desired in our study. This is the reason KOH solution is not used in our experiment.

The Secco chemical etching appears more appropriate to highlight the planar defects [9]. Secco etchant is extremely sensitive to defects and is able to remove defects on all surfaces. In fact, it removes defects and weak bonds created with hydrogen ion near the surface of Si-Cr interface.

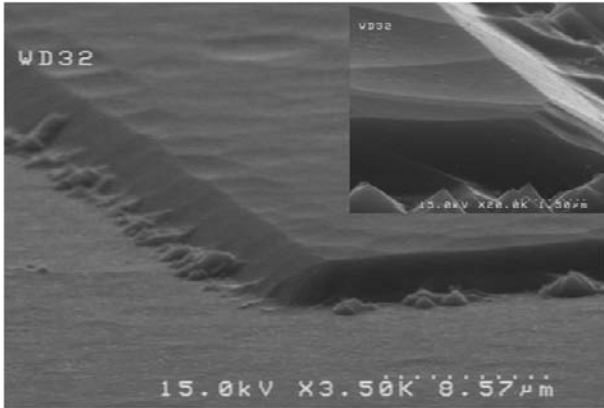


Figure 5: SEM image of hydrogenated sample after use of KOH solution. Inset shows closer view of the sample.

Chemical reactions taken place during etching in Secco can be summarized as follows. The potassium dichromate oxidizes silicon, forming silicon dioxide which will be dissolved in HF. Since the defected area is under higher stress, it will be etched more quickly than the bulk silicon. In most cases, the result is elliptical pits on substrate at the location of the defects [9].

To examine the effects of hydrogenation, two samples are prepared with the same procedure. The only difference is that the first one is bombarded with hydrogen ions with power of  $2.78 \text{ W/cm}^2$  and pressure of 1 Torr while the other one is not hydrogenated at all. The effect of hydrogen bombardment on defect formation is shown in figure 6.

#### A. Formation of Hydrogen-Induced Defect

During hydrogenation of silicon, hydrogen atoms break the Si-Si bonds and form Si-H. The energy needed for this reaction is provided either by plasma or by thermal energy of hydrogenation process.

Noticing the crystalline structure of silicon, one can figure out four intrinsic vacancies in each unit cell [8]. During hydrogen ion bombardment, these vacancies play an important role in formation of defects, i.e. hydrogen ions, which are much smaller than Si atoms and therefore intrinsic vacancies, can be trapped by these vacancies and form VH (Vacancy-Hydrogen) and  $\text{VH}_2$ . Hydrogen molecules trapped in Si crystal can be served as a source of creation of larger defects [8, 10]. These defects create a damaged layer near the surface of Si wafer which is removed by use of proper solution at the end.

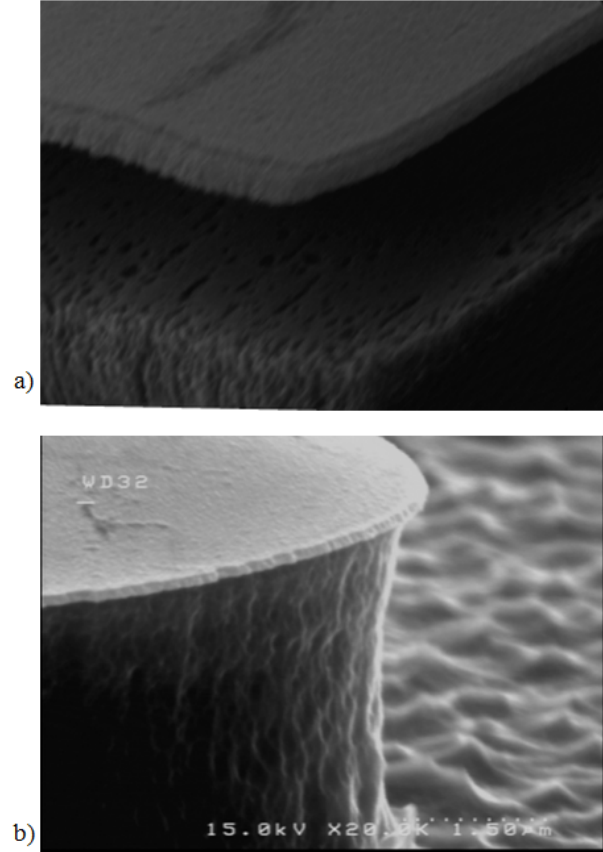


Figure 6: SEM images of the samples after dissolution in Secco a) with hydrogenation and b) without hydrogenation.

It should be noted that in smart cut technology to create defects in depth of 100 nm below the surface, considering the buried thick oxide, energy of about 60 keV is needed in comparison with energies of about 300 eV which is required in our method. In fact, absence of thick oxide layer in the proposed technique leads to lower energies required for defect formation. Besides, high temperature annealing step used in smart cut to localize defects is not employed here. These facts make our proposed technique very simple and commercial.

#### B. Effect of Temperature on Layer Separation

The effect of temperature in this process is very significant to be taken into account. As temperature increases, energy of hydrogen ions which break Si-Si bonds and form defects increases. However, the number of hydrogen molecules escaping from sample increases, as well. So, the time in which samples are exposed to hydrogen ion bombardment at high temperature should be decreased. In fact, as the temperature increases most of the hydrogen-induced defects are formed underneath the interface. This leads to separation of chromium layer from silicon substrate in Secco solution [10].



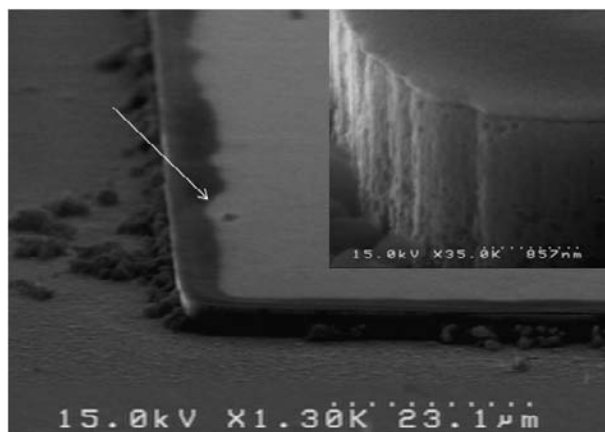


Figure 7: Separation of chromium layer from the bottom Si-layer under high temperature, i.e. above 600°C. The border of separated layers is shown in inset.

Figure 7 illustrates this effect. In this figure, the change in the color of chromium layer, shown by the arrow, specifies the border between the two layers, i.e. chromium layer and Si-layer. Temperature window, in which hydrogen-induced defects are formed on the desired depth of Si substrate and corresponding time needed for formation of these defects, is now under investigation.

### C. EDX Analysis

Figure 8 demonstrates EDX results of the separated multilayer sheet which consists of a Si layer with a thickness of about 100 nm and a 140 nm thick chromium layer on top. Regarding this figure, it is obvious that the thin layer remained under Cr layer is definitely silicon which has been separated from the substrate. To perform this analysis, the top released multi-layer shown in figure 4 was completely separated from the substrate and placed in EDX system.

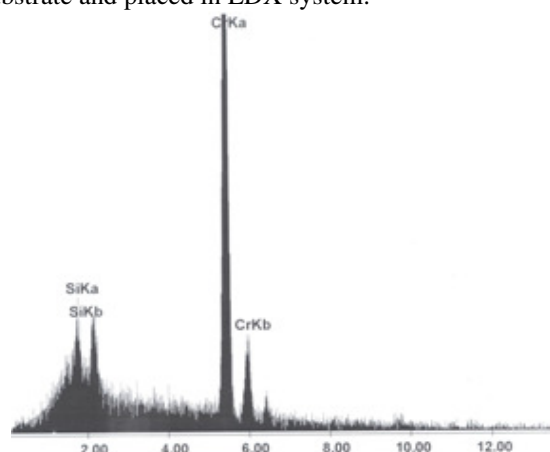


Figure 8: EDX analysis to prove existing of Si-layer underneath of chromium layer.

## IV - Conclusion

Lateral micromachining of (100) Si by combining hydrogenation and chemical removal of damaged silicon planes in Secco etchant is reported. Using this method, a thin silicon layer of about 100nm thickness is separated from the silicon substrate. The proposed technique provides an efficient way to fabricate suspended structures on (100) Si wafers with no need of 3D lithography or SOI wafer. In this method, separation of silicon layers with higher thicknesses demands higher energy which is not available in conventional DC plasma systems and requires ion implantation, leading to complexity and higher cost.

## References

- [1] F. Laermer and A. Schilp, U.S. Patent 5501893, Mar. 26, 1996.
- [2] A. Samak, S. Azimi, N. Izadi, B. K. Hosseini, and S. Mohajerzadeh, J. Microelectromech. Syst., vol. 16, no. 4, pp. 912–918, Aug. 2007.
- [3] M. J. de Boer, J. G. E. Gardeniers, H. V. Jansen, E. Smulders, M.-J. Gilde, G. Roelofs, J. N. Sasserath, and M. Elwenspoek, J. Microelectromech. Syst., vol. 11, no. 4, pp. 385–401, Aug. 2002.
- [4] K. Murakami, Y. Wakabayashi, K. Minami, and M. Esashi, in Proc. IEEE MEMS Conf., Fort Lauderdale, FL, Feb. 1993, pp. 65–70.
- [5] A. Ebrahimi, S. Darbari, S. Mohajerzadeh and S. Azimi, Asia-Pacific Conference on Transducers and Micro-Nano Technology, Tainan, June 2008.
- [6] M. Jurczak, T. Skotnicki, M. Paoli, B. Tormen, J. Martins, J. L. Regolini, D. Dutartre, P. Ribot, D. Lenoble, R. Pantel, and S. Monfray, IEEE Trans. Electron Devices, vol. 47, pp. 2179–2187, Nov. 2000.
- [7] N. M. Johnson, F. A. Ponce, R.A. Nemanich, Phys. Rev., B 35, pp. 4166–4169, 1987.
- [8] Feng, X.Q., Huang, Y., Int. J. Solids. Struct. 41, 4299–4320, 2004.
- [9] A. Abbadie, S. W. Bedell, J. M. Hartmann, O. Kononchuk, D. K. Sadana, F. Brunier, C. Figuet and I. Cayrefourcq, J. Electrochemical society, vol. 154, pp. 713–719, June 2007.
- [10] F. Di, Y.Q. Wang, M. Nastasi, F. Rossi, L. Shao, and P.E. Thompson, Appl. Phys. Lett. 93, 254104, 2008.

# AFM-BASED MECHANICAL CHARACTERIZATION OF FBAR CANTILEVERS AS FIRST STEP TOWARDS DEVELOPING OF FORCE SENSORS

CJ. Camargo, H. Campanella, J. Montserrat, J. Esteve

<sup>1</sup>*Instituto de Microelectrónica de Barcelona IMB-CNM (CSIC); Campus UAB, 08193, Bellaterra, Barcelona, Spain*

**Abstract —** In this paper the spring constant of three FBAR cantilevers were found through an accurate mechanical characterization method based on AFM. The need of this post-fabrication procedure was demonstrated because of that fabrication deviations make unviable an accurate characterization by traditional methods. AFM's force mode was employed for extracting curves Force vs FBAR's deflection and consequently the constant  $k$  is obtained through Hooke's Law; results differ markedly of FEA-based simulated data. This work opens a wide route towards developing FBAR-based force sensors and establishes a reference for mechanical characterization of acoustic resonators and complex MEMS structures in future.

**Keywords:** spring constant, FBAR, force sensor, Atomic Force microscopy

## I - Introduction

In recent years, thin-film bulk acoustic resonators (FBAR) have overtaken to other kind of MEMS devices due to their higher performance in gas sensing applications [1], localized mass detectors [2] and more recently in inertial force detection [3], among others. That performance is mainly determined by both the acoustic and mechanical properties of the structure; even so, majority of experimental studies have been routed to electromechanical characterization when resonator is operating in dynamic state (RF). Parallel to this, the low frequency mechanical characterization has always been carried out based on experimental procedures converging on mathematical models that are made under the assumption of precise geometries and materials properties. This does not apply only to FBAR but also to other MEMS structures that are slightly characterized in this field.

The affirmations above are true and valid when the geometry and configuration of a multi-layer FBAR is the typical (rectangular layers of equal areas), however, when these variables are changed and FBARs have unconventional geometries, there are no precise mathematical models allowing the relationship of resonant frequency with geometry. Hence, the importance of *post-fabrication characterization*, which also takes into account the deviations of the process on the electromechanical properties and materials originally estimated. For example, when evaluating modes of mechanical or acoustic resonance, an *a priori* knowledge of Young's modulus, density, and the effective mass, among others, it is essential to achieve an accurate characterization of the spring constant  $k$  [4].

Besides it, Atomic Force Microscopy (AFM) has become one of the most powerful characterization tools in recent years, no limited to surfaces but also being widely applied in MEMS field, where precisely, some techniques have been developed and successfully used for vibratory systems characterization, as mechanical oscillators [5] and wave acoustic resonators [6].

According to above, and considering the potential of FBAR as piezoelectric detectors in mechanical sensing applications [3], the study of  $k$  takes relevance because it allows evaluating the force and frequency sensitivity of the devices. The characterization method proposed in this paper allows us: (a) to facilitate the extraction of  $k$  of complex structures, and (b) ignoring the prior knowledge of the physical constants of materials (which, in fact, could be determined from the  $k$  experimentally measured [7]).

Thus, the main purpose of this study is to use the AFM in force mode (by taking advantage of its irreplaceable vertical resolution – *out-of-plane*- and the –*in-plane*- resolution available for tip location) to characterize accurately the elastic constant of FBAR with non conventional geometries, as first step towards developing of FBAR-based force sensors. These measurements will also allow analyzing the consequences of stress induced during fabrication process by the deposition of the layers that make up the FBAR, which will be explored in future stages.

## II – FBAR Fabrication technology

Fabrication process of FBAR is based on reactive ion etching (RIE) of silicon. Hence, FBAR devices were implemented as a sandwich with 700 nm thick aluminum nitride (AlN) as active layer, sputtered on top of a titanium/platinum (Ti/Pt) layer (30/150 nm thick) which has been deposited on a silicon (Si) substrate. A final Ti/Pt layer acts as top electrode.

A schematic of the step-by step FBAR process is depicted in figures 1(a)–(f). First, an isolating silicon dioxide layer (SiO<sub>2</sub>) is deposited on the silicon substrate to provide electrical isolation between electrical contacts of electrodes and substrate (a). This oxide layer is etched to provide a window through silicon, in order to perform releasing of the FBAR in the last step of the process (b). Next, a first Ti/Pt layer is deposited on top of the SiO<sub>2</sub> layer and patterned by lift-off to conform the bottom electrode of the FBAR (c). Once the electrode area is defined, an AlN piezoelectric layer is deposited by RF sputtering and wet etched in a TMAH-like solution (d). The top Ti/Pt electrode follows the same processing steps described for the bottom electrode (e).

Finally, releasing of the FBAR is done by micromachining of the silicon substrate, by means of silicon RIE in a SF<sub>6</sub> and O<sub>2</sub> atmosphere inside the RIE-machine chamber - Alcatel 610 - (f).

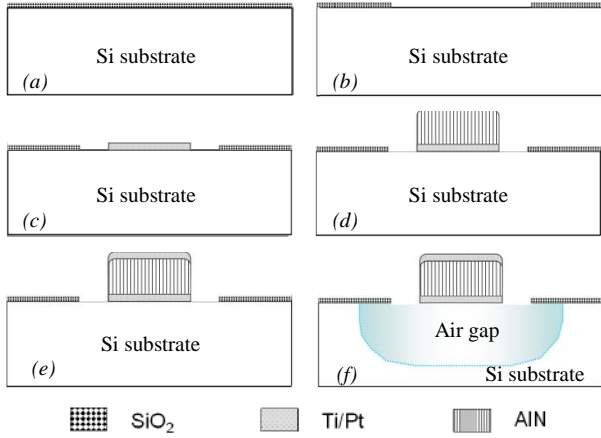


Figure 1: *Fabrication process of the FBAR: (a) oxidation of substrate, (b) etching of silicon oxide, (c) deposition and lift-off of Ti/Pt-made bottom electrode, (d) deposition and etching of AlN, (e) deposition and lift-off of top electrode and (f) reactive ion etching of silicon.*

Regarding this process, it should be said that no layer planarization was performed in any step of the fabrication. For this reason, a lack of uniformity in the thickness of the different layers was expected. In this sense, the AlN layer thickness was measured using a Nanospec system implementing standard spectrographic techniques with angstrom resolution. The topographic profile of figure 2, shows how the thickness of the AlN layer changes as a function of the distance of the measured point to the center of the 100 mm wafer (sputtering timing and conditions were adjusted to obtain a nominal width of 1  $\mu$ m). As suggested by this plot, a mechanical post-fabrication characterization must be performed if is desired an accurate description of the device before they are used as force sensors.

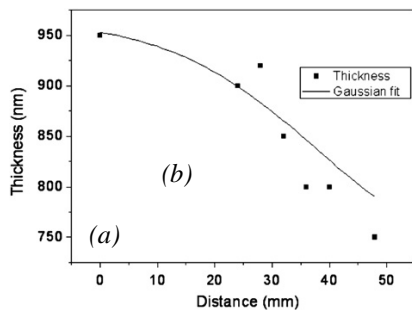


Figure 2: *AlN thickness variation due to process deviations as function of the distance of the measured point from wafer's center.*

Moreover, in Figure 3 are shown the FBAR cantilever structures that were characterized and a sample of the un-loaded frequency response of FBARs. This was characterized using a coplanar probe station and micro-

wave network analyzer connected to the Ground-Signal-Ground (GSG) pads of the test structure.

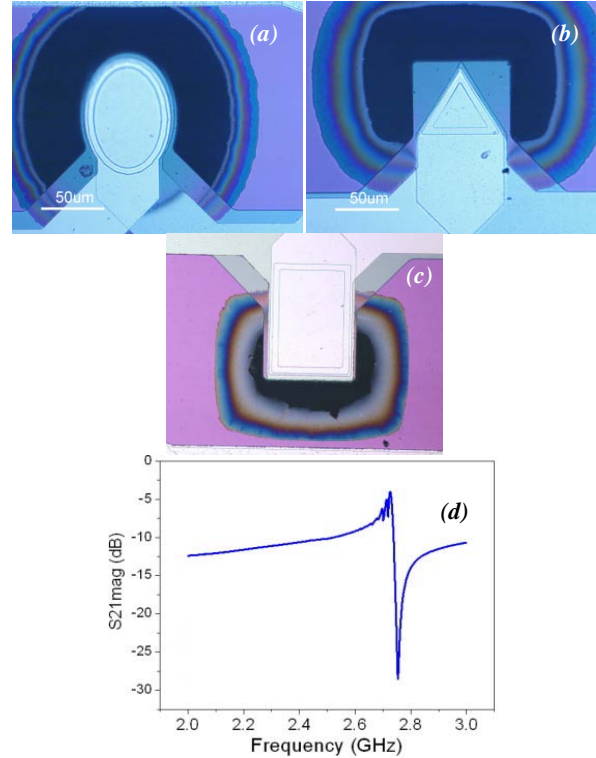


Figure 3: *First prototypes of FBAR-cantilevers to develop force sensors. (a) Ellipsoidal (S1), (b) triangular (S2) and (c) rectangular (S3), and (d) frequency response of a FBAR: Resonance frequency of 2.7 GHz with quality factor of 500*

### III – Description of the method

As was mentioned above, generally the elastic constant of MEMS structures is slightly characterized, even when it could be a laborious but simple procedure; moreover, the continuous trend in developing multilayer structures and atypical geometries requires of establishing accurate methods to test and evaluate their mechanical properties. The method is based on the measurement of deflection of the FBAR cantilever when a force load is applied by an AFM tip on a point of interest for us (It's not necessarily the end). This force is controlled by the AFM piezoelectric through an accurate position variation when it is operated in force mode which consists in to apply a ramp voltage to AFM Z piezo so tip gets down and up on the surface where is located. The total displacement of the AFM tip is the sum of its own deflection and the bending of the studied surface/structure.

For small deformations, the behavior of both the AFM beam and FBAR cantilever can be described by Hooke's law, where the global spring constant of the AFM/FBAR system is the resulting constant of a combination in series as (1) shows, where,  $K_{eq}$  is the spring constant of the system.

$$\frac{1}{K_{eq}} = \frac{1}{K_{AFM}} + \frac{1}{K_{FBAR}} \quad (1)$$

Writing Hooke's law for this system under a loading force, results

$$F = K_{eq} \cdot z = K_{AFM} \cdot \delta \quad (2)$$

where  $z$  is the total displacement of the AFM tip and  $\delta$  is the measured deflection. Thus, the curve region in Fig. 4 where AFM tip and FBAR are in contact is defined by eq. 3 and it is called relative deflection of the system. But, as what we desire is to find  $K_{FBAR}$ , Eqs. (1) and (3) are related to obtain (4):

$$\delta_s = \delta/z = K_{eq}/K_{AFM} \quad (3)$$

$$K_{FBAR} = \delta_s \cdot K_{AFM} / (1 - \delta_s) \quad (4)$$

#### IV – Experimental Section

##### A. Calibration of Force Mode

With the purpose of apply an accurate force, a correct spring constant calibration of AFM tip is performed. About it, there are several techniques and methods to calculate the cantilever's spring constant but only the most accurate are of interest for us. According to Ohler [8], Sader and Thermal tune methods are the most reliable and additionally are supported on Veeco Dimension 3100 through Nanoscope V system, which is the equipment available at the IMB-CNM(CSIC).

Sader's formula is shown (5),

$$k = 7.5246 \rho_f w^2 L Q f_0^2 \Gamma_t (Re) \quad (5)$$

$$Re = \frac{2\pi\rho_f f_0 w^2}{4\eta_f} \quad (6)$$

where  $\rho_f$  is the density of the fluid in which the measurement is taken (air in this case),  $\eta_f$  is the viscosity of that fluid,  $Q$  is the quality factor of the cantilever oscillation,  $f_0$  is the resonance frequency and  $\Gamma_t$  is the imaginary component of the hydrodynamic function, which is a function of the Reynolds number,  $Re$ . [9]

At first appearance, Sader's formula describes a geometrical method and it is only applicable to rectangular cantilevers (which is our case, since OTESPA -by Veeco- is our tip reference). On the other hand, thermal tune method is based on modeling the cantilever as a simple harmonic oscillator (what makes it applicable for any geometry); it uses the equipartition theorem [10] so thermal motion of cantilever's fundamental oscillation is related with its thermal energy. Boltzman constant  $k_B$  ( $1.38 \times 10^{-23} J/K$ ), the temperature  $T$  and the mean square displacement of the cantilever  $\langle z^2 \rangle$  are the components in Eq. 3. Last quantity is found by performing a power spectral density analysis (PSD) of cantilever oscillations and integrating the area under fundamental resonant peak. Eq. 7 is a final corrected equation given by Ohler.

$$k = 0.817 \frac{k_B T}{\langle z^2 \rangle} \quad (7)$$

A confocal microscope (296PLU04 by Sensofar) was used for measuring of AFM cantilever geometry, and so it was obtained a sharper and better resolved image of typical resolution of 100nm;  $w=49,6\mu m$ ,  $L=168,3\mu m$  are the AFM cantilever dimensions. Next, with the support of *thermal tune* mode from Nanoscope V system  $f_0=309.63kHz$ ,  $Q=599.89$ , were obtained. With these dates spring constants of 71,7N/m and 70,07N/m were found, using Sader and Thermal methods respectively; last one is used for calculations.

Before applying force to FBAR cantilevers, a previous calibration of photodetector sensitivity is required and this is made locating the tip on a rigid surface (SiO<sub>2</sub> on substrate in our case) and using force mode. We can see in Fig.4 that the vertical distance descended by tip ( $x$  axis) starting from the moment when it contacts the surface is equal to the vertical deflection measured by AFM system (as was expected from eq.3). Sensitivity calculated is  $70,5 \pm 0,5$  nm/V

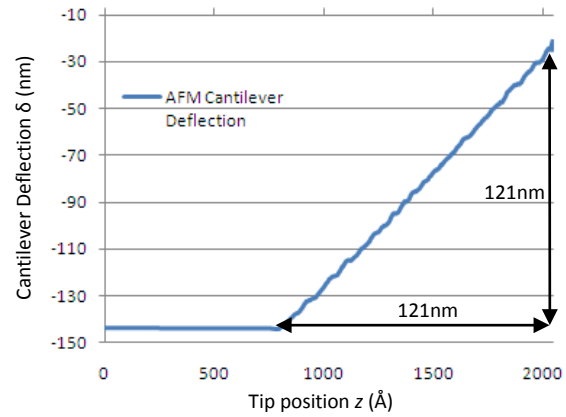


Figure 4: AFM Cantilever deflection versus Z tip position when AFM is operating in Force Mode on a rigid surface.

##### B. Experimental Results

With all these, mechanical characterization of FBAR is possible. The process that follows consists in carefully location of the tip on the point of interest for us (as Figure 5 shows); for that, a contact scanning around edge is done ( $10 \times 10\mu m$ ) and from that scanning the desired tip location is achieved.

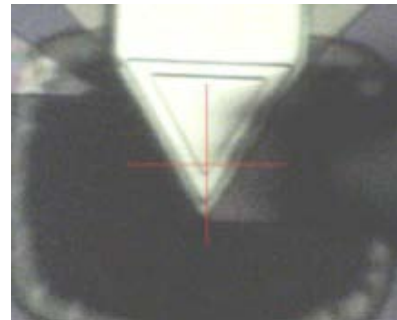


Figure 5: AFM tip location on triangular FBAR-cantilever.

Next, force mode is operated with constant Scan Range (200nm) and new sensitivities are obtained.



Figure 6(a) shows a comparison between FBAR sensitivities; as could be seen, slope keeps constant and force is directly related to Z tip position and calculated spring constants are written in Table 1.

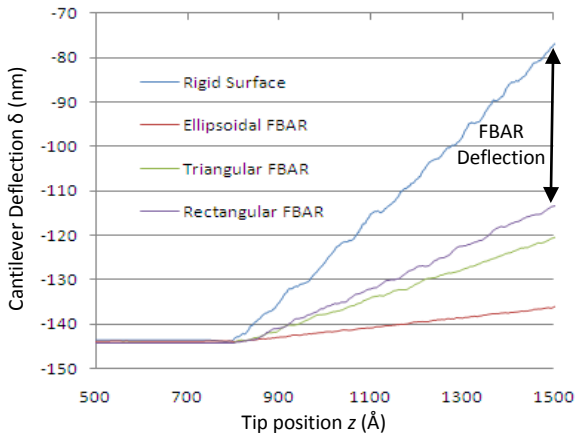


Figure 6: AFM Cantilever deflections against vertical tip position, when Force Mode is operated on different FBAR cantilever and rigid surface.

Table 1: Measured and simulated dates of the FBARs under discussion and comparison with the reference.

Data	AFM	S1	S2	S2
Sensitivity (nm/V)	70.5	566.97	193.88	149.96
Experimental K (N/m)	70.07	7.72*	25.48	32.94
Simulated K (N/m)	-	10.65	32.72	43.37
Simulated K – thick. adj.(N/m)	-	8.54	27.47	34.48
Max. Force load (μN)	-	1.15	3.82	4.94

\*Finally for ellipsoidal FBAR, a softer AFM cantilever (SCM-PIT –by Veeco-  $k=3,46\text{N/m}$ ) was used for its characterization due to method limitations [8].

A Finite Element Analysis (FEA) in ANSYS was performed with the aim to compare simulated spring constants with experimental results. First, an ideal geometry was simulated and results are highly distorted, showing deviations of up 37%. Considering the fabrication deviations mentioned before, a new FEA was carried out for these structures; even when results showed an improved modeling, deviations from 4,5% were observed. Also, the maximum force load possible was calculated for each structure taking in account the limitation of Hooke's law for cantilevers (vertical displacement  $\ll$  structure thickness; 0.15:1 was assumed).

The authors would like to mention that presentation of the force sensor concept that gave birth to this work will be presented in the final paper and electrical measurements will supplement the experimental results.

## IV - Conclusion

Three FBAR cantilevers with complex structures were mechanically characterized through a simple method based on AFM. The main virtue of this method is the thoroughness with which it was made; depending of desired precision in the study about force loading and/or force detection, a FEA model could be enough (taking the fabrication effects into account), but when the aim is developing force sensor and the resolution is crucial, an accurate calibration of the structures is required. Future development of this work involve two fields: on one hand, further optimization of the process to make it applicable to miniature FBAR (five-fold smaller), besides to fabrication of FBAR integrated in an AFM chip-size to take advantage of the potential of thermal tuning characterization by Nanoscope system. On the other hand, characterization of piezoelectric conversion of FBAR cantilevers when they are force-loaded is the next step towards developing FBAR-based force sensors and method presented here is an important part of the process.

## References

- [1] M. Penza, P. Aversa, G. Cassano, D. Suriano, W. Wlodarski, M. Benetti, D. Cannata, F. Di Pietrantonio, and E. Verona, IEEE Trans. Electron Device **55**, 1237 (2008)
- [2] H. Campanella, J. Esteve, J. Montserrat, et al. Appl. Phys. Lett. 89 (2006) 033507.
- [3] H. Campanella, J.A. Plaza, J. Montserrat, A. Uranga, J. Esteve. Microelectronic Engineering, Volume 86, Issues 4-6, April-June 2009, Pages 1254-1257
- [4] Y.W. Lin, S. Lee, S.S. Li, et al. Series-resonant VHF micromechanical resonator reference oscillators, IEEE J. Solid State Circuits **39** (2004) 2477-2491
- [5] F. Sthal and R. Bourquin, Appl. Phys. Len. 77, pp. 1792-1794 (2000)
- [6] A. San Paulo, X. Liu, J. Bokor, Atomic force microscopy characterization of electromechanical properties of RF acoustic bulk wave resonators, in: Proc. IEEE Intl. Conf. MEMS, Maastrich, The Netherlands, 25–29 January, 2004, pp. 169–172.
- [7] C. Serre, A. Perez-Rodriguez, J.R. Morante, P. Gorostiza, J. Esteve. Sensors and Actuators A: Physical 74 (1) (1999) 134–138.
- [8] Ohler, B. "Practical advice on the determination of cantilever spring constants". Application Note 94, Rev A0, Veeco Instruments (2007)
- [9] J.E. Sader. Frequency response of cantilever beams immersed in viscous fluids with applications to the atomic force microscope. Journal of Applied Physics 84 (1) (1998) 64–76.
- [10] J.L. Hutter, J. Bechhoefer, Calibration of atomic-force microscope tips, Rev. Sci. Instrum. 64 (1993) 1868-1873.

## POST-PROCESSING OF LINEAR VARIABLE OPTICAL FILTER ON CMOS CHIP AT DIE-LEVEL

A. Emadi, H. Wu, G. de Graaf and R. F. Wolffenbuttel

Faculty EEMCS, Department ME/EI, Delft University of Technology, Mekelweg 4, 2628 CD, Delft, The Netherlands

**Abstract** — The fabrication of a Linear Variable Optical Filters as a post-process on CMOS chips at the die-level is presented in this paper. The CMOS chip contains a 128-element Photodiode array. The LVOF deposited on the top of the photodiode array will make each of the photodiodes sensitive to a specific wavelength, which changes linearly along the array. A one-mask process based on trench etching in resist and subsequent reflow is used to fabricate a tapered cavity layer for the LVOF on top of the photodiode array. A special process has been designed to allow lithography and wafer processing on pre-fabricated CMOS dies, based on die bonding to a carrier wafer and reflow planarization. The result is an on-chip spectrometer. The technique can be generally applied to chips from a multi-chip design processed at an external foundry service that supply chips only.

**Keywords :** on-chip, micro-spectrometer, post-processing, Linear Variable Filter

### I - Introduction

Single-chip optical micro-spectrometers have huge potential in many applications, such as identification of bio-molecules, gas detection and in chemical analysis, because of their properties such as low-cost and low sample volume [1]. A small Linear Variable Optical Filter (LVOF) integrated with an array of optical detectors is a very suitable candidate for a micro-spectrometer that should feature both low unit cost and high resolving power [2]-[3]. Although grating based micro-spectrometers generally outperform optical resonance based systems, such as the Fabry-Perot etalon or the LVOF-based micro-spectrometer, in case of operation over a wide spectral bandwidth, LVOF-based micro-spectrometers are more suitable for operation with high resolving power over a narrow spectral band, as is required in spectral analysis around an absorption line [4]. IC-Compatible fabrication enables the fabrication of LVOFs as a post-process in CMOS. Having the detector array and electronic circuits realized in CMOS prior to application of the post-process offers opportunities for low unit costs in case of a high production volume.

Early versions of LVOFs have been fabricated on glass substrate and mounted on a commercial CMOS camera for characterization and spectral measurements [5]-[7]. To prove the principle and IC-compatibility of the process an LVOF has been fabricated on CMOS chips at the die-level. The technique can be generally applied to chips from a multi-chip design processed at an external foundry service that supplies chips only.

### II – Principle of operation

Figure 1 shows the principle of operation of a LVOF.

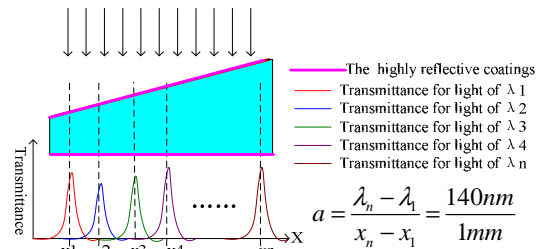


Figure 1: Principle of operation of a Linear Variable Optical Filter (LVOF).

The LVOF is basically a one-dimensional array of many Fabry-Perot (FP)-type of optical resonators. Rather than a huge number of discrete devices, the LVOF has a center layer (the resonator cavity) in the shape of a strip and a thickness that changes over its length. Dielectric mirrors are on either side. The spectral resolution of a Fabry-Perot interferometer is determined by surface flatness, parallelism between the two mirror surfaces and mirror reflectivity. Theoretically, it is possible to have a high number of narrowly spaced spectral channels in a LVOF spectrometer to result in a spectral resolution better than 0.2 nm in the visible spectrum, using signal processing techniques. However, for a Fabry-Perot type of LVOF, the thickness variation of the cavity layer has to be in order of quarter of the wavelength and very well controlled, which makes fabrication of miniature LVOFs a technological challenge. The theoretical limit for the spectral resolving power of the LVOF-based spectrometer is the spectral bandwidth divided by the number of channels in the detector array. However, this is difficult to achieve when considering the Signal to Noise Ratio. This simple geometric optimum is only approached in case of a high SNR.

### III – Fabrication of LVOF

LVOF fabrication is based on reflow of a specially patterned layer of resist. Figure 2 shows the process steps for the fabrication of an IC-Compatible LVOF. The process starts with deposition of the lower dielectric mirror stack and the oxide layer that results in the cavity layer. Photoresist is spin coated as the next step and lithography is applied to define the strip-like structure in the resist layer to be reflowed. A series of trenches of constant width and with variable spatial frequency or trenches of variable width and constant pitch are etched over the length of the strip of resist to vary the effective

amount of resist per unit area. The subsequent reflow transfers this gradient volume of resist into a smooth tapered resist layer [8]. The topography of the tapered resist layer is transformed into the thick oxide cavity layer by an appropriate plasma etching process. The process is completed by deposition of the top dielectric mirror stack. This first prototype of the LVOF was fabricated on a glass substrate. Figure 3 shows a photograph of LVOF fabricated on glass substrate.

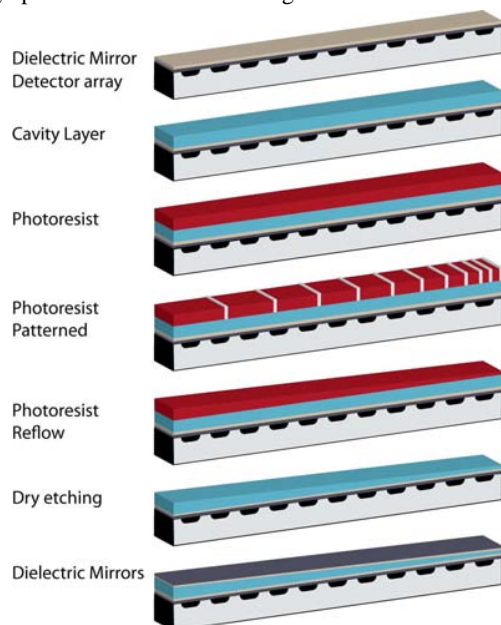


Figure 2 Process flow for fabrication of a Linear Variable Optical Filter (LVOF).

The LVOF design presented here is based on operation in the wavelength range between 570 nm to 720 nm. Spectrometers in this wavelength range are suitable for applications such as fluorescence spectroscopy of plants and H- $\alpha$  spectroscopy. The performance characterization of the LVOF and related micro-spectrometer in this wavelength range can be tested using a Neon lamp, which has most of its major peaks in this wavelength range.

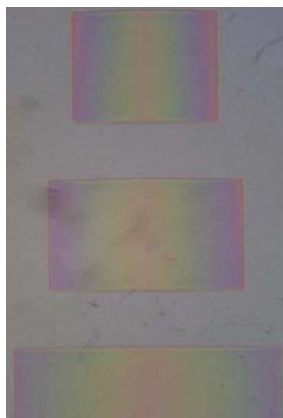


Figure 3 Photograph of LVOFs fabricated on a glass substrate.

The same principle of design and fabrication can be applied to other wavelength ranges in visible, IR and UV. The difference would be in the choice of dielectric materials for the LVOF filter and suitable detector array. For near-infra red region, for example PolySi and SiO<sub>2</sub> are to be used as dielectric materials and MEMS fabricated thermopile arrays as detectors.

#### IV – Integrating LVOF to CMOS at die-level

A chip with 128-element photodiode array and read-out circuitry has been designed and fabricated in a 0.35 CMOS process [9]. Figure 4a shows the block diagram of the integrated system and Fig. 4b a photograph of the chip.

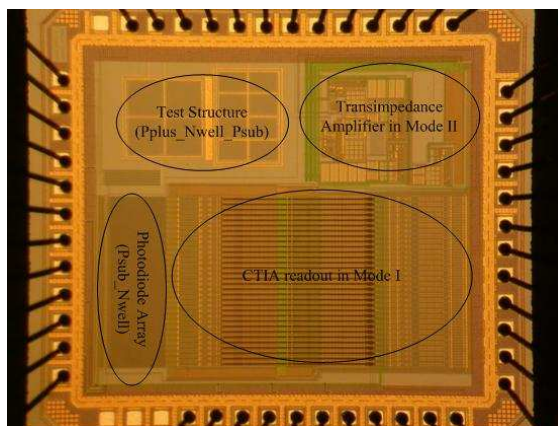
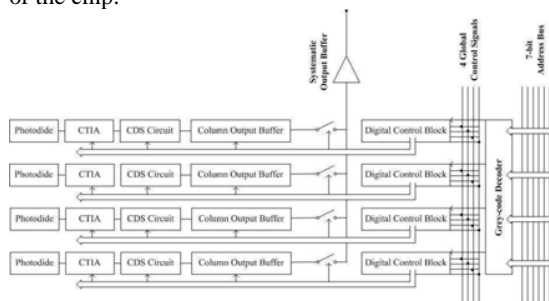


Figure 4 a) block diagram of the integrated system b) the die photo of the 128 CTIA-APS linear array

Since the 2×2 mm<sup>2</sup> CMOS chips are too small for handling in process, they have to be initially mounted on a substrate. Using SU-8 as an adhesive material the chips are glued to 1×1 cm<sup>2</sup> Silicon or Glass substrates. The SU-8 is heated to reflow and planarize the sharp edges on the chip. This is necessary to enable subsequent spin coating of photoresist and processing. Figure 5 shows a photograph of a chip after bonding to the substrate by SU-8 and planarization.

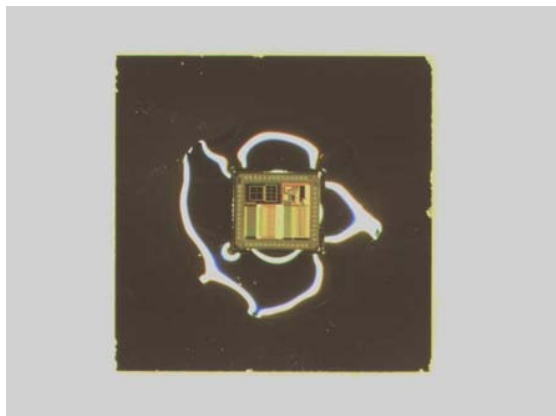


Figure 5 Chip die bonded to substrate with SU-8

The benefit of using SU-8 is that it is not removed by the AZ resist developer during subsequent lithography steps. The lithography step is required for covering the bonding pads with photoresist before deposition of dielectric layers. Lift-off processing has been applied with AZ 5214E photoresist after image reversal. Planarization of the die sharp edges makes it possible to spin coat photoresist on the die. Figure 6 shows the photoresist mask opening on the photodiodes array part of the CMOS chip, while covering the bonding pads. The thickness of the resist layer is 5.5  $\mu\text{m}$ .

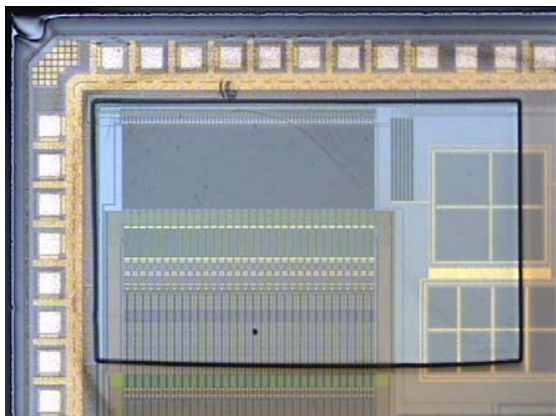


Figure 6 Photoresist lift-off mask opening on the photodiode array, covering the bonding pads.

The LVOF consist of 15 alternating layers of  $\text{TiO}_2$  and  $\text{SiO}_2$ . The layers are sputter deposited using a FHR MS150. The 2 % precession control of the thicknesses and optical properties are essential for a reliable interference-based optical filter.

Table 1: Layer structure of the Linear Variable Filter

Layer Material	Layer thickness
$\text{TiO}_2$	67 nm
$\text{SiO}_2$	112 nm
$\text{TiO}_2$	67 nm
$\text{SiO}_2$	112 nm
$\text{TiO}_2$	67 nm
$\text{SiO}_2$	112 nm
$\text{TiO}_2$	67 nm
$\text{SiO}_2$	850 nm – 1000 nm
$\text{TiO}_2$	67 nm
$\text{SiO}_2$	112 nm
$\text{TiO}_2$	67 nm
$\text{SiO}_2$	112 nm
$\text{TiO}_2$	67 nm

The obvious disadvantage of sputtering is a difficult lift-off process is the non-directional deposition, which causes coating of the sidewalls of the patterned photoresist and reduced access of the acetone. Figure 7 shows a photograph of CMOS die chip after deposition of the first stack of dielectric layers.

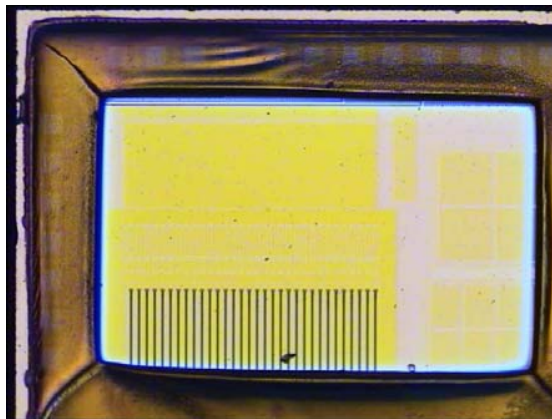


Figure 6 dielectric layers deposited on the CMOS die through photoresist lift-off mask..

The lift-off is done in an ultrasonic bath with Acetone heated to 50° C. The complete lift-off takes about 3 hours. The use of Shipley remover 1165, which can potentially help in an easier lift-off, was avoided due to the fact that it can etch the Aluminum bonding pads. Figure 7 shows the photograph of a die after the lift-off process.



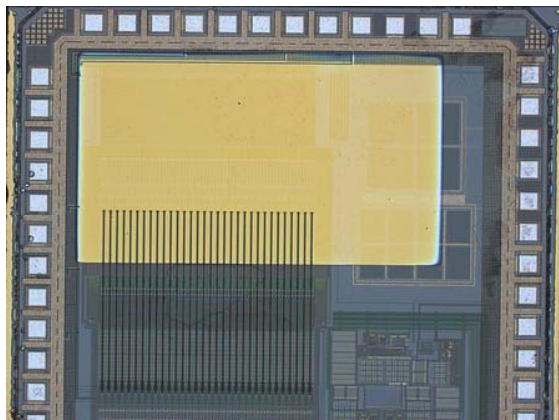


Figure 7 dielectric layers deposited on the CMOS die.

As it can be seen, the dielectric layers are covering all the photodiode pixels on the chip and bonding pads, while the remainder of the chip is kept clear. In the next step, lithography is applied for the fabrication of the tapered cavity layer. Initially, a lithography step is done on the chip using low viscosity SU-8 2002 to cover the bonding pads. Subsequently, lithography is done using S1813 photoresist to result in a tapered photoresist layer as described in [8].

As mentioned before, the exposed SU-8 is not removed in the Shipley MF 322 which is used for development of AZ5214E and S1813. This allows us to do implement two subsequent lithography steps: the first with SU-8 2002 used for protection of the bonding pads and the second with S1813 to form the tapered resist layer. After completion of the lithography and reflow processing, the tapered resist layer is transferred into the underlying  $\text{SiO}_2$  layer. Samples are cleaned in Acetone after dry etching step to remove photoresist residuals. Exposed SU-8 is removed in Acetone provided that it is not hard-baked. This also causes the die to detach from the substrate and the SU-8 covering the bonding pads is also cleaned. The die chips are bonded to a substrate again and a lift-off mask using AZ 5214E is made with the same procedure for the deposition of the second stack of dielectric layers, layers 9-15 in table 1. The process is completed after the lift-off.

#### IV - Conclusion

Bonding of a CMOS chip fabricated using a foundry service and a multi-chip design to a carrier wafer and reflow planarization can be applied for making the device suitable for lithography and subsequent Linear Variable Optical Filter deposition. The result is an on-chip micro-spectrometer. Spectral measurements using the chip are the subject of future work.

#### Acknowledgement

This work has been supported in part by the Dutch technology Foundation STW under grant DET.6667.

Part of this work has been done at the Nanofabrication Laboratory of MC2, Chalmers University of Technology, through MC2ACCESS programme.

#### References

- [1] G. Minas, R. F. Wolffenbuttel and J. H. Correia. An array of highly selective Fabry-Perot optical channels for biological fluid analysis by optical absorption using a white light source for illumination, *Journal of Optics A: Pure and Applied Optics*, IOP Publisher, 8, pp.272-278.
- [2] R. McLeod, T. Honda. Improving the spectral resolution of wedged etalons and linear variable filters with incidence angle, *Optics Letters*, Vol. 30, No. 19 (2005), pp 2647-2649.
- [3] S.F. Pellicori, US Patent 4957371 - Wedge-filter spectrometer
- [4] S. Grabarnik, Optical microspectrometers using imaging diffraction gratings, PhD thesis, 2010, Delft University of Technology, ISBN: 978-90-9025048-9
- [5] Arvin Emadi, Huaiwen Wu, Ger de Graaf, and Reinoud F. Wolffenbuttel, "CMOS-compatible LVOF-based visible microspectrometer", *Proc. SPIE 7680*, 76800W (2010)
- [6] Arvin Emadi, Semen Grabarnik, Huaiwen Wu, Ger de Graaf, Karin Hedsten, Peter Enoksson, Jose Higinio Correia, and Reinoud F. Wolffenbuttel, "Spectral measurement using IC-compatible linear variable optical filter", *Proc. SPIE 7716*, 77162G (2010)
- [7] Arvin Emadi, H. Wu, S. Grabarnik, G. De Graaf, K. Hedsten, P. Enoksson, J.H. Correia, R.F. Wolffenbuttel, Fabrication and characterization of IC-compatible linear variable optical filters with application in a micro-spectrometer, *Sensors and Actuators A: Physical*, In Press, Accepted Manuscript, Available online 7 May 2010
- [8] A Emadi *et al* 2009," Vertically tapered layers for optical applications fabricated using resist reflow" *J. Micromech. Microeng.* **19** 074014
- [9] Chi Liu, Arvin Emadi, Huaiwen Wu, Ger de Graaf, and Reinoud F. Wolffenbuttel, "A CMOS 128-APS linear array integrated with a LVOF for high sensitivity and high-resolution micro-spectrophotometry", *Proc. SPIE 7726*, 772616 (2010)

## MEMS BASED GRAVIMETERS AND GRAVITY GRADIOMETERS

R. Cuperus<sup>1</sup>, F.F. Flokstra<sup>1</sup>, R.J. Wiegerink<sup>2</sup>, and J. Flokstra<sup>1</sup>

<sup>1</sup>University of Twente, Interfaces and Correlated Electron systems, Enschede, Netherlands

<sup>2</sup>University of Twente, Transducers Science and Technology, Enschede, Netherlands

**Abstract** — Measuring the gravity field of the Earth or planetary objects provides us with important information about the composition of the crusts. Present available instruments are heavy and have a large volume and therefore they cannot always be applied. A reduction to a small scale instrument is an urgent need and will open new application areas. In this paper we describe our developments on MEMS-based gravimeters and gravity gradiometer.

**Keywords:** MEMS, gradiometer, gravimeter, gravity, silicon

### I – Introduction

In this paper we concentrate on small scale instruments for both gravity and gravity gradient measurements to be applied for earth and planetary observations. The aim is to develop MEMS-based systems that can compete in sensitivity with the present large and heavy instruments. These new instruments will open new application areas both for earth and space research.

Although in physics we like to consider the Earth as a homogeneous sphere, this is in reality not the case due to minerals deposited in various concentrations locally around the Earth and to the rough surface structure caused by mountains and trenches. Several physical properties can be used to differentiate between the different areas: density, magnetization, conductivity, chargeability, radioactivity and seismic velocity [1]. Although we will only focus on detecting gravity variations in this paper, usually those measurements need to be combined with other measurements to provide a clear picture.

In general there are two ways of determining gravity fields. One is to scan a complete area from the air or from a ship at a fixed time, and the other is to measure the gravity in situ with a fixed setup as a function of time. This fixed setup is usually located on the surface, but there are also sensors which are suitable to be used inside a borehole into the Earth. The gravity itself can be measured in two different ways. The first is to measure the local acceleration. If this accelerometer is specifically tuned to measure the gravity this is commonly called a gravimeter. The second option is to measure the gradient in the gravity field by measuring the gravity acceleration at two (or more) points and fitting a gradient through these measurements. Such a device is commonly called a gravity gradiometer.

The big advantage of the gravimeter is that it provides an absolute value of the gravity, but it is very sensi-

tive to environmental acceleration noise, thus making it less suitable for usage on a moving platform. With the gravity gradiometer it is relatively easy to reduce environmental acceleration noise but the signal itself is much lower.

In the explorative industry there is need for a small and cheap devices which can be deployed in the field. These can then be used for long term monitoring of for example oil fields. If these are specially prepared then there is also an application for them inside boreholes and small unmanned submarines for deep sea exploration.

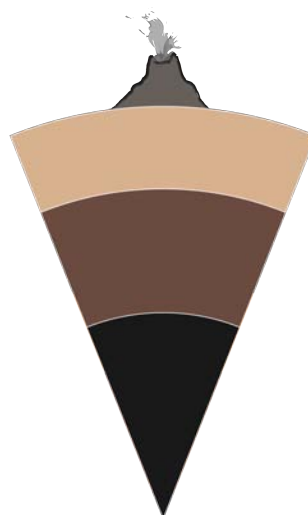


Figure 1: A cross section of a sample planet showing different interesting gravity research goals: the volcano as a relative small feature and the internal layering as a planetary scale topic.

The objectives for space missions are comparable with those on Earth: determining what structures of minerals are underneath the surface of a planet. For example, the surface of Jupiter's moon Europa could be caused by a hidden ocean, but this needs to be confirmed by detailed gravity measurements from orbit looking at the tides of such an ocean [2].

In figure 1 we present a standard model for the different layers inside a planet and a large volcano representing the surface roughness. Gravity field mapping can only be done with gradiometers for the orbiter is in free fall. The space instrument should also have a small size, low weight and low power consumption. Our MEMS-based gravity gradiometer will fulfill these requirements.

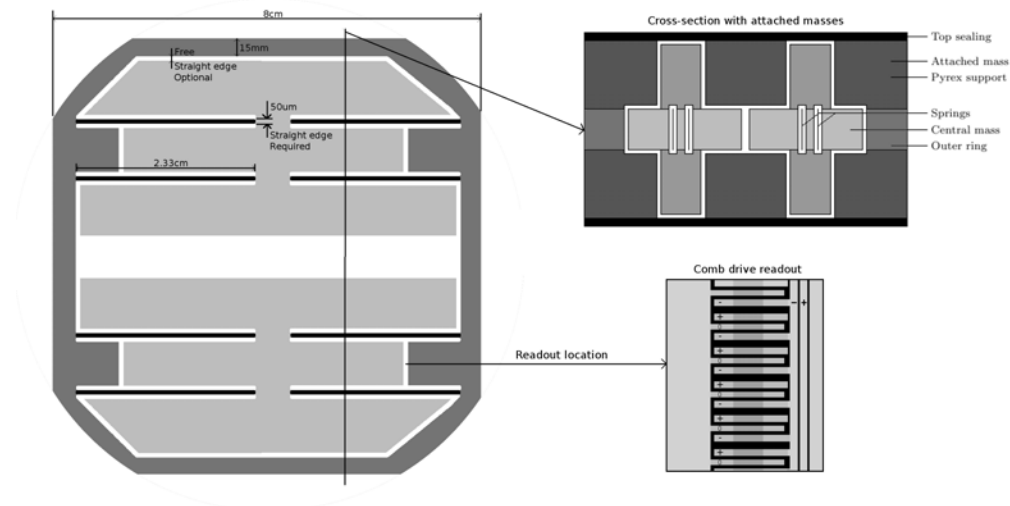


Figure 2: Design of a gravity gradiometer showing a top-view on the left side. The springs are shown in the black, the masses in grey, and the frame in dark grey. A cross section of this device, with attached masses, is shown in the top-right. Finally, one of the locations of the comb drives is indicated bottom right.

## II – Gravity Gradiometer

As introduced in the previous section, a gravity gradiometer is a device which measures the gradient in the gravity acceleration. The principle of this is schematically shown in figure 3 in which two masses  $m$  are separated with a baseline distance  $b$ . The masses are connected to the frame by springs with spring constant  $k$ . The gravity gradient is a tensor defined by  $\Gamma = \nabla \vec{g}$  which usually carries the unit Eötvös ( $E = 10^{-9}/s^2$ ).

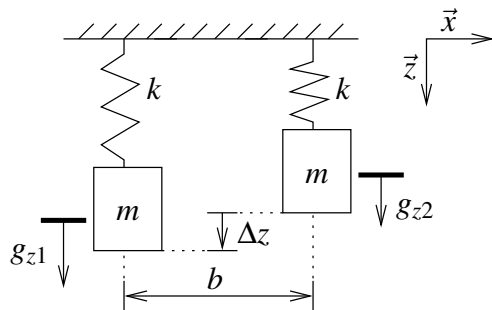


Figure 3: Schematic drawing of a gravity gradiometer measuring the  $\Gamma_{xz}$  component.

The sensitivity of the gradiometer is determined by the noise and can be expressed in the power spectral density function as follows [3]:

$$S_{\Gamma} = \Gamma_n^2 = \frac{8}{mb^2} \left[ \frac{k_B T 2\pi f_0}{Q(f)} + \frac{(2\pi f_0)^2 \epsilon_A(f)}{2\beta_N} \right]. \quad (1)$$

Here,  $f_0$  is the mechanical resonance frequency of the differential mode,  $Q$  the quality factor of the resonance mode,  $\epsilon_A(f)$  the sensor noise energy,  $\beta_N$  the energy-coupling factor of the sensor and  $f$  as the operating frequency. The first term in the equation is the mechanical noise and the second term the noise from the read out system. Both terms are proportional to  $T$ .

The possible size and mass are limited in the target applications, so the main design parameters are spring

constant and quality factor. The bandwidth of the measurements must be in the range of 1mHz to 1Hz [4] for a space application. This means that the resonance frequency of the device must be low but above 1Hz. To get a low resonance frequency, very weak springs need to be used. This brings great difficulties for the manufacturing and testing processes. To get a spring with low spring constant in the sensitive direction, but stiff enough in the direction on which the gravity acts on the ground, a very long spring is needed. To reach the required low resonance frequency, these stiffened springs are not weak enough, so extra (gold) masses must be added which can be seen in the cross-section in figure 2.

A quality factor of  $10^5$  is needed to reach a good sensitivity. This can be realized by using monocrystalline springs in a vacuum environment. This also means that it is not possible to add any extra layers over the springs for conduction of signals. The last free design parameter, temperature, is chosen at 77K because this temperature can be obtained in space with small effort.

The noise in state-of-the-art capacitive readout is calculated. The accuracy with which the distance variations can be measured with the capacitive plates is assumed to be 0.1pm [5]. Using these variables in our model, we derived that it is possible to reach a Brownian noise level of  $107mE/\sqrt{Hz}$  and a readout noise level of  $53mE/\sqrt{Hz}$  giving a total sensitivity of  $119mE/\sqrt{Hz}$  [4].

Small differences in response between the two accelerometers have a significant influence on the amount of environmental acceleration which couples into the device. This means that the springs and masses of both accelerometers within the gradiometer need to be matched very well. Our simulations have shown that the allowed difference, including control effects, should be below  $1 : 10^5$  for an environmental acceleration noise of  $10^{-5}m/s^2/\sqrt{Hz}$ .

A MEMS test structure showing the mechanical principles but with stiffer springs is being manufactured at this moment.

### III – Gravimeter

Gravimeters based on the Zero Length Spring (ZLS) principle as patented by LaCoste [6] include a spring which is operated in a working point with a specific requirement: the spring must have an unstretched length of 0m as viewed from the workpoint. This type of spring makes it possible to create mechanical systems with very low resonance frequency as will be shown in the next subsection. An example of such a device is the “Air-Sea gravity system II” of LaCoste which has a sensitivity of 1 mGal with dimensions of 71 x 56 x 84 cm and a weight of 86kg [7].

In the following we describe the mathematical model of the ZLS, a scale model of a miniaturized system and the MEMS-based gravimeter that is under development.

#### A. Mathematical model

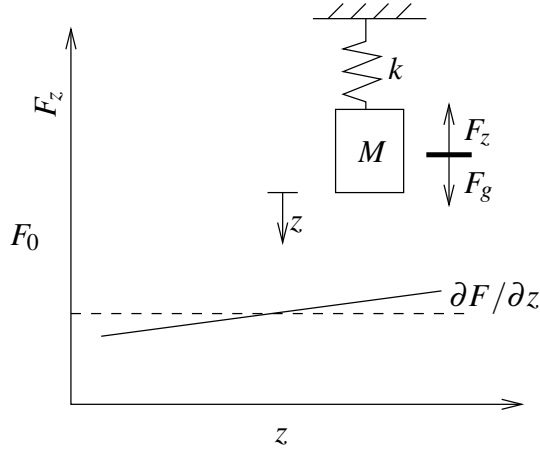


Figure 4: Equilibrium of force while counteracting gravity

The main challenge for any gravimeter is to measure small variations in acceleration with a large 1g background field. Gravimeters can solve this by providing a very stable reference force on their test mass and having a low force gradient in the direction of measurement ( $\partial F/\partial z \simeq 0$ ). This is demonstrated in figure 4 using a basic setup of a test mass suspended from a spring. In this setup, the  $\partial F/\partial z$  is equal to  $k$ , and the total force is equal to  $k$  times the displacement  $z$ . This means that when a large force needs to be counterbalanced, either a large spring constant is needed, which reduces the sensitivity, or the displacement needs to be large, which is incompatible with a small device.

The ZLS design uses a rotating structure which reduces the effective gravity force when the mass is out of the equilibrium point in such a way that a large spring constant is fully compensated. The model shown in figure 5 shows a 2D model of a beam which can rotate about the origin. The end of this beam is connected with a spring to a fixed attachment point above the origin. The proof mass is attached to the beam at the point where the spring is connected.

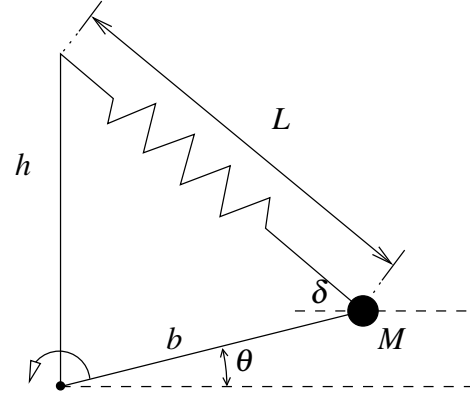


Figure 5: Schematic drawing of a zero length spring design gravimeter

We use ideal conditions to derive an equation of motion, so we assume no damping, rigid beam, and weightless spring and beam. Using torsions in a rotating frame:

$$-mgb\cos(\theta) + k(L - L_0)b\sin(\delta) - mb^2\ddot{\theta} = 0. \quad (2)$$

with  $b$  the length of the beam,  $g$  the local gravity acceleration,  $\theta$  the angle of deflection of the beam,  $k$  the spring constant of the spring,  $L$  the actual length of the spring,  $L_0$  the length of the spring at rest,  $\delta$  the angle between the beam and the spring. Deriving the equation of motion around an equilibrium leads to:

$$\ddot{\theta} - \frac{k}{m} \frac{hL_0}{L_{eq}^2} \cos(\theta_{eq}) \Delta\theta = 0 \quad (3)$$

The resonance frequency for this system is:

$$\omega = \sqrt{\frac{k}{m} \frac{hL_0}{L_{eq}^2} \cos(\theta_{eq})} \quad (4)$$

It's interesting to note that when  $L_0$  of the spring goes to zero, the resonance frequency goes to zero as well.

When a small gravity deviation  $g = g_0 + \Delta g$  is taken into account when deriving equation 3 and again requiring steady state ( $\ddot{\theta} = 0$ ) the deviation can be found as follows:

$$\Delta\theta = -\frac{L_{eq}^2}{hL_0} \frac{m\Delta g}{bk} \quad (5)$$

In here it is obvious that a spring of zero length ( $L_0 = 0$ ) will cause a maximum deflection of the beam, but on the other hand, this will cause instability in the setup and requires a restriction on the movement and feedback to keep it in the equilibrium position.

Equation 3 was derived around a steady state. The dimensions of the gravimeter in this steady state are given by:

$$\frac{kh}{m} = g_0 \quad (6)$$



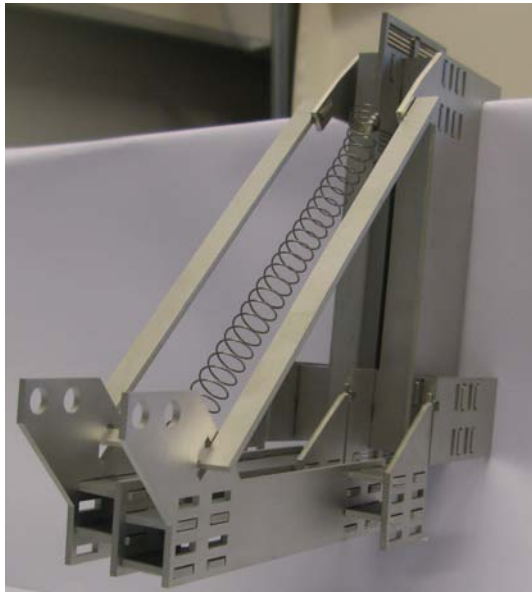


Figure 6: *Stainless steel scale model of the MEMS gravimeter B. Scale model*

A scale model of the MEMS based gravimeter (see figure 6) was fabricated. The model is built of RVS (stainless steel) components with thickness of 2mm, and has a total dimension of about 5.9x15.9x20.2cm (wxhxd). The components have been shaped by a laser cutting machine and then assembled with glue. The device will be suspended by the hooks which are in the top/back of the picture. The model contains three hinges and one spring in order to oscillate. A mass can be added to create an appropriate mass/spring ratio. The characteristic properties will be determined and presented at the conference.

#### C. MEMS based gravimeter

Parallel with the scale model we are producing the same parts from silicon. This is done with a DRIE process and will produce parts a factor of 4 smaller. Also it should be possible to manufacture the springs directly, instead of using outside parts.

Our designed mechanical system has a target sensitivity of  $21 \text{ nrad/mgal}$ . If a capacitive readout with a sensitivity of  $1 \text{ pm}$  is located  $1 \text{ cm}$  from the rotation from the rotation point, this means that a sensitivity of  $5 \mu\text{gal}$  is possible.

#### IV – Conclusion

MEMS technology is a promising technology offering sufficient sensitivity for many applications on both Earth and in space. For space we have shown a gravity gradiometer design, and for applications on Earth we have proposed a MEMS-based gravimeter based on the zero length spring principle.

#### References

- [1] K. Ford, P. Keating, and M.D. Thomas. Overview of geophysical signatures associated with canadian ore deposits. 2006. <http://cgc.rncan.gc.ca/mindep/method/geophysics/pdf/methods.geophysics.ford.pdf>.

[ca/mindep/method/geophysics/pdf/methods.geophysics.ford.pdf](http://cgc.rncan.gc.ca/mindep/method/geophysics/pdf/methods.geophysics.ford.pdf).

- [2] C. Sotin, J. Head, and G. Tobie. Europa: Tidal heating of upwelling thermal plumes and the origin of lenticulae and chaos melting. *Geophys. Res. Lett.*, 29, 8:74–1 – 74–4, 2002.
- [3] M.V. Moody, H.J. Paik, and E.R. Canavan. Three-axis superconducting gravity gradiometer for sensitive gravity experiments. *Review of Scientific Instruments*, 73:3957–74, Nov 2002.
- [4] J. Flokstra, R. Cuperus, R.J. Wiegerink, and M.C. van Essen. A mems-based gravity gradiometer for future planetary missions. *Cryogenics*, 49(11):665–668, 11 2009. 2009.
- [5] X. Jiang, F. Wang, M. Kraft, and B.E. Boser. An integrated surface micromachined capacitive lateral accelerometer with  $2 \mu\text{G}/\sqrt{\text{Hz}}$  resolution. *Solid-State Sensor, Actuator and Microsystems Workshop*, June 2-6:202–205, 2002.
- [6] Lucien J.B. La Coste and Arnold Romberg. Force measuring instrument, June 1945. US PATENT 2377889.
- [7] Micro-g LaCoste, Inc. Air-sea gravity system II. <http://www.lacosteromberg.com/airseafeatures.htm>.

## A MUSICAL INSTRUMENT IN MEMS

J. B. C. Engelen<sup>1</sup>, H. de Boer<sup>1</sup>, J. G. Beekman<sup>1</sup>, A. J. Been<sup>1</sup>, G. A. Folkertsma<sup>1</sup>, L. C. Fortgens<sup>1</sup>,  
D. B. de Graaf<sup>1</sup>, S. Vocke<sup>1</sup>, L. A. Woldering<sup>1</sup>, L. Abelmann<sup>1</sup>, and M. C. Elwenspoek<sup>1,2</sup>

<sup>1</sup>Transducer Science and Technology, MESA<sup>+</sup> Institute for Nanotechnology, University of Twente, Enschede, the Netherlands

<sup>2</sup>Freiburg Institute for Advanced Studies (FRIAS), Albert-Ludwigs-Universität Freiburg, Freiburg im Breisgau, Germany

**Abstract** — In this work we describe a MEMS instrument that resonates at audible frequencies, and with which music can be made. The sounds are generated by mechanical resonators and capacitive displacement sensors. Damping by air scales unfavourably for generating audible frequencies with small devices. Therefore a vacuum of 1.5 mbar is used to increase the quality factor and consequently the duration of the sounds to around 0.25 s. The instrument will be demonstrated during the MME 2010 conference opening, in a musical composition especially made for the occasion.

**Keywords** — Musical instrument, capacitive sensor, comb drive

### I – Introduction

In 1997, researchers at Cornell University fabricated the world's smallest guitar, about the size of a human blood cell [1]. Two years later, a micro harp was made [2]. In 2003, laser light was used to strum the 'strings' of a nanoguitar [3]. However, no human has heard the sound of these instruments; the strings vibrate at frequencies on the order of tenths of megahertz. With the advent of a microphone for MEMS structures [4], there seems to be a growing interest in the field of MEMS musical instruments.

In this work we describe a MEMS instrument, consisting of micromechanical mass-spring resonators that can be 'plucked' using electrostatic comb-drive actuators. The instrument's vibrations are sensed by capacitive displacement sensors using comb structures as sensing elements. The measured capacitance is used as the audio signal.

In the following, first the design of the instrument will be explained, after which measurements of the MEMS instrument's tone will be discussed.

### II – Theory and design

Our instrument consists of individual resonators for each note, similar to a harp. The resonators are (relatively large) masses suspended by folded flexures. Each resonator is actuated by a comb drive. A resonator behaves according to the well known differential equation

$$m \frac{d^2x}{dt^2} + \gamma \frac{dx}{dt} + kx = F_{\text{comb}}, \quad (1)$$

where  $m$  is the mass of the resonator,  $x$  the displacement,  $\gamma$  the coefficient of viscous damping by air,  $k$  the

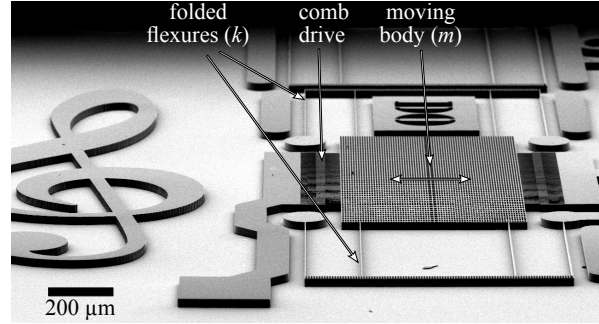


Figure 1: Scanning electron micrograph of one of the resonators of the MEMS instrument. The perforated structure is the moving body (mass  $m$ ), suspended by folded flexures on both sides. The mass is 'plucked' by a comb drive on one side, and the mass's displacement is measured by a comb drive on the other side.

suspension spring constant, and  $F_{\text{comb}}$  the comb-drive force. The solution of (1) is the expected comb-drive displacement after it has been excited,

$$x(t) = e^{-\alpha t} \sin(2\pi f_0 t), \quad (2)$$

with  $\alpha = \gamma/2m$ . The free resonance frequency for an underdamped system is

$$f_1 = \frac{1}{2\pi} \sqrt{\frac{k}{m} - \alpha^2} \approx f_0 \left(1 - \frac{1}{8Q^2}\right), \quad (3)$$

with  $f_0 = 2\pi\sqrt{k/m}$ , and  $Q = \pi f_0/\alpha$ . The approximation is correct for low damping. Tailoring the mass and spring constant, resonators with different resonance frequencies are made. In order to obtain resonance frequencies in a range from 400 Hz to 1000 Hz, large structures are needed compared with common MEMS structure sizes.

#### A. Scaling issues — $Q$ -factor

For our mass-spring-damper system resonators, the quality factor equals

$$Q = \frac{\sqrt{mk}}{\gamma}. \quad (4)$$

The duration of a note after being excited/struck, is proportional to the  $Q$ -factor and inversely proportional to the resonance frequency.

Scaling the dimensions of the mass with factor  $l$ , the mass scales cubically,  $m \propto l^3$ . The spring constant should scale proportionally to the mass in order to maintain the same resonance frequency, hence  $k \propto m$ . The viscous

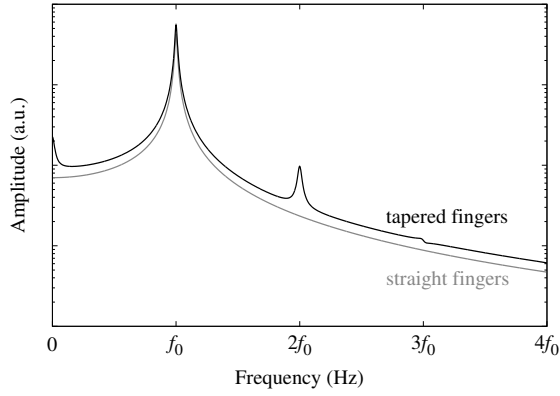


Figure 2: The Fourier transform of the simulated capacitance of comb drives with straight and tapered fingers for an exponentially decaying sinusoid displacement. The non-linear capacitance versus displacement of tapered fingers gives rise to higher harmonics besides the fundamental (first harmonic).

damping is proportional to the area of the mass,  $\gamma \propto l^2$ . Consequently, the Q-factor scales with  $l$ ; reducing the dimensions of the system results in a proportionally reduced Q-factor. In general, at equal resonance frequencies, a smaller mass-spring oscillator will experience more damping and will sound a shorter note than a larger oscillator. To solve this issue of small MEMS instruments, we decrease  $\gamma$  by placing the instrument in a vacuum chamber.

### B. Capacitive read-out

We use a comb drive together with capacitance measurement circuitry to generate the audio signal. Besides ease of fabrication, the use of a comb drive allows us to adjust the timbre of the note, by modifying the comb-drive finger shape. For straight comb drive fingers, the capacitance is linearly proportional to the displacement. However, the capacitance of a comb drive with tapered fingers depends non-linearly on the displacement  $x$  [5],

$$C_{\text{tapered}} = 2\epsilon_0 h \frac{x + x_0}{g - (x + x_0) \tan \alpha}, \quad (5)$$

where  $x_0$  and  $g$  are the initial overlap and gap between fingers respectively,  $h$  is the comb-drive height, and  $\alpha$  the angle of the tapering. This non-linearity gives rise to higher harmonics in the audio signal, resulting in a more interesting tone. The upper bound on the angle  $\alpha$  is set by fabrication limits;  $\alpha = 0.72^\circ$  for our designs. Figure 2 shows the Fourier transform of the simulated capacitance for both straight and tapered fingers using (2) for displacement  $x$ . Besides the fundamental, the second harmonic is clearly present. However, the relative amplitude of the second harmonic is small due to the small angle  $\alpha$ .

### C. Instrument design

The designed instrument contains six resonators at different frequencies. The instrument is designed such that

the notes form part of a major diatonic scale. We chose six notes with  $n = \{0, 2, 4, 5, 7, 12\}$ , where  $n$  indicates the number of semitones above a ‘C’ [6]: Do, Re, Mi, Fa, So, and (high) Do. The instrument is not tuned to a particular existing instrument. A frequency for our ‘C’ is chosen at 396 Hz, from which the subsequent note frequencies follow from [6],

$$f_n = 2^{\frac{n}{12}} \times 396 \text{ Hz}. \quad (6)$$

The general layout of our instrument chip is shown in Figure 3. Both the suspension spring stiffness  $k$  and the moving body mass  $m$  of the resonators are adjusted to obtain the desired resonance frequencies. The spring stiffness of the folded flexure suspension equals [7]

$$k = \frac{2Ehb^3}{L^3}, \quad (7)$$

where  $E$  is the effective Young’s modulus of silicon,  $h$  the spring height,  $b = 3 \mu\text{m}$  the spring width, and  $L$  the spring length. The effective mass of the resonator  $m_{\text{eff}}$  is equal to the moving body mass plus the folded flexure truss mass. Because the folded flexure trusses move only half the distance, only half their mass contributes to the effective mass. The moving body and trusses need to be perforated because of the used fabrication process. The perforation consists of  $5 \mu\text{m} \times 5 \mu\text{m}$  square with  $3 \mu\text{m}$  silicon beams in between. This results in an area reduction  $R_{\text{perf}}$  of approximately

$$R_{\text{perf}} \approx \frac{8^2 - 5^2}{8^2}. \quad (8)$$

Only one dimension of the moving body is adjusted. Referring to Figure 3,  $B = 1.2 \text{ mm}$  is fixed,  $W$  is adjusted. The area of the perforated trusses  $A_{\text{truss}}$  is the product of the width and length,  $32 \mu\text{m}$  and  $W + 333 \mu\text{m}$ , respectively. The total area  $A_{\text{fingers}}$  of the comb-drive fingers on both sides of the resonator equals  $3.84 \times 10^{-8} \text{ m}^2$ . We find for the effective mass,

$$m_{\text{eff}} = \rho_{\text{Si}} h \cdot [A_{\text{fingers}} + R_{\text{perf}} (WB + A_{\text{truss}})]. \quad (9)$$

First  $L$  is chosen such that the resonators fit on the chip, according to the layout shown in Figure 3. Subsequently,  $W$  is adjusted. The dimensions are listed in Table 1.

## III – Experimental Details and Results

The MEMS instrument is fabricated from a (100) single-crystal highly boron-doped silicon-on-insulator wafer, with a  $50 \mu\text{m}$  thick device layer (determining height  $h$  of the comb drive and springs) and an oxide thickness of  $3 \mu\text{m}$ . The structures are made by deep reactive-ion etching (DRIE) [8, 9], after which the (movable) structures are released by HF vapour phase etching [10] of the oxide layer. Large structures, like the moving body of the resonator, need to be perforated to allow etching of the underlying silicon oxide. The result is shown in Figure 1.

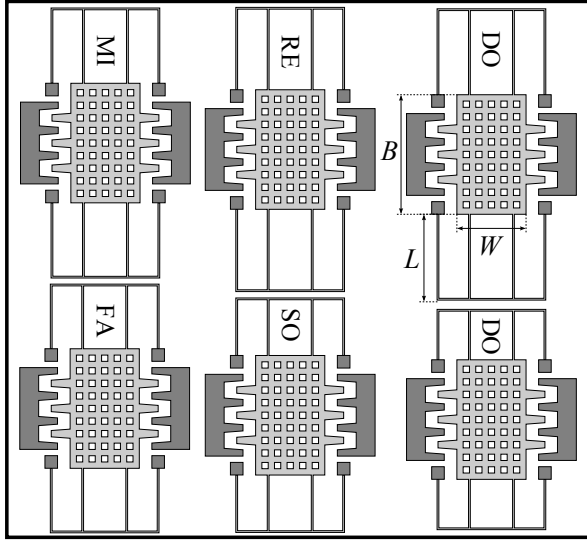


Figure 3: Layout of the 7 mm  $\times$  7 mm instrument chip. Six resonators fit on the chip. The comb drives and length  $B$  are equal for all resonators, only the spring length  $L$  and mass width  $W$  are varied to obtain the correct resonance frequencies.

Table 1: Frequencies of the instrument notes and the resulting design parameters for the spring length  $L$  and moving body size  $W$ . The measured frequencies and the relative deviation from the design are listed on the right.

Note	$f_0$ (Hz) design	$L$ ( $\mu\text{m}$ )	$W$ ( $\mu\text{m}$ )	$f_0$ (Hz) meas.	out-of-tune
Do	396	1050	670	475	20%
Re	445	950	718	592	33%
Mi	499	890	693	-	-
Fa	530	840	735	695	31%
So	595	770	758	778	31%
Do 2	788	690	589	1031	31%

The measurement setup, shown in Figure 4, consists of a charge amplifier, lock-in amplifier and an additional amplifier with band-pass filter. The resulting audio signal can either be played through a loudspeaker or recorded using the soundcard of a PC.

The resonators are actuated by a programmable microcontroller with a D/A-converter and a high-voltage amplifier. At rest, the applied voltage is 0 V. A note is ‘plucked’ by ramping the applied voltage in about 8 ms up to the actuation voltage  $V_{\text{act}}$ , and subsequently rapidly reducing the applied voltage back to 0 V. The ramp prevents sounding a note upon both the increase and decrease of the applied voltage. This simulates manually pulling back the resonator and releasing it, similar to plucking a string. The height of the actuation voltage  $V_{\text{act}}$  is determined from the velocity parameter received in the MIDI messages from the MIDI keyboard.

Figure 5 shows the recorded audio signal of the low Do resonator, for two pressures of respectively 1.5 mbar and 20 mbar. The audio signal is a decaying sine wave,

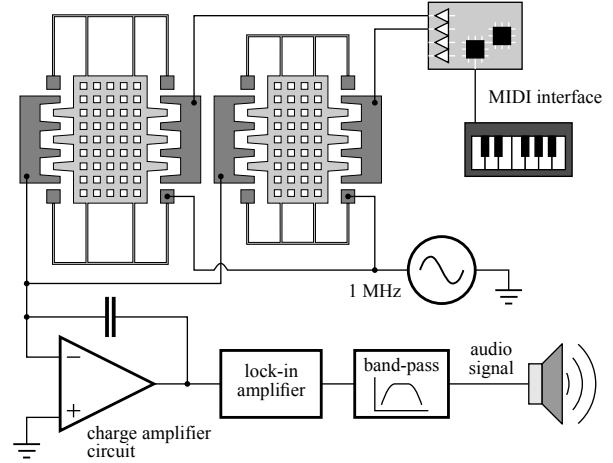


Figure 4: Simplified drawing of the used measurement setup. The displacement of a resonator is measured from the comb-drive capacitance, using a charge amplifier circuit and lock-in amplifier. In total, six resonators are connected in parallel to one charge amplifier circuit (only two resonators are drawn). The resonators are actuated by high-voltage amplifiers that are controlled through a MIDI interface.

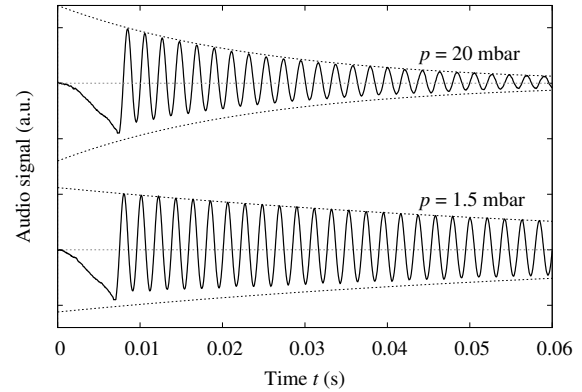


Figure 5: The recorded tone of the low Do note at two different vacuum pressures. The sine frequency equals 475 Hz. The dashed curves are equal to  $\pm e^{-\alpha t}$ , with  $\alpha$  equal to  $13 \text{ s}^{-1}$  at 1.5 mbar and  $40 \text{ s}^{-1}$  at 20 mbar.

that is slightly asymmetric due to the non-linearity of the sensing comb drive. The damping  $\alpha$  is estimated by fitting an exponential curve to the decaying sine;  $Q$  equals 115 and 37 at 1.5 mbar and 20 mbar, respectively. Clearly, the duration of the note is greatly increased at a reduced pressure. At ambient pressure, only a very brief oscillation was measured.

The Fourier transform of the audio signal at 1.5 mbar is shown in Figure 6. The fundamental frequency equals 475 Hz. As expected from the non-linear capacitance versus displacement curve of the tapered comb-drive fingers, a second peak at double the resonance frequency (951 Hz) is visible, compare with Figure 2. The measured resonance frequencies of the other resonators are listed in Table 1. There is no measurement of the Mi resonator as it broke before it was measured. All notes



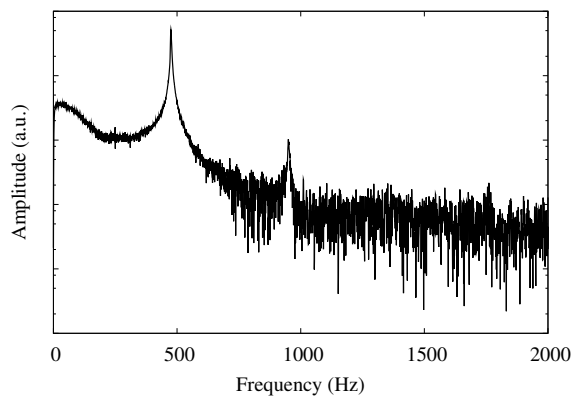


Figure 6: *Fourier transform of the audio signal of the low Do note, showing a large peak at 475.1 Hz. A second peak at 951 Hz is visible, caused by the non-linear capacitance versus displacement curve of the tapered comb-drive fingers.*

resonate at a much higher frequency than the design predicted. However, the instrument is still largely in-tune with itself, because the frequency increased with an almost equal factor for Re, Fa, So and the high Do. The instrument is pitched close to a C5 major scale (except for the low Do, that is closest to A $\sharp$ 4). It should be noted however, that a second chip was more out of tune. The large increase in frequency may be explained by a strong increase in spring stiffness, because their thickness was larger than originally designed.

#### IV – Discussion

Because of intrinsic uncertainties in fabrication, there is a large uncertainty in the resonance frequencies after fabrication. Clearly, tuning of the instrument is necessary. There are several methods of tuning. Because the comb-drive finger shape is tapered, applying an offset voltage to both the actuating and sensing comb drives would result in a lower spring stiffness [11]. Another method to lower the spring constant is heating the springs, which lowers the Young's modulus of the silicon [12], for example by flowing an electrical current through the springs. Large frequency adjustments can be realised through subsequential mass fine-tuning performed by manually depositing additional material on the moving body.

#### V – Conclusion

In this work we show that it is possible to make a musical instrument in MEMS. Viscous damping by air is relatively large for micro resonators at audible frequencies, resulting in a short tone. A vacuum of 1.5 mbar was required for a short note around 0.25 s. The frequencies of the fabricated notes are 20% to 33% higher than expected, however, the instrument is still mostly in-tune with itself. Improvement of the fabrication method is necessary to correctly tune the device by design, without the need for tuning after fabrication.

#### References

- [1] Cornell University Science News, “World’s smallest silicon mechanical devices are made at Cornell,” 1997. [Online]. Available: <http://www.news.cornell.edu/releases/july97/guitar.ltb.html>
- [2] D. W. Carr, S. Evoy, L. Sekaric, H. G. Craighead, and J. M. Parpia, “Measurement of mechanical resonance and losses in nanometer scale silicon wires,” *Appl. Phys. Lett.*, vol. 75, no. 7, pp. 920–922, 1999, doi:[10.1063/1.124554](https://doi.org/10.1063/1.124554).
- [3] B. Steele, “New nanoguitar offers promise of applications in electronics, sensing,” 2003. [Online]. Available: [http://www.news.cornell.edu/Chronicle/03/11.20.03/new\\_nanoguitar.html](http://www.news.cornell.edu/Chronicle/03/11.20.03/new_nanoguitar.html)
- [4] D. R. Yntema, J. Haneveld, J. B. C. Engelen, R. A. Brookhuis, R. G. P. Sanders, R. J. Wiegerink, and M. Elwenspoek, “Listening to MEMS: An acoustic vibrometer,” in *Proc. IEEE MEMS 2010*, Hong Kong, China, Jan. 24–28 2010, pp. 663–666, doi:[10.1109/MEMSYS.2010.5442319](https://doi.org/10.1109/MEMSYS.2010.5442319).
- [5] J. Mohr, P. Bley, M. Strohrmann, and U. Wallrabe, “Microactuators fabricated by the LIGA process,” *J. Micromech. Microeng.*, vol. 2, no. 4, pp. 234–241, 1992, doi:[10.1088/0960-1317/2/4/003](https://doi.org/10.1088/0960-1317/2/4/003).
- [6] R. W. Young, “Terminology for logarithmic frequency units,” *J. Acoust. Soc. Am.*, vol. 11, no. 1, pp. 134–139, 1939, doi:[10.1121/1.1916017](https://doi.org/10.1121/1.1916017).
- [7] R. Legtenberg, A. W. Groeneveld, and M. C. Elwenspoek, “Comb-drive actuators for large displacements,” *J. Micromech. Microeng.*, vol. 6, no. 3, pp. 320–329, 1996, doi:[10.1088/0960-1317/6/3/004](https://doi.org/10.1088/0960-1317/6/3/004).
- [8] F. Laermer and A. Schilp, “Method of anisotropically etching silicon,” German Patent DE 4 241 045, 1994.
- [9] H. V. Jansen, M. J. De Boer, S. Unnikrishnan, M. C. Louwerse, and M. C. Elwenspoek, “Black silicon method X,” *J. Micromech. Microeng.*, vol. 19, no. 3, p. 033001, 2009, doi:[10.1088/0960-1317/19/3/033001](https://doi.org/10.1088/0960-1317/19/3/033001).
- [10] P. J. Holmes and J. E. Snell, “A vapour etching technique for the photolithography of silicon dioxide,” *Microelectron. Reliab.*, vol. 5, no. 4, pp. 337–341, 1966, doi:[10.1016/0026-2714\(66\)90162-4](https://doi.org/10.1016/0026-2714(66)90162-4).
- [11] B. D. Jensen, S. Mutlu, S. Miller, K. Kurabayashi, and J. J. Allen, “Shaped comb fingers for tailored electromechanical restoring force,” *J. Microelectromech. Syst.*, vol. 12, no. 3, pp. 373–383, 2003, doi:[10.1109/JMEMS.2003.809948](https://doi.org/10.1109/JMEMS.2003.809948).
- [12] C.-H. Cho, “Characterization of Young’s modulus of silicon versus temperature using a “beam deflection” method with a four-point bending fixture,” *Curr. Appl. Phys.*, vol. 9, no. 2, pp. 538–545, 2009, doi:[10.1016/j.cap.2008.03.024](https://doi.org/10.1016/j.cap.2008.03.024).

# MICROFLUIDIC CHIP DEVELOPMENT FOR AN AUTONOMOUS FIELD DEPLOYABLE WATER QUALITY ANALYSER

D. Maher<sup>1</sup>, J. Healy<sup>1</sup>, J. Cleary<sup>1</sup>, G. Carroll<sup>2</sup>, and D. Diamond<sup>1</sup>

<sup>1</sup>CLARITY: Centre for Web Sensing Technologies, Dublin City University, Dublin 9, Ireland

<sup>2</sup>EpiSensor Ltd., Moylish Park, Limerick, Ireland

**Abstract** — This paper presents the ongoing development of a microfluidic chip for a low cost field deployable phosphate analyser for water. The phosphate analyser is a fully integrated system incorporating fluid handling, microfluidic technology, colorimetric chemical detection, and real time wireless communications in a compact and rugged portable device. No commercially available water quality monitoring system can provide this type of functionality in a field deployable system at a comparable cost. The system uses microfluidic technology to have reagent and battery life in excess of one year. The development of a microfluidic chip for this system presents a significant challenge. The phosphate analyser is a commercial product, hence cost reduction and ease of manufacture are major design constraints. In addition sensing system robustness in the presence of air bubbles must be achieved. In this paper we examine different manufacturing approaches, difficulties encountered and solutions found.

**Keywords:** Microfluidics, Water Quality, Environmental Monitoring, Phosphate

**I – Introduction** Increased demand for environmental monitoring has resulted in the need for in-situ real time measurements [1]. Environmental legislation such as the European Union Water Framework Directive establishes a legal framework to protect and restore clean water across Europe [2]. The legislation calls for continuous monitoring to provide a broad understanding of the health of water bodies by 2015. Low cost, widely distributed, autonomous sensors are required as manual sample collection and analysis techniques cannot provide the spatial and temporal resolution to effectively monitor water resources [3].

A prototype field deployable autonomous phosphate analyser has been developed as previously reported in [4, 5]. The system has been extensively field trialled both in natural waters and at waste water treatment plants [6, 7]. The next generation system, shown in figure 1, is a commercial version of the prototype system. The commercial analyser is a compact, portable system with an internal volume of 2.3L and a mass of 1.7Kg. Cost reduction, ease of manufacture and ruggedisation were major considerations during the design of the system. The sensing system is based on the molybdenum yellow method for phosphate detection. Mixing a phosphate containing sample with a reagent containing

ammonium molybdate and ammonium metavanadate results in the formation of vanadomolybdophosphoric acid, a yellow coloured compound. The absorbance of the compound is measured using an ultra violet (UV) light emitting diode (LED) and photodiode. The absorbance is proportional to the phosphate concentration in the sample. The reagent lifetime has been shown to extend to more than 1 year [8].

The issues facing the use of microfluidic devices for in situ environmental monitoring are well documented in [1]. Here we report the development of the phosphate analyser microfluidic chip to date. Different manufacturing methods are first presented followed by a discussion on the performance of the different chips and the issues encountered in the design of a robust, low cost microfluidic chip which can be easily scaled up for volume production.

**II – Experimental Details** The microfluidic chip of the phosphate analyser serves three functions. Mixing of the reagent and sample is first carried out in the micro channels of the chip during the pumping cycle. A stopped flow reaction is then carried out for between 4-7 minutes in the optical cuvette of the chip. The optical detection system carries out an absorbance measurement on the reacted sample using a 380nm UV LED and



Figure 1: Left to Right: Analyzer Internals, Analyzer and Communications Housing, Wireless Communications Gateway



Figure 2: *Prototype Phosphate System Microfluidic Chip*

photodiode. The system also carries out a two point calibration each reaction cycle using two known phosphate concentrations (Typically 0ppm and 10ppm phosphate solutions). As a result the microfluidic chip has 6 inlets (low standard and reagent, sample and reagent, high standard and reagent) and one outlet (waste). Pumping is provided by three dual-channel peristaltic pumps with a maximum flow rate of  $3.7 \mu\text{l/s}$ .

The prototype phosphate analyser [5] microfluidic chip is shown in figure 2. The microfluidic chip consists of 3 layers of polymethyl methacrylate (PMMA) 20x35mm in size. A numerically controlled micromill is employed for manufacturing the chip layers. The microchannels are machined on a PMMA substrate. Channel sizes range from  $200 \mu\text{m}$  to 1mm. The PMMA layers are bonded directly after treating the mating surfaces with UV radiation. The layers are placed under a UV lamp with a wave length less than 180nm. This causes the surface to become hydrophilic. The chip is then assembled and clamped. The chip layers bond after 2 hours at room temperature. To increase the strength of the bond the chip can be heated up to  $90^\circ\text{C}$  while it is under pressure. This caused no significant deformation to the microfluidic channels. The optical cuvette has a 1mm diameter and a 3.5mm path length.

The prototype microfluidic chip provides good reliability and does not suffer from excessive bubble problems. The time required to manufacture a single chip is in excess of 5 hours. This manufacturing method is not scalable or cost effective for mass production. This prompted a redesign not only of the chip but also the chip manufacturing method.

The feasibility of manufacturing the chip using injection moulding techniques is first investigated. Injection moulding eliminates the time consuming micro machining stage from the chip production. The chip is redesigned to be manufacturable in two parts. The injection moulded chip allows mass production of the chip halves from PMMA. The chip has six  $300 \mu\text{m}$  inlet channels and one 1mm outlet channel. The chip injection mould can be seen in figure 3. The mould is machined from brass using electrical discharge machining (EDM). The chip is bonded using thermal bonding. The injection moulded chip halves are clamped together



Figure 3: *Microfluidic Chip Injection Mould*



Figure 4: *Injection Moulded Chip and Detection System*

and heated to  $110^\circ\text{C}$  in an oven for 12 hours. The assembled injection moulded chip mounted on the analyser detection system is shown in figure 4.

A second manufacturing approach is investigated which involved the use of simple drilling operations in PMMA rod. The inlets, outlets and optical cuvette of the system are drilled using a micro pillar drill. The ends of the cuvette are sealed using 1mm diameter PMMA plugs. The drilled chip is shown in figure 5. The chip is relatively easy to manufacture and assemble. This chip uses microbore polyether ether ketone (PEEK) tubing to form the micro inlets thus eliminating the need for micro machining. Tubing is self sealing through the use of interference fits on the inlet and outlet holes allowing rapid assembly without the need for any bonding processes. The chip is also simplified by eliminating T-mixers from the chip design and pumping reagent and sample directly into the optical cuvette for mixing.

To produce a more robust chip in the presence of air bubbles a polydimethylsiloxane (PDMS) casting technique is employed to produce cuvettes with constant cross sections and eliminate corners in the cuvette. This technique involved casting the UV LED, photodiode and copper wire in PDMS. The casting is cured in an oven at  $60^\circ\text{C}$  for 2 hours. Once cured the copper wire is pulled from the cast PDMS block to leave the optical cuvette between the LED and photodiode. Figure 6 shows a chip manufactured using this method. The chip is designed to be a detection chip only, mixing is carried out in a separate PDMS cast mixing chip (figure 7).



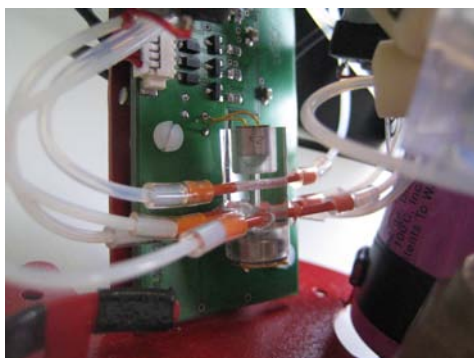


Figure 5: Micro drilled PMMA chip and detection system

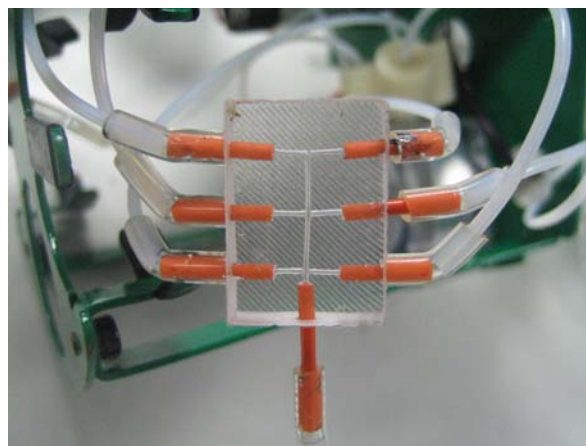


Figure 7: PDMS Cast Mixing Chip

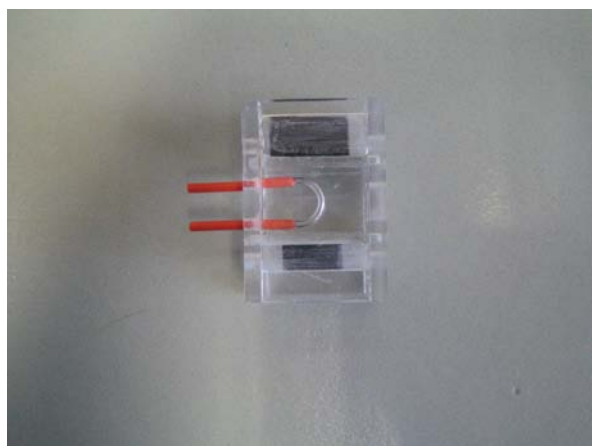


Figure 6: PDMS Cast Chip

The mixing chip uses a simple T-mixing setup and the PDMS material allows the inlets and outlets to be self sealing without the need for any bonding procedure. This simplified chip construction and also produced a robust chip seal.

**III – Results and Discussion** Air bubble entrapment within the optical cuvette proved to be a significant problem with the system. Changes in pressure due to the peristaltic pumping system and also temperature changes during normal operation result in the formation of air bubbles in the system plumbing. Due to the limited battery life and reagent volume in the phosphate analyser, excessive flushing of the optical cuvette to eliminate bubbles, proves detrimental to the overall deployable lifetime of the system. Bubbles were found to become trapped in the optical cuvette especially when the cuvette cross section deviated from a circular cross section. A bubble in a cylindrical optical cuvette will tend to block the channel and as a result the fluid pressure behind the bubble will push the bubble through the cuvette. Bubble entrapment occurs predominantly at the inlet and outlet ports of the optical cuvette where more complex cuvette geometries are seen, fluid was found to flow around the bubbles trapped at these locations and not push them out of the cuvette.

The effect of air bubbles on the phosphate system

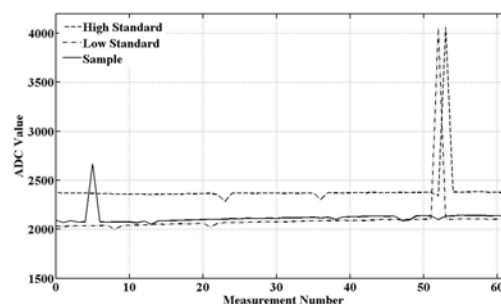


Figure 8: Phosphate System Bubble Events

signal can be seen in figure 8. The graph shows the raw high standard, sample and low standard signals for 62 individual measurements. Major bubble events are indicated by the three large spikes in the raw data at measurement points 5, 52 and 53. The analogue to digital conversion (ADC) scale is inverted here so a bubble present in the cuvette results in a major drop in light transmittance through the optical cuvette and hence photodiode signal. These large spikes are due to bubbles completely blocking the optical cuvette light path. These events are easily detectable at sensor level and can be eliminated. A number of smaller drops in ADC values are seen in the raw data (at measurement points 8,13,21,36 for example). These are smaller bubble events which are difficult to detect at sensor level and contribute to an overall noisy sensor signal. The calculated phosphate concentration from the raw data is seen in figure 9. Although the underline signal is relatively noise free the bubble events contribute to a low signal to noise ratio(SNR).

The injection moulded chip showed significant bubble entrapment problems. This was believed to be due to the surface roughness of the cuvette walls and also the deviation in the optical cuvette from a perfect cylinder. The drilled PMMA chip allowed manufacture of the chip body in one single part. This eliminated bonding operations from the chip manufacturing procedure. This produced a more robust chip as chip bond integrity



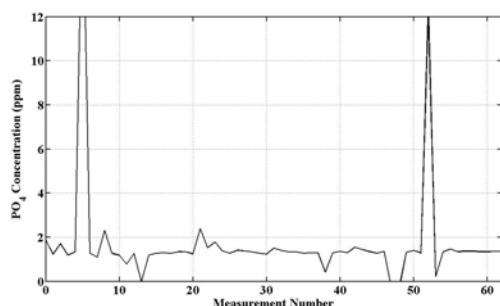


Figure 9: Calculated Phosphate Concentration

was not an issue. This chip was an improvement over the injection moulded chip from a bubble entrapment point of view. The drilling operation produced a cuvette surface finish superior to the injection moulded chip. The nature of the drilling procedure produced sharp corners at the inlets and outlets of the chip. This resulted in intermittent bubble problems with this chip design.

The PDMS casting technique produced an excellent surface finish inside the optical cuvette. The elimination of sharp corners inside the cuvette also contributed to more robust performance in the presence of bubbles. The uniform cuvette circular cross section produced using this manufacturing methods encourages bubbles to pass through the cuvette. The major drawback of this chip design is the optical transparency of the cuvette. The angle of incidence of the light entering the cuvette deviates from  $90^\circ$  and so light refraction and reflection effects at the cuvette boundaries effect the transmission of light through the cuvette and can result in a weak signal at the photodiode. A PDMS chip was produced with a 2mm diameter cuvette perpendicular to the light path. This eliminated refraction problems and produced results comparable with the prototype phosphate system microfluidic chip. Manufacturing time was significantly reduced with assembly time of approximately 10 minutes before curing.

#### IV – Conclusion

The development of a low cost microfluidic chip for a field deployable phosphate analyser for water is presented here. The phosphate analyser is a low cost commercial system designed for long term field trials in remote locations. The entrapment of air bubbles in the microfluidic chip optical cuvette proved to be problematic. The chip needed to be designed to ensure air bubbles could pass through the optical path without lodging in the cuvette. Sample laboratory results have shown the detrimental effect of bubbles on the phosphate analyser data. Three manufacturing methods were examined, PMMA injection moulding, drilling of PMMA rod and PDMS casting. Both the injection moulded chip and PMMA rod chip suffered from bubble problems. Bubbles lodged in the optical cuvette for multiple sample measurements and could not be easily removed by extended pumping. The PDMS chip provided a more robust chip from a bubble point of

view. Occurances of bubbles lodging in the cuvette were significantly reduced due to the smooth cuvette walls and constant cuvette circular cross section produced using this manufacturing method. Tubing inlets and outlets were self sealing allowing for ease of manufacture. Chip assembly time was reduced to approximately 10 minutes. Future work will look at field trialling of the system to assess the chip robustness and performance under operating conditions.

#### References

- [1] L. Marle and G.M. Greenway. Microfluidic devices for environmental monitoring. *TrAC Trends in Analytical Chemistry*, 24(9):795 – 802, 2005.
- [2] Directive 200/60/ec of the european parliament and of the council of 23 october 2000 establishing a framework for community action in the field of water policy. *Official Journal L 327/1*, 2000.
- [3] P. Jordan, A. Arnscheidt, H. McGrogan, and S. McCormick. Characterising phosphorus transfers in rural catchments using a continuous bank-side analyser. *Hydrology and Earth System Sciences*, 11(1):372–381, 2007.
- [4] C.M. McGraw, S.E. Stitzel, J. Cleary, C. Slater, and D. Diamond. Autonomous microfluidic system for phosphate detection. *Talanta*, 71(3):1180 – 1185, 2007.
- [5] C. Slater, J. Cleary, C.M. McGraw, W.S. Yerazunis, K.T. Lau, and D. Diamond. Autonomous field-deployable device for the measurement of phosphate in natural water. In *Proceedings of SPIE*, volume 6755, 2007.
- [6] J. Cleary, C. Slater, C. McGraw, and D. Diamond. An autonomous microfluidic sensor for phosphate: on-site analysis of treated wastewater. *IEEE Sensors Journal*, 8(5):508 – 515, 2008.
- [7] J. Cleary, D. Maher, C. Slater, and D. Diamond. In situ monitoring of environmental water quality using an autonomous microfluidic sensor. In *IEEE Sensors Applications Symposium (SAS)*, pages 36 – 40, 2010.
- [8] M. Bowden and D. Diamond. The determination of phosphorus in a microfluidic manifold demonstrating long-term reagent lifetime and chemical stability utilising a colorimetric method. *Sensors and Actuators B: Chemical*, 90(1-3):170 – 174, 2003.

# A NOVEL MULTISITE SILICON PROBE FOR LAMINAR NEURAL RECORDINGS WITH IMPROVED ELECTRODE IMPEDANCE

A. Pongrácz<sup>1</sup>, G. Márton<sup>1</sup>, L. Grand<sup>2,3</sup>, É. Vázsonyi<sup>1</sup>, I. Ulbert<sup>2,3</sup>, G. Karmos<sup>2,3</sup>, S. Wiebe<sup>4</sup>, G. Battistig<sup>1</sup>

<sup>1</sup> Research Institute for Technical Physics and Materials Science, Hungarian Academy of Sciences, H-1525, P.O. Box 49, Budapest, Hungary

<sup>2</sup> Péter Pázmány Catholic University, Faculty of Information Technology, H-1083, 50/A Práter St., Budapest, Hungary

<sup>3</sup> Institute for Psychology of the Hungarian Academy of Sciences, H-1068, 83-85 Szondi St., Budapest, Hungary

<sup>4</sup> Plexon Inc., 6500 Greenville Ave., Suite 730, Dallas, TX 75206, USA

**Abstract** — A multisite silicon neural electrode was designed, realized and tested for laminar neural recording. The combination of wet etching methods results in a minimally invasive probe shaft having rounded edges and yacht-bow like sharp tip, which provides unique capabilities to record high-resolution signals simultaneously from multiple, precisely defined locations within neural tissue. Fast response and increased sensitivity of the electrode network were enhanced by reduction of the impedance of the biointerface. Improved property of the interface between the brain tissue and the metal contacts will be presented.

**Keywords:** neural probe, multisite extracellular electrode, carbon nanotubes, CNT coating

## I - Introduction

The efficiency of silicon (Si) substrate as brain electrode carrier has been confirmed, as the Si based multi-site structures are not only suitable for batch fabricating and have uniform small dimensions, but numerous contacts can be placed precisely at different points along each probe [1]. Moreover, they offer the potential to integrate signal processing circuits on them and the applied thin films as silicon dioxide and silicon nitride are biocompatible with the brain tissue [2].

## II - Probe design and fabrication

A novel multisite neural electrode was developed, using MEMS technology that offers the same advantages as existing Si micromachining processes [3-5]: highly reproducible batch fabrication with uniform small dimensions, multisite structure formation and compatibility with other CMOS circuit integration technologies. Moreover, the probe dimensions are highly scalable, and it is minimally invasive thanks to its special shape.

An advanced MEMS process flow consisting of 38 steps was carried out for the construction of multisite Si based neural interface [6]. Fig. 1 shows a schematic plan view of a probe with only one shaft projecting from

the base. Fig. 2 shows the design of the top side electrode array.

Standard <100> oriented, p-type silicon wafers with a diameter of 3 inch and the thickness of 200  $\mu\text{m}$ , polished on both sides were used for the probe fabrication that proceeded in four phases. The initial phase consists of thin-film depositions to form the bottom insulating layers, the electrodes, the passivation layer and the contact holes and bonding pads. During the subsequent two phases, combination of anisotropic and isotropic wet chemical etching was applied to shape the probe in order to obtain sharp tip with rounded edge. The special isotropic etching method results in a minimally invasive probe shaft having rounded edges and yacht-like sharp tips.

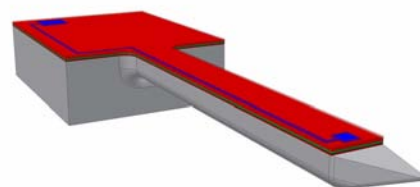


Fig. 1: Simplified 3D view of the probe. The Pt contact placed nearest to the tip of the shaft, the corresponding Pt lead and the bonding pad is clearly visible.

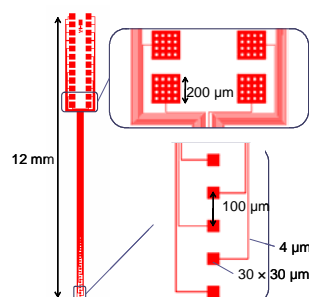


Fig.2. Main dimensions of the designed Pt wiring.

The applied etching method ensures a wide variety of thickness and length dimensions for this neural interface. Current probe (Fig. 3) was designed with definite geometry namely, the length of the probe exceeded 12 mm, the height and width to 80  $\mu\text{m}$  and 280  $\mu\text{m}$ , respectively. The distance between the tip and

the middle of the first contact window is 660  $\mu\text{m}$ . The probe body that can be inserted into the brain tissue extends to 7 mm in length. Our design supports 24 square shaped Pt sites with 100  $\mu\text{m}$  site spacing.

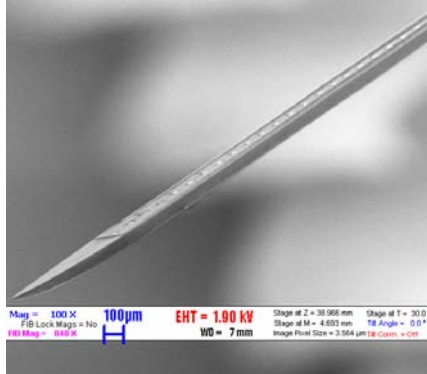


Fig. 3: Scanning Electron Microscope image of the realized silicon probe shows the yacht-like probe tip and the Pt recording sites.

### III – Testing of the probe

The rounded, minimally invasive shape of the probe provided high resolution and good quality recording. The body of the probe can easily be cleaned and reused because of its good mechanical properties; it could simply penetrate through dura and pia mater without bending or causing serious bleeding. The investigated electrodes exhibit excellent in vivo performance in Local Field Potential (LFP), Multi-unit (MUA) and Single-unit (SUA) activity recordings.

### IV - Reduction of impedance

The reduction of electrode impedances offers distinct advantages in terms of lowering noise, calibrating stimulation, and minimizing artifacts [7]. For this purpose, electrochemical etching and carbon nanotube (CNT) coating have been applied.

Initial impedance between each probe site and a counter platinum electrode had been measured. Average site impedance and standard deviation was calculated to be  $1195.12 \pm 113.1$  k $\Omega$ .

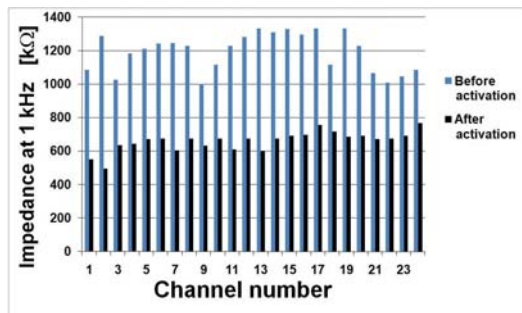


Fig. 4: The impedance values of the channels have been decreased by electrochemical etching

### A. Electrochemical etching

Decreasing the impedance values of the channels of the electrode is possible by a simple electrochemical etching method when -2V is applied on the probe and +2V is applied through an electrode immersed into Saline for 10 seconds. The passing current did not exceed 30  $\mu\text{A}$ . The average impedance of the probe dropped to  $659.04 \pm 59.47$  k $\Omega$ , which is 55.14% of the initial value (Fig.4.).

### B. Carbon nanotube coating

Beside their extremely large surface areas (700–1000  $\text{m}^2/\text{g}$ ), carbon nanotubes have high conductance and aspect ratios. These properties suggest that micro-electrodes coated with CNTs may have low impedance and high charge transfer characteristics [8]. Nanotubes have been electrochemically deposited by Plexon Inc. onto every second site of one of the herein presented probe. The coating decreased the impedances of the targeted channels significantly, to an average of  $44 \pm 6.9$  k $\Omega$ , while the impedances of the non-targeted sites also changed to an average of  $514 \pm 220$  k $\Omega$ . The impedance values of the electrode have been measured after a two hour-long in-vivo experiment as well (Fig. 5). The results of this measurement suggest that the coating was stable enough to withstand the mechanical and chemical effects caused by the implantation.

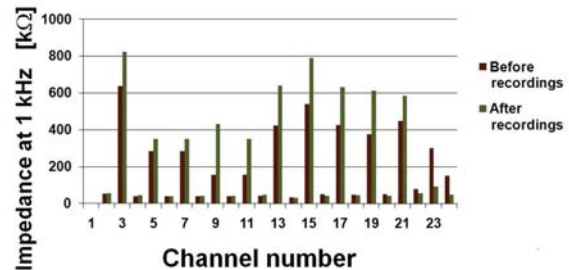


Fig. 5: The effect of carbon nanotube deposition on electrode impedance. The surface of every second site has been coated with carbon nanotubes. The 1<sup>st</sup> channel was damaged. No significant changes can be seen in the targeted channels' impedances. CNT coating was mechanically stable and chemically inert.

### V - Conclusion

With the efficient application of a special wet etching process the micromachining of a multichannel neural probe has been demonstrated here, which is suitable for good quality LFP, MUA and SUA recordings in vivo. Response and sensitivity of the electrode network was improved by reduction of the impedance of the Pt site using either electrochemical etch or CNT coating.

Considering the advantageous properties of the technological process in dimensional scaling and shap-

ing of the silicon probes, as well as the good mechanical properties of our probes, we expect to be able to produce silicon-based devices for deep brain recording/stimulation in the future. Finding the trade-off between small dimensions and stable mechanical properties is not obvious but rather a long-term challenge that we can accomplish by fabricating and testing single- and multi-shank probes with different width, thickness and length.

## Acknowledgements

The authors would like to thank for the staff of the MEMS Lab of MTA MFA for their continuous support in the clean room.

## References

- [1] Wise, K.D., *Engineering in Medicine and Biology Magazine, IEEE*, vol. 24 (5), pp. 22-29, 2005.
- [2] D. T. Kewley, M. D. Hills, D. A. Borkholder, I. E. Opris, N. I. Maluf, C. W. Storment, J. M. Bower and G. T. A. Kovacs, *Sensors and Actuators A*, vol. 58, pp. 27-35, 1997.
- [3] K. Najafi, *et al.*, *IEEE Trans Electron Devices*, vol. 32, pp. 1206- 1211, 1985.
- [4] P. K. Campbell, *et al.*, *IEEE Trans Biomed Eng*, vol. 38, pp. 758-68, Aug 1991.
- [5] P. Ruther, *et al.*, *Proc 13th Conf IFESS*, vol. 53, pp. 238-240, 2008.
- [6] G. Battistig, L. Grand, G. Karmos, K. Payer, A. Pongrácz, I. Ulbert, and É. Vázsonyi, *Hungarian patent application (Nr. P0900774)*, 10 December, 2009.
- [7] J. D. Ross, S. M. O'Connor, R. A. Blum, E. A. Brown and S. P. DeWeerth, *Proceedings of the 26th Annual International Conference of the IEEE EMBS*, San Francisco, CA, USA, pp. 4115-4117, 2004.
- [8] Edward W. Keefer, Barry R. Botteman, Mario I. Romero, Andrew F. Rossi, Guenter W. Gross. *Nature Nanotechnology*, vol. 3, pp. 434 – 439, 2008.



# LARGE DEFLECTION ACTUATOR FOR VARIABLE-RATIO RF MEMS POWER DIVIDER APPLICATION

Y. Li<sup>1</sup>, S. Kühne<sup>1</sup>, D. Psychogiou<sup>2</sup>, J. Hesselbarth<sup>2</sup>, C. Hierold<sup>1</sup>

<sup>1</sup>*Micro- and Nanosystems, Department of Mechanical and Process Engineering, ETH Zurich, 8092 Zürich, Switzerland*

<sup>2</sup>*Laboratory for Electromagnetic Fields and Microwave Electronics, Department of Information Technology and Electrical Engineering, ETH Zurich, 8092 Zürich, Switzerland*

**Abstract** — In this paper, we present the design and fabrication of a large deflection MEMS actuator for the application as a variable ratio RF power divider, to be directly integrated into a waveguide. The device is based on a micro tilting plate suspended by SU-8 springs and driven by a vertical comb drive actuator. The fabricated devices are characterized by laser Doppler vibrometer and white light interferometer measurements. The dynamic measurements confirm the resonance frequency of the tilting mode being around 345Hz, which demonstrates the correct operation of the device. Static actuation measurements evidenced micro plate deflection angles of 3° (vertical plate displacement of ~52 µm) with a DC voltage of 30V and using half of the comb drive.

**Keywords:** RF power divider, Micro mirror, vertical comb drive

## I - Introduction

RF power dividers are multi-port passive components to divide a RF signal at one input port to several output ports. Traditionally, RF power is divided evenly and coherently by simple T junctions or hybrid junctions [1]. Unequal ratio power dividers were implemented by T junction with different output impedance [2] and micro strip transmission line ring hybrid junctions [3]. All these dividers realize perfect impedance match at the input and output ports, and large isolation between the output ports due to the inclusion of dissipative elements (resistors). Concepts of variable power dividers using tuning elements can be easily developed if non-perfect impedance match and non-perfect output port isolation are acceptable. MEMS tuning elements in planar RF circuits show increasing dissipative loss at higher frequencies. A practical approach to reduce the loss of RF MEMS effectively has been proposed by mounting them into a waveguide structure [4,5].

However, such active elements in waveguides require a metallization thicker than the skin depth of the RF signal, as well as large out-of-plane movements. Tilting micro plates are a type of MEMS device, which could meet these requirements. Electrostatic comb drive actuation for the tilting movement has been adopted for many of the devices, because of advantages such as relatively large actuation force, low power consumption, and no pull-in force compare to the electrostatic parallel plate actuators [6]. Especially high-aspect-ratio vertical

comb drives, fabricated by bulk micromachining allow the device to achieve large tilting angles [6]. Also, in order to increase the deflection angle of the micro mirrors under moderate actuation voltage, research has been conducted to optimize the geometry of the comb drives and the design of the suspension spring [7]. Recently, polymer springs have been employed instead of the conventional silicon springs; the low stiffness of polymers has efficiently increased the deflection of the micro devices [8,9].

Here we propose to mount a micro tilting plate device into a waveguide, to steer the path of the RF signals. A thick metal layer will be integrated onto the top of the device according to the skin depth of the RF signal, and another metal layer will be deposited at bottom as a shielding layer. Therefore, by the actuation of the vertical comb drives, the metallic plate surface will be tilting into the waveguide and achieve the function of a variable-ratio RF MEMS power divider. The power divider will work at a frequency of 80 GHz with low dissipative loss, maintaining good but non-perfect characteristics in terms of impedance match and port isolation [10]. In this paper, we will report the design, fabrication, and electromechanical characterization of the micro tilting plate device.

## II - Experimental Details

### A. Device design

The micro tilting plate device is designed to be mounted at the bottom of an air-filled metallic waveguide, as can be seen in figure 1 (a). The waveguide test fixture is made of four gold plated brass parts (Figure 1 (b)). The fixture embraces the MEMS chip and will allow for the connection of millimeter-wave transmitters and receivers using standard WR10-type connectors. For MEMS and waveguide integration, a top metallization is needed on the mirror plate for steering the RF signal as well as on the plate-surrounding area as an interface to the waveguide. The metallization interface prevents the RF signal to come into direct contact with silicon, which will generate additional loss. The thickness of the metallization must be larger than the RF skin depth  $\delta$  to avoid RF loss. The calculated skin depth of Au at the operation frequency of 80GHz is 280 nm. A bottom metallization is also performed under the static combs as a shielding layer to prevent the RF signal from penetrating the device. In order to facilitate the design of an efficient and low-loss device, the dimensions of

the mirror plate should be roughly a quarter to a half of the wavelength of the RF signal. Considering the free-space wavelength at a frequency of 80 GHz being 3.75 mm, the size of the tilting plate is chosen to be 1.8 mm x 0.4 mm.

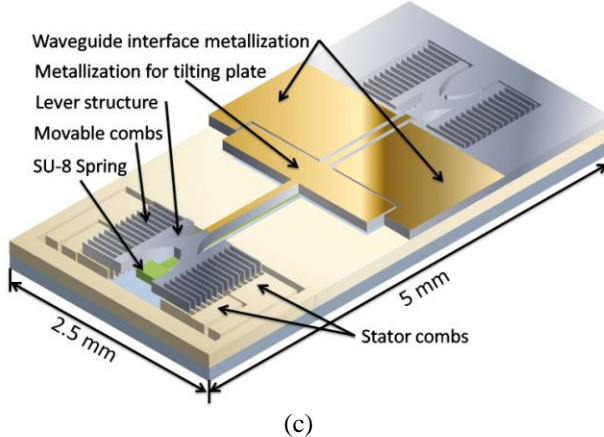
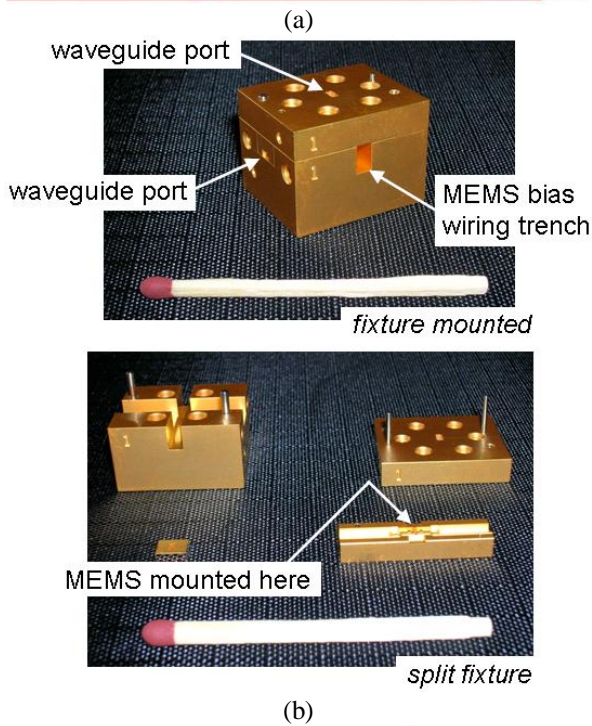
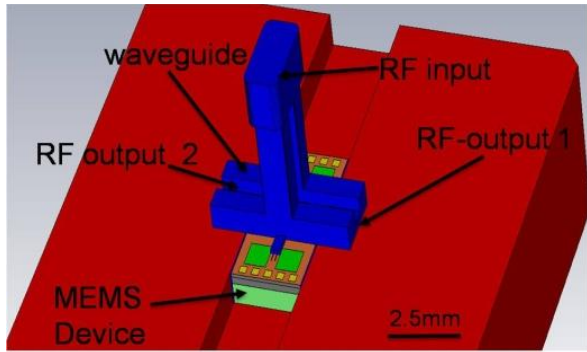


Figure 1: (a) Schematic illustration of Micro plate mounted into a waveguide; (b) photo of a waveguide test structure; and (c) Schematic illustration of the micro tilting plate, with half of the topmost frame removed.

A schematic view of the presented device is shown in figure 1 (c). Half of the frame around the movable combs and the mirror plate has been removed for a clearer view. The design of the micro tilting plate includes a soft SU-8 polymer spring for the suspension of the movable comb drive and mirror plate in order to increase the deflection angle of the tilting plate [8, 9]. Additionally a lever structure between the rotational axis and the movable combs has been designed to increase the electrostatic actuation torque while maintaining the stability of the system. The four stator comb drives are each divided into an electrode pair by completely etched through isolation trenches. For actuation, a positive and negative voltage is applied to the electrode pair, since the movable combs are not electrically connected [10].

### B. Fabrication process

The presented device is composed of a stack of 3 double side polished silicon wafers with different thicknesses, and was fabricated with a 5 mask process. The fabrication process is depicted in figure 2. Alignment marks on the back side of a 400  $\mu\text{m}$  thick silicon

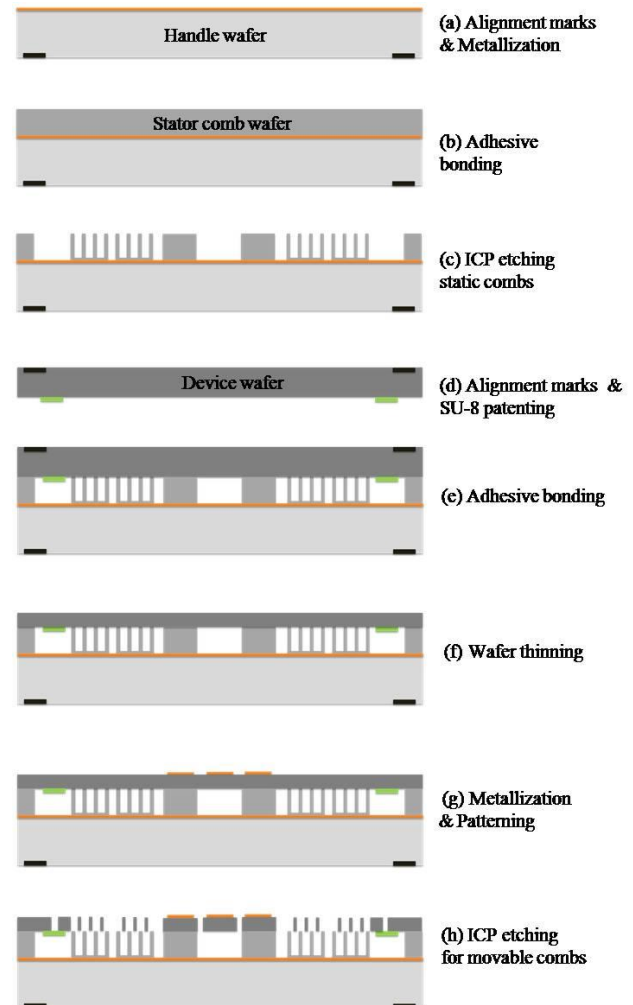


Figure 2: Fabrication process flow for the presented device

handle wafer are patterned first with an Inductively Coupled Plasma (ICP) dry etching process. Then the metallization of 300nm Au is evaporated on to the handle wafer as a shielding layer for the RF signals (figure 2 (a)). Additionally a layer of Lift-off Resist (LOR) is spin coated on the Au which will serve as an etch stop for the successive ICP etching. The handle wafer is then bonded with a 200  $\mu\text{m}$  thick silicon wafer for the stator comb drive layer by adhesive bonding with Benzocyclobutene (BCB) (figure 2 (b)). ICP etching with a Bosch process is then performed to structure the high-aspect-ratio stator combs and the cavity for the micro plate (figure 2 (c)). Afterwards, alignment marks on the back side of a 200  $\mu\text{m}$  thick silicon device wafer is patterned by ICP, and the SU-8 spring is fabricated by photolithography (figure 2 (d)). This device wafer with SU-8 springs is then bonded with the stack of stator comb and handle wafers, by BCB adhesive bonding (figure 2 (e)). A wafer thinning process is performed to reach a final device layer thickness of 100  $\mu\text{m}$  by an isotropic dry etching (figure 2 (f)). Then the top metallization of 300 nm Au is evaporated and structured by a lift-off process (figure 2 (g)). At the end, the movable comb drive and micro tilting plate are released by dry etching (ICP Bosch process) (figure 2 (h)).

### III - Results and Discussion

#### A. Fabrication results

The presented fabrication process flow was successfully validated, as evidenced by microscope photos. Figure 3(a) shows the microscope photo of the wafer with stator combs and cavity for the tilting plate. It can be seen that the profile of the combs as well as the electrical isolation trenches between the stator comb electrodes are well defined. The brighter part of the photo is the Au metallization under the stator combs and in the cavity. The dark color region between the stator combs indicates that the stator combs are not fully released which is also part of the design and enhances the stability of the combs in the subsequent wet processes. Figure 3(b) is a microscope photo taken from the top of the fabricated device. It shows the movable combs, the stator combs as well as the good alignment between them. The bright part of the photo is the Au top metallization for both the micro plate and the waveguide interface area around the plate. The SU-8 spring for the suspension of movable combs and the micro plate can also be seen. The through-holes forming the wire bonding pad on the stator comb electrodes have been etched by ICP during the device layer release.

#### B. Dynamic actuation characterization

The dynamic behavior of the device is measured with a Laser-Doppler Vibrometer in atmospheric air. The measurements are performed at wafer-level and the periodic chirp excitation signal is applied to only half of

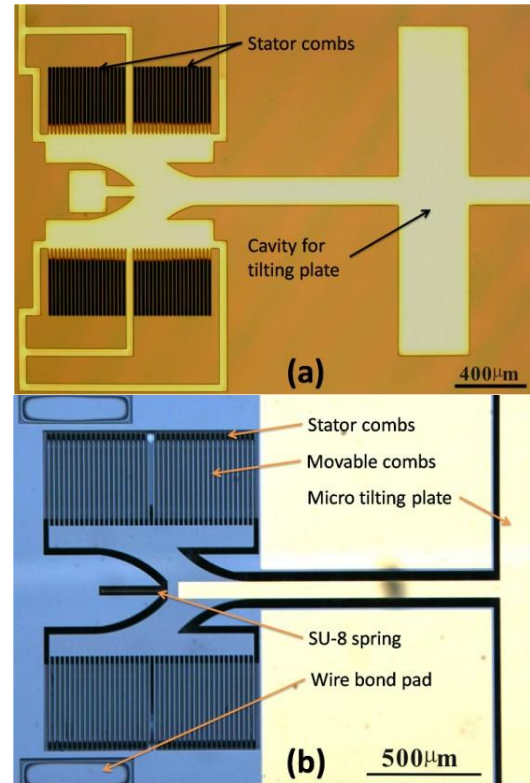


Figure 3: Microscopic photo of: (a) the stator comb drive and plate cavity, (b) movable comb drive and micro plate.

the comb drive on one side of the device. The result of the dynamic measurement is shown in figure 4. The two first resonance peaks have been observed, one at 345 Hz and another above 3000Hz, which is in good agreement with the model values. The amplitude of the first resonance mode, which is the desired out-of-plane tilting mode, is much higher than that of the second resonance mode, which is the out-of-plane piston-motion mode. The dominating first resonance mode and the large frequency separation between the two modes demonstrate the correct function of the micro plate device.

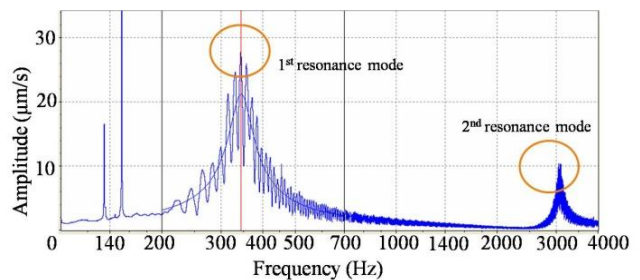


Figure 4: Frequency spectrum of the micro tilting plate.

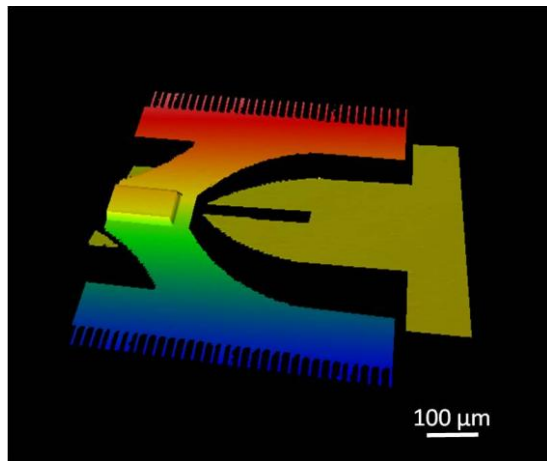
#### C. Static actuation characterization

The static actuation behavior of the device is measured with a White Light Interferometer (WLI) in atmospheric air and on wafer-level. The actuation voltages are applied on only half of the comb drives on one side of

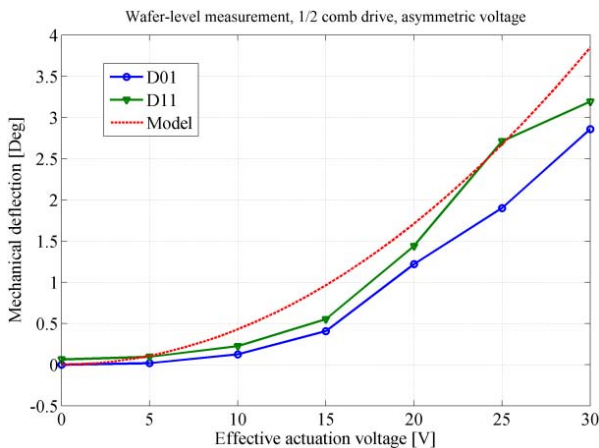


the device, and the deflection of the micro plate is measured with the WLI. Figure 5(a) shows a WLI measurement of the device with an actuation voltage of 15 V on half the comb drive. The parts of the device, which are visible in the image, are the movable combs, the anchor, and the end of the metallization of the middle bar. The measured deflection angle of the micro plate is  $0.55^\circ$ . Figure 5(b) represents the calculated and measured deflection angle of the micro plate as a function of the actuation voltage for two fabricated devices with the same geometry. A deviation between the calculated and measured deflection angles has been observed. The deviation may come mainly from two aspects: firstly, only half of the comb drive is used for actuation, the applied torque was correspondingly asymmetrical. Secondly, the non-vertical profile of the comb sidewalls due to over etching changes the lateral gap distance between the stator and movable combs.

In figure 5(b), a maximum deflection of around  $3^\circ$  was obtained with an actuation voltage of 30V. However, the achievable deflection angle by using both comb drives at one side of the device should be  $6^\circ$  at 30V, since the deflection angle is directly proportional to the number of comb fingers [11]. A deflection of  $6^\circ$  is sufficient for the RF power divider operation.



(a)



(b)

Figure 5: (a) WLI measurement of a micro plate actuated by a voltage of 15V; (b) measured deflection angle of the device as a function of actuation voltage.

#### IV - Conclusion

A micro tilting plate device has been designed and fabricated, and tailored for the application as variable ratio RF power divider. The device features an SU-8 suspension and a lever structure, which enhanced the actuation efficiency of the high-aspect-ratio vertical comb drive. The presented device is composed of a stack of 3 double side polished silicon wafers and is fabricated with a 5 mask process. Two metal layers have been integrated into the device for steering and shielding the RF signal, respectively. The fabricated device is characterized on a wafer-level with a laser Doppler vibrometer and a white light interferometer. Dynamic measurements suggest the resonance frequency of the device is around 345Hz, which demonstrates the correct functionality of the device. Static actuation measurements show that the micro plate is tilted by an angle of  $3^\circ$  with a DC voltage of 30V, applied on half of the comb drives on one side of the device only, which satisfies the specification for the application as RF power divider.

#### Acknowledgement

The authors would like to thank the operational team of FIRST-CLA, ETH Zurich, Switzerland; and Mr. Donat Scheiwiller for his technical support.

#### References

- [1] E. J. Wilkinson, *IRE Trans. on Microwave Theory and Techniques*, vol. MTT-8, Pp 116–118, Jan 1960.
- [2] L. I. Parad and R. L. Moynihan, *IRE Trans. Microwave Theory Tech.*, vol. 8, no. 1, pp.91–95, Jan. 1965.
- [3] J. S. Roy, D. R. Poddar, A. Mukherjee, and S. K. Chowdhury, *Microwave and Optical Technology Letters*, Vol. 3, No. 4, pp. 119-122, 1990
- [4] M. Daneshmand, R.R. Mansour, *IEEE Transactions Microwave Theory Techniques*, pp. 3531 – 3537, 2005.
- [5] M. Daneshmand, R.R. Mansour, *Proc. IEEE Int. Microwave Symp.*, pp. 935-938, June 2005
- [6] U. Krishnamoorthy, D. Lee, and O. Solgaard, *MEMS/ NEMS Handbook Techniques and Applications*, pp. 1718-1745, 2007.
- [7] X. Huikai, P. Yingtian, G.K. Fedder, *J. Microelectromechanical Systems*, vol. 12, pp. 450 – 457, 2003.
- [8] D. Bachmann, S. Kühne, C. Hierold, *IEEE 20th Annual Int. Conf. on Micro-Electro-Mechanical-Systems, MEMS 2007*, Jan. 21-25, Kobe, Japan, pp. 723 -726, 2007.
- [9] S. Kühne, R. Blattmann, and C.H. Hierold, *IEEE 22nd Annual Int. Conf. Micro-Electro-Mechanical-Systems, MEMS 2009*, Jan. 25-26, Sorrento, Italy, pp. 673 -676, 2009.
- [10] J. Hesselbarth, R. Vahldieck, *Proc. Int. Conf. Device Packaging*, pp. TP26, Scottsdale/AZ, March 2009.
- [11] R. A. Conant, *Micromachined Mirrors*, Boston: Kluwer Academic Publishers, 2003



# PVDF MICRO HEAT EXCHANGER MANUFACTURED BY ULTRASONIC HOT EMBOSSEING AND WELDING

K. Burlage, C. Gerhardy, W.K. Schomburg

*RWTH Aachen University, Konstruktion und Entwicklung von Mikrosystemen (KEmikro), Germany*

**Abstract** — In this paper we present for the first time a polymer multilayer micro fluidic system manufactured by the new fabrication process ultrasonic hot embossing and welding. Each fabrication step is performed in a few seconds and the machine and tools are comparatively cheap, allowing for economic fabrication even in small-scale production. A counter flow heat exchanger is fabricated from structures with six parallel channels embossed into polymer films using a metal mold. Three layers of these channel structures are welded on top of each other, creating a counter flow heat exchanger with two coolant layers and a middle layer. The channels have a width of 600  $\mu\text{m}$ , a height of 400  $\mu\text{m}$  and a length of 10 mm. The polymer used for the heat exchanger is polyvinylidene fluoride (PVDF), which offers high chemical and temperature stability and is biologically inert and thus suitable for a wide range of chemical, biological and medical applications. At a temperature difference of 44  $^{\circ}\text{C}$  between warm fluid and coolant and a flow rate of 50 mL/h of the warm fluid, the heat exchanger achieved a heat transfer of 1 W.

**Keywords :** Ultrasonic hot embossing, micro heat exchanger, chemical microreactor, multilayered polymer structures

## I - Introduction

Ultrasonic welding is an established friction welding technology and is employed for welding metals and thermoplastic polymers. Ultrasonic vibration causes frictional heat in the workpieces, which are locally melted and welded together. At KEmikro the same technology has been employed for embossing micro structures into polymer films [1]. Various open micro structures and single layer sealed structures have been realized. The micro heat exchanger presented here is the first multilayer micro fluidic device manufactured by this method.

Depending on conditions of use, polymer micro structures manufactured by ultrasonic hot embossing can in many cases supplant products manufactured from more expensive materials and by technologies such as micro milling, micro injection molding or etching which are expensive and thus often not practical for small scale businesses or research facilities. The micro heat exchanger presented in this paper is a case in point.

Micro heat exchangers have an increased surface-to-volume ratio compared to large scale heat exchangers, which improves heat transfer. Moreover, when the heat exchanger is used as a chemical micro reactor, the small

volume of the channels is advantageous for controlling exothermal chemical reactions, avoiding runaway of the chemical reactor and reducing undesirable byproducts. Compared to micro heat exchangers manufactured from metal or glass by etching, micro milling or micro grit-blasting, production of the presented PVDF micro heat exchanger is cheap and simple. New designs can be realized and tested in a matter of hours which expedites research and development, and once a mold is fabricated, even cost effective batch production is feasible. Furthermore, attachments for connecting the inlets and outlets of the micro heat exchanger with tubes are welded onto the layered structure with the same method.

In this paper, we describe the production process of ultrasonic hot embossing and welding and present the findings of test-stand experiments conducted on the developed PVDF micro heat exchanger.

## II – Ultrasonic Hot Embossing and Welding of the PVDF Micro Heat Exchanger

### A. Basic Principles of Ultrasonic Hot Embossing and Welding of Thermoplastic Polymers

Ultrasonic hot embossing is a manufacturing method derived from conventional ultrasonic welding which is suitable for structuring thermoplastic films. By applying compressive force and ultrasonic vibration, frictional heat is induced in the polymer films which locally melt and adapt to the structures of a mold. The machine used for the production of the micro heat exchanger is the Dynamic 745 by Rinco Ultrasonics, a 35 kHz machine with amplitudes between 7 and 12  $\mu\text{m}$  and a compressive force of up to 745 N. The frictional heat is due to both boundary friction between the films and protruding structures on the tool and between the films themselves, and inner friction on a molecular level inside the polymer.

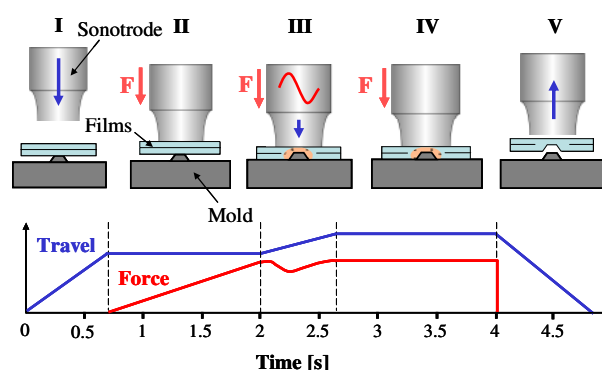


Figure 1: Ultrasonic Hot Embossing.

Fig. 1 shows a schematic of the production process of ultrasonic hot embossing, which consists of five steps. After the ultrasonic horn has been driven onto the workpiece (I), the compressive force is increased until a set value is reached (II) and the ultrasonic vibration is switched on (III). Due to the melting of the polymer, the compressive force drops and the sonotrode travels further down, pressing the molten polymer into the mold. After a subsequent cooling phase with a set force (IV) the sonotrode is retracted and the molded part can be removed. As the diagram indicates, the whole process only takes a few seconds. In contrast to conventional hot embossing the energy input of ultrasonic hot embossing is constricted to the areas where melting of the polymer is desired. The sonotrode, the mold and the area of the polymer films which is not in contact with the mold remain almost constantly at room temperature. Thus, the embossed structure is solidified in less than a second and can be manually demolded immediately after retraction of the sonotrode. Due to the directed energy input achieved by the protruding structures of the mold, these structures are also called energy directors.

#### B. Production Process of the PVDF Micro Heat Exchanger

The first step of the production process is the mold-part and tool design for the components of the heat exchanger. The counter flow heat exchanger was projected to consist of stacked fluid-carrying layers with alternate layers for tempering fluid. Each layer was designed with six parallel channels, which converge at both ends into an inlet respectively outlet. The channels have a width of 600  $\mu\text{m}$ , a height of 400  $\mu\text{m}$ , and a length of 10 mm, respectively. To feed different fluids into alternating layers and to permit mounting of inlets and outlets for both liquids on the top cover of the heat exchanger, two laterally reversed layer designs A and B with lead-throughs for adjoining layers were created (fig.2).

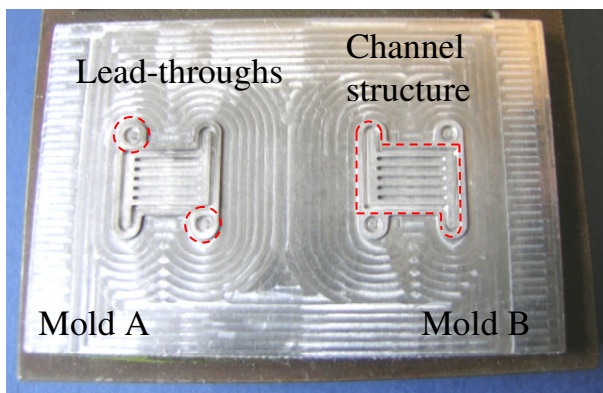


Figure 2: Molds for channel structures A and B.

For the mold design, the shrinkage caused by ultrasonic hot embossing was neglected and demolding bevels and shrinkage allowance were dispensed with.

Previous tests showed that channel structures in this scale with right angled walls can be manufactured without problems. Accordingly, the pattern of the mold is composed of indentations (which later form the walls of the heat exchanger) and protruding bars (which form the channels) with rectangular cross sections.

Whereas welding a lid film on a single-layer structure can be achieved by using a tool with an energy director in the position of the weld seam, welding multi-layered structures requires energy directors on the workpieces themselves. When two layers are positioned on top of each other, the ultrasonic process leads to melting of these energy directors and the layers are joined.

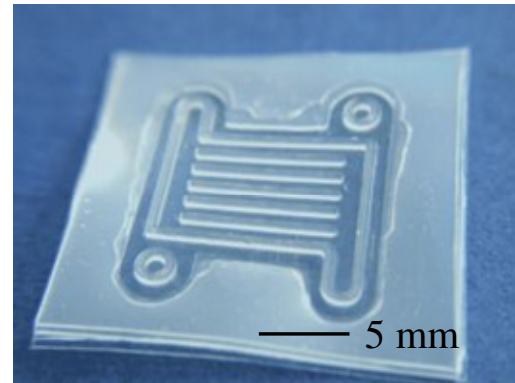


Figure 3: Embossed structure A.

Consequently, the design for the mold in fig. 2 includes grooves for energy directors (not visible in the figure) around the outer contours of each layer and on the walls between the separate channels. The mold was manufactured from aluminum by micro milling. The grooves for the energy directors were milled with a micro ball end milling cutter with a diameter of 150  $\mu\text{m}$ . The production of cone shaped energy directors was also tried but rejected due to the oversized width of the tips of standard engraving tools.

After manufacturing of the molds, suitable embossing and welding parameters were determined by experiments. The start values were based on experiences from similar embossing and welding tasks and adjusted to achieve optimal results. Figure 3 shows one layer of the heat exchanger molded from mold A in fig. 2.

Table 1: Parameters for embossing and welding

Parameter	Embossing	Welding
Force Buildup [N/s]	250	25
Trigger Force [N]	250	25
Ultrasonic Time [ms]	290	100
Holding Force [N]	1500	500
Energy [Ws]	$\approx 100$	$\approx 10$

For welding the layers together, the structures were aligned and fixed on a flat surface beneath the sono-

trode. The welding process starts with the lid and the first structure, then the second layer is welded beneath these and finally the third layer is joined. All layers except for the bottom one have drilled holes at the ends of the channel structures and at the lead-throughs.

Cuts through an embossed channel structure with energy directors and through three layers welded on top of each other sealed with a lid film are shown in fig. 4.

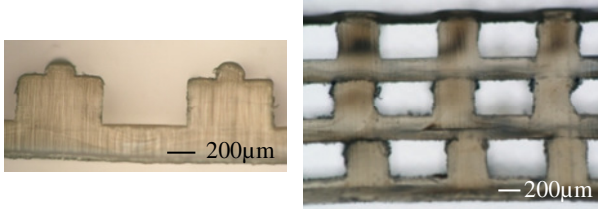


Figure 4: Cut through a channel with surrounding walls with energy directors and through three channel structures welded together.

Each layer of the micro heat exchanger was manufactured by embossing into a stack of four layers of PVDF with a thickness of 150 µm each. For the inlets and outlets of the micro heat exchanger, a massive cylindrical piece of PVDF with a thickness of 10 mm and a diameter of 20 mm with drilled holes for connecting tubes was employed. This was welded to the first layer of the heat exchanger using the same parameters as mentioned in table 1.

### III – Characteristics of the PVDF Micro Heat Exchanger

#### A. Generic Physical and Chemical Properties of PVDF

PVDF is a partially crystalline thermoplastic polymer. It is suitable for long-run operation temperatures between -50 and 140 °C and short-run temperatures up to 150 °C, its melting point is at about 175 °C. PVDF is resistant against a multitude of chemical agents, among others sulfuric acid up to a concentration of 95 %, hydrochloric acid, glycerine, and various oils and fats [2]. It has low moisture absorption of 0.03 to 0.04 %. As most polymers, it has a low heat conductivity of 0.2 W/(K m) compared to high alloyed steel with 15 W/(K m) and glass 0.76 W/(K m).

#### B. Experimental Analysis of the PVDF Micro Heat Exchanger

For basic tests of the capabilities of the micro heat exchanger, the inlet of the middle layer was connected to a syringe pump filled with water at 50 °C with a maximum flow rate of 99 mL/h.

The inlet of the two surrounding coolant layers was connected to a constant flow of 12 mL/min of water at a temperature of 6 °C. The temperature at inlet and outlet of the warm layer was measured with thermocouples (fig. 5). The cooling results achieved by the micro heat exchanger are shown in fig. 6. Depending on the flow

rate of the 50 °C warm water, cooling of 6 to 18 °C was realized.

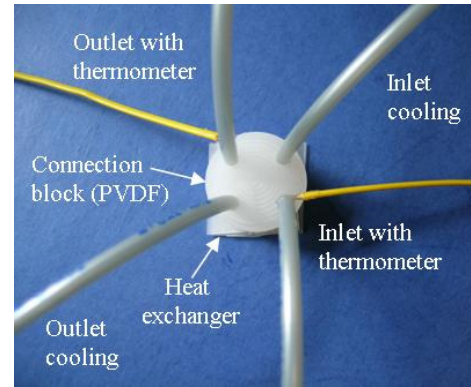


Figure 5: Micro heat exchanger with fluid connections

The heat exchange can be calculated with the specific heat capacity  $c_w$  (4.18 kJ/(kg °C)) and density  $\rho$  (1000 kg/m<sup>3</sup>) of water. At a flow rate of 50 mL/h and cooling of  $\Delta T = 18$  °C the heat exchange is

$$\Delta Q = c_w \cdot \rho \cdot \Delta T \cdot \dot{V} = 1.05 \text{ W}.$$

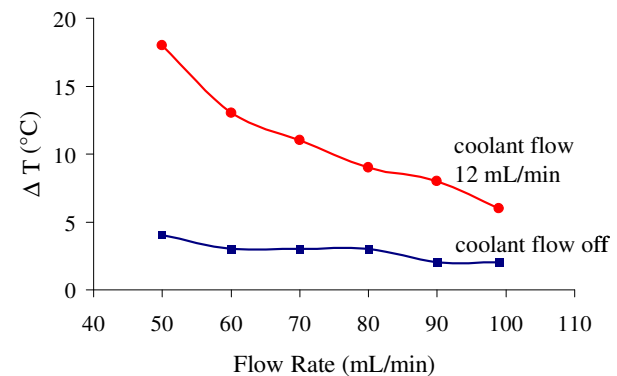


Figure 6: Cooling performance of the PVDF micro heat exchanger with 50 °C inlet temperature as a function of the flow rate.

The flow resistance  $R_{fl}$  of a single layer of the heat exchanger was determined by feeding it with a hydrostatically driven flow of water and using the following equation:

$$R_{fl} = \frac{\Delta p}{\dot{V}} = \frac{9 \text{ kPa}}{20 \text{ ml/min}} = 27 \text{ kPa} \cdot \text{s/ml}$$

The pressure difference  $\Delta p$  between inlet and outlet was 9 kPa and the measured flow rate was 20 mL/min.

Finally, to test the pressure stability of the heat exchanger, the outlets were sealed and the inlets connected to an air pressure source and a flow meter to detect leakage. A pressure of 200 kPa did not result in any measurable leakage. Furthermore, the heat exchanger could be stabilized with an outer housing for use at higher pressures.

## IV - Conclusion

Ultrasonic hot embossing is applicable for a wide range of polymers and designs. The investment costs for a table top machine are comparatively low, each embossing and welding step only takes seconds and molds can be manufactured by different methods which are readily available. Thus, ultrasonic hot embossing is a cost effective and expeditious method and exceptionally suitable for the production of prototypes and small series. Contrary to injection molding and hot embossing, which require complete melting of the polymer, the directed energy input and locally restricted melting achieved by ultrasonic hot embossing lead to shorter cycle times and reduced shrinkage, which facilitates tool design and reduces energy consumption.

The successful fabrication of micro heat exchangers by ultrasonic hot embossing shows that multilayer structures can be fabricated which are leak-proof and suitable for various applications. Besides this, it is a large advantage that inlets and outlets can be welded directly onto the structures avoiding additional manufacturing steps. Thus, ultrasonic hot embossing and welding open up the way for an economic production of micro from thermoplastic polymers even in small scale series and for research and development.

## References

- [1] P. Khuntontong, T. Blaser, W.K. Schomburg "Ultrasonic micro hot embossing of thermoplastic polymers", Proc. 24<sup>th</sup> Annual Meeting of the Polymer Processing Society, PPS24, Salerno, Italy, June 15-19 (2008) p. II.364.
- [2] Bürkle GmbH „Chemische Beständigkeit von Kunststoffen“, 2010 [www.buerkle.de/de/chemische-bestaendigkeit.html](http://www.buerkle.de/de/chemische-bestaendigkeit.html)



# A COMB BASED IN-PLANE SIGE CAPACITIVE ACCELEROMETER FOR ABOVE-IC INTEGRATION

L. Wen<sup>1</sup>, K. Wouters<sup>1</sup>, L. Haspeslagh<sup>2</sup>, A. Witvrouw<sup>2</sup>, R. Puers<sup>1</sup>

<sup>1</sup>ESAT-MICAS, Katholieke Universiteit Leuven, Leuven, Belgium

<sup>2</sup>IMEC, Kapeldreef 75, Leuven, Belgium

**Abstract** — MEMS above-IC monolithic integration can yield very compact device with good cost-effectiveness. One of the major challenges for this technology is to protect the CMOS from the heat introduced by the MEMS fabrication. In this paper, we present the design and fabrication of a novel lateral capacitive accelerometer, utilizing a low thermal budget SiGe MEMS technology. The accelerometer features a 4μm SiGe structural layer thickness with a shock protector gap of 500nm. Benefiting from the low temperature (~450 °C) SiGe MEMS technology, this inertial device demonstrates the achievability of fabricating above-IC mechanical sensors by 3D stacking. In this paper, the accelerometer design will be introduced first, followed by the introduction of the low thermal budget SiGe MEMS fabrication process. The fabricated devices have been characterized with a network/spectrum analyzer. Both a frequency sweep and a DC voltage sweep have been conducted. These electrostatic characterization results will be analyzed and compared with the design model.

**Keywords :** Capacitive accelerometer, SiGe, Low thermal budget MEMS, MEMS above-IC

## I - Introduction

Inertial sensors have been widely used in many sectors of industry and consumer electronics. Techniques such as bulk and surface micromachining have allowed the performance of accelerometers to be much improved [1]. Meanwhile, CMOS compatible accelerometer research has become a promising research field, by which the monolithic integration of a micro-sensor and the related interfacing integrated circuit can be realized [2]. This integration can boost the device performances in many ways. For example, due to the shortening of the signal path for the sensor-IC integration, the parasitic capacitance in the signal path can be greatly reduced. Compared to other CMOS compatible technologies, MEMS above-IC monolithic integration has advantages concerning the use of standard CMOS, size and possibly cost [3, 4]. On the other hand, among all the detection principles, capacitive differential accelerometers feature high sensitivity, stable DC-characteristics, low drift, low power dissipation and low temperature sensitivity [5]. Therefore, to realize differential capacitive accelerometer above-IC integration shows great promise.

The major restriction for a post-CMOS integration technology is to find the proper material with a low processing thermal budget. Poly-SiGe turns out to be a promising choice since it possesses similar mechanical

properties as poly-silicon and can be deposited on top of CMOS due to its low processing temperature (~450 °C) [6].

This paper presents a lateral differential capacitive accelerometer fabricated with a 4μm thick poly-SiGe structural layer. Figure 1 shows Schematic view of the designed accelerometer. The device possesses 100 sensing fingers on the proof mass, which are 110μm in length and 2μm in width. On each side of a proof mass finger a stationary finger is located. All these fingers can be connected to form the differential sensing pair  $C_{s1}$  and  $C_{s2}$ . The proof mass is suspended by four folding beams. The length of each beam is 100 μm plus 125μm. Two groups of electrodes on both ends of the proof mass can be used as self-testing electrodes. To protect the device from harsh shock damages, four shock protectors are placed to limit the movement range of the proof mass with respect to the substrate. The gap between the fingers in this design is 1.5μm, while the finger overlapping is 100μm.

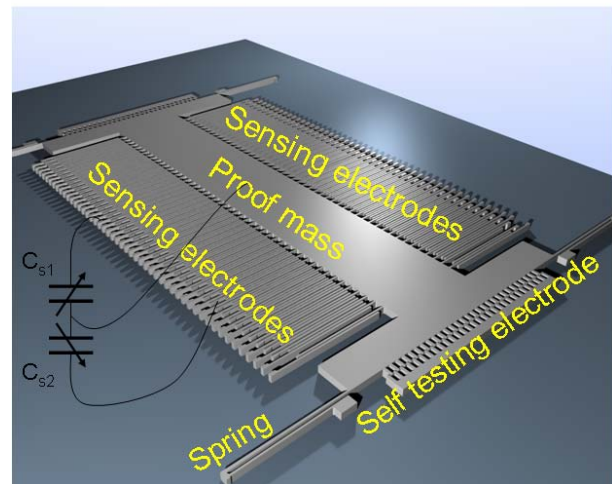


Figure 1: Schematic view of the poly-SiGe lateral capacitive accelerometer with self-testing electrodes and shock protectors

## II – Device fabrication

Figure 2 shows the fabrication process flow of the poly-SiGe lateral capacitive accelerometer. The fabrication process is starting from a silicon wafer with a silicon oxide layer to mimic the CMOS backend and a SiC passivation layer. SiC layer is used to protect the oxide layer from the HF release step later on. On the SiC layer, the SiGe electrode layer is deposited by CVD (Chemical Vapor Deposition) and patterned, Figure 2 (1). Then the sacrificial oxide layer is deposited and

patterned thereafter, Figure 2 (2). Openings are made to place the anchors. The following step is to deposit the structural SiGe layer. A 4 $\mu$ m thick structural layer is realized by CVD and PECVD (Plasma Enhanced CVD) deposition of four 1 $\mu$ m layers [7], with chamber cleaning step in between of each layer, Figure 2 (3). After the structural layer roughness reduction by CMP, an additional oxide deposition can be conducted for the metal bond-pad via, Figure 2 (4). The bond pad layer is then deposited on top and patterned thereafter, Figure 2 (5). The SiGe structural layer is then patterned, being masked by the oxide layer on top, Figure 2 (6). The last step is to release the whole stack with HF, Figure 2 (7).

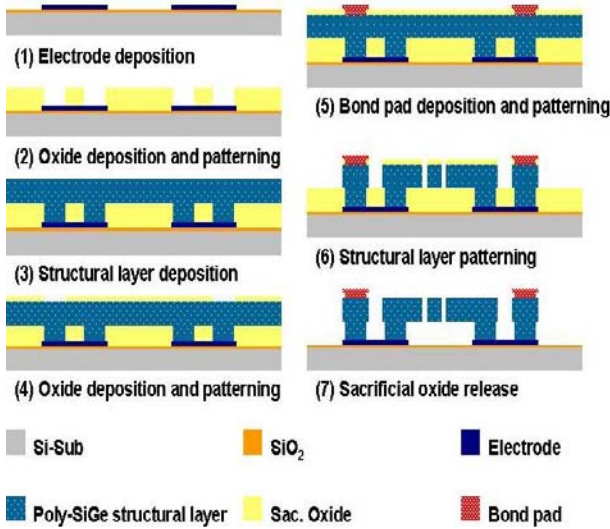


Figure 2: Fabrication process flow of the poly-SiGe lateral capacitive accelerometer

This prototyping process is to demonstrate the feasibility of the above-IC MEMS concept. With the electrode layer, the MEMS device signal can be then conducted to the bond pads. For the wafer level inspection and the individual device characterization, this bond pad scheme offers the easy access to the MEMS device, which doesn't hinder the future use of this technology to above-IC applications.

Figure 3 shows a SEM view of the fabricated poly-SiGe lateral capacitive accelerometer. All the sensing fingers are well defined as shown in Figure 3 (a), while on each inner side of the proof mass, the shock protecting stopper feature can be clearly observed. The interconnections are fabricated in the electrode layer, which can be seen in Figure 3 (b). Figure 3 (b) also shows nicely the free-standing gap beneath the proof mass. On the proof mass, etch holes were designed to speed up the final release time, which can also protect the oxide layer under the SiC passivation layer from the HF attack. The small square shaped the islands in the Figure 3 (b) are the dummy islands. Under the dummy islands, the anchor layer and the electrode layer can be seen with ease.

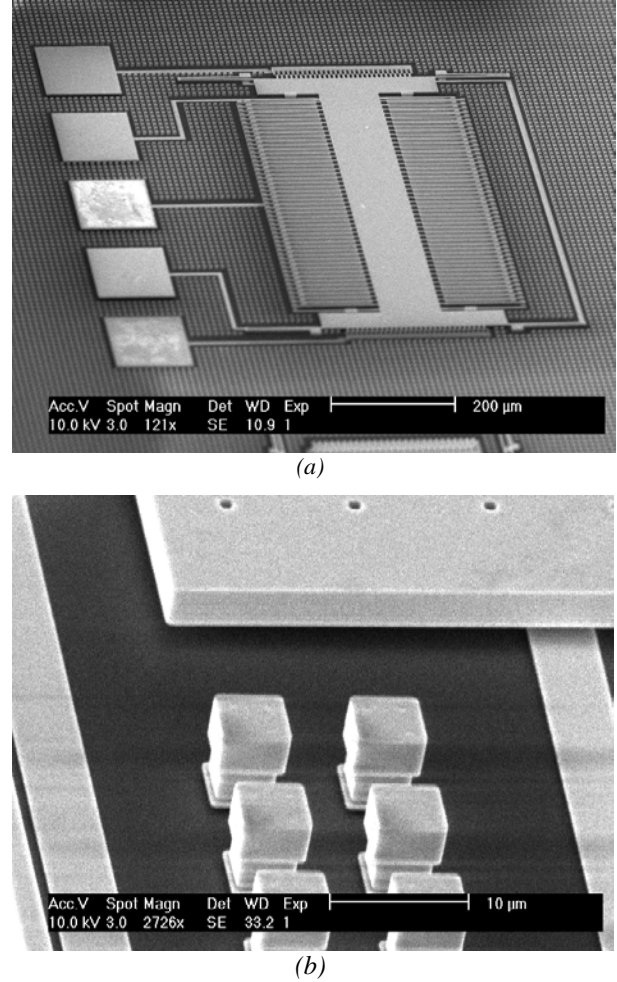


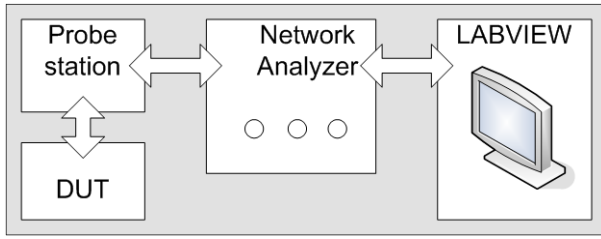
Figure 3: SEM view of the fabricated poly-SiGe lateral capacitive accelerometer

### III – Device characteristics and discussion

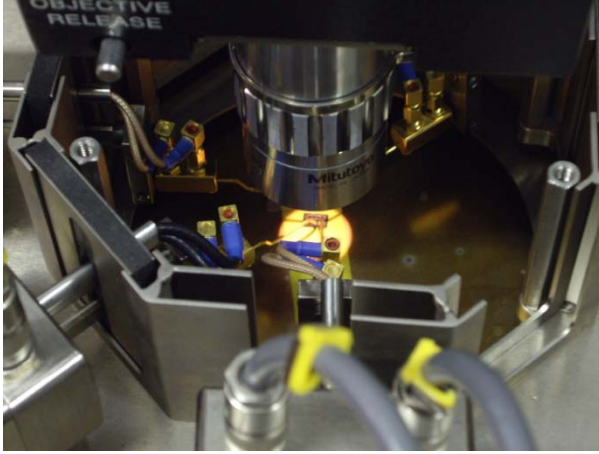
The fabricated devices have been characterized using both a frequency sweep and a DC voltage sweep with a HP4195A network/spectrum analyzer. The testing setup has been constructed as shown in Figure 4 (a). The device under test (DUT) is positioned on the probe station chuck, Figure 4 (b), with the probe signals feeding to the analyzer which is interfaced by a Lab-view program to the computer.

The frequency sweep is conducted by an AC oscillation across a range of 5 kHz, centered at 8 kHz, and the oscillation level is 0.5V, with a 2V DC bias voltage. Figure 5 shows a typical real part of the admittance response of the DUT during the frequency sweep. The peak position is corresponding to the resonance frequency of the accelerometer. In this case the resonance frequency is around 7.9 kHz. According to the design, the total spring constant of the folding beams is:

$$k = 4 \times \frac{EHW^3}{L_1^3 + L_2^3} \quad (1)$$



(a)



(b)

Figure 4: Diagram of the electrostatic measurement setup with the view of the fabricated DUT during the measurement

Where the  $E$  is the young's modulus of the deposited SiGe,  $H$  is the thickness of the structural layer,  $W$  is the width of the spring,  $L_1$  and  $L_2$  are the length of each part of the folding beam. With these design specs,  $k$  is  $6.07 \text{ N/m}$ . On the other hand, the resonance frequency of the accelerometer is

$$f = \frac{1}{2\pi} \sqrt{\frac{k}{m}} \quad (2)$$

With the proof mass  $m = 1.69 \times 10^{-9} \text{ kg}$ , the designhn resonance frequency is  $9.64 \text{ kHz}$ .

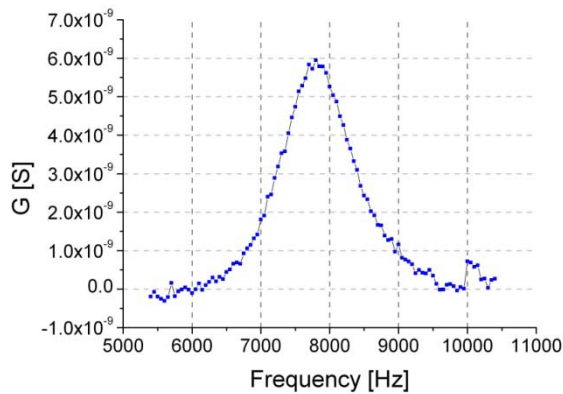


Figure 5: Frequency response of the DUT under the frequency sweep test

The tested resonance is in the same order of the calculated resonance frequency from of design.

Figure 6 shows a SEM close-up of the shock protectors of the fabricated poly-SiGe lateral capacitive accelerometer. The gap between the stopper and the proof mass in this design is  $500\text{nm}$ , which is well defined with teeth feature to miniaturize the contact surface area between the proof mass and the stopper. From this figure, the springs and fingers can also be clearly observed. Attention has been paid to all the  $90$  degree corners of the device. Triangular patches have been added to all the fragile corners to prevent them from probable fractures during the processing and during the related testing or even during the possible usage afterwards.

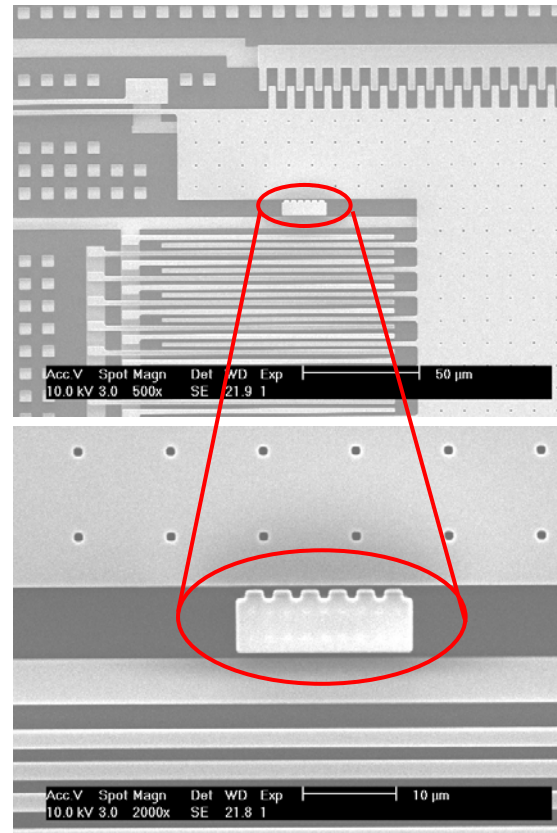


Figure 6: SEM view over the positioning of the shock protectors of the fabricated poly-SiGe lateral capacitive accelerometer

A HP 4195A network analyzer is used to characterize the electrostatic response of the device to a DC bias voltage, sweeping across one pair of its counter electrodes. The spot frequency is  $10\text{MHz}$ , with an oscillation level of  $0.5\text{V}$ . Figure 7 shows the measured C-V characteristics with up and down DC voltage sweep across one pair of the sensing electrodes of the fabricated poly-SiGe lateral capacitive accelerometer.



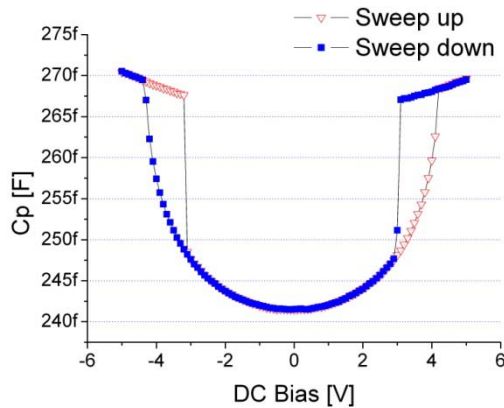


Figure 7: Measured CV characteristics with up and down DC voltage sweep across one pair of the sensing electrodes of the fabricated poly-SiGe lateral capacitive accelerometer

From Figure 7 a clear pull-in and release cycle can be seen, the pull in occurs around 4.10V, while the designed pull-in voltage is 4.14V. In the sweep up direction of the curve, after the pull-in occurred, the C-V curve still increase with a slower rate. This is related to the positioning of the stopper. Because the stoppers are positioned 500nm away from the proof mass, which is a third of the 1.5 $\mu$ m finger gap, that distance equals to the pull-in position. The finger will bent into each other after the proof mass hit the stopper. That bending is the cause of the slope after pull-in on both ends of the C-V curve. The tested capacitive change is 25fF.

#### IV - Conclusion

This paper presents the design, fabrication and characterization of a CMOS compatible lateral capacitive accelerometer, fabricated with a low thermal budget poly-SiGe MEMS technology. The in-plane single axial device features a small outline profile, low cross talk and a precise shock protection. The released devices have been electro-statically analyzed, with an impedance analyzing system. The frequency response of the DUT is found to be 7.9 kHz, which is in the same order of magnitude as the calculated resonance frequency of 9.6 kHz. The DC bias voltage sweep response of the DUT is tested also. The tested capacitive change of 25fF together with the pull-in voltage of 4.10 V is precisely within the design specs.

#### Acknowledgments

This work has been carried out in the frame of SBO-program project 060046, Gemini, sponsored by the 'Instituut voor de aanmoediging van Innovatie door Wetenschap en Technologie in Vlaanderen' (IWT), Belgium. This work is also supported by the Hercules initiative for large equipment (AKUL034, Cluster for micro and nanolithography). The authors wish to acknowledge Jeroen De Coaster at IMEC Belgium for his help and support.

#### References

- [1] Wim Claes, Willy M. C. Sansen, Robert Puers, Design of wireless autonomous datalogger IC's, Springer (2005), ISBN1402032080, 9781402032080
- [2] Robert Modlinski, Ann Witvrouw, Agnes Verbist, Robert Puers and Ingrid De Wolf, Mechanical characterization of poly-SiGe layers for CMOS-MEMS integrated application, J. Micromech. Microeng. 20 (2010) 015014
- [3] Witvrouw A, CMOS-MEMS integration: why, how and what, ICCAD'06 (San Jose, CA, 5-9 November 2006), pp 826-7
- [4] <http://www.mems.sandia.gov/tech-info/mems-overview.html>
- [5] Lianggong Wen, Kristof Wouters, Frederik Ceysens, Robert Puers, A CMOS-compatible self-aligning capacitive accelerometer with Epoclad polymer on silicon (POS) technology, in Proceedings of MicroMechanics Europe Workshop, 20, Toulouse, France, 2009
- [6] A. Schreurle, T. Fuchs, K. Kehr, C. Leinenbach, S. Kronmüller, A. Arias, J. Ceballos, M. A. Lagos, J. M. Mora, J. M. Muñoz, A. Ragel, J. Ramos, S. Van Aerde, J. Spengler, A. Mehta, A. Verbist, B. Du Bois and A. Witvrouw, A 10  $\mu$ m thick poly-SiGe gyroscope processed above 0.35  $\mu$ m CMOS, Proc. IEEE MEMS 07, 39-42.
- [7] G. Claes, G. Van Barel, R. Van Hoof, B. Du Bois, M. Gromova, A. Verbist, T. Van der Donck, S. Decoutere, J.-P. Celis and A. Witvrouw, Stacked Boron Doped Poly-Crystalline Silicon-Germanium Layers: an Excellent MEMS Structural Material, Mater. Res. Soc. Symp. Proc. Volume 1075E, 2008, 1075-J05-02



# SURFACE-MICROMACHED GAS SENSOR USING THERMOPILES FOR CARBON DIOXIDE DETECTION

S. Chen, H. Wu, G. de Graaf and R. F. Wolffenbuttel

*Delft University of Technology, Faculty of EEMCS, Department of ME/EI, Mekelweg 4, 2628 CD Delft, The Netherlands*

**Abstract** — The results of simulation, fabrication and measurement of a thermal conductivity gas sensor are presented. IC-compatible surface-micromachining MEMS technologies have been used for fabrication. The simulation and measurement results show that the output Seebeck voltage increases with the carbon dioxide concentration in air, thus gas detection is accomplished. The simulation results show that an increase in the carbon dioxide concentration in air from 0% to 30% leads to an increase in the output Seebeck voltage of 2.5mV at 1.2mW input power. The measurement results indicate that an increase in the carbon dioxide concentration in air leads to an increase in the output Seebeck voltage of 2.6mV at 1.2mW input power.

**Keywords:** gas sensor, surface-micromachining, thermal conductivity, sensitivity

## I - Introduction

In recent years, gas sensors are increasingly used in the growing markets of automotive industry and environmental monitoring [1, 2]. The most widely used commercial gas sensors are chemical gas sensors, such as metal oxide-based gas sensors [2, 3, 4]. Chemical gas sensing is based on the measurement of a change in electrical conductance or other physical properties of the sensing material due to the chemical interaction between the gas and the sensing material [5, 7].

However, one of the major drawbacks of chemical gas sensors is the limited long-term stability due to for instance contamination of the interface during chemical interaction [3, 5, 6]. The operation of physical gas sensor relies on the direct measurement of a physical property of a measured gas, which offers possibilities for an enhanced long-term stability. Especially, the thermal conductivity sensor is such a good solution. Although thermal conductivity sensors are generally not as sensitive as chemical sensors [7], they are more reliable since they will not be contaminated when they sense the gases.

Thermal conductivity gas sensors are particularly suitable for detecting hydrogen, since the thermal conductivity of hydrogen (0.1805 W/(m·K) [10]) is approximately 7.5 times that of the air (0.02394 W/(m·K) [10]). That implies even very low concentration of hydrogen can be detected in air. Therefore, gas sensors based on thermal conductivity are especially

suitable in safety applications, such as automotive combustion or fuel cell applications [9]. In such systems, leakage of hydrogen needs to be detected before hydrogen concentrations reach the lower explosive limit LEL of 4% [8] in air.

In order to detect carbon dioxide (thermal conductivity 0.01465 W/(m·k) [10]), a higher concentration is required. For a low concentration of carbon dioxide detection, the sensitivity of thermal conductivity gas sensors should be relatively high. The carbon dioxide gas sensors should be placed as low as possible during measurement. The reason is that the density of carbon dioxide (1.977 kg/m<sup>3</sup> [8]) is approximately 1.5 times of the density of the air (1.2754 kg/m<sup>3</sup> [8]), and thus the carbon dioxide concentration is highest at the lowest location in the measurement chamber.

## II - Design

The fabricated thermal conductivity gas sensor is shown in Figure 1, while the parameters of this sensor structure are shown in Table 1.

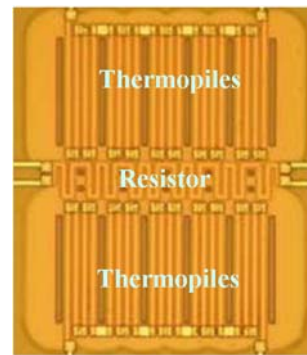


Figure 1: A photograph of the fabricated thermal conductivity gas sensor.

Table 1: Parameters of the sensor structure

Parameter	Value
Sensor length	232μm
Sensor width	154μm
Beam length	102μm
Beam width	154μm
Thermocouples length	100μm
Number of thermocouples	10

Gas detection using the thermal conductivity gas sensor is accomplished as follows. By feeding current into the resistor in the center of the sensor, the resistor is heated up and becomes a “hot element”. The heat is transferred from the hot resistor to the cold edge via

heat conduction through the measured gas and the beams that are used to support the suspended structure containing the resistor from the heat sink at ambient temperature. The suspended structure should be designed to reduce the heat loss through the beams to negligible values to ensure that the corresponding temperature difference between the hot resistor and the cold edge only depends on the thermal conductance of the measured gas.

At a fixed input power, the temperature difference between the hot resistor and the cold edge is determined by gas concentration. The temperature difference is measured by using thermocouples with well-characterized thermo-electric properties and a Seebeck output voltage is generated.

Although metal based resistors are superior in terms of low temperature coefficient of resistivity (TCR) and, therefore, have a better defined heat generation, while Pt resistors are more reproducible in temperature measurement, these materials are poorly IC-process compatible. Therefore, P-type poly-silicon is utilized here for its acceptable linearity with temperature variation and relatively low thermal conductivity [12]. The meandered shape of the resistor enables high electrical resistance while occupying small area.

The materials of the thermocouples determine the output performance of the sensor. The P-type poly-silicon (Seebeck coefficient  $-120 \mu\text{V/K}$ ) and N-type poly-silicon (Seebeck coefficient  $170 \mu\text{V/K}$ ) thermocouples are used here. They are connected in a thermopile configuration with ten pairs of thermocouples to increase the total Seebeck voltage.

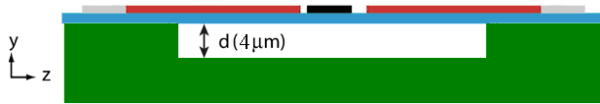


Figure 2: Bridge shaped thermopile (cross-sectional view).

The sensor can be analyzed using a two-dimensional temperature distribution analysis, because the elements of this sensor are all composed of very thin films in which the effect of thickness can be disregarded. The heat transferred in two directions, one is in z-direction through the measured gas, and the other is in y-direction through the beam. Thus the transferred heat is given by:

$$H_t = G_{\text{gas}}(T_{\text{hot}} - T_{\text{cold}}) + G_{\text{beam}}(T_{\text{hot}} - T_{\text{cold}}) \quad (1)$$

where,  $G_{\text{gas}}$  is the thermal conductance of the gas,  $G_{\text{beam}}$  is the thermal conductance of the beams,  $T_{\text{hot}}$  and  $T_{\text{cold}}$  are the temperature of the hot resistor and the cold edge, respectively.

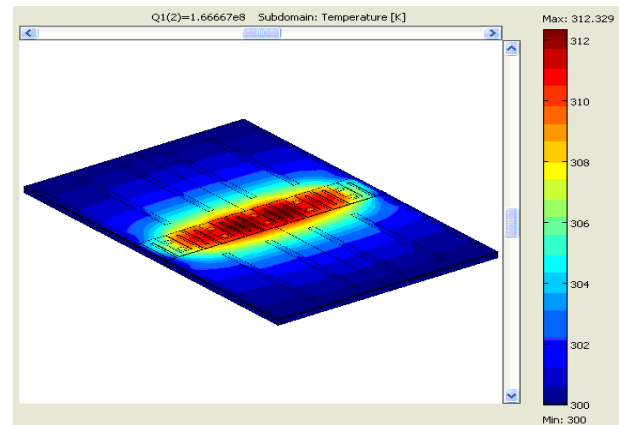
The sensitivity of the sensor is defined as the ratio of the change in the output Seebeck voltage to the change in the carbon dioxide gas concentration of the entire measurand gas at a fixed input power, which is expressed by:

$$S_{\text{sensor}} = \frac{\Delta U_{\text{seebeck}}}{\Delta V_{\text{gas}} / V_{\text{gas}}} \quad [\text{mV}] \quad (2)$$

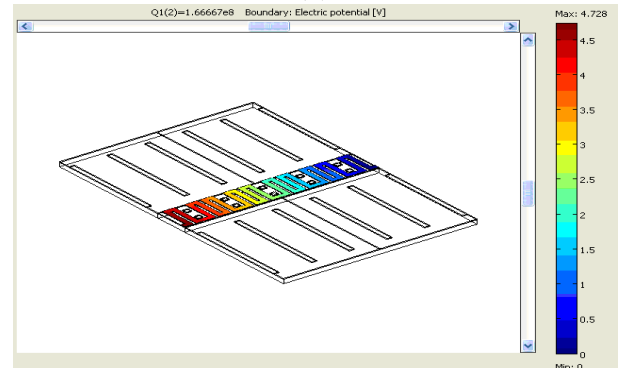
where,  $V_{\text{gas}}$  is the volume of the entire measurand gas,  $\Delta V_{\text{gas}}$  is the volume change of carbon dioxide,  $\Delta U_{\text{seebeck}}$  is the change in the output Seebeck voltage of the thermopile.

### III -Simulation

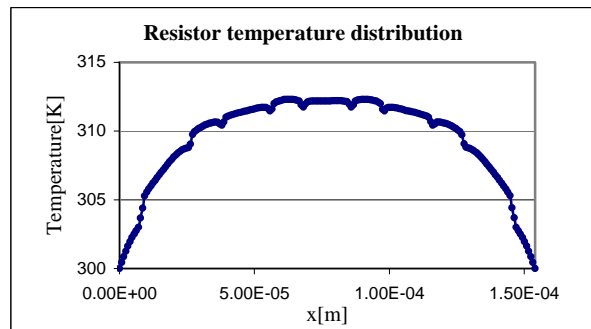
COMSOL Multiphysics software is used for simulation, which basically solves the equations involved in the Joule-heating and the thermo-electric interactions. The sensor temperature distribution, sensor electric potential distribution and resistor temperature distribution when supplying 0.2mA current into the central resistor are shown in Figure 3.



(a)



(b)



(c)

Figure 3: Electro-thermal interaction simulation, (a) sensor temperature distribution, (b) sensor electric potential distribution and (c) temperature distribution of the resistor.

As shown in Figure 3(c), the temperature of the resistor is not homogeneously distributed. The reason is that the temperatures at the two short ends of the resistor are significantly influenced by the cold edges.

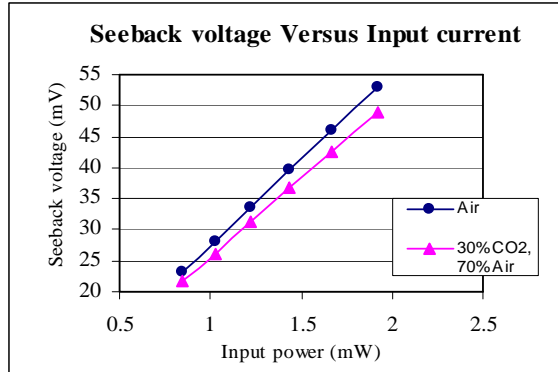


Figure 4: COMSOL simulation results for carbon dioxide detection.

The simulation results in Figure 4 clearly show the output Seebeck voltage changes with the carbon dioxide concentration in air. An increase in the carbon dioxide concentration in air from 0% to 30% leads to an increase in the output Seebeck voltage of 2.5mV at 1.2mW input power.

#### IV - Fabrication

The fabrication was done in DIMES facility of TU-Delft. The process sequence is shown simplified in Figure 5.

1. TEOS 4  $\mu\text{m}$  & Reflow



2. 700 nm SiN->Doped & Patterned 300 nm PolySi



3. Contact opening-> Al 600 nm sputtered & patterned



4. RIE and stop on TEOS



5. 73% Hydrogen Fluoride



Figure 5: Fabrication processing steps (cross-sectional view).

The fabrication starts with a 4  $\mu\text{m}$  PECVD TEOS as the sacrificial layer [11]. 700 nm of low stress SiN film

formation and several process steps followed. Firstly, a 300 nm low-stress PolySi layer was grown by LPCVD. Secondly, boron was implanted at 40 keV to realize p-type PolySi. After cleaning procedure, n-type Poly-Si was formed by phosphorous doping. In the next step, 100 nm low-stress SiN was deposited by LPCVD to make the isolation between metal contacts and Poly-Si. Aluminum was deposited and patterned on top to define connection of thermocouples and bonding pads. Finally, the wafer was processed with 73% HF for 10 minutes for the surface-micromachining.

#### V - Results and Discussion

##### A. Measurement Results

As shown in Figure 6, a Keithley 2400 is used as the current source to feed current into the resistor, while measuring the voltage, current and resistance of the resistor. An Agilent 34220A nanovoltmeter measures the output Seebeck voltage from the thermocouples. The measurement results in Figure 7 indicate that the output Seebeck voltage changes with the carbon dioxide concentration in air. An increase in the carbon dioxide concentration in air leads to an increase in the output Seebeck voltage of 2.6mV at 1.2mW input power. And the measurement results are in accordance with the COMSOL simulation results as shown in Figure 7.

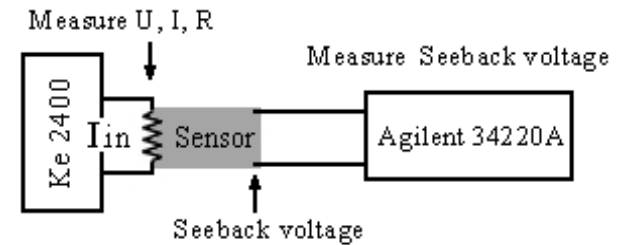


Figure 6: Measurement setup for carbon dioxide detection.

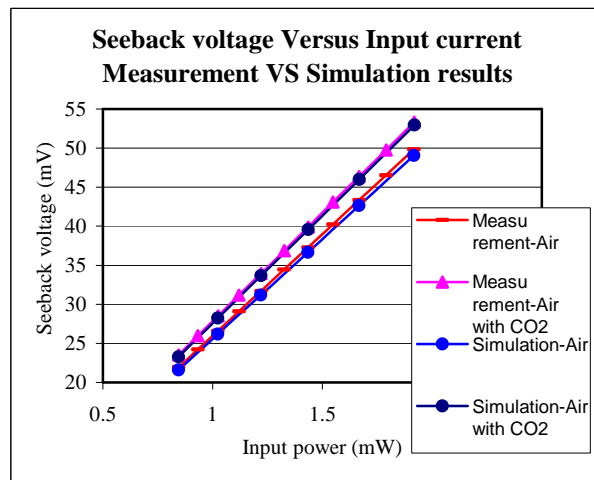


Figure 7: Comparison between measurement results and simulation results.

### B. Improvement of Sensor Sensitivity

Sensor sensitivity can be improved by reducing the heat loss of the beams. The thermocouples should not be placed near the cold edges on the beam. The reason is that on the two ends of the resistor, the temperature distribution is significantly influenced by the cold edges, and will not change as rapidly with changes in the measured gas as the temperature in the middle part of the heater.

As shown in Figure 8, an improved sensor based on a single-clamped bridge is adopted instead of double-clamped structure, while larger gas opening are placed on the edges of the other beam. These measures allow the detected gas to flow in the chamber underneath the sensor more easily and increase the thermal isolation of the membrane.

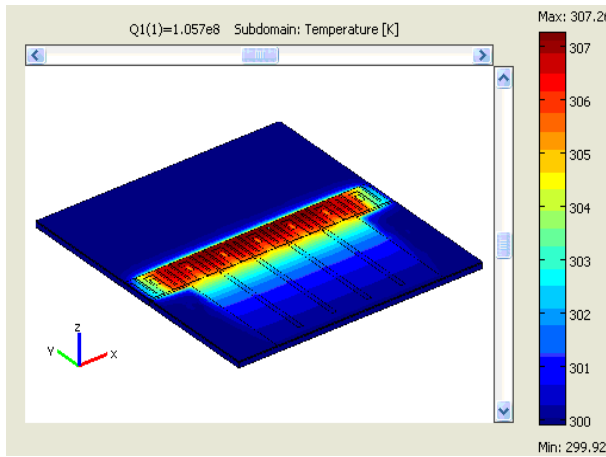


Figure 8: Temperature distribution of the improved sensor

The simulation results in Figure 9 clearly show the sensitivity of the improved sensor is approximately twice of that of the previous one under the same conditions. At 1.2mW input power, the sensitivity increases by 83.2% with a 30% change of carbon dioxide concentration in air.

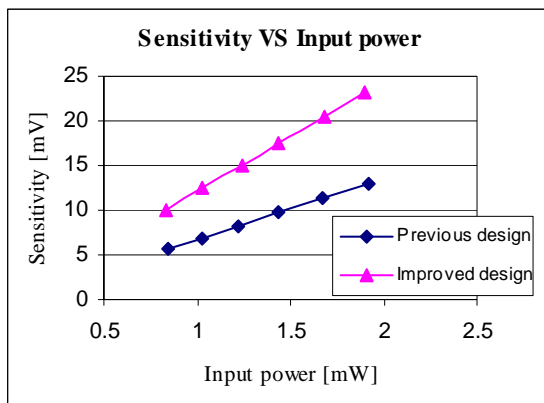


Figure 9: Comparison of sensitivity between the improved design and the previous design.

### VI – Conclusion

The results on simulation, fabrication and measurement of a surface-micromachining MEMS thermal conductivity gas sensor are presented. IC-compatible surface-micromachining MEMS technologies are used for fabrication of the gas sensor. The simulation and measurement results show that the output Seebeck voltage increases with the carbon dioxide concentration in air, thus gas detection is accomplished. The simulation results show that an increase in the carbon dioxide concentration in air from 0% to 30% leads to an increase in the output Seebeck voltage of 2.5mV at 1.2mW input power. The measurement results indicate that an increase in the carbon dioxide concentration in air leads to an increase in the output Seebeck voltage of 2.6mV at 1.2mW input power. An improved single-clamped bridge sensor is introduced. The sensitivity of the improved sensor increases by 83.2% with a 30% change of carbon dioxide concentration in air at 1.2mW input power.

### References

- [1] Edward Gobina, *BCC Research*, April 2005.
- [2] J. Spannake, A. Helwig, O. Schulz, and G. Müller, *Solid State Gas Sensing*, pp.1-46, 2009.
- [3] M. Baraton, *SPIE Newsroom*, 2009.
- [4] S. Capone, A. Forleo, L. Francioso, R. Rella, P. Siciliano, J. Spadavecchia, D. S. Presicce and A. M. Taurino, *Journal of Optoelectronics and Advanced Materials*, vol.5, pp.1335–1348, 2003.
- [5] P. Tardy, J. Coulon, C. Lucat and F. Menil, *Sensors and Actuators B: Chemical*, vol. 98, pp.63-68, March 2004.
- [6] S. J. Kim, *Journal of Physics D: Applied Physics*, vol.39, pp.3026-3029, 2006.
- [7] I. Simon and M. Arndt, *Sensors and Actuators A: Physical*, vol.97-98, pp.104-108, 2002.
- [8] <http://encyclopedia.airliquide.com/Encyclopedia.asp>
- [9] L. Brett, *European Commission's Joint Research Center*, 2003.
- [10] F. P. Incropera, D. P. DeWitt, T. L. Bergman, and A. S. Lavine, John Wiley and Sons, New York, 2006.
- [11] H. Wu, S. Grabarnik, A. Emadi, G. de Graaf and R. F. Wolffenbuttel, *J. Micromech. Microeng.*, 2008.
- [12] Y. C. Tai, C. H. Mastrangelo and R. S. Muller, *Journal of Applied Physics*, vol.63, pp.1442-1447, 1988.



# SUBWAVELENGTH NANOPYRAMIDS FOR SURFACE ENHANCED RAMAN SCATTERING

M. Jin<sup>1</sup>, V. Pully<sup>2</sup>, C. Otto<sup>2</sup>, A. van den Berg<sup>1</sup> and E T. Carlen<sup>1</sup>

<sup>1</sup> BIOS/Lab-on-a-Chip Group, <sup>2</sup>Medical Cell Biophysics Group, <sup>1,2</sup> MESA+ Institute for Nanotechnology, <sup>2</sup>MIRA Institute for Biomedical Technology and Technical Medicine, University of Twente, Enschede, The Netherlands

**Abstract** — We present novel nanotextured surfaces with periodically spaced subwavelength nanogroove and nanopyramid structures with precisely defined pitch  $\lambda_g$  that form high density arrays of scattering sites ideal for surface enhanced Raman scattering (SERS). The simple fabrication technique requires a single lithography step and wet anisotropic etching. Numerical calculations predict Raman enhancement factors  $G \sim 10^7$  for Ag surfaces with  $\lambda_g = 50$  nm. Measured  $G \sim 10^6$  for rhodamine 6G (R6G) on Au surfaces with  $\lambda_g = 200$  nm are consistent with numerical calculations.

**Keywords** : SERS, Plasmonics, Nanostructures

## I - Introduction

Since the discovery of surface enhanced Raman scattering (SERS) on metal surfaces [1,2,3], a new era for Raman spectroscopy has emerged for the molecular identification and detection at low sample concentrations, which provides a unique capability for the lab-free-detection and identification of a variety of different analytes. The electromagnetic enhancement is the dominant factor due to the localized surface plasmon resonance (LSPR) of metal nanostructures with optical excitation [4]. The LSPR that the metal surface can support is dependent on the size, spacing, geometry, and orientation of the nanostructure, as well as the dielectric function of the metal and dielectric material in direct contact with surface; all of which participate in the overall ability of the surface to enhance the Raman scattering cross-section of molecules absorbed on the metal surface. Various colloidal suspensions of nanoparticles have been extensively reported with various shapes and sizes [5,6,7,8,9,10] and set the stage for single molecule resonance Raman measurements [7,8,9,10]. Although, colloidal nanoparticle suspensions are attractive SERS substrate, due to the easy preparation, they suffer from poor reproducibility because of a lack of control in nanoparticle dimensions, dimer spacing and orientation with respect to the excitation polarization. Many different types of SERS solid-support substrates have been reported over the last three decades, such as electrochemically-roughened surfaces, template colloidal films [11,12], deposited metal island films, and lithographically defined thin films. Lithographically patterned SERS-active substrates still constitute one of the most promising and reproducible manufacturing methods. Current methods include nanosphere lithography [13], metal coated etched silicon surfaces [14,15,16], microscale metal coated

pyramidal pits electron beam lithography patterned metal, nanoimprint lithography and focused ion beam milling. Despite the impressive progress that has been made over the last three decades there is still strong demand for SERS substrates with large number of scattering sites with large Raman enhancements accompanied by high reproducibility and stability.

We have realized two subwavelength surfaces with highly reproducible *hot-spots*: nanogratings (1D surface) and nanopyramid arrays (2D surface) with ultra-precise pitch  $\lambda_g$ , and most importantly, sharp nanoscale crevices that consist of etched gaps with controlled spacing  $\sim 2$  nm that form a high-density array of SERS hot-spots ( $10^8$  hot spots/mm<sup>2</sup>). The advantage of this approach is that the spacing between nearest nanopyramid neighbors is not controlled by lithographic patterning, but rather by extremely precise etching of the silicon substrate due to the large etch selectivity between the (111) and (100) crystal planes of high purity silicon substrates.

## II - Experimental Details

Periodic arrays ( $40 \times 40 \mu\text{m}^2$ ) of nanoholes were patterned in a spin-coated electron sensitive photoresist layer on a conventional silicon (100) wafer using electron-beam lithography. A Cr layer was then transferred to the exposed silicon regions thus forming an array of Cr disks over the entire surface (Fig. 1a, step i) and subsequently the exposed silicon regions were etched in a potassium hydroxide solution. The different crystal planes etch anisotropically by hydroxide ions in an alkaline solution where (111) planes have the lowest etch rate where the (100), and (110) planes both have higher etch rates [17]. Precise alignment of the nanohole array is not required due to the regularity of the single crystal silicon, which facilitates the precise formation of the two-dimensional nanopyramids (pentahedrons) (Fig. 1b) that are spontaneously formed with precisely controlled  $\lambda_g$  (Fig. 1a, step ii). The gold layer ( $\sim 70$  nm) was sputtered-coated from a high purity Au target in Ar plasma (1 nm/min).

High resolution SEM and atomic force microscopy were applied to characterize the nano crevices between two nanopyramids. The different concentrations of R6G water solutions were applied for SERS measurement and Raman enhancement factor study. All samples of varying concentrations were diluted from  $10^{-2}$  M R6G ([9-(2-ethoxycarbonylphenyl)-6-(ethylamino)-2,7-dimethylxanthen-3-ylidene]-ethylazanium chloride, Aldrich, R4127) deionized water (dH<sub>2</sub>O) solutions. The  $10^{-2}$  M R6G solution is prepared by dissolving 4.8 mg R6G in deionized water. b) All data were smoothed with

an FFT smoothing algorithm with  $n=3$  data points c) Sample concentration  $10^{-7}$  M and  $10^{-5}$  L volume results in  $0.5 \times (10^{-7} \text{ mol L}^{-1}) \times (10^{-5} \text{ L}) \times (6.02 \times 10^{23} \text{ mol}^{-1}) \approx 3 \times 10^{11}$  molecules.

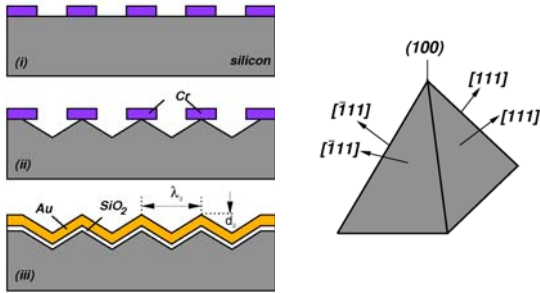


Figure 1: Nanotextured surfaces. (a) Fabrication overview. (b) Silicon nanopyramid surface facets.

### III - Results and Discussion

#### A. Nano grooves and Nano pyramids

Figures 2a-2b show high resolution scanning electron microscopy (HRSEM) images of representative patterned two-dimensional surfaces at increasingly higher zoom, thus demonstrating the effectiveness of this simple method to produce highly regular and reproducible nanotextured surfaces. One-dimensional nanogroove surfaces have been realized (Fig. 2c). A high-resolution transmission electron microscopy (HRTEM) image of a nanocrevise with separation  $\sim 2$  nm between adjacent nanostructures (Fig. 2d).

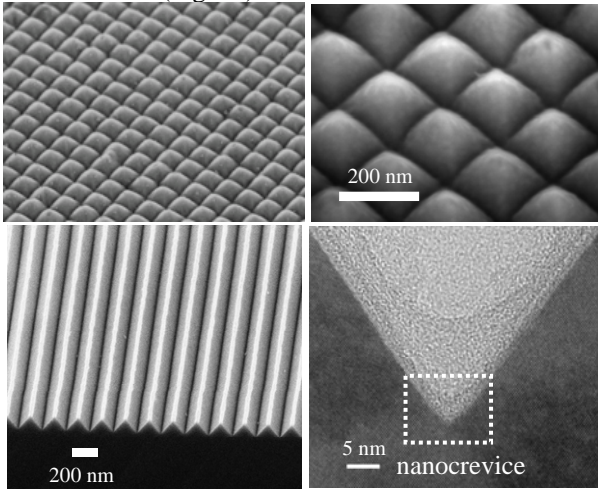


Figure 2: Nanotextured surfaces. (a)-(c) HRSEM images of subwavelength nanotextured silicon surfaces. (a) and (b) Two-dimensional nanopyramid surfaces. (c) One dimensional nanograting surfaces. (d) HRTEM image of crevice region. Inset: diffraction image silicon crystal [110] direction. Scale bar: 5 nm.

Scaling the nanostructures to smaller lateral dimensions of  $\lambda_g \sim 30$ -50 nm is achievable with refinement of the lithography procedure. The surfaces are thermally oxidized with a 10 nm layer on the exposed (111) facets and a 70 nm thick Au layer is subsequently deposited directly on the surface (Fig. 1a, step iii). An optically thick metal film prevents radiation damping of the SPP into the substrate supporting the metal film. Figure 2 shows an atomic force microscopy image and profiles of

a typical nanopyramid array surfaces before and after metal deposition. The surface roughness of the Au layer is evident. For array pitches  $\lambda_g \sim 150$  nm, the crevice shape is not significantly altered for  $t_{Au} \sim 70$  nm (Fig. 2b) and in some cases reduces the nanocrevise gap distance, which will result in increased field enhancements at the base of the crevice. For smaller  $\lambda_g$  the metal layer deposition procedure requires careful control to ensure that the crevice shape is maintained or improved with smaller gap distances. We are currently studying the effects of varying degrees of surface roughness with respect to electromagnetic field enhancements, which is important for scaling to smaller dimensions. Methods currently exist to reduce the Au surface roughness.

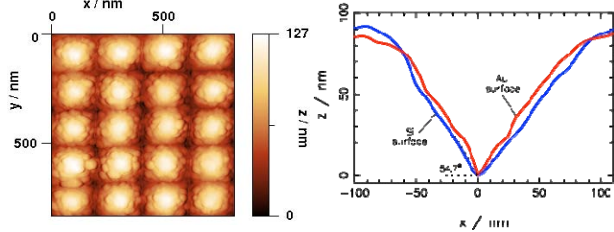


Figure 3: High-resolution atomic force microscopy images. (a) Au coated surface map. (b) Crevice profiles of etched silicon surface (blue) and following Au deposition (red).

#### B. Surface enhanced Raman scattering

A significant amount of insight has been gained about the optical properties of metals and the excitation of LSPR and surface plasmon polaritons (SPP), fundamental electromagnetic excitations located at a metal-dielectric interface [19]. Periodically roughened surfaces facilitate the SPP excitation such that the momentum of photons in the dielectric is increased by the in-plane periodicity to phase-match to the SPP. When the nanostructure periodicity is smaller than the excitation wavelength, the diffraction is zero-mode, however, an evanescent field is generated with a decay length proportional to the period of the grating that results in electromagnetic field enhancements near the metal surface [20]. Subwavelength periodic patterned surfaces have been shown to form standing SPP waves in narrow crevices with large localized electromagnetic field enhancements near the base of the crevice [19, 21]. In all reported subwavelength grating or patterned surfaces, large localized electromagnetic field enhancements were reported near the base of the nanocrevices due to strong coupling between surface charges from the opposing sides of the nearest-neighbor structures. The electromagnetic Raman scattering enhancement can be estimated in first order as  $G \approx |E_{tot}(x,z,\omega)/E_0(x,z,\omega)|^4$ , where  $E_0(\omega)$  is the electric field of the incident excitation [4]. Nanopyramid surface cross-sections with  $\lambda_g = 200$  nm, 10 nm  $\text{SiO}_2$  layer, and 70 nm thick Au layer have been modeled using two-dimensional finite difference time domain calculations to determine the total electric  $E_{tot}(x,z)$ , and magnetic  $H_y(x,z)$  field distributions near the metal surface of the fabricated structures (Fig. 3a, inset). The excitation source is a normally incident plane wave with transverse-magnetic polarization where the magnetic field intensity  $H_y$  points along the length

of the cavity. The complex frequency-dependent dielectric function  $\epsilon_m(\omega)$  of Au is included in the simulation code. The dielectric region is water with a relative permittivity  $\epsilon_d=1.77$ . It should be noted that the electromagnetic field enhancement is dependent on the excitation polarization due to the rectangular geometry involved, similar to the polarization dependent enhancement of closely spaced metal nanoparticles [22]. Smooth Au surfaces are assumed in all simulations. Figure 3a shows the Raman enhancement as a function of excitation wavelength showing a maximum enhancement  $G \sim 5 \times 10^5$  at an excitation wavelength of  $\lambda_0=740$  nm (1.7 eV) at the base of the crevice. Additional calculations predict Raman enhancements  $G \sim 10^7$  for Ag nanopryamid surfaces  $\lambda_g=50$  nm. The largest electromagnetic enhancement is localized at the base of the nanocrevise due to strong SPP coupling between adjacent surfaces of nearest neighbor nanostructures with small separation distances. Not only the calculated enhancements are large, but the entry angle  $2\gamma_g$  is also large, in this case. From a surface accessibility perspective, a larger entry angle is preferred, which makes the *hot-spots* more accessible for molecular adsorption compared to narrow and deep cavity structures. Scaling the pattern dimensions  $\lambda_g < 50$  nm results in increased electromagnetic enhancements.

Raman spectra of physically adsorbed R6G on flat and patterned nanopryamid surfaces coated with Au layer, diluted in deionized water (dH<sub>2</sub>O) solutions of varying concentrations, have been measured. Although SERS of R6G on Ag surfaces has been extensively reported [23,24,25,26], we used Au surfaces, despite its lower enhancement SERS performance. A  $10^{-5}$  L aliquot of each solution was placed in the center of the nanopryamid surface ( $50 \text{ mm}^2$ ) and immediately covered with a glass slide ( $25 \times 25 \text{ mm}^2$ , Menzel-Glaser). Each sample was incubated for 15 minutes at room temperature prior to a measurement. The sample was then placed under the objective of the previously described confocal Raman microscope [27] and horizontal nanocrevises were aligned perpendicular to the excitation polarization. The acquisition time for all measurements is 30 seconds. Figure 3 shows representative measurements of R6G (in dH<sub>2</sub>O) on flat and nanopryamid Au surfaces. The molecular structure of R6G is shown in Fig. 3b. Figure 3c shows the Raman spectra for a  $5 \times 10^{-6}$  M R6G sample solution; the lower trace shows the measured sample response from a flat Au surface, which consists of the deposited Au film on a flat SiO<sub>2</sub>/Si surface using identical measurement conditions. The measured spectral characteristics of R6G on the nanopryamid surfaces include 611, 773, 1011, 1184, 1311, 1363, 1568, and  $1650 \text{ cm}^{-1}$ . The 611, 773, and  $1184 \text{ cm}^{-1}$  modes are associated with C–C–C ring in-plane, out-of-plane bending, and C–C stretching vibrations, respectively, and the 1363, 1568, and  $1650 \text{ cm}^{-1}$  modes are associated with aromatic C–C stretching vibrations [23], however, the  $1650 \text{ cm}^{-1}$  mode is reported to have contributions from C–H bending modes of the xanthene ring and the  $1011 \text{ cm}^{-1}$  mode is associated with the phenyl ring and

COOC<sub>2</sub>H<sub>5</sub> side groups [28]. The measured vibrational spectra compare well with previous reports with the exception of the  $1011 \text{ cm}^{-1}$  mode [23,25].

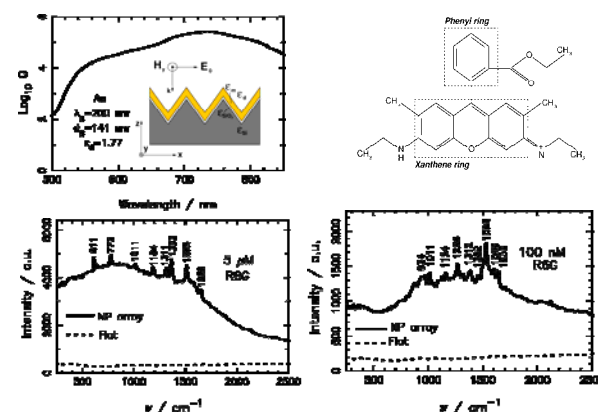


Figure 3: Calculated and measured results from nanopryamid surfaces. (a) 2D steady state FDTD simulation results of Raman enhancement of triangular cross-section with  $\lambda_g=200$  nm,  $t_{\text{SiO}_2}=10$  nm,  $t_{\text{Au}}=70$  nm, and  $\epsilon_d=1.77$  (inset: surface cross-section) (b) R6G molecule. (c), (d) Raman measurements of R6G adsorbed on flat (dotted) and nanopryamid (NP) (solid) surfaces (c) solution concentration  $[C_{\text{SERS}}]=5 \times 10^{-6}$  M (d)  $[C_{\text{SERS}}]=10^{-7}$  M.

It should be noted that most previous studies were conducted under surface enhanced resonance Raman conditions with an excitation wavelength near the peak absorption wavelength of R6G ( $\sim 532$  nm). Raman spectra for a  $10^{-7}$  M R6G concentration in dH<sub>2</sub>O (Fig. 3d) include the 934, 1011, 1124, 1266, 1312, 1382, 1525, 1599, and  $1636 \text{ cm}^{-1}$  modes, where all modes have been previously reported [23,25,29], except for the  $1011 \text{ cm}^{-1}$  and  $1525 \text{ cm}^{-1}$  modes; the  $1525 \text{ cm}^{-1}$  mode has not been previously reported under SERS or resonant SERS conditions and is associated with vibration of the xanthene ring and NHC<sub>2</sub>H<sub>5</sub> end groups [28]. The  $1636 \text{ cm}^{-1}$  mode has not been previously assigned and is likely related to the  $1650 \text{ cm}^{-1}$  xanthene ring mode.

All measurements are accompanied by a broadband *white* continuum under the Raman lines as previously reported, which can be explained by continuous scattering from the underlying metal [25,30], however, is not present on the flat metal surfaces. Since each measurement was performed with a known sample volume, we estimate an upper limit of  $\sim 760$  R6G molecules adsorbed on the nanopryamid surface in the confocal imaging area. It should be noted that the electromagnetic enhancement occurs only for the field polarization perpendicular to the length of the cavity, and therefore, a much smaller region of the total excitation region provides the large electromagnetic enhancement, and therefore, the measured response is due to a much smaller number of molecules. A more precise assessment of the number of molecules represented in the  $10^{-7}$  M measurement (Fig. 3d) is not possible with the current measurement system since the exact location of the active region of the crevice is not known, however, the measured spectra of the  $10^{-7}$  M R6G concentration is associated with just a few R6G molecules in dH<sub>2</sub>O. For low sample concentrations ( $<10^{-6}$  M) the measurements



are consistent with the population averaging effect [23]. For R6G sample concentrations ranging from  $10^{-6}$  M to  $10^{-4}$  M (not all data shown), the measured spectra are very consistent and repeatable with respect to location and time. The enhancement factor has been estimated by comparing the peak heights of vibration spectra on the nanopillar array surfaces with peak heights from reference measurements in solution while maintaining the same laser power (135  $\mu$ W), microscope, spectrometer configuration, and R6G sample. In order to compare the peak heights, a larger R6G concentration is used for the normal Raman reference measurement. The resulting enhancement factor can be roughly estimated as  $EF \approx S_{SERS}[C_R](S_R[C_{SERS}])^{-1}$ , where  $S_{SERS}$  and  $[C_{SERS}]$  are the intensity amplitude and R6G concentration from the SERS substrate, respectively, and  $S_R$  and  $[C_R]$  are the intensity amplitude and R6G concentration from the normal Raman reference measurement. Due to the pre-resonance activity of R6G and low required laser power, enhancement factors at all measured vibration modes was not possible, however, an  $EF \sim 10^6$  has been measured for the  $\nu=1310\text{ cm}^{-1}$  mode and we consider this to be a lower bound for the Raman scattering enhancement.

#### IV - Conclusion

In conclusion, large area nanotextured surfaces with periodically spaced subwavelength nanogroove and nanopillar structures with precisely defined pitch  $\lambda_g$  and adjacent nanostructure spacing that form high density ( $>10^8$  crevices  $\text{mm}^{-2}$ ) arrays of scattering sites ideal for surface enhanced Raman scattering (SERS) have been presented. The simple fabrication technique requires a single lithography step and wet anisotropic etching. Measured Raman enhancement factors in  $\text{dH}_2\text{O}$  of  $G \sim 10^6$  for R6G on Au surfaces with  $\lambda_g=200\text{ nm}$  are consistent with numerical calculations of the electromagnetic field enhancement. Scaling to smaller dimensions  $\lambda_g < 50\text{ nm}$  on Ag surfaces results in  $G > 10^7$ .

#### References

- [1] Fleischm.M, P. J. Hendra and Mcquilla.Aj, *Chem. Phys. Lett.*, 26,163-166, 1974.
- [2] D. L. Jeanmaire and R. P. Vanduyne, *J. Electroanal. Chem.*, 84, 1-20, 1977.
- [3] M. Moskovits, *J. Chem. Phys.*, 69, 4159-4161, 1978
- [4] M. Moskovits, *J. Raman Spect.*, 36, 485-496, 2005
- [5] S. Link and M. A. El-Sayed, *J. Phys. Chem. B*, 103, 4212-4217, 1999.
- [6] J. B. Jackson and N. J. Halas, *Proc. Natl. Acad. Sci.*, 101, 17930-17935, 2004.
- [7] Y. Lu, G. L. Liu, J. Kim, Y. X. Mejia and L. P. Lee, *Nano Lett.*, 5, 119-124, 2005.
- [8] H. Wang, D. W. Brandl, F. Le, P. Nordlander and N. J. Halas, *Nano Lett.*, 6, 827-832, 2006.
- [9] J. M. McLellan, Z. Y. Li, A. R. Siekkinen and Y. N. Xia, *Nano Lett.*, 7, 1013-1017, 2007.
- [10] L. Rodriguez-Lorenzo, R.A. Alvarez-Puebla, I. Pastoriza-Santos, S. Mazzucco, O. Stephan, M. Kociak, L.M. Liz-Marzan and F.J.G. de Abajo, *J. Am. Chem. Soc.*, 131, 4616, 2009.
- [11] S. Coyle, M. C. Netti, J. J. Baumberg, M. A. Ghanem, P. R. Birkin, P. N. Bartlett and D. M. Whittaker, *Phys. Rev. Lett.*, 87, 176801, 2001.
- [12] S. Shanmukh, L. Jones, J. Driskell, Y. P. Zhao, R. Dluhy and R. A. Tripp, *Nano Lett.*, 6, 2630-2636, 2006.
- [13] J. C. Hulthen and R. P. Vanduyne, *J. Vacuum Sci. Tech A*, 13, 1553-1558, 1995.
- [14] N. M. B. Perney, J. J. Baumberg, M. E. Zoorob, M. D. B. Charlton, S. Mahnkopf and C. M. Netti, *Optics Exp.*, 14, 847-857, 2006.
- [15] H. W. Gao, J. Henzie, M. H. Lee and T. W. Odom, *Proc. Natl. Acad. Sci.*, 105, 20146-20151, 2008.
- [16] T. H. Lin, N. C. Linn, L. Tarajano, B. Jiang and P. Jiang, *J. Phys. Chem. C*, 113, 1367-1372, 2009.
- [17] H. Seidel, L. Csepregi, A. Heuberger and H. Baumgartel, *J. Electrochem. Soc.*, 137, 3612-3626, 1990.
- [18] S. Y. Chen, J. G. Bommer, W. G. van der Wiel, E. T. Carlen and A. van den Berg, *ACS Nano*, 3, 3485-3492, 2009.
- [19] H. Raether, *Springer Tracts in Modern Physics*, 111, 1-133, 1988.
- [20] W. L. Barnes, A. Dereux and T. W. Ebbesen, *Nature*, 424, 824-830, 2003.
- [21] M. B. Sobnack, W. C. Tan, N. P. Wanstall, T. W. Preist and J. R. Sambles, *Phys. Rev. Lett.*, 80, 5667-5670, 1998.
- [22] M. Inoue and K. Ohtaka, *J. Phys. Soc. Jpn*, 52, 1457-1468, 1983.
- [23] P. Hildebrandt and M. Stockburger, *J. Phys. Chem.*, 88, 5935-5944, 1984.
- [24] S. M. Nie and S. R. Emery, *Science*, 275, 1102-1106, 1997.
- [25] A. M. Michaels, J. Jiang and L. Brus, *J. Phys. Chem. B*, 104, 11965-11971, 2000.
- [26] C. L. Haynes, C. R. Yonzon, X. Y. Zhang and R. P. Van Duyne, *J. Raman Spec.*, 36, 471-484, 2005.
- [27] V. V. Pully and C. Otto, *J. Raman Spec.*, 40, 473-475, 2009
- [28] H. Watanabe, N. Hayazawa, Y. Inouye and S. Kawata, *J. Phys. Chem. B*, 109, 5012-5020, 2005.
- [29] A. M. Michaels, M. Nirmal and L. E. Brus, *J. Am. Chem. Soc.*, 121, 9932-9939, 1999.
- [30] J. Jiang, K. Bosnick, M. Maillard and L. Brus, *J. Phys. Chem. B*, 107, 9964-9972, 2003.



# A MICRONEEDLE-BASED MINIATURE SYRINGE FOR TRANSDERMAL DRUG DELIVERY

C. O'Mahony, J. Scully, A. Blake, and J. O'Brien

*Tyndall National Institute, University College Cork, Ireland.*

**Abstract** — Hollow microneedles have the potential to revolutionize the transdermal delivery of a range of therapeutic agents. This paper describes the fabrication of a micromachined transdermal delivery syringe, the primary component of which is an array of hollow silicon microneedles fabricated using a combination of wet- and dry-etching techniques. The needles are bonded to a PDMS reservoir, which incorporates a flexible membrane and which may be filled with a pharmaceutical agent. Using light pressure to actuate the membrane, the drug cargo is forced through the hollow needles and into the skin beyond the stratum corneum barrier.

Preliminary experiments have been carried out in-vivo on human volunteers. Skin piercing using the microsyringe was verified and delivery of dye beneath the stratum corneum was successfully demonstrated.

**Keywords :** Microneedles, transdermal drug delivery, bulk micromachining

## I - Introduction

The outer layer of the skin, the stratum corneum (SC), is only 10-20 $\mu$ m thick but yet poses a major barrier to the transdermal delivery of drugs to the viable epidermis that lies immediately beneath, Figure 1. Largely composed of dead, keratin-filled cells embedded in lipid bilayers and moisture that have migrated outward from the basal layer, the SC prevents the transdermal diffusion of most therapeutic agents, meaning drug delivery via the skin is currently limited to a small number of low dose, low molecular weight drugs such as nicotine, testosterone and fentanyl [1].

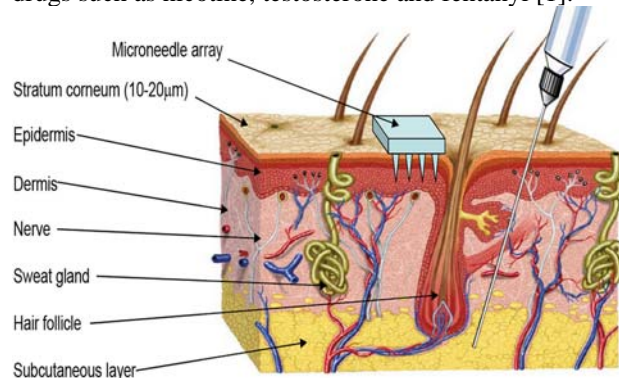


Figure 1: Structure of the skin. Microneedles are sufficiently long to enable perforation of the stratum corneum, but not large or long enough to stimulate the nerve endings underneath.

It is expected that the development of microneedle technology will eventually circumvent these barriers. Microneedles are sharp protrusions, generally ranging in height from 100 $\mu$ m-500 $\mu$ m, and manufactured using microfabrication technologies in a range of materials as diverse as silicon, titanium, polymers and sugars. Microneedles can be designed to be sufficiently tall to penetrate the SC yet not stimulate nerve endings that populate the underlying dermis, and recent clinical trials have shown that drug delivery using microneedles is a viable alternative to syringe-based delivery methods [2].

Although solid microneedles are straightforward to fabricate and are easily applied, in certain treatments, such as insulin delivery, a controllable, time-varying infusion using hollow microneedles is desirable. The concept of a self-administrable, painless microsyringe is an attractive one, as this technology could simultaneously eliminate both the need for trained healthcare personnel and the problems of syringe disposal in developing countries.

It has been evaluated by a number of groups, most notably in [3], where DRIE-etched needles and a PDMS reservoir were described, and in [4], where a pressure-driven multi-reservoir device was presented.

This paper describes the extension of our microneedle research to the development and fabrication of a silicon-based hollow microneedle drug delivery system, based on the convex corner undercutting and dry etching of <100> silicon to form microneedles, and subsequent bonding to a PDMS reservoir and flexible membrane to form a microneedle-based syringe. The device is capable of holding up to 320 $\mu$ L, and incorporates a 9 x 8 array of 280 $\mu$ m tall hollow microneedles. Preliminary results have demonstrated successful SC rupture and delivery of a model drug.

## II – Solid Microneedle Fabrication

The microneedle arrays were fabricated at the Tyndall National Institute by using potassium hydroxide wet-etching techniques [5]. The starting material is a 525 $\mu$ m thick, boron doped, 100mm diameter monocrystalline silicon wafer, orientated in the <100> direction and into which marks denoting the precise crystal alignment have previously been etched. A layer of 350A silicon oxide is grown using thermal oxidation as a stress-relief layer, before a subsequent low-pressure chemical vapour deposition of 1000A silicon nitride. A positive photoresist layer is then deposited and patterned in square masks using standard photolithography

techniques; the dimensions of these square masks determine the array pitch and needle geometry. The mask pattern is etched into the nitride layer using a plasma etch process before the resist is stripped and the oxide layer then removed in the open areas using hydrofluoric acid (HF).

The patterned silicon wafer is then etched using a 29% w/v aqueous KOH solution at a temperature of 79°C. Needle formation is based on the anisotropic etch behaviour of monocrystalline silicon in KOH, a property of the crystal structure that causes each group of crystal planes to etch at a different rate. The sides of the square nitride mask are precisely aligned to the particularly slow-etching  $\langle 111 \rangle$  plane; the faster-etching  $\langle 112 \rangle$  planes are exposed to the KOH at the convex corners of the square. As two of these fast-etching planes are etched from each corner, an octagonal needle shape is generated when the eight planes meet. The final needle is comprised of eight  $\langle 263 \rangle$  planes, a base of  $\langle 212 \rangle$  planes and has a height:base diameter aspect ratio of 3:2. The needles are 280  $\mu\text{m}$  tall and are illustrated in Figure 2.

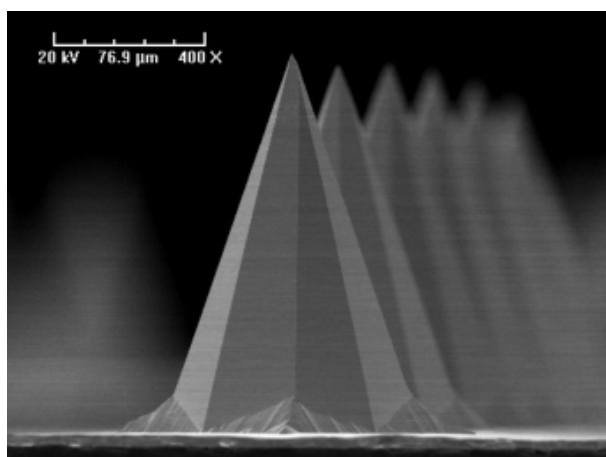


Figure 2: Solid silicon microneedles

### III – Needle Bore Etching

Hollow needles are fabricated by using wafers as outlined in Section II. The original oxide and nitride masking layers are removed after completion of the wet chemistry fabrication steps. A thick PECVD oxide coating of 3  $\mu\text{m}$  is deposited onto the back silicon wafer face, followed by a deposition of 2  $\mu\text{m}$  sputtered aluminium on the front side of the wafer to act as an etch stop layer. After patterning of the 3  $\mu\text{m}$  back oxide, by UV lithography and subsequent dry etch pattern transfer into the oxide etch mask, capillary tubes are then micro-machined from the back side of the wafer using an Surface Technology System [STS] ASE ICP dry etching tool incorporating BOSCH dry etching technology. The etch gases are  $\text{SF}_6$  and  $\text{C}_4\text{F}_8$ , and the etch time using this process technology is approximately 80 minutes. In this case, the resultant needle bore is 54  $\mu\text{m}$  in diameter. The

aluminium layer and thick oxide layers are then stripped from the front and back sides of the wafer, respectively.

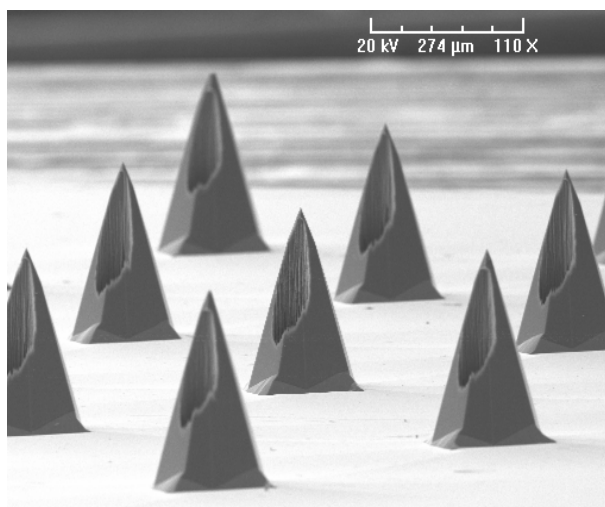


Figure 3: Scanning electron microscope image of hollow needle array.

### IV – Reservoir Fabrication

In order to provide a drug container and a fluidic interface to the hollow needle array, a reservoir was also fabricated. A mould was first manufactured by machining a block of polytetrafluoroethylene (PTFE) so that protrusions measuring 8mm x 8mm x 5mm high stood proud of the base. Polydimethylsiloxane (PDMS) was used as the reservoir material. After curing, the reservoir was peeled from the mould and cut to size. The reservoir membrane depends on the thickness of the poured PDMS, but in this instance was approximately (900 $\pm$ 100)  $\mu\text{m}$  thick. A completed microsyringe is shown in Figure 4.



Figure 4: Completed microsyringe. The reservoir is filled with a solution of methylene blue dye.

We achieved a strong bond between the reservoir and needle array by using a second, thin layer of PDMS as the bonding agent; this was also cured at 100°C for one hour.

A solution of 1% w/v methylene blue was used as the model drug. This was injected into the reservoir using a narrow BD Micro-Fine 29-gauge conventional syringe; the current maximum volume of the microsyringe reservoir is 320µL. Upon withdrawal of the syringe needle, the microsyringe reservoir was observed to be self-sealing, thereby negating the need for an additional sealing step.

## V – Analysis and Discussion

Following informed consent, preliminary experiments of drug infusion on healthy human volunteers were also performed. For these tests, a 9x8 array of 280µm tall hollow microneedles was used; the self-sealing reservoir was filled with 250µL of 1% w/v methylene blue dye.

No skin preparation was carried out before the microsyringe was applied to the back of the hand and the membrane was depressed using light finger pressure for 20 seconds. Upon removal of the microsyringe, some excess dye was seen to have leaked from the needles and this was removed using alcohol wipes before the skin was imaged under an Olympus SZX12 stereomicroscope as shown in Figure 5.

The presence of blue dots clearly indicates that SC rupture has taken place and that dye has been delivered using the microsyringe.



Figure 5: The presence of methylene blue dots in the skin indicates SC rupture and dye delivery. The spacing between the dots is 940µm.

Future work is required to assess PDMS bond strength, chamber reliability, microneedle penetration forces and drug efficacy.

## VI – Conclusion

The fabrication of a microneedle-based microsyringe has been described. Hollow silicon microneedles have been fabricated by firstly using KOH wet etching techniques to define an octagonal needle, followed by a dry etch to create a capillary through the needle. A PDMS reservoir and flexible membrane were then bonded to the microneedle array to create a microsyringe. Reservoir filling was achieved using a conventional 29-gauge syringe and the reservoir is self-sealing after filling.

Initial work on human volunteers indicates that stratum corneum piercing has taken place and that dye has been delivered to the epidermis.

## References

- [1] M. R. Prausnitz and R. Langer, "Transdermal Drug Delivery," *Nature Biotechnology*, vol. 26, pp. 1261-1268, 2008.
- [2] D. P. Wermeling, S. L. Banks, D. A. Hudson, H. S. Gill, J. Gupta, M. R. Prausnitz, and A. L. Stinchcomb, "Microneedles permit transdermal delivery of a skin-impermeant medication to humans," *PNAS*, vol. 105, pp. 2058-2063, 2008.
- [3] U. O. Häfeli, A. Mokhtari, D. Liepmann and B. Stoeber., "In vivo evaluation of a microneedle-based miniature syringe for intradermal drug delivery," *Biomedical Microdevices*, vol. 11, pp. 943-950, 2009.
- [4] A. Hoel, N. Baron, G. Cabodevila and M.-C. Jullien, "A microfluidic distribution system for an array of hollow microneedles," *J. Micromechanics and Microengineering*, vol. 18, 065019, 2008.
- [5] N. Wilke, M. L. Reed and A. Morrissey, "The Evolution from Convex Corner Undercut Towards Microneedle Formation: Theory and Experimental Verification," *J. Micromechanics and Microengineering*, vol. 16, pp. 808-814, 2006.



# On the processing aspects of high performance hybrid backside illuminated CMOS imagers

J. De Vos, K. De Munck, K. Minoglou, P. Ramachandra Rao, M. A. Erismis,  
P. De Moor and D. S. Tezcan

*Imec, Kapeldreef 75, 3001 Heverlee, Belgium  
E-mail: Joeri.DeVos@imec.be*

**Abstract** — In this paper we present a successful integration scheme of a backside illuminated 1024x1024 pixel, 30 $\mu$ m thin, sensor array that is flip chipped on a ROIC die with 10 $\mu$ m diameter Indium micro bumps, where the pixel pitch is 22.5 $\mu$ m. A novel backside alignment strategy to avoid glass as temporary carrier for wafer thinning is described. Further special attention is given to critical steps leading towards high broadband quantum efficiency. It is shown that through introduction of a high aspect ratio pixel separating trenches, inter pixel electrical crosstalk can be avoided.

**Keywords:** backside illuminated imager, high broadband quantum efficiency, thinned imager, high aspect ratio trenches for low electrical crosstalk

## I - Introduction

CMOS image sensor arrays have developed to the point where they are offering an advantageous alternative to CCDs for many applications. Their high suitability as a detector for a broad wavelength range promises a very significant reduction in weight, volume and power consumption [1].

Backside (BS) illumination, as compared to front side (FS) illumination, results in a large gain in quantum efficiency (QE) since no incoming light is lost due to reflections on the metal interconnects, leading to a 100% fill factor. Also anti-reflective coatings (ARC) on the Si BS can be optimized independently of the backend structure on the FS, thus maximizing the light coupling to the substrate. As a result BS illuminated imagers have a wider spectral response than FS illuminated imagers. On the other hand, however, BS illuminated imagers require more complex post processing because the detector array has to be thinned down to 30 $\mu$ m or less.

For hybrid imagers, the detector array is separately processed from the read-out IC (ROIC) and optimized to the needs of the application. As such special substrates or epi layers can be chosen, the pixel separating trenches can be added for crosstalk reduction, etc. This additional degree of freedom has the advantage to produce photodiodes which are not available as standard for monolithic imagers fabricated in commercial foundries.

In this paper the process integration of a hybrid backside illuminated 1024x1024 pixel imager is presented. The sensor array, thinned to 30 $\mu$ m, is flip chipped on top of a ROIC with 10 $\mu$ m diameter Indium micro bumps, where the pixel pitch is 22.5 $\mu$ m. The

detector IC was produced at imec and the ROIC at a commercial foundry, both in a 0.35 $\mu$ m technology.

## II – Processing scheme

The fully hybridized backside illuminated imager consists of two components: a 30 $\mu$ m thin detector array which is flipped and mounted on a ROIC. The two components are precisely aligned and connected together by means of Indium micro bumps.

Starting from 200mm p-type wafers, a 30 $\mu$ m graded epi-layer was grown to introduce a built-in electrical field to pull generated carriers from the non-depleted substrate [2,3].

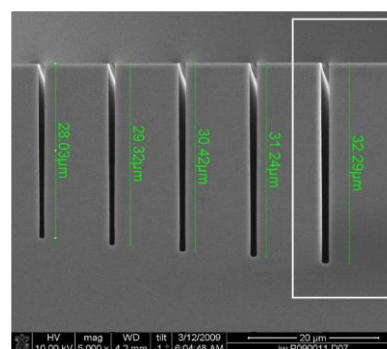


Figure 1: Bosch DRIE etch to form pixel separating trenches. The right hand trench is 1.2 $\mu$ m wide and 32 $\mu$ m deep.

To reduce cross-talk, pixel separating trenches are foreseen. These high aspect ratio (1.2 $\mu$ m wide, 32 $\mu$ m deep) trenches are etched before all front-end steps, using an oxide hard mask based Bosch DRIE process (alternating steps of SF<sub>6</sub> etching and C<sub>4</sub>F<sub>8</sub> passivation). In Figure 1, the trenches are shown for widths varying from 0.8 $\mu$ m to 1.2 $\mu$ m. These trenches are filled with highly boron doped poly-Si. Good contact to the substrate ensures a lateral electrical field, which blocks the pixel to pixel carrier diffusion. Planarization by means of chemical mechanical polishing and oxide hard mask removal finalizes the trench definition.

All following front end and backend steps run in a standard 0.35 $\mu$ m technology (Figure 2). Only the implantation conditions are dedicated for the diodes.

After finalizing the metallization and nitride passivation, the edge of the wafer is trimmed by dicing. As explained in Figure 3, edge conditioning of the wafer before thinning will avoid chipping of the edge after thinning.



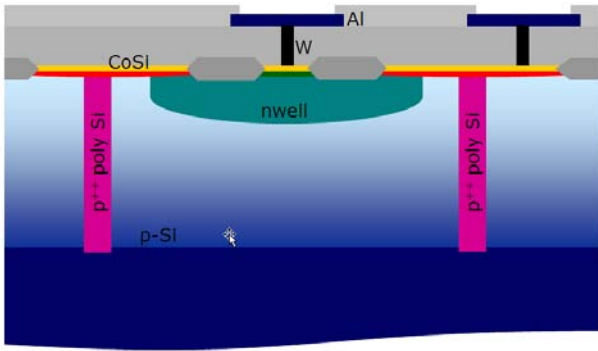


Figure 2: Schematic cross section view of a detector pixel. Pixel separating trench definition is followed by front-end and back-end in a  $0.35\mu\text{m}$ .

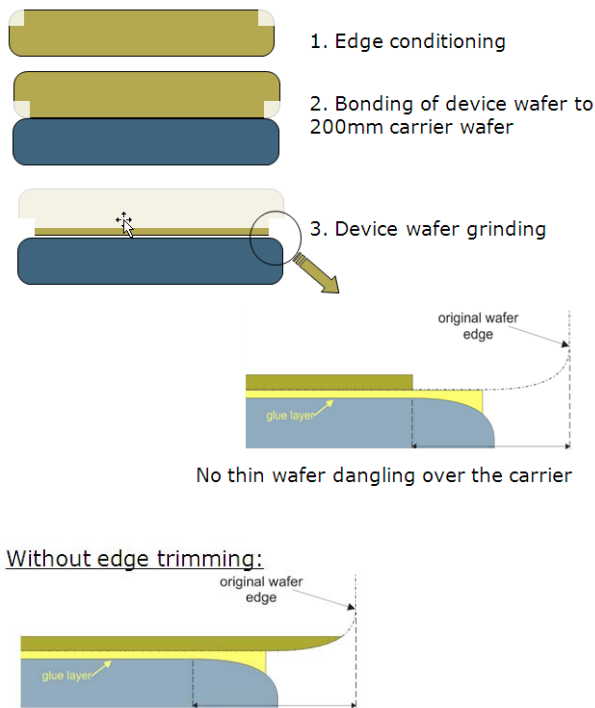


Figure 3: Edge conditioning. Without edge trimming wafer to carrier misalignment can lead to overhanging wafer edge which is sensitive to chipping.

After edge trimming, the device wafer is bonded face down on a temporary carrier by means of a temporary glue (Quickstick 135). In order to align the Aluminum light shield on the backside of the thinned wafer to the diode array on the front side (Figure 4C), normally a (CTE matched) glass temporary carrier is used. Glass is however not compatible with high-end Si process environment due to its fragile, non conductive and (Na) contaminating nature. Therefore a novel backside alignment strategy is introduced, avoiding glass as temporary carrier for thinning. In this novel strategy the

device wafer is bonded to a Si carrier. After thinning by grinding down to  $30\mu\text{m}$  (Figure 4A), large cavities are etched through the thinned Si on the position of the front side alignment marks (Figure 4B). Then these exposed marks are transferred to the silicon backside next to the cavities by DRIE (to introduce topography). The new alignment marks are used to align the Al metal shield (Figure 4C). By using this method, misalignment of the Al backside light shield to front side metal layer is limited to  $5\mu\text{m}$ , which is far below the allowed  $22.5\mu\text{m}$  (i.e. 1 pixel pitch) misalignment.

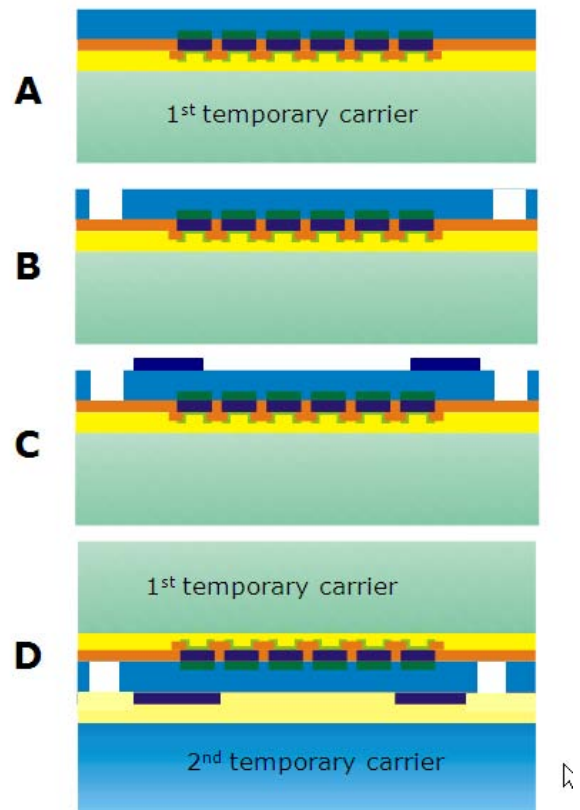


Figure 4: Post-processing of the detector array

A: Bonding to 1st temporary Si carrier + thinning to  $30\mu\text{m}$  + post grinding clean

B: DRIE of large cavities to open front side alignment marks + DRIE new backside alignment marks next to cavities + implantation + laser annealing

C: Aluminum light shield patterning, aligned to the new marks

D: Bonding to 2nd temporary Si carrier

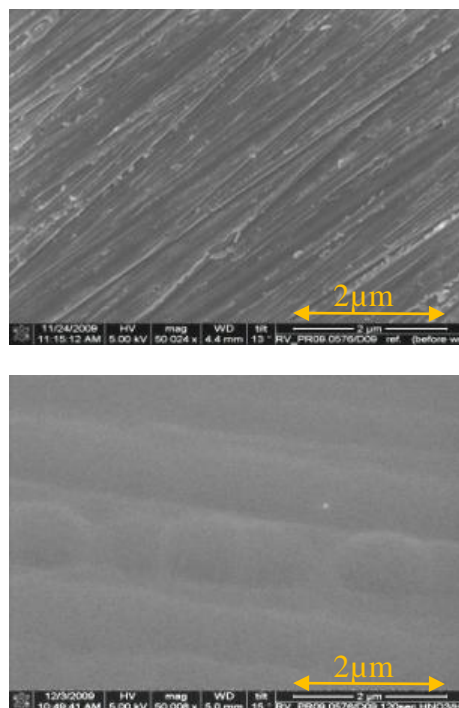


Figure 5: Smoothing of the ground surface using an optimized  $\text{HF}/\text{HNO}_3$  wet etch.

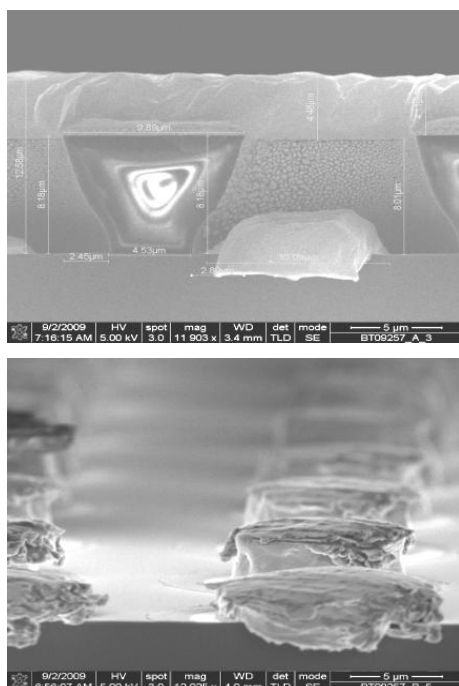


Figure 6 (Top) Patterning for lift-off definition of Au/In bumps. For lift-off a negative resist profile is desired. (Bottom)  $10\mu\text{m}$  diameter bumps defined after lift-off ( $10\mu\text{m}$  spacing)  
Due to its soft nature, indium was smeared out over the wafer edge during sample preparation.

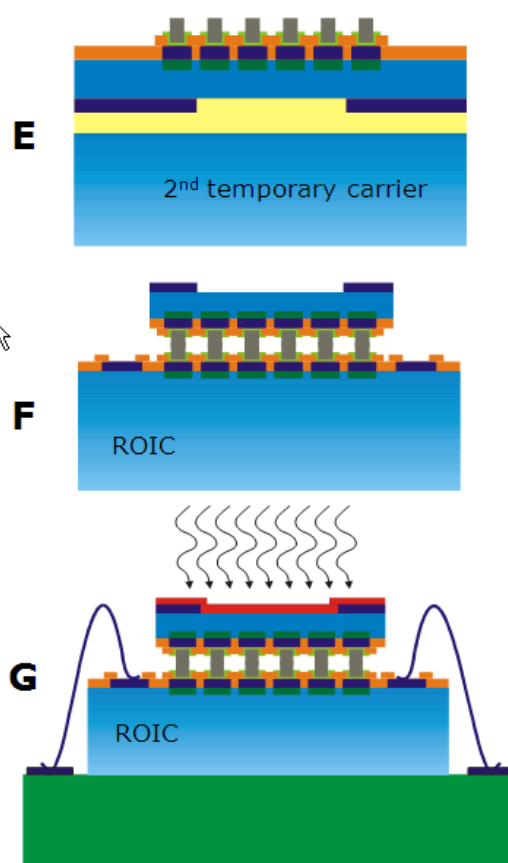


Figure 7: Post-processing of the detector array

E: Waferflip - Debonding of 1st temporary Si carrier + Indium bump definition

F: Dicing of detector array on carrier + flip chip assembly on the ROIC + debonding of 2nd temporary Si carrier

G: Mounting on PCB + wire bonding + ARC deposition

Special attention is given to conditioning the backside Si surface after grinding. As shown in Figure 5, an optimized  $\text{HF}/\text{HNO}_3$  wet etch process smoothens the rough ground surface. This smooth surface, in combination with shallow implantation and laser annealing, is very important to keep the QE high [2]. Any damage induced at the backside of the imager is detrimental for the QE since defects act as recombination centers for the light generated electron-hole pairs. Shallow implantation followed by laser anneal introduces an electrical field which is shielding generated carriers from the recombination centers at the backside surface. As shown in section III, these treatments will lead towards a high performance optical sensor.

After defining the Aluminum light shield (Figure 4D), the wafer is bonded to a 2<sup>nd</sup> temporary Si carrier using a 2<sup>nd</sup> glue, followed by debonding of the 1<sup>st</sup> carrier.

After this waferflip operation (Figure 7E), Au-based under bump metallization together with Indium bumps are formed by lift-off. In Figure 6 the resist pattern for

10 $\mu$ m bumps, 10 $\mu$ m spacing is shown, together with the defined bumps after lift-off.

Further the detector arrays are diced on carrier and flip-chipped on the ROIC dies. The second carrier is removed followed by a thorough cleaning of the detector surface. This step is crucial to ensure low photon response non-uniformity. Processing is finalized after mounting the hybrid imager on a PCB by wire bonding and ARC deposition (Figure 7G).

### III - Results and Discussion

Besides an excellent QE and low pixel-to-pixel cross-talk (see below), a 99.93% high bump yield on the 1024x1024 imager and low diode dark currents of 300pA/cm<sup>2</sup> @ 25°C were measured.

#### A. Quantum Efficiency

In the wavelength range of 400-850nm a QE above 80% was measured (Figure 8). These excellent values were obtained by applying the discussed backside surface treatment (post-grinding clean, implantation and laser annealing) and an optimized ZnS/MgF<sub>2</sub> ARC [2]. The measurements are amongst the highest broadband QE's reported for CMOS imagers [1] and CCD camera's [4].

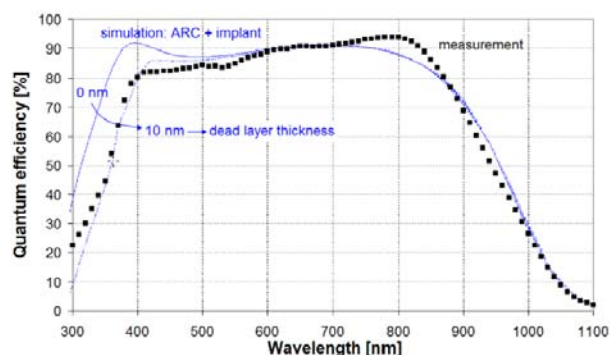


Figure 8 Excellent broadband QE was measured. The results are in agreement with simulations [2].

#### B. Crosstalk

Crosstalk can be defined as the ratio of the output signal of neighboring pixels to the output signal of the central pixel when illuminating only the center pixel. For the non-trenched imager, a large part of the signal is captured by the neighboring pixels. Introducing pixel separating trenches dramatically reduces, i.e. better, avoids cross-talk (Figure 9)

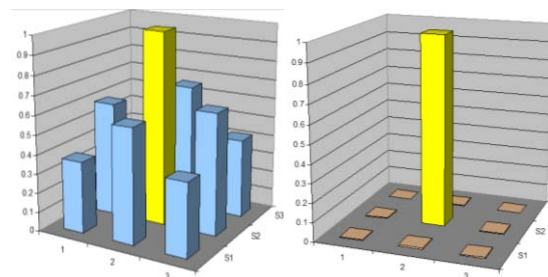


Figure 9: Cross-talk measurement for a non-trenched and a trenched detector array using single pixel illumination.

### IV – Acknowledgement

The development of these imagers was done in the framework of an ESA funded project (16764/03/NL/EC).

### V – Conclusion

A successful processing scheme of a hybrid backside illuminated 1024x1024 imager with a pixel pitch of 22.5 $\mu$ m is presented. All process optimizations that are implemented lead towards excellent broadband quantum efficiency above 80%. Cross-talk reduction can be obtained by introducing high aspect ratio pixel separating trenches. Finally a novel backside alignment strategy to avoid the use of glass substrate as temporary carrier for thinning is presented.

### References

- [1] Y. Bai, S.G. Bernd, J.R. Hosack, M.C. Farris, J.T. Montroy, J. Bajaj, SPIE's 48<sup>th</sup> Annual Meeting, San Diego, California, 2003.
- [2] K. De Munck, J. Bogaerts, D.S. Tezcan, P. De Moor, S. Sedky, C. Van Hoof, IEEE Electronics Letters, Vol. 44 No. 1, 2008.
- [3] B. Dierickx, J. Bogaerts, Proceedings of the SPIE, vol. 5301, No. 1, pp. 205-212, 2004
- [4] R. Jorden, P. Pool, R. Holtom, Proceedings 4th ESO Workshop on Optical detectors for Astronomy, pp. 227, 1999

# FABRICATION AND CHARACTERIZATION OF CARBON NANOTUBE COMPOSITES FOR STRAIN SENSOR APPLICATIONS

F. Ceyssens<sup>1</sup>, M. De Volder<sup>2</sup>, G. Keulemans, J.W.Seo<sup>3</sup>, R. Puers<sup>1</sup>

<sup>1</sup>KULeuven, dept. ESAT-MICAS, Kasteelpark Arenberg 10, 3001 Leuven, Belgium.

<sup>2</sup>KULeuven, dept. Mech. <sup>2</sup>Eng, Celestijnenlaan 300B, 3001 Leuven, Belgium

<sup>3</sup>KULeuven, dept. MTM, Kasteelpark Arenberg 14, Leuven, Belgium

**Abstract** — This paper reports on the fabrication of carbon nanotube (CNT) composites based on polydimethylsiloxane (PDMS). Composites using both bulk and vertically aligned multi wall carbon nanotubes (MWCNTs) as conductive filler elements have been investigated. The PDMS composites using bulk MWCNTs show a quasi-linear piezoresistance response with gauge factors between 0.8 and 2.3. The vertically aligned MWCNTs composites behave in a similar way realizing a gauge factor of 1.4. This gauge factor can be explained by only considering the geometrical change of the CNT composites during strain. The dense network of vertically aligned MWCNTs limits the contraction or transverse strain during axial strain of the PDMS composites. Poisson's ratio drops from 0.45 for pure PDMS to 0.2 for VACNT/PDMS composites. Conclusions about the suitability of these materials for use in MEMS are presented.

**Keywords :** Carbon Nanotubes, CNTs, VACNTs, Strain sensors, piezoresistivity

## I - Introduction

Carbon nanotubes (CNTs) have extraordinary mechanical, electrical and thermal properties [1-3]. When used as conductive filler in polymers, CNTs not only enhance the mechanical properties but also introduce new functionality.

Indeed, conductive CNT composites are sensitive to various external stimuli, such as the chemical environment, pressure, temperature and mechanical perturbation (axial and shear stresses) [4]. The sensitivity of CNT composites enables the application of these composites as 'smart' materials in various sensors.

CNT composites have the promise to realize a higher sensitivity to strain (i.e. a higher gauge factor) in comparison to commercial strain gauges based on a meander structure of Cu – Ni or Ni – Cr [5].

This paper reports on our research aimed at the fabrication and characterization of such composites for use in sensor applications and MEMS[6-7]

The most important issues here are the efficient production of homogeneous and stable CNT composites and their piezoresistive properties.

Further important properties of CNT composites are the influence of temperature and ambient atmosphere on the conductivity, the conduction mechanism and scaling effects [6].

## II - Experimental Details

### A. MWCNT / PDMS composites.

Polydimethylsiloxane (PDMS) is an inert silicon based polymer which has excellent hydrophobic, isolating and biocompatible properties [9]. It is also a relative low cost material. Its very low Young's modulus makes it interesting for use in large area flexible and stretchable devices as well.

The fabrication of multi wall carbon nanotubes - PDMS composites relies on the common solvent evaporation method [3]. First multiwalled carbon nanotubes plied from Nanocyl (MWCNTs grade NC7000) are mixed with the solvent tetrahydrofuran (THF) in a ratio of 300 mg MWCNTs for 20 ml THF and sonificated for 60 minutes (Branson 1510). Afterwards PDMS (Sylgard 184) from Dow Corning is added. Shear mixing (Ika Labortechnik Ultra-turrax T25) for 15 min diminishes the number of macroscopic CNT clusters still present after ultrasonification.

After shear mixing the CNT dispersion are spin coated on a Pyrex substrate to control the thickness of the composite samples. A lift-off resist (LOR30B) is needed to easily remove the MWCNT/PDMS composite after curing. Finally the free MWCNT/PDMS layers are cut in dimensions of 4 cm by 1 cm and silver epoxy contacts are applied. A plasma activation step of the surface of MWCNT/PDMS composites is necessary to guarantee a reliable electrical contact. The final MWCNT/PDMS composite samples have thicknesses between 300 and 600  $\mu\text{m}$ . Figure 2 shows a photograph of a MWCNT/PDMS composite sample used during piezoresistance measurements.



Figure 1: Photograph of MWCNT / PDMS composite test sample.



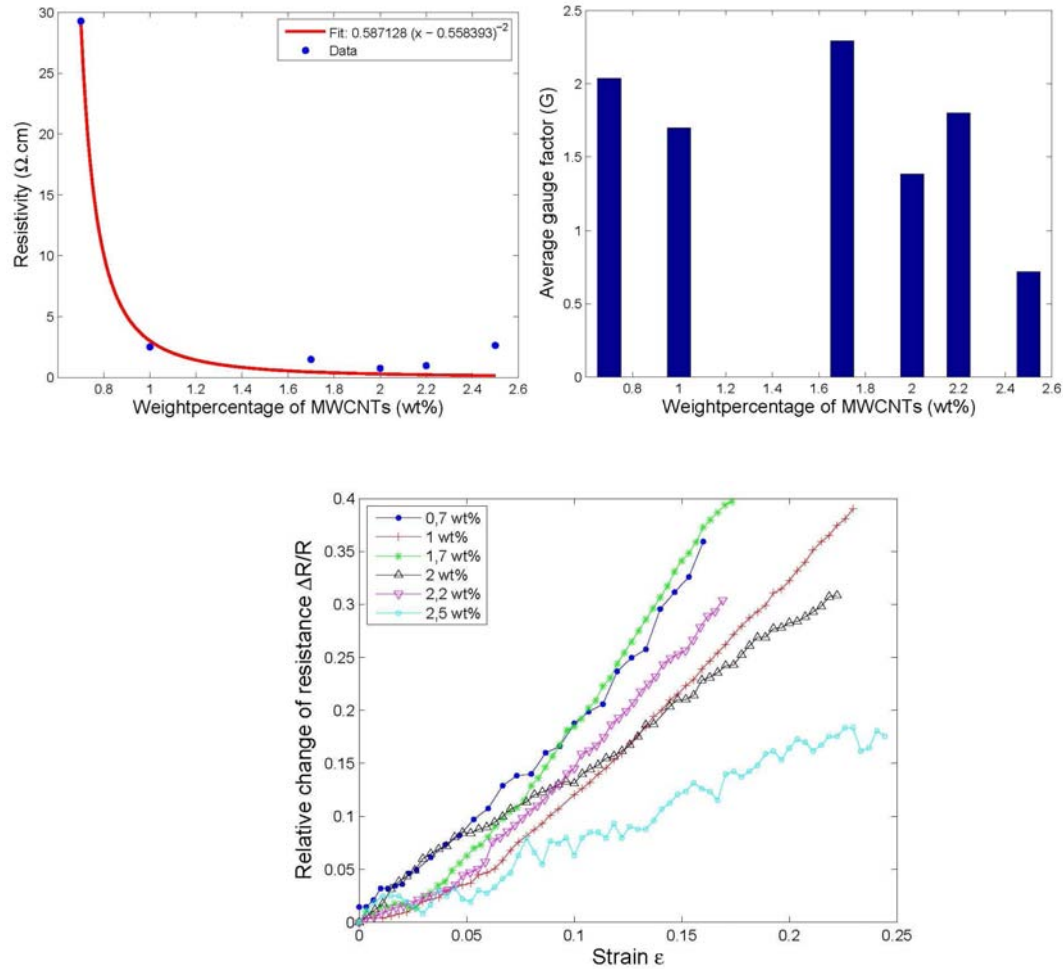


Figure 2: Measured piezoresistive behavior of MWCNT/PDMS composites for different weight percentages of MWCNT.

The processing times mentioned above are derived from microscope inspection of the layers formed with the process. When no further improvement in uniformity and the presence of clusters was detected, ultrasonification and shear mixing times were no longer increased to limit possible damaging of the nanotubes.

### B. VACNT / PDMS composites

Vertically aligned carbon nanotubes (VACNTs) have already an initial uniform distribution and alignment. VACNT composites were fabricated by drop coating the PDMS prepolymer over the VACNT forests grown by thermal chemical vapour deposition (CVD) on silicon substrates [10]. The VACNTs have an average length of 9.3  $\mu\text{m}$  and a diameter of 15.6 nm. The amount of capillary induced wetting is dependent on the angle of contact between the polymer and the VACNTs, the viscosity of the polymer and the diameter and density of the VACNTs [81]. Vacuum is necessary to sufficiently wet the VACNTs and to remove remaining air bubbles in the polymer and to allow penetration of the PDMS prepolymer between the VACNTs. After

curing, the VACNT/PDMS composites can be peeled off the Si substrate.

Sylgard 186 PDMS (Dow Corning) is used instead of Sylgard 184 due to the better mechanical properties of the former. Sylgard 184 breaks when trying to peel off the VACNT/PDMS composites for the Si substrate. Finally silver epoxy contacts are applied after surface activation using oxygen plasma. Figure 3 shows a photograph of a VACNT/PDMS composite sample used for piezoresistance measurements.

## III - Results and Discussion

### A. Piezoresistivity theory

In measurements straining MWCNTs to their breaking point, no intrinsic piezoresistive behavior was found [12-13]. Therefore, the piezoresistance of MWCNTs can only be caused by charge carrier tunneling between individual CNTs [14], or by changes in the geometry of the composite layer due to the applied forces.

### B. Measurement results

Figure 2, top left shows the measured percolation behavior of the resistance of MWCNT/PDMS composites with respect to concentration of MWCNTs (expressed as weight percentage or wt%). With our dispersion process, the percolation threshold for MWCNTs from Nanocyl MWCNTs and PDMS lies around 0.5 wt%. The relative change of the resistance of MWCNT/PDMS composites with different concentrations of MWCNTs with respect to the applied strain ( $\epsilon$ ) is shown on the bottom of in figure 2. MWCNT/PDMS composites with MWCNT concentration closer to the percolation threshold should generally have higher sensitivity for strain than MWCNT/PDMS composites with higher concentrations of MWCNTs, as explained by percolation theory.

The top right plot on figure 2 shows the average gauge factor for different concentrations of MWCNTs which lie between 0.8 and 2.3. The fact that some MWCNT/PDMS composites with a higher MWCNT concentration have a higher gauge factor than composites with a lower MWCNT concentration could be explained by an incomplete dispersion of the MWCNTs and the presence of larger clusters.

If large clusters separate due to strain, there will be a large increase in the resistance. Also the overall trend of the piezoresistive behavior is linear, in contradiction to the expected exponential dependence [4] [14]. This could also be a consequence of a nonuniform dispersion of MWCNTs.

Figure 4 shows the measured linear piezoresistive behaviour of the VACNT/PDMS composites, displaying a gauge factor of 1.4. A fit that only considers the geometrical change of the composite during strain approximates the measurement data quite well if a Poisson ratio ( $\nu$ ) of 0.2 is assumed. This makes sense, as the vertically aligned carbon nanotubes limit the contraction of the composite during strain, lowering the Poisson ratio with respect to standard PDMS ( $\nu = 0.45$ ). The linear dependence can be explained the fact that the carbon nanotubes are not vertically aligned to the substrate but bent due to the high length and form contacts with multiple surrounding carbon nanotubes. Due to the high density of the carbon nanotubes only a few contacts get broken during strain.

### C. Integrated sensor applications

Plasma and reactive ion etch processes useful for PDMS patterning are well-known [15]. We have verified that these oxygen / fluorine based processes work equally well on the MWCNT/PDMS composites presented here.

Thus, it is possible to pattern the MWCNT / PDMS composites for use in an integrated sensor or other MEMS. In our laboratories, a MWCNT / PDMS composite based 'artificial skin' is under development.

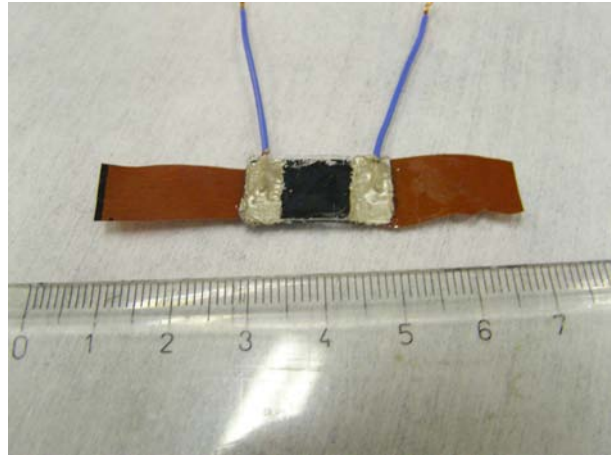


Figure 3: photograph of a VACNT / PDMS composite test sample

However, especially when finer sensor structures are required, the VACNT composites have clear advantages. First, as the VACNTs can be grown in situ on spots defined by lithography, patterning by etching is often not required. Their most significant advantage is their excellent regularity, which is especially important for limiting the variations in small sensor structures.

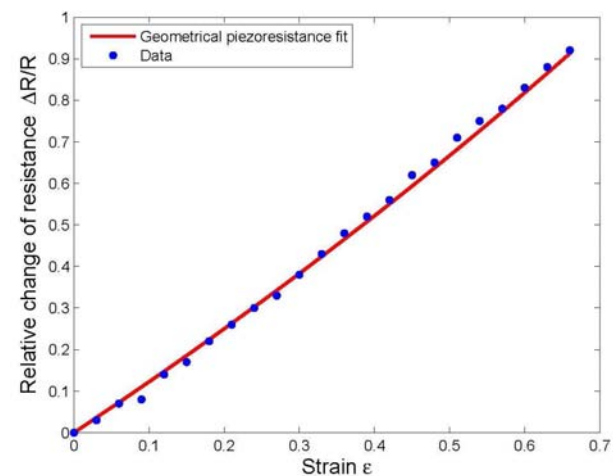


Figure 4: Measured piezoresistive behavior of VACNT / PDMS composites

On the negative side, the gauge factors found are inferior than those naturally present in silicon or even polysilicon. Therefore, we do not expect these composite materials to be used to replace silicon in classic MEMS devices such as pressure sensors unless major improvements are achieved. For high sensitivity applications, the sensors based on single nanotubes by for instance Stampfer et al. [16] are more promising.

However, when the fabrication cost of relatively large areas of VACNTs becomes acceptable, we do see a future for these composite materials in large-area flexible organic electronics, e.g. in artificial skin or intelligent textile.

## IV – Conclusions

This paper reports the fabrication and electromechanical characterization of carbon nanotube composites based on polydimethylsiloxane (PDMS). MWCNT/PDMS composites show a quasi-linear piezoresistive response with gauge factors between 0.8 and 2.3. However, the still inhomogeneous dispersion and presence of larger clusters results in a large variability.

Vertically aligned carbon carbon nanotubes can be considered as an easy way to get uniform dispersions of aligned carbon nanotubes in polymers approaching the ideal morphology. VACNT/PDMS composites show a linear piezoresistivity up to high strain values and a gauge factor of 1.4.

Although the current gauge factor for VACNT/PDMS composites is lower than for commercial strain gauges (gauge factors around 2), vertically aligned carbon nanotubes composites have the potential to generate uniform localized CNT composites, a requirement for application in MEMS.

Further research should go to the influence of length, density and diameter of the vertically aligned carbon nanotubes on the piezoresistivity of the VACNT polymer composites.

## Acknowledgements

This research was supported by the Fund for Scientific Research – Flanders (FWO) and equipment provided by the Hercules fund of Flanders.

## References

- [1] R. H. Baughman, A. A. Zakhidov and W. A. de Heer, Carbon nanotubes – the route toward applications, *Science* 297: 787-792, 2002.
- [2] I.P.Kang et al., Introduction to carbon nanotube and nanofiber smart materials, *Compos. Pt. B-Eng.* 37, 382-394, 2006.
- [3] S. G. Advani. Processing and properties of nanocomposites. World Scientific Publishing, 2007. ISBN: 981-270-390-X.
- [4] R. Zhang, M. Baxendale, and T. Peijs. Universal resistivity-strain dependence of carbon nanotube/polymer composites. *Phys. Rev. B*, 76(19):195433, 2007.
- [5] G. T. Pham, Y. B. Park, Z. Liang, C. Zhang, and B. Wang. Processing and modeling of conductive thermoplastic/carbon nanotube films for strain sensing. *Compos. Pt. B-Eng.*, 39(1):209–216, 2008.
- [6] Prasad Dharap, Zhiling Li, Satish Nagarajaiah, and E V Barrera Nanotube film based on single-wall carbon nanotubes for strain sensing *Nanotechnology* 15, 379–382, 2004.
- [7] Inpil Kang, Mark J Schulz, Jay H Kim, Vesselin Shanov and Donglu Shi, A carbon nanotube strain sensor for structural health monitoring *Smart Mater. Struct.* 15, 737–748, 2006.
- [8] X. Li, C. Levy, and L. Elaadil. Multiwalled carbon-nanotube film for strain sensing. *Nanotechnology*, 19(4):045501, 2008.
- [9] C. L.Wu, H. C. Lin, J. S. Hsu, M. C. Yip, and W. L. Fang. Static and dynamic mechanical properties of polydimethylsiloxane/carbon nanotube nanocomposites. *Thin Solid Films*, 517(17):4895–4901, 2009.
- [10] M.. De Volder, D. Vidaud, E. Meshot, S. Tawfick and A. J. Hart, Self-similar organization of arrays of individual carbon nanotubes and carbon nanotube micropillars, *Microelectronic Engineering* 87, 1233-1238, 2010.
- [11] B. L. Wardle, D. S. Saito, E. J. Garcia, A. J. Hart, R. G. de Villoria, and E. A. Verploegen. Fabrication and characterization of ultrahigh-volume-fraction aligned carbon nanotube-polymer composites. *Adv. Mater.*, 20(14):2707–+, 2008.
- [12] T.W.Tombler et al. , Reversible electromechanical characteristics of carbon nanotubes under local-probe manipulation, *Nature* 405, 769-772, 2000.
- [13] S. Paulson et al., In situ resistance measurements of strained carbon nanotubes, *Appl.Phys.Lett.* 75, 2936-2938, 1999
- [14] N. Hu, Y. Karube, C. Yan, Z. Masuda, and H. Fukunaga. Tunneling effect in a polymer/carbon nanotube nanocomposite strain sensor. *Acta Mater.*, 56(13):2929–2936, 2008.
- [15] J. Garra, T. Long, J. Currie, T. Schneider, R. White and M. Paranjape, Dry etching of polydimethylsiloxane for microfluidic systems, *J. Vac. Sci. Technol. A* 20(3), pp. 975-982, 2002.
- [16] C. Stampfer, T. Helbling, D. Obergfell, B. Schöberle, M. K. Tripp, A. Jungen, S. Roth, V. M. Bright, and C. Hierold, Fabrication of Single-Walled Carbon-Nanotube-Based Pressure Sensors *Nano Lett.*, 6 (2), pp 233–237, 2006.

## Fluidic variable inductor using SU8 channel

I. El Gmati<sup>1,3</sup>, P. Calmon<sup>1,2</sup>, R. Fulcran<sup>1</sup>, S. Pinon<sup>1</sup>, A. Boukabache<sup>1,2</sup>, P. Pons<sup>1,2</sup>, A. Kallala<sup>3</sup>

<sup>1</sup> LAAS-CNRS, 7 avenue du Colonel Roche, 31077 Toulouse, France

<sup>2</sup> Université de Toulouse ; UPS, INSA, INP, ISAE ; LAAS ; F-31077 Toulouse, France

<sup>3</sup> Laboratoire instrumentations Monastir, Tunisie

Contact author: [ielgmati@laas.fr](mailto:ielgmati@laas.fr)

### Abstract

A variable inductor based on liquid tuning has been fabricated and characterized. The fabrication process used SU8 channel obtained by spin coating and lamination. The inductance can be tune from from 5.4 nH to 2.6nH with a quality factor between 12 and 6.

**Keywords :** Tunable inductor, Fluidic tuning, SU8 channel

### I- Introduction

The tuning of passive RF circuits is often a critical issue. In wireless communication equipment such as cellular phones, wide range tuning is necessary for channeling. Narrow range tuning is required for precise impedance matching or when the fabricated circuits are unable to meet the required performance due to process parameters deviation of the process parameters.

In both types of tuning, not only variable capacitors but also variable inductors can be used. The main requirement for these components is a high variation ratio with continuous states.

MEMS technology has been already used to fabricate variable capacitor and inductors [1-15], but most of them have drawbacks like low quality factor and/or low tuning range.

Even if liquids are used recently in RF components [16-20], few studies are focused on liquid variable inductors.

In this paper we propose a liquid based RF MEMS inductor where salt-water is used to modify the capacitive coupling between metal spires.

### II- Principle and design

The proposed inductor (*Figure 1*) is a dual circular coil and has an inductance of few nH. The metallic lines of the inductor have 20µm width, spaced by 10µm. The inside (outside) coil diameter is around 600µm (1200µm). The dual spires are fabricated inside 70µm width channels. When liquid moves along this channel, it change the capacitive coupling between inter-spires leading to reduction of the stored magnetic energy, and hence the inductance. The inductance value varies according to the liquid position, which can be rise from zero to the total spiral length.

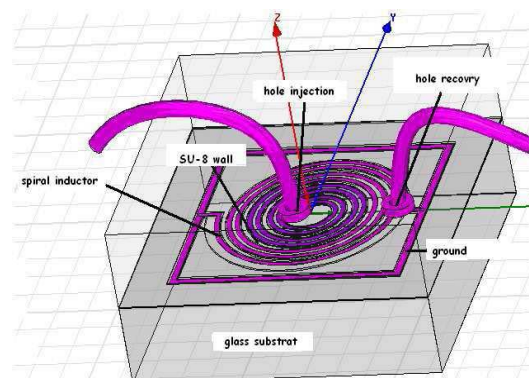


Figure 1 : Top view of the 3D inductor

### III- Process fabrication

Figure 2 shows a schematic cross section view of the technological steps developed to fabricate thick gold spiral inductors embedded in a glass substrate. The fabrication process requires six masks.

#### • Gold spiral inductors

A Ti/Au (500Å/500Å) seed layer was homogeneously sputtered on top side of a 500µm thick glass substrate (Fig. 2a). The Ti layer was deposited to improve the adhesion, and a positive photoresist (AZ 4562) was subsequently patterned in order to create the electroplating mould (thickness ≈ 5.5 µm). Finally, 2 µm thick gold, were electroplated into the resist mould. The photoresist mould was then removed and the seed layer was chemically etched (Fig. 2b-d).

#### • Microfluidic channel

A 10 µm thick SU8 films was obtained by spin coating using 4 ml of SU-8 3005 at 900rpm with a 900rpms<sup>-1</sup> acceleration for 30s. The resist was then soft baked for 1 min at 65°C, ramped at a rate of 10°C min<sup>-1</sup> up to 95 °C, held at 95°C for 7 min and finally cooled down to room temperature. The resist was then exposed to UV light, and post-baked for 1 min at 65°C and 3 min at 95 °C to cross-link the photoresist. Finally, the resist was developed in SU-8 developer (*Propylene Glycol Methyl Ether Acetate*, PGMEA) (Fig. 2e). A photosensitive SU-8 dry film, 10 µm in thickness, was then laminated and patterned on the top side to close the channel. Holes are performed in this laminated SU8 in order to realize the fluidic access (Fig. 2f).



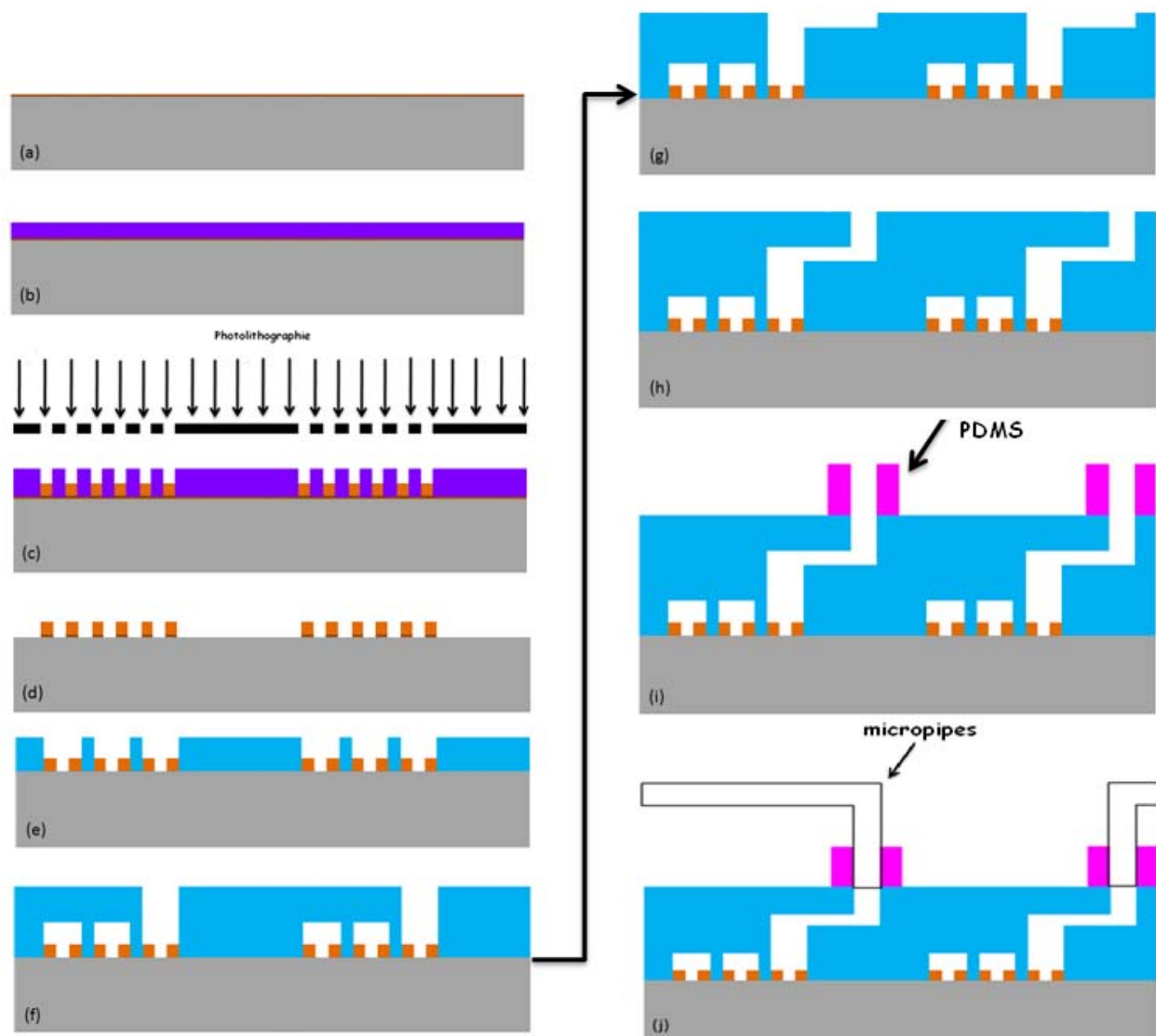


Figure 2 : Top view of the 3D inductor

- Microfluidic access

Microfluidic access channel was then performed by lamination technique. A second SU-8 dry film (10  $\mu\text{m}$  in thickness) was laminated and patterned in order to realize the access channel walls (Fig. 2g). Finally, a 10 $\mu\text{m}$  thick SU-8 dry film was laminated and patterned to close the access channel and create access holes for the fluid (Fig. 2h).

- Fluidic connexion

In order to perform fluidic connection between to micro-pipe and fluidic channels, *polydimethylsiloxane* (PDMS) disks was sealed at the microchip inlet and outlet using photo curable glue (Fig. 2i-j).

Figure 3 shows an example of spiral inductor inside the SU8 channel.

Figure 4 presents a global view of a four inches wafer after the end of the process fabrication (only one inductance is connected here).

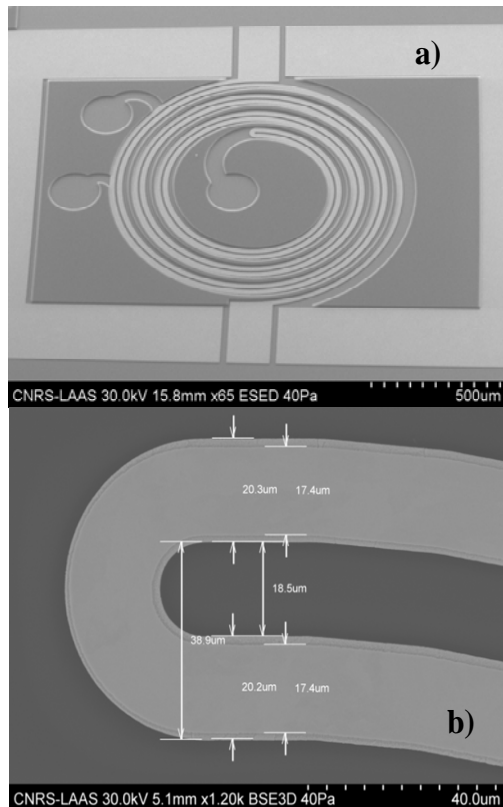


Figure 3: MEM image of one inductor after step 2e (a) and zoom of dual coil (b)

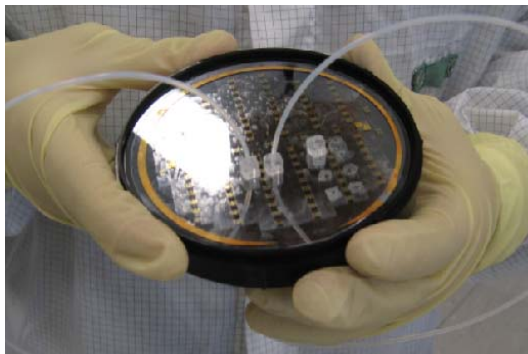


Figure 4: 4'' wafer photo after step 2j

#### IV- Inductance characterization

Figure 5 presents the RF test bench used for the characterization. The S-parameters were measured from 40 MHz to 20 GHz with an Agilent 8510 network analyzer and cascade Microtech GSG probes.

The micro-pipe are connected to a manual syringe pump which allows to push the liquid inside the micro-channels

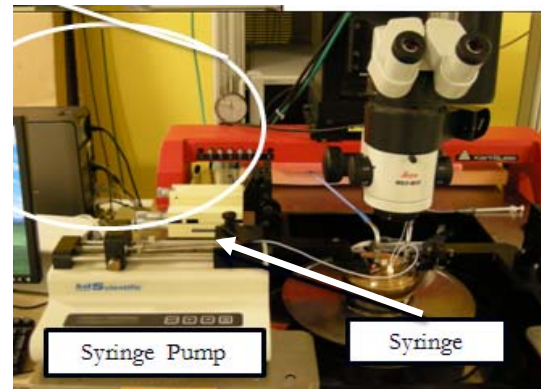


Figure 5 : Test bench

Measurement has been performed using salt water with conductivity of 75S/m. Six liquid positions has been used for the characterization has shown in Figure 6.

Figure 7 presents the measured quality factor and inductance between 0.1GHz to 6GHz for the six liquid position (Q and L is without liquid). At 1.6GHz, the inductance can be tuned from 5.4 nH to 2.6nH with a quality factor between 12 and 6.

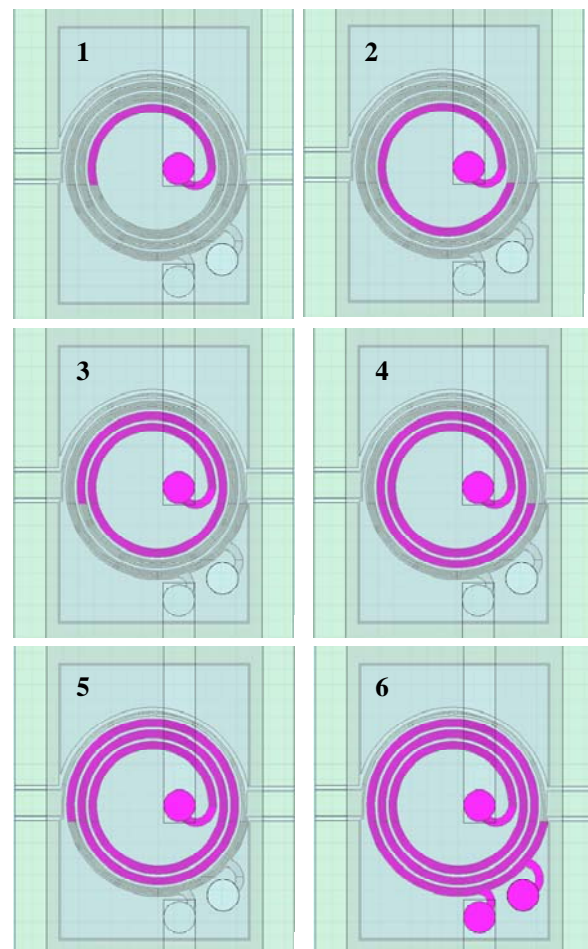


Figure 6 : Different liquid positions inside the channel

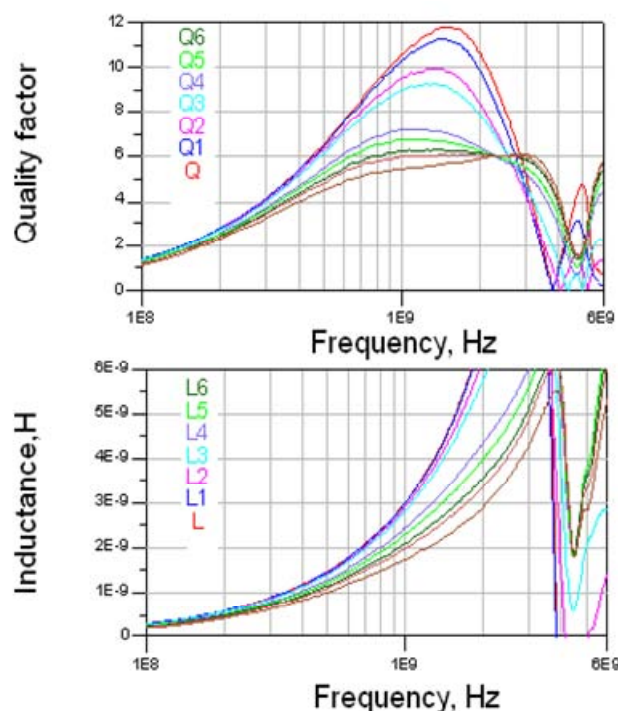


Figure 7 : Measured quality factors a) and inductance b)

## V- Conclusion

On chip micro-variable inductor using photosensitive lamination process and MEMS technology has been fabricated and characterized. The tuning range of the inductance is around 107 % with a Q-factor between 6 and 12.

New devices with non toxic conductive liquid (galinstan) are under fabrication. This conductive liquid will allow improving the inductor performances as shown by simulation.

## VI- References

- [1] A. Dec and K. Suyama, "Micromachined electro-mechanically tunable capacitors and their applications to RF IC's," IEEE Trans. Microw. Theory Tech., vol. 46, no. 12, pp. 2587–2596, Dec. 1998.
- [2] Y. Yoshihara, H. Sugawara, H. Ito, K. Okada, and K. Masu, "Wide tuning range LC-VCO using variable inductor for reconfigurable RF circuit," IEICE Trans. Fundam. Electron., Commun. Comput. Sci., vol. E-88A, no. 2, pp. 507–512, Feb. 2005.
- [3] Y. Ito, Y. Yoshihara, H. Sugawara, K. Okada, and K. Masu, "A 1.3–2.8 GHz wide range CMOS LC-VCO using variable inductor," in Proc. IEEE Asian Solid-State Circuits Conf., Nov. 2005, pp. 265–268.
- [4] S. Lucyszun, I. D. Robertson, "High performance MMIC Narrow band filter using tunable active inductors", IEEE Microwave and Millimeter-wave monolithic circuits Symposium, 1994.
- [5] S. Hara, T. Tokumitsu, M. Aikawa, "lossless Broadband Monolithic Microwave floating active inductor", IEEE Transaction on MTT, vol.28, n°1, 1992
- [6] S. Zhou, X. Q. Sun, W. N. Carr, "A monolithic variable inductor network using microrelays with combined thermal and electrostatic", Journal of Micromechanics and Microengineering, vol.9, 1999.
- [7] T. Velden, D. Stefan, E. Obermeier, "Micro-coil with movable core for application in an inductive displacement sensor", Journal of Micro-mechanics in and Microengineering, vol.9, 1999
- [8] V. Luberck, B. Barder, E. Chan, D. Lopez, M. Gross, P. Gammel, "Self-assembling MEMS variable and fixer RF inductors", IEEE Transactions on MTT, vol.49, n°11, 2001
- [9] C. H. Chien, C. H. Wang, "Fabricated tunable inductor by microfabrication technology", Proceedings de la conference DTIP, Montreux, Suisse, 2004
- [10] M. GEL, S. Takeuchi, I. Shimoyama, "Fabrication methode for out-of-plane, micro-coil by surface micromachining", sensors and actuators A: physical, vol.97-98, pp702-708, 2002.
- [11] I. Zine-El-Abedine, M. Okoniewski, J. G. Mc Roy, "A new class of tunable RF MEMS inductors", Proceeding of the international conference on MEMS, NANO and Smart systems, pp. 114-115, 2003
- [12] H. Sugawara, Y. Yoshira, H. Ito, K. Okada, K. Masu, "wide-Range RF variable inductor on Si CMOS chip with MEMS Actuation", IEEE European Microwave Conference, pp.701-704, 2004.
- [13] C.-M. Tassetti, M. Bensetti, G. Lissorgues, J.-P. Gilles, Y. Le Bihan, C. Marchand, and P. Nicole. Design, modeling and measurement of tunable MEMS inductors. In Symposium on Design, Test, Integration and Packaging of MEMS and MOEMS, Montreux, pages 259–263, 2004.
- [14] K. Okada, H. Sugawara, H. Ito, K. Itoi, M. Sata, H. Abe, T. Ito, and K. Masu. "On-chip high-Q variable inductor using wafer-level chip-scale package technology". IEEE Transactions on Electron Devices, 53(9) :2401–2406, September 2006.
- [15] Jeong-Il Kim, and Dimitrios Peroulis "Tunable MEMS Spiral Inductors with Optimized RF Performance and Integrated Large-Displacement Electrothermal Actuators; IEEE transactions on microwave theory and techniques, vol. 57, no. 9, september 2009.
- [16] Chung-Hao Chen, and Dimitrios Peroulis "Liquid RF MEMS Wideband Reflective and Absorptive Switches" IEEE Transactions on Microwave Theory and Techniques, vol. 55, no. 12, december 2007.
- [17] Xiaoguang Liu, Linda P. B. Katehit and Dimitrios Peroulis "MEMS Liquid Metal Through-wafer Microstrip to Microstrip Transition" 978-1-4244-1780-3/08/\$25.00 ©2008 IEEE
- [18] Chung-Hao Chen, and Dimitrios Peroulis "Liquid RF MEMS Wideband Reflective and Absorptive Switches" IEEE Transactions on microwave theory and techniques, vol. 55, no. 12, december 2007.
- [19] C. Chen and D. Peroulis, "Electrostatic liquid-metal capacitive shunt MEMS switch," in IEEE MTT-S Int. Microw. Symp. Dig., Jun. 2006, pp. 263–266.
- [20] C. Chen, J. Whalen, and D. Peroulis, "Non-toxic liquid-metal 2–100 GHz MEMS switch," in IEEE MTT-S Int. Microw. Symp. Dig., Jun. 2007, pp. 363–366.



# LOW-COST BEVEL-SHAPED SHARP TIPPED HOLLOW POLYMER-BASED MICRONEEDLES FOR TRANSDERMAL DRUG DELIVERY

B. Paul Chaudhri<sup>1,2</sup>, F. Ceyssens<sup>1</sup>, P. De Moor<sup>2</sup>, C. Van Hoof<sup>1,2</sup> and R. Puers<sup>1,2</sup>

<sup>1</sup>ESAT, Department of Electrical Engineering, Katholieke Universiteit Leuven, 3001 Leuven, Belgium

<sup>2</sup>IMEC, Kapeldreef 75, 3001 Leuven, Belgium

**Abstract** — Microneedles are one of the more feasible and painless methods for transdermal drug delivery. Microneedles when inserted into the skin can by-pass the stratum corneum which forms the main barrier for large-molecule drugs to diffuse through the skin, and thus proteins and hormonal drugs can be delivered to the bloodstream. In this paper we present for the first time sharp tipped hollow SU-8 microneedles with bevel shaped tips, fabricated using a low-cost process. The bevel shaped tips were further facilitated by a novel triangular cross-sectional based design of the microneedle. They were fabricated by a combination of molding technique with KOH-etched-pits and photolithography. Microneedle heights of around 300  $\mu\text{m}$  with a wall thickness of around 10  $\mu\text{m}$  have been achieved.

**Keywords :** Microneedle, SU-8, bevel-shaped tips, molding, transdermal drug delivery

## I – Introduction

Protein drugs or hormonal drugs cannot be ingested orally like conventional drugs because they get digested in the gastrointestinal (G.I.) tract. Thus, alternative routes for delivery such as intranasal [1,2], transdermal, buccal [3], intraocular and pulmonary, are the other methods being investigated. But most of them come with the downside of the adverse effects associated with applying these drugs on the pulmonary or mucosal surfaces which limits their usefulness [4]. Transdermal drug delivery using microneedles are one possible solution. The outermost layer of the skin, called the stratum corneum, provides the toughest resistance to any drug formulation applied on the skin with the objective of allowing it to diffuse through the skin layers till it reaches the blood vessels. With microneedles designed for suitable lengths (depending on where on the body the drug needs to be delivered), the barrier of stratum corneum can be circumvented once the microneedle is inserted inside the skin. Microneedles come in different shapes and sizes with different cross-sectional areas. Sharp tipped needles require a lesser insertion force which directly translates into lesser pain for the patient. One of the approaches to fabricating sharp tipped hollow polymer microneedles in the past has been using a process of laser drilling through bore of the solid polymer needle [5]. This process is expensive and would have limited scalability. Another approach was by SU-8 molding on polydimethylsiloxane (PDMS) master templates [6]. Here the

average microneedle tip diameters obtained was between 15 to 25  $\mu\text{m}$ . In contrast, what we report here are much sharper tips with tip diameters averaging under 2  $\mu\text{m}$ . They were fabricated using a combination of molding and photolithography. Pyramidal shaped trenches were etched in a Si wafer using KOH anisotropic etching. SU-8 polymer was next cast on these trenches followed by lithography on SU-8. This was followed by development resulting in out-of-plane sharp-ended microneedles. SU-8 is a negative photoresist which enables it to be patterned directly without any additional step. Furthermore, a novel design feature here is the use of triangular cross-section of the microneedle structure in aiding the formation of the desired sharp bevel-tip.

## II – Design

Anisotropic etching with KOH on Si <100> wafer results in a pyramidal pit, the walls of which are at an angle of  $54.74^\circ$  in accordance with properties of anisotropic etching of <100> Si wafer. The SU-8 microneedles were aligned such that their tips should coincide with the sharp tips of the pyramidal grooves on the wafer, in order for them to form a sharp tip, as shown in Figure 1.

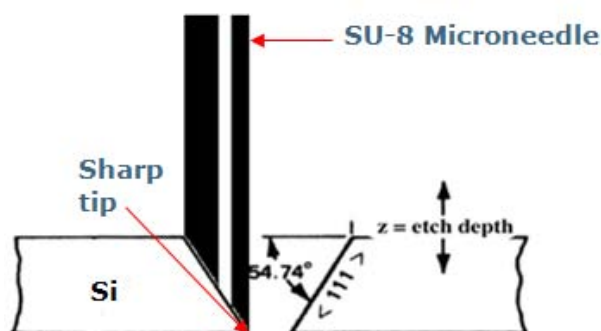


Figure 1. Principle behind molding the microneedles on the KOH-etched pyramidal pits to form a sharp ended tip.

Furthermore, to facilitate an even more pronounced formation of the bevel-shaped sharp tips, triangular cross-sectional design of the microneedle with a triangular cross-sectional bore was adopted. The main reason behind this idea was that the triangular shaped geometry would aid naturally in the formation of bevel-shaped tips. The cross-section shape was designed as a right-angled isosceles triangle with base 92  $\mu\text{m}$  and sides 65  $\mu\text{m}$  each, with a wall thickness of 10  $\mu\text{m}$ , such that one of the  $45^\circ$  vertices coincides with the pyramidal pit's



sharp bottom point. The main reason why bevel-shaped tips were desired is because the microneedle is based on a biomimetic design inspired from that of that of a mosquito proboscis tip [7].

The height of the microneedle was designed for 300  $\mu\text{m}$  mainly as an initial test to demonstrate primarily the concept of tip sharpening by molding.

### III – Fabrication

The basic fabrication principle as reported earlier for high-aspect ratio microneedles [7] still remained the same with a few additional steps. Here, first windows were patterned on an oxidized <100> Si wafer in order to create openings for the KOH-etch step as shown in Figure 2a. Then KOH etching was carried out in a KOH solution of 30% by weight at a temperature of 60°C. These parameters were chosen in accordance with values from literature for silicon oxide masked KOH etching [8].

It is to be noted from Figure 1 that at the step of UV-exposure on the SU-8, there is a very high risk of the UV light getting reflected off the inclined plane of the pyramidal pit wall and in turn cross-linking the entire microneedle bore. This is highly undesirable. To solve this problem, an anti-reflective coating of chromium-black (Cr-black) was used. Cr-black has a very low reflectance of only 5% in the UV region and was very suitable for our purpose.

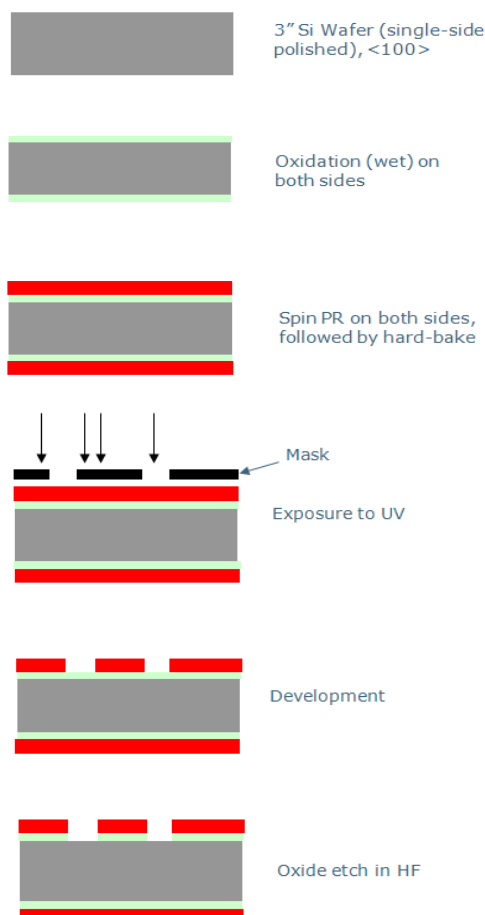


Figure 2a. Process steps – Part 1

This Cr-black coating was done by electrodeposition [9]. Prior to this step, an adhesive layer of Ti followed by a seed layer of Cu was sputtered as shown in Figure 2b.

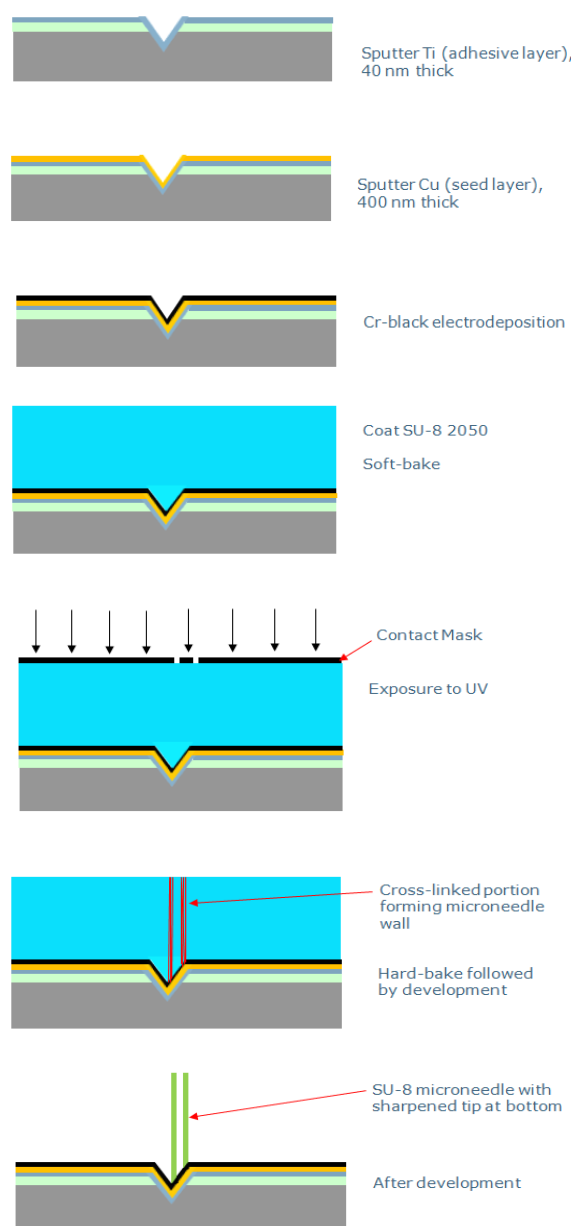


Figure 2b. Process steps – Part 2

Once Cr-black was coated, the wafer was ready for the subsequent steps of SU-8 processing. SU-8 2050 (Mi-

croChem Inc., US) has been used here. Since it has been earlier observed that very thick layers of SU-8 require a two-step soft-bake as has been reported before [7], the same was embarked upon here. First, a soft bake was carried out at 95°C for 7 hours on a hot plate, followed by cooling to room temperature for the next 24 hours. The solvent content percentage is calculated and should it be less than 10% only, should the baking be stopped.

$$\text{Solvent content}\% = \left[ 1 - \frac{0.735(W_{in})}{W_{fin}} \right] \times 100$$

where,  $W_{in}$  is the initial net weight of the SU-8 and  $W_{fin}$  is the final net weight of SU-8 after the pre-bake. For this step, a stainless steel plate was utilized instead of a Si wafer. Second, this entire mass of semi-dried SU-8 material was scraped out and collected in the form of 'dry chips'. These dry chips were now placed on the KOH-etched Si wafer and heated to 110°C in a vacuum oven. The vacuum is applied to eliminate the large number of air bubbles that accumulate as a result of the last heating step. This heating causes reflow and melting of the SU-8 dry chips which in turn allows the SU-8 to fill the KOH-etched pits completely. This is crucial for without this the entire purpose behind the molding step would be defeated. Once done, the SU-8 is ready for UV exposure. A h- and g-line exposure wavelengths were used, by filtering out wavelengths at 365 nm and below. This is followed by hard-bake and subsequent development in propylene glycol monomethyl ether acetate (PGMEA) solution for 30 minutes. After development the microneedles were observed standing out-of-plane on the wafer.

Prior to carrying out the entire process, a short-loop test was executed to test the molding capability of SU-8 on a test Si-wafer with prior-etched KOH-etched grooves and a release was done as shown in Figure 3. This proved that SU-8 could indeed be used suitably as a molding material with a good reproducibility of the sharp edges.

#### IV – Results and Discussion

Triangular-cross-sectional microneedles with bevel-shaped sharp tips have been fabricated. As this is a part

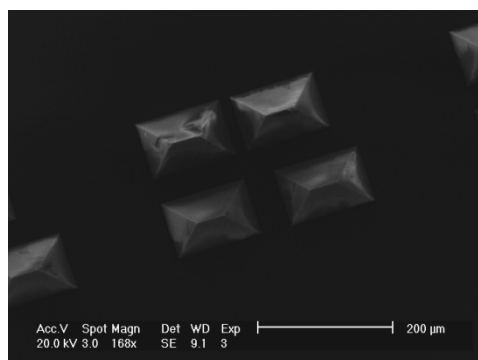


Figure 3. Top view of molded SU-8 test structures. The sharp edges prove the good mold- reproducibility quality of SU-8.

of an on-going work, the microneedles have not yet been released from the wafer at this stage and appear as needles standing on KOH-etched pits as shown in Figure 4.

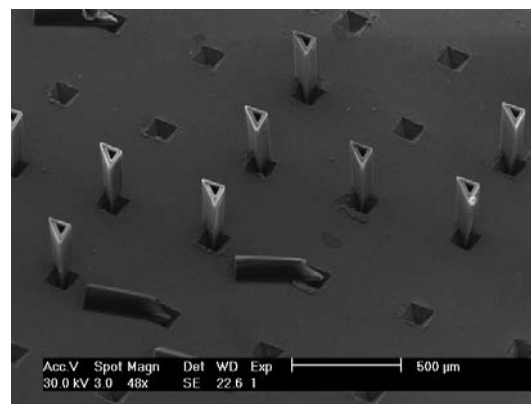


Figure 4. An array of triangular cross-section microneedles standing out-of-plane on the KOH-etched pits. The ones that have fallen off prove that their end lying inside the KOH-etched pit, is the sharpened tip. It is to be noted that the entire wafer surface here is covered with Cr-black.

Close-up views of the released microneedles prove that they do indeed have a sharpened bevel-shaped sharp tip as shown in Figure 5 and 6.

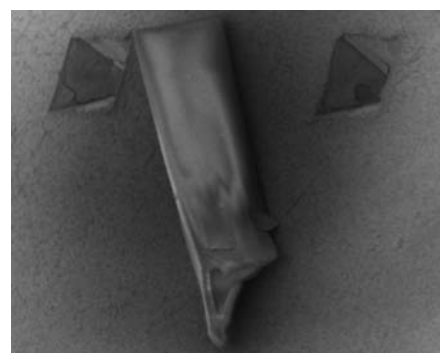


Figure 5. The bevel-shaped tip of a loosened microneedle is prominent here. The bore opening at the sharp tip is also clear indicating the ends are not clogged.

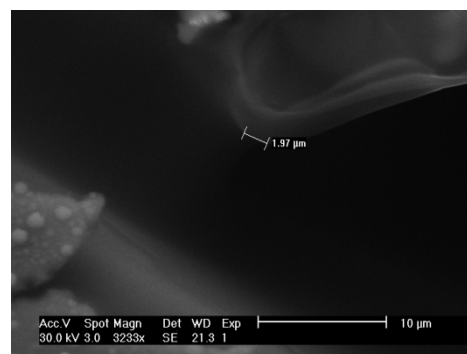


Figure 6. Close-up view of the bevel-shaped needle tip showing a tip diameter of 1.97 μm.

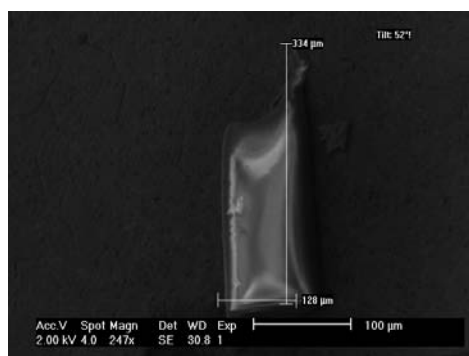


Figure 7. Side view of the fabricated microneedle. Measured needle length of 334  $\mu\text{m}$  of and base of 128  $\mu\text{m}$ , viewed at a tilt of 52°. Needle wall thickness is 10  $\mu\text{m}$ .

The lengths of the needle obtained were around 300  $\mu\text{m}$  with a base-length of around 128  $\mu\text{m}$ , as shown in Figure 7. Further, from Figure 6, it is proven that the fabricated microneedles are quite sharp at 1.97  $\mu\text{m}$  needle tip diameter. For a molding process such as this, this is a significant achievement. However, should it be desired to release the microneedles from the substrate here, a simple Cr etching would suffice.

## V – Conclusion

Sharp-tipped bevel-shaped hollow microneedles have been fabricated successfully with SU-8 polymer, using a combination of molding and photolithography techniques. The molding step can easily be scaled up for mass production and together with a cheap polymer-based structural material like SU-8, serves as a low-cost means for producing these microneedles. As it is impractical to handle individual needles, it was refrained from releasing microneedles from the substrate at this stage. The next stage of the work involves creating a platform for the microneedle base which has holes continuous with the bore of the microneedle, so that the system can be used further for integrating with microfluidics for transdermal drug delivery. It is envisaged, in keeping in line with a monolithic material-based system design, that the platform would be made of SU-8 too. Then the entire system comprising the platform and microneedles array would be released from the wafer.

## References

- [1] Torres-Lugo M and Peppas NA (2000). Transmucosal delivery systems for calcitonin: a review. *Biomaterials* 21, 12, 1191-6.
- [2] O'Hagan DT and Illum L (1990). Absorption of peptides and proteins from the respiratory tract and the potential for development of locally administered vaccine. *Crit Rev Ther Drug Carrier Syst* 7, 1, 35-97.
- [3] Sayani AP and Chien YW (1996). Systemic delivery of peptides and proteins across absorptive mucosae. *Crit Rev Ther Drug Carrier Syst*, 13, 1-2, 85-184.
- [4] Richard Soltero and Nnochiri Ekwuribe (2004). The oral delivery of protein and peptide drugs. *Innovations in Pharmaceutical Technology*, pp 106-110.
- [5] Wijaya Martanto *et al*, Side-Opening Hollow Microneedles for Transdermal Drug Delivery (2005), IEEE Proceedings.
- [6] Po-chun Wang *et al*, Hollow Polymer Microneedle Array Fabricated by Photolithography Process Combines with Micromolding Technique, 31<sup>st</sup> Annual International Conference of the IEEE EMBS Minneapolis, USA, September 2-6, 2009.
- [7] Buddhadev Paul Chaudhri *et al*, A high aspect ratio SU-8 fabrication technique for hollow microneedles for transdermal drug delivery and blood extraction on 2010 *J. Micromech. Microeng.* 20 064006
- [8] R. Hull [Properties of Crystalline Silicon (INSPEC, London, 1999)]
- [9] M.R. Bayati *et al* Design of chemical composition and optimum working conditions for trivalent black chromium electroplating bath used for solar thermal collectors. *J. Renew Energy* 2005; 30: 2163-2178.

# NON-INVASIVE DRY ELECTRODES FOR EEG

M.F. Silva, N.S. Dias, A.F. Silva, J.F. Ribeiro, L.M. Goncalves, J.P. Carmo, P. M. Mendes, J.H. Correia

University of Minho, Dept. Industrial Electronics, Campus Azurem, 4800-058 Guimaraes, Portugal

**Abstract** - This paper presents a non-invasive dry electrode for electroencephalogram (EEG) acquisition. These electrodes can be integrated in a wearable braincap for wireless EEG that can be used for a long time by patients avoiding the contact gel. This wearable braincap will allow mobility to the patients, while simultaneously having their electrical brain activity monitored. The fabricated dry electrodes are based on iridium oxide ( $\text{IrO}_x$ ) deposited by reactively pulsed sputtering. The electrode employs an array of microtips that penetrate the outer skin layer (i.e. *stratum corneum*) that is 10  $\mu\text{m}$  thick. The microtips (100-200  $\mu\text{m}$  deep) were micromachined through a bulk-micromachining process based on a KOH solution.

**Keywords:** dry electrodes,  $\text{IrO}_x$  electrode.

## I - Introduction

The electrodes are key elements for acquiring EEG signals. The high demand on non-invasive EEG electrodes for monitoring, diagnostics and treatment of patients with neural diseases, such as epilepsy, is driving the research of electrodes fabricated in different materials and with very low impedance.

The Ag/AgCl standard electrodes present a low impedance in the interface skin-electrode and good stability through its life span. However, these electrodes require a previous preparation in the outer skin (i.e. *stratum comeum*) and a gel to provide a good contact between electrode and skin to minimize the insulating effect of the *stratum comeum* layer. The standard Ag/AgCl gel electrodes have limited use because they suffer from dehydration, which leads to a modified electrode impedance and consequently, generates noise and other artifacts in the measured signals. Furthermore, the gel can cause skin irritation and support bacterial growth [1]. A dry Ag/AgCl electrode was proposed for acquiring biopotentials with promising results [2]. Nevertheless, despite the good electrochemical characteristics, the AgCl is toxic and presents an infection risk because it dissolves in contact with the skin [3].

This paper presents a non-invasive dry electrode for EEG. The brain electrical activity occurs between neurons as well as in muscles. The neuroscience field has been demanding invasive electrodes that are implanted in single and multiple recording sites [4]. Electrodes with microtips are presented in Figure 1(b). The microtips length is about 100-200  $\mu\text{m}$  for providing the penetration of the outer skin layer (i.e. *stratum corneum*) that is 10  $\mu\text{m}$  thick.

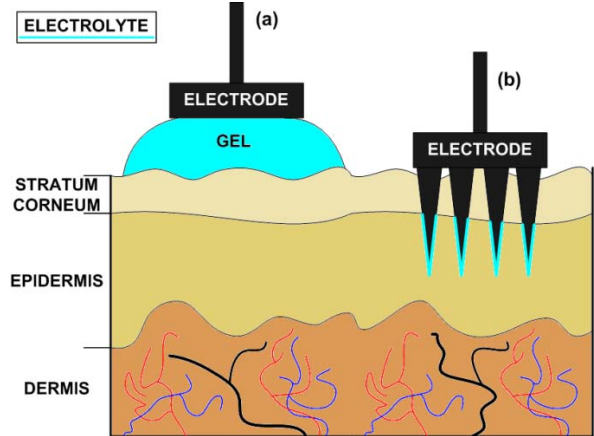


Figure 1: Application of biopotential electrodes: (a) standard EEG electrode; (b) EEG dry electrode with microtips.

## II – Design

The design of the dry electrode consists in a pyramidal structure. The penetration of the microtips in the skin requires a specific pressure [5]. The pressure in the microtip, when an axial load is applied, is given by:

$$P = \frac{F}{A} \quad (1)$$

where  $P$  is the pressure resulted in the solid structure (i.e. microtip),  $F$ , the perpendicular force applied, and  $A$ , the section where the force is applied. The force necessary to insert and remove the electrode is about 10 N [5]. The Figure 2 shows the pairs of action-reaction forces, established in the electrode when inserted in skin (the distribution of the force is uniform on the electrode through the 4x4 microtips array - 0.625 N per microtip). The base of the microtip structure is subjected to a pressure of 15.6 MPa. Therefore, every microtip achieves a maximum pressure endured by silicon at 165  $\mu\text{m}$  from the base (red section in Figure 2). The average height of the pyramidal structures is about 200  $\mu\text{m}$ .

## III – Fabrication

### A. Etching

Each microtip in the dry electrode has a three dimensional structure, which is fabricated by a wet-etching process in silicon through a liquid solution of potassium hydroxide (KOH). The microtips desired shape is obtained by the undercut effect in the etching, where the planes of fast etching are revealed. It was used a [100]-type silicon wafer with a thickness of 500  $\mu\text{m}$ . Also, two layers of silicon nitride (SiN) on the top and on bottom were used as masks for the etching. The Figure 3 shows the microtips fabrication steps.



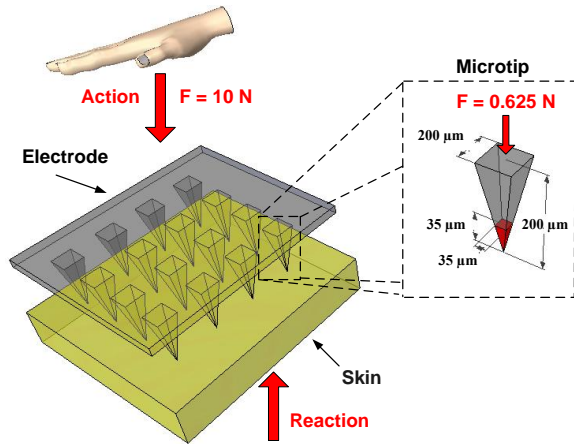


Figure 2: Pairs of action-reaction forces on a electrode with an array of 4x4 microtips.

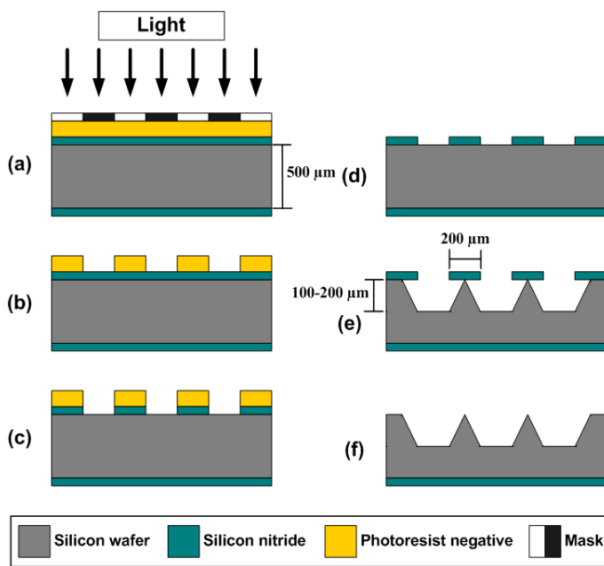


Figure 3: Fabrication of the microtips.

In the Figure 3(a), a mask, with 200  $\mu\text{m}$  square openings, was used to define the microtips by lithography process. The photoresist was removed in the second step (b) from the uncovered areas. Then, the opened window in the SiN layer allowed the exposition to its elimination in the third step (c) whereas the photoresist is removed afterwards (d). The Si wafer is etched during the step (e). The remaining areas with SiN worked out as a protection layer for the etching process of the Si wafer. The etching solution of KOH was by 30% at a temperature of 87  $^{\circ}\text{C}$ , ensuring an etching rate of 1.6  $\mu\text{m}/\text{min}$ . Finally, the remaining layer of SiN was removed (f).

#### B. $\text{IrO}_x$ Sputtering

The iridium oxide ( $\text{IrO}_x$ ) electrodes were deposited by means of pulsed magnetron sputter using  $\text{Ar}/\text{O}_2$  plasma prior to which, a Ti adhesion layer (with a thickness of 50 nm) was deposited on the substrate [6]. The  $\text{IrO}_x$  resistance in a 270 nm thick film was  $349 \times 10^{-6} \Omega\text{cm}$ . The film thicknesses were determined via liftoff process with a *Tencor Pa-10* profilometer.

The thin film resistance was measured in a classic four-point probe system.

### IV – Experimental Results

#### A. Electrode Microtips Fabrication

The Figure 4 shows the emerged microtips by optical microscopy every 30 minutes through the undercut effect on the etch process.

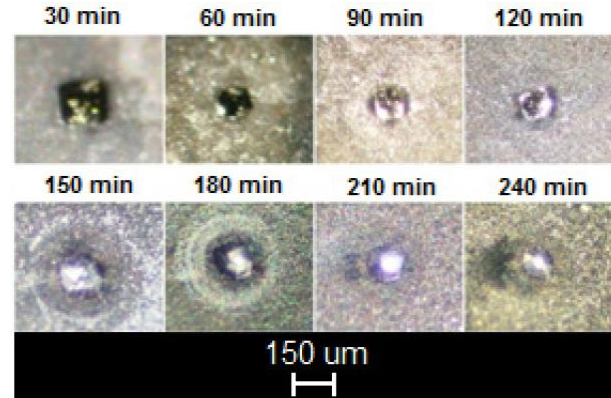


Figure 4: Top view of etching progression stages with 30 minutes intervals.

The etching process employed is anisotropic, with an angle of  $54.7^{\circ}$  between the [111] and the [100] planes. The microtip pyramidal structure due to the anisotropic process is presented in the Figure 5. One can observe the etching of square corners to an hexagonal shape as its final structure. The final microtip was 150-200  $\mu\text{m}$  wider with a height around 100-200  $\mu\text{m}$ .

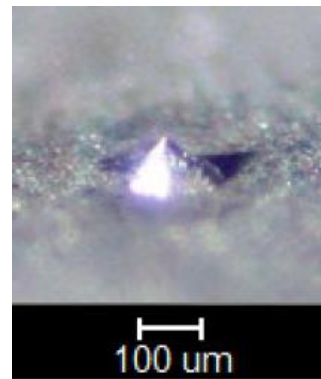


Figure 5: Microtip structure with a pyramidal shape.

#### B. Electrode Characterization

The deposition sessions were done in a *Nordiko NS 2550* sputtering system and pulse generator *ENI RPG-100* at 180 W. The plasma uses argon (Ar) at 100 sccm of flow with a pressure of  $10^{-4}$  Pa. The target of pure iridium (Ir) has a resistivity of  $5.3 \times 10^{-8} \Omega\text{m}$ .

The Table 1 lists the characteristics of the thin-films made of  $\text{IrO}_x$ . The resistivity of the thin-films is one of the main characteristic for determining the quality of the electrode, and it was measured via the *van der Pauw* method [7].

Table 1: The session parameters in the sputtering depositions at frequency of 50 kHz.

O <sub>2</sub> flow (sccm)	2	3.5	6.5	10
Deposition rate (nm/min)	13.5	14	33	28
Thickness (nm)	265	349	526	199
Resistivity ( $\Omega\text{m}\times 10^{-7}$ )	1.926	1.664	2.487	4.914

It would be expected that the increase of O<sub>2</sub> would result in an increase of the films resistivity. Such result would be expected as the increase of O<sub>2</sub> decreases the film purity. However, around 3.5 sccm of O<sub>2</sub>, a lower film resistivity was obtained.

The SEMs in the Figure 6 may induce a justification for the lower resistivity at 3.5 sccm of O<sub>2</sub> flow.

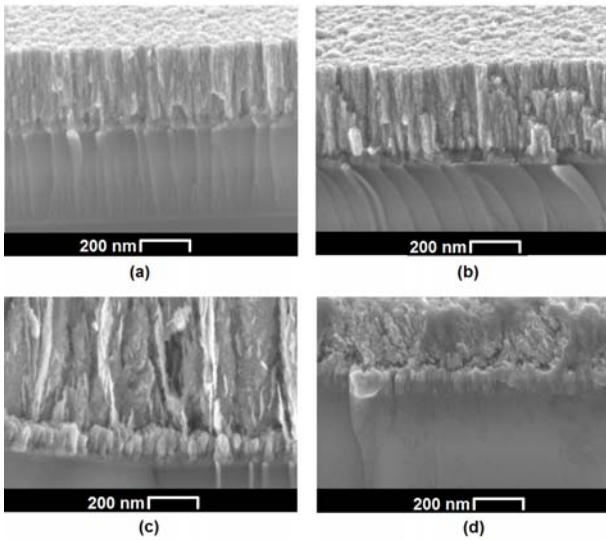


Figure 6: SEM images in cut-view of IrO<sub>x</sub> thin-film deposited at different O<sub>2</sub> flows: (a) 2 sccm; (b) 3.5 sccm; (c) 6.5 sccm; (d) 10 sccm.

Apparently, the transition point between stable and unstable thin-film structures happens with an O<sub>2</sub> flow around 3.5 sccm. It appears that in the region of this O<sub>2</sub> flow, the film permittivity increases ensuring lower resistivity than the other samples. Under this flow, the structure is very consolidated which leads to an increased resistivity. Above this flow, the irregular surface induces the highest resistivity obtained. Consequently, 3.5 sccm was the selected flow for coating the electrodes under evaluation.

The O<sub>2</sub> in IrO<sub>x</sub> allows the utilization of these electrodes for other application besides recording. As IrO<sub>x</sub> has four states of oxidation in reversible chemical reactions, it enables functional stimulation [8].

The Figure 7 shows the variation of current density versus the applied voltage in the IrO<sub>x</sub> thin-films when submerged in a NaCl solution with 0.9 % concentration.

These results allow the evaluation of the electrical activity for stimulation of the IrO<sub>x</sub> dry electrodes. The results showed good electrochemical properties for 2 and 3.5 sccm O<sub>2</sub> flows.

The charge capacity versus the O<sub>2</sub> flow was plotted in Figure 8. The maximum charge capacity occurs for

3-4 sccm of O<sub>2</sub> flow, for a sputtering frequency of 50 kHz.

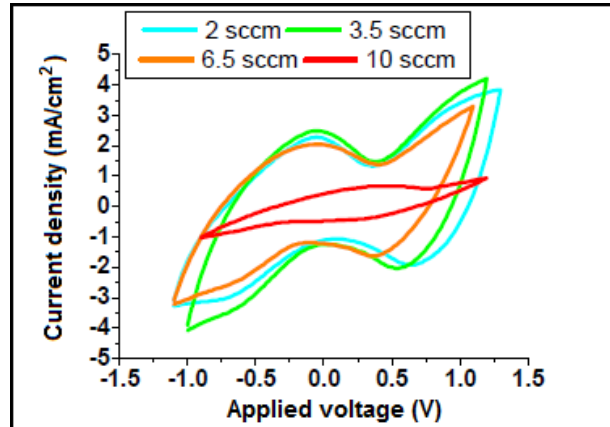


Figure 7: Current density vs. applied voltage for four different O<sub>2</sub> flows at 50 kHz sputtering frequency.

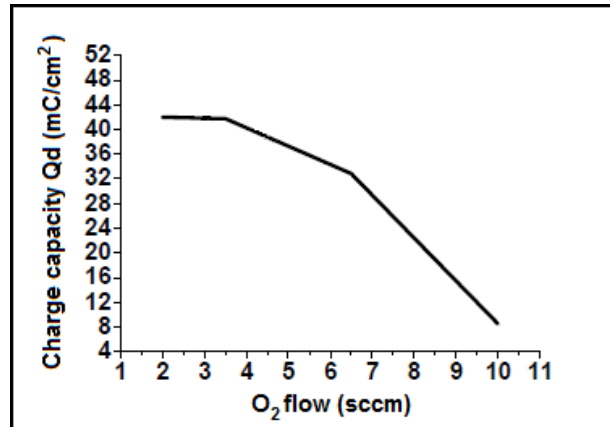


Figure 8: Comparison between charge capacity vs. O<sub>2</sub> flow at 50 kHz.

## V – Conclusions

This paper proposes a non-invasive IrO<sub>x</sub> dry electrode for EEG acquisition fabricated in bulk-micromachining technology. This electrode can avoid the skin preparation with gel due to its microtips structure, which penetrates through the *stratum corneum* layer.

After the fabrication and the characterization of the electrodes, the optimum deposition conditions were obtained for O<sub>2</sub> flows between 2-3.5 sccm and at 50 kHz sputtering frequency. Also, the developed microtips showed a good mechanical behaviour and strength to penetrate the skin.

The iridium oxide had an excellent overall performance not only for biopotential recordings but also functional stimulation application due to charge delivery capacity, low-constant transition impedance and low-resistivity. Thin-films made of IrO<sub>x</sub> demonstrated long-term mechanical stability and good corrosion resistance.

## Acknowledgments

The authors would like to thanks the Portuguese Foundation for Science and Technology for sponsoring the project FCOMP-01-0124-FEDER-010909 (ref<sup>a</sup>. FCT/PTDC/SAU-BEB/100392/2008).

## References

- [1] A. Searle and J. Kirkup, "A direct comparison of wet, dry and insulating bioelectric recording electrodes", *Physiological Measurement*, Vol. 21, pp. 271 – 283, 2000.
- [2] P. Griss, H.K. Tolvanen-Laakso, P. Meriläinen, and G. Stemme, "Characterization of micromachined spiked biopotential electrodes", *IEEE Transactions on Biomedical Engineering*, Vol. 49, pp. 597-604, 2002.
- [3] T.C. Ferree, P. Luu, G.S. Russell, and D.M. Tucker, "Scalp electrode impedance, infection risk, and EEG data quality", *Clinical Neurophysiology*, Vol. 112, pp. 536-544, 2001.
- [4] A. Lebedev and M.A.L. Nicolelis, "Brain-machine interfaces: past, present and future", *TRENDS in Neurosciences*, Vol. 29, No. 9, pp. 536-546, July 2006.
- [5] S. Henry, D.V. Mcallister, M.G. Allen, and M.R. Prausnitz, "Microfabricated Microneedles: A Novel Approach to Transdermal Drug Delivery", *Journal of Pharmaceutical Sciences*, Vol. 87, No. 8, pp. 922-925, August 1998.
- [6] B. Wessling, W. Mokwa, and U. Schnakenberg, "RF-sputtering of iridium oxide to be used as stimulation material in functional medical implants", *Journal of Micromechanics and Microengineering*, Vol. 16, pp. 142–148, 2007.
- [7] L.J. van der Pauw, "A method of measuring the resistivity and Hall coefficient on lamellae of arbitrary shape", *Philips Research Reports*, Vol. 20, pp. 220-224, 1958.
- [8] E. Slavcheva, R. Vitushinsky, W. Mokwa, and U. Schnakenberg, "Sputtered iridium oxide films as charge injection material for functional electrostimulation", *Journal of the Electrochemical Society*, Vol. 151, No. 7, pp. 226-237, May 2004.

# APPLICATION OF SILICON MICRO-NEEDLES IN LIQUID-BASED SENSORS AND VAPOR TRANSPORT

Z. Sanaee and S. Mohajerzadeh

*University of Tehran, School of Electrical and Computer Eng,  
Nano-electronic Center of Excellence, Thin Film and Nano-Electronic Lab,  
Tehran, Iran, mohajer@ut.ac.ir*

**Abstract** — A self-defined method for the formation of hollow needles and micro-cylindrical structures on silicon substrates is reported which uses the combination of high aspect ratio vertical etching of silicon in a hydrogen-assisted reactive ion etching with a small angle vacuum deposition technique. These structures can be used as the media to transfer gas and liquid through their tiny holes. A cavity-based capacitance has been realized with a value 8 pF and the presence of water droplet inside this cavity would raise the capacitance to 10 pF. The capillary force has been minimized using a Cr coating of the inner parts of the holes. The structures have been used to study the transport of vapors where an enhanced transient injection is observed.

**Keywords :** Hollow needles, Slant deposition, Silicon membrane, capacitance, vapor transport

## I - Introduction

Smart drug delivery lends its success to the evolution of hollow micro-needles [1]. The transfer of drug through little holes inside such structures allows a safe replacement for regular injection needles at macroscopic scale, which could cause pain as well as non-programmable injection. The evolution of micro-needles allows the transfer of drug in a programmable fashion and without pain [2]. They have also been proposed as possible electrodes for biological and medical applications [3]. In addition, in electro-cardiograph units the use of microneedles has been investigated as a replacement for applying external gel and skin preparation [4]. Apart from biological applications, the cup-like structures can be used as gas and vapor transfer media for mass spectroscopy and as an ionization source [5].

Silicon micromachining has been an important step in realizing complex high aspect ratio features. Deep reactive ion etching (DRIE) of silicon has been used to form silicon-based structures. Recently we have developed a modified deep reactive ion etching technique which replaces the polymeric passivation in Bosch process by a combination of hydrogen/oxygen and  $\text{SF}_6$  gases to obtain high aspect ratio features [6].

In this paper, we use our high-resolution vertical etching process, to realize needles at deep micrometer and nanometer scale. Depending on the process, the formation of hollow needles or cup-like structures is possible using a self-defined slant angle deposition and with no need to a three-dimensional lithography. The fabricated structures have been exploited to realize a

liquid-based inclination sensor. In addition the transport of various vapors such as acetone and alcohol show an abnormal behavior which could be due to an enhanced transient injection. The physical characteristics of the fabricated structures has been studied using Hitachi SE4160 filed emission scanning electron microscope operating at 15-30kV and with secondary electron spectroscopy.

## II - Experimental Details

For these investigations, single-side polished p-type  $\langle 100 \rangle$ -oriented Si substrates with a resistivity of 1-5ohm-cm and a thickness of 520 $\mu\text{m}$  are used. The silicon wafers are cleaned using an RCA#1 solution ( $\text{NH}_4\text{OH}:\text{H}_2\text{O}_2:\text{H}_2\text{O}$ , 1:1:5) for 12mins followed by rinsing in de-ionized water and blow-drying. The cleaned samples are placed in an e-beam evaporation unit to deposit a 40 nm chromium layer as the mask for the subsequent processing steps. For this investigation features of the order of 2 $\mu\text{m}$  and inner diameter of 0.5 $\mu\text{m}$  have been realized. These features are circular rings and the high precision lithography allows the formation of rims with a width well below 0.6 $\mu\text{m}$  that can be further reduced to values of the order of 200nm with an extra step of oxygen plasma ashing.

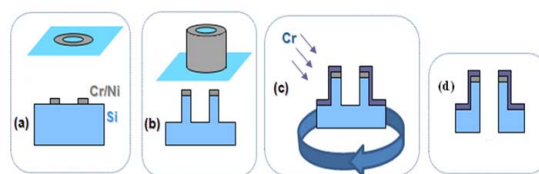


Figure 1: Schematic process flow for the formation of hollow needles and cuplike structures, (a) formation of rings, (b) vertical etching of Si and (c) deposition of Cr using a rotating small angle deposition method to coat the outer sides of the recessed craters while inner parts and especially the inner bottom remains uncoated. (d) For hollow needle formation, the vertical etching process continues on the silicon membrane to realize via holes.

Figure 1 demonstrates the procedure for the formation of hollow needles or cup-like structures on silicon membranes. The creation of hollow needles requires fabrication of Si membranes using standard anisotropic etching in a KOH solution. For this step a 30% molar solution of KOH in water is used at a temperature of 60°C. A combination of  $\text{SiO}_2/\text{Si}_3\text{N}_4/\text{Cr}$  layers with respective thicknesses of 200/300/400 nm is suitable for



protection during this long etching process.  $\text{Si}_3\text{N}_4$  is deposited using a low-pressure chemical vapor deposition at  $800^\circ\text{C}$  using a mixture of  $\text{SiH}_4$  and  $\text{NH}_3$  diluted in  $\text{H}_2$  with gas flows of 10, 25 and 100 sccm, respectively.

As seen from Fig. 1, the formation of hollow structures continues by an etching process from the top surface of the silicon substrate. Once the desired ring-like features are created on the top Cr layer, the silicon is removed in a vertical fashion and by means of a our recently developed deep reactive ion etching [6]. Following the vertical etching step, one can arrive at cup-like cylindrical structures where the bottom of the recessed features is not hollow. As seen in parts (c) and (d) of Fig. 1, the formation of hollow structures requires coating the whole silicon surface except for the very bottom of the inner part of the circular cylinders. Since for this purpose, lithography is not easy with high aspect ratio features and especially for sub-micrometer structures, we used a rotating small angle deposition method to coat the outer walls as well as the outer surfaces of the silicon substrate selectively, while leaving the inner bottom of the little cylindrical features uncoated.

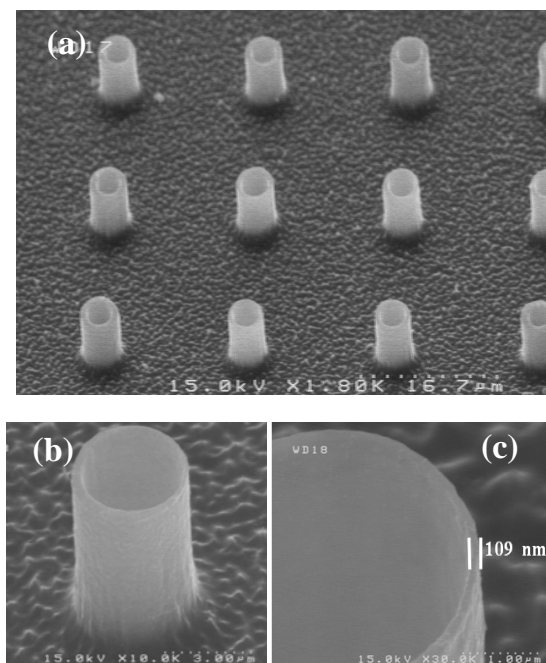


Figure 2: The formation of hollow-needle and cup-like structures on silicon substrates with high aspect ratio features. (a) the array of hollow structures, (b) a close view at one of the features and (c), the formation of side-walls with 100nm width, while the height is 7 $\mu\text{m}$ .

The vertical etching of silicon can proceed with no need to a lithography step and at this stage, only the inner side is etched away to achieve hollow silicon needles. The overall depth of the needles depends on the original thickness of the silicon-based membrane. Figure 2 shows the SEM images of several cup-like structures with ultra-fine features made on a silicon substrate. The formation of side-walls with 109nm

width and a height of 7-10 $\mu\text{m}$  is possible. The fabrication process has been implemented both on silicon substrates and silicon membranes. Figure 3 collects the SEM images of hollow needles on a silicon membrane where the inner diameter of the holes is 15 $\mu\text{m}$ . The thickness of the membrane is set to be 30 $\mu\text{m}$ .

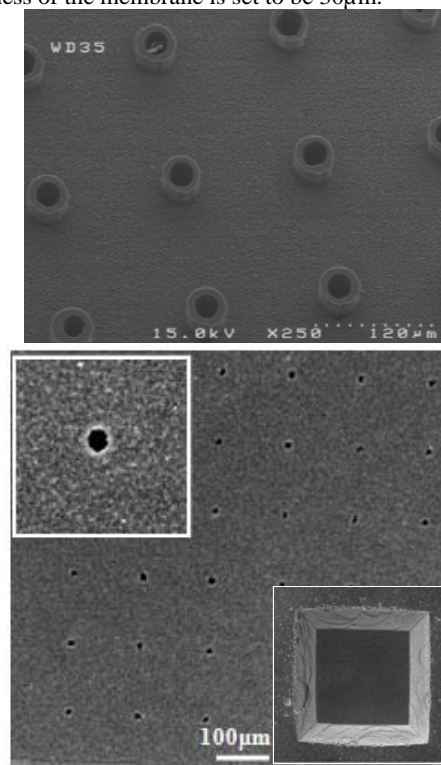


Figure 3: (Top) the formation of array on the same membrane from the top side. (bottom) the SEM image of the backside of the Si membrane where the micro-needles are placed on its front side. Insets in this figure show the evolution of holes as well as the crystallographic etching of the whole membrane.

### III - Results and Discussion

Since the silicon membrane is part of a cavity, it can be filled with a proper liquid to observe the penetration of liquid through the little hollow needles. The fully etched holes can be used as possible liquid-based capacitors. By first oxidizing the needle-containing silicon sample followed by depositing a metal layer (Cr here) on the backside of the membrane, one can form a capacitor between the silicon membrane and an opposite plate located just on top of the silicon substrate. This deposition step has been carried out in an e-beam evaporation technique while the substrate is placed in the line of sight of the source. Figure 4 shows, schematically how this capacitor is formed and how a liquid can be inserted into the cavity to affect the value of the capacitance. The capacitance is formed between the backside of the silicon membrane and the top electrode, which is a piece of glass coated with chromium and patterned. The value of the capacitor depends on the

thickness of the membrane and the height of the cylindrical needles. By inserting a water droplet onto the cavity, part of the water would penetrate through the hole and as a result, the total value of the capacitance would rise. This is mainly because the relative permittivity of water ( $\epsilon$ ), which has been inserted into the hole, is far more than silicon and air.

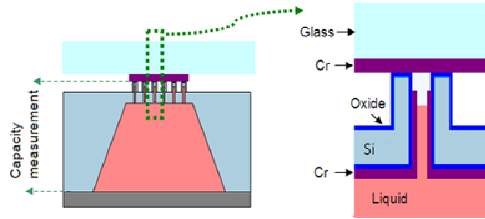


Figure 4: Schematic presentation of liquid-stimulated capacitance measurement. Inclusion of a water droplet into the backside cavity of the sample would yield in the penetration of liquid into the little holes, increasing the effective permittivity ( $\epsilon$ ) which in turn leads to an increase in the capacitance value.

Since the inner diameter of the holes is quite small, the capillary force becomes quite significant, hampering the operation of the device. We have used a Cr coating step to alleviate this effect. Figure 5 presents an optical image of a Cr-coated silicon/SiO<sub>2</sub> surface where a droplet of water has been placed on it. The wetting angle is measured to be around 90 degree which seems most suitable for the capacitance measurement. As a consequence and under similar conditions, the capillary force becomes negligible.

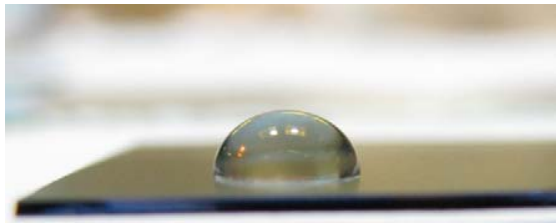


Figure 5: The formation of water droplet on a Cr-plated surface, indicating a 90-degree angle where the capillary force becomes negligible.

Figure 6 collects the results of capacitance voltage characteristics of the samples before and after water inclusion. The capacitance value remains around 8 pF for the dry sample (bottom curve in part (a)) whereas the wetted sample shows a rise to 10 pF because of raising water through the little holes (the top curve). To highlight this anomalous behavior even better we have re-plotted the top curve and presented it in part (b) of this figure. As seen from this figure, the capacitance shows a local decrease at values close to zero which is believed to be due to the extension of depletion region at the sidewall silicon body. We have also tilted the sample with a small angle of 5 degree and repeated the capacitance measurement, as seen in part (c) of this figure. The value of the capacitance shows a higher rise

to 13 pF due to further penetration of water into micro-needle holes.

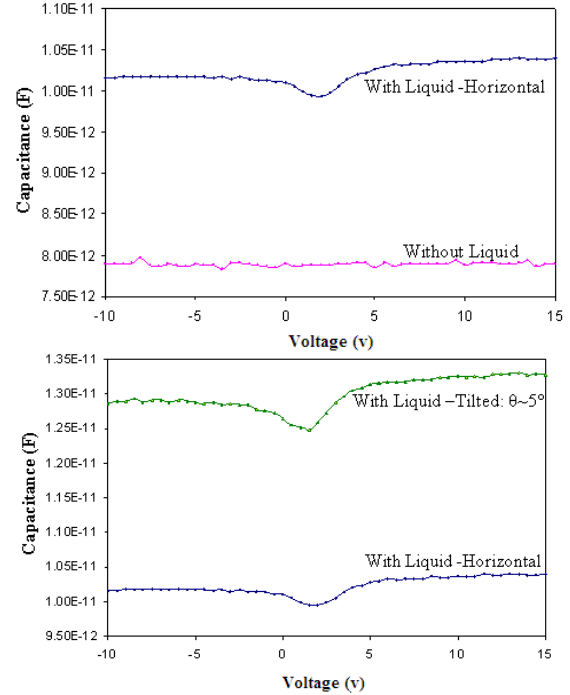


Figure 6: Capacitance voltage characteristics of the liquid-stimulated capacitor. (a) C-V with and without liquid. (b) The measured C-V results in the presence of water and after a slight tilt. A significant increase is observed in the value of the capacitance as a result of the tilting.

In Fig. 7 the results of the measured capacitance with respect to the inclination angle has been plotted showing the high sensitivity of the device. It has been observed that at tilts higher than 10 degrees, the capacitance shows an abnormal behavior which could be due to the leakage of water through the holes into the upper surfaces which hampers the electrical performance of the device. Further investigation of the water penetration through these needles and their side effects are being pursued.

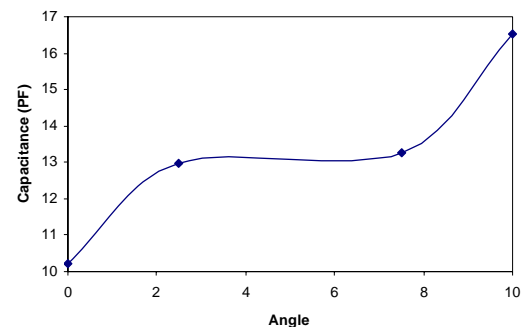


Figure 7: Sensor response to tilting. For values above 10 degree, a sharp and abnormal rise in the capacitance is observed which could be due to water penetration through the hole into the upper surfaces, hampering the electrical response of the device.

# Metallic layer for EM Pressure Sensor Sensitivity Improvement

Sofiene Bouaziz<sup>1,2</sup>, Mohamed Mehdi Jatlaoui<sup>1</sup>, Ding Mingli<sup>1</sup>, Patrick Pons<sup>1</sup>, and Hervé Aubert<sup>1,2</sup>

<sup>1</sup> CNRS ; LAAS ; 7 avenue du Colonel Roche, F-31077 Toulouse, France

<sup>2</sup> Université de Toulouse ; INP ; LAAS ; F- 31077 Toulouse, France

## Abstract

Passive wireless electromagnetic pressure sensor with very high sensitivity has been designed (250MHz/ $\mu\text{m}$ ). This result has been obtained by adding a thin metallic layer on the top side of the silicon membrane in order to improve the coupling between the coplanar resonator and the membrane.

**Keywords :** Passive Pressure sensor, Electro-magnetic Transduction

## I- Introduction

Today, the demand for wireless sensors is growing hugely to address in particular sensors network applications [1-2]. But for several cases, the sensors life time is limited by embedded energy. In order to overcome this problem, passive wireless sensors have been developed as Radio Frequency IDentification (RFID) tags and Surface Acoustic Wave (SAW [3-4]. But the main drawback of these sensors is the low interrogation distance.

In previous works, reported by the authors, the functioning and feasibility of an electromagnetic pressure sensor has been validated [5]. The sensor will be remotely interrogated by an FMCW radar reader. The interrogation technique is based on the correlation between the RCS (Radar Cross Section) level measurement and the applied pressure [6-7].

The purpose of this paper is to improve the sensor sensitivity to pressure by adding a metallic layer on the top of the silicon membrane.

## II- Sensor principle and design

The sensor is based on a coplanar metallic resonator, deposited inside a Pyrex cavity (Figure 1, Figure 2). A high resistivity silicon membrane, bonded upper the resonator, modifies the resonance frequency. This frequency shift is linked to the membrane deflection which induces a change in the effective permittivity inside the structure [1].

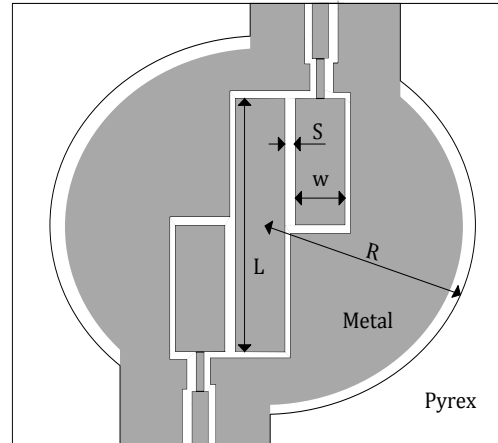


Figure 1 : Coplanar quarter wave coupled line resonator in Pyrex circular cavity

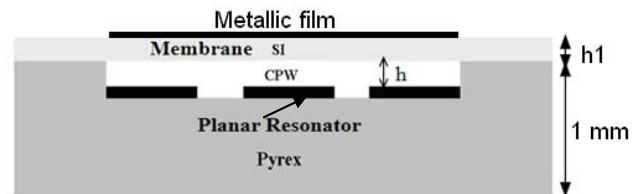


Figure 2 : Cross section of the EM sensor

To be in the FMCW radar frequency range (26~29.8GHz), the length (L) of the coplanar quarter wave coupled lines resonator is kept to 2300 $\mu\text{m}$ . To obtain a 50 $\Omega$  line, the resonator width (w) is equal to 300 $\mu\text{m}$  and the gap (s) separating lines is fixed at 10 $\mu\text{m}$ . The circular Pyrex cavity radius (R) is equal to 1700 $\mu\text{m}$ , while, the thickness of air gap (h) is kept at 6 $\mu\text{m}$  without deflection.

The membrane thickness (h1) used in this study is chosen to 50 $\mu\text{m}$  to cover 0 to 6bar pressure range. A metallic layer is added on the top side of the silicon membrane to improve the coupling between the membrane and the resonator and then to improve the sensor sensitivity.

### III- Results

Ansoft HFSS (High Frequency Structure Simulator) has been used to quantify the impact of this metallic film on the sensor response.

Preliminary simulations have shown that 0.8μm thick metal layer is necessary to suppress the EM field outside the silicon membrane. *Figure 3* and *Figure 4* present a cross sectional views of the E-field distribution for the sensor structure respectively without and with a metallic layer (0.8μm thick) on the top side of the membrane. It's clearly shown that without metallic layer, a part of the E-field is going through the membrane to be finally radiated in the air. With metallic patch on the top side of the membrane, the E-field is still confined inside the structure and precisely in the air gap above the central line. In this case, the E-field magnitude is notably increased.

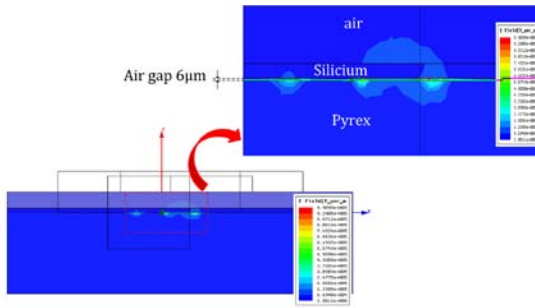


*Figure 3 : E-field density distribution in a cross section view (without metallic layer)*

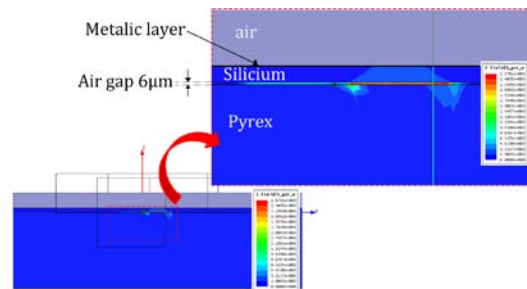


*Figure 4 : E-field density distribution in a cross section view (with metallic layer 0.8μm thick)*

HFSS simulations have been performed taking into account the real membrane deflection under hydrostatic pressure. The deflection for a circular membrane is modeled by:

$$W(r) = W_0 \cdot W_N(r) \quad (1)$$

Where  $W_0$  is the maximum deflection in the center of the membrane and  $W_N(r)$  is a function of the radius position (r).  $W_0$  and  $W_N(r)$  can be written as:

$$W_0 = \frac{12 R^4 (1 - \nu^2)}{64 E h_1^3} P; W_N(r) = \left(1 - \frac{r^2}{R^2}\right)^2 \quad (2)$$

Where  $P$  is the pressure,  $E$  is Young modulus and  $\nu$  is Poisson's ratio.

The normalized deflection ( $W_N$ ) has been introduced in HFSS through analytical description. The center deflection ( $W_0$ ) is taken as an input parameter.

*Figure 5* and *Figure 6* show the simulated  $S_{11}$  parameter versus frequency for different membrane deflection values. We can see that the metallic layer increase both the resonance frequency shift and the quality factor.

*Figure 7* compares the resonance frequency shift versus the center deflection ( $W_0$ ) with and without the metallic layer. The metallic layer improves the sensor sensitivity by a factor 2.5 (100MHz/μm to 250MHz/μm).

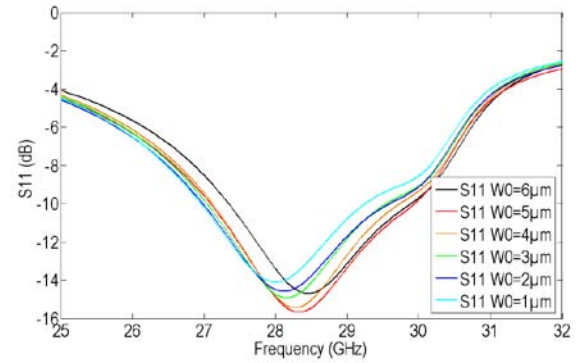


*Figure 5: Simulated S parameters under different deflections (without metallic layer).*

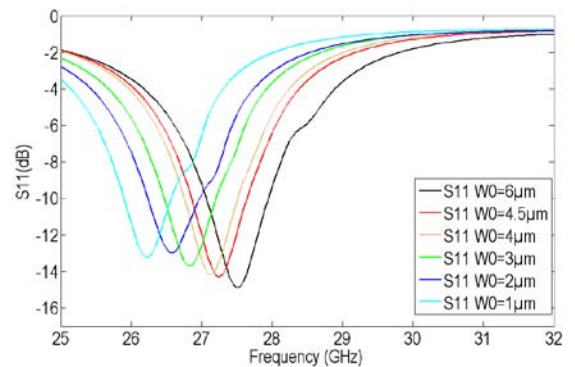


*Figure 6: Simulated S parameters under different deflections (with metallic layer)*



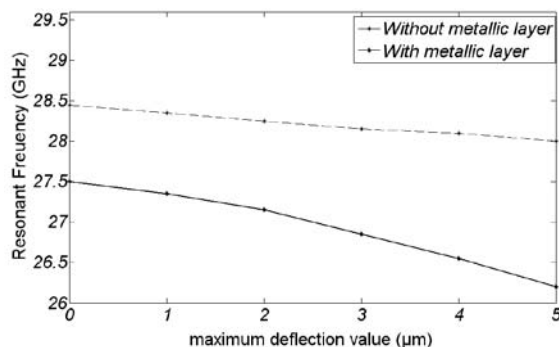


Figure 7: Simulated resonance frequency shift with and without metallic layer

#### IV- Conclusion

Previous work, reported by the authors, demonstrated the feasibility of such original pressure micro-sensor based on EM transduction. We have shown here that the sensor sensitivity can be improved hugely by adding a metallic layer on the upper side of the silicon membrane.

Ongoing studies are focused on the impact of the metallic layer for different silicon membrane thicknesses, in order to identify if there is an optimum configuration to improve the sensor sensitivity.

#### V- References

- [1] Sir Magdi Yacoub, 'Body Sensor Networks', Springer-Verlag London Limited 2006
- [2] Elena Gaura & Robert Newman, 'Smart MEMS and Sensor Systems', 2006 by Imperial College Press.
- [3] Leonhard Reindl, Gerd Scholl, Thomas Oster-tag, Holger Scherr, Ulrich Woland Frank Schmidt, 'Theory and Application of Passive SAW Radio Transponders as Sensors', IEEE transactions on ultrasonics, ferroelectrics, and frequency control, vol. 45, no. 5, september 1998.
- [4] Alfred Pohl, 'A Review of Wireless SAW Sensors', IEEE transactions on ultrasonics, ferroelectrics, and frequency control, vol. 47, no. 2, march 2000.
- [5] M.M.Jatlaoui, F. Chebila, I.Gmati, P.Pons, H.Aubert. "New Electromagnetic Transduction Micro-sensor Concept For Passive Wireless Pressure Monitoring Application" The 15th Conference on Solid-State Sensors, Actuators & Microsystems, Transducers 2009, June 21-25 2009, Denver, Colorado, USA.
- [6] M. M. Jatlaoui, F. Chebila, P. Pons, H. Aubert, "Pressure Sensing Approach Based on Electromagnetic Transduction principal", 2008

IEEE Asia Pacific Microwave Conference, pp. 16-19, Hong Kong, December 2008.

- [7] M. M. Jatlaoui, F. Chebila, P. Pons, H. Aubert, "Original Identification technique of passive EM Sensors using Loaded Transmission Delay Lines", The 13th European Microwave Week 2010, Paris.

# MICROFABRICATION AND CHARACTERIZATION OF THIN-FILMS SOLID-STATE RECHARGEABLE LITHIUM BATTERY

J. F. Ribeiro<sup>1</sup>, M. F. Silva<sup>1</sup>, L. M. Goncalves<sup>1</sup>, M. M. Silva<sup>2</sup>, and J. H. Correia<sup>1</sup>

<sup>1</sup>University of Minho, Algoritmi Centre, Guimarães, Portugal

<sup>2</sup>University of Minho, Chemistry Centre, Braga, Portugal

**Abstract** — This paper presents the microfabrication and materials characterization of thin-film solid-state rechargeable lithium batteries. Film solid-state batteries are ideal power sources for stand-alone microsystems where a high-level of integration is required. Solid-state thin-film batteries are intrinsically safe, have a larger life cycle, a faster charge/discharge cycling and a bigger capacity by  $\text{cm}^3$  than the conventional ones. The fabrication materials used are  $\text{LiCoO}_2$ , LIPON and metal lithium in cathode, electrolyte and anode respectively. The  $\text{LiCoO}_2$  and LIPON films were deposited by RF magnetron sputtering technique and the metal lithium by thermal-evaporation technique.

**Keywords** : Solid-state films battery, integrated batteries, energy-harvesting microsystems

## I - Introduction

There is a great interest in size reduction of batteries due it integration with portable microsystems [1-2] for biomedical Microsystems [3-4] such as wireless neural electrodes [5]. Solid-state batteries are intrinsically safe and have advantages in life time, capacity, power and cost [6-7].

In this paper a battery fabricated by thin-film techniques in a Si (silicon) substrate is presented. The materials used are  $\text{LiCoO}_2$  (lithium-cobalt oxide), LIPON (lithium-phosphorus oxynitride) and metal Li (lithium), for the cathode, electrolyte and anode respectively. Platinum current collectors of cathode and anode ensure good electrical contact without reacting with the electrodes. A silicon-nitride ( $\text{Si}_3\text{N}_4$ ) encapsulation ensures oxidation protection. An artwork of the battery is presented in Figure 1. The  $\text{LiCoO}_2$  is the material commonly used as cathode in batteries [8, 9] because of the good electrochemical cycling stability and the capacity of insertion and extraction of  $\text{Li}^+$  ions without losing the structural stability [10].

The solid electrolyte ensures the intrinsically safe operation. LIPON is a good alternative due to its high-electrical resistivity and high-ionic conductivity. A good electrochemical stability in contact with lithium also makes the LIPON an excellent material for electrolyte in solid-state batteries [11, 12, 13].

The anode of battery is metallic Li because it exhibits the highest capacity and discharge rate [14], despite the fast oxidation in contact with air.

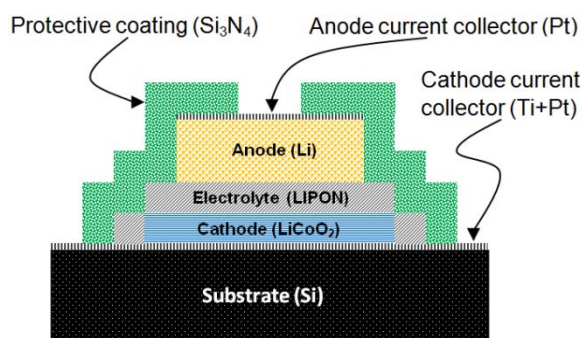


Figure 1: Artwork of the battery, with  $\text{LiCoO}_2$  cathode, LIPON electrolyte and Li anode, between Pt current collectors, covered by a protective  $\text{Si}_3\text{N}_4$  film.

## II - Fabrication Details

The active material of the battery was deposited using PVD (Physical Vapor Deposition) techniques in a [100] silicon substrate. The platinum cathode current collector with 70 nm thick was deposited by E-Beam technique. In order to improve adhesion between silicon and platinum, a 30 nm thick titanium layer was deposited between them by the same technique.

The cathode of the battery was deposited by RF magnetron sputtering technique (a RF power source 13.56 MHz at 150 W, a pressure of 0.2 Pa in a 30 sccm flow of Ar and 10 sccm flow of  $\text{O}_2$ ). A  $\text{LiCoO}_2$  target was used for depositing a layer 1  $\mu\text{m}$  thick. A crystalline structure of  $\text{LiCoO}_2$  is desirable for a good cathode. Three different temperatures were tested (873 K, 973 K and 1023 K) and crystalline structure compared in: 30 min annealing at vacuum atmosphere.

Electrolyte (LIPON) was deposited by RF magnetron sputtering technique (a layer 1  $\mu\text{m}$  thick). A  $\text{Li}_3\text{PO}_4$  target was used in a 20 sccm reactive nitrogen flow. The power source (13.56 MHz) was biased at 200 W and three different pressures were tested (Table 1).

Table 1: Parameters used in LIPON deposition

LIPON film	Target	$\text{N}_2$ (SCCM)	RF power (W)	Pressure (Pa)
#1	$\text{Li}_3\text{PO}_4$	20	200	1
#2	$\text{Li}_3\text{PO}_4$	20	200	0.7
#3	$\text{Li}_3\text{PO}_4$	20	200	0.3

The anode of the battery (metallic Li) was deposited by thermal evaporation. The platinum anode current collector, with 100 nm thick was deposited by e-beam. The protection layer,  $\text{Si}_3\text{N}_4$  film, was deposited by low-temperature CVD [15].

### III – Experimental Results

#### A. $\text{LiCoO}_2$ films

After annealing,  $\text{LiCoO}_2$  films exhibit a polycrystalline structure with strong orientation in the [104] planes and fewer at [003] and [101] planes [16]. This structure improves the ion diffusion. Figure 2 shows the X-ray diffraction pattern (XRD).

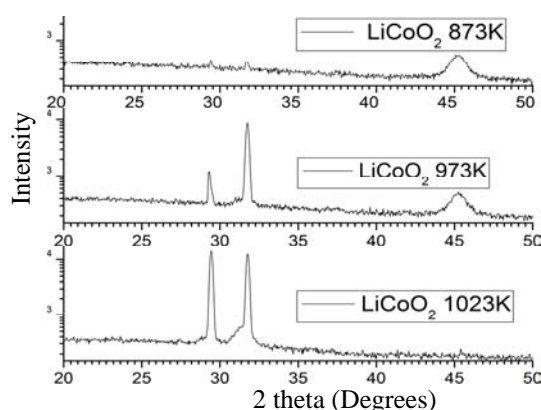


Figure 2: XRD diffraction of  $\text{LiCoO}_2$  films after annealing at temperatures of 873, 973 and 1023 K.

A SEM image of  $\text{LiCoO}_2$  film was also performed and can be seen in Figure 3. The in-plane resistivity of  $2.5 \Omega\text{cm}$  was measured using the Van der Pauw technique (Figure 4). The  $\text{LiCoO}_2$  cathode has a capacity of  $140 \text{ mAhg}^{-1}$  (about 1 Li per 2  $\text{CoO}_2$ ).

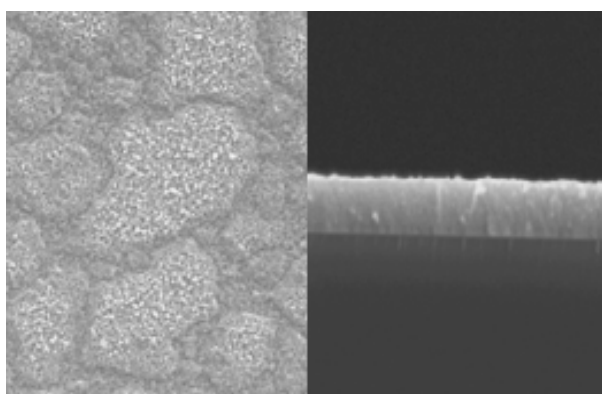


Figure 3: Cross-section and surface SEM images of  $\text{LiCoO}_2$  film.

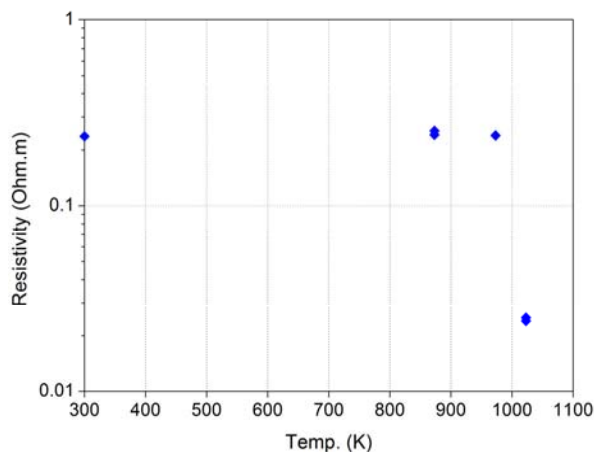


Figure 4: Resistivity of  $\text{LiCoO}_2$  films, as function of annealing temperature (left point represents the deposition without annealing). The resistivity decreases with temperature annealing above 1000 K.

#### B. LIPON films

The deposition pressure in LIPON depositions was correlated with ionic conductivity. The ionic conductivity of LIPON was measured with Nyquist diagrams of impedance, performed at different temperatures (Figure 5).

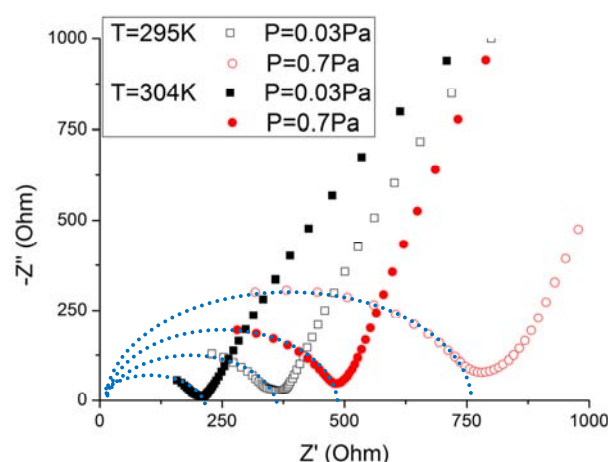


Figure 5: Nyquist (impedance) diagram of LIPON films, deposited at  $\text{N}_2$  pressures of 0.03 (#3) and 0.7 Pa (#2), measures at temperatures of 295 K and 304 K. Dashed lines show fitting for ionic conductivity calculation.

When the dashed lines in Nyquist diagram of impedance cross the x-axis, the resistivity of the film at different conditions of pressure and temperature can be measured. The best result of ionic conductivity of LIPON was achieved with a pressure of 0.03 Pa (#3) and a temperature of 304 K. The best ionic conductivity was achieved between  $10^{-7}$  and  $10^{-6} \text{ Scm}^{-1}$  (Figure 6).

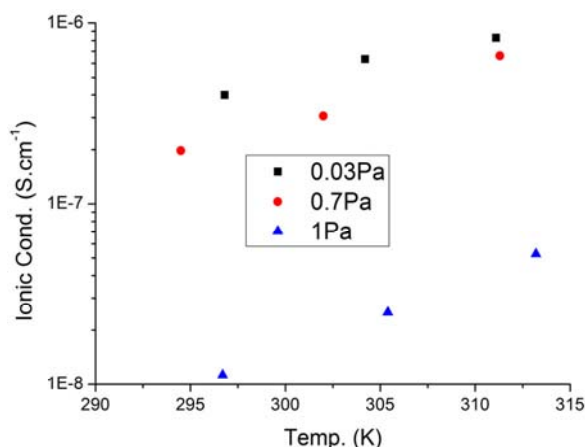


Figure 6: Ionic conductivity of LIPON deposited at  $N_2$  pressures of 0.03 (#3), 0.7 (#2) and 1 Pa (#1) measured in temperature range of 295-315 K.

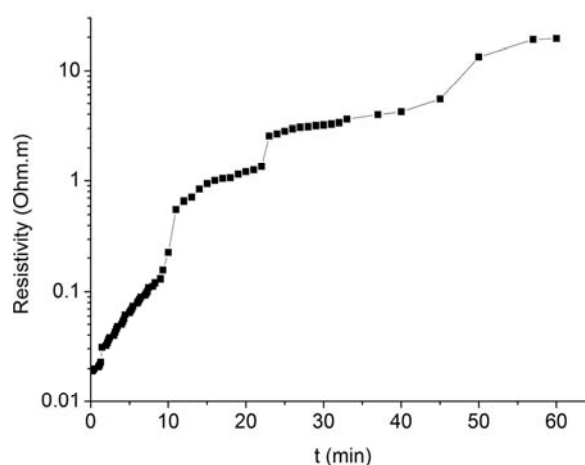


Figure 8: Resistivity of Li as function of time at room atmosphere.

### C. Li Films

The Li resistance was measured during the deposition using a four point setup and values between 2.5  $\Omega$  and 3.5  $\Omega$  were measures for 3  $\mu\text{m}$  thick layers (Figure 7).

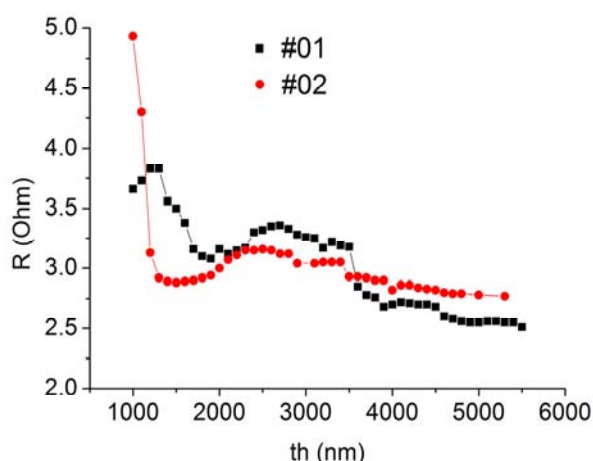


Figure 7: Resistance of Li in function of thickness during the deposition.

After the deposition, the resistivity of Li was measured at room atmosphere without any protective layer in order to evaluate the oxidation of Li (Figure 8). Results show that a protective layer is essential to keep the battery functional.

### IV - Conclusions

This paper presented the microfabrication and characterization of materials for thin-films solid-state rechargeable lithium battery. RF magnetron sputtering, e-beam and low-temperature CVD was used in the deposition of the layers. The battery is composed of a  $\text{LiCoO}_2$  cathode, a LIPON electrolyte and a Li anode. The contacts are made of Pt to avoid unwanted reactions. A  $\text{Si}_3\text{N}_4$  protective layer protects the battery layers.

$\text{LiCoO}_2$  films show different phases, as function of annealing temperature. Best results were obtained with annealing on vacuum, at temperature above 1000 K. A resistivity of 2.5  $\Omega\text{cm}$  was measured. The best LIPON films have an ionic conductivity of  $2\text{E}^{-6} \text{ S cm}^{-1}$ , deposited at 20 sccm flow of  $N_2$  and 0.03 Pa of pressure. The Li anode deposited by thermal evaporation has a low resistivity (0.02  $\Omega\text{cm}$ ), however, a rapid oxidation occurs in contact with atmosphere. These materials have good properties as standard large-sized batteries, and are suitable for the fabrication of lithium thin-film batteries.

Thin-films solid-state rechargeable battery show a high-cycle life, a high charge/discharge rate and are intrinsically safe. This is a special concern in biomedical applications such as wireless neural microsystems.

### Acknowledgements

The authors would like to thanks the Portuguese Foundation for Science and Technology for sponsoring the project FCOMP-01-0124-FEDER-007226 (with the previous reference PTDC/EEA-ENE/66855/2006) and FCOMP-01-0124-FEDER-010909 (with the previous reference FCT/PTDC/SAU-BEB/100392/2008), and CRIOLAB company.



## References

- [1] J. P. Carmo, R. P. Rocha, A. F. Silva, L. M. Gonçalves, and J. H. Correia, A thin-film rechargeable battery for integration in stand-alone microsystems, *Procedia Chemistry*, vol. 1, pp. 453-456, 2009.
- [2] G. Nagasubramanian, and D. H. Doughty, Electrical characterization of all-solid-state thin film batteries, *Journal of Power Sources*, vol. 136, pp. 395-400, 2004.
- [3] Roger Latham, Roger Linford, and Wasliria Schlindwein, Biomedical applications of batteries, *Solid State Ionics*, vol. 172, pp. 7-11, 2004.
- [4] Peter H. L. Notten, Fred Roozeboom, Rogier A. H. Niessen, and Loïc Baggetto, 3-D Integrated All-Solid-State Rechargeable Batteries, *Advanced Materials*, vol. 19, pp. 4564-4567, 2007.
- [5] João Paulo Carmo, Nuno Sérgio Dias, Helder Raul Silva, Paulo Mateus Mendes, Carlos Couto, and José Higino Correia, A 2.4-GHz Low-Power/Low-Voltage Wireless Plug-and-Play Module for EEG Applications, *IEEE Sensors Journal*, vol. 7, pp. 1524-1531, 2007.
- [6] M. Armand, and J. M. Tarascon, Building better batteries, *Nature*, vol. 451, pp. 652-657, 2008.
- [7] Colin A. Vincent, Lithium batteries: a 50-year perspective, 1959–2009, *Solid State Ionics*, vol. 134, pp. 159-167, 2000.
- [8] H. Y. Park, S. R. Lee, Y. J. Lee, B. W. Cho, and W. I. Cho, Bias sputtering and characterization of Li-CoO<sub>2</sub> thin film cathodes for thin film microbattery, *Materials Chemistry and Physics*, vol. 93, pp. 70-78, 2005.
- [9] Jong-Ki Lee, Seung-Joo Lee, Hong-Koo Baik, Heon-Young Lee, Serk-Won Jang, and Sung-Man Leeb, Substrate Effect on the Microstructure and Electrochemical Properties in the Deposition of a Thin Film LiCoO<sub>2</sub> Electrode, *Electrochemical and Solid-State Letters*, vol. 2, pp. 512-515, 1999.
- [10] L. Predoana, A. Barau, M. Zaharescu, H. Vasilchina, N. Velinova, B. Banov, A. Momchilov, Advanced Techniques for LiCoO<sub>2</sub> Preparation and Testing, *Proceedings of the International Workshop "Advanced Techniques for Energy Sources Investigation and Testing"*, Sofia, Bulgaria, September 4 – 9, 2004.
- [11] Y. Hamon, A. Douard, F. Sabary, C. Marcel, P. Vinatier, B. Pecquenard, A. Levasseur, Influence of sputtering conditions on ionic conductivity of LiPON thin films, *Solid State Ionics*, vol. 177, pp. 257-261, 2006.
- [12] Ho Young Park, Sang Cheol Nam, Young Chang Lim, Kyu Gil Choi, Ki Chang Lee, Gi Back Park, Seong-Rae Lee, Heesook Park Kim, and Sung Baek Cho, Effects of sputtering pressure on the characteristics of lithium ion conductive lithium phosphorous oxynitride thin film, *Journal Electroceram*, vol. 17, pp. 1023-1030, 2006.
- [13] W. C. West, J. F. Whitacre, and J. R. Lim, Chemical stability enhancement of lithium conducting solid electrolyte plates using sputtered LiPON thin films, *Journal of Power Sources*, vol. 126, pp. 134-138, 2004.
- [14] N. J. Dudney, B. J. Neudecker, Solid state thin-film lithium battery systems, *Solid State and Materials Science*, vol. 4, pp. 479-482, 1999.
- [15] P. Alpuim, L. M. Gonçalves, E. S. Marins, T. M. R. Viseu, S. Ferdov, J. E. Bourée, Deposition of silicon nitride thin films by hot-wire CVD at 100 °C and 250 °C, *Thin Solid Films*, vol. 517, pp. 3503-3506, 2009.
- [16] J. B. Bates, N. J. Dudney, B. Neudecker, A. Ueda, and C. D. Evans, Thin-film lithium and lithium-ion batteries, *Solid State Ionics*, vol. 135, pp. 33-45, 2000.

## DETERMINATION OF YOUNG'S MODULUS OF PZT – INFLUENCE OF CANTILEVER ORIENTATION

H. Nazeer<sup>1</sup>, L.A. Woldering<sup>1</sup>, L. Abelman<sup>1</sup> and M.C. Elwenspoek<sup>1,2</sup>

<sup>1</sup>MESA+ Research Institute, University of Twente, P.O. Box 217, 7500 AE Enschede, The Netherlands

<sup>2</sup>FRIAS, Albert-Ludwigs University, Albertstr. 19, 79104 Freiburg, Germany

**Abstract** — Calculation of the resonance frequency of cantilevers fabricated from an elastically anisotropic material requires the use of an effective Young's modulus. In this paper a technique to determine the appropriate effective Young's modulus for arbitrary cantilever geometries is introduced. This technique is validated using a combined analytical and finite element simulations (FEM) approach. In addition, the effective Young's modulus of  $\text{PbZr}_{0.52}\text{Ti}_{0.48}\text{O}_3$  (PZT) thin films deposited on dedicated micromachined cantilevers was investigated experimentally. The PZT films were deposited on the cantilevers by pulsed laser deposition (PLD). The change in flexural resonance frequency of the cantilevers was measured both before and after deposition of the PZT thin film. From this frequency difference we determined the Young's modulus of PZT deposited by PLD to be  $103 \pm 2$  GPa. Even though the PZT is grown epitaxially, this value is independent of the in-plane orientation.

**Keywords:** Cantilever, resonance frequency, anisotropic, Young's modulus, FEM, PZT, PLD.

### I – Introduction

Piezoelectric thin films are widely used in the MEMS industry for both actuation and sensing purposes [1, 2]. Many micro sized structures such as cantilevers, membranes and bridges have been employed for fabrication of the micro sensors and actuators using PZT thin films as an active material. These PZT films can be deposited by processes [3] like sol-gel, sputter deposition and pulsed laser deposition. Recently, excellent ferroelectric properties have been published about PZT deposited by PLD [4]. However, accurate determination of the mechanical properties of the PZT thin film is being hampered by the fact that up to now only mm-square areas can be deposited uniformly. Micrometer sized measurement devices provide a solution to this limitation.

The effective Young's modulus of the thin film is an important parameter to be known accurately when designing micro transducers. We devised a method to accurately determine the Young's modulus of PZT thin films by using the shift in the resonance frequency of cantilevers. An analytical relation for the determination of the effective Young's modulus of the PZT thin film was developed and experiments were conducted to measure the resonance frequency of cantilevers both before

and after the deposition of PZT thin films.

We took extra care to eliminate the errors in the determination of the effective Young's modulus of the PZT thin film. At this precision, conventional analytical expressions to calculate resonance frequencies of silicon cantilevers might not be accurate enough. 3D FEM simulations were performed to estimate the deviations between these simulations, that use anisotropic elastic properties of silicon, and the values calculated analytically for our cantilevers. The appropriate effective Young's modulus to be used in the resonance frequency calculation of our cantilevers was determined along with the corresponding errors.

### II – Theory

The resonance frequency of a cantilever without PZT is calculated by using the analytical relation defined in equation (1) [5]:

$$f_n = \frac{C^2 t_s}{2\pi L^2} \sqrt{\frac{E_s^*}{12\rho}} \quad (1)$$

here  $f_n$  is the resonance frequency,  $C$  is a constant which depends on the vibration mode  $C = 1.875$  for fundamental resonance frequency ( $f_0$ ),  $E_s^*$  is the effective Young's modulus,  $\rho$  is the density of silicon,  $t_s$  is the thickness and  $L$  is the length of the cantilever. Calculation of the resonance frequency of silicon cantilever depends on the use of appropriate effective Young's modulus. However, single crystal silicon is elastically anisotropic. Therefore the effective Young's modulus of silicon is different for different crystal orientations. Consequently, the resonance frequencies of the cantilevers depend on their orientation with regards to the crystal lattice. For the effective Young's modulus we can either take the biaxial modulus  $E/(1-\nu)$  or plate modulus  $E/(1-\nu^2)$ , depending on the geometry of the cantilevers. Both are however approximations.  $E$  and  $\nu$  are the Young's modulus and Poisson's ratio of silicon in the particular crystal direction of silicon, see Table 1 [6]. The appropriate effective Young's modulus for our cantilevers was determined by calculating the resonance frequencies using equation (1) and by FEM simulations results for the silicon cantilevers aligned parallel to the  $\langle 110 \rangle$  and  $\langle 100 \rangle$  crystal directions of the silicon crystal lattice.

Full 3D finite element simulations were carried out using the COMSOL software package to verify the analytical results obtained using equation (1). To define cantilevers aligned parallel to the  $\langle 110 \rangle$  orientation

Table 1: Elastic anisotropic properties of single crystal silicon.

Crystal plane {100}				
Direction	Young's modulus GPa	Poisson's ratio	$E/(1-\nu)$ GPa	$E/(1-\nu^2)$ GPa
$\langle 110 \rangle$	168.9	0.064	180.4	169.8
$\langle 100 \rangle$	130.2	0.279	180.4	141

in COMSOL, the cantilever geometry was drawn in the xy-plane with the length axis parallel to the x-axis and then rotated  $45^\circ$  around the z-axis. For the  $\langle 100 \rangle$  cantilevers, no rotation was given to the cantilever. Standard anisotropic elastic properties of single crystal silicon as defined in the material section of the COMSOL were used for the simulations. The elastic stiffness coefficients are identical to values quoted in literature[6].

Table 2 lists the analytical calculations of resonance frequencies using equation (1) and the results of the FEM simulations of a silicon cantilever. The analytical values of the resonance frequencies calculated using a plate modulus  $E/(1-\nu^2)$  agree with the FEM simulations to within 0.04 % for the  $\langle 110 \rangle$  direction, and deviate by only 3 % for the  $\langle 100 \rangle$  direction. The FEM results are 17 % lower when using the biaxial modulus  $E/(1-\nu)$  for  $\langle 100 \rangle$  aligned cantilevers. The results verify that the effective Young's modulus that we apply should be the plate modulus for the cantilever geometry which we have used in this work.

Addition of the PZT thin film on the cantilever affects the flexural rigidity and increases the mass. Both affects result in a change in the resonance frequency of the cantilever. The effective Young's modulus of the PZT thin film is calculated using the resonance frequency both before and after deposition of the PZT thin film. We developed an analytical relation for the determination of Young's modulus of PZT as described in equation (2). The equation was based on a shift of the neutral axis and on the assumptions that the cantilever has a uniform cross section and that there is small cantilever deflection [5, 7]:

$$E_f^* = \frac{1}{t_f^3} \left[ 6(t_s \rho_s + t_f \rho_f) B - 2E_s^* t_s^3 - 3t_f E_s^* t_s^2 - 2E_s^* t_s t_f^2 + \sqrt{\frac{E_s^* t_s^2 t_f^4 + 3E_s^* t_s^3 t_f^3 + (4E_s^* t_s^4 - 3AB) t_f^2 + (3E_s^* t_s^5 - 9AB t_s) t_f + E_s^* t_s^6 - 6AB t_s^2 + 9(t_s \rho_s + t_f \rho_f)^2 B^2}{}} \right] \quad (2)$$

where

$$A = E_s^* t_s (t_s \rho_s + t_f \rho_f) \quad \text{and} \quad B = \left( \sqrt{\frac{E_s^* t_s^3}{12 t_s \rho_s}} - 0.568 \pi \Delta f_o L^2 \right)^2$$

the symbols  $E^*$ ,  $t$ ,  $L$  and  $\rho$  are the effective Young's modulus, thickness, length and density respectively.

Subscripts  $s$  and  $f$  denotes the silicon and PZT thin film.  $\Delta f_o$  is the difference in the fundamental resonance frequency of the cantilever before and after the deposition of PZT. By taking this difference, any potential uncertainties in the thickness of the cantilever can be eliminated and a more accurate result is obtained [8].

Table 2: Comparison of the fundamental resonance frequency of silicon cantilevers with length,  $L = 300 \mu\text{m}$ , thickness,  $t_s = 3 \mu\text{m}$  and width,  $w = 30 \mu\text{m}$ .

Orientation	Calculated resonance frequency (Hz) for $E/(1-\nu)$	Calculated resonance frequency (Hz) for $E/(1-\nu^2)$	FEM simulation 3D, Anisotropic (Hz)
$\langle 110 \rangle$	47369	45956	45978
$\langle 100 \rangle$	47369	41878	40541

### III – Fabrication

To ensure precise control of the dimensions of the cantilevers, we fabricated our  $3 \mu\text{m}$  thick silicon cantilevers in a dedicated SOI/MEMS fabrication process. The fabricated cantilevers vary in length from  $250 \mu\text{m}$  to  $350 \mu\text{m}$  in steps of  $10 \mu\text{m}$ . Cantilevers were etched on the front side of the SOI wafer as detailed in Figure 1 with the following sequence. SOI wafer was selected to use the buried oxide as an etch stop (a). Application and patterning of the photoresist for defining the cantilevers (b) and (c). Deep reactive ion etching (DRIE) of the cantilevers (d). Photoresist was removed by oxygen plasma (e). Polyimide pyralin, a photoresist material, was coated as the protective layer on the front side (f).

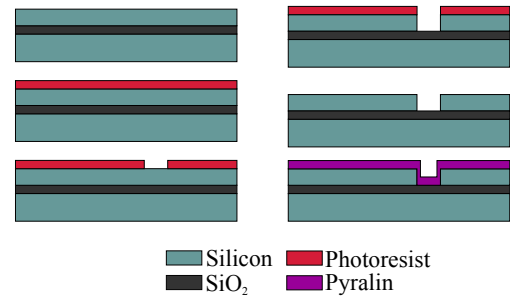


Figure 1: Fabrication process for defining cantilevers on the front side of the wafers. (a) SOI wafer, (b) application of photoresist, (c) patterning of photoresist, (d) DRIE of the silicon device layer, (e) photoresist removal, (f) application of protective layer polyimide pyralin.

Subsequently, cantilevers were released from the handle wafer by making through holes from the backside of the wafer according to the steps shown in Figure 2. Application and patterning of the photoresist for defining the holes (a) and (b). Etching of the backside of the wafer using DRIE (c). Removal of photoresist material from the top and back sides of the wafer by oxygen plasma (d). In last step the cantilevers were released by etching 500 nm of buried oxide layer using

Vapour HF (e). To measure resonance frequencies in the  $\langle 110 \rangle$  and  $\langle 100 \rangle$  directions, cantilevers were fabricated from a (100) single crystal silicon wafer and oriented parallel to the  $\langle 110 \rangle$  and  $\langle 100 \rangle$  directions of the silicon crystal lattice, see Figure 3. Buffer layers of Yttria-Stabilized Zirconia and  $\text{SrRuO}_3$ , each 10 nm thick, were deposited by PLD on the cantilevers. These layers ensured that a high quality 100 nm PZT film could be grown epitaxially on the silicon by PLD.

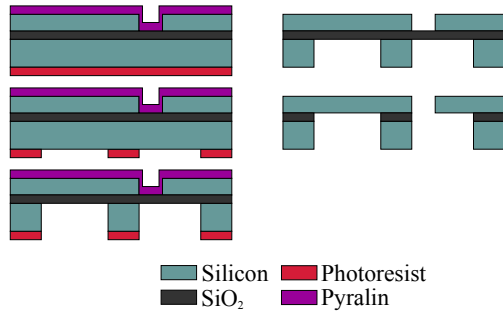


Figure 2: Fabrication steps on the backside of the wafers for releasing the cantilevers. (a) application of photoresist, (b) patterning of photoresist, (c) wafer through DRIE, (d) photoresist removal from front and back sides, (e) etching of buried oxide layer.

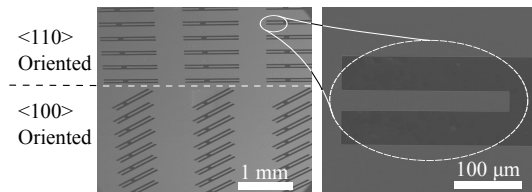


Figure 3: Scanning electron micrographs of the fabricated cantilevers. The cantilevers vary in length from 250  $\mu\text{m}$  to 350  $\mu\text{m}$  in steps of 10  $\mu\text{m}$ . The cantilevers are aligned parallel to the  $\langle 110 \rangle$  and  $\langle 100 \rangle$  crystal orientations of silicon.

#### IV – Experimental Details

The resonance frequency of the cantilevers was measured by using a MSA-400 Micro System Analyser scanning laser-Doppler vibrometer. The measured resonance frequency before the deposition of the PZT for similar cantilevers aligned parallel to the  $\langle 110 \rangle$  and  $\langle 100 \rangle$  crystal orientations of silicon are shown in Figure 4. The difference of the fundamental resonance frequency for two differently oriented cantilevers can be seen clearly from the Figure 4. This difference is solely caused by the different effective Young's modulus for the two directions.

The resonance frequency of the cantilevers was again measured after the deposition of PZT. Due to the addition of the PZT thin film on the cantilevers, the resonance frequency was changed as expected, see Figure 5.

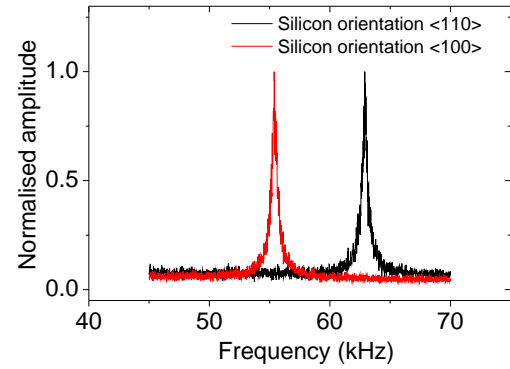


Figure 4: The difference in resonance frequency of similar cantilevers, aligned in the  $\langle 110 \rangle$  and  $\langle 100 \rangle$  crystal directions of the silicon crystal lattice.

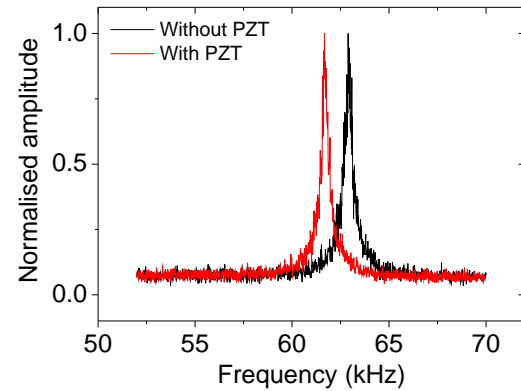


Figure 5: Measured resonance frequency before and after deposition of the PZT. The amplitude is normalised to the maximum value. The resonance frequency with PZT is lower than for the cantilevers without PZT, which is as expected.

#### V – Results and Discussion

Figure 6 shows that the experimentally measured resonance frequencies for the range of cantilevers length agrees well with the FEM simulations and the analytically calculated values when using the plate modulus as the effective Young's modulus of silicon.

The Young's modulus of PZT calculated by using the measured change in resonance frequency, was found to be 103 GPa with a standard error of  $\pm 2$  GPa (measured on 11 cantilevers). This value is in the same order as values quoted in literature for sol-gel [9] and sputter deposited [10] PZT. The expected change in resonance frequency, corresponding to the effective Young's modulus of PZT, was also obtained from FEM simulations. It was found that the measured change in resonance frequency is 5 to 8 % higher when compared to what is obtained from FEM simulations for different lengths of cantilevers. The origin of this discrepancy is not known



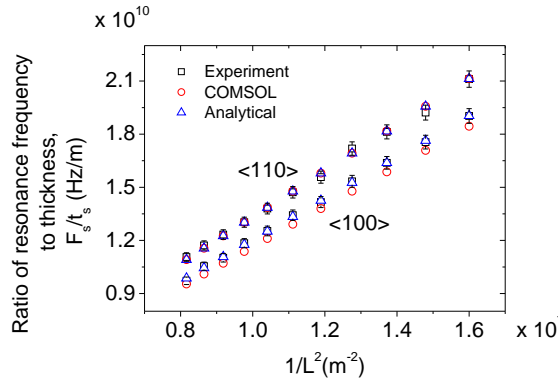


Figure 6: Analytically calculated, simulated and measured resonance frequencies for cantilevers of varying length. The cantilevers are aligned parallel to the  $\langle 110 \rangle$  and  $\langle 100 \rangle$  crystal directions of silicon.

to us yet.

A thorough error analysis was performed to calculate the propagation of errors in the parameters to the calculated values for the effective Young's modulus. The cumulative error found in the calculated value of the effective Young's modulus is in the order of 6 to 8 GPa for individual cantilevers. The 3 % error in the  $\langle 100 \rangle$  effective Young's modulus of silicon propagates as 3.7 % error in the value of the effective Young's modulus of PZT. This suggests that a correction of the plate modulus model for the  $\langle 100 \rangle$  direction might be necessary.

## VI – Conclusions

In conclusion, we determined the effective Young's modulus of PZT thin films using the resonance frequency of the cantilevers both before and after the deposition of PZT. The effective Young's modulus of PZT is 103 GPa with a standard error of  $\pm 2$  GPa in both the  $\langle 110 \rangle$  and  $\langle 100 \rangle$  directions of silicon. We also validated by FEM simulations and experimental measurements that the plate modulus has to be used for the calculation of the effective Young's modulus of silicon for our measured cantilevers. The analytical relation for resonance frequency calculation of silicon cantilevers is very precise in the  $\langle 110 \rangle$  direction. For the  $\langle 100 \rangle$  direction, the deviation of analytical value compared to the simulation is only 3 %. The inaccuracy in the model however lies below the uncertainty in the measured parameters. This method of determining the appropriate effective Young's modulus is generally applicable for arbitrary cantilever geometries.

## Acknowledgements

The authors gratefully acknowledge the support of the SmartMix Program (SmartPie) of the Netherlands Ministry of Economic Affairs and the Netherlands Ministry of Education, Culture and Science. The authors

also thank M.J. de Boer for etching, R.G.P. Sanders for laser Doppler vibrometer measurement, J.G.M. Sanderink for assistance with SEM, and M.D. Nguyen for depositing PZT by PLD.

## References

- [1] J.R. Bronson, J.S. Pulskamp, R.G. Polcawich, C.M. Kroninger, and E.D. Wetzel. In *22nd IEEE International Conference on Micro Electro Mechanical Systems, MEMS 2009*, pages 1047–1050, Sorrento, 2009.
- [2] H.-J. Nam, Y.-S. Kim, C.S. Lee, W.-H. Jin, S.-S. Jang, I.-J. Cho, J.-U. Bu, W.B. Choi, and S.W. Choi. *Sensors and Actuators A: Physical*, 134(2):329–333, 2007.
- [3] Y.C. Zhou, Z.Y. Yang, and X.J. Zheng. *Surface and Coatings Technology*, 162(2-3):202–211, 2003.
- [4] M. Dekkers, M.D. Nguyen, R. Steenwelle, P.M. te Riele, D.H.A. Blank, and G. Rijnders. *Applied Physics Letters*, 95(1):012902–012902–3, 2009.
- [5] E. Volterra and E.C. Zachmanoglou. *Dynamics of vibrations*. CE Merrill Books, 1965.
- [6] W.A. Brantley. *Journal of Applied Physics*, 44(1):534–535, 1973.
- [7] J.M. Gere. *Mechanics of Materials*. 6th. Toronto, Canada: Thomson-Engineering, 2006.
- [8] J.-A. Schweitz. *Journal of Micromechanics and Microengineering*, 1(1):10–15, 1991.
- [9] B. Piekarski, D. DeVoe, M. Dubey, R. Kaul, and J. Conrad. *Sensors and Actuators A: Physical*, 91(3):313–320, July 2001.
- [10] T.H. Fang, S.R. Jian, et al. *Journal of Physics: Condensed Matter*, 15:5253–5259, 2003.

## TUNGSTEN-SILICONNITRIDE MEDIUM FOR MEGA- TO GIGAYEAR DATA STORAGE

Jeroen de Vries<sup>1</sup>, Leon Abelmann<sup>1</sup>, Andreas Manz<sup>2</sup>, Miko Elwenspoek<sup>1,2</sup>

<sup>1</sup>MESA+ Institute for Nanotechnology, University of Twente, Enschede, The Netherlands

<sup>2</sup>Freiburg Institute for Advanced Studies, School of Soft Matter Research, Freiburg, Germany

**Abstract** — Throughout the ages humanity has stored data in order to preserve important information for generations to come. As the years have progressed the amount of data that can be stored efficiently has increased tremendously, the lifespan of this type of data storage however is severely limited. Within this paper we investigate the possibility to store data by encapsulating W in a SiN matrix. We show that using accelerated thermal aging the possible lifespan of this medium can be investigated and expected to reach well into the millions of years, preserving data for thousands of future generations. The first steps into fabrication of such a medium are discussed.

**Keywords:** Gigayear data storage, Silicon nitride, Human document project

### I – Introduction

Literature, newspapers or science use the internet, paper and written language for documenting their contents and trading it down to the readers. The time scale for this is typically a human generation or much less. Technically speaking, printed paper as such will not necessarily survive very much longer. The computerized modern world has gotten a boost towards storing and accessing much more information. However, this has not improved the survival time scale. Heart beat frequency, body size of the organism and time scales of reaction may correlate. We have developed a civilization which overcame these biological hurdles through, e.g., medicine and technology for self-protection. However, human thinking is mostly limited to short timescales, in its best case to 1-2 generations ahead. Long-term documentation has only occurred related to religion and the idea of “eternal life”, or purely by accident. Ancient cultures documented themselves on cave paintings, petroglyphs and rock carvings. Clay plates and large architectural objects have demonstrated lifetimes of thousands of years. At least, that is how it appears to be today. We simply have no evidence of other forms of communication, since most of that has disappeared with time. We can find that Homo erectus or Homo neandertalensis was able to prepare fire, because this is documented in inorganic traces. However, perhaps there was a scientific understanding or expression of art, which may have vanished over the years. How can we know? What will remain of today’s efforts of the arts and sciences, not to speak about the many aspects of everyday life, in say 1,000,000 years? It may be comparable to the remains we currently have of Homo

erectus and his lifestyle. Computers will have corroded (except a few silicon chips), paper is all gone, houses disappeared and with it most other items we use in everyday life. Of course, we can hope for a community which trades down information as the medieval monasteries did in copying Aristoteles’ books. However, we have no guarantee that there will be a smooth transition or continuous development in Homo sapiens, as we can observe in the last 1 million years. Historians speak of hundreds of years, archaeologists of 100,000s of years and astronomers or geologists handle the real time scales, which we currently believe play no role for Homo sapiens. That might be wrong. In a similar way as there was centuries of debate about geocentric versus heliocentric viewpoint for astronomy, there could be a debate about relevant timescales... We may not have a (very geological) prehistory of much more than 1 million years, but we may have a future of intelligent life on this planet of much more!

To attempt to create a system which will store information about the human race for future intelligences has many scientifically interesting aspects. These question range from philosophical “What actually does define humanity?” and “How do we transfer information to an intelligence which might have a completely different, and unknown, framework?” to historical “What are the main events in human history” to linguistic “How do we teach an unknown intelligence to read English?” to technical “How do we store information for over one million years, how can we prove it will still be there?”. This contribution deals with the latter question, and is part of the larger Human Document Project ([www.humandocument.org](http://www.humandocument.org)).

### II – Theory

All data is volatile. Even the largest engraving in marble will erode with time. By experience we know however that the more energy we use to write data, the longer it will hold (marble is better than sand-stone). In modern data storage, this fact is becoming painfully apparent in magnetic data storage. With decreasing bit size, the energy stored in one single bit is getting smaller[1]. As a result, the lifetime of data is magnetic media has dropped below ten years, despite intense efforts of the magnetic recording industry to maintain stability. It could well be that with continuing progress in density, we will reach the point that no magnetic material will be strong enough to hold the data, and the magnetic hard disk will disappear.

Fortunately, the efforts of scientist working in mag-

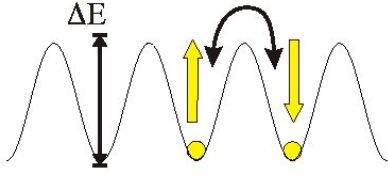


Figure 1: Data is stored in the state of a system, which can be in two or more energy minima

netic storage has led to a broad knowledge on data stability. A simple, but effective, theory can be defined, which might be extrapolated to over a million years. We assume that a bit of information is stored in a single entity. The information is stored in one of the energy minima in the system, which are separated by an energy barrier  $\Delta E$  (Figure 1). (The entity might be a magnetic needle, which can be magnetized in two stable directions). At 0 K, the system will stay in one of the energy minima indefinitely, but at elevated temperatures the probability that the system will jump to another minimum after a time  $t$  is given by the Arrhenius law [2]:

$$P_{sw}(t) = 1 - \exp(-t/\tau(T)), \quad (1)$$

$$\tau(T) = f_0^{-1} \exp(\Delta E/kT) \quad (2)$$

where  $k$  is Boltzmann's constant,  $T$  the absolute temperature and  $f_0$  is the attempt frequency which is related to atomic vibrations, and in the order of  $10^9$  Hz for magnetic particles [3]).

We assume that the probability of switching is low, so that secondary processes like switching back to the correct minimum can be neglected. In that case the number of incorrect bits in a large set of data  $N$  simply is  $P_{sw}N$ . In modern data storage systems, errors up to fractions  $\alpha$  of  $10^{-5}$  can be comfortably corrected by suitable error codes. Rewriting equation 1

$$\tau > -t/\ln(1 - \alpha) \approx t/\alpha \text{ for } \alpha \ll 1 \quad (3)$$

$$\text{and } \Delta E/kT > \ln(t f_0/\alpha) \quad (4)$$

For data storage over 1 million years, with  $\alpha=10^{-5}$  and  $f_0=10^9$  Hz,  $\Delta E$  should be  $63 kT$ , for 1 billion years the energy barrier should be raised to  $70 kT$  (1.8 eV at room temperature). These values are well within range of today's technology.

To prove that the data will remain without errors for over a million of years is quite another challenge. Even though PhD projects tend to run over time, we should not have to wait for a million years and devise some kind of accelerated test. Starting from equation 3 there are three variables we can act upon: the testing time  $t_t$ , the observed number of errors during the test  $\alpha_t$  and the temperature at which the test is performed  $T_t$ .

$$\Delta E/kT_t > \ln(t_t f_0/\alpha_t) \quad (5)$$

Storage period	1 Week Test	1 Year Test
$10^6$ years	770 K	550 K
$10^9$ years	980 K	700 K

Table 1: Testing at elevated temperature to prove data retention at  $T=300$  K

By observing many bits, we can determine error rates lower than  $10^{-5}$  and extrapolate from there when this value will be reached. By testing at higher temperature, we can increase the number of errors per time unit. Combining equations 3 and 5, the temperature at which the test is performed

$$T_t > T \frac{\ln\left(\frac{t}{\alpha}\right)}{\ln\left(\frac{t_t}{\alpha_t}\right)} \quad (6)$$

which indeed is independent on the attempt frequency. Taking for instance an observed error rate ten times better than the desired rate (so  $\alpha_t=10^{-6}$ ), the required testing temperature to prove that the data is stable for a million years within a year is 550 K. Table 1 lists values for different testing and storing times, which are well within experimental range.

From this simple theory, we can conclude that it should be possible to prove that data will be retained for at least one million year by an elevated temperature test. The main question is however whether this theory above can be extrapolated to such time-scales. Moreover, we assume that the system only possesses global minima, where local minima might exist which can serve as intermediate steps towards overcoming the energy barrier between global minima states. Data in phase change media (such as DVD) is stored in the position of atoms, which can reside in a huge number of local minima. The assumption that attempt frequencies are independent of temperature might also be invalid. In order to answer these question, we need to perform the actual accelerated test on a real medium which should be able to withstand temperatures up to 1000 K. In this contribution, such a medium is realized.

### III – Medium design

We expect that the data that will be preserved for the coming thousands of generations will be carefully selected and will not be subject to constant change. If updates are made, we expect that new media can be written. Because it might be necessary to view the information multiple times it should be possible to read back the data many times without altering or destroying its content. For this reason we chose a write once, read multiple (WORM) type medium.

To create a sample which can withstand the ravages of the ages, suitable materials have to be carefully chosen. The data should be stored on a stable medium which can withstand and endure large changes in temperature, mechanical influences and various other

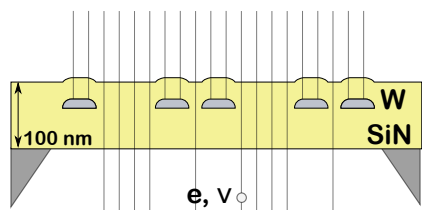


Figure 2: W-SiN WORM medium, which is transparent to electron or photon beams

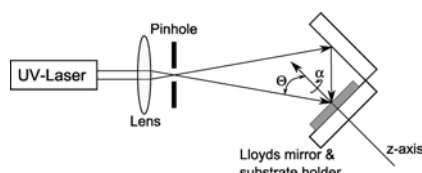


Figure 3: Schematic view of the laser interference lithography (LIL) setup

forms of abuse over long periods of time. Because the data itself should be stable for a very long time we require a medium where a large amount of energy is needed to change the information that is written. This will limit the degradation of the information through the ages. Two materials which possess these traits are silicon nitride for the medium and tungsten to store the data.

Because the medium needs to be written only once a W-SiN medium is created where the information, stored in W, is encapsulated in SiN. SiN has a high strength over a large temperature range and a high fracture toughness whereas the high melting point of W together with its high activation energy makes it suitable for storing information for long periods of time. The created medium will be opaque and it will be possible to read back the data by electron beams or photons without modifying or degrading its content (Figure 2).

#### IV – Fabrication process

For the initial test sample a medium with W lines encapsulated within a SiN medium is created. This medium does not contain data yet but can be used for the elevated temperature tests. The line pattern is created by laser interference lithography which makes it possible to create lines over a large area by a short exposure step. A schematic view of the LIL setup can be seen in figure 3[4]. The thin high aspect ratio lines make it possible to quickly compare the thermally treated sample and the reference sample.

The process steps for the test sample creation can be seen in figure 4. First a layer of 230 nm SiN is deposited on a cleaned silicon wafer by a LPCVD process. A layer of 20 nm W is magnetron sputtered on the SiN substrate. Next we spin a layer of DUV 30-8 bottom anti-reflective coating (BARC) which limits the

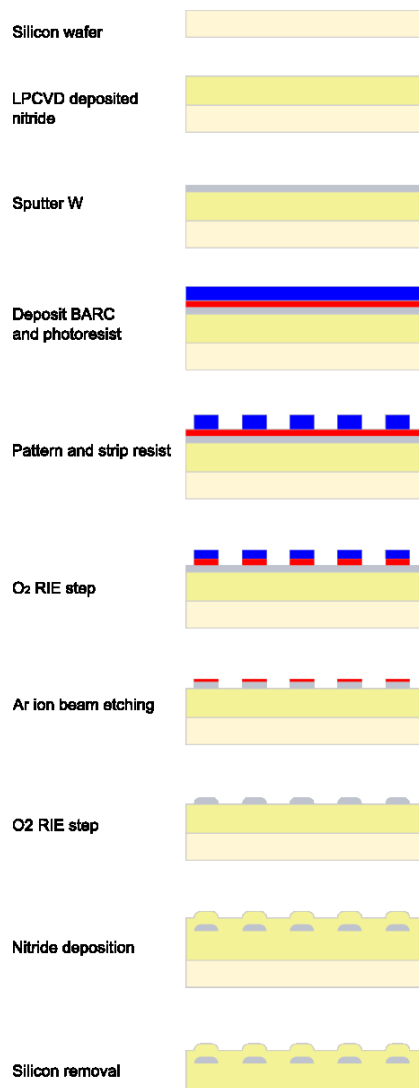


Figure 4: Fabrication process steps for the W-SiN test sample

standing waves in the resist and improves the vertical sidewalls with a layer of MA-N 2403 resist on top. By laser interference lithography (LIL) a pattern of 100 nm wide lines is created in the resist. A short O<sub>2</sub> reactive ion etching (RIE) step is used to remove the BARC layer and the pattern is transferred into the W by an Ar ion beam etching (IBE) step. A short O<sub>2</sub> RIE step is used to remove the remaining BARC layer. The whole sample is now covered with SiN by a PECVD process to encapsulate the W lines. In the final step the silicon is removed from the bottom of the sample and an opaque medium with encapsulated W lines remains.

#### V – Fabrication results

In figure 5 a scanning electron micrograph of the test sample can be seen before etching. In the image the domain structure of the W layer can be clearly seen together with the SiN layer below and the BARC layer on top.

In the initial attempt to create a test sample the RIE



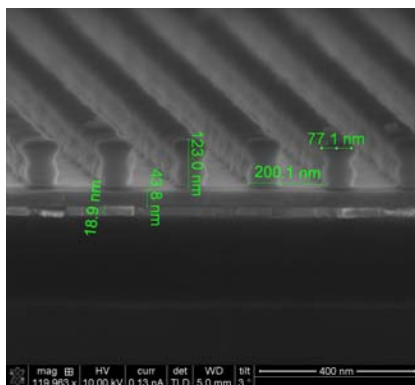


Figure 5: Scanning electron micrograph of the test sample before etching

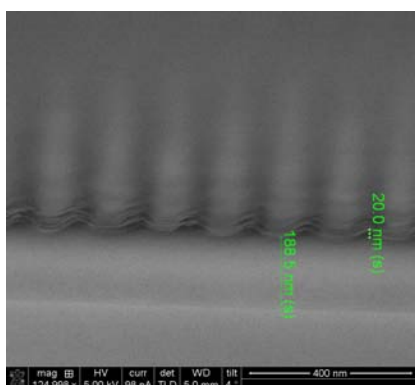


Figure 6: Scanning electron micrograph of the test sample after etching

etch steps were omitted and the sample was directly etched using IBE. Unfortunately this approach did not give the desired result and the sample was destroyed as can be seen in figure 6. During the RIE step both Si and W were monitored using secondary mass ion spectrometry (SIMS) in order to stop when etching after the first layer of BARC and W were removed. Unfortunately BARC proved tougher to remove than expected and the negative resist could not withstand the long etching time and began to spread out due to the local increase in temperature. This decreased the aspect ratio of the resist lines which caused the W which were covered by the resist to start etching before the first layer of W was completely removed. This resulted in a continues W signal in the SIMS instead of two separated peaks and made it impossible to stop etching at the right moment.

In the near future a sample will be fabricated using a positive resist (PEK 500) which does not spread during etching. Before the ion beam etch step a reactive ion etching step is used to remove the bottom anti reflective coating and maintain the high aspect ratio of the lines in the W. The resulting sample will be covered by PECVD deposited SiN and thermally aged during one week at elevated temperatures.

## VI – Conclusion

Initial calculations shows that it is possible to store data for over 1 million years, or even 1 billion, with reasonable energy barriers in the order of 70 kT. To prove that the data will not disappear over this time period, one can perform accelerated tests at moderately elevated temperatures (550 K for 1 million year). As a first attempt for such a medium, we designed a medium in which data is stored in W dots embedded in a SiN matrix. Initial attempts to etch submicron W lines failed due to the high etch resistance of W. Once the etch problem is solved, the medium will be exposed to high temperature acceleration test.

## References

- [1] S. H. Charap, P. L. Lu, and Y. He. Thermal stability of recorded information at high densities. *IEEE Trans. Magn.*, 33(1):978–983, 1997.
- [2] W. Wernsdorfer, E. Bonet Orozco, K. Hasselbach, A. Benoit, B. Barbara, N. Demoncy, A. Loiseau, H. Pascard, and D. Mailly. Experimental evidence of the Néel-Brown model of magnetization reversal. *Phys. Rev. Lett.*, 78(9):1791, 1997.
- [3] Dieter Weller and Andreas Moser. Thermal effect limits in ultrahigh-density magnetic recording. *IEEE Trans. Magn.*, 35:4423–4439, 1999.
- [4] R. Lutge, H. A. G. M. van Wolferen, and L. Abelmann. Laser interferometric nanolithography using a new positive chemical amplified resist. *J. Vac. Sci. Technol. B*, 25:2476–2480, 2007.

# CONTROLLED INCREASE AND STABILISATION OF THE TUNING RANGE OF RF-MEMS CAPACITORS WITH AN ACTIVE LID ELECTRODE

John Love<sup>1</sup>, Martin Hill<sup>1</sup> and Conor O'Mahony<sup>2</sup>

<sup>1</sup>Adaptive Wireless Systems Group, Cork Institute of Technology, Bishopstown, Cork, Ireland

<sup>2</sup>Tyndall National Institute, University College Cork, Ireland

**Abstract** - This paper demonstrates improved performance of RF-MEMS tunable capacitors by applying bidirectional tuning electrostatic forces on the MEMS moveable part. It also presents simulated results for a closed loop control system to compensate the tuned capacitance for RF induced actuation forces. The device employs a triple plate MEMS structure, utilising a metal encapsulation thin film as the third electrode, to allow bidirectional actuation of the plate. For a 20µm wide, 532 µm long fixed-fixed beam tuning ranges were measured as 45% (bidirectional tuning) and 29.9% (unidirectional tuning) for applied voltages of less than 15V. 3D finite-element simulations gave tuning ranges of 57.8% and 30.9% respectively. A mathematical model of a parallel plate system is presented. The model is used to evaluate the operation of a closed loop controller to minimise the disturbance in beam deflection from a given setpoint by RF power induced actuation forces. It was found that the controller compensated for the variations with a steady state error of 1fF. This dual electrode technique could also be useful for temperature compensation and for improved control of RF-MEMS switch pull-in.

**Keywords** : MEMS, tunable capacitor, fixed-fixed beam, bidirectional tuning, triple plate.

## I – Introduction

RF-MEMS is evolving as an exciting technology for providing improved solutions in the development of RF wireless applications due to its proven superior performance over existing solid state technology [1-4]. MEMS tunable capacitors operate by varying the gap between two metal plates using electrostatic actuation. Devices of this type, often referred to as tunable electrostatic parallel plate capacitors, are unstable due to the electrostatic pull-in effect which limits the tuning range that can be achieved to 50% [1, 2].

Previous methods used to extend the tuning range include using two moveable beams [5]. The continuous tuning range reported was 117% and further tuning after pull-in gave an overall tuning range of 280%. In [6] a triple plate configuration is used where the top and bottom plates are fixed and the middle plate moves between the fixed plates with a measured tuning range of 40%. This paper will demonstrate a similar triple plate tunable capacitor configuration where the fixed top plate is a metal encapsulation layer used for wafer level packaging of the MEMS devices.

An additional benefit of the triple plate structure is the ability to actuate in two directions and this can be used in a control system to minimise the RF self actuation effect. A system model is presented and the operation of a closed loop proportional controller is investigated by simulation.

## II - Principle of Operation

The device can be described as a moveable beam actuated by applying bidirectional electrostatic forces ( $F_{eu}$ ,  $F_{ed}$ ) due to applied voltages ( $V_u$ ,  $V_d$ ) respectively as seen in Figure 1. Deflection due to these forces is balanced by the beam mechanical compliance forces ( $F_{mu}$ ,  $F_{md}$ ). With  $V_d$  set to zero, the beam can be deflected upwards due to an applied voltage  $V_u$  with the electrostatic force,  $F_{eu}$ , balanced by the downward mechanical restoring force,  $F_{md}$ . The device capacitance,  $C_d$ , can thus be reduced by increasing  $V_u$ . When voltage  $V_u$  is reduced to zero and the applied voltage  $V_d$  is increased, the beam is deflected downwards, increasing  $C_d$ , until equilibrium between the opposing forces  $F_{ed}$  and  $F_{mu}$  is reached. The beam tuned capacitance range is from an upwards minimum value to a downwards maximum value before the pull-in instability causes the beam to collapse into contact with the actuation pad.

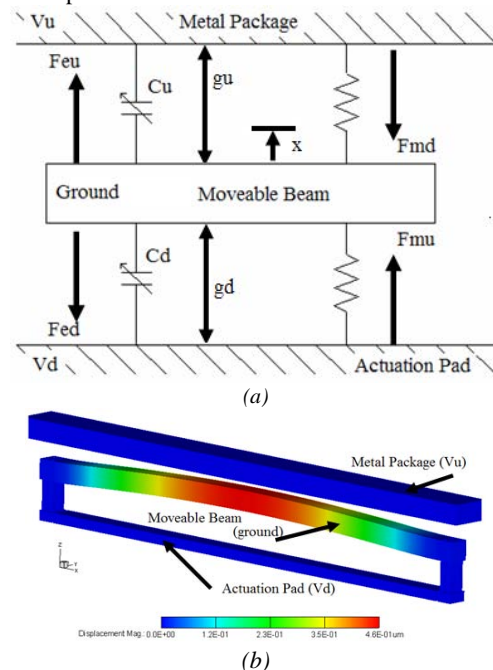


Figure 1, (a): Forces acting on the RF-MEMS tunable capacitor moveable beam (b): Voltage biasing applied to the RF-MEMS tunable capacitor during testing

The tuned capacitance range ( $TR$ ) is the percentage change between the minimum upwards deflected capacitance and the maximum downwards deflected capacitance before pull-in and is given in Equation 1.

$$TR[\%] = \frac{C_{\max} - C_{\min}}{C_{\min}} \times \frac{100}{1} \quad (1)$$

### III - Device Fabrication

The device is manufactured by first fabricating the 1  $\mu\text{m}$  thick aluminium movable beam on a first sacrificial layer of polyimide, which is then covered with a second layer of polyimide, which is encapsulated by a second aluminium film as shown in Figure 2.

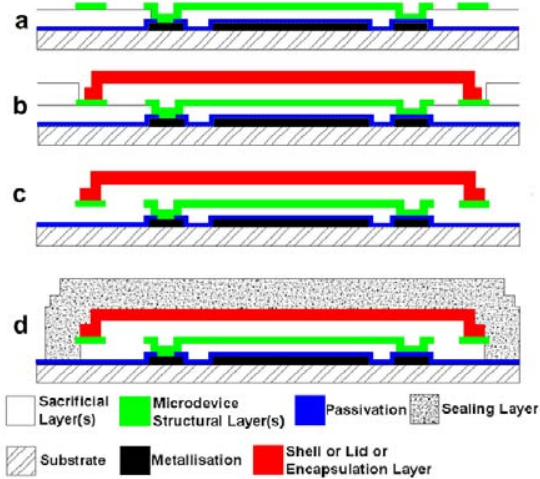


Figure 2: Fabrication flow schematic: (a) device and etch channel formation; (b) second sacrificial layer deposition and encapsulation layer patterning; (c) simultaneous removal of both sacrificial layers; (d) sealing of encapsulation shell.

Both sacrificial layers are simultaneously removed using an oxygen plasma [7]. Encapsulated devices are shown in Figure 3(a) where the encapsulation layer is oxide for optical inspection, and Figure 3(b) where the encapsulating layer is aluminium.

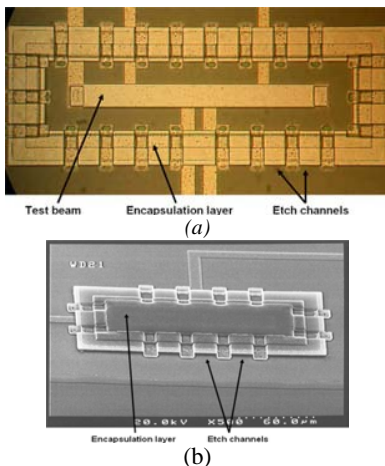


Figure 3, (a): An Optical view of a fully etched device (b): A SEM image of an encapsulated device.

For this fabrication batch only narrow beams were encapsulated as the etch channels in the side wall were designed for vacuum sealing and only lateral etching could be performed. The lateral etch is only effective for narrow structures and will not remove the sacrificial layer at the centre of a wide structure.

### IV - Verification of Triple Plate Operation

Triple plate operation was verified by comparison of simulated and measured pull-in voltages and capacitance tuning curves. Due to the lateral etch restrictions described above a  $532\mu\text{m} \times 20\mu\text{m}$  beam under 48MPa tensile stress with a down gap of  $2\mu\text{m}$  and an up gap of  $1\mu\text{m}$ , was used for this verification.

#### A. Pull-in Voltage

The triple plate structure was simulated in CoventorWare [8] with a  $10\mu\text{m}$  element tetrahedral mesh as shown in Figure 1(b). The results are shown in Figure 4. The initial capacitance can be seen to decrease with increasing  $V_u$ . The downwards pull-in voltage increases with increasing  $V_u$  as the down force is balanced by the mechanical and downward electrostatic forces. The effect of varying  $V_u$  on the initial beam capacitance,  $C_d$ , is highlighted in the figure.

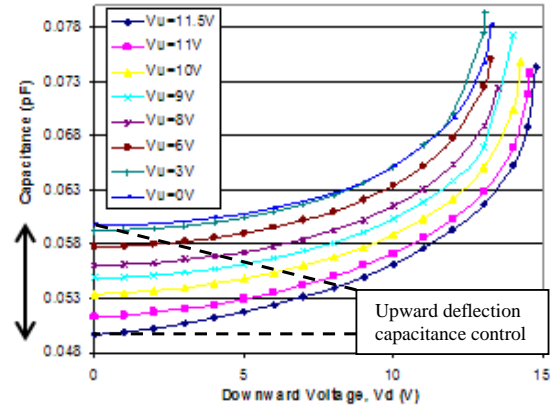


Figure 4: Simulated  $C_d$  as a function of downwards voltage ( $V_d$ ) for varying  $V_u$  which also causes  $C_d$  to change

A test setup comprising of two voltage supplies and an HP4275A LCR meter was used to take capacitance measurements. The tuned capacitance  $C_d$  was measured while  $V_d$  was swept beyond pull-in.  $V_u$  was increased in one volt increments between measurements. The results from this experiment are displayed in Figure 5.

The initial capacitance of the beam is slightly higher compared with simulated results which could be attributed to parasitic capacitances in the fabricated structure (the lid surrounds the beam) while simulations calculate the capacitance with only a top beam present. It can be observed that the measured initial  $C_d$  is lower for higher values of  $V_u$  and the pull-in voltage is increased. A significant shift between the  $V_u=0\text{V}$  trace and the other traces could indicate dielectric charging occurring after pull-in.

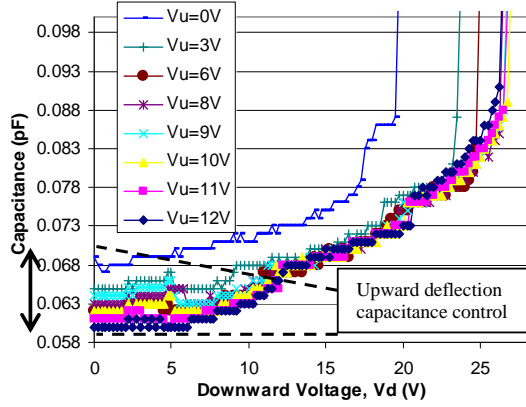


Figure 5: Measured  $C_d$  as a function of downwards voltage ( $V_d$ ) for varying  $V_u$  which also causes  $C_u$  to change.

### B. Capacitance Tuning Curve

The data from Figure 4 was used to graph the extended tuning range of the device. Tuning by upward beam deflection is quantified using the change in initial capacitance with  $V_d=0$ . This upward deflection is shown in Figure 6 by changing the sign of the  $V_u$  voltage to negative. Tuning by downward deflection uses the trace for  $V_u=0V$  and is shown in Figure 6 with a positive sweep voltage. The tuning range extends from 49.6fF to 78.2fF and equates to a 57.8% tuning range. The simulated tuning range without the upper electrode was 30.9% (only  $V_d$  is used).

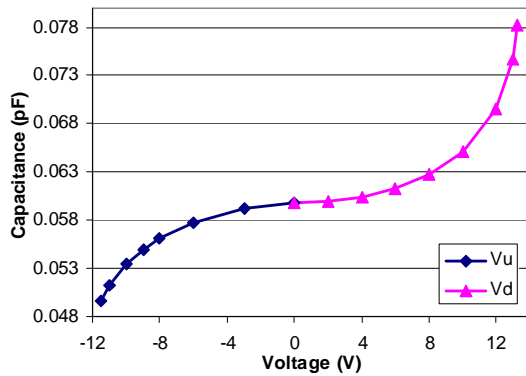


Figure 6: Simulated  $C_d$  as a function of upward voltages ( $V_u$  - plotted as negative) and downward voltage ( $V_d$  - plotted as positive).

Figure 7 demonstrates the measured data from Figure 5 using the same technique as in Figure 6. The tuning range extends from 60fF to 87fF which equates to a 45% tuning range. A 29.9% tuning range was measured with only  $V_d$  applied to the beam. The measured tuning range is consistent with the simulated data. The simulated triple plate tuning range is greater than the measured value and this is attributed to non-idealities in the fabricated device. Both the simulated and measured tuning ranges are low compared with the tunable electrostatic parallel plate capacitor's tuning range of 50%. The reasons for this are that these devices are not ideal and the beams are tethered

by high spring constant anchors which force the beam to bend in the centre when  $V_d$  is applied across the entire actuation pad as described by Olszewski [9].

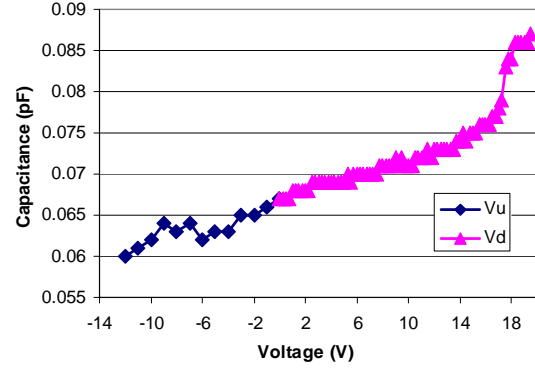


Figure 7: Measured  $C_d$  as a function of upward voltages ( $V_u$  - plotted as negative) and downward voltage ( $V_d$  - plotted as positive).

### V – Triple Plate Control

The capacitance of a tunable capacitor will vary due to changes in RF power. In the triple plate design this change in capacitance can be offset by using the top electrode to pull the beam back to the correct position.

#### A. Modelling

A parallel plate capacitor mathematical model in [10] was used to formulate the triple plate model in Equation 2.

$$m \frac{d^2 x}{dt^2} = F_{eu} - F_{ed} - d_c \frac{dx}{dt} - F_s \quad (2)$$

In this equation  $F_s$  is the mechanical restoring force acting against the displacement. The resulting acceleration is given in Equation 3.

$$\frac{d^2 x}{dt^2} = \frac{{}_0V_u^2 A}{2m(g_u - x)^2} - \frac{{}_0V_d^2 A}{2m(g_d + x)^2} - \frac{d_c}{m} \frac{dx}{dt} - \frac{kx}{m} \quad (3)$$

where  $m$  is the moveable electrode mass,  $d_c$  is the damping coefficient of the air surrounding the moveable electrode,  $k$  is the electrode's spring constant,  $\epsilon_0$  is the permittivity of free space,  $A$  is the area of the moveable electrode,  $g_u$  and  $g_d$  are the up and down gaps respectively and  $x$  is the displacement of the beam. The model was built in Simulink [11], a block diagram simulator program using the dimensions given for the  $532\mu m \times 20\mu m$  beam above.

#### B. Closed Loop Control

Closed loop proportional control of the position of the moveable beam and hence the capacitance was modelled with a feedback loop for displacement,  $x$ , added to the Simulink block diagram as displayed in Figure 8. The required displacement setpoint is calculated from the applied tuning voltage  $V_d$  using a fitted 4<sup>th</sup> order function which relates  $V_d$  to  $x$ .

The control loop was tested by comparing the open loop and closed loop response with setpoint step input of



$V_d=12V$  at time  $t=0$  with a disturbance ( $V_{RF}$  disturbance) step input of amplitude 4V at 0.03ms. The response curves are shown in Figure 9.

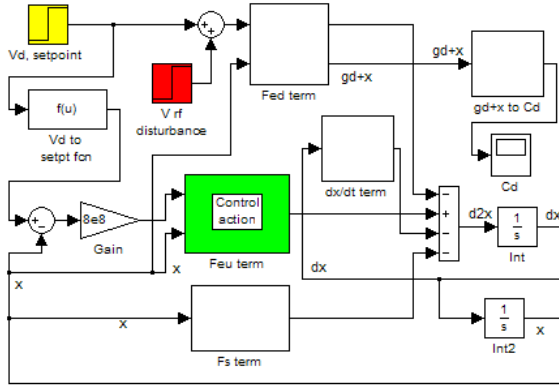


Figure 8: A Simulink block diagram of a closed loop control system of the triple plate model

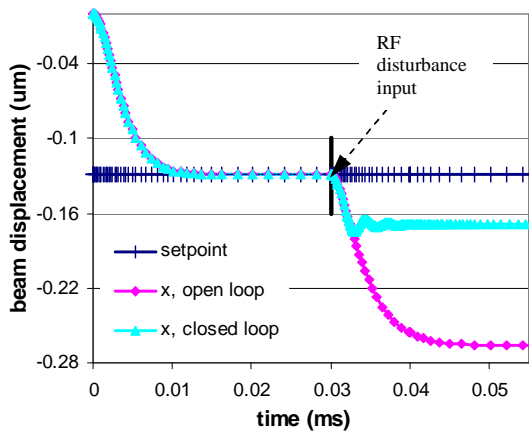


Figure 9: A graph of moveable beam displacement under open loop and proportional closed loop control when a  $V_{RF}$  disturbance was added at 0.03ms (the beam being below its rest position results in negative values for  $x$ )

In both open and closed loop operation the system has settled at the required beam displacement ( $-0.13\mu m$ ) after 0.01ms. In the open loop response the effect of RF power disturbance is to shift the displacement from the desired setpoint to  $-0.27\mu m$ . In closed loop operation the proportional controller operates so that beam displacement below the setpoint due to the disturbance, results in an increase in  $V_u$  to pull the beam back up towards the setpoint. A 0-30V supply is used for  $V_u$  to eliminate controller action for displacement above the required setpoint. In proportional control the steady state error observed in Figure 9 is inevitable and could be reduced using a higher gain or by adding integral action. In the system modelled here, the steady state error is  $0.04\mu m$  which equates to a capacitance error of 1fF.

## VII - Conclusions

The principle of a triple plate MEMS structure utilising a thin film metal encapsulation to increase the tuning range of a simple fixed-fixed beam has been

demonstrated. Due to fabrication constraints a long narrow beam was used to verify the operating principle. The beam was simulated and it was found to have a tuning range of 57.8% when two voltages were applied to it compared to 30.9% when only one voltage was applied. The tuning ranges from measured results are 45% (two voltages) and 29.9% (one voltage).

The examination of a simulated closed loop proportional only control mechanism for regulating RF power changes has shown that a 33% increase in  $V_d$  (12V to 16V) can be compensated for, however there is a steady state error of  $0.04\mu m$  which equates to 1fF.

The fabrication of the spring tethered MEMS structure is the next step in improving the tunable capacitor and this is currently at the design stage. The investigation of a proportional integral controller to eliminate the steady state error and the use of a cascade control loop involving  $V_u$  and  $V_d$  as improved control techniques are on going.

## Acknowledgements

The authors would like to acknowledge SFI NAP (National Access Program) and Tyndall National Institute for device fabrication and testing facilities.

## References

- [1] H. A. C. Tilmans, W. De Raedt and E. Beyne, *MEMS for wireless communications: from RF-MEMS components to RF-MEMS-SiP*, J. Micromech. Microeng. 13, pp. S139-S163, 2003.
- [2] S. Lucyszyn, *Review of radio frequency microelectromechanical systems technology* IEE Proc. Sci. Meas. Technol. 151, pp. 93-103, 2004.
- [3] G.M. Rebeiz, *RF MEMS Theory, Design and Application*, New Jersey, John Wiley and Sons 2003.
- [4] C. G. Christodoulou, *RF-MEMS and its Applications to Microwave Systems, Antennas and Wireless Communications* Proc. SBMO/IEEE MTT-S IMOC pp.525-531, 2003
- [5] M. Baki-Kassem and R. R. Mansour *Two movable plate nitride loaded MEMS variable capacitor*, 2003 IEEE MTT-S Digest pp. 283-286
- [6] A. Dec and K. Suyama *Electro-mechanical properties of a micromachined varactor with a wide tuning range*, IEEE 1998 pp. IV369-IV372,
- [7] C. O'Mahony, M. Hill, Z. Olszewski, A. Blake, *Wafer-level thin-film encapsulation for MEMS*, Microelectronic Engineering 86, pp. 1311-1313, 2009
- [8] www.coventorware.com
- [9] Olszewski, Z, et al, *Characterisation, modelling and performance evaluation of CMOS integrated Multielectrode Tunable Capacitor (MTC)*, JMM 2005
- [10] Saucedo-Flores, E, et al, *Study of the Pull-In Voltage for MEMS Parallel Plate Capacitor Actuators*, MRS Fall Meeting, Boston, Dec. 1-5 2003
- [11] www.mathworks.com

# TWO-DEGREE-OF-FREEDOM CAPACITIVE MEMS VELOCITY SENSOR: INITIAL TEST MEASUREMENTS

Ali Alshehri<sup>1</sup>, Michael Kraft<sup>1</sup>, and Paolo Gardonio<sup>2</sup>

<sup>1</sup> ECS, University of Southampton, Southampton, SO17 1BJ, UK

<sup>2</sup> DIEGM, Università degli Studi di Udine, Via delle Scienze, 208 – 33100 Udine (IT)

**Abstract** — This paper presents the initial test results of a novel Micro Electro Mechanical System (MEMS) velocity sensor with capacitive transduction, which benefits from a two-degree-of-freedom (2-DoF) structure. The principle operation of the 2-DoF sensor is described; its main function is to produce an output signal proportional to the velocity of the object of interest. A discussion on the design and microfabrication process follows. Finally, initial optical measurements on a microfabricated prototype are presented, showing the response of the open-loop operating mode of the 2-DoF device.

**Keywords:** Two degree of freedom MEMS sensor, Velocity sensor, MEMS

## I - Introduction

This paper presents the design, micromaching, and initial tests of a two-degree-of-freedom (2-DoF) Micro Electro Mechanical System (MEMS) velocity sensor with an internal feedback loop that uses capacitive sensing and electrostatic actuation. The aim of this work is to conceive and develop a new 2-DoF design, which enhances the performance of the piezoresistive MEMS velocity sensor described in references [1], [2]. This piezoresistive velocity sensor was intended to be used in pair with piezoelectric patch actuator in order to implement a velocity feedback loop on a structure that reduces its vibrational response by means of active damping.

If a collocated and dual actuator and velocity sensor pair is used, the feedback loop is bound to be unconditionally stable [3], [4]. The design and functionality of the MEMS velocity sensor can be paired with an actuator to offer good collocation and duality conditions [2]. The 2-DoF MEMS velocity sensor is capable to generate an output signal proportional to the opposite of the velocity at its base in a wide frequency band between a lower limit of about 20 Hz and an upper limit of about 2 kHz, which is determined by the fundamental resonance frequency of the transducer. Also, the peak of the fundamental resonance is well damped so that, above the fundamental resonance, the response monotonically rolls off with a  $-90^\circ$  phase lag (instead of the  $180^\circ$  lag of ordinary seismic sensors).

The MEMS velocity sensor in [1] was fabricated using a piezoresistive transduction technique. The piezoresistive transduction technique suffers from temperature changes and has low sensitivity compared with the capacitive transduction technique [5].

This paper focuses on a novel capacitive MEMS 2-DoF velocity sensor. It presents a theoretical description and analysis of the 2-DoF sensor and a brief review of the electronic circuit required to operate the device to measure velocity. A presentation of the fabrication process follows. Finally, the test configuration is described along with initial optical test measurements.

## II – Velocity sensor

### A. 2-DoF capacitive MEMS operation concept

The 2-DoF MEMS velocity sensor is formed by two mass-spring-damper systems attached to each other, as shown in the block diagram in Figure 1. The bottom spring-mass system is referred as the principal sensor while the top spring-mass system is referred as the control sensor, which is used to implement a negative velocity feedback loop on the mass of the principal sensor. The block masses and lumped springs are designed in such a way that the first resonance is controlled by the natural frequency and mode of the principal sensor while the second resonance is controlled by the natural frequency and mode of the control sensor. As shown in Figure 1, the capacitive transducers  $C_{sa}$  and  $C_{ss}$  are used to detect the displacements of the two block masses relative to the frame of the velocity sensor:  $x = w_{c2} - w_{c1}$  and  $y = w_{c3} - w_{c1}$ .

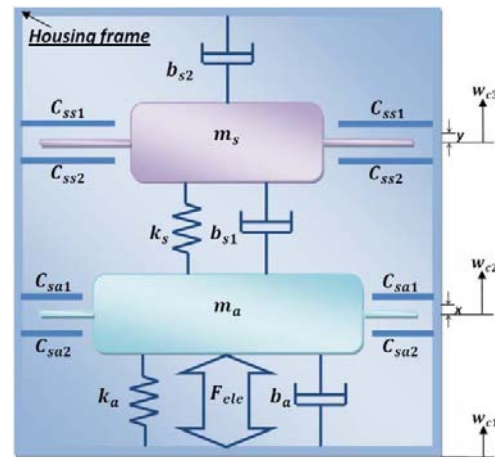


Figure 1. Block diagram of the mechanical design of the 2-DoF capacitive MEMS velocity sensor

The output of the velocity sensor is provided directly by the output signal of the principal sensor, thus it is proportional to the relative displacement between the block mass of the principal sensor and the frame of the velocity sensor  $x = w_{c2} - w_{c1}$ . Thus, if the internal feedback loop is left open it provides the acceleration of the frame of the velocity sensor. The control signal for

the internal feedback loop is given by the difference of the output signals from the principal and control sensors, thus it is proportional to the relative displacement between the two block masses  $z = y - x = w_{c3} - w_{c2}$ . In other words, it provides the acceleration of the block mass of the principal actuator. As shown in the block diagram of Figure 2, the control signal is time-integrated, inverted and then fed back to a capacitive electrostatic actuator that produces a reactive force between the frame of the sensor and the mass of the principal sensor. Thus the internal velocity feedback loop produces sky-hook active damping on the principal mass of the sensor.

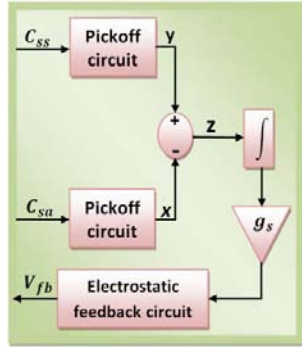


Figure 2. Interface and feedback control circuit block diagram of the 2-DoF velocity sensor

As discussed in references [1,2] this active damping action produces three important effects:

- at frequencies below the resonance frequency of the principal sensor, the output signal of the sensor is proportional to the velocity of the sensor frame;
- the resonance peak of the principal sensor is rounded off;
- above the resonance peak produced by the principal sensor the output signal of the sensor falls down monotonically with a phase lag of  $-90^\circ$  instead of  $180^\circ$ ;

These three properties are of great importance to improve the stability of velocity feedback loops used to reduce the vibrational response of flexible structures.

### B.2-DoF theoretical analysis

The equations of motion for the 2-DoF system are obtained by applying Newton's second law for each mass:

$$m_a \ddot{w}_{c2} = -b_a (\dot{w}_{c2} - \dot{w}_{c1}) - k_a (w_{c2} - w_{c1}) + f_{ele} + b_{s1} (\dot{w}_{c3} - \dot{w}_{c2}) + k_s (w_{c3} - w_{c2}) \quad \dots (1)$$

$$m_s \ddot{w}_{c3} = -b_{s1} (\dot{w}_{c3} - \dot{w}_{c2}) - k_s (w_{c3} - w_{c2}) - b_{s2} (\dot{w}_{c3} - \dot{w}_{c1}) \quad \dots (2)$$

Considering the definitions given above for the measured signals with the capacitive sensors, that is

$$x = w_{c2} - w_{c1} \quad \dots (3)$$

$$y = w_{c3} - w_{c1} \quad \dots (4)$$

$$z = y - x = w_{c3} - w_{c2} \quad \dots (5)$$

equations (1) and (2) can be rewritten in terms of the relative displacement  $z = y - x$  as follows:

$$m_a \ddot{x} = -m_a \ddot{w}_{c1} - b_a \dot{x} - k_a x + f_s + b_{s1} (\dot{y} - \dot{x}) + k_s (y - x) \quad \dots (6)$$

$$m_s \ddot{y} = -m_s \ddot{w}_{c1} - b_{s1} (\dot{y} - \dot{x}) - k_s (y - x) - b_{s2} \dot{y} \quad \dots (7)$$

The electrostatic control force produced on the mass of the principal sensor is given by

$$f_{ele} = -g_s \left( \frac{1}{1 + j\omega\tau} \right) (y - x) \quad \dots (8)$$

Where  $-g_s$  is the negative gain of the feedback loop,  $1/(1 + j\omega\tau)$  is the transfer function of a real time-integrator (with corner frequency  $1/\tau$ ) and  $z = y - x = w_{c3} - w_{c2}$  is the control signal obtained by subtracting the signal  $x$  to the signal  $y$  measured with the capacitive transducers. The open and closed loop frequency response function of the velocity sensor is derived by transforming equations (6), (7), and (8) to the Laplace domain and manipulating these equations to obtain the relation between the relative displacement of the principal mass  $X$  with the velocity of the base  $sW_{c1}$ , as follows:

$$\frac{X}{sW_{c1}} = \frac{B_1 M_a - A_2 M_s}{B_1 A_1 - B_2 A_2} \quad \dots (9)$$

Where,  $s$  is the Laplace domain operator,  $X$  is the relative displacement of the principal mass,  $sW_{c1}$  is the base velocity in the Laplace domain, and

$$M_a = m_a s, \quad M_s = m_s s, \quad I = \frac{1}{1 + s\tau}$$

$$A_1 = -m_a s^2 - (b_a + b_{s1})s - (k_a + k_s) + g_s I,$$

$$A_2 = b_{s1}s + k_s - g_s I,$$

$$B_1 = -m_s s^2 - (b_{s1} + b_{s2})s - k_s, \quad B_2 = b_{s1}s + k_s$$

Tables 1 and 2 list these parameters for the prototype MEMS sensors considered in this study.

Table 1: Principal sensor model parameters

Parameter	Value
Mass ' $m_a$ ' (kg)	1.0485 $\mu$
Damping coefficient ' $b_a$ ' (N/m/s)	0.257m
Spring constant ' $k_a$ ' (N/m)	143.604

Table 2: Control sensor model parameters

Parameter	Value
Mass ' $m_s$ ' (kg)	0.4823 $\mu$
Damping coefficient ' $b_{s1}$ ' (N/m/s)	35.51n
Damping coefficient ' $b_{s2}$ ' (N/m/s)	0.1707m
Spring constant ' $k_s$ ' (N/m)	249.383

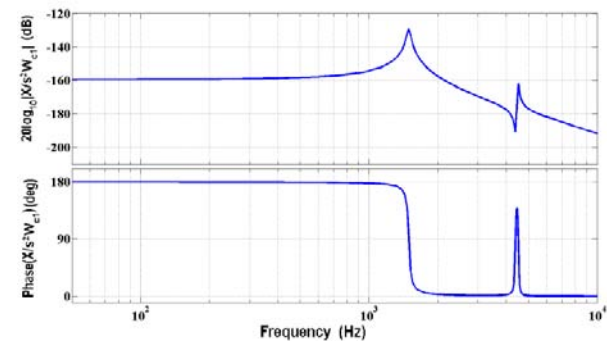


Figure 3. Theoretical Bode plot of the open-loop 2-DoF velocity sensor represented with the transfer function in equation (9). The plot shows the relation between the principal mass's relative displacement  $X$  with the base acceleration  $s^2 W_{c1}$ .

Since the aim of this study is to assess if the newly designed and fabricated prototype MEMS velocity sensor produces the desired dynamic response the open loop frequency response function has been measured and then contrasted with that simulated from Eq. (9) assuming  $g_s = 0$ . As shown in Figure 3 the predicted open-loop frequency response function shows two resonance peaks at 1.49 kHz and 4.52 kHz.

The 2-DoF velocity sensor is designed with a second resonance frequency well above the first resonance, allowing the control sensor to measure the acceleration of the principal mass.

### III – Prototype 2-DoF velocity sensor

The velocity sensor was fabricated in the Nanofabrication centre at the University of Southampton, with Silicon - On - Insulator (SOI) wafer of a 6 inch diameter. Its device layer of phosphorous doped n-type silicon has a resistivity of 0.001–0.0015  $\Omega\text{cm}$ . The silicon dioxide sacrificial layer of 2  $\mu\text{m}$  thickness rests between two silicon layers.

The microfabrication of the sensor was performed with two lithography masks; the top side mask defines the structure of the sensor with a structure layer of 50 $\mu\text{m}$  thickness. The bottom side mask, used for the back etching, defines the back areas to be exposed for the DRIE process. This allows the etching agent to go through the deep 200 $\mu\text{m}$  substrate silicon layer up to the silicon dioxide layer, thus enhancing the releasing. Also, a large silicon structure such as proof mass does not require etching holes on the top side.

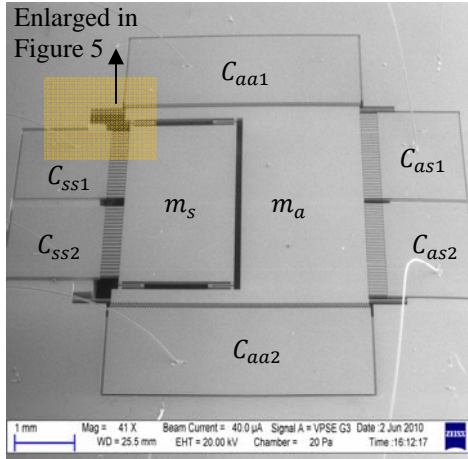


Figure 4. SEM of the SOI-fabricated 2-DoF velocity sensor

Figure 4 shows the SEM picture of the velocity sensor, including the control sensor of mass  $m_s$  encapsulated inside the principal sensor, the principal mass  $m_a$  suspended with four beams to the anchors, and the principal sensor designed with two sets of differential capacitors. The first represents the sensing capacitors ( $C_{as1}$  and  $C_{as2}$ ) designed with parallel electrodes. The second set represents the actuating capacitors ( $C_{aa1}$  and  $C_{aa2}$ ) designed with lateral comb electrodes. The control sensor, suspended inside the

principal mass with four folded beams, has differential sensing capacitors denoted with  $C_{ss1}$  and  $C_{ss2}$ . These are designed with a parallel electrode structure.

Each device has been released individually to avoid harming the fragile structure during the releasing process, which was performed using the HF Vapor-Phase Etcher.

Figure 5 shows one of four beams holding the principal mass, and one of the four folded beams holding the control mass inside the principal sensor. It also depicts the lateral comb capacitor and the parallel capacitor.

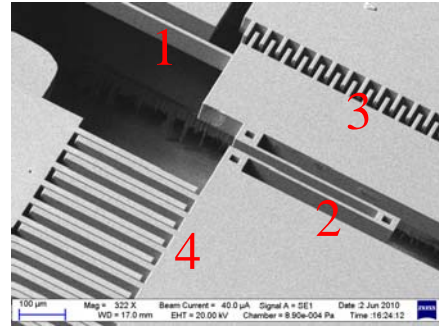


Figure 5. SEM photo of 1) the beam of the principal mass, 2) the folded beam of the control mass, 3) the actuating lateral comb capacitors of the principal sensor, and 4) the parallel sensing capacitor of the control sensor

The sensor is fixed with crystal bond on a PCB package with a transparent plastic lid designed in house and wire bonded to the appropriate pads on the PCB as shown in Figure 6.

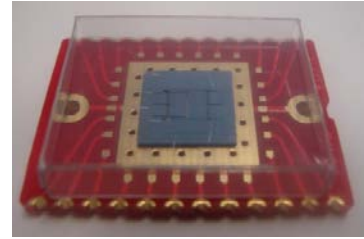


Figure 6. 2-DoF velocity sensor placed on PCB package and wire bonded to the PCB bonding pads

### IV – Optical measurements

The 2-DoF velocity sensor block was successfully micromachined and initially tested using the MSA400 microsystem analyzer. The test was performed by applying an excitation AC signal ( $V_{ex}$ ) on the principal mass, with bias voltages ( $\pm V_b$ ) connected to the differential sensing capacitor of the principal sensor. Figure 7 shows this configuration.

The value of the excitation and bias voltages were carefully calculated in order to avoid collapsing the capacitor electrodes. The amount of the voltage can be deduced by equating the testing electrostatic force ( $F_{es}$ ) generated by  $V_{ex}$  and  $\pm V_b$  with the principal sensor's spring force ( $F_{spring}$ ). If mass displacement  $x$  is assumed very low compared with the air gap  $d$  between the parallel electrodes ( $x \gg d$ ), the simplified electrostatic force of the differential capacitor is given by [6]:



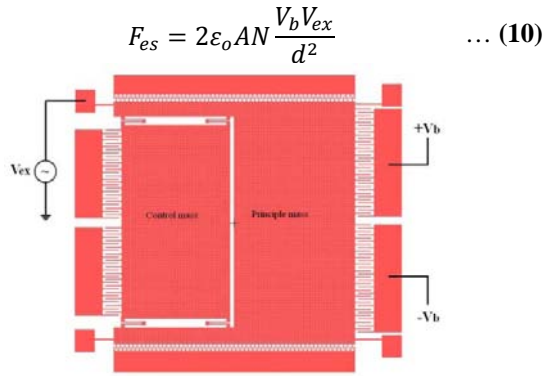


Figure 7. Testing electrical wiring configuration of the 2-DoF velocity sensor

where  $\epsilon_o$  is air permittivity,  $A$  is the overlap area of the two parallel electrodes, and  $N$  is the number of capacitors.

The spring force is given by:

$$F_{spring} = xk \quad \dots (11)$$

Where  $k$  is the spring constant, and  $x$  is the deflection of the spring.

Using equations (10) and (11), the excitation voltage can be given by:

$$V_{ex} = \frac{xkd^2}{2\epsilon_oANV_b} \quad \dots (12)$$

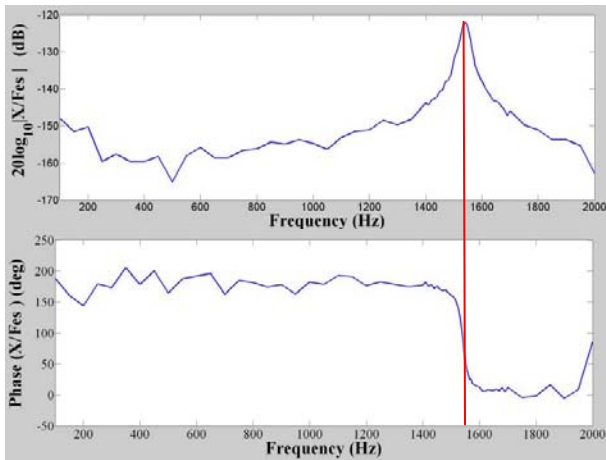


Figure 8. FRF optical measurement of the 2-DoF velocity sensor between the principal mass displacement 'X' and the applied electrostatic force ' $F_{es}$ '. The figure shows the first resonance peak at 1540Hz.

The optical FRF results shown in Figure 8 and Figure 9 has been obtained by applying  $V_{ex}=3v$  and  $V_b=\pm 10v$ . These voltages excite the velocity sensor with a varying frequency electrostatic force  $F_{es} \approx 9\mu N$ , equivalent to 0.87g. The optical results show the frequency response of the 2-DoF velocity sensor as a relation between the displacement  $x$  of the principal mass and the electro-static force equivalent to base acceleration. The measured frequency response function shows a flat response with  $180^\circ$  phase up to the first resonance. The obtained results are close to the theoretical one shown in Figure 3, and the two resonance peaks are at 1.540 kHz and 4.225 kHz.

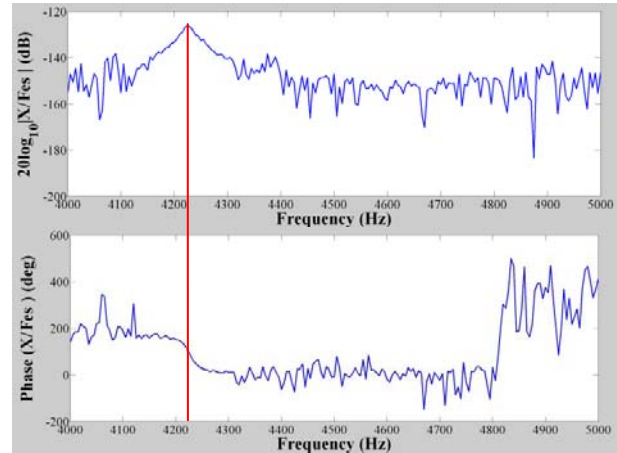


Figure 9. FRF optical measurement of the 2-DoF velocity sensor between principal mass displacement 'X' and applied electrostatic force ' $F_{es}$ '. The figure shows the second resonance peak at 4225Hz.

## V – Conclusion

This paper described the 2-DoF velocity sensor with an internal feedback loop in terms of operating concepts and offered a brief description of the associated electronic circuit, fabrication process, and testing configuration, along with the initial optical test results.

The results show a close match to the predicted open loop response, where the theoretical 2-DoF resonant frequencies are on 1.493 kHz and 4.512 kHz, while the optical test result shows two resonant frequencies on 1.540 kHz and 4.225 kHz.

Currently, further testing and measuring continue to explore the design and implementation of the close-loop 2-DoF velocity sensor.

## References

- [1] Gavagni, M., Gardonio, P., Elliot, S.J. "Design and fabrication of a micro-velocity sensor for direct velocity feedback control systems." In, Proceedings of the Sixth International Symposium on Active Noise and Vibration Control, Adelaide, Australia, 2006.
- [2] Gardonio, P.; Gavagni, M.; Bagolini, A., "Seismic Velocity Sensor With an Internal Sky-Hook Damping Feedback Loop," Sensors Journal, IEEE, vol.8, no.11, pp.1776-1784, Nov. 2008
- [3] Sun, J. Q., "Some observations on physical duality and collocation of structural control sensor and actuators", Journal of Sound and Vibration - 194, pp.765-770, 1996.
- [4] Holterman, J., De Vries, T. J. A. "Active Vibration Control based on Collocation" In Proceedings of the eighth Mechatronics Forum International Conference, pp.1038-1047, Enschede, The Netherlands, 2002
- [5] Yazdi, N.; Ayazi, F.; Najafi, K., "Micromachined inertial sensors," Proceedings of the IEEE, vol.86, no.8, pp.1640-1659, Aug 1998
- [6] Beeby, S., Ensell, G., Kraft, M., White, N., "MEMS Mechanical Sensors", Artech House, Inc, 2004.

## COMPUTATIONAL ANALYSIS OF MICROPARTICLE SEPERATION IN STRAIGHT CHANNELS

Huseyin Kizil<sup>1</sup>, Levent Trabzon<sup>2</sup>, Levent Yobas<sup>3</sup>, Mustafa Yilmaz<sup>1</sup>, Arzu Ozbey<sup>2</sup>

<sup>1</sup>Department of Materials and Metallurgical Engineering, Istanbul Technical University, Istanbul 34469, Turkey

<sup>2</sup>Department of Mechanical Engineering, Istanbul Technical University, Istanbul 34469, Turkey

<sup>3</sup>Department of Electronic and Computer Engineering, Hong Kong University of Science and Technology, Hong Kong

**Abstract** — This study is aimed to show the effects of channel parameters to particle separation in straight channels. In addition to the momentum change along with channel geometry, the  $Re_p$  will increase or decrease due to change in the fluid flow rate. Using an appropriate channel design, particles can be separated along the microchannel by just controlling the fluid flow rate. It was found that particles with  $Re_p \gg 1$  at any point the particle will move laterally, and particles with  $Re_p \ll 1$  will follow the streamlines. This study proved that particle separation in a micro channel system could be accomplished by changing the particle Reynolds number. It was found that width, percent contraction, and length of the expansion have crucial roles for the efficiency of particle separation.

**Keywords :** *microparticle, microchannel, inertial particle separation, inertial lift force, drag force.*

### I - Introduction

Micro particle separation techniques have received significant importance for biomedical, chemical and medical applications. Most common separation techniques are centrifugation and membrane based filtration techniques in macro scale systems. The main problem for filtration is the limitations of membrane clogging and the necessity to use excess amount of fluids.

Recently, inertial migration based particle separation techniques have been reported to achieve high throughput particle separation [1-2]. Under the influence of inertial forces, neutrally buoyant particles flowing in a microchannel migrate to a stable equilibrium position along the channel periphery. This single particle stream can later be extracted by employing bifurcated outlets. DiCarlo et al. [3] investigated the inertial focusing in a straight microchannel and showed that uniformly distributed particles in rectangular channels migrate across the streamlines of four symmetric equilibrium positions at the centers of the sides of channel and move closer to the channel walls as  $Re_p$  (particle Reynolds

number) increases. Kim et.al. [4] observed that particles focused to a narrow band along the perimeter, which is about  $0.2 D_h$  (Hydraulic diameter) away from the walls of the square channels, and have low Reynolds numbers ( $Re < 20$ ). Recently, Askar et al. [5-6] found that the inertial focusing positions of particles in a straight microchannel also depend on the channel aspect ratio. They found that particles equilibrate into two focused streams along the longer sidewalls for both  $H / W > 1$  (H: Height, W: Width) and  $W / H > 1$  at the same  $Re_c$  (channel Reynolds number). Park et al. [7] investigated the inertial focusing of particles with

using two sided multiorifice type micro channels in a series of narrow and wide sections. Having vortex flows at the side wall corners of wide sections make another particle focusing position apart from that in straight channels. They observed that particles which have  $Re_p$  in a range of 0.8 to 2.3 were focused at two side positions and particles with  $Re_p$  in a range of 3 to 3.5 were focussed at the centerline.

### II - Experimental Details

The major forces acting on neutrally buoyant particles flowing through microchannel are the viscous drag force and the inertial lift forces. The drag force due to the viscous nature of the fluid acts in the opposite direction of the flow velocity thus responsible for ordering particles along the flow streamlines. The inertial lift forces act in the positive and negative directions and cause lateral migration of particles across the flow streamlines.

The first experiment about lateral migration due to the inertial lift forces was done by Segre and Silberberg [8]. They observed that particles migrated to a radial equilibrium position at the pipe radius (R) of 0.62 from the axis of the pipe. This effect is known as the Tubular Pinch Effect (TP), which is a result of competition of inertial lift forces acting on a particle. Matas et al. [9] experimentally confirmed TP effect for a wide range of Reynolds numbers and found that equilibrium positions shift towards the wall with increasing  $Re$ .

The dominant inertial lift forces are the shear – gradient induced lift force ( $F_{SG}$ ) and wall induced inertial lift force ( $F_{WL}$ ) shown in Figure 1. In Poiseuille flow, the parabolic velocity profile results in  $F_{SG}$  acting on the particles. The flow velocity vectors relative to the particles are larger on the centerline than that of on the wall side. This causes the particles to rotate and migrate towards to the wall of channel. In addition to  $F_{SG}$ , particles are also affected from wall induced inertial lift force as they get closer to the wall. Rotating particle in a fluid system imparts a rotational component to the immediately surrounding fluid which results in the formation of symmetric wake around the particle. As particles move closer towards the channel wall under the influence of  $F_{SG}$ , the presence of the channel wall disrupts this rotational wake. The asymmetric wake vorticity induces high pressure on the channel wall side and  $F_{WL}$  drives the particle away from the wall towards to the channel centerline (Figure 1) [3,6,8,10]

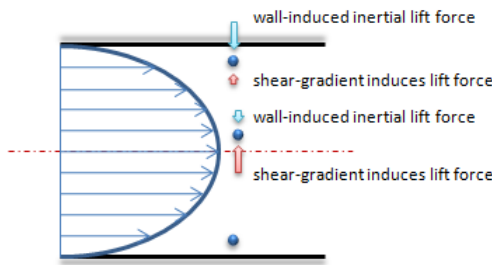


Figure 1. Inertial lift forces acting on the spherical particles in Poiseuille flow

It has been well determined with the studies that variable channel geometry induces a fluctuation in the fluid flow and so on the particle. With a change in the fluid speed the Reynolds number and the particle Reynolds number will also change and so does the behavior of the particle. Park et al. [13] studied experimentally a two-sided contraction / expansion based multiorifice microchannel. In the expansion part of the channel the Reynolds number decreases with the hydraulic diameter of the channel so that streamlines of the fluid flow will be expanded. The movement of particles along the just formed fluid streamlines affects the momentum of the particles in the stream.

In addition to the momentum change along with channel geometry, the  $Re_p$  will increase or decrease due to change in the fluid flow rate. Using an appropriate channel design, particles can be separated along the microchannel by just controlling the fluid flow rate.

### III - Results and Discussion

This study is aimed to show the effects of channel parameters to particle separation in straight channels. COMSOL Multiphysics software was used for simulations, MATLAB and MS Excel were used for various computational analysis. Minitab is used for statistical analysis. Main variables kept constant in the analyses are given in Table 1.

Table 1. Constant variables in the computational analysis

Variable	Value
Fluid properties	Behaves as Water
Particle 1 diameter/mass	6 $\mu\text{m}$ / $1.02 \times 10^{-12}$ kg
Particle 2 diameter/mass	14 $\mu\text{m}$ / $1.29 \times 10^{-11}$ kg
Particles density	1125 kg/m <sup>3</sup>

#### A. COMSOL Simulations for Separation

Microfluidics module of COMSOL Multiphysics simulation tool was used for simulating the flow in a microchannel with contraction and expansion at one side of the channel. It was considered that with only allowing one sided contraction and expansion in microchannel, a wall effect induced inertial lift will be exerted on the particle, which then will increase the lateral movement in the expansion part of the channel. A basic schematic view of the proposed microchannel design is given in Figure 2.

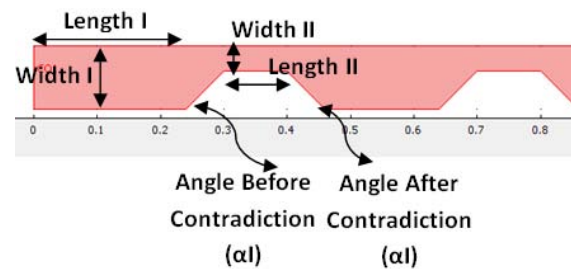


Figure 2. Channel design parameters for the simulations given in Table 2.

Incompressible Navier–Stokes method was chosen and all the simulations were solved as non-linear. Fluid input velocity was set as 0.01 m/s. First simulation run was done for fluid properties without any particle in the system. Basic design parameters and the resulting flow velocities can be found in Table 1.

The velocity values given in Table 2 can be defined as follows: maximum velocity is the velocity at the center of contraction part of the channel, minimum velocity is

the velocity at the corner point of the expansion/contraction region and maximum velocity at expansion is the velocity at the center of expansion part of the channel.

Table 2. Fluid flow simulations run on different channel geometries.

Width I [μm]	Width II [μm]	Length I [μm]	Length II [μm]	$\alpha_1$	$\alpha_2$	velocity at expansion channel	velocity at contraction channel
100	40	300	100	90	90	0.0463	0.0195
100	40	300	100	45	90	0.0462	0.0195
100	40	300	100	45	45	0.0459	0.0195
200	20	100	300	45	45	0.167	0.0653
200	80	200	50	90	90	0.0597	0.0209
100	30	200	300	60	90	0.0595	0.0194

As seen from the Table 2 the velocity of fluid in the channel can be controlled by changing the channel geometry yet some of the design parameters are not affecting the fluid properties. For this reason statistical study was done for determining the optimum design parameters of microfluidic channel.

Figure 3 gives the particle trajectories for the channels given in the Table 2.

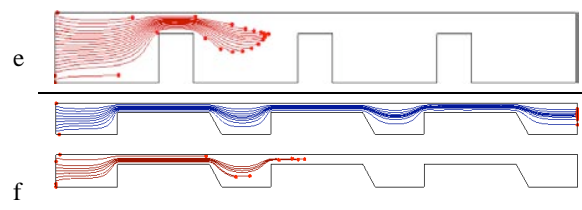
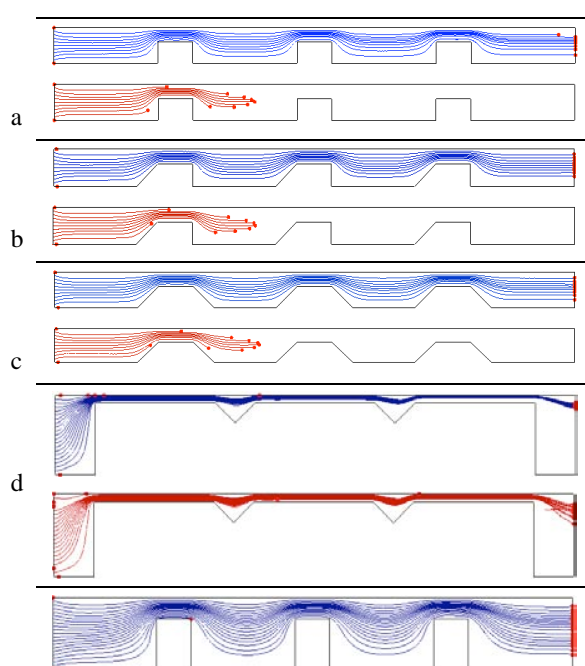


Figure 3. Particle trajectories of the simulations given at Table 2 (Blue: 14 μm particle, Red: 6 μm particle)

The particle trajectories are determined with using particle-tracking module of the post processing analysis of COMSOL Multiphysics. It can be seen that the particles are following a streamline and both particles are following a different streamline at the expansions of the channel. The problem causing the discontinuity of the particle 1 was due to meshing in the simulation runs.

#### B. Computational Mathematics with MATLAB and MS Excel

Since COMSOL does not exactly provide the particle trajectories, MATLAB was used to solve the exact trajectories changing with time. Particles with 6 and 14 microns in diameter were fed from the same point as shown in Figure 4 design (a), and the trajectories of the particles calculated in MATLAB are shown in Figure 4.

MS Excel environment is used for calculating the  $Re_p$  of the particles. The fluid flow velocities were gathered from COMSOL and used as input into MS Excel to calculate the  $Re_p$  numbers with respect to channel geometries. It was found that particles with  $Re_p \gg 1$  at any point the particle will move laterally and particles with  $Re_p \ll 1$  will follow the streamlines. The figure 5 is an example of an analysis of MS Excel environment.

In this analysis minimum and maximum points of the graphic is the contraction and expansion parts of the channel (minimums are expansion points, maximums are contraction points). This analysis showed that particles with larger radius are affected more from the channel geometry as their  $Re$  numbers grow higher. Furthermore it can be thought that particles with larger radius will move much more laterally in the fluid flow.



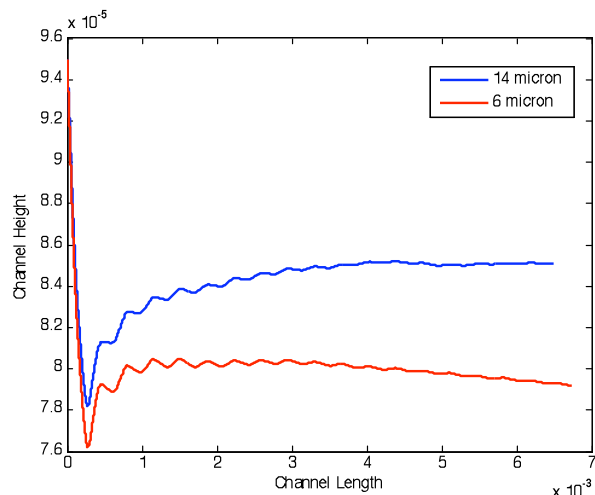


Figure 4. Matlab computation for design (a) where both particles are fed from 95 microns in height and 50 microns in width.

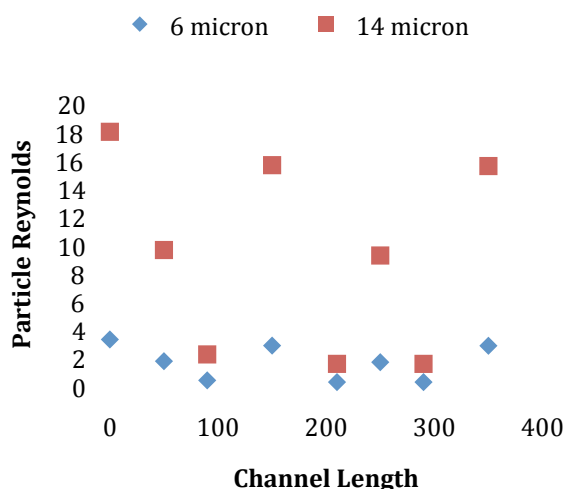


Figure 5. Particle Reynolds number difference in entire channel

#### IV - Conclusion

This study proved that particle separation in a micro channel system could be accomplished by changing the particle Reynolds number. It was found that width, percent contraction, and length of the expansion have crucial roles for the efficiency of particle separation.

#### References

1. T. Kulrattanak , R.G.M van der Sman, C.G.P.H. Schroën, R.M. Boom "Classification and evaluation of microfluidic devices for continuous suspension

- fractionation" Advances in Colloid and Interface Science 142 , 53–66 (2008).
2. Nicole Pamme "Continuous flow separations in microfluidic devices" Lab Chip, 7, 1644–1659 2007.
3. Dino Di Carlo, Daniel Irimia, Ronald G. Tompkins, and Mehmet Toner "Continuous inertial focusing, ordering, and separation of particles in microchannels" Proc. Natl. Acad. Sci. U.S.A 2007, 104, 18892-18897.
4. Kim and J. Yoo, "The lateral migration of neutrally-buoyant spheres transported through square microchannels," J. Micromech. Microeng. 18, 065015 (2008).
5. Ali Asgar S. Bhagat, Sathyakumar S. Kuntaegowdanahalli, and Ian Papautsky "Enhanced particle filtration in straight microchannels using shear-modulated inertial migration" Phys. Fluids 20, 101702 (2008).
6. Ali Asgar S. Bhagat, Sathyakumar S. Kuntaegowdanahalli, and Ian Papautsky "Inertial microfluidics for continuous particle filtration and extraction" Microfluid Nanofluid, 7:217–226, (2009).
7. Park J, Song S, Jung H Continuous focusing of microparticles using inertial lift force and vorticity via multi-orifice microfluidic channels. Lab Chip 9:939–948, (2009).
8. G. Segre and A. Silberberg, "Radial particle displacements in Poiseuille flow of suspensions," Nature (London) 189, 209 (1961).
9. P. Matas, J. Morris, and E. Guazzelli, "Inertial migration of rigid spherical particles in Poiseuille flow," J. Fluid Mech. 515, 171 (2004).
10. Ali Asgar, S. Bhagat, Sathyakumar S. Kuntaegowdanahalli, Ian Papautsky Continuous particle separation in spiral microchannels using dean flows and differential migration. Lab Chip Lab Chip, 8, 1906–1914 (2008).
11. E. Asmolov, "The inertial lift on a spherical particle in a plane Poiseuille flow at large channel Reynolds number," J. Fluid Mech. 381, 63 (1999).
12. Ali Asgar S. Bhagat, Sathyakumar S. Kuntaegowdanahalli Necati Kaval, Carl J. Seliskar, Ian Papautsky "Inertial microfluidics for sheath-less high-throughput flow cytometry." Biomed Microdevices DOI 10.1007/s10544-009-9374-9
13. Park J., Jung H. (2009) "Multiorifice Flow Fractionation: Continuous Size – Based Separation of Microspheres Using a Series of Contraction / Expansion Microchannels" Anal. Chem, 81, 8280 – 8288, (2009).

# FABRICATION OF CANTILEVER ARRAYS WITH TIPS FOR PARALLEL OPTICAL READOUT

W.W. Koelmans<sup>1</sup>, T. Peters<sup>1</sup>, L. Abelman<sup>1</sup> and M. C. Elwenspoek<sup>1,2</sup>

<sup>1</sup>MESA+ and IMPACT Research Institutes, University of Twente, Enschede, The Netherlands

<sup>2</sup>Freiburg institute for Advanced Studies, Albert-Ludwigs-Universität Freiburg, Freiburg, Germany

**Abstract** — We report on progress in the fabrication of cantilever arrays with tips. The process features only one lithographic step for the definition of both the tips and cantilevers. The tips have a uniform height distribution and are placed by self-alignment on the cantilever. The arrays are fabricated for an optical readout technique under development in which the cantilever arrays serve as diffraction gratings. This work describes our ongoing effort in array fabrication as well as preliminary results on optical readout of a previously fabricated batch of tipless cantilever arrays using Fraunhofer diffraction.

**Keywords** : Cantilever array, Tip fabrication, Optical readout

## I - Introduction

Arrays of microcantilevers are fast and highly sensitive transducers having enormous potential in a variety of applications, among which probe-based data storage [1], probe based nano-lithography and nanomanufacturing. There are many challenges related to maturing cantilever array technology for application purposes. In this work we are concerned with two major consequences of scaling up from a single cantilever to a cantilever array.

Firstly, fabrication tolerance will result in deviation in tip height across the array. This is not only caused by the actual height of the tip, but also by the cantilever that supports it. When trying to utilize such an array one has to apply a higher loading force in order to make all cantilever tips touch the sample underneath. Meaning that tolerance in tip height will directly translate into different loading forces on the tips while operating them. Variation in loading force across an array will, in turn, results in reduced overall performance.

Secondly, many applications require readback of cantilever motion and readback techniques have to be able to handle arrays. A common way of detecting cantilever motion is by integrating a sensor into the cantilever and then wiring, in a matrix fashion, each sensor [2]. The most used sensors include piezoelectric [3], thermal [4] and magnetoresistive sensors. However, such a sensor integration will not only add to the complexity of the fabrication process, it also poses extra demands on cantilever probe design and possibly puts a limit on admissible fabrication steps.

In this work we aim to reduce the complexity which arises from fabricating and reading out cantilever arrays.

We show progress on the fabrication of cantilever arrays where only one mask is used to define both tip and cantilever. The fabrication process is partly based on [5]. The tip is self-aligning on the cantilever and its height is defined by a wet etching step. Therefore we expect to obtain a small deviation in tip height and position across an array. Next, we propose an optical readout method that can read out cantilevers in parallel, while not posing extra demands on the cantilever design, unlike an optical readout solution reported in [6]. The optical readout technique is non-invasive and is easily replaceable in case of breakdown. Whereas integrated sensors cannot be replaced. First experimental results on optical readout of previously fabricated tipless cantilever array are presented.

## II - Fabrication Details

The cantilever arrays are fabricated using silicon on insulator wafers with a device layer thickness of 10  $\mu\text{m}$  that has a  $\langle 100 \rangle$  orientation. The process flow for the fabrication of the cantilever arrays is shown in figure 1. A layer stack of 25 nm silicon rich nitride (SiRN), 100 nm silicon oxide and 20 nm SiRN is deposited. The top layer of SiRN is patterned with a first lithographic step. A wet etch in buffered HF is applied to locally remove the silicon oxide layer and we purposefully create about 1  $\mu\text{m}$  of undercut under the top SiRN layer. This undercut sharpens the corner that will house the tip, effectively increasing the resolution of our lithography process, which is limited to 1  $\mu\text{m}$ . Consequently, the final tip apex will be more precise defined and also its position is set more accurately. After removal of the top SiRN layer by a phosphoric acid etch, the cantilever is cryogenically etched out of the device layer. The cryogenic etch is a critical step in the fabrication process, because it creates two side walls of the tip. Most important is the transfer of the hard mask into the first hundreds of nanometers of silicon. Any amount of undercut will reduce the height of the tip when the KOH etch is performed. By optimisation of the cryogenic etching process a nice, straight etch profile is obtained, as shown in figure 2. The cryogenic etch is performed with an ADIXEN AMS100 SE. At a temperature of  $-100^\circ\text{C}$  and at a pressure of  $1.3 \cdot 10^{-2}$  mbar an  $\text{SF}_6$  flow of 100 sccm and an oxygen flow of 12 sccm is applied to etch the silicon 5  $\mu\text{m}$  down.

After the cryogenic etch, the sidewalls of the cantilever are protected by local oxidation. Now a wet, anisotropic KOH etch creates the tips. This is possible

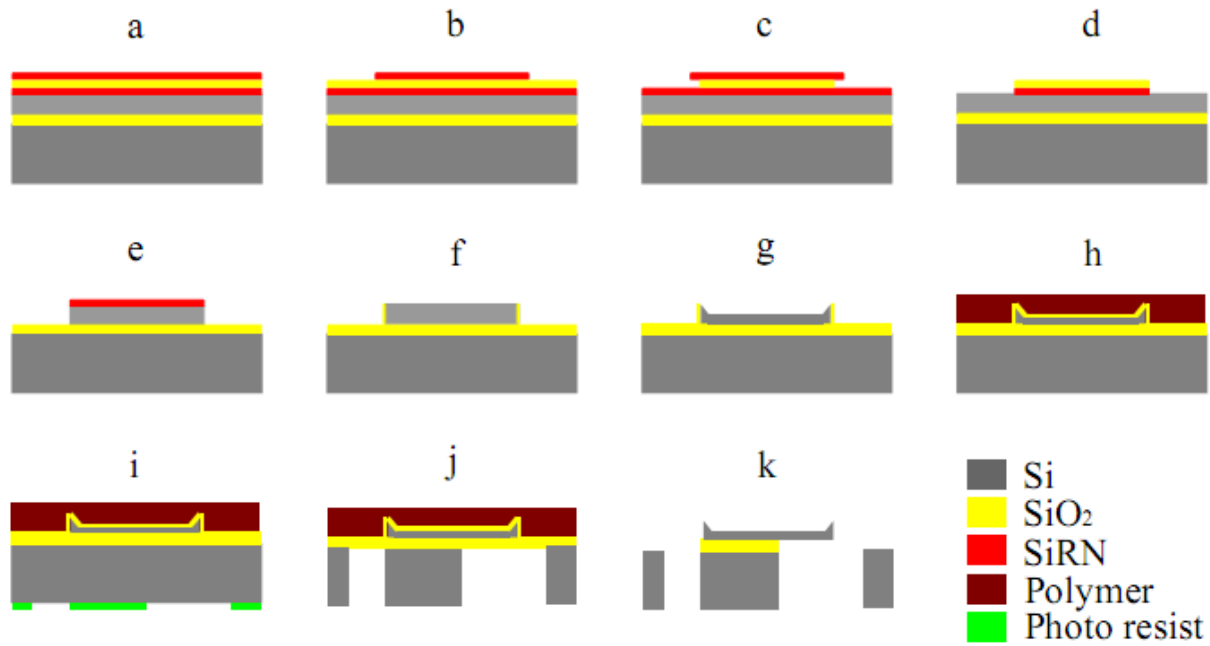


Figure 1: Process flow of the fabrication process of the cantilever arrays with tips. (a) Deposition of 25 nm SiRN, 100 nm SiO<sub>2</sub> and 20 nm SiRN layers. (b) Patterning of top SiRN. (c) BHF etch of SiO<sub>2</sub>. (d) Phosphoric acid etch removes SiRN locally. (e) Cryogenic etch defining cantilever outline. (f) SiRN removal and oxidation to 100 nm. (g) KOH etch creating tips. (h) Oxidation to 100 nm and spray coating of a polymer film protection layer. (i) Backside patterning in second lithographic step. (j) Backside etch until the buried oxide layer. (k) Removal of pyralin and local removal of SiO<sub>2</sub>.

since the cantilever is aligned with the  $\langle 110 \rangle$  direction and the triangular shape of the tip end yields the tip due to the slow etching of the  $\{111\}$  plane. Due to the uniformity of the KOH etching step, tip height is expected to show little variation within one array. The KOH etch also defines the final thickness of the cantilever. Another oxidation step grows 100 nm of silicon oxide to both protect as well as sharpen the tips. A polymer film (DuPont MX5000) is applied by lamination to add additional protection to the tips during the backside etch procedure.

A second lithographic step is now used to pattern a 3.5  $\mu\text{m}$  thick layer of photo resist on the backside of the wafer. A wafer-through backside etch is performed using a deep reactive ion etch. A pulsed process is used with SF<sub>6</sub> (400 sccm, 4 s) and C<sub>4</sub>F<sub>8</sub> (25 sccm, 0.5 s). The polymer film is then removed by oxygen plasma stripping. Finally, both the protective oxide layer, as well as the exposed parts of the buried oxide layer are etched away in 1% HF. This final step releases the cantilevers.

## II – Current Fabrication Results

We have completed a successful test run where silicon wafers have been used instead of silicon on insulator wafers. The process flow is exactly the same, except for the final few steps, i.e. figure 1 (j) and (k). As a result cantilevers with tips are created on top of a silicon wafer and cannot be released, as shown in figure 3.

A disadvantage of the described process is the occurrence of a ridge that stands on the sides of the cantilever, see figure 2 (a). These ridges are caused by the slow etching of the  $\{111\}$  plane, just like the formation of the tip plane. We solve this issue by adding a small

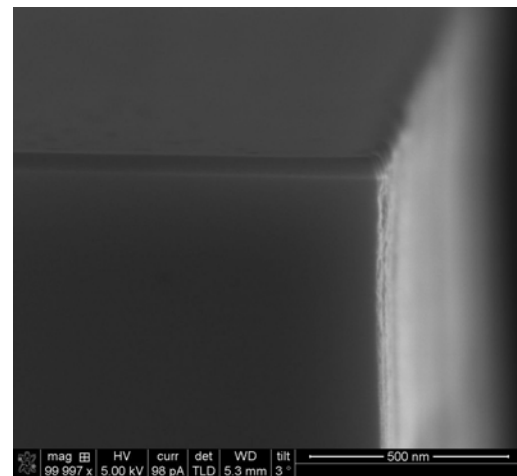


Figure 2: SEM image of a well defined straight etch profile obtained by cryogenic etching after the etching procedure has been optimized. Important is the lack of undercut, since undercut will influence the tip height in a later stage of the process.

taper to the width of the cantilever. Figure 2 (b) shows that an angle of 10 degree is sufficient to remove the ridge. Note that remainders of the SiO<sub>2</sub> protection layer are still present.

## III – Experimental Details

The cantilever arrays are fabricated for optical read-out experiments where the array serves as a diffraction grating. The medium topography is transferred into bending of the cantilevers hereby modifying the diffraction grating, which results in a change in a detectable change in the diffraction pattern. We have constructed

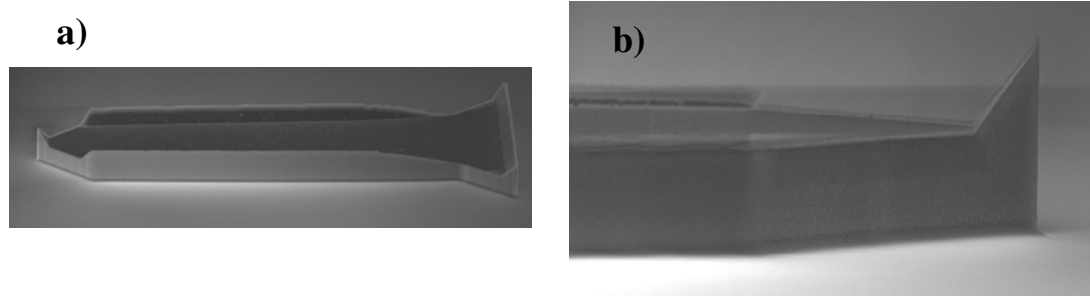


Figure 3: (a) SEM photograph showing a fabricated cantilever with tip and standing ridge at the cantilever sides and base. The cantilever has not been released from the substrate. (b) SEM photograph showing a cantilever design where the ridge is effectively prevented at the sides of the cantilever by adding a taper of  $10^\circ$  to the width of the cantilever. Note that the silicon oxide protection layer is still visibly present.

an optical setup to readout a one dimensional array of cantilevers. A schematic depiction of the optical path is shown in figure 4. The spot from a diode laser with a wavelength of 635 nm and 5 mW power is expanded five times using a beam expander. The beam is sent through a rectangular shaped slit and then focussed in one direction by a cylindrical lens with a focal distance of 200 mm. A prism reflects the beam on the cantilever array, which is positioned in the focal point of the cylindrical lens. The laser spot is now line shaped and illuminates each of the cantilevers in the array. The reflected light from the cantilever array creates a one dimensional Fraunhofer diffraction pattern. The pattern is reflected by a second prism into a second cylindrical lens with a focal distance of 60 mm. This lens is rotated 90 degrees with respect to the first cylindrical lens. This second lens determines the width of the diffraction pattern on the CCD camera. The CCD camera is connected to a computer equipped with software capable of reading back the data from the CCD camera.

The cantilever array is positioned inside a measurement chamber that can be sealed off using a glass window. Depending on the experiment the chamber can either be air filled, pumped to a high vacuum or filled with nitrogen gas. Current measurements are taking

place with the glass cover removed.

The first optical readout experiments are performed using previously fabricated cantilever arrays. The arrays have been fabricated much along the lines of the current fabrication process, however they lack tips. The aim of these experiments is to verify whether Fraunhofer diffraction theory is applicable to an array of cantilevers and to quantify the quality of the optical patterns recorded by our newly constructed setup.

#### IV – Experimental Results and Discussion

Figure 5 shows the intensity profile obtained from the diffraction pattern of an array consisting of three cantilevers. The cantilevers are  $30\ \mu\text{m}$  wide and are spaced  $10\ \mu\text{m}$  apart. In the same figure a simulation of the expected profile is shown. The error of fit between the measurement and a calculated Fraunhofer diffraction profile is 0.87%. Although difficult to see at this scale, it is noted that at larger angles of diffraction ( $\theta$ ), the deviation between the measured and simulated pattern increases. We attribute this deviation to aberration of the second cylindrical lens.

Other authors have presented diffraction profiles from cantilevers before; however these profiles were

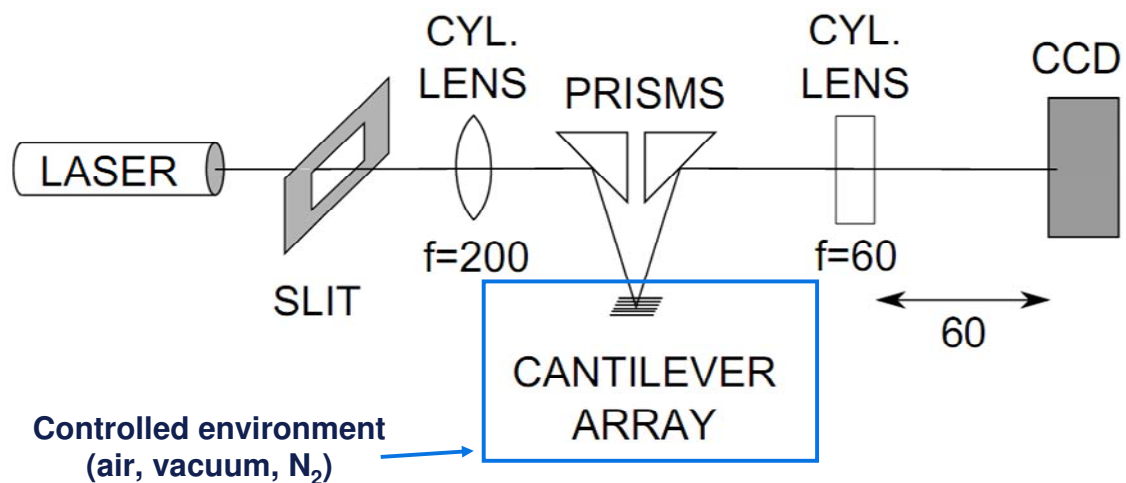


Figure 4: Schematic depiction of the optical readout setup for cantilever arrays. A rectangular laser spot is focused by a cylindrical lens into a line shaped beam, illuminating all cantilevers within the array. A second cylindrical lens (rotated 90 degree with respect to the first) shapes the diffraction pattern to fit the active CCD area.



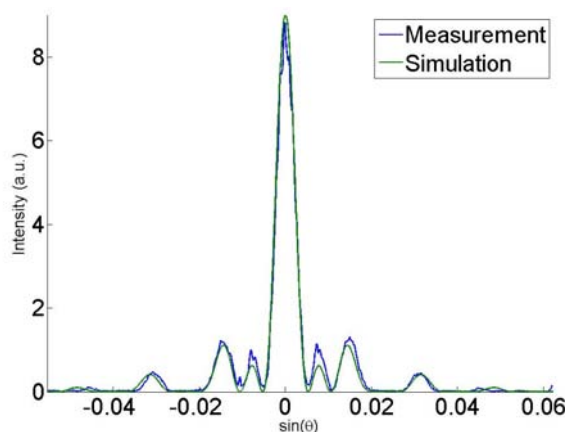


Figure 5: Intensity profile of the diffraction pattern of a cantilever array consisting of three cantilevers. The blue line is the measurement which fits very well (0.87% fitting error) with Fraunhofer diffraction theory (green line).

produced using a grating that is fabricated within every cantilever [6]. Here the array itself serves as a grating. This approach actively makes use of the complete array of cantilevers, in contrast to the approach of previous work to start off by reading out one cantilever and then gradually add more cantilevers.

Based on our calculations we expect that small cantilever deflections will result in only very small changes in the diffraction profile. This makes the optical readout method less suitable for applications in which nanometer sized deflections have to be measured. For applications such as indentation based probe storage the technique offers a distinct advantage. Since indentations are ideally all of the same depth, the deflection of each cantilever is either one of two possibilities: undeflected or deflected by the indentation depth. This eases the task of retrieving cantilever positions from the diffraction profile greatly.

## V – Conclusions

In conclusion we have shown significant progress in the fabrication of cantilever arrays with tips using only one mask to define both tips and cantilevers. A corner sharpening step is included in the process to overcome the 1  $\mu\text{m}$  resolution limit of our lithography tools. Cryogenic etching has been optimised to create straight etch profiles that will define the sidewalls of the tip. A KOH wet etch anisotropically etches the cantilever tips, self-aligned in the corner at the free end of the cantilever.

Also we have proposed an optical readout method capable of reading out cantilevers in parallel without any modification to the cantilever design. Illuminating the complete array by line shaped laser beam has been shown to result in a diffraction pattern obeying Fraunhofer diffraction theory. This opens up the way to readback of cantilever motion in a parallel fashion.

## Acknowledgments

The authors gratefully acknowledge Martin Siekman for experimental support, Johnny Sanderink for SEM imaging, Kechun Ma for help with the cleanroom work and, Meint de Boer and Erwin Beerenschot for their contribution to the fabrication process.

This work is supported by the European Union within the FP6 project Probe based Terabit Memory – ProTeM.

## References

- [1] P. Vettiger, G. Cross, M. Despont, U. Drechsler, U. Duerig, B. Gotsmann, W. Haeberle, M. A. Lantz, H. E. Rothuizen, R. Stutz and G. K. Binnig, *IEEE Trans. Nanotechnol.*, vol 1, pp. 39-54, 2002.
- [2] M. Despont, J. Brugger, U. Drechsler, U. Duerig, W. Haeberle, M. Lutwyche, H. Rothuizen, R. Stutz, R. Widmer, H. Rohrer, G. Binnig, P. Vettiger, *Sens. Actuators A*, vol. 80, pp. 100-107, 2000.
- [3] C. S. Lee, H.-J. Nam, Y.-S. Kim, W.-H. Jin, S.-M. Moon Cho and J. Bu, *Appl. Phys. Lett.*, vol. 83, pp. 4839-4841, 2003.
- [4] W. P. King, T. W. Kenny, K. E. Goodson, G. L. W. Cross, M. Despont, U. T. Duerig, H. Rothuizen, G. Binnig and P. Vettiger, 2002.
- [5] M. Kitazawa and A. Toda, *Jpn. J. Appl. Phys.*, vol. 41, pp. 4928-4931, 2002.
- [6] T. Sulchek, R. J. Grow, G. G. Yaralioglu, S. C. Minne, C. F. Quate, S. R. Manalis, A. Kiraz, A. Aydine and A. Atalar, *Appl. Phys. Lett.*, vol. 78, pp. 1787-1789, 2001.

# MORPHOLOGICAL CHARACTERISATION OF MICROMACHINED FILM BULK ACOUSTIC RESONATOR STRUCTURES MANUFACTURED ON GAN/SI

A. Cismaru<sup>1</sup>, A. Stavrinidis<sup>2</sup>, A. Stefanescu<sup>1</sup>, D. Neculoiu<sup>1</sup>, G. Konstantinidis<sup>2</sup> and A. Müller<sup>1</sup>

<sup>1</sup> *IMT-Bucharest, 32 B, Erou Iancu Nicolae str., 077190 Bucharest, Romania*

<sup>2</sup> *FORTH-IESL-MRG Heraklion, PO Box 1527, Crete, Greece*

**Abstract** — This paper presents the morphological characterization of very thin GaN membranes used in the manufacturing of film bulk acoustic resonator (FBAR) structures. Analysis has been developed using optical profile characterization using WLI (white light interferometry) technique.

Membrane deflection as function of the metallization thickness is analyzed.

Recently developed FBAR resonators manufactured on GaN/Si wafers, with an operation frequency beyond 5 GHz, are used as test structures for the morphological characterization.

**Keywords :** Micromachining, FBAR, morphology characterization, microwave

## I - Introduction

Conventional technologies for FBAR (film bulk acoustic resonator) devices are based on ZnO sputtered layers. This material is not compatible with monolithic integration with other circuit elements and is restricted to frequencies below 2 GHz.

The development, in the last years, of wide band gap (WBG) semiconductor technologies has opened the possibility to manufacture FBAR (film bulk acoustic resonator) and SAW (surface acoustic wave) devices for application in the GHz frequency range. Currently the cellular phone is evolving from the third generation (3G) to the fourth generation (4G) system with an expected operating within the 3-6 GHz frequency range. Wireless local area networks (WLAN), for high speed computer interconnections are another area of application for FBAR and SAW structures operating around 5 GHz.

Lately, the quality of highly oriented thin AlN and GaN piezoelectric films, sputtered or deposited by MOCVD, on semiconductor crystals, has improved dramatically. It became possible the development of acoustic devices (SAWs and FBARs) based on these semiconductor films. One clear advantage is the possibility to grow thin GaN or AlN layers on high resistivity silicon wafers, which offers compatibility with conventional semiconductor technology. This means that also processes such as MEMS, nanolithography and monolithic integration (with different passive and active circuit elements), can be included in the fabrication protocol.

Micromachining techniques can be used to manufacture thin, high quality self-sustainable membranes, which allow the increase of the resonance frequency of FBAR structures processed on these materials [1].

Compared with other substrates, the manufacturing of thin AlN and GaN membranes starting from GaN/Si or AlN/Si structures is an easier task. The advantages of the well known silicon micromachining technologies can be used and very thin GaN and AlN membranes can be manufactured. Taking into consideration the sound velocity for these materials, the resonance frequency becomes higher than 2 GHz if the membrane thickness is lower than 1  $\mu\text{m}$ . So in order to increase the resonance frequency of FBAR structures manufactured on AlN or GaN thin layers it is necessary to obtain very thin and reliable membranes

Recently FBAR structures manufactured on an AlN/diamond layer, working at 8 GHz has been reported [2].

The first GaN based FBAR resonators, manufactured on a 2.2  $\mu\text{m}$  thin GaN membrane and working at 1.3 GHz, has been reported by the authors ([3]-[4]). Recently we have reported the manufacturing of a FBAR structure working at 6.3 GHz [1].

Up to now a lot of effort has been devoted to device development, but the morphological analysis of the GaN membrane is missed. This paper presents fabrication and morphological characterization of very thin GaN membranes used in the manufacturing of film bulk acoustic resonator (FBAR) structures. Analysis has been developed using optical profile characterization, using WLI (white light interferometry) technique.

Membrane deflection as function of its thickness and as function of the backside metallization thickness is analyzed.

## II - Technology and characterization of FBAR structures manufactured on GaN/Si

Two different GaN/Si wafers, purchased from NTT AT Japan, have been processed. The layer structure for the first wafer is presented in Fig.1a: first the buffer (composed of AlN and AlGaIn layers) is deposited on high resistivity (111) oriented silicon and next the undoped GaN layer is deposited. The buffer layer thickness was 0.2  $\mu\text{m}$  for both wafers. The thickness of the GaN layer was 0.34  $\mu\text{m}$  for the first wafer and 0.2  $\mu\text{m}$  for the second wafer.

The layout of the FBAR test structure is shown in Fig.1b. The test structure was a series connection of two FBAR structures. Each structure is a square with sides of  $100\text{ }\mu\text{m}$ . The gap between the resonators was  $50\text{ }\mu\text{m}$ , and the series connection was obtained by a floating backside metallization.

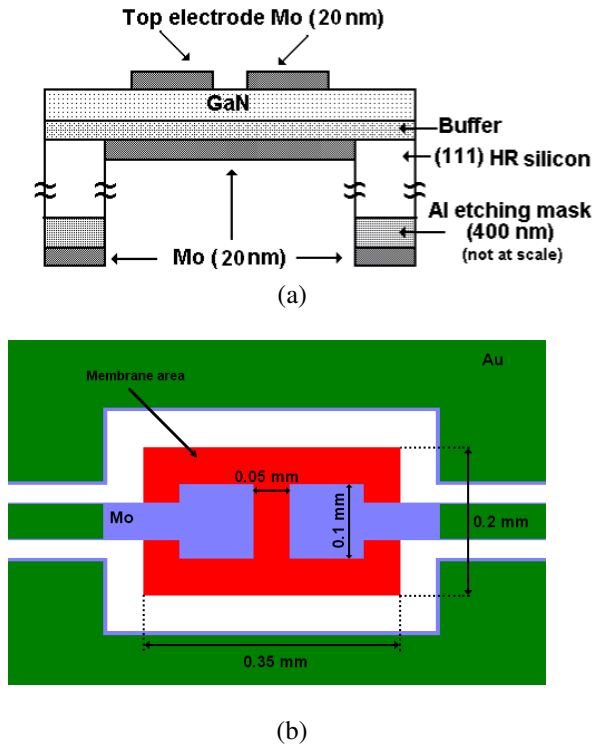


Figure 1. (a) Cross section of FBAR structure, (b) layout of FBAR structure

The resonators are fed by means of  $50/100/50\text{ }\mu\text{m}$  coplanar waveguide transmission lines. In the fabrication process, first a molybdenum layer  $50\text{ nm}$  thick was deposited on the top side and patterned using lift off techniques. A second mask was used to cover the molybdenum with a  $500\text{ nm}$  gold layer, overall excepting the FBAR squares. The thin molybdenum layer is essential for maximizing the performances of the resonator structure. It is demonstrated in reference [5] that electrodes with high acoustic impedance suppress the spurious responses and confines the longitudinal acoustic wave of the FBAR; this has as an effect the increase of the quality factor. The silicon wafer was thinned down to  $150\text{ }\mu\text{m}$  and an Al mask was subsequently deposited on the backside of the substrate, in order to serve as reactive ion etching (RIE) mask, for bulk micromachining. Membranes  $0.54\text{ }\mu\text{m}$  thin have been obtained on the first wafer and  $0.4\text{ }\mu\text{m}$  thin on the second one. Backside floating metallization,  $60\text{ nm}$  thick, was realized on the first wafer. For the second wafer 3 different backside metallization thicknesses ( $20\text{ nm}$ ,  $40\text{ nm}$  and  $90\text{ nm}$ ) have been used, in order to analyze their influence on the microwave performances of the structures but also to analyze the influence of the metallization on the membrane morphology.

The S parameters have been measured using a 37397D vector network analyzer from Anritsu, equipped with PM5 on wafer set-up from Suss Microtec.

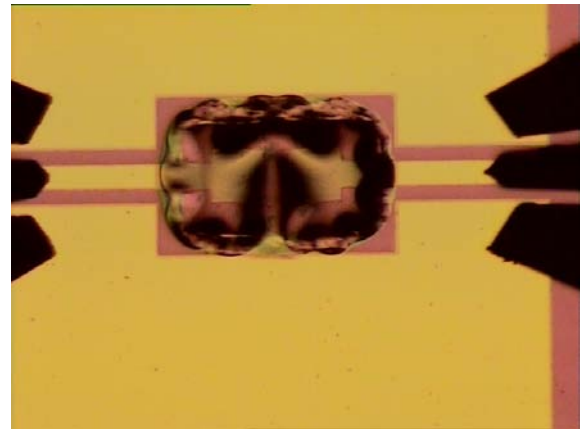


Figure 2. FBAR photo taken during the measurement procedure

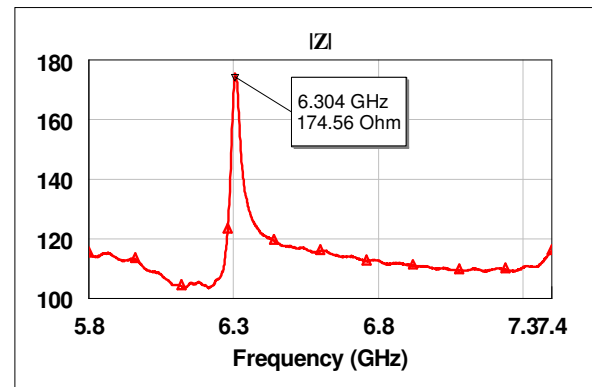


Figure 3. Z module for the FBAR structure having the  $60\text{ nm}$  Mo thin layer electrodes metallization thickness ( $0.54\text{ }\mu\text{m}$  GaN plus buffer thin membrane )

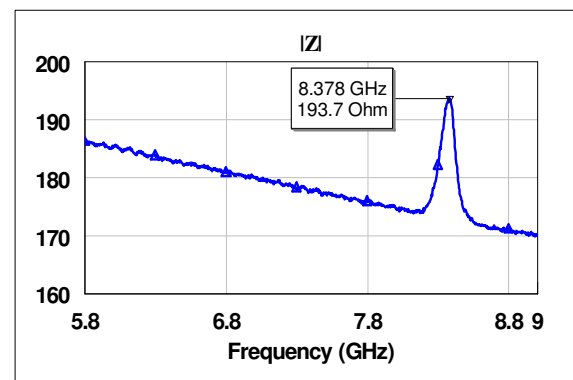


Figure 4. Z module for the FBAR structure having the  $20\text{ nm}$  Mo thin layer electrodes metallization thickness ( $0.4\text{ }\mu\text{m}$  GaN plus buffer thin membrane )

The FBAR structure photo taken during the microwave measurements of the S parameters is presented in Fig. 2. For the  $0.54\text{ }\mu\text{m}$  thick membrane FBAR structures having the  $60\text{ nm}$  Mo thin layer electrodes metalli-

zation thickness and the backside metallization also 60 nm thick resonance frequency was at 6.3 GHz ( fig 3); these results have been reported in [1]. For the 0.4  $\mu\text{m}$  thick membrane the three different type of structures FBAR structures ( with different backside metallization thickness) It has been demonstrated that as long as the thickness of the electrodes metallization is decreasing, the resonance frequency is increasing reaching the highest response ever reported for FBAR structures at 8.38 GHz (fig 4), for the structures with a20 nm thin backside metallization.

### III – Deflection analysis of thin GaN membranes obtained by micromachining of GaN/Si

The deflection of the thin GaN membrane has been analyzed using a white light interferometer (WLI) – Photomap 3D from Fogale. The 3D topography of the FBAR structure working at 6.3 GHz (manufactured on the first wafer) is presented in Fig. 5, where the “A” area indicates the pressure of the electrodes metallization of thin GaN membrane.

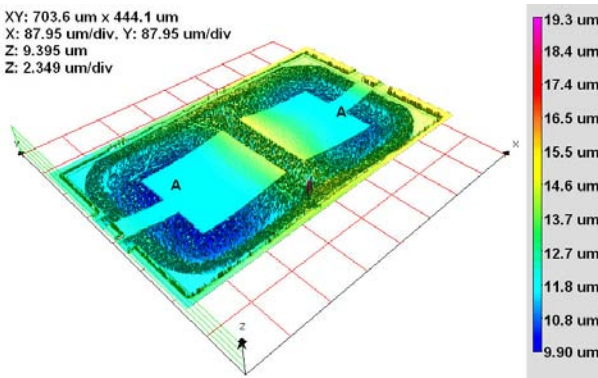


Figure 5. 3D topography of the FBAR structure in the membrane area (0.54  $\mu\text{m}$  GaN plus buffer thin membrane )

in Fig. 7, where the “A” area indicates the pressure of the electrodes metallization of thin GaN membrane.

The characterization of the membrane deflection, for the three structures with different thicknesses of the backside Mo layers, has been performed. The profile of the structure is presented in Fig. 8, where it is obvious that metallization thickness has an influence on membrane deflection.

The profile characterization demonstrates three different pressures of the electrodes metallization respectively  $h_1 = 3.30 \mu\text{m}$  for 90 nm,  $h_2 = 2.70 \mu\text{m}$  for 40 nm and  $h_3 = 2.50 \mu\text{m}$  for 20 nm depending of the molybdenum thickness. The maximum deflection, of  $H=5.3 \mu\text{m}$ , appears in the GaN membrane regions covered with the 90 nm thin molybdenum metallization layer only which are in compressive stress. Such a deflection, for a membrane having an area of  $350 \times 200 \mu\text{m}$ , is low enough not to have a significant influence on the mechanical stability of the structure and on the resonance frequency (mainly determined by the membrane thickness).

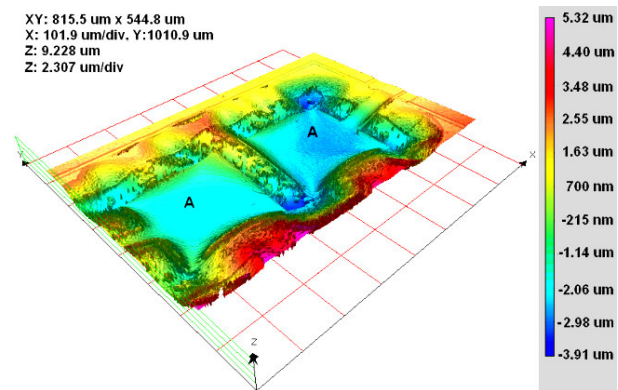


Figure 7. 3D topography of the FBAR structure in the membrane area (0.4  $\mu\text{m}$  GaN plus buffer thin membrane )

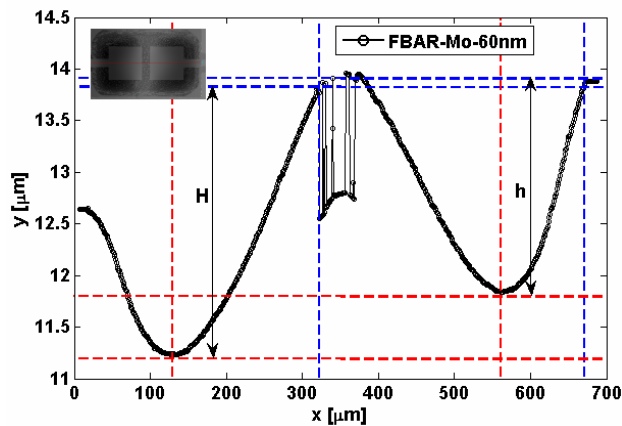


Figure 6. Optical profile of the FBAR structures in the membrane area with 60 nm Mo thicknesses of electrodes metallization(0.54  $\mu\text{m}$  GaN plus buffer thin membrane )

One can see that the maximum deflection is  $H = 2.50 \mu\text{m}$  and the minimum deflection is  $h = 2.20 \mu\text{m}$  (Fig. 6).

The 3D topography of the FBAR structure working at 8.3 GHz (manufactured on the first wafer) is presented

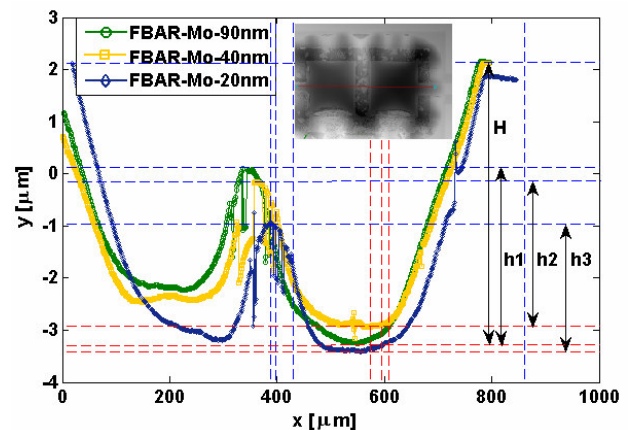


Figure 8. Optical profile of the FBAR structures in the membrane area with three different thicknesses of electrodes metallization (0.4  $\mu\text{m}$  GaN plus buffer thin membrane )



## V -Conclusion

Using micromachining technologies, thin GaN membranes can be used to manufacture FBAR devices having resonance frequencies up to 8 GHz, and possible more. The morphological analysis of thin GaN membranes, manufactured by micromachining of GaN/Si has evidenced the strong influence of the metal thicknesses on the membrane deflection. This is important for the device designer because the thickness of the metal can be used for frequency tuning, in FBAR based filter structures. Also it was evidenced that a thinner GaN membrane has a higher deflection than thick membrane.

The membrane deflection even at the 0.4  $\mu\text{m}$  thin membrane is low enough and we are sure that the membrane thickness can be further reduced without major influence on its self-sustainability.

## Acknowledgement

The authors acknowledge the European Commission (project 202897 “MIMOMEMS”) and the National Romanian Authority for Research (projects MIMFOMEMS and GIGASABAR -PNII) for the support in this work.

## References

- [1] A. Muller, D. Neculoiu, G. Konstantinidis, A. Stavriniadis, D. Vasilache, A. Cismaru, M. Danila, M. Dragoman, G. Deligeorgis, K Tsagaraki, *IEEE Electron Device Letters*, vol.30, pp. 799 – 801, August 2009
- [2] R. Lanz, P. Muralt, *IEEE Trans. on UFFC*, Vol. 52, pp. 946–946, June 2005
- [3] A. Muller, D. Neculoiu, D. Vasilache, D. Dascalu, G. Konstantinidis, A. Kostopoulos, A. Adikimenakis, A. Georgakilas, K. Mutamba, C. Sydlo, H.L. Hartnagel, and A. Dadgar, *Superlattices & Microstructures*, vol 40, pp. 426-431, Oct. 2006
- [4] D. Neculoiu, G. Konstantinidis, A. Müller, A. Kostopoulos, D. Vasilache, K. Mutamba, C. Sydlo, H. L. Hartnagel, L. Bary, R. Plana, *International Microwave Symposium Digest, IEEE MTT-S*, 2007, pp. 877-880.
- [5] M. C. Chao, Z. Wang, Z. N. Huang, S. Y. Pao and C. S. Lam, *Proc of the 2003 IEEE Int Frequency Control Symposium*, pp. 794-801, 2003

# STATIC CRACK GROWTH AND FATIGUE MODELING FOR SILICON MEMS

W. Merlijn van Spengen<sup>1,2</sup>

<sup>1</sup>*TU Delft, 3mE-PME, Mekelweg 2, 2628CD, Delft, The Netherlands*

<sup>2</sup>*also with Falco Systems, Gelderlandplein 75L, 1082LV, Amsterdam, The Netherlands*

**Abstract** — One of the two main hypotheses to describe the origin of the experimentally observed fatigue in silicon MEMS says that it is caused by stress corrosion cracking (SCC) of the native surface oxide. SCC is a known life-limiting phenomenon in high-quality optical fibers. In this paper it is investigated to which extent the existing theory on fracture lifetime of glass objects under tensile stress can be applied to silicon MEMS for predicting their reliability. It turns out that at room temperature SCC is not of concern for typical conditions in silicon MEMS. However, when the MEMS structure is mechanically stressed to the point where the normally compressively stressed thin native oxide layer becomes tensile, the lifetime of silicon MEMS can be severely affected by SCC. The model is shown to be consistent with published measured lifetime data.

**Keywords :** MEMS, fracture, fatigue, stress corrosion cracking, reliability

## I - Introduction

It has been known for a long time that glass is prone to slow fracture due to SCC in a humid environment at stress levels lower than its yield strength for sudden fracture [1]. Fatigue occurs due to stress-assisted hydrolysis of silicon dioxide, and has been the subject of considerable research, especially for the study of the long-term deterioration of optical fibers.

In MEMS, for structural components that have to resist large stresses, silicon is often used. Silicon by itself does not exhibit SCC due to humidity [2]. However, in air, silicon is always covered by a thin native oxide layer, which can be susceptible to SCC. Connolly, Brown and Van Arsdel [2-3] were the first to investigate the fatigue due to cyclic stresses in

silicon MEMS, and found indications that SCC in thin film silicon does indeed occur. A whole body of experimental and Si/SiO<sub>2</sub> bilayer modeling papers have appeared that take SCC combined with repetitive stress oxide thickening as the cause for silicon fatigue, calling it reaction layer fatigue (RLF) [4-5].

There is an alternative hypothesis, which says that, even though silicon is an almost ideal brittle material, fatigue cracks appear due to wedging by asperities on the crack surfaces [6]. Both theories are supported, among other things, with vacuum experiments: in the literature both fatigue in silicon and its absence have been observed. The experimental evaluation of the question is still open [7]. Also, it has been claimed that the failures are cycle-dependent instead of time-dependent [5], but the wide scatter in existing measurement data produce convincing graphs both as a function of time and as a function of frequency.

In this paper it is shown that it is possible to calculate the expected time to failure of silicon components under mechanical stress, assuming that the underlying mechanism is SCC. This time depends on the properties of the surface of the MEMS device. The predictions of the model are consistent with a well-known experimental lifetime study by Muhlstein et al. [4]. By using the insights presented here, it should be possible to design reliable MEMS devices that will not suffer from SCC during their operational life.

## II – Crack growth in silicon due to SCC

The fracture of silicon MEMS structures due to SCC is expected to happen in the following way. A small crack in the SiO<sub>2</sub> surface layer can grow due to SCC if this layer is under tensile stress. Because the native SiO<sub>2</sub> layer typically has an intrinsic compressive stress [8], this can only happen if a stress is

applied externally, e.g. by actuating a MEMS device. The silicon of the actuated structure is then stressed, and its SiO<sub>2</sub> surface layer as well. When the applied stress is so large that it forces the stress in the SiO<sub>2</sub> layer to become tensile, SCC may occur in the SiO<sub>2</sub>, in which case crack growth will be observed. As the crack propagates, the silicon comes closer to the SiO<sub>2</sub>/air interface, thereby facilitating the oxidation of the silicon deeper in the structure. The crack can grow further in the SiO<sub>2</sub>, which itself now extends further in the structure. This process goes on, until the remaining part of the structure can no longer stand the concentrated stress, and fractures (Fig. 1). At the same time, the oxide layer of the entire stressed area becomes thicker [9]. It may be attributed to direct oxidation of stressed silicon, or to small oxidizing cracks. Static crack growth recently seems to have been observed as well [10].

SCC in brittle solids is also sometimes called static fatigue, because a cyclically varying applied stress is not required for the crack growth to occur; the presence of a (sometimes non-varying) tensile stress is enough. Note that this effect can take place in both mono- and polycrystalline silicon, as the reaction region is the amorphous SiO<sub>2</sub> layer in both cases.

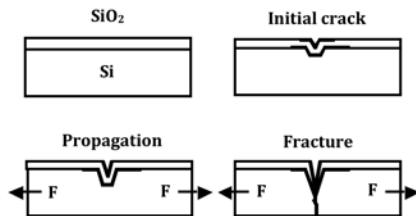


Figure 1: SCC failure mechanism in silicon

### III – Molecular aspects of the stress corrosion cracking of glass

Under stress-free conditions at room temperature, SiO<sub>2</sub> does not react significantly with H<sub>2</sub>O. The bond of the Si-O tetrahedral is too strong for hydrolysis to take place. If the bonds are highly stressed, like they are near a crack tip, the bond strength can be lowered considerably. The Michalske-Freiman model [11] assumes that a molecule should have the following properties to be able to react with the SiO<sub>2</sub> in the tip region. It should have a

non-bonding spare electron pair (Lewis base), a weakly bound proton (Brønsted acid), and the distance between the reactive sites should be about the same as the Si-O bond length. This means that not only water, but also chemicals like ammonia should be able to enhance crack growth in glass. Only small molecules will fit in the crack tip, which is assumed to be a ring of Si-O bonds with a diameter of ~0.5 nm.

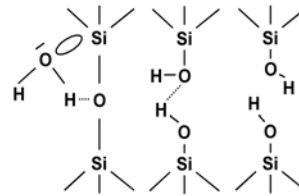


Figure 2: Hydrolysis of SiO<sub>2</sub>

Hydrolysis takes place in steps (Fig. 2). First, the water will penetrate in the crack opening until it arrives at the crack tip. When it has arrived at the crack tip, its lone electron pair interacts with the silicon, while H-bridging occurs between the labile proton and the oxygen in SiO<sub>2</sub>. Then the Si-O bond in the glass and O-H bond in the water molecule break to give two silanol groups. The remaining H-bridge is subsequently cleaved, and the crack has propagated one atomic bond.

In a later paper, Michalske and Bunker [12] used the model to predict the crack propagation rate versus the applied stress intensity factor. They confirm the underlying principles of Wiederhorn's [13] Arrhenius relation for SCC in glass,

$$v = v_0 \exp \left[ \frac{-E^* + aK_I}{RT} \right] \equiv v'_0 \exp(bK_I)$$

in which  $v$  is the crack propagation rate,  $R$  is the gas constant,  $T$  is the absolute temperature, and  $K_I = Y\sigma\sqrt{\pi c}$  is the stress intensity factor at the crack tip, with  $Y$  the Young's modulus of the material,  $\sigma$  the tensile stress, and  $c$  the crack length.  $E^*$  is the activation energy in the case of unstrained bonds,  $v_0$  is an 'attempt frequency' required to obtain the right crack propagation rate and  $a$  is the factor governing the behavior in the stressed case. The factors  $a$  and  $b$  are used to simplify the equations.

From the equation of Wiederhorn, we see that we can accelerate the crack propagation rate by using a high temperature. This may be important in reliability tests to discover whether MEMS under test suffer from SCC. Because the Wiederhorn data [13] give a lower crack growth rate than the data of Michalske and Bunker [12], we will use the latter data to be on the safe side. For  $\text{SiO}_2$ ,  $a = 2.7 \cdot 10^{-22}$  and  $b = 7.3 \cdot 10^{-5}$ .

#### IV- SCC and the reliability of MEMS: acceleration and critical crack length

When the native oxide layer on the silicon is under compressive stress, as it will usually be in rest, SCC will hardly occur. It is only when the applied stresses are so large that a compressive to tensile transition point of the  $\text{SiO}_2$  surface layer is reached, that SCC may become significant. This is a very nice property, because it suggests the possibility of silicon structures with ‘infinite’ lifetimes with respect to SCC, especially because the compressive stress in  $\text{SiO}_2$  is large, usually about 1 GPa [8]. As long as the stress is lower than this ‘threshold’, fracture of the structure due to SCC will never occur.

The Wiederhorn model for SCC in  $\text{SiO}_2$  predicts the crack propagation rates versus stress intensity factor plotted in Fig. 3. This graph was constructed using  $a$  and  $b$  given by Michalske and Bunker [12], and  $E^* = 319$  kJ/mole given by Wiederhorn [13]. Only stresses beyond the compressive-tensile transition point will add to the stress intensity factor.

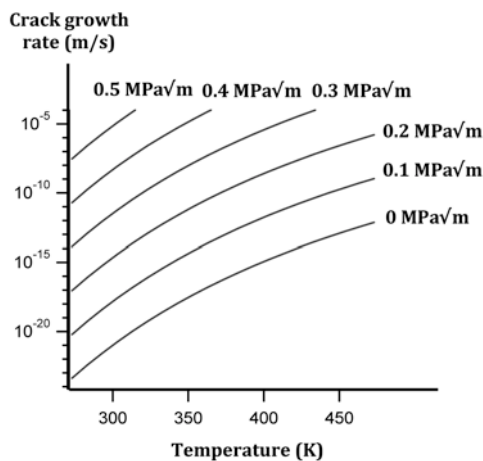


Figure 3: Temperature dependency of crack growth rate as a function of the stress intensity factor

We can go further and predict the crack growth rate as a function of both crack length and temperature, the latter suggesting the possibility to do accelerated lifetime tests. The surface roughness and/or small pre-existing cracks will act as a crack initiation site. The maximum initial  $K_I$  depends on the depth of the ‘effective’ surface crack. The crack propagation rate as a function of the crack length  $c$

$$\text{is then } v = v_0 \exp \left[ \frac{-E^* + aY\sigma\sqrt{\pi c}}{RT} \right].$$

To simplify the equations, we define  $b' \equiv bY\sqrt{\pi}$  and obtain for the crack propagation rate  $v = v'_0 \exp(b'\sigma\sqrt{c})$ .

During the growth of a crack,  $K_I$  will increase, because the crack length  $c$  changes. Michalske et al. [1] have calculated by integration the time to failure  $t_f$ ,

$$t_f = \frac{-2}{v'_0} \left[ \frac{\exp[-b'\sigma x]}{(b'\sigma)^2} (b'\sigma x + 1) \right]_{x=\sqrt{c_{\text{initial}}}}^{x=\sqrt{c_{\text{critical}}}}.$$

The crack will grow slowly from its initial value  $c_{\text{initial}}$ , until at a certain crack length  $c_{\text{critical}}$  the stress intensity value of the material is exceeded and sudden fracture occurs.

The lowest stress intensity level required for the sudden fracture of silicon reported in the literature [14] is  $0.7 \text{ MPa}\sqrt{\text{m}}$ . The corresponding  $c_{\text{critical}}$  is given in Fig. 4. Note that the stress in this figure is the stress required *above* the compressive to tensile transition stress value of the native surface oxide layer.

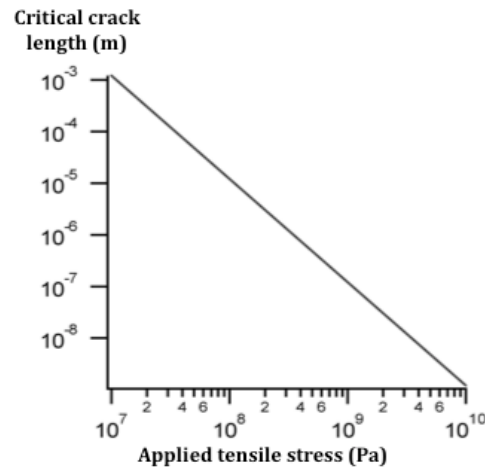


Figure 4: Critical crack length for sudden fracture at  $0.7 \text{ MPa}\sqrt{\text{m}}$



From the previous discussion, we can derive new insights in the reliability of silicon microstructures under stress. According to Fig. 4, for small cracks (<100 nm) and reasonable stresses (< 300 MPa) in excess of the transition point stress at 1 GPa, SCC at room temperature will not be a large problem. Only at relative large stresses and “deep” cracks, SCC will show up as a detrimental effect. On the other hand, we know from Fig. 3 that the reaction has a large temperature dependence. In Fig. 5, it is shown that even at an excess stress level of 100 MPa, causing no reliability problems at room temperature, the SCC effect can be a problem at elevated temperatures.

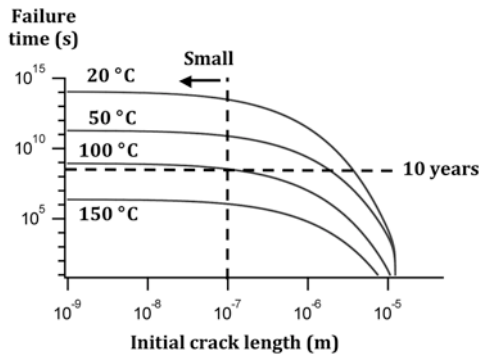


Figure 5: Temperature dependence of the SCC failure time at 100 MPa excess stress

It seems therefore a good idea never to exceed the transition stress of ~1 GPa in a Si MEMS structure. If unavoidable, we have to make sure that no water can enter the MEMS package, or the lifetime of the component can be compromised at high temperatures.

## V- SCC and the reliability of MEMS

The validity of the modeling can be tested by comparing its predictions to the measured lifetime data obtained by Muhlstein et al. [4] (Fig. 6). To do this, we have to calculate the effective static stress equivalent to the cycling varying stress of this experiment, the details of which will be discussed elsewhere [15]. When we assume a transition stress of 1 GPa, the solid line gives the predicted values for a 26 nm ‘effective’ initial surface crack (roughness and/or pre-existing cracks) at room temperature. The scatter is most probably due to the fact that the initial effective crack length is not exactly the same for each sample.

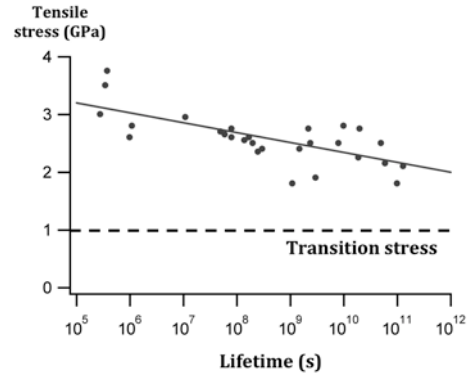


Figure 6: Lifetime data as a function of mechanical stress by Muhlstein et al. [4], replotted in stressing time instead of number of cycles, and the predicted line of the new model

## VI- Conclusion

We have shown that the existing theory on the slow fracturing of glass can provide the insights required to predict the time to failure for silicon MEMS devices under stress. There is a critical stress in the device, above which SCC may occur. If the stress in the device is kept below this transition, where the oxide surface layer turns from its intrinsic compressive stress to tensile, there will be no problems due to SCC. Above this value, ~1 GPa, silicon MEMS are expected to be severely affected by SCC, especially at elevated temperatures. The model presented fits well with the measured lifetime data for SCC failures in literature. For optimal reliability assessment, the native surface oxide layer stress needs to be known.

## References

- [1] T. A. Michalske et al., J. Am. Ceram. Soc. Vol. 74, 1991, p. 1993
- [2] W. W. Van Arsdel and S. B. Brown, J. MEMS Vol. 8, 1999, p. 319
- [3] A. Connolly and S. B. Brown, Science Vol. 256, 12 June, 1992, p. 1537
- [4] C. L. Muhlstein et al., Sens. Act. A 94, 2001, p. 177
- [5] D. H. Alsem et al., Adv. Eng. Mater. Vol. 9, 2007, p. 15
- [6] H. Kahn et al., Scr. Mater. Vol. 59, 2008, p. 912
- [7] H. Kahn et al., Science Vol. 298, 2002, p. 1215
- [8] B. Stark (ed.), MEMS reliability assurance guidelines for space applications, NASA and JPL, CIT, Pasadena, California, USA, 1999, p. 55.
- [9] M. Budnitski and O. N. Pierron, Acta Mater. Vol. 57, 2009, p. 2944
- [10] E. K. Baumert et al., Acta Mater. Vol. 58, 2010, p. 2854
- [11] T. A. Michalske and B. C. Bunker, J. Appl. Phys. Vol. 56, 1984, p. 2686
- [12] T. A. Michalske and B. C. Bunker, J. Am. Ceram. Soc. Vol. 76, 1993, p. 2613
- [13] S. M. Wiederhorn et al., Met. Sci. Vol 14, 1980, p. 450
- [14] R. Ballarini et al., J. Mater. Res. Vol. 12, 1997, p. 915
- [15] W. M. van Spengen, to be published

# DEVELOPMENT OF A NOVEL MICROMIRROR WITH HIGH STATIC ROTATION ANGLE FOR MEASUREMENT APPLICATIONS

S. Weinberger, O. Jakovlev, C. H. Winkelmann, E. Markweg, T. Polster, M. Hoffmann

Ilmenau University of Technology, IMN MacroNano®, Department of Micromechanical Systems,  
Max-Planck-Ring 12, 98693 Ilmenau, Germany

**Abstract** — Micromirrors using silicon torsion springs have an excellent performance in the dynamic mode, but in the static mode the possible rotation angle is usually low. We have developed a new concept, using aluminum nitride for the torsion springs. The excellent mechanical behavior of aluminum nitride makes it possible to fabricate torsion springs at nano-scale thickness, which allows high static rotation angles at low operating voltages.

**Keywords** : micromirror, aluminum nitride, torsion spring

## I – Introduction

In numerous technical applications, e.g. projectors or scanners, electrostatically actuated micromirrors are used for light deflection. Most of them are based on silicon torsion springs in resonant mode [1, 2]. For controlled beam deflection, a high static rotation angle of the micromirror is necessary.

Tracking of an object for measurement purpose requires static deflection rather than dynamic deflection. Unfortunately the static rotation angle of common micromirrors is as low as about 3 to 6 ° [3, 4, 5]. To overcome this limitation, we develop a micromirror based on a common design with planar plate electrodes but aluminum nitride torsion springs. The deposition of aluminum nitride is CMOS compatible and inexpensive by using reactive sputtering. Because of the nanocrystalline structure, the sputtered aluminum nitride has excellent mechanical properties [6]. Hence it is possible to fabricate 500-nm thin torsion springs with low polar moment of inertia and therefore a static rotation angle as large as more than 10 °, at low operating voltage.

## II – Development of a common micromirror

For comparison, an electrostatic comb-drive actuated micromirror (Figure 1) made of silicon springs is fabricated and tested. The simple technology of this micromirror is advantageous combined with a high rotation angle in the resonant mode by low voltage. The drawback is the small range of electrostatic attraction of the interdigital electrodes and therefore the small resulting static rotation angle with less than 1 °.

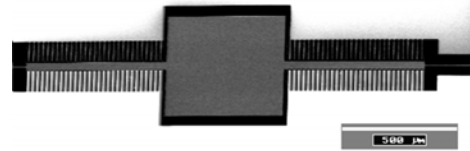


Figure 1: Electrostatic comb-drive actuated micromirror with silicon springs

### A. Technology

In the following the fabrication technology pictured in Figure 1 is described. An SOI-Wafer with a device layer thickness of 8 μm is used. A simplified process flow chart is shown in Figure 2. The KOH etch mask consists of 20 nm thermal SiO<sub>2</sub> and 80 nm LPCVD-Si<sub>3</sub>N<sub>4</sub>. Aluminum is used for the contact pads as well as for the reflection layer. Before KOH etching, the device layer is coated by PECVD-SiO<sub>2</sub> and mounted into a single-side etching box. The handle wafer is thinned in KOH down to a thickness of about 20 μm and fully etched by DRIE. Finally, the SiO<sub>2</sub> is removed in HF vapor etching.

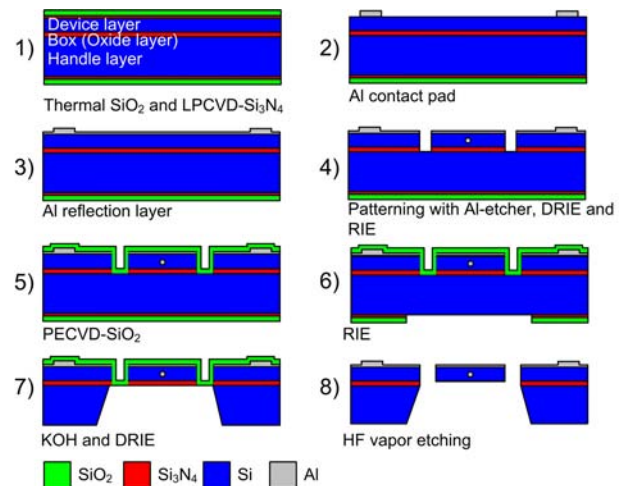


Figure 2: Flow chart of the common micromirror

### B. Experimental Results

Figure 3 shows the schematic drawing of the test equipment. The mirror samples are fixed on a vacuum chuck and contacted by probe tips. A focused laser beam is directed to the mirror and the beam deflection can be measured on a screen. The distance between micromirror and screen as well the height difference can be controlled. Knowing the distance, height difference and measuring the beam deflection on the screen, the rotation angle can be calculated.

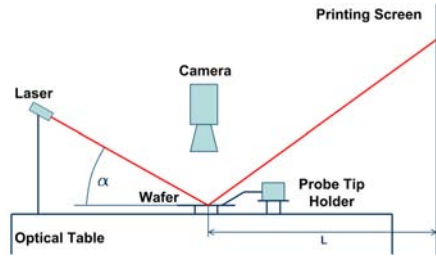


Figure 3: Schematic drawing of the test stand

Figure 4 shows the dependence of the maximum rotation angle from driving frequency. In resonant mode, high rotation angles at low voltage (Figure 5) are achieved whereas the static rotation angle is limited to less than  $1^\circ$  (Figure 6).

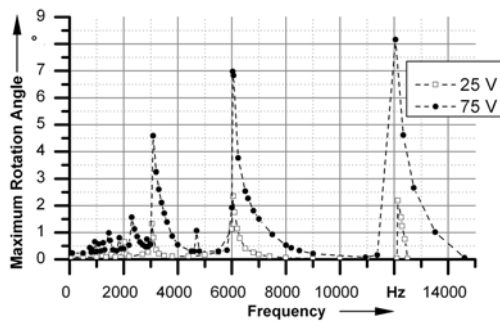


Figure 4: Measurement of maximum rotation angle for different frequencies

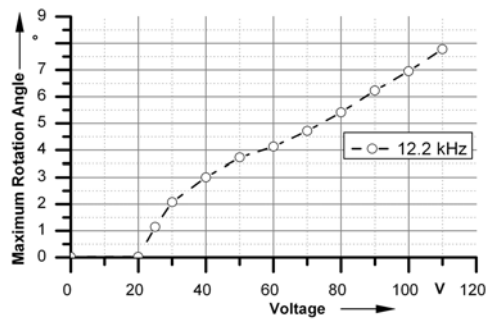


Figure 5: Measurement of maximum rotation angle for different operating voltages in resonant mode

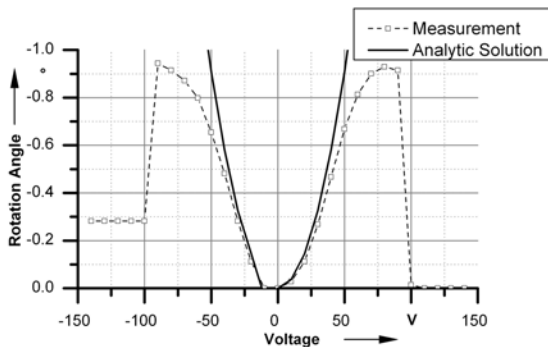


Figure 6: Rotation angle for different operating voltages in static mode

### III – Development of an innovative micromirror

For large static deflection of light, electrostatic comb-drive actuators are not adequate. An alternative are parallel plate electrode actuators.

#### A. Design

Figure 7 shows different electrode designs [7]. The advantage of the inclined electrodes (variant a)) is the low operating voltage in comparison to the planar electrodes (variant b)), but in both cases the maximum rotation angle is limited by the pull-in effect. The pull-in effect describes the system instability caused by an increased electrostatic torque larger than the mechanical restoring torque of the spring. The maximum angles limited by the pull-in effect could be described by the following equations [7, 8]:

Variant a)

$$\varphi_{\max} = \frac{1}{3} \varphi_0$$

Variant b)

$$\varphi_{\max} \approx 0.4404 \arcsin \frac{2 \cdot z_0}{b}$$

Thereby follows for the case of variant a), etched by KOH in a {100}-Wafer, a maximum angle of  $18^\circ$  and for variant b) of  $40^\circ$ .

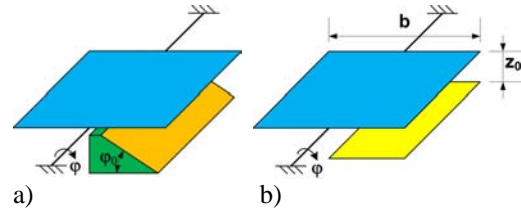


Figure 7: Schematic drawing of possible plate electrode designs

Because of the increased maximum rotation angle and the simple fabrication, planar electrodes are selected.

For a maximum static rotation angle, the electrode distance has to be optimized. An optimal electrode distance is reached by limiting the maximum rotation angle with a mechanical stop close to the pull-in angle. Because of the large electrode distance, usually high operating voltages are necessary in static operation mode. So it is important to minimize the polar moment of inertia. Figure 8 shows a solution: Torsion springs with a 500 nm thick aluminum nitride layer have been successfully fabricated. The potential of this technology is demonstrated in Figure 10, where the necessary operating voltage is clearly reduced by a 5 times smaller spring length than in silicon.

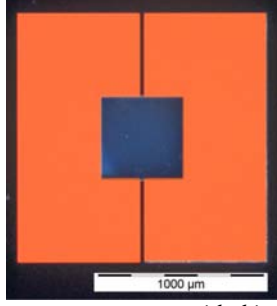


Figure 8: Micromirror test structures with thin aluminum nitride torsion springs (500 nm thick, 30 μm wide and 500 μm long)

### B. Simulation of a 1D mirror

The torques must be in balance:  $T_{el} = T_{mech}$

$$T_{el} = \frac{1}{2} \cdot V^2 \cdot \epsilon \cdot \Delta y \cdot \int_c^d \frac{x \cdot dx}{(z_0 - x \cdot \tan \varphi)^2}$$

with  $c = x_1$  and  $d = x_2$

$$T_{mech} = 2 \cdot K \cdot \varphi$$

$$\text{with the stiffness: } K = \frac{G \cdot I}{l}$$

and the polar moment of inertia for  $w \geq t$  [9]:

$$I \approx w \cdot t^3 \cdot \left( \frac{1}{3} - \frac{0.21 \cdot t}{w} \cdot \left( 1 - \frac{t^4}{12 \cdot w^4} \right) \right)$$

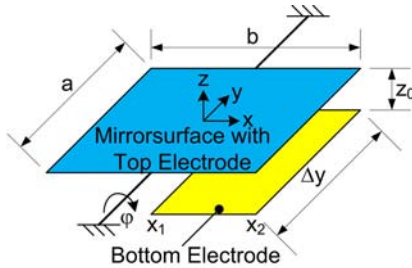


Figure 9: Schematic drawing of the electrode position

Table 1: List of symbols

$T_{mech}$	mechanical torque	$T_{el}$	electrical torque
$V$	voltage	$\varphi$	rotation angle
$a$	length of mirror surface	$b$	width of mirror surface
$x_1, x_2$	begin and end of bottom electrode width	$\Delta y$	length of bottom electrode
$K$	stiffness	$G$	shear modulus
$I$	polar moment of inertia	$t$	spring thickness
$w$	spring width	$l$	spring length
$z_0$	distance between rotation axis and bottom electrode	$\epsilon$	permittivity

Figure 10 compares the simulation result of micromirrors with AlN torsion springs to micromirrors with minimized silicon springs. The simulation parameters of Table 2 are used. The analytical equation neglects the

film stress which has an important role for the mechanical behavior.

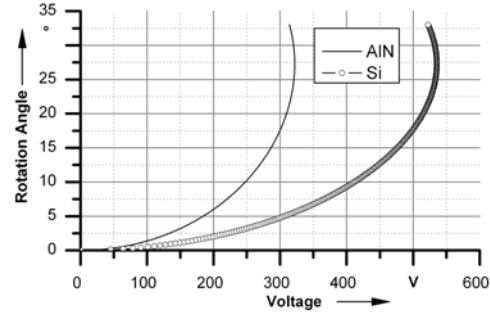


Figure 10: Simulation of the rotation angle for a micromirror with silicon and aluminum nitride torsion springs

Table 2: Simulation parameters

	AlN springs	Si springs
$a, b, \Delta y$ (μm)	2000	2000
$z_0$ (μm)	525	525
$x_1$ (μm)	100	100
$x_2$ (μm)	400	400
$l$ (μm)	200	1000
$w$ (μm)	20	2
$t$ (μm)	0.5	8
$G$ (GPa)	126	79.55
$\epsilon$ (As/Vm)	$8.85 \cdot 10^{-12}$	$8.85 \cdot 10^{-12}$

In the example of Table 2 the position of the bottom electrodes is optimized. The pull-in angle is not reached, because the rotation angle is limited by a mechanical stop close to the pull-in angle.

### C. Aluminum Nitride

The used aluminum nitride (AlN) is deposited by reactive sputtering of Al with N<sub>2</sub> and Ar by a process temperature less than 400 °C and crystallizes in the wurtzite structure [6]. Because of the strong chemical bonds and the nanocrystalline structure, AlN has excellent mechanical properties. Figure 11 shows the homogenous texture of sputtered aluminum nitride. By changing of the process parameter setting, it is possible to vary the film stress [6]. A high tensile stress increases spring stiffness but also reduces the electrostatic deflection of the spring. In further studies the optimum film stress must be found by experiments in combination with simulations.

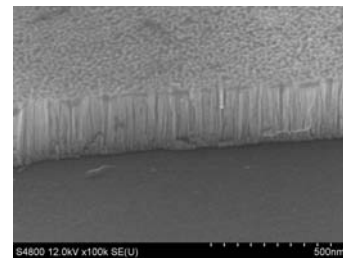


Figure 11: Homogenous texture of aluminum nitride



#### D. Flow chart of a micromirror with AlN torsion springs

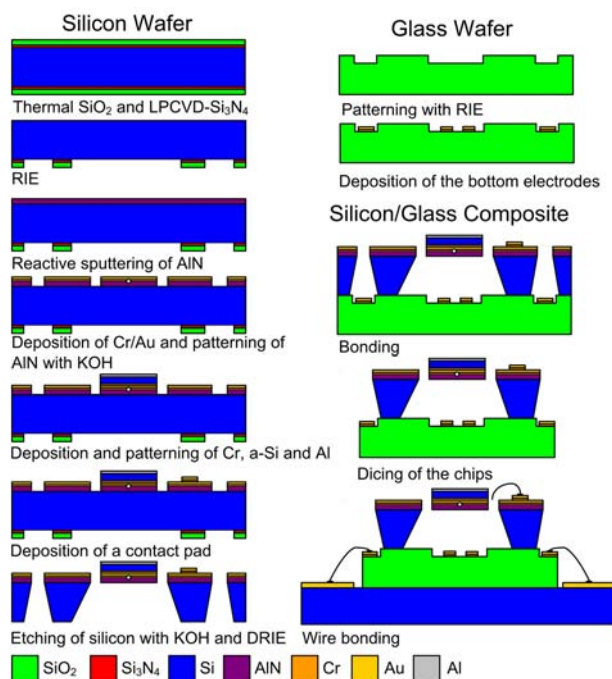


Figure 12: Flow chart of the micromirror with AlN torsion springs

A process flow of the micromirror with AlN torsional springs is shown in Figure 12. For the fabrication a silicon and a glass wafer are used. KOH etching is performed with a  $\text{SiO}_2 / \text{Si}_3\text{N}_4$  mask. The deposition of the 500 nm aluminum nitride functional layer follows by reactive sputtering. As electrode material, 20 nm Cr and 80 nm Au are deposited. This electrode layer is used as a mask for the wet etching of AlN with KOH. To get a mechanically stiff mirror surface, Cr and a thick PECVD silicon are deposited. A sputtered 100 nm Al film is used as reflective layer. With wet etching and reactive dry etching the film stack is finally patterned. For the mirror electrode, a bond pad consisting of Cr/Au or Al is deposited using a shadow mask. The 525  $\mu\text{m}$  thick standard silicon wafer is etched in KOH followed by a DRIE process.

The glass wafer is patterned with RIE and the bottom electrodes (Cr/Au or Al) are deposited and patterned. The both wafers are aligned and bonded. After that, the wafer stack is separated, the chips are mounted on a PCB and finally, the electrical contacts are realized by wire bonding.

#### IV – Conclusion

The challenge of high rotation angle in static mode at low operation voltage for micromirrors is described. A common micromirror based on silicon springs driven by an electrostatic comb-drive actuator is demonstrated and the measurements show good performance in resonant mode, but low rotation angles in static mode. Therefore a new technological concept based on alumi-

num nitride torsion springs with planar plate electrodes is presented. The key to this novel concept is the excellent mechanical behavior of aluminum nitride. Simulations predict an excellent static performance. The fabrication of first samples is ongoing.

The key application for these static mirrors with large deflection is a microtracker system, that allows to measure the 3D position of a tool center point (TCP) by trilateration of a cat eye at the TCP. Thus the mirrors must be able to provide a large static deflection as well as a fast dynamic actuation.

This project is funded by the Ministry of Education and Research (BMBF) within the project cluster "Kompetenzdreieck Optische Mikrosysteme, Spitzenforschung und Innovation in den Neuen Ländern".

FKZ: 16SV3701

#### References

- [1] M. H. Kiang et al: Electrostatic Combdrive-Actuated Micromirrors for Laser-Beam Scanning and Positioning, *Journal of Micromechanical Systems*, Vol. 7, No. 1, pp. 27-37, 1998
- [2] A. Rober et al, A flat high-frequency scanning micromirror, in *Proc. Tech. Dig. Solid-State Sensor and Actuator Workshop*, Hilton Head, SC, 2000, pp. 6-9.
- [3] M.R. Dokmeci et al: Two-Axis Single-Crystal Silicon Micromirror Arrays, *Journal of Micromechanical Systems*, Vol. 13, No. 6, pp. 1006-1017, 2004
- [4] H. Dooyoung: A self-aligned vertical comb-drive actuator on an SOI wafer for a 2D scanning micromirror, *Journal of Micromechanics and Microengineering*, Vol. 14, pp. 1148-1156, 2004
- [5] D. Hah et al: Low-Voltage, Large-Scan Angle MEMS Analog, *Journal of Microelectromechanical Systems*, Vol. 13, No. 2, pp. 279-289, 2004
- [6] T. Polster et al: Thin Free Standing AlN Membranes-Mechanical Stable and Flexible Structural Material for MEMS Devices, *MME*, Aachen, pp. 85-88, 2008
- [7] H. Camon et al: Fabrication, simulation, and experiment of a rotating electrostatic silicon mirror with large angular deflections, *Proceedings of the IEEE micro electro mechanical systems*, pp 645-650, 2000
- [8] O. Degani et al: Pull-In Study of an Electrostatic Torsion Microactuator, *Journal of Microelectromechanical Systems*, Vol. 7, No. 4, pp. 373-376, 1998
- [9] W. C. Young, et al: *Roark's Formulas for Stress and Strain*, New York, McGraw-Hill, 2002

# APPLICATIONS OF ALL-(111) SURFACE SILICON NANOWIRES

M. N. Masood, S. Chen, E. T. Carlen and A. van den Berg

BIOS Lab on a Chip, MESA+ Institute for Nanotechnology, University of Twente, Enschede, the Netherlands.

**Abstract** — Selective chemical modification on all-(111) surface silicon nanowires has been achieved using covalently linked C-Si monolayers that offer several advantages for biosensing compared to nanowire biosensors with conventional dielectric layers: 1. Ligands conjugated exclusively on the nanowire surfaces results in high sensor selectivity, 2. Si (111) surfaces have low interface trap densities for H-Si and C-Si interfaces, 3. Elimination of fixed charge that is present near SiO<sub>2</sub>-Si interfaces, 4. Improved detection sensitivity compared to SiO<sub>2</sub>-Si interfaces as the ligands are within ~1 nm from the sensing surface, and 5. Resistant to acidic and basic solutions.

**Keywords:** Silicon-nanowires, Si-C monolayers, biosensing

## I – Introduction

Silicon nanowire (Si-NW) field-effect biosensors have been reported extensively for the highly sensitive, label-free, and real time detection of biomolecular binding of ssDNA, proteins, and viruses [1-4]. The high detection sensitivity of Si-NW biosensors has been attributed to the large surface-to-volume ratio and three-dimensional multi-gate structure; both contribute to the improved sensitivity compared to conventional planar devices [5, 6]. The transformation of a nanowire into a biosensor requires surface functionalization, such that biologically active ligands are conjugated to the sensor surface [7, 8]. In conventional Si-NW biosensors, the ligand conjugation is done directly to a silicon dioxide (SiO<sub>2</sub>) layer using silane attachment chemistry.

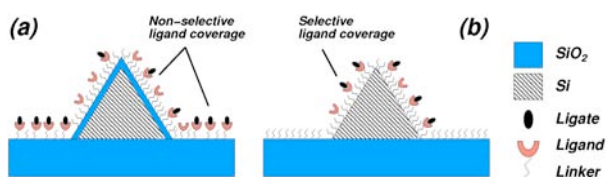


Figure 1: Si-NW biosensor surface configurations. (a) Conventional non-selective homogeneous surface functionalization (b) Selective heterogeneous functionalization with ligands conjugated exclusively to the Si-NW sensor.

However, conjugating to the SiO<sub>2</sub> layer reduces the sensor selectivity because the entire substrate surface is most often a homogeneous oxide surface. Figure 1a shows the conventional non-selective ligand functionalized Si-NW biosensor where the ligands cover the homogeneous surface thus drastically reducing the ligate selectivity to the biosensor surface. Figure 1b shows the selective heterogeneously functionalized Si-NW biosensor where the ligands are conjugated exclusively to the silicon surface.

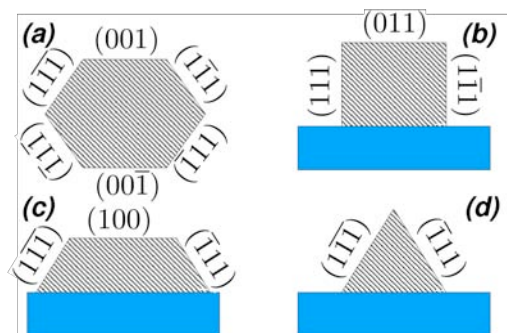


Figure 2: Various Si-NW fabrication dependent cross-section shapes. (a) Bottom-up VLS synthesized, (b) Top-down rectangular, (c) Top-down trapezoidal, and (d) Top-down triangular.

It is well known that the Si (111) surface is preferred for the covalent alkylation of organic monolayers due to the surface atomic arrangement, which leads to densely packed layers and low density of dangling bonds [9-12]. However, existing reports of alkyl monolayer formation on Si-NWs have been conducted on a mixture of surface orientations due to limitations in fabrication technology [2]. Figure 2 shows cross-sections of commonly reported Si-NW shapes and the corresponding surface crystal orientation of the exposed facets, which is dependent on the fabrication technology. Bottom-up vapor-liquid-solid (VLS) synthesis of Si-NWs has been reported to have hexagonal cross-sections consisting of a mixture of surface orientations (Fig. 2a) [13]. Top-down fabricated Si-NWs patterned with electron-beam lithography and formed with plane-dependent etching using Si (011) substrates (Fig. 2b) [14] and Si (100) substrates (Fig. 2c) [15] also have more than one type of exposed surface orientation. Figure 2d shows the triangular Si-NW used in this letter that consist exclusively of Si (111) exposed surfaces. It should be noted that H-Si (111) surfaces have the lowest reported surface recombination velocity [16] and improved electronic performance compared to Si (100) surfaces with SiO<sub>2</sub> interfaces [17], and therefore, will further improve the Si-NW biosensor performance.

In this paper, we present a new Si-NW biosensor platform consisting of our recently reported Si-NWs with all-Si (111) exposed surfaces [18] with an alkyl monolayer interface that is suitable for functionalization with any biomolecular moiety [19]. Figure 3 shows examples of the all-(111) exposed surface Si-NWs that are fabricated with a *soft* top-down technology that results in Si (111) surfaces on the faces of the triangle that are atomically smooth [18]. The base of the Si-NW is anchored to the SiO<sub>2</sub> layer of the silicon-on-insulator substrate.

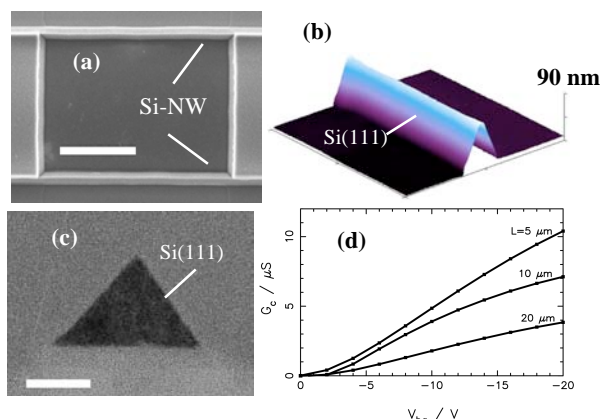


Figure 3: (a) High-resolution scanning electron microscopy (HRSEM) image of triangular Si-NWs (scale bar: 1  $\mu m$ ) (b) Tapping-mode atomic force microscopy image of single Si-NW (NW height: 90 nm) (c) High-resolution transmission electron microscopy image of Si-NW cross-section (scale bar: 20 nm) (d) Si-NW Conductance modulation as a function of back-gate voltage  $V_{bg}$ .

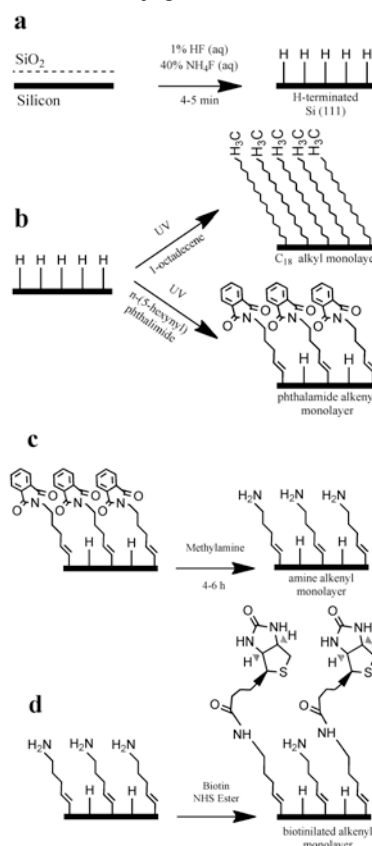
Direct covalent bonding of organic molecules to reconstructed silicon surfaces can be done using ultra high vacuum (UHV) or wet chemistry methods [20]. Carbon silicon (C-Si) coupling reactions performed using wet chemistry methods are very attractive due to the simple apparatus required and the high reaction rates due to presence of high reactant fluxes in solution; however, careful control of surface cleanliness is required. The first step in forming a covalent C-Si bond is the formation of stable H-Si surfaces, which is most often done by removing the native oxide on the silicon surface with hydrofluoric acid (HF) and followed by ammonium fluoride ( $NH_4F$ ) etching the silicon surface. Once a stable H-Si surface has been formed, the C-Si monolayer can be formed with an appropriate precursor and a free radical initiation using ultraviolet (UV) irradiation, heating, electrochemical reaction, transition metal complexes, or Lewis acid catalysts [21]. Many reports of C-Si monolayer formation on H-Si surfaces using a variety of methods, such as a refluxed precursor solution of 1-hexadecene in mesitylene [22], neat solution and UV-irradiation [23], and a two-step hydrosilylation reaction with Grignard reagents [21]. Monolayers formed with Grignard reagents may impart unwanted metal contaminants to the surface. Monolayers formed by Lewis acid catalysis involve lower surface coverage as compared to the coverage obtained by heating, photochemical irradiation and Grignard reaction schemes [22]. Here we utilized Si-alkyl and Si-alkenyl monolayers for selective functionalization of the all-(111) silicon nanowires.

## II - Experimental Details

### A. Surface preparation and monolayer formation.

Two types of C-Si monolayers on H-Si (111) surfaces have been formed using photochemical UV hydrosilylation. The monolayer formation with UV-initiated photochemical hydrosilylation is based on the

high reactivity of the C=C bond to the bare silicon promoted by the cleavage of the H-Si at room temperature (19). First, a  $C_{18}$  alkyl monolayer with methyl end groups was formed from a 1-octadecene precursor. The second monolayer consists of amine-terminated ( $NH_2$ ) alkyne monolayer from an n-(5-hexynyl) phthalimide precursor. Scheme 1 shows the steps used to form both C-Si monolayers. The H-Si surface is first formed followed by the UV initiated hydrosilylation with 1-octadecene and n-(5-hexynyl) phthalimide precursors to form the different C-Si monolayers. Following removal of the phthalimide groups (deprotection) with a methylamine solution, an amine terminal group ( $NH_2$ ) was released for further conjugation.



Scheme 1: C-Si (111) monolayer formation. (a) Si-H surface formation: remove native  $SiO_2$  with 1% HF (aq) followed by surface preparation with 40%  $NH_4F$  (aq) (b) Hydrosilylation UV reaction forming  $C_{18}$  alkyl and phthalimide alkenyl monolayers (c) Deprotection of amine terminal groups (d) Conjugate biotin to amine groups.

The samples were first cleaned to remove organic and metal impurities. The p-type planar Si (111) samples were cleaned with acetone and sonicated (10-20 min) and etched in 1% HF (1-2 min) to remove the native oxide. Etched silicon samples were rinsed with deionized water ( $dH_2O$ ) and further cleaned with piranha solution ( $H_2O_2$  30%,  $H_2SO_4$  in 1:1 ratio) at 90  $^{\circ}C$  for 10 min and rinsed thoroughly with  $dH_2O$ . This procedure was repeated three times. The contact angle of the resultant surface was found to be zero. The p-type Si-NW samples were first cleaned with methanol, isopropanol, acetone and acetonitrile with low power sonica-



tion (5-20 min). The Si-NW samples were further cleaned with oxygen plasma (100W, 10 min). Silicon nanowire and planar samples were etched with 1% HF and  $\text{NH}_4\text{F}$  for 4-5 min and then rinsed thoroughly with  $\text{dH}_2\text{O}$  and placed into a custom-made vacuum vessel and the surface dried with a combination of vacuum ( $\sim 1$  mTorr) and heating with an infrared lamp (Scheme 1a). The vacuum vessel was continuously purged with argon during the drying step. A thin layer of precursor solution was deposited onto the samples and irradiated for 4 hours with a UV lamp ( $4.4 \text{ mW/cm}^2$  at 254 nm, Jelight Co., USA). The 40%  $\text{NH}_4\text{F}$  etchant and 0.2 M precursor solution in mesitylene were bubbled with pure argon gas for 1 hour before the hydrosilylation reaction. After the hydrosilylation reaction, the samples were exposed to ambient air and sonicated with dichloromethane, chloroform, methanol, and acetonitrile. For deprotection of the phthalimide groups, samples were placed in a 30% methylamine solution in ethanol for 6-8 h (Scheme 1c). Following the reaction, the samples were rinsed with triethylamine and ethanol, and subsequently nitrogen dried. Activated biotin (Sigma Aldrich) was conjugated to the amine-terminated surfaces by placing the samples in a 3 mM solution of activated biotin / dimethylformamide (DMF) for two hours at room temperature, followed by sonication in DMF, ethanol, and acetone (5-10 min). Gold nanoparticles conjugated with streptavidin (0.25 ml streptavidin conjugated Au nanoparticles in solution with 5 nm average diameter, Ted Pella, Inc. USA) was diluted to 100 ml of solution by adding 20 mM Tris buffer, 154 mM NaCl, and  $\text{dH}_2\text{O}$ . The biotinylated surfaces were immersed with the labeling solution for 12 hours at room temperature. Monolayers prepared by 1-octadecene do not include a deprotection step and biotinylation.

### III - Results and Discussion

The quality of the as-prepared monolayers was verified by using sessile drop contact angle measurements and x-ray photoelectron spectroscopy (XPS) on planar samples. A contact angle of  $109^\circ$  for the  $\text{C}_{18}$  alkyl monolayer indicates a high quality ordered monolayer and effective surface preparation on both planar and Si-NW surfaces. The XPS spectra were taken just after monolayer formation or after storage in a dry nitrogen purged container. An etched piece of silicon was used as a reference blank. The survey spectrum of a phthalimide monolayer on Si (111) (Fig. 4a) shows the expected elements (Si, C, N and O) indicating a clean contamination free surface. The silicon reference shows a small amount of carbon deposited on the surface, however, not the N1s peak (400 eV) thus discriminating the phthalimide monolayer. Figure 4b shows the least amount of oxidation for the silicon surface that was exposed to UV irradiation for monolayer formation (red) as compared to the H-Si reference and piranha treated samples (blue and black, respectively).

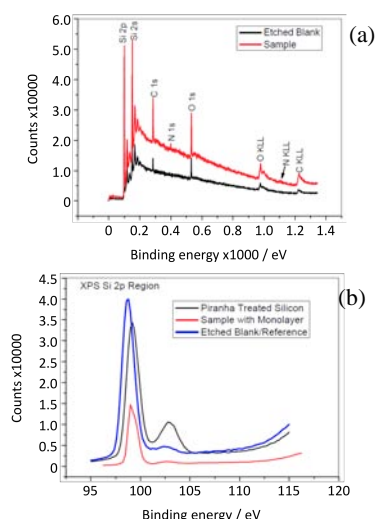


Figure 4: XPS measurements (a) Survey spectrum of phthalimide monolayer on Si (111) surface (red) and control sample (black) (b) Si2p region (peak at 103 eV) shows oxidation of the silicon surface.

Figure 5 shows representative XPS data for experimental samples. Following deprotection, the overall area percentage of C-N peak (286.57 eV) increases compared to the area of C-C (284.77 eV) as the carbon number decreased from 14 to 6. The peak at 288.55 eV (C=O) is expected to disappear after deprotection, but shows a decrease in percent area due to partial deprotection or some physically adsorbed C=O moieties on the surface.

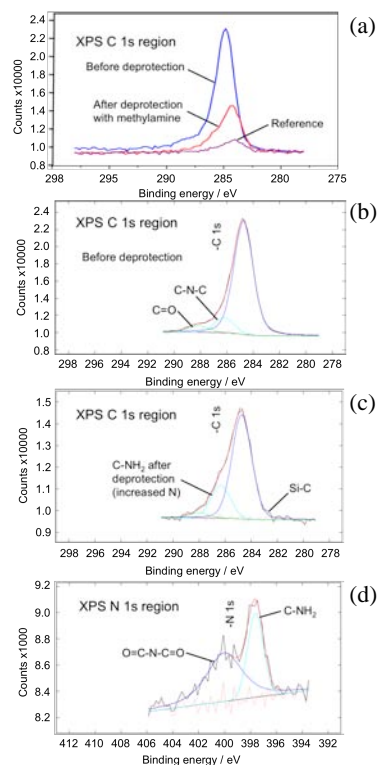


Figure 5: XPS results (a) C1s region of the spectrum showing a comparison before and after deprotection (b, c) C1s region shows fit for different functional bonds in the monolayer before and after deprotection (d) N1s region after deprotection.



High resolution scanning electron microscopy (HRSEM) was used to image the selective Au nanoparticles conjugation to the all-(111) Si-NW surfaces via a C-Si monolayer. This step requires the removal of the phthalimide protection groups, which exposes the  $\text{NH}_2$  functional groups. Activated biotin was then conjugated to the  $\text{NH}_2$ -terminated surfaces. Gold nanoparticles conjugated with thiolated-streptavidin were then introduced to the biotinylated surfaces in solution. Figure 6a shows an HRSEM image of a clean non-conjugated Si-NW. Figure 6b shows the selective conjugation of Au nanoparticles to the all-(111) surface Si-NWs using the C-Si monolayer. Figure 6c shows a zoomed image of the selectively Au nanoparticles conjugated Si-NW surfaces.

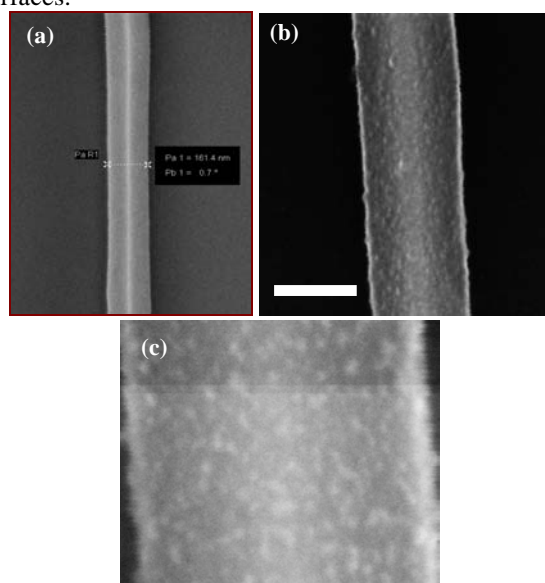


Figure 6: HRSEM images (a) blank Si-NWs (b) Si-NW surfaces following the conjugation of 5 nm diameter Au nanoparticles (scale bar: 100 nm) (c) zoomed view of Si-NW surface.

#### IV – Conclusion

The selective chemical modification of C-Si monolayers on all-(111) surface Si-NWs has been demonstrated, which presents a new Si-NW sensing platform that offers advantages for biosensing compared to conventional nanowire biosensors with dielectric layers. The direct ligand conjugation exclusively on the Si-NW surfaces that ensures the highest possible selectivity. The Si-NW platform consists of exposed surfaces that are exclusively Si (111), and therefore, provide a low density of interface states for H-Si and C-Si interfaces and combined with the elimination of fixed charge that is present near  $\text{SiO}_2$ -Si interfaces provide an opportunity to reduce the doping concentration of the depletion type devices to achieve the highest sensitivity while maintaining proper device operation [18]. Additionally, the short ligand lengths  $\sim 1$  nm means that hybridized ligand-ligate pairs are close to the sensing surface ensuring high detection sensitivity.

#### Acknowledgments

Thanks to Johan Bomer, Jan van Nieuwkastele, and Hans de Boer for technical assistance with silicon nanowire fabrication and construction of the reaction vessel and thanks also to Gerard Kip for XPS measurements and Mark Smithers for high resolution scanning electron microscopy imaging.

#### References

- [1] Cui, Y.; Wei, Q.Q.; Park, H.K.; Lieber, C.M. *Science*, 293, 1289, 2001.
- [2] Bunimovich, Y.L.; Shin, Y.S.; Yeo, W.; Amori, M.; Kwong, G.; Heath, J.R. *J. Am. Chem. Soc.*, 128, 16323, 2006.
- [3] Gao, Z.Q.; Agarwal, A.; Trigg, A.D.; Singh, N.; Fang, C.; Tung, C.H.; Fan, Y.; Buddharaju, K.D.; Kong, J.M. *Anal. Chem.*, 79, 3291, 2007.
- [4] F. Patolsky, F.; Lieber, C.M. *Mater. Today* April 2005.
- [5] Wanekaya, A.K.; Chen, W.; Myung, N.V.; Mulchandani, A. *Electroanal.*, 18, 533, 2006.
- [6] Tong, H. D.; Chen, S.; van der Wiel, W. G.; Carlen, E. T.; van den Berg, A. *Nano Lett.*, 9, 1015-1022, 2009.
- [7] van der Voort, D.; McNeil, C.A.; Renneberg, R.; Korf, J.; Hermens, W.T.; Glatz, J.F.C. *Sensor Actuat B-Chem.*, 105, 50, 2005.
- [8] Bunimovich, Y.L.; Ge, G.; Beverly, K.C.; Ries, R.S.; Hood, L.; Heath, J.R. *Langmuir*, 20, 10630, 2004.
- [9] Kar, S.; Miramond, C.; Vuillaume, D. *Appl. Phys. Lett.*, 78, 1288, 2001.
- [10] Weldon, M.K.; Queeney, K.T.; Eng Jr., J.; Raghavachari, K.; Chabal, Y.J. *Surf. Sci.*, 500, 859, 2002.
- [11] Leão, C.R.; Fazzio, A.; da Silva, A.J.R. *Nano Lett.*, 7, 1172, 2007.
- [12] Scheres, L.; Giesbers, M.; Zuilhof, Z. *Langmuir*, 26, 4790, 2010.
- [13] Wu, Y.; Cui, Y.; Huynh, L.; Barrelet, C.J.; Bell, D.C.; Lieber, C.M. *Nano Lett.*, 4, 433, 2004.
- [14] Choi, Y-K.; Lee, J.S.; Zhu, J.; Somorjai, G.A.; Lee, L.P.; Bokor, J. *J. Vac. Sci. Technol. B*, 21, 2951, 2003.
- [15] Stern, E.; Klemic, J.F.; Routenberg, D.A.; Wyrembak, P.N.; Turner-Evans, D.B.; Hamilton, A.D.; LaVan, D.A.; Fahmy, T.M.; Reed, M. A. *Nature*, 445, 519, 2007.
- [16] Yablonovitch, E.; Allara, D.L.; Chang, C.C.; Gmitter, T.; Bright, T.B. *Phys. Rev. Lett.*, 57, 249, 1986.
- [17] Cheng, Y.C. *Prog. Surf. Sci.*, 8, 181, 1977.
- [18] Chen, S.; Bomer, J.G.; van der Wiel, W.G.; Carlen, E.T.; Van den Berg, A. *ACS Nano*, 3, 3485, 2009.
- [19] Buriak, J.M. *Chem. Rev.*, 102, 1272, 2002.
- [20] Bent, S.F. *Surf. Sci.*, 500, 879, 2002.
- [21] Puniredd, S.R.; Assad, O.; Haick, H. *J. Am. Chem. Soc.*, 130, 13727, 2008.
- [22] H. Zuilhof, H.; Sudholter, E.J.R. *Adv. Mater.*, 12, 1457, 2000.
- [23] Ciero, R.L.; Chidsey, C.E.D. *Langmuir*, 18, 305, 2002.

# A MICROMIRROR FOR OPTICAL PROJECTION DISPLAYS

R.A.Brookhuis<sup>1</sup>, M.J. de Boer<sup>1</sup>, M. Dijkstra<sup>1</sup>, A.A. Kuijpers<sup>2</sup>, D. van Lierop<sup>2</sup> and R.J. Wiegerink<sup>1</sup>

<sup>1</sup>MESA+ institute for nanotechnology, University of Twente, Enschede, The Netherlands

<sup>2</sup>Philips Applied Technologies, Eindhoven, The Netherlands

**Abstract** — In this paper we present a tilting micro mirror with a large mirror surface of up to 2.5 mm x 1.0 mm and a large rotation angle of  $\pm 10^\circ$  as needed for optical projection displays. The mirror is driven by vertical comb-drive actuators which were realized by deep reactive ion etching (DRIE) fabrication technology based on a combination of deep reactive ion etching and a buried mask to provide self-alignment of the stator and rotor fingers in a silicon on insulator (SOI) wafer. Measurement results are shown for various realized mirror designs.

**Keywords:** micromirror, vertical comb-drive, SVC, DRIE, laser display, pocket projector.

## I - Introduction

Miniature laser projection or pico projection is one of the most promising technologies [1] for displaying information from small electronic devices like mobile phones, PDA's and multi-media players. The current possibilities with micro technology and the availability of tiny light sources which can be modulated at high frequencies give the possibility of making an efficient projection system in a very small form factor. This is of interest for mobile applications or other applications where weight, low power consumption and form factor are important design rules.

The micro mirror presented in this paper is meant for a bidirectional scanning system with a small 'fast' mirror for the horizontal scan direction and a larger 'slow' mirror for the vertical direction. The 'fast' mirror, which operates in resonance, has been presented earlier [2-3]. A solution for the 'slow' mirror is presented in this paper. This mirror will not be driven in resonance, but with a 50 Hz saw-tooth signal, which means that the bandwidth should be in the order of 1 kHz. In Figure 1 a schematic diagram is shown of a laser based projection display. The projector consists of three light sources and two mirrors which deflect the light beam. One mirror deflects the light over the horizontal axis and the other mirror deflects the light over the vertical axis. Doing so, the light can be steered over a 2D plane. To be able to create a color and differences in brightness, the three light sources are modulated at high frequency to vary the intensity.

An overview of previously published micromirrors can be found in [4-5].

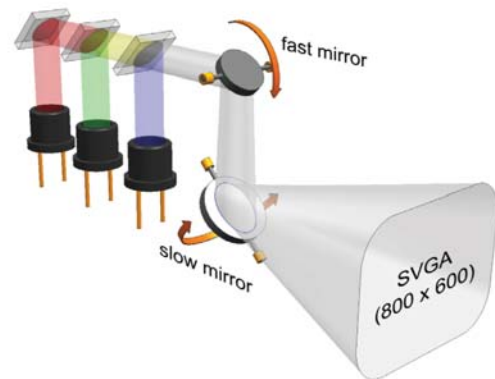


Figure 1: Model of a laserdiode based projection system consisting of 3 laser diodes (red, green, blue) and two mirrors to deflect the light over two perpendicular axes. Color is created by modulating the light source with an on-off signal to vary its intensity (image taken from [2]).

## II - Design

### A. Mirror Design

In Figure 2 the model of the micromirror is shown. The mirror is suspended by two torsion axes with a rectangular cross-section and the actuation is done by a staggered vertical comb-drive (SVC) [6-8]. To create two nicely defined levels, an SOI wafer is used. The mirror surface should have good reflective properties and must ensure that the reflection characteristics are such that the resolution of the whole system is diffraction limited. The static flatness is determined by the residual stress in the mirror surface. The dynamic flatness is determined by the rigidity of the mirror surface and the angular acceleration. Due to the moment of inertia of the mirror, the surface will deform in an s-curve as shown in [9]. The deflection due to angular acceleration together with the initial curvature of the mirror should not exceed  $\lambda/10$ , which means that the flatness should be below 40 nm. Table 1 summarizes the target specifications for the mirror device.

Table 1: Target mechanical and electrical properties

Property	Symbol	Specification
Mirror width	$w_m$	1000 $\mu\text{m}$
Mirror length	$l_m$	2500 $\mu\text{m}$
Maximum rotation angle	$\theta_{\max}$	$-10^\circ$ to $+10^\circ$ (mechanical)
Maximum actuation voltage	$u_{\max}$	60 Volt
Mirror flatness	$\delta_{\max}$	$\lambda/10$ ( $< 40$ nm)

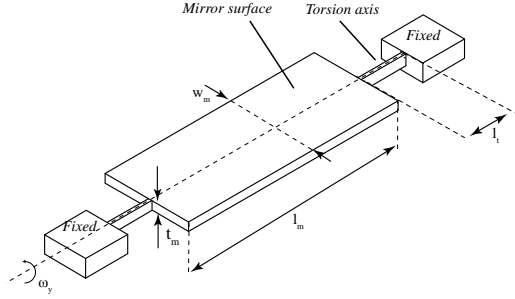


Figure 2: Model of the 1D micromirror

### B. Comb-drive Actuator

The mirror will not be operated in resonance. This means that the SVC actuator must actuate the mirror surface over the full range. The maximum static rotation angle which can be achieved is determined by the height and length of the comb-fingers. This maximum occurs where the overlapping area between the stator and rotor comb has a maximum. Due to the geometry, the change in area is not fully linear up to the maximum overlap. The angle for which the change in area is assumed to be linear occurs at  $\theta_{\text{mlin}}$  where the right-most corner of the rotor comb is at the same height as the topside of the stator comb finger, see Figure 3. To express the capacitance as function of the angle of rotation  $\theta$ , the model will be simplified by defining the rotation axis on the same horizontal plane as the bottom of the stator comb. This yield the following expression for the capacitance as function of the angle  $\theta$ :

$$C_{\text{svc}}(\theta) = N_f \frac{\epsilon_0 \epsilon_r (l_f^2 - l_{so}^2)}{g_{rs}} \theta \quad (1)$$

Where  $N_f$  is the number of fingers,  $l_f$  the length of the rotor finger,  $l_{so}$  the offset of the stator from the center of rotation and  $g_{rs}$  the gap spacing between the rotor and the stator. From this equation the torque exerted by the vertical comb-drive as a function of the applied voltage can be expressed when taking the derivative of the capacitance to  $\theta$  at constant voltage  $u$  while neglecting the fringing field effect:

$$\tau_{el} = N_f \frac{\epsilon_0 \epsilon_r (l_f^2 - l_{so}^2)}{2g_{rs}} u^2 \quad \text{if } 0 \leq \theta \leq \theta_{\text{mlin}} \quad (2)$$

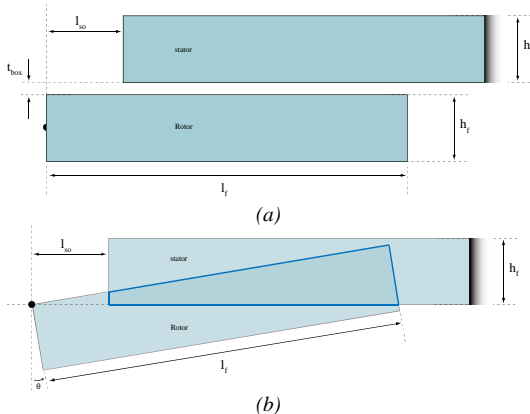


Figure 3: Schematic view of the vertical comb-drive actuator with (a) initial position (b) model for actuated comb-drive.

Figure 4 shows the calculated capacitance using FEM simulations. The resulting curve is almost identical to the analytical expression given by (2).

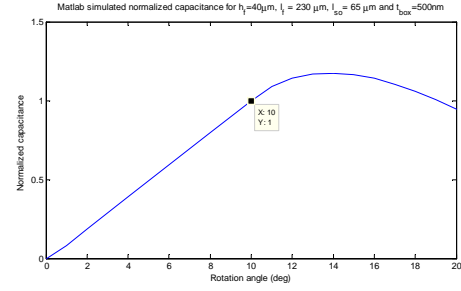


Figure 4: FEM results showing normalized change in capacitance versus rotation angle for  $h_f = 40 \mu\text{m}$ ,  $l_f = 230 \mu\text{m}$ ,  $l_{so} = 65 \mu\text{m}$  and  $t_{\text{box}} = 500 \text{ nm}$ . The capacitance is normalized at  $\theta_{\text{mlin}} = 10^\circ$ .

### C. Position Sensing

For controlling the mirror and the projector, the angle of rotation of the mirror needs to be known. For SVGA resolution the required angular resolution is 0.03 degrees. Commonly used position sensing mechanisms are capacitive sensing, piezo-electric sensing [10-11] and thermal displacement sensing. Capacitive rotation angle measurement is compatible with the fabrication process. If designed well, the parasitic effects of a capacitive measurement can be suppressed by a differential measurement which suppresses all common mode signals. A disadvantage of a capacitive sensing method is that the measurement introduces parasitic forces which can be suppressed by using differential measuring methods with frequencies way above the mechanical bandwidth of the system. To cancel out the actuation signal, two actuator groups are realized on each side of the mirror. One group is actuated by a positive signal, the other group by the same signal with opposite polarity.

## III - Fabrication

### A. Process flow

Figure 5 shows the outline of the process flow. (a) The base material is a SOI wafer with a device layer of 40  $\mu\text{m}$ , a handle layer of 340  $\mu\text{m}$  and a buried oxide layer of 500 nm. (b) The handle layer will be etched until there is a thickness equal to  $h_f = 40 \mu\text{m}$  left. This etch determines the height of the rotor comb-fingers and the thickness of the mirror surface. (c) A 1200 nm TEOS  $\text{SiO}_2$  layer is deposited, to form a stopping layer which is needed later (in steps k and l). LPCVD  $\text{SiO}_2$  is chosen because this is, after deposition, slightly tensile compared to silicon. A layer of 150 nm Chromium is deposited on the backside. This is to ensure good thermal conductivity which is required for releasing the mirror in step k and l. (d,e) Patterning of photoresist and etching of  $\text{SiO}_2$  in which the stator fingers are defined and all other features which should not be etched during all the steps. In this step, the width of the stator fingers

is 2  $\mu\text{m}$  wider than the final width. This allows a tolerance in the alignment between the lithography steps *i* and *g*. **(f,g)** Second photoresist patterning step and  $\text{SiO}_2$  etch in which the rotor fingers and mirror surface are defined. The pattern must be deposited within 2  $\mu\text{m}$  alignment of the previous step. The misalignment is etched away by a second  $\text{SiO}_2$  etch. At the places where there is no masking layer, the silicon will be completely etched to the  $\text{SiO}_2$  stopping layer. Everywhere where there is only photoresist, the silicon will be etched to the buried oxide (BOX) layer. **(h)** First DRIE step (DRIE-1), which will stop on the BOX layer. The recipe for etching DRIE-1 must have straight sidewall profiles and no notching. **(i)** Removal of the buried oxide layer. As described in [12], etching  $\text{SiO}_2$  in high aspect ratio trenches can lead to unexpected results. For this step a custom recipe has been developed which make use of argon. **(j)** Second DRIE step (DRIE-2), which will stop on the  $\text{SiO}_2$  stopping layer. When the silicon is etched away, the mirror surface is only connected to the substrate by the torsion axis. Since high energies are involved in the etching process the mirror surface will heat up and eventually the torsion axis will be damaged due to thermal effects. Therefore a layer of chromium is deposited in step c. **(k)** Stripping of photoresist. Important in this step is that the fluorocarbon sidewall projection will not be affected otherwise the structure will be damaged in the next etching step. Last DRIE step (DRIE-3), which will remove the upper part of the rotor comb-fingers. **(p)** Removal of the chromium thermal support layer by  $\text{O}_2$  plasma. Vapor HF isotropic etch of Silicon Dioxide stopping layer.

### B. Fabrication results

Figure 6 shows a photograph of the scanning micromirror and a close-up of the actuator part.

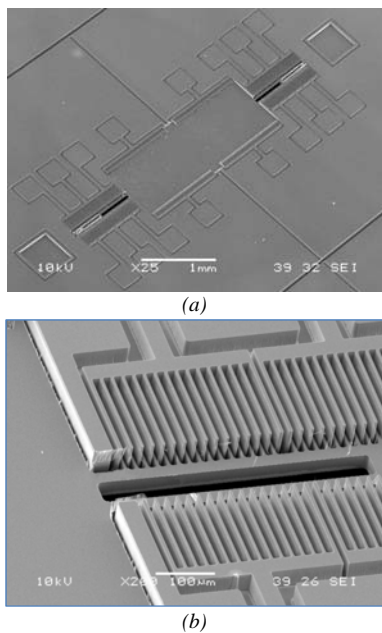


Figure 6: SEM photo showing (a) total overview of the fabricated micromirror. (b) close-up of the vertical comb-drive actuator.

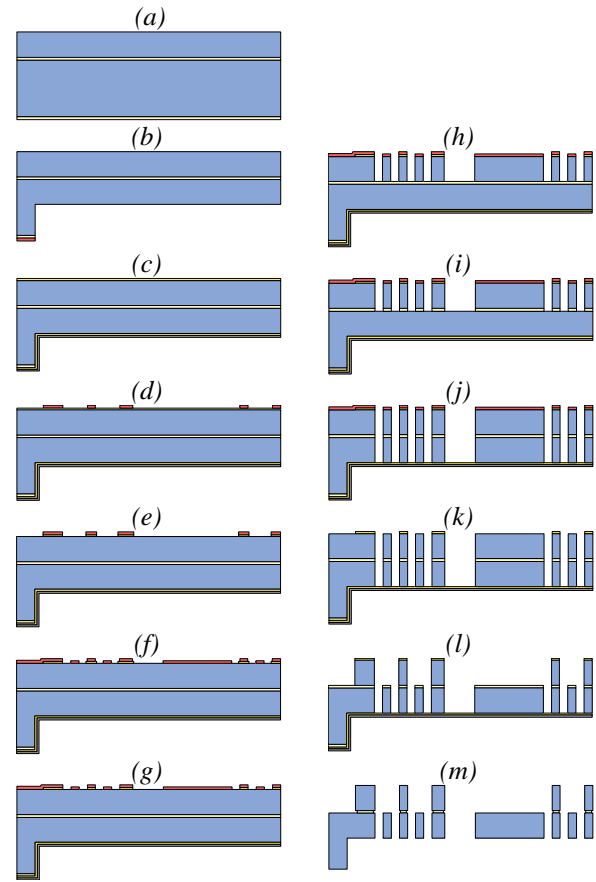


Figure 5: Process outline (see text)

## IV - Characterization

### A. Static behavior

For all samples the static and dynamic properties are determined. Figure 7 shows the measured rotation angle as a function of the actuation voltage for a typical sample with the dimensions shown in table 1. The measured resonance frequency of this device is 243 Hz. It has a finger gap spacing of  $g_{rs} = 5 \mu\text{m}$  and the number of fingers for static actuation ( $N_f$ ) is 30. In the same figure, the plot of the analytical model with the same bandwidth and gap spacing is shown. As can be seen, the measured values are slightly lower than the analytical values. This is the result of undercut of the comb-fingers due to the DRIE process. An undercut increases the gap distance and will therefore result in a lower torque.

### B. Dynamic behavior

In Figure 8 the frequency response of various mirror types is shown. Two resonance peaks can be observed the first resonance peak is the desired torsional mode. The second peak in the figure is the out-of-plane sliding mode, where the mirror slides up and down in the direction perpendicular to the mirror surface. Two other higher modes the in-plane sliding and rotational mode



[9] could not be measured with the vibrometer, since these are in-plane motions.

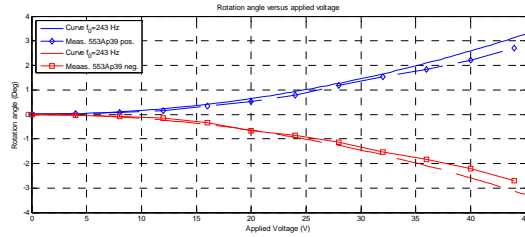


Figure 7: Rotation angle versus voltage for a sample with resonance frequency of  $f_0 = 243$  Hz, and the solid line shows the plot of the analytical model for  $f_0 = 243$  Hz,  $N_f = 30$  and  $g_s = 5$   $\mu\text{m}$

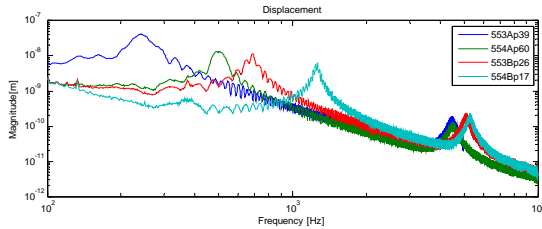


Figure 8: Polytec MSA 400 vibrometer measurement with a periodic chirp from 1 Hz to 10 kHz for various mirror versions.

553A: mirror size 2.5x1.0mm, torsion axis width 3  $\mu\text{m}$ .  
554A: mirror size 2.5x1.0mm, torsion axis width 4  $\mu\text{m}$ .  
553B: mirror size 1.75x0.7mm, torsion axis width 3  $\mu\text{m}$ .  
554B: mirror size 1.75x0.7mm, torsion axis width 4  $\mu\text{m}$ .

### C. Mirror flatness

Figure 9 (a) shows the three dimensional profile of the silicon mirror surface with 2500  $\mu\text{m}$  length and 1000  $\mu\text{m}$  width. The mirror shows a hollow profile with a maximum deflection  $\delta_m$  of 30 nm over the length of the mirror and 8 nm over the width of the mirror. Both deflections are below the requirement of 40 nm. In Figure 9 (b) the deflection is plotted against the position on the mirror surface where the center of the mirror surface is the origin. Note that the measurements are performed on a mirror surface without reflective coating.

## IV - Conclusions

In this paper we have discussed the design, fabrication and characterization of an electrostatically actuated scanning MEMS micromirror for a system based on a two-mirror (2x1D) architecture. The measured resonance frequencies were lower than predicted by the analytical model, which was mainly due to undercut and side-wall tapering in the DRIE process. Current research focuses on techniques to reduce the mass of the mirror without sacrificing static and dynamic flatness in order to reach a 1 kHz resonance frequency also for the largest mirrors.

## Acknowledgements

This work has been sponsored in part by the Dutch government within the Point-One framework MEMS-Land.

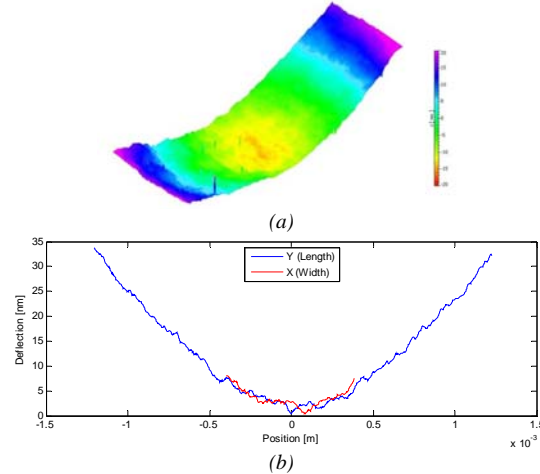


Figure 9: (a) Three dimensional profile of the silicon mirror surface of 2500x1000  $\mu\text{m}$  without reflective layer measured with the polytech MSA400 white light interferometer. (b) Height profile in x-direction and y-direction of silicon mirror of 2500x1000  $\mu\text{m}$  without reflective layer.

## References

- [1] C. Chinnock, "The picoprojector gold rush," *Information Display*, vol. 24, p. 12, 2008.
- [2] R. Sanders, *et al.*, "Design and fabrication of a MEMS mirror for miniature laser projection," in *OEMS and Miniaturized Systems VIII*, 2009.
- [3] A. Kuijpers, *et al.*, "Towards embedded control for resonant scanning MEMS micromirror," *Procedia Chemistry*, vol. 1, pp. 1307-1310, 2009.
- [4] K. Hane and M. Sasaki, "Micro-Mirrors," in *Comprehensive microsystems*, ed: Elsevier B.V., 2007, p. 2100.
- [5] P. Patterson, *et al.*, "Scanning micromirrors: An overview," 2004, p. 195.
- [6] R. Conant, *et al.*, "A flat high-frequency scanning micromirror," 2000, pp. 6-9.
- [7] K. Kumar and X. Zhang, "CMOS-compatible 2-axis self-aligned vertical comb-driven micromirror for large field-of-view microendoscopes," 2009, p. 1015.
- [8] D. Hah, *et al.*, "Self-aligned vertical comb-drive actuator," *Journal of Micromechanics and Microengineering*, vol. 14, pp. 1148-1156, 2004.
- [9] H. Schenk, "Ein neuartiger Mikroaktor zur ein- und zweidimensionalen Ablenkung von Licht," 2000.
- [10] M. Sasaki, *et al.*, "Piezoresistive rotation angle sensor integrated in micromirror," *Japanese journal of applied physics*, vol. 45, p. 3789, 2006.
- [11] T. Sandner, *et al.*, "Integrated Piezo-resistive Positionssensor for Microscanning Mirrors," 2007, pp. 195-196.
- [12] D. Hah, *et al.*, "A self-aligned vertical comb-drive actuator on an SOI wafer for a 2D scanning micromirror," *Journal of Micromechanics and Microengineering*, vol. 14, p. 1148, 2004.

# FREQUENCY SHIFT OF MEMS ELECTROMECHANICAL RESONATORS INDUCED BY PROCESS VARIATION

F. Casset<sup>1</sup>, J. Arcamone<sup>1</sup>, A. Niel<sup>1</sup>, E. Lorent<sup>1</sup>, C. Marcoux<sup>1</sup>, Y. Civet<sup>3</sup>, C. Durand<sup>2</sup>, E. Ollier<sup>1</sup>, P. Renaux<sup>1</sup>, JF. Carpentier<sup>2</sup>, P. Ancey<sup>2</sup> and P. Robert<sup>1</sup>

<sup>1</sup>CEA, LETI, MINATEC, F-38000 Grenoble, France

<sup>2</sup>STMicroelectronics, F-38926 Crolles, France

<sup>3</sup>TIMA, CNRS, Grenoble INP, UJF, F-38000 Grenoble, France

**Abstract** — MEMS resonators can bring an important added value in many fields of application. For example, MEMS resonators are good candidates to replace quartz oscillators. In this paper, we present MEMS resonator designs and measurements at various frequencies while they were built using the same process. We put in exergue the frequency shift induced by resonator sizes variation such as process inaccuracy. This measured frequency shift proves the need for a frequency shift compensation method for industrial perspectives.

**Keywords** : MEMS resonator, multi-frequency, frequency accuracy.

## I - Introduction

ONE of the major advantage of MEMS resonators reside on the possibility to obtain multi-frequency components on a single wafer using the same process. It enables the possibility of obtaining compact and integrated multi-frequency front end modules, for example for multi-band systems or multi-time reference applications. State-of-the-art MEMS resonators [1]-[3] already present impressive performances. In order to compare state-of-the-art demonstrators, we use a figure of merit based on the resonant frequency (F) multiplied by the quality factor (Q). This F×Q product represents one criteria of excellence in RF applications. Figure 1 shows that bulk mode MEMS resonators present the highest performances in terms of F×Q product (data measured at ambient temperature and under vacuum atmosphere). In this paper we describe the design and realization of bulk mode disk and plate resonators which present compact sizes (for integration purposes), high performances and high power handling.

Nevertheless, today, the frequency accuracy after process integration is still a key challenge for industrial perspectives. For example, time reference applications require frequency accuracy of some parts per million (ppm). In this context, we present in this paper MEMS resonators with distinct frequencies, built using the same process. We put in exergue the frequency shift induced by resonator sizes variation such as process inaccuracy (photolithography or/and etch step). This measured frequency shift then allows us to specify the frequency shift compensation method needed for industrial perspectives.

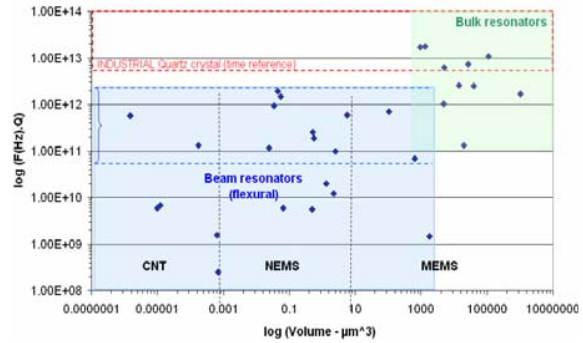


Figure 1: CNT, NEMS and MEMS resonators state of the art

## II – MEMS resonator design

### A. Simple analytic equations

Many different resonator designs were studied for many years: flexural beam [4], bulk mode disk [5] or plate [6], bulk mode SiBar [7]. All these devices present a resonant frequency following the generic equation (1):

$$F_R = \frac{1}{2\pi} \sqrt{\frac{k}{m}} \quad (1)$$

k and m are respectively the effective stiffness and mass. The resonant frequency of bulk mode disk and plate resonators is function respectively of its radius R as described by equation (2) [5], and of the plate size L as described by equation (3) [6]:

$$F_{R \text{ Disk}} = \frac{k}{2\pi R} \sqrt{\frac{E}{\rho(1-\nu^2)}} \quad (2)$$

$$F_{R \text{ Plate}} = \frac{1}{2L} \sqrt{\frac{Y_{2D}}{\rho}} \quad (3)$$

Table 1 describes the parameters included in equation (2) and (3) and gives typical value for single crystal silicon.

Table 1: Parameters and values

Symbol	Parameter	Value (single crystal silicon <110> direction)
K	Frequency constant	1.6002
E	Young's modulus	169 GPa
Y <sub>2D</sub>	Effective Young's modulus for a 2D expansion	181 GPa [2]
ν	Poisson's ratio	0.29
ρ	Density	2330kg/m <sup>3</sup>

Our interest here is the resonant frequency dependence upon the photolithographically defined sizes of the vibrating element (radius or length). Thus, we can provide several frequencies on a single wafer by changing the resonator size. Table 2 lists the difference of resonance frequencies obtained by FEM and analytical equation (2) and (3).

### B. FEM simulations

We used the FEM Coventor® software to study two kinds of bulk mode resonators: wine-glass mode disk and Lamé mode plate. We used *Extruded bricks* elements using the *Split and merge* algorithm to mesh our structures, and we performed modal analysis. The following Figure 2 shows the vibration shape of the considered mode. With support beams clamped at the corners corresponding to nodal points (in blue, and presenting nearly zero displacement), energy losses due to the anchoring of the resonator can be minimized.

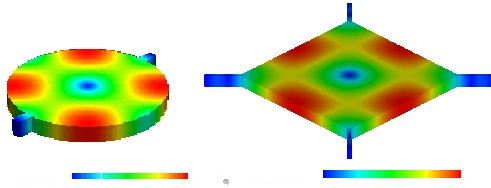


Figure 2: Bulk mode wine glass disk ( $R=14.7\mu\text{m}$ ) and Lamé plate ( $L=41.05\mu\text{m}$ ) vibration shape.

Frequencies extracted from Coventor® are compared with analytical calculation (Table 2). We note that we have a good agreement between analytical calculation and FEM, with a discrepancy less than 3% for disk and less than 8.2% for plate (in this last case, anchor influence or parameters inaccuracy can explain the higher discrepancy between analytical calculation and FEM).

### III – Technological realization

Demonstrators were built at the CEA, LETI, MINATEC using 200mm facilities. [3] describes the process flow used in order to obtain the studied devices as well as 100 MHz bulk mode resonators. Figure 3 summarizes the main steps of the process integration. It consists first in the patterning of released holes on a  $3\mu\text{m}$  thick silicon (SOI wafer) followed by oxide filling. Then the resonators are etched and an ultra-thin sacrificial oxide layer is deposited followed by the deposition, patterning and etching of polycrystalline silicon electrodes. Finally, after metal contact deposition and etching, the mechanical structures are released by etching the buried and the sacrificial oxide.

Figure 4 gives some SEM views of electrical demonstrators.

Table 2: Resonator design: Analytical and FEM comparison

ANALYTIC Frequency (MHz)	FEM Frequency (MHz)	$\Delta$ (%)	Design & Sizes
154	150	2.6	Disk D16, $R=14.7\mu\text{m}$ Thickness= $3\mu\text{m}$ 2 Anchors: $1.7\times 3\mu\text{m}^2$
324	314	3	Disk D17, $R=7\mu\text{m}$ Thickness= $3\mu\text{m}$ 4 Anchors: $0.8\times 2\mu\text{m}^2$
105	102	2.8	Disk D4, $R=21.6\mu\text{m}$ Thickness= $3\mu\text{m}$ 4 Anchors: $0.8\times 10\mu\text{m}^2$
278	303	8.2	Plate P23, $L=14\mu\text{m}$ Thickness= $3\mu\text{m}$ 4 T anchors: $2\times 3\mu\text{m}^2 + 1\times 3\mu\text{m}^2$
95	102	6.8	Plate P4, $L=41.05\mu\text{m}$ Thickness= $3\mu\text{m}$ 4 Anchors: $0.8\times 10\mu\text{m}^2$

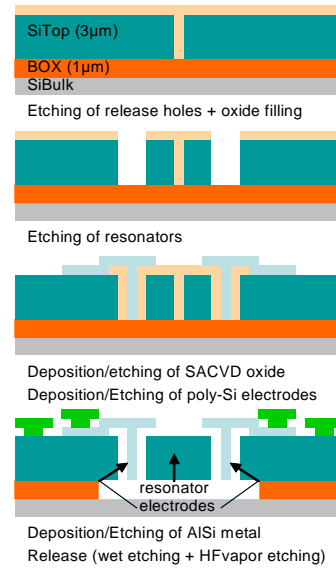


Figure 3: Process flow used to build demonstrators [3].

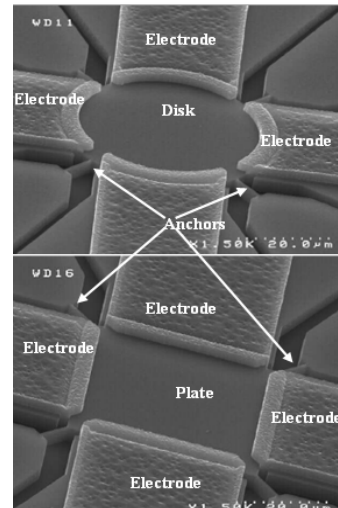


Figure 4: SEM views of released demonstrators.

#### IV – RF characterization and discussion

We used the measurement setup detailed in [8] to characterize our demonstrators. Table 3 shows some electrical results on bulk mode disk and plate resonators. Resonant frequencies extracted from measurement, ranging from 144 to 300MHz, are in good agreement with FEM design. The discrepancy between measurement and FEM simulation is less than 5%.

One of the design presenting the thinner anchor (design D17, anchor width=0.8 $\mu$ m) allows to obtain the higher F $\times$ Q factor ( $3.61 \times 10^{12}$ ) due to energy loss minimization through the anchoring area. This result, in the same F $\times$ Q range than those coming from the state of the art (Figure 1), proves that the technology used here allows obtaining performing multi-frequency components on a single wafer.

The discrepancy between FEM simulations and measurements can be explained by model inaccuracy (Young's modulus value, meshing), but equally by effective resonator sizes variation. Indeed, as shown by equations (2) and (3), the resonant frequency depends on the photolithographically defined sizes of the vibrating element. Process integration (photolithography and/or etch step) can introduce inaccuracy in the final resonator sizes which will impact the resonant frequency. Figure 5 gives an example of resonator to electrode gap enlargement, which induces resonator sizes modification due to technological inaccuracy [9].

#### Technological realization

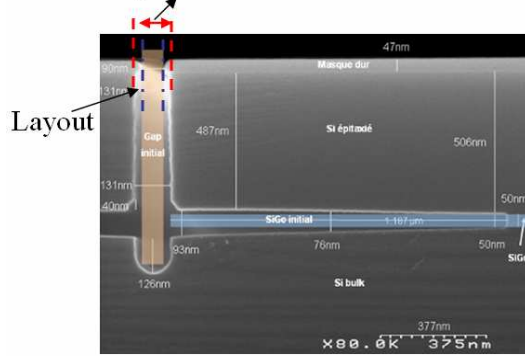


Figure 5: SEM view of resonator to electrode gap enlargement due to process inaccuracy [9].

This process inaccuracy depends on the process used to build demonstrators and its maturity. To study its impact in the worst case, we intentionally introduced sizes variation (<400nm) on two devices in order to measure the frequency shift induced by resonator sizes variation. Figure 6 shows a plate resonator frequency variation of 941.9kHz induced by a plate length variation of 400nm, in good agreement with the 950kHz predicted by equation (3).

Figure 7 show the frequency shift induces on a disk resonator when its sizes varies from 21.6 to 21.8 $\mu$ m. The measured frequency shift of 901kHz is in good agreement with the analytic calculation (963kHz).

Table 3: Resonator measurement and FEM comparison

Measurement	FEM Comparison
	<p>D16 disk device</p> <p><math>\Delta F_{\text{measure/FEM}}=3.8\%</math></p>
	<p>D17 disk device</p> <p><math>\Delta F_{\text{measure/FEM}}=4.6\%</math></p>
	<p>P23 plate device</p> <p><math>\Delta F_{\text{measure/FEM}}=5.2\%</math></p>

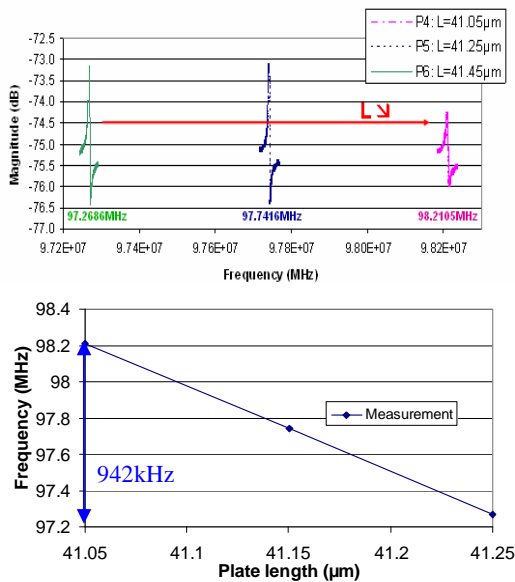


Figure 6: RF measurement ( $V_{DC}=3V$ ) of the frequency shift induced by plate resonator sizes variation.



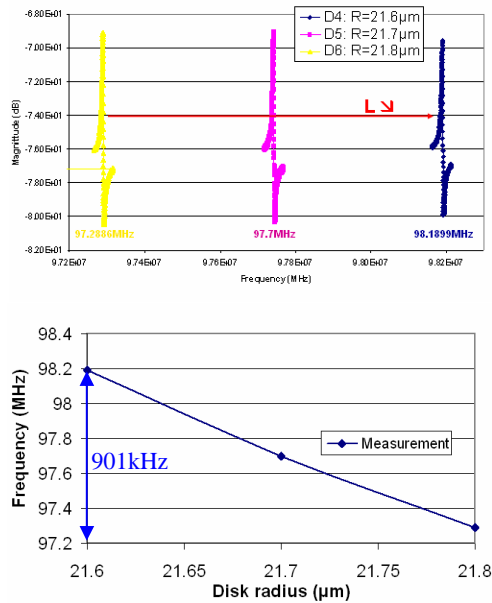


Figure 7: RF measurement ( $V_{DC}=5V$ ) of the frequency shift induced by disk resonator sizes variation.

To accurately design a MEMS resonator, the discrepancy between measurement and FEM (equal to device-layout mismatch) can be easily corrected for example by layout adjustments (resonator sizes correction on the layout). Nevertheless, the frequency dispersion between nominally identical devices which can be as high as 1% (400nm resonator sizes variation) put in exergue the need for a frequency compensation method to be implemented at the end of the fabrication process in order to meet the drastic specification in term of frequency accuracy for industrial perspectives. [10] presents a material coating-based frequency compensation method with promising results, hence reducing the frequency dispersion linked to process variations from 7% to around 0.1%. The final frequency tuning could be done by adjusting the polarization voltage which enables a frequency tuning around 0.1% in case of bulk mode resonators.

## V – Conclusion

In this paper, we measured various bulk mode resonators built using the same technology and presenting different resonant frequencies. We estimate at around 5% the inaccuracy between measurement and FEM model. This inaccuracy could be easily compensated by layout adjustments. We additionally observed a frequency shift of around 1%, induced by process variation that has to be corrected in order to reach some parts per million (ppm) as required for industrial purposes. One of the promising possibilities for reducing process dispersion is to use a material coating compensation method.

## References

- [1] YW Lin, S Lee, SS Li, Y Xie, Z Ren, CTC Nguyen, “60-MHz Wine-Glass Micromachined-Disk Reference Oscillator”, *IEEE International Solid-State Circuits Conference (ISSCC)*, Feb. 15-19, 2004, pp. 322-323.
- [2] V Kaajakari, T Mattila, A Oja, J Kiihamäki, H Seppä, “Square-Extentional Mode Single-Crystal Silicon Micromechanical Resonator for Low Phase Noise Oscillator Applications”, *IEEE Electro Device Letter*, Vol. 25, n. 4, April 2004, pp. 173-175.
- [3] E Ollier *et al.* “IC-integration-compatible single-crystal silicon 100-300MHz MEMS resonators with 60nm air gap and sub 5V polarization voltage”, *Workshop on MEMS for Millimeter Wave Communication (Memswave)*, June 2010, to be published.
- [4] C. Durand *et al.*, “In plane Silicon on Nothing Suspended Gate MOSFET for in IC integration perspectives”, *IEEE Electron Device Letters*, Vol 29, n 5, May 2008.
- [5] Z. Hao, S. Pourkamali, F. Ayazi, “VHF Single-Crystal Silicon Elliptic Bulk-Mode Capacitive Disk Resonator – Part I: Design and Modeling”, *Journal of Microelectromechanical Systems*, vol. 13, n 6, December 2004, pp. 1043-1053.
- [6] M. Palaniapan, L. Khine, “Micromechanical resonator with ultra-high quality factor”, *Electronics Letters*, Vol. 43, n°20, September 2007.
- [7] HM. Lavasani, AK. Samaroo, G. Casinovi, F. Ayazi, “A 145MHz low phase noise capacitive silicon micromechanical oscillator”, *IEEE International Electron Devices Meeting*, December 2008, pp. 675–678.
- [8] J. Arcamone, E. Colinet, A. Niel, E. Ollier, “Enhanced capacitive detection of bulk mode MEMS resonators by active cancellation of feedthrough capacitance”, *IEEE IFCS 2010*, to be published.
- [9] C. Durand *et al.*, “Silicon on nothing MEMS electromechanical resonator”, *In Proceedings of the 2007 Symposium on Design, Test, Integration and Packaging of MEMS/MOEMS (DTIP)*, April 2007, pp. 326-331
- [10] Y. Civet, F. Casset, JF. Carpentier, S. Decossas, T. Haccart, S. Basrour, “MEMS resonator frequency compensation by “in-line” trimming”, *Workshop on MEMS for Millimeter Wave Communication (Memswave)*, June 2010, to be published.

# WET ETCHING OPTIMIZATION FOR ARBITRARILY SHAPED PLANAR ELECTRODE STRUCTURES

H. Rattanasonti<sup>1</sup>, R. C. Sterling<sup>2</sup>, P. Srinivasan<sup>1</sup>, W. K. Hensinger<sup>2</sup>, and M. Kraft<sup>1</sup>

<sup>1</sup>*School of Electronics and Computer Science, University of Southampton, Southampton, U.K*

<sup>2</sup>*Department of Physics and Astronomy, University of Sussex, Brighton, U.K*

**Abstract** — In this paper we present a simple fabrication process to realize arbitrarily shaped in-plane structures at micro scales. The structure consists of an array of isolated high aspect ratio Cr/Au islands of varying geometry and topology created on a SOI (Silicon-on-Oxide Insulator) wafer by a chemical wet etching process. We optimized the wet etching recipe to minimize the undercutting effect on the critical features of the isolated islands. The fidelity of the developed process to transfer the mask patterns was studied by comparing the dimensions of micromachined features at critical locations with that of the mask. Preliminary microscopic measurements revealed that the deviation in the geometry of the islands at critical locations was within 7%. Such a simple cost-effective etch process is potentially promising for realizing metalized microelectrode structures in a large scale atom/ion trap applications.

**Keywords:** Ion traps, quantum computation, micro-fabrication, wet etching

## I - Introduction

Realizing ASPES (arbitrarily shaped planar electrode structures) at micro scales without appreciable etch lag and undercuts is very challenging from a wafer level processing standpoint. Creating such electrode structures is of great interest in many interesting applications such as atom/ion traps for Quantum Information Processing (QIP) [1-4], dielectrophoresis [5-8, 10] and particle mixing/manipulation [9, 10]. The feasibility of achieving such structures depends on the materials considered for processing and their thicknesses. Present generation silicon micromachining technology provides ample opportunities to realize ASPES through dry/plasma etching processes [11, 14]. Creating metallization on such electrode structures improves the device performance by reducing the operating voltage. However, the relevant processes to realize such metalized ASPES are very limited on a wafer level due to difficulty in controlling the etch rate across the wafer. Hence it is timely and pertinent to develop a suitable process for creating metalized ASPES for exploring new design opportunities which forms the principal motivation of the present work.

Thin film metallic ASPES on silicon are promising for applications such as atom/ion traps [11-14]. Although various device configurations [16-18] have been studied for ion traps, the potential of surface

micromachined planar microelectrode structures cannot be overstated [15, 16]. Metalized ASPES structures are commonly accomplished either by lift-off procedures or by wet etching. The ability to successfully implement lift-off process for creating high aspect ratio thin film metallization on ASPES is dictated by the area to be lifted off and the thickness of the substrate materials which is usually about  $\sim 1\mu\text{m}$ . Although there was a limited success for lifting off large film thickness i.e. about a few microns [19-20], the process available is not very matured. Consequently, non-standard chip level processing has been preferred to retain better control on the feature sizes which is a technological barrier for the scalability of the device structures.

The present work investigates the suitability of wet etching process for creating Au/Cr metallization on ASPES micromachined on a SOI wafer to realize large scale asymmetric ion traps on wafer level. The effects of relevant process parameters (resist thickness, concentration of the etchant, etch duration and agitation) on the quality of the metalized electrode structures were studied by comparing the deviation in the dimensions of critical features caused by undercut to the corresponding features on the mask. The key objective of the work is to develop a robust process to accommodate the variation in the dimensions of the electrode gaps (2.5 to 7.5  $\mu\text{m}$ ) i.e. the distance between the ASPES islands at critical locations which have a significant bearing on the electric field generated to trap ions.

Based on the computational analyses of electric field vectors necessary to create a trap of required depth, the geometry and topology of the electrode structures were obtained which was discussed elsewhere [21]. This work discusses exclusively on the microfabrication processes associated with an array of a specific type of asymmetric microelectrodes achieved by creating metalized (Cr/Au) ASPES on a SOI wafer. Development of a simple cost-effective process to create such structures will serve as a technological platform for realizing atom/ion traps on a large scale which forms the basic building block of quantum (qubit) computing.

This paper is organized as follows. Section II explains the relevant micromachining processes to create microelectrode structures on a wafer level. Section III discusses on the outcome of the fabrication process by comparing the dimensions of the critical features on the processed wafer to the corresponding feature on the mask. Section IV lists the concluding remarks drawn from this study.

## II. Fabrication Processes

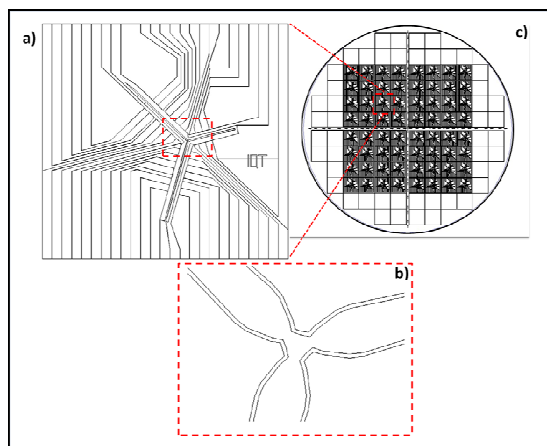


Figure 1: Schematic of microelectrode structures used for ion trap application. a) Asymmetric Y-electrode structure, b) Blown out picture of the central region of the trap, c) Layout of the mask considered for wafer level processing

The present study focuses on a particular type of a device structure to be used for generating asymmetric electric fields by applying rf potentials. It consists of an arrangement of microelectrode structures which forms a Y-shape at the centre as shown in Figure 1a. Each electrode forms a bond pad at the periphery of the device to provide electrical contacts. The geometry and the topology of each of the microelectrode structures vary appreciably within a chip. Figure 1b shows the zoom in picture of the arrangement of the Y-electrodes at the central region the chip. The critical features of the Y-electrode were in shown in Figure 1b which is a region of interest in our study. The actual mask layout consists of an array of such chips with different dimensions at the critical locations of each of the chip as shown in Figure 1c.

Figure 2 shows the fabrication process flow for creating the devices. The process sequence starts with the cleaning of a wafer by immersing in a bath of fuming nitric acid (FNA) for 90 sec to remove the organic contaminants. This is followed by a quick rinse in de-ionised (DI) water and an evaporative drying in an oven maintained at 210 °C for 1 hr. The second step is the deposition of Cr/Au layers of about 40/500 nm respectively by e-beam evaporation using Evaporator Balzers BAK 600. The Cr layer was created at a deposition rate of  $0.06 \text{ nm.s}^{-1}$  using a beam current of 21 mA at 5 kV. The Au layer was deposited at a rate of  $0.23 \text{ nm.s}^{-1}$  using a beam current of 113 mA at 5 kV. The thickness of Au layer obtained from e-beam evaporation process varies within 10% from the centre to the periphery of the wafer. The third step is the spin coating of a positive photo resist (Shipley S1813) on the wafer at a speed of 5000 rpm for 30 sec which results in a resist layer of 1.8

$\mu\text{m}$  thickness. The spinning is followed by a pre-bake of 98 °C for a minute. The fourth step is the patterning of the photoresist by UV lithography using EVG 620T. A pressure of 1bar was applied for creating a vacuum and hard contact during photolithography for exposure duration of 3 sec. The fifth step consists of developing the exposed photo resist using Microposit™ MF™ -319 metal-ion-free developer (Rohm and Hass Electronics materials LLC) 20 sec. The sixth step involves removal of Au layer using a mixture of Au etchant ( $\text{KI} < 25\% + \text{I}_2$  1-10% +  $\text{H}_2\text{O}$  remaining, OM Group Ultra Pure Chemicals) and DI water in the ratio of 1:2 by volume. The seventh step is the removal of Cr layer using Cr etchant (Acetic acid 1-10% + Ceric ammonium nitrate 10-30% +  $\text{H}_2\text{O}$  remaining, OM Group Ultra Pure Chemicals).

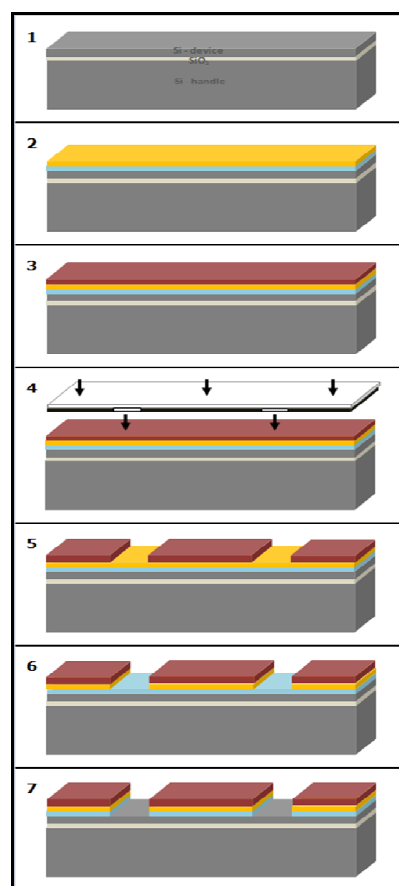


Figure 2: Fabrication process flow to micromachine ASPES for ion trap application.

## III - Results and Discussion

The process discussed in the previous section was obtained after several trials by varying the concentration of the Au etchant ( $\text{KI} < 25\% + \text{I}_2$  1-10% +  $\text{H}_2\text{O}$  remaining) by mixing with DI water and thickness of the photoresist. Figure 3 shows the outcome of one of

the trials obtained by etching a wafer patterned with a positive photoresist of  $\sim 3 \mu\text{m}$  thick. The Au etchant was used as it without mixing with the DI water and the wafer was etched for 60 sec.

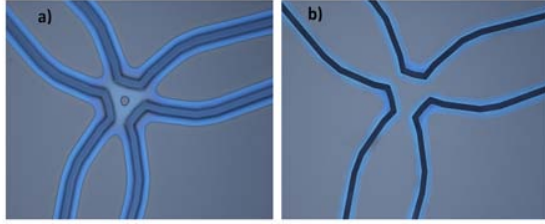


Figure 3: Comparison of a severe undercut at the crucial trap region after Au etching step between two different feature size a) the electrode feature size of  $9.5 \mu\text{m}$  width,  $7.5 \mu\text{m}$  gap width b) the electrode feature size of  $15.0 \mu\text{m}$  width,  $5.5 \mu\text{m}$  gap width (An undercut can be seen in a microscope as a bright outline of the edges of the trenches in a dark-sharp outline).

It is clearly evident from Figure 3 that there was severe undercutting through the electrode structures due to etch lag associated with the size of mask features. This is attributed to the availability of more ions to etch the Au layer through large exposed (Figure 3a) areas compared to that of the smaller areas (Figure 3b). Consequently, deep undercuts were formed by the time the Au layer was etched completely at the locations of the small openings thereby causing a significant deviation in the geometry of the critical Y-shaped electrodes.

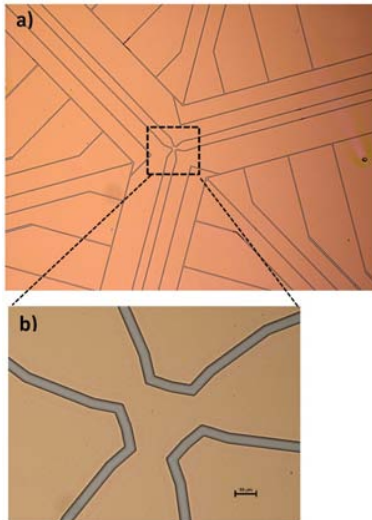


Figure 4: a) Micromachined metalized ASPES for ion traps application b) Microscopic image of the central Y-electrode region of the trap (Si surface appears in a dull gray region after Au/Cr etch)

To obtain a relatively uniform etching across the wafer, the concentration of the etchant was varied by adding DI water. Figure 4a shows the etch results obtained by using an optimised process discussed in

Figure 2. The etchant and DI water in the ratio of 1:2 by volume was employed for etching the Au layer for 15 sec. This was followed by Cr etching using Cr etchant (Acetic acid 1-10% + Ceric ammonium nitrate 10-30% +  $\text{H}_2\text{O}$  remaining) for another 15 sec. It is clearly evident from Figure 4a that a relatively uniform etching is accomplished minimising the undercut effects with this etch condition. Microscopic examination revealed that the central Y-electrode region as shown in Figure 4b was formed with relatively lesser undercut than experienced by the previously discussed etch conditions. Development of a suitable process to realise thin film arbitrary shaped metalised electrode structures by wet etching is the key contribution of the present work. We believe by changing the etch concentration it is possible to achieve arbitrary shaped metalized electrode structures with in-plane complexities using wet etching process.

Points	Top devices			Bottom devices			Schematic Y-electrodes
	Etched	Mask	Offset	Etched	Mask	Offset	
A	14.82	15.00	1.2%	9.63	9.50	1.4%	
B	14.93	15.00	0.5%	10.00	9.50	5.3%	
C	15.44	15.00	2.9%	9.91	9.50	4.3%	
D	5.08	5.00	1.6%	7.71	7.50	2.8%	

\* Unit in micron ( $\mu\text{m}$ )

Table 1: Comparison of the in-plane dimensions of the Y-shaped RF electrodes between the etched and mask features

Type	Area	Device	Electrode dimensions ( $\mu\text{m}$ )				Gap ( $\mu\text{m}$ )	Max Offset (%)	Schematic of Y-electrode
			electrode #1	electrode #2	electrode #3	electrode #4			
Etched	A	Top	115.7	101.1	61.1	204.5	5.3	6.6%	
		Bottom	113.2	101.5	55.7	202.0	7.8	3.8%	
	B	Top	114.5	101.8	60.2	202.5	4.8	4.9%	
		Bottom	112.2	101.7	55.9	202.4	7.2	3.6%	
Mask	A/B	Top	409.8				10.2	2.4%	
		Bottom	409.2				10.2	2.4%	
	C	Top	112	100	60	200	5.0		
		Bottom	110	100	55	200	7.5		

Table 2: Comparison of the proximity of DC control electrodes between the etched and the mask features.

The fidelity of the process for creating electrode structures with geometry close to that designed is critical for ion trap applications. Hence comparison were made between the etched features to the corresponding features in the mask by making in-plane microscopic measurements. The microscopic measurements were taken at two regions namely: a) the critical dimensions of Y-shaped electrodes at the centre where rf potentials would be applied, b) the proximity of the DC control electrodes from the centre to periphery. Table 1 shows the comparison between the in-plane dimensions of the etched features to the corresponding features on the mask obtained by microscopic measurements. Perhaps the most important contribution is the ability to realise the complex Y-shaped electrode structures with in-plane dimensional variation  $< 5.3\%$  which is potentially promising for ion trap applications. Table 2 shows similar such



measurements on the proximity of the DC control electrode structures. The maximum deviation in the proximity of the DC control electrodes was found to be 6.6%.

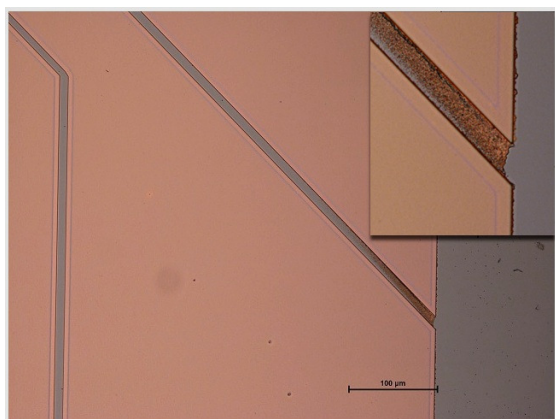


Figure 5: Incomplete Au removal at the gap between the electrodes on the periphery of the device.

The process developed left an issue to be addressed. Very thin layer of Au of few tens of nanometers were left between the electrode gaps after the Au etching step along the periphery of a few devices. This may lead to an inadvertent short circuit of the adjacent electrodes which is undesirable for ion traps. Figure 5 shows one such location at the periphery of the chip close to the region D shown in Table 2. It is clearly evident from the inset shown that Au was not completely removed after etching step. This may be attributed to the incomplete removal of photo resist subsequent to the development process. This can be overcome by an intermediate descumming procedure before Au etching step to ensure complete removal of monolayers of photo resist if any, left after the development. Continuous efforts are required to improve the developed process in order to overcome this issue. Nevertheless, the process discussed here will serve as a baseline study to realise other arbitrarily shaped surface micromachined structures which is the key contribution of the present work.

#### IV - Conclusion

In this study, we discussed on an optimised process to realise surface micromachined ASPES. These structures consist of an array of isolated high aspect ratio Cr/Au islands with a complex in-plane geometry and topology. The Au layer was etched using Au etchant ( $KI < 25\% + I_2$  1-10% +  $H_2O$  remaining) of varying concentration obtained by mixing it with DI water. Preliminary microscopic measurement indicates a variation in the in-plane dimensions within 5.3% at the critical Y-electrode region and 6.6% at the peripheral locations. The issue of incomplete gold etching at the periphery need to be addressed in the future research work. The surface micromachined Au structures would serve as a pattern for the subsequent processes namely,

the DRIE (Deep reactive ion etching) of Si layer followed by the BOE (Buffered oxide HF etch) of the sandwiched oxide layer of the SOI. This in turn will enable to create shielded dielectrics between the electrode structures. Future work involves scaling down of these electrode structures to create few thousands of ion traps which serves as a platform for a demonstrating the functionality of quantum computing.

#### Acknowledgement

The authors would like to thank the research colleagues of the Nano research group, School of Electronics and Computer Science, University of Southampton, U.K for their help and support during microfabrication. Due thank to the governing funding bodies which enabled to pursue this work.

#### References

- [1] D. Kielpinski, *et al.*, Nature 417, 709 (2002)
- [2] J. I. Cirac, *et al.*, Nature 404, 579 (2000)
- [3] R. Folman, *et al.*, Phys. Rev. Lett. 84, 4749 (2000)
- [4] M. Trinker, *et al.*, Appl. Phys. Lett. 92, 254102 (2008)
- [5] S. Fiedler, *et al.*, Anal. Chem. 70, 1909 (1998)
- [6] J. Yang, *et al.*, Anal. Chem. 71, 911 (1999)
- [7] P. R. Gascoyne, and J. Vykoukal, Electrophoresis 23, 1973 (2002)
- [8] M. P. Hughes, Electrophoresis 23, 2569 (2002)
- [9] A. Bezryadin, *et al.*, Appl. Phys. Lett. 71, 1273 (1997)
- [10] C. H. Kua, *et al.*, Innovation in Manufacturing Systems and Technology (IMST), 2005-01 (URI: <http://hdl.handle.net/1721.1/7464>)
- [11] J. Britton, *et al.*, arXiv:quant-ph/0605170 (2006)
- [12] S. Seidelin, *et al.*, Phys. Rev. Lett. 96, 253003 (2006)
- [13] C. E. Pearson, *et al.*, Phys. Rev. A 73, 032307 (2006)
- [14] D. R. Leibbrandt, *et al.*, Quant. Inf. Comp. 9, 0910 (2009)
- [15] J. M. Amini, *et al.*, New J. Phys. 12, 033031 (2010)
- [16] M. Brownnutt, *et al.*, New J. Phys. 8, 232 (2006)
- [17] W. K. Hensinger, *et al.*, Appl. Phys. Lett. 88, 034101 (2006)
- [18] D. Stick, *et al.*, Nat. Phys. 2, 36 (2006)
- [19] B. Lev, *et al.*, Quant. Inf. Comput. 3, 450 (2003)
- [20] S. Groth, *et al.*, Appl. Phys. Lett. 85, 2980 (2004)
- [21] J. Chiaverini, *et al.*, Quant. Inf. Comput. 5, 419 (2005)

# THERMAL BEHAVIOUR OF THREE DIMENSIONAL SINGLE CRYSTALLINE FORCE SENSORS

G. Battistig<sup>1</sup>, T. Weidisch<sup>2</sup>, T. Retkes<sup>2</sup>, M. Ádám<sup>1</sup>, I. Bársony<sup>1</sup> and T. Mohácsy<sup>1</sup>

<sup>1</sup>Research Institute for Technical Physics and Materials Science - MFA, Hungarian Academy of Sciences

<sup>2</sup>Department of Electron Devices of the Budapest University of Technology and Economics, Hungary

**Abstract** — A piezoresistive-type integrable single-crystalline sensor was developed for 3D force sensing. The piezoresistance effect is inherently temperature-dependent, therefore thermal properties of the device have to be studied. Furthermore, the elastic cover and the packaging strongly affect the thermal behaviour of the sensor.

The temperature dependence of the offset and the sensitivity were measured and the value of Temperature Coefficient of Offset (TCO) and Sensitivity (TCS) calculated. In case of a bare sensor TCO is  $0.9 \pm 1.17 \times 10^{-4}/^{\circ}\text{C}$  and with the elastic cover  $-0.98 \pm 1.04 \times 10^{-3}/^{\circ}\text{C}$ . In point of sensitivity we found a non-linear relationship and a remarkable drop over the temperature of  $45^{\circ}\text{C}$ .

There are less demanding applications, where - in spite their temperature sensitivity - the force sensors are appropriate, however, for precise tasks a temperature compensation is indispensable. On this reason a new perforated membrane force sensor design was proposed and manufactured, providing the necessary signals for obtaining temperature compensated outputs.

**Keywords :** 3D force sensors, Temperature coefficient, Temperature compensation, Piezoresistivity

## I - Introduction

Transducers accomplishing 3D force sensing receive increasing attention among sensors. Shear force sensors to be implemented for instance in robotic arms, require the development of special micromachined construction. Owing to their unique construction 3D force sensors developed and manufactured by MFA are most suitable for such applications. Thermal stability of the sensor assemblies, however, is a prerequisite in integrated system application.

In order to establish the exact thermal behaviour of the sensor, various measurements were employed, including thermal imaging of the warming-up process by applying a thermographic IR camera. The change in offset and sensitivity of the device affected by warming caused by the power dissipation and environmental heat were extensively analysed.

The elastic covering and the sensor structure plays a crucial role in the protection and operation of the force sensor device [1]. It significantly influences, however, its thermal behaviour, too. The side effects originating from the thermal expansion and relaxation of the cover material during operation, i.e. by the application of

mechanical force, are substantial. At temperatures in excess of  $45^{\circ}\text{C}$  in assembled sensors equipped with a cover a remarkable sensitivity drop and offset-shift was observed. This indicates the requirement for temperature compensation.

## II - Measurements

Fig.1. shows the schematic drawing of a sensing element. The perforated membrane-type device consists of a (100) n-type Si central plate, suspended by four bridges of the same type and orientation over an etched cavity. Since relative to the bridges the central part of the membrane is rigid, when loading the centre, the suspended structure allows deformation of the bridge elements. [110] oriented p<sup>+</sup>-type piezoresistors - as independent strain gauges - are embedded in the bridges. Each of the piezoresistors in the suspension membrane acts as the variable leg in a resistive half-bridge circuit, while the respective reference resistors are formed in the non-stressed Si bulk. The intermediate node voltages ( $V_{0i}$ ) provide the readings for resolving the vector components of the load. A detailed description of operation was recently reported by some of the authors [2].

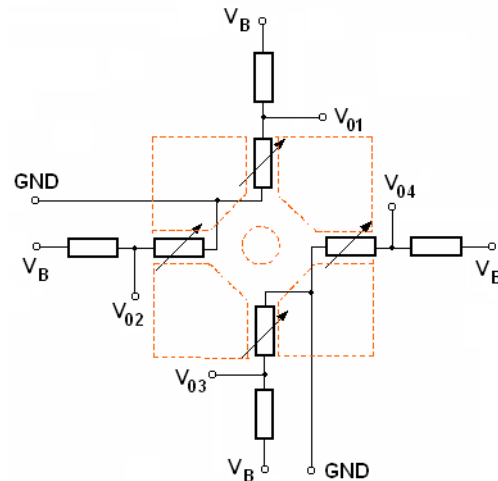


Figure 1: Scheme of a piezoresistive-type 3D force sensing element

### A. Offset shift

First the Offset Warm-up Shift, i.e. the change in output offset voltage that may occur when the sensor is powered was analysed.

For monitoring the warming-up of an elastic material covered and packaged 3D force sensor we used an analogue IR camera. The offset signals and thermographic images of the camera were recorded simulta-

eously.

The obtained images at different moments after start are presented in Fig. 2.

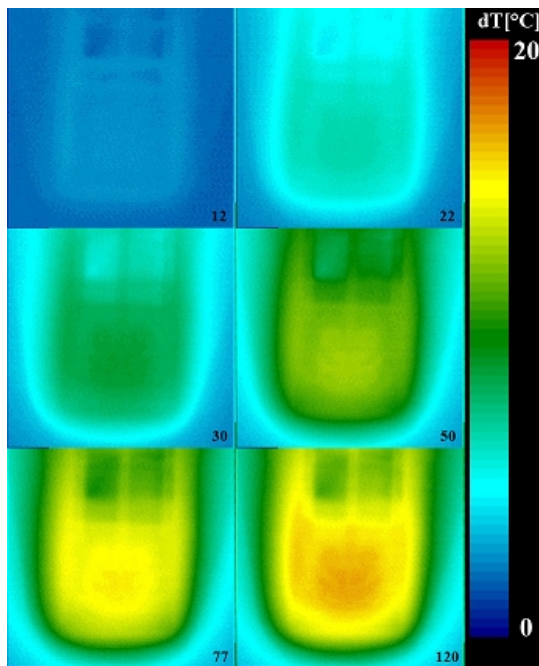


Figure 2: Temperature maps of a force sensor after powering with 5V. The figures at the bottom-right corners mark the elapsed time from start in seconds.

According to thermographic measurements, the self heating itself is responsible for the rise in temperature by ca. 15°C. Fig. 3. shows the time dependence of the sensor temperature. On the vertical axis offset signal is plotted as well. Both temperature and offset reflect an exponential growth with time.

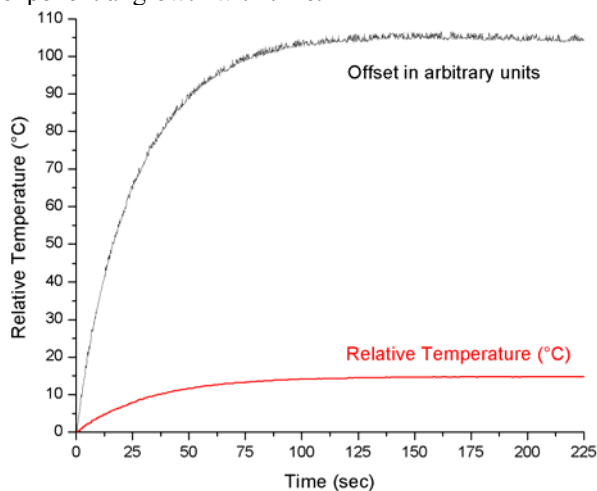


Figure 3: Changing of temperature of the sensor during warming-up. The offset signal was calculated from the node voltages and plotted in arbitrary units.

The effect of power supply on the warm-up shift was examined, too. As expected, the higher the input power, the bigger the offset shift in Fig. 4. While the rate of change is approximately uniform, the sign of the offset voltage shift is clearly reversed by the cover.

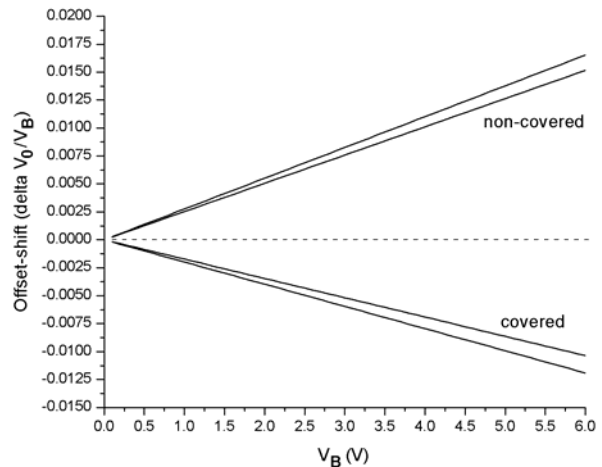


Figure 4: Offset-shifts of bare and covered sensor vs. power supply.

### B Temperature Coefficient of Offset (TCO)

There is also a primary influence of the ambient temperature on the offset signal of the sensors. This was investigated by using external heating. Change of offset voltage in a typical bare (a) and elastic rubber covered (b) sensor element is shown in Fig. 5.

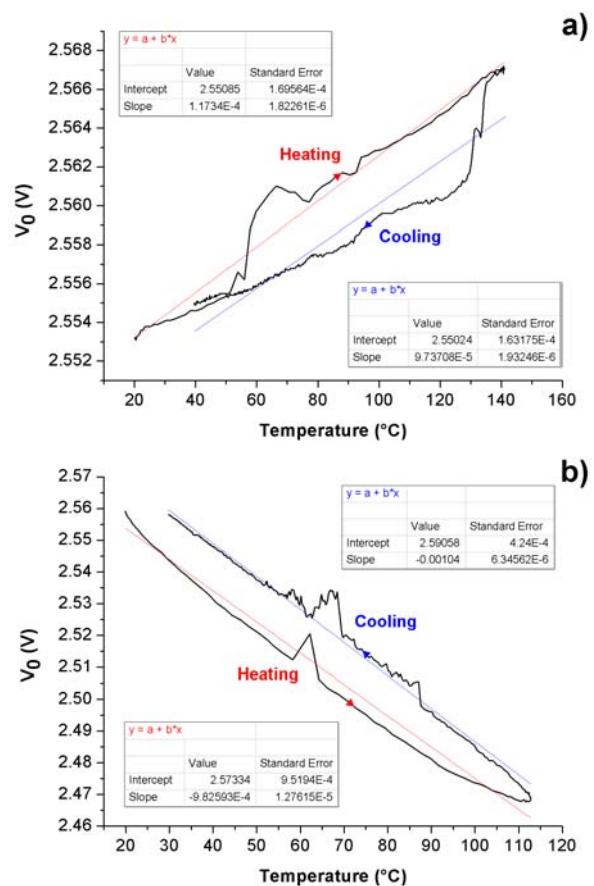


Figure 5: Measured and fitted offset-shift of bare (a) and covered (b) sensor vs. ambient temperature.

The difference between heating-up and cooling-down offset values, the apparent hysteresis of 2mV is just the effect of measurement uncertainty in case of

bare devices (Fig.5.a). In case of the covered sensors the discrepancy of ca. 10mV is to be ascribed mostly to non-saturated thermal capacitances rather (Fig.5.b).

### C. Sensitivity

The sensitivity change of the device was analyzed by applying load at different ambient temperatures. The output signals of a packaged, elastic rubber covered sensor were recorded. Readings on the unloaded device and at a static load of 200 gram normal to the membrane surface were taken while heating up at 25, 35, 41, 50, 58°C and during cooling down at 45, 37, 28°C, respectively (Fig. 6).

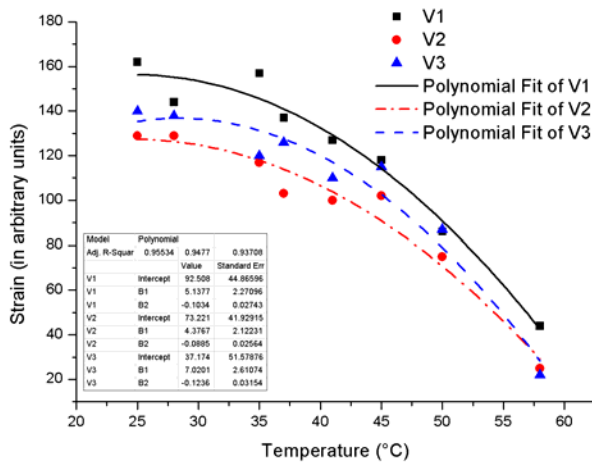


Figure 6: The output signals of the sensor at different temperature.

## III - Results and Discussion

We found fundamental differences between the thermal properties of bare and covered 3D bulk micromachined force sensors.

- Non-covered chips have a positive, while the elastic rubber covered ones a negative Offset Warm-up Shift. Up to 5V bias the rate of the change is about equal for both sensor types.
- TCO is  $0.9 \div 1.17 \times 10^{-4}/^{\circ}\text{C}$  in case of bare sensor and  $-0.98 \div -1.04 \times 10^{-3}/^{\circ}\text{C}$  with elastic cover. Not only the sign but also the value of the shift in the offset voltage indicates a remarkable difference depending on the material parameters of the cover. After cooling down the offset behaviour returns back to the initial state.

The reason for the above thermal phenomena in bare sensors is in the difference of temperature of the sensing and reference resistors. Reference resistors are placed in the heat-sinking bulk Si while the sensing resistors lie on the thermally more isolated membrane, under different thermal conditions. Even at unloaded condition of both, increasing temperature causes significant discrepancy in their resistance leading to offset voltage shift. By elevated temperature mechanical strain will be generated by the thermo-mechanical stresses, which is capable to alter the resistivity of the piezoresistors.

In case of covered chips offset shift may even be

produced by mechanical stress originating from the difference in thermal expansion coefficients of silicon and the elastomer used.

- The sensitivity decreases in a nonlinear manner, and above the temperature of 45°C a remarkable sensitivity drop occurred in the assembled, covered sensor structure.

## IV – New design

Temperature sensitivity is a major concern for piezoresistive sensors, the value of TCS is much higher than acceptable in precise application.

To eliminate the effects originating from differing thermal boundary conditions in the reference and sensor elements a new structure was proposed.

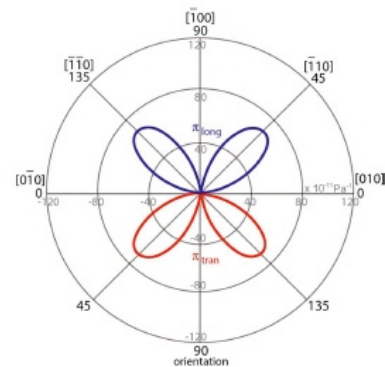


Figure 7: Strong orientation dependence of piezoresistivity in silicon [3].

When the reference resistors are aligned to [100] or equivalent directions, they remain insensitive to mechanical stress. Therefore, they can be formed in thin bridges, where they operate at identical thermal conditions with the sensor elements on the same perforated membrane.

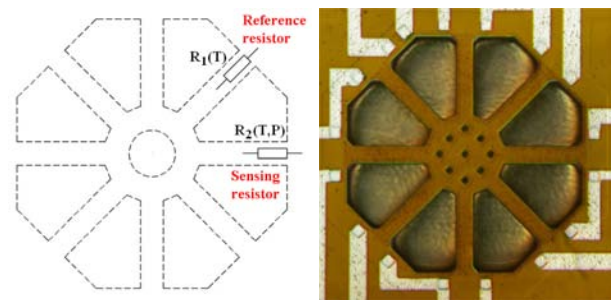


Fig. 8: Schematic top view and optical microscope image of the proposed and manufactured new 3D force sensor design.

### Method of thermal compensation

A resistor pair consists of a thermally sensitive reference resistor  $R_1(T)$  and a sensor element depending from both temperature and pressure  $R_2(T,P)$ . Driven by two independent but equal current sources the voltage drops



$V_1(T)$  and  $V_2(T,P)$  are obtained, respectively. These two voltages can be described as:

$$V_1(T) = I(T) R_1(T) \quad (1)$$

and

$$V_2(T,P) = I(T) R_2(T,P) \quad (2)$$

where  $I(T)$  denotes the temperature dependent current of the sources. As the current generators are realized by depletion mode MOS transistors with zero gate-source bias voltages applied, from the characteristics of the MOS transistors the forced current can be described as:

$$I(T) = \mu_i(T) C_{ox} \frac{W_i}{L_i} V_T^2 \quad (3)$$

where  $\mu_i(T)$  is the temperature dependent mobility of charge carriers,  $C_{ox}$  is the specific capacitance of the gate-oxide normalized to the area,  $W_i/L_i$  is the width-length ratio of the transistors' channel, and  $V_T$  the threshold voltage. For the mobility of charge carriers, the empiric relation [4]

$$\mu_i(T) = \mu_i(T_0) \left( \frac{T_0}{T} \right)^{\frac{3}{2}} \quad (4)$$

applies where  $T_0$  denotes the arbitrary assigned reference temperature – 300 K for the most simple case –, and  $\mu_i(T_0)$  is the mobility measured at this temperature. According to (1) and (2) the ratio of the voltages is

$$\frac{V_1(T)}{V_2(T,P)} = \frac{R_1(T)}{R_2(T,P)} = \frac{G_2(T,P)}{G_1(T)} \quad (5)$$

where  $G_1(T)$  and  $G_2(T,P)$  denote conductance of resistors, respectively. Knowing the specific conductance, and the geometry these can be calculated. Former is the product of the hole charge  $q$ , the mobility  $\mu_i(T)$  and  $\mu_2(T,P)$  in the resistors and the concentration of charge carriers  $h$ . The latter can approximately be taken as a constant, which is independent of temperature and pressure, considering that most acceptors are ionized. Geometric data means the depth of the  $p^+$  diffusion  $x_j$  – which also can be considered constant being independent of temperature and pressure – and the ratio of the resistors  $W_R/L_R$  – just like in case of transistors. These geometric data of the reference and sensor elements are equivalent with each other.

Applying (4) on the charge carrier mobilities, the conductances can be described as:

$$G_1(T) = G_1(T_0) \left( \frac{T_0}{T} \right)^{\frac{3}{2}} \quad (6)$$

where

$$G_1(T_0) = q \mu_1(T_0) h x_j \frac{W_R}{L_R} \quad (7)$$

and

$$G_2(T,P) = G_2(T_0,P) \left( \frac{T_0}{T} \right)^{\frac{3}{2}} \quad (8)$$

where

$$G_2(T_0,P) = q \mu_2(T_0,P) h x_j \frac{W_R}{L_R} \quad (9)$$

By substituting (6)...(9) into (5) we obtain

$$\frac{V_1(T)}{V_2(T,P)} = \frac{G_2(T,P)}{G_1(T)} = \frac{G_2(T_0,P)}{G_1(T_0)} = \frac{R_1(T_0)}{R_2(T_0,P)} \quad (10)$$

After rearrangement of (10) for the calculation of the thermally independent resistance component  $R_2(T_0,P)$  of the sensor element the reference resistance  $R_1(T_0)$  will be the ratio of the voltage and current ( $V_1(T_0)/I(T_0)$ ),

$$R_2(T_0,P) = \frac{V_2(T,P)}{V_1(T)} \frac{V_1(T_0)}{I(T_0)} \quad (11)$$

Thus for the calculation of the thermally independent pressure sensitive component of the sensor element the continuous measurement of the voltage  $V_1(T)$ ,  $V_2(T,P)$  and the storage of  $V_1(T_0)$  and  $I(T_0)$  – both measured at  $T_0$  – is required.

## Conclusion

Upon thorough analysis of the basic thermal phenomena in practical - assembled and packaged – devices it clearly emerged that thermal compensation in the 3D bulk micromachined force sensors for demanding, sensitive applications is a must. A novel approach is proposed based on utilisation of anisotropy of piezo-sensitivity in silicon. The suggested method is appropriate for realisation by the perforated thin Si membrane technology. The basics and design considerations of the manufactured sensor were introduced in detail.

## Acknowledgement

The support of the Hungarian Research Fund OTKA grant No. NK73424. and the ENIAC JTI project SE2A is acknowledged.

## References

- [1] G. Vászrhelyi, M. Ádám, É. Vázsonyi, I. Bársony, Cs. Dücső: *Effects of the elastic cover on tactile sensor array* Sensors and Actuators A 132 (2006) 245
- [2] G. Vászrhelyi, M. Ádám, É. Vázsonyi, Zs. Vízváry, A. Kis, I. Bársony, Cs. Dücső: *Characterization of an Integrable Single-Crystalline 3-D Tactile Sensor*, IEEE Sensors Journal, Vol. 6, No. 4, Aug. 2006, pp. 928
- [3] S. M. Sze, *Semiconductor Sensors*, Wiley, New York, 1994, pp. 169
- [4] P. Antognetti, G. Massobrio: *Semiconductor Device Modeling with SPICE*, McGraw-Hill, 1988, pp. 199

# INCORPORATION OF IN-PLANE ELECTRICAL INTERCONNECTS TO THE REFLOW BONDING

B. Moğulkoç<sup>1</sup>, H. V. Jansen<sup>1</sup>, H. J. M. ter Brake<sup>1</sup> and M. C. Elwenspoek<sup>1,2</sup>

<sup>1</sup> *Institute of Mechanics Processes and Control – Twente (IMPACT) and MESA+ Institute for Nanotechnology, University of Twente, PO Box 217, 7500AE Enschede, The Netherlands*

<sup>2</sup> *Freiburg Institute for Advanced Studies (FRIAS), University of Freiburg, D-79194 Freiburg, Germany*

**Abstract** — This paper elaborates on the incorporation of in-plane electrical interconnects to the reflow bonding. After joining the tubes to silicon substrates, the electrically conductive lines will allow probing into the volume confined by the tube. Therefore methods of fabrication of electrical interconnects, which would survive the bonding and not alter the quality of the bond interface, are investigated.

**Keywords :** Reflow bonding, electrical interconnects, fluidic interconnects

## I - Introduction

The reflow bonding is the joining technology of glass tubes to silicon substrates [1, 2] to be used as fluidic interconnects to microfluidic devices. The connections can be operated at high pressures and are inherently hermetic. However, integrated microfluidic devices incorporate a lot of functionality with electrical interconnects for sensing and actuation. Typical mechanical applications are microvalves, pumps and flow sensors [3]. Integrated devices for chemical and biological analysis, optical sensing elements, cooling of electronics [4] and manipulation of fluids through electrowetting or electrophoresis [5] are other applications that might require electrical interconnects. Therefore, in this chapter, the incorporation of in-plane electrical interconnects to reflow bonding is investigated.

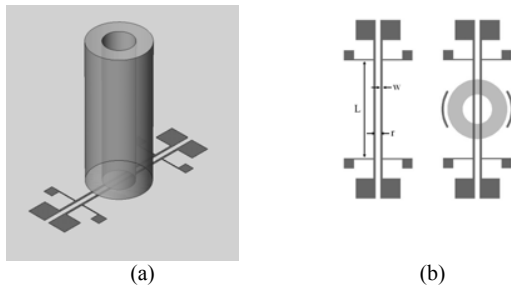


Figure 1: (a) Schematic representation of incorporation of in-plane electrical interconnects. (b) Top view of one of the structures in the mask design.

The electrical lines start outside the tube and run through the bond interface allowing access to the volume encapsulated by the tube as depicted in Figure 1(a). The connections should be able to survive the bonding process and preserve the bond quality. The fabricated interconnects should stay conductive and should not produce any direct leak paths or cause reduction in the package strength.

## II - Fabrication

Two types of in-plane electrical interconnects are fabricated for integration to reflow bonding. The first design is to fabricate boron doped lines in an n-type substrate and the second one is to deposit metal lines. The mask consists of two sets of nine different structures with varying parameters. The structural parameters are labeled in Figure 1(b). The length of the metallic lines,  $L$ , is 10 mm and always kept the same. The line widths,  $w$ , of 100, 200 and 500  $\mu\text{m}$  are tested with separations,  $r$ , of 200, 500 and 1000  $\mu\text{m}$ . The glass tubes are bonded to one set of the lines, while the second set acted as a reference point for comparison.

### A. Doped Lines

The selected substrate wafers are lightly n-type doped,  $\langle 100 \rangle$  oriented, Single Side Polished (SSP) wafers of 380 micron thick. The first step is to grow 2  $\mu\text{m}$  thick silicon oxide by wet thermal oxidation in a tube oven. Secondly, this oxide layer is patterned in buffered hydrofluoric acid (BHF) using a hard baked photoresist mask. After removing the photoresist in 100% nitric acid ( $\text{HNO}_3$ ), the doping can be performed in a tube oven.

Boron nitride wafers are used as solid sources [6]. This process is constant-source diffusion and we name it as solid source dotation (SSD) in this text. After the doping, wells of  $p^+$ -type are created in junction with the n-type substrate. We have performed SSD at 1000  $^\circ\text{C}$ , 1050  $^\circ\text{C}$  and 1100  $^\circ\text{C}$  for 60 minutes. After the dotation, the boron containing residue on the doped regions is cleaned by initially dipping the wafers in 50% HF for 2 minutes. The doped regions were still hydrophilic. Therefore the wafers are briefly oxidized at 800  $^\circ\text{C}$  for 30 minutes and etched for another 2 minutes in 50% HF. After this procedure, whole silicon surface was clean and hydrophobic. The step height between the protected and the doped regions are measured by Dektak profiler to be approximately 30 nm, 50 nm and 100 nm for the wafers treated respectively at 1000  $^\circ\text{C}$ , 1050  $^\circ\text{C}$  and 1100  $^\circ\text{C}$  for 60 minutes.

### B. Metallic Lines

The selected substrate wafers are  $\langle 100 \rangle$  oriented, Single Side Polished (SSP) wafers of 525 micron thick. The first step is to grow 310 nm thick silicon oxide by dry thermal oxidation in a tube oven. The oxide layer will act as a diffusion barrier between the metals and the silicon substrate to prevent formation of silicide [7]. After standard lithography, the metal lines are sputtered

in Argon plasma. In all of the samples, 10 nm thick Titanium is deposited on SiO<sub>2</sub>/Si stack as the adhesion layer or the bond layer as it is known to react directly with silicon oxide [7]. The second metallic layer is the functional layer and is chosen to be either platinum or rhodium due to their high melting temperature and resistance to oxidation. The thickness of the platinum layer was about 310 nm and the thickness of the rhodium layer was about 270 nm. The photoresist mask is lift-off to release the metallic interconnects. For removal of the photoresist, the wafers are put in acetone and isopropanol at 50 °C in ultrasonic bath for 0.5 hours each and let dry in laminar flow bench.

### III - Results and Discussion

After the fabrication of both designs, their electrical resistances are measured and the tube bonding is performed by annealing the samples at 700 °C for 30 hours in air environment [1] to test their performance and integrability to the reflow bonding. The electrical resistances of these lines are measured both before and after the tube bonding. The hermeticity of every bonded tube is tested by a helium leak detector. The last step of characterization is to measure the burst pressures of the bonded tubes to check if the in-plane electrical interconnects caused any reduction in the strength of the package and change in the fracture behavior of the silicon membranes.

#### A. Electrical Resistivity

The electrical resistances of the fabricated structures are measured with four-point probe method by obtaining current-voltage curves and by multimeter measurements. The electrode configuration is exemplified in Figure 1(b), where the connections on the side are used to couple current and the connections on the ends are used to measure the voltage drop. The electrical resistances of the doped lines are measured in dark to minimize photo-currents and the junction depths of the diffused layers are measured by the groove-and-stain method [6]. The resistance of doped lines with respect to the line width is plotted in Figure 2 with the sheet resistances and junction depths. The deviation of the measurements was less than 5%. The accuracy was limited by the uniformity of the process.

The surface dopant concentration remains the same during the high temperature diffusion and is determined by the solid-solubility limit of boron in silicon [6]. For temperatures higher than or equal to 1000 °C, the diffusion coefficient of boron becomes dependent on its local concentration [8, 9, 10]. Therefore, the dopant concentration profile deviates from complementary error function curves and extra measure has to be taken to calculate the junction depth. This effect has been studied and formulated by Fair [11]. If the values of the solid-solubility limit of boron in silicon [8], the intrinsic diffusion coefficient of boron in silicon [11] and the intrinsic-carrier concentration of silicon [12] are substituted in the corrected junction depth [11] formula for diffusion temperatures of 1000 °C, 1050 °C and 1100

°C and time of 60 minutes, the corresponding junction depths can be calculated as 0.84, 1.55 and 2.72 microns. These values are quite close to our experimental measurements displayed in Figure 2, especially considering that the diffusion coefficient of boron will be changing more than a decade during the diffusion process at the mentioned temperatures [13].

After the analysis of the SSD process, the electrical resistances of the doped lines are measured after the reflow bonding is performed at 700°C for 30 hours. The bonding is performed in air environment and therefore the silicon wafers are oxidized about 20 – 30 nm [14]. That oxide layer was thick enough to insulate the test probes from the diffused layer. Therefore, the wafers are dipped in dilute HF solution after the tube bonding in order to remove the surface oxide layer before the resistance measurements. The measurement results after the tube bonding showed that the resistance values increased 3% on the average. This increase is within the uniformity limits of the doping process.

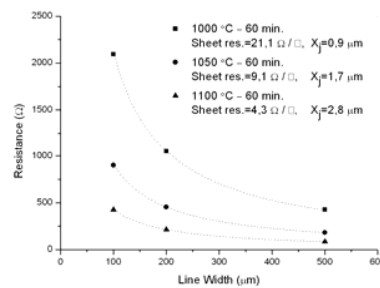


Figure 2: Electrical resistances of 10 mm long boron doped lines at different temperatures with respect to the line widths.

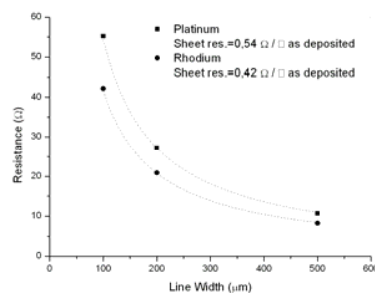


Figure 3: Electrical resistances of 10 mm long metallic lines with respect to the line widths.

For the fabrication of metallic line stacks, titanium is used as the adhesion layer to form continuous and smooth coverage [7]. The resistance of metal lines with respect to the line width is plotted in Figure 3 with the sheet resistances. The deviation of the measurements was less than 2%. The accuracy was limited by the uniformity of the process. The sheet resistance of the rhodium stack is slightly less than the platinum stack, while both of them were about one tenth of the lowest sheet resistance of the boron doped lines. After the initial resistivity measurements of the metallic lines,

their electrical resistance are measured after the reflow bonding is performed at 700°C for 30 hours. Since the bonding is performed in air environment, oxygen was present in the environment during high temperature annealing.

The platinum lines stayed conductive and their resistance has decreased 13% on the average presumably due to healing of the defects and the grain growth [15]. An Atomic Force Micrograph (AFM) of the surface of platinum layer after the bonding is displayed in Figure 4(a). The grain growth and hillock formation in the platinum layer are clearly visible in the topography. The Scanning Electron Micrograph (SEM) of the cross-sectional view of the stack in Figure 4(b) indicates the porosity of the large grains. Olowolafe et al. [16] and Kreider et al. [17] observed that platinum layer remained unreacted during the Post-Deposition Annealing (PDA) of Pt/Ti/SiO<sub>2</sub>/Si stack at high temperature. In conformity with them, our energy dispersive x-ray analysis confirmed that the platinum layer was not oxidized. Relevantly, the base thickness of the platinum layer is observed to remain constant after the reflow bonding.

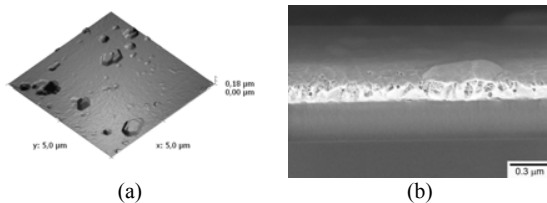


Figure 4: The platinum layer is annealed at 700 °C for 30 hours in air environment for the tube bonding. (a) The surface is examined in an atomic force microscope and (b) the cross-section is examined in a scanning electron microscope.

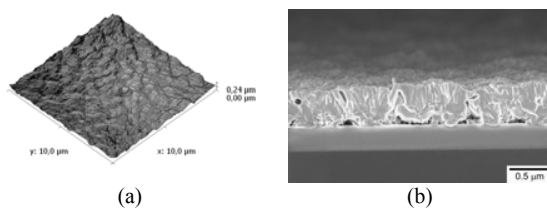


Figure 5: The rhodium layer is annealed at 700 °C for 30 hours in air environment for the tube bonding. (a) The surface is examined in an atomic force microscope and (b) the cross-section is examined in a scanning electron microscope.

The rhodium lines lost their conductivity. In presence of oxygen, rhodium starts to oxidize above 600 °C [18]. At and above 700 °C, the oxide layers are explicitly growing on the surface in the form of Rh<sub>2</sub>O<sub>3</sub> which is a stable product until around 1000 °C [18]. Although, the lines on which the tubes were bonded showed lower resistivity, their sheet resistances were higher than 1000 Ω/□. An AFM of the surface of rhodium layer after the bonding is displayed in Figure 5(a) with a SEM of the cross-sectional view of the stack in Figure 5(b). Our energy dispersive x-ray analysis confirmed that the rhodium layer was oxidized. The base layer thickness of

the rhodium layer was measured to be 580 nm, which is higher than twice its initial thickness. The reason is ascribed to the volume gain during oxidation.

### B. Hermeticity

The hermeticity of every bonded tube is tested by a Leybold UL 500 helium leak detector. The tubes are connected to the detector through a flange and pumped down to the background pressure of 0.5 Pa. The bond between the glass tube and the silicon is sprayed with Helium gas. If there is an apparent leak, helium molecules can migrate through direct paths and the detector will read a signal if the leak is above 10<sup>-9</sup> Pa m<sup>3</sup> sec<sup>-1</sup>. The maximum signal is obtained by continuously spraying helium to the leaky region and the rates are recorded. As the result of leak tests, all of the tubes bonded to the boron doped lines did not cause any instant leak and were found to be hermetic. However, all of the tubes bonded to the metallic electrical interconnects were found to be leaking. The maximum level of flux was measured to be about 10<sup>-6</sup> Pa m<sup>3</sup> sec<sup>-1</sup> for Pt/Ti/SiO<sub>2</sub>/Si stack and 3 10<sup>-6</sup> Pa m<sup>3</sup> sec<sup>-1</sup> for Rh/Ti/SiO<sub>2</sub>/Si stack. No correlation between the structural parameters of the metal lines and the leak values could be found.

### C. Bond Strength

The electrical interconnects running through the bond interface might reduce the maximum pressure to which the assembly can be subjected and cause change in the fracture behavior of the silicon membranes. Therefore, the burst pressure of every bonded tube is tested to measure the effect of in-plane electrical interconnects on the strength of the package, as has been done for non-processed wafers [1].

The burst pressures of the silicon-glass assembly containing the boron doped electrical interconnects are measured and the results are shown in Table 1. All of the pressurized samples were found to fracture in the silicon plate. The values are similar to those obtained by testing non-processed 380 micron thick silicon wafers [1]. The step between the protected and the doped regions were completely filled by the softened glass and the fracture mechanism of the silicon substrates with boron doped lines was the same as non-processed substrates. Therefore, the doped lines can be said to cause no reduction in the strength of the bonds and no change in the failure mechanism of the assembly.

The burst pressure of the silicon-glass assembly containing the metal electrical interconnects are measured and the results are shown in Table 2. All of the pressurized samples were found to fracture in the silicon plate. The burst pressures of the samples containing platinum lines were similar to those obtained by testing non-processed 525 micron thick silicon wafers [1]. However, it is good to notice that the burst pressures of the samples containing rhodium lines are more scattered and lower than non-processed wafers.

During the PDA of Pt/Ti/SiO<sub>2</sub>/Si stack, the titanium layer at the interface can oxidize [16]. The loss of



titanium bond layer will lead to coalescence problem in platinum layer and the loss of adhesion can be observed in addition to surface roughening in the platinum layer [17]. In conformity with the literature, we have seen that the platinum layer was peeled off the underlying substrate. A SEM of partly stripped platinum layer is shown in Figure 6(a) from an oblique view. This is the edge of the sample presented in Figure 4. Another example is displayed in Figure 6(b), which is the surface of a ruptured silicon piece containing platinum lines. The crack initiated in the glass tube near its inner rim before propagating into the silicon and the lines at the interface are stripped off the silicon piece during the fracture of pressurized assembly. The stiction problem of platinum layer after the annealing is a possible explanation for apparent leaks discussed in the previous section.

During the PDA of Rh/Ti/SiO<sub>2</sub>/Si stack, the rhodium layer is oxidized [18] and thickened from 270 nm to 580 nm. Similar to the platinum lines, the rhodium lines lost their adhesion to underlying silicon substrates. In addition, the rhodium lines at the glass tube–substrate wafer interface were cracked. The oxidation and the cracking behavior of these lines are thought to have altered the electrical resistance measurements.

Table 1: Burst pressures of <100> single side polished silicon wafers of 380  $\mu\text{m}$  thick, containing boron doped lines at different temperatures, after the tube bonding.

	1000°C ; 60 min.	1050°C ; 60 min.	1100°C ; 60 min.
Burst press. (MPa)	5.71 $\pm$ 0.16	5.71 $\pm$ 0.18	5.66 $\pm$ 0.1

Table 2: Burst pressures of <100> single side polished silicon wafers of 525  $\mu\text{m}$  thick, containing different types of metallic lines, after the tube bonding.

	Platinum	Rhodium
Burst press. (MPa)	7.53 $\pm$ 0.53	6.79 $\pm$ 0.74

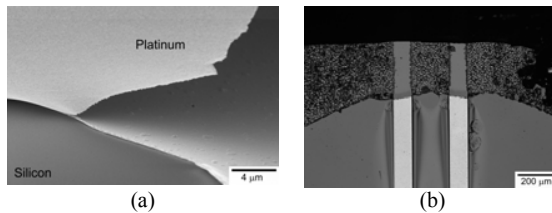


Figure 6: (a) Oblique view of the platinum layer, which is peeled off the silicon substrate after annealing at 700 °C for 30 hours in air environment. (b) Top view of the edge of a fractured silicon plate containing platinum lines after the tube bonding and burst pressure test.

#### IV - Conclusion

The incorporation of electrical interconnects to reflow bonding is required for probing to the volume encapsulated by the tube and is therefore investigated. Two types of electrical lines were tested for integrability to tube bonding. The first design was to fabricate boron doped lines in an n-type substrate. The sheet resistances between 5–20  $\Omega/\square$  were obtained after doping. The conductivity of the lines did not change after the reflow bonding. The doped lines did not cause any leakage or reduction in the strength of the tube–silicon assembly.

The second design was to deposit metal lines. Platinum or rhodium metallic lines were deposited on oxidized silicon using titanium adhesion layer to form Pt/Ti/SiO<sub>2</sub>/Si or Rh/Ti/SiO<sub>2</sub>/Si stack. The sheet resistances of both types of metal were about 0.5  $\Omega/\square$  after deposition. After the reflow bonding, the resistivity of platinum lines slightly reduced while the rhodium lines lost their conductivity. Both types of metallic interconnect caused direct leak paths through the bond interface. Although the presence of these metallic lines did not considerably affect the strength of the glass tube–silicon joint, both types of metals lost adhesion to the underlying silicon substrate after the post-deposition annealing of the reflow bonding.

In light of the presented test results, we conclude that the doping process is easily integrable to the reflow bonding, as they survive the bonding process and preserve the bond quality. However, the platinum and rhodium lines suffered from loss of adhesion after the reflow bonding. Although the platinum lines stayed conducting, the rhodium lines were oxidized during the annealing in air environment.

#### References

- [1] B Moğulkoç, H V Jansen, J W Berenschot, H J M ter Brake, K M Knowles, and M C Elwenspoek, J. Micromech. Microeng. 19, 085027 (2009).
- [2] S Unnikrishnan, H V Jansen, J W Berenschot, B Moğulkoç, and M C Elwenspoek, Lab Chip 9, 1966 (2009).
- [3] P Gravesen, J Branebjerg, and O S Jensen, J. Micromech. Microeng. 3, 168 (1993).
- [4] D Erickson, and D Li, Anal. Chim. Acta 507, 11 (2004).
- [5] T M Squires, and S R Quake, Rev. Mod. Phys. 77, 977 (2005).
- [6] R C Jaeger, Introduction to microelectronic fabrication (Addison–Wesley, Reading, 1993), pp 49–83.
- [7] M Liehr, F K LeGoues, G W Rubloff, and P S Ho, J. Vac. Sci. Technol. A 3, 983 (1985).
- [8] A Armigliato, D Nobili, P Ostojia, M Servidori, and S Solmi, Semiconductor Silicon 1977, pp 638–47.
- [9] G L Vick, and K M Whittle, J. Electrochem. Soc. 116, 1142 (1969).
- [10] R B Fair, Semiconductor Silicon 1977, pp 968–87.
- [11] R B Fair, J. Electrochem. Soc. 122, 800 (1975).
- [12] F J Morin, and J P Maita, Phys. Rev. 96, 28 (1954).
- [13] S Matsumoto, Y Ishikawa, Y Shirai, S Sekine, and T Niimi, Jpn. J. Appl. Phys. 19, 217 (1980).
- [14] B E Deal, and A S Grove, J. Appl. Phys. 36, 3770 (1965).
- [15] D–S Lee, D–Y Park, H–J Woo, S–H Kim, J Ha, and E Yoon, Jpn. J. Appl. Phys. 40, L1 (2001).
- [16] J O Olowolafe, R E Jones Jr, A C Campbell, R I Hegde, C J Mogab, and R B Gregory, J. Appl. Phys. 73, 1764 (1993).
- [17] K G Kreider, and G Gillen, Thin Solid Films 376, 32 (2000).
- [18] L A Carol, and G S Mann, Oxid. Met. 34, 1 (1990).

# PIEZOELECTRIC POWER HARVESTING DEVICE WITH MULTIPLE RESONANT FREQUENCIES

Zhengjun Chew and Lijie Li<sup>1</sup>

<sup>1</sup>Swansea University, School of Engineering; Swansea, SA2 8PP, UK

**Abstract** — This paper reports design and characterization of a new piezoelectric scavenging device that has multiple resonant frequencies in the low frequency range. The structure is constructed with the most accessible off-the-shelf piezoelectric cantilevers. The device has been characterised using both self-excitation and a customised shaker table. Power conditioning circuits for the scavenging device have been designed and analysed. The experimental results show that the 9-beam structure has at least 7 resonant peaks from frequency range of 100 Hz to 1000 Hz. A maximum DC voltage of 3.58 V has been measured subject to 130 Hz external vibration.

**Keywords** : Piezoelectric energy scavenging device, Multiple resonant frequency structures

## I - Introduction

Vibration based MEMS power scavenging devices are increasingly important, as they have the advantages such as long lasting time and no harm to the environment. Due to the very low energy density, they have the potential to be used in wireless sensors [1]. Previously tremendous works surrounding this type of energy harvesting methodology based on transduction principles including piezoelectric [2], electromagnetic [3], and electrostatic [4] have been conducted. The key issue for micro vibration power scavenging devices is that the resonant frequency of the devices mismatches ambient vibration frequency band. The frequencies of ambient vibration vary between several hertz to several hundred hertz, however the resonant frequency of most of micro structures are around several thousand hertz, moreover most of micro structures have very narrow resonant bandwidth. Therefore effort has been devoted to develop wide band micro structures for achieving high efficiency energy scavenging devices. A wide bandwidth piezoelectric energy scavenging device was demonstrated with bandwidth ranging from 160 Hz to 400 Hz [5]. An electromagnetic wideband vibration energy scavenging device was achieved with bandwidth ranging from 4 kHz to 5 kHz [6]. A micro electromagnetic energy scavenging prototype that can generate 18 mV at its resonant frequency of 55 Hz has been demonstrated [7]. Wide bandwidth piezoelectric energy scavenging devices were achieved by combining an array of piezoelectric cantilevers [8]; the bandwidth of the device was reported from around 600 Hz to 615 Hz. Kulah and Najafi [9] reported a new structure for converting low frequency vibration to high frequency vibration of the micro structures to increase the energy transfer efficiency. A piezoelectric multifrequency

energy converter that has been constructed by an array of piezoelectric cantilevers (four cantilevers in that case) for power scavenging was reported in reference [10].

In this paper, we report design and characterisation of a multiple resonant frequency micro structure for energy scavenging applications. Section 2 of this paper shows the design of the structure, section 3 presents the detailed characterisation of the device, and conclusion is described in section 4.

## II - Design

The structure consists of a series of piezoelectric beams connected each other shown schematically in Figure 1. It is seen that a piezoelectric bimorph beam taken from commercial product (BM15015-06HC) is fixed at its one end onto a PCB board and another end is suspended on which another identical piezoelectric bimorph element is fixed at its one end using epoxy glue. (It is noted that the bimorph vibration element 6L15mm x W1.4mm x D0.6mmö can be used for strain to electrical and electrical to strain converter) The third identical bimorph beam is fixed at its one end onto the free end of the second beam (Figure 1a). The fourth beam is fixed on the third beam, so are the beams 5-9 (Figure 1b). The whole structure looks like a mechanical spring structure. Two sets of this type of structure have been constructed, one has three piezoelectric beams (Figure 1a), and the other has 9 piezoelectric beams (Figure 1b).

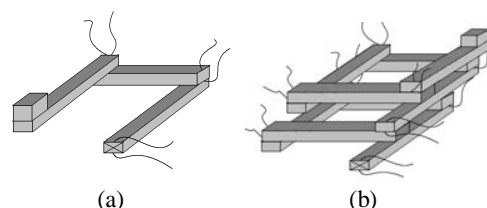


Figure 1: Schematic diagram of the multiple resonant frequency structure for energy scavenging

## III – Characterization of the devices

### A. Characterization of the devices using self-excitation

First of all, characterisation of a single piezoelectric beam has been conducted to demonstrate its dynamic behaviour. In the experiment, a piezoelectric beam is fixed on a breadboard using glue at one end while a mass is attached on the other edge. A function generator is used to produce waveform which acts as the input to

the piezoelectric cantilever. The voltage is set to be constant throughout the experiment while the frequency of the waveform will be varying. The piezoelectric cantilever is placed on the stage of an electronic microscope. There is a camera embedded in the microscope which is connected to computer allowing observer to view the specimen through computer screen. Displacement of the piezoelectric cantilever can be acquired from an interferometer. The interferometer keeps tracking the reflected laser signal that had been directed to the cantilever. The piezoelectric beam is then connected to the function generator without concern about its polarity as it would not disrupt the outcome of results. A 5 V peak-to-peak sinewave produced using the function generator is fed into the piezoelectric cantilever. Frequency of the 5V<sub>pp</sub> sinewave will be varying starting from 10 Hz to 1200 Hz with an incremental of 10 Hz. Finally, observation is made by looking at the measurements taken from oscilloscope. Output voltage corresponding to the input frequency is recorded. Actual peak to peak displacement of the transducer is obtained by multiplying the corresponding voltage to a constant indicated on the vibrometer controller. Recorded data in voltage is converted to desired form which is displacement by multiplying the constant 2 m/V. A plot of displacement vs. frequency is shown below as Figure 2. The graph shows that the device has a fundamental frequency of 1030 Hz.

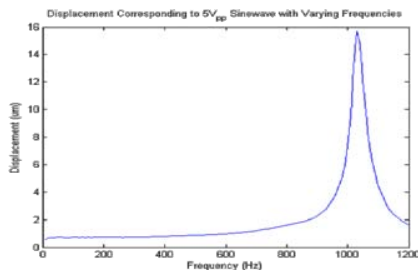


Figure 2: Displacement vs. frequency in 5 V<sub>pp</sub> sinewave ranging from 10Hz to 1200 Hz

After knowing the dynamic behaviour of a single piezoelectric beam, experiment is conducted on the three-beam piezoelectric structure. First of all, the experiment is conducted by applying electrical signal to the beam 1, hence this beam is acting as a vibration source. The outputs of the rest of beams are monitored through the oscilloscope. Set 1 as shown in Figure 3a is a piezoelectric energy scavenging device which consists of three beams. Meanwhile, set 2 incorporated nine beams where one beam acts as input while the remaining are output as in Figure 3b. All the beams are attached one by one at the tip at right angle. A proof mass is attached on the edge of the last beam.

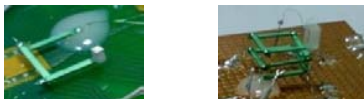


Figure 3: Piezoelectric energy scavenging device which comprises three beams (a), nine beams (b).

A TTI 40 MHz Arbitrary Waveform Generator TGA 1242 is used to produce waveform which acts as the input to the piezoelectric cantilever. Two different voltage amplitudes but with the same frequency are used. Finally, the output signals are observed using a Tektronix TDS 2024 Four Channel Digital Storage Oscilloscope. The beam which is glued on the circuit board where it is denoted as beam 1 is connected to the waveform generator. From the previous experiment, it is known that a piezoelectric material will produce movement subject to electrical energy. This beam 1 acts as a vibration source here in the absence of a shaker table. The remaining beams will be denoted as beam 2 for the centre one and beam 3 for the one with a mass attached on it for set 1. For set 2, the numbering is still the same but it would up to beam 9 that is attached with the mass. Both beams for set 1 are connected to the oscilloscope to observe the voltages generated due to the vibration of beam 1. The same procedure is carried out four times for set 2 as only two outputs can be measured at a time. To start with, a 5V peak-to-peak sinewave produced by the function generator is used as the input. Frequency of the 5V<sub>pp</sub> sinewave varies from 20 Hz to 1500 Hz with an incremental of 20 Hz. The experiment is repeated using a 10V peak-to-peak sinewave having the same frequency range. Observation on the output voltages and frequencies corresponding to the input frequency are recorded. For set 1, beam 2 and beam 3 are connected to channel 1 and channel 2 of the oscilloscope respectively where the generated signals from both piezoelectric cantilevers can be observed simultaneously. For set 2, beam 2 and beam 3, beam 4 and beam 5, beam 6 and beam 7 and lastly beam 8 and beam 9 are the pairs to be examined at a time.

Data acquired for set 1 is presented in graphs as in Figure 4 and Figure 5. It is seen from these graphs that the three-beam structure has resonant peaks at around 260 Hz and 600 Hz, which meets the expectations: 1), the three-beam structure has more resonant peaks; 2), these resonant peaks are lower than that of single beam structure.

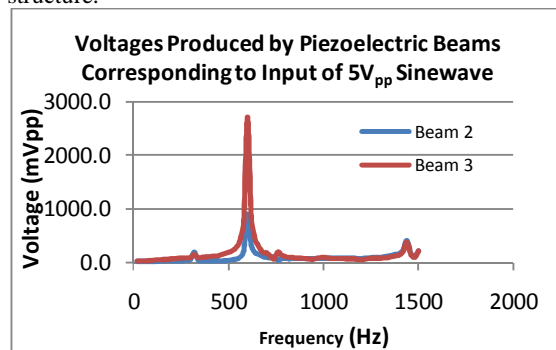


Figure 4: Voltages vs. frequency plot subjected to a 5 V<sub>pp</sub> sinewave input for set 1.

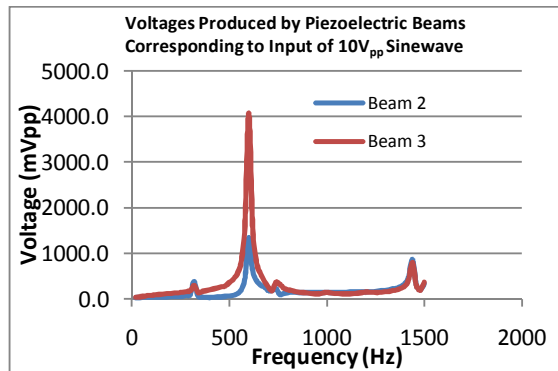


Figure 5: Voltages vs. frequency plot subjected to a 10 Vpp sinewave input for set 1.

Data acquired for set 2 is presented in graphs as in Figure 6 and Figure 7. Again, the results indicate that 9-beam structure has even more resonant peaks than three-beam structure, and it can reach resonant at frequencies around 100 Hz which is close to some of ambient vibrations.

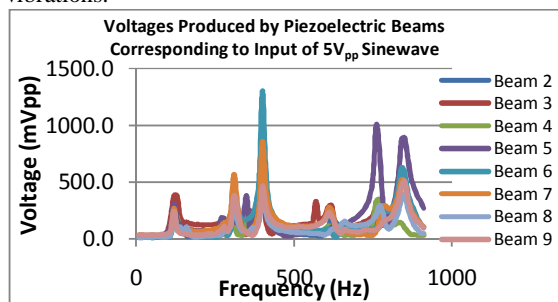


Figure 6: Voltages vs. frequency plot subjected to a 5 Vpp sinewave input for set 2.

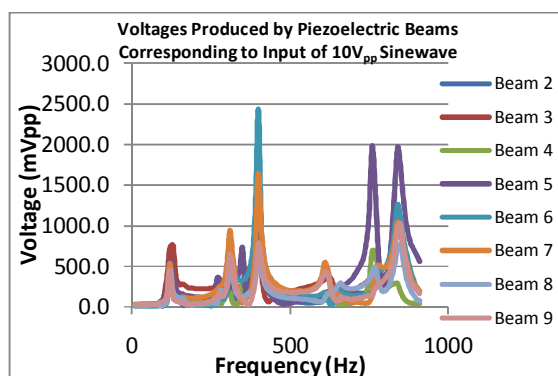


Figure 7: Voltages vs. frequency plot subjected to a 10 Vpp sinewave input for set 2.

### B. Characterization of devices using an external excitation

After utilising the transduction properties of piezoelectric to examine the generated voltage, a customised shaker table was built to examine the above

devices. Dynamic response of the energy scavenging devices can be examined through the accurate and consistent movement of the motor. The same multiple output piezoelectric energy converter is used to carry out this experiment.

The shaker table is comprised of an electric motor, which is constituted of a SMAC LAC-1 controller and motor and a TRUST - 16427 6 Adapter. The power supply is set to give 24Vdc, 3A output as this is the minimum power required by the motor to work. Starting from left in Figure 8 below, is the motor, the controller, power supply and an oscilloscope at far end.



Figure 8: Shaker motor system for generating vibrations to MEMS energy harvesters.

The measurement results are shown in the Figure 9. Compared to previous experiment using the beam 1 as the vibration source, the overall output voltage is much higher using a motor as direct physical force is exerted in the form of vibration. Result shows that frequency response of the piezoelectric energy scavenging device is still the same regardless of the vibration source. The same peak and trough manner is exhibited except that with higher magnitude. It is also shown in the result that some useful resonant peaks are appeared at around 90 Hz, 115 Hz and 130 Hz.

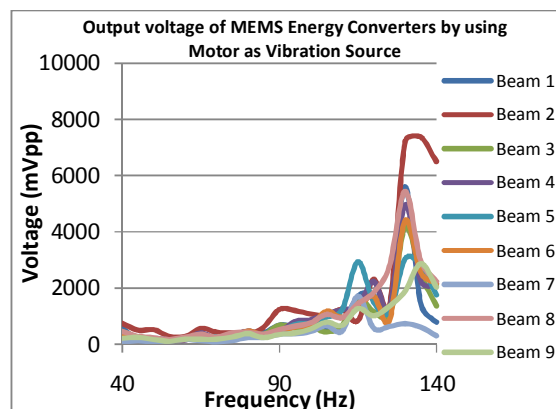


Figure 9: Voltage vs. Frequency plot for piezoelectric energy harvester using motor.

Most observations are same as experiment with the self-excitation. Apart from conclusions drawn from prior investigation, it is noticed that besides frequency, displacement of vibration does affect the outcome where they have a linear relationship. From section 3(A), the maximum displacement is only 14  $\mu$ m using



vibration from a piezoelectric cantilever while the displacement is set to be 0.1mm for the customised shaker table, which is about 7 times higher.

#### IV – Power Conditioning Circuits

After verification of possible configurations through simulation, it is decided that generated AC output from piezoelectric converter ought to be connected in parallel. This is mainly due to the unpredictable phase shift of each produced voltage. Experimental results show that parallel connection gives higher output than serial connection. These measurements match the simulated results where voltages with different phases in series counteract giving a lower resultant voltage. Paralleled open  $\delta$  circuited voltage is measured to be  $3.58V_p$  whereas serial connected rectifier gives only  $1.30V_p$ . Smoothed output becomes  $2.5V_{dc}$  and  $0.6V_{dc}$  respectively. Voltages across the  $1k\Omega$ ,  $10k\Omega$  and  $100k\Omega$  resistors are found to be  $80mV_{p-p}$ ,  $640mV_{p-p}$  and  $160mV_{p-p}$  respectively. Simulation of voltage changes with respect to resistance is then carried out to verify this statement.

Capacitor with high capacitance is desirable to store energy from the transducers. As long as capacitance of storage capacitor is 100 times higher than capacitance of piezoelectric beam [11], it would not have evident effect on output voltage. Increasing the capacitance will only increase charging time of capacitor. Although the capacitance of piezoelectric energy converter is not known here, based on past researchers literature, it is found that this parasitic capacitance usually range in pico Farad (pF). So, capacitance of micro Farad ( $\mu F$ ) is minimum value to be used. Experiment has verified this argument where  $1\mu F$ ,  $10\mu F$  and  $100\mu F$  capacitors perform just as well. Also, capacitors can smooth out ripple of rectified voltage in which higher capacitance gives better smoothing capability. Rectification is utmost essential power conditioning as this process converts AC voltages to DC voltages, which is a usable form by most electronics devices. Therefore it is important to devise a rectifier circuit which is highly efficient. Findings from simulations and experiments carried out include:

- Connecting sources with different phases in series impair the resultant voltage as these voltages counteract with each other.
- Connecting sources with different phases in parallel only introduce phase shift to resultant output.
- Potential drop across diodes cause significant loss to output if the magnitude AC source is low.
- Resistance of diodes have to be taken into consideration in designing rectifiers to ensure that minimum losses in rectifiers.
- Load of energy harvester shall be carefully selected for maximum power transfer.
- Charging time of capacitors increases with capacitance.

#### V – Conclusion

A design of a multiple resonant frequency structure for energy scavenging applications has been proposed in this paper. The structure has been fully characterised using both the self-excitation and the external excitation using a customised shaker table based on an electromagnetic motor. Investigation of different power conditioning circuitries has been conducted, it is concluded that the parallel connection for the multiple output structure is optimal and has been subsequently used in the experiment. It is found from the experiment that the 9-beam structure has at least 7 noticeable resonant peaks from 100 Hz to 1000 Hz. Subject to a 130 Hz vibration, the open-circuit output voltage from the parallel connection is measured to be  $3.58V_p$  while the open-circuit output from series connection gives only  $1.30V_p$ . Smoothed outputs from the parallel connection and the series connection become  $2.5V_{dc}$  and  $0.6V_{dc}$  respectively. From the parallel connection, the voltages across the  $1k\Omega$ ,  $10k\Omega$  and  $100k\Omega$  load resistors are found to be  $80mV_{p-p}$ ,  $640mV_{p-p}$  and  $160mV_{p-p}$  respectively.

#### References

1. P. D. Mitcheson, E. M. Yeatman, G. K. Rao, A. S. Holmes, T. C. Green, *Proceedings of The IEEE*, 96 (2008), pp. 1457-1486.
2. P. Glynn-Jones, S. P. Beeby, N.M. White, *IEEE Proceedings-Science Measurement and Technology*, 148(2001), pp. 68-72.
3. S. Kulkarni, E. Koukharenko, R. Torah, J. Tudor, S. Beeby, T. O'Donnell, S. Roy, *Sensors and Actuators A*, 145 (2008), pp. 336-342.
4. A. M. Paracha, P. Basset, D. Galayko, F. Marty, T. Bourouina, *IEEE Electron Device Letters*, 30 (2009), pp. 481-483.
5. B. Marinkovic and H. Koser, *Smart and a wide bandwidth vibration energy harvesting platform*, *Applied Physics Letters* 94, 103505 (2009).
6. I. Sari, T. Balkan, H. Kulah, *An electromagnetic micro power generator for wideband environmental vibrations*, *Sensors and Actuators A*, 145-146 (2008), p. 405-413.
7. P. Wang, K. Tanaka, S. Sugiyama, X. Dai, X. Zhao, J. Liu, *A micro electromagnetic low level vibration energy harvester based on MEMS technology*, *Microsystems Technology*, 15 (2009), pp. 941-951.
8. J. Liu, H. Fang, Z. Xu, X. Mao, X. Shen, D. Chen, H. Liao, B. Cai, *A MEMS-based piezoelectric power generator array for vibration energy harvesting*, *Microelectronics Journal*, 39 (2008), pp. 802-806.
9. H. Kulah and K. Najafi, *Energy scavenging from low-frequency vibrations using frequency up-conversion for wireless sensor applications*, *IEEE Sensor Journal*, 8 (2008), pp. 261-268.
10. M. Ferrari, V. Ferrari, M. Guizzetti, D. Marioli, and A. Taroni, *Piezoelectric multifrequency energy converter for power harvesting in autonomous microsystems*, *Sensors and Actuators A*, 142 (2008), pp. 329-335.
11. S. J. Roundy, *Energy scavenging for wireless sensor nodes with a focus on vibration to electricity conversion*, *PhD dissertation*, The University of California, Berkeley, 2003.

# RELIABILITY MODELLING OF MEMS CANTILEVER SWITCHES UNDER VARIABLE ACTUATION STRESS LEVELS

P.Fitzgerald<sup>1</sup>, Dr. Martin Hill<sup>2</sup>

<sup>1</sup>Cork Institute of Technology Ireland & Analog Devices, <sup>2</sup>Cork Institute of Technology, Cork, Ireland

**Abstract** — In this paper we present the development and verification of an actuation yielding model, which allows prediction of device reliability for different designs and materials, which is of concern for many MEMS devices. To develop the model, gold cantilevers with inherent actuation stress variations, due to out of plane deflection variations after processing. The distribution of deformations was quantified by measuring the tip-gap of the cantilevers, or the cantilever pull-in voltage which was related to the tip-gap value. Device reliability was assessed by measuring the reduction over time in pull-in voltage for long term hold-down tests. During hold-down, cantilevers with larger tip-gap spacing have a larger actuation stress. A strong correlation was found between long term actuated yielding of the beams, and the peak initial actuation stress. Using the initial actuation stress figure, and the tip-gap change versus time, a creep model was fitted which was then used to extrapolate the tip-gap change over extended periods of time (10+years). For a 10% gap change in a 10 year period, the model suggests a max peak actuation stress of 20MPa.

**Keywords** : Actuation Stress, Gold, MEMS cantilever

## I – Introduction

Metal MEMS actuators show huge potential in areas such as RF switches where MEMS can offer wide bandwidth, high isolation and better linearity compared with solid state devices [1], and for power relay's where devices need lower cost and smaller size [7]. An example of a cantilever MEMS switch is shown in Figure 1. In this device, the metal cantilever beam can be electrostatically actuated by applying voltage to an electrode positioned underneath the beam (Gate). On actuation, contact is made at the tip (Drain), and an electrical contact is made allowing conduction from Source to Drain.

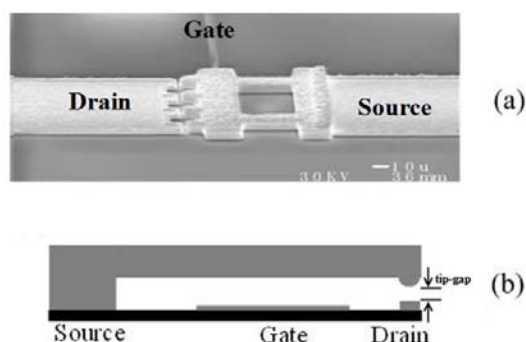


Figure 1: SEM of a device(a), beam schematic(b)

Much work has been carried out on the contact reliability of similar MEMS switches, to achieve high toggle counts. Power relay's have been well characterized in terms of current handling or hot switch opening[9]. Little information in the literature deals with the beam material and failure due to deformations or creep.

Under actuation, stress is induced in the beam. If these stresses exceed the yield stresses of the material, permanent deformation can occur. Over time, these deformations reduce the tip-gap and opening force of the beam, leading to reduced performance or eventual failure to open. This is particularly a problem with MEMS structures manufactured on soft metals such as copper or gold where plastic deformation is generally the first material failure to occur in the beam. To increase reliability, a thorough understanding of the stress limits is essential when designing a structure.

In this project, hold-down tests were carried out on multiple devices, by applying voltage in excess of the actuation voltage or  $V_{pi}$  of the devices, over extended periods of time.  $V_{pi}$  is measured and recorded at various intervals to monitor the status of the devices. It was noted, that  $V_{pi}$  drops over time and sometimes leads to failure or sticking on. Strong correlations were found between  $V_{pi}$ , tip-gap of a device and actuation stress of the devices. Larger  $V_{pi}$  devices, have larger tip-gaps, thus larger stresses, and the larger stress structures tended towards failure more rapidly. These correlations helped create a model relating actuation stress to eventual failure.

Another use for the model is predicting the tip-gap or failure of a device over operating lifetime. In practice, tests can only be carried out over a short period of time. The observed drift in measured early life behaviour, suggests that the model can predict performance over the course of many years.

## II – Device Description

### A. Materials, dimensions and process

The beam is built using electroplated 8 $\mu$ m gold. The contact material can be gold or a hardwearing material chosen for reliability purposes. Thin metals on the substrate form the gate electrode and the drain connection.

The structure consists of an anchor which is connected to the substrate. Two tethers then connect the main beam plate to the anchor. These tethers bend when the beam closes.

The device under characterization has as standard a 0.3 $\mu$ m tip-gap, 0.6 $\mu$ m gate to beam gap, and is 8 $\mu$ m

thick. It is 100µm long and 60µm wide. The tip-gap is the gap between the tip on the beam, and the substrate contact. This gap, dictates the distance the beam will need to move to close, which is critical when determining stresses on the beam.

### B. Tip-gap variation post processing

Following device manufacture, a significant spread in  $V_{pi}$  is noted on the devices under test. This spread in  $V_{pi}$  was found to correlate with a spread in the tip-gaps of the devices. Tip-gaps of the devices under examination were measured using an interferometer, and then plotted vs  $V_{pi}$ . The data is shown in Figure 2.

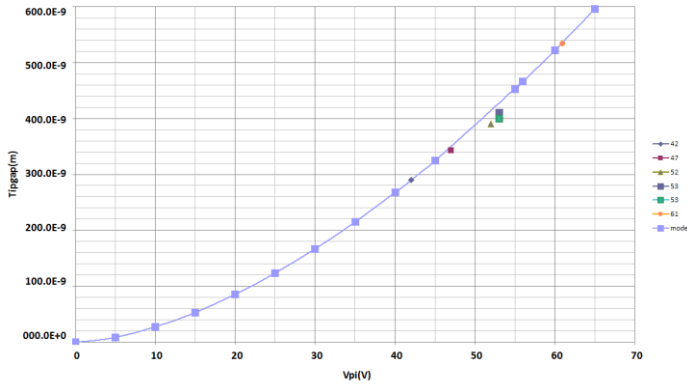


Figure 2: measured tip-gaps vs  $v_{pi}$  including fitted curve

Using curve fitting methods, the tip-gap equation which converts  $V_{pi}$  to tip-gap was derived empirically.

$$Tip-gap = \left\{ \frac{V_{pi}}{385000} \right\}^{1.65} \quad (1)$$

From basic cantilever mechanics, the peak actuation stress induced in the device, is proportional to the deflection of the tip [4]. Therefore, this inherent  $V_{pi}$  or tip-gap variation correlates to an inherent stress variation in the sample of devices. This stress variation can be used to measure and model the various effects of these stresses. The next section discusses the use of a 3D finite element model to accurately derive these stresses.

### C. Device Simulation

The measured device was simulated using CoventorWare [5]. A 3D mesh model is created, and force is mechanically applied to the tips to put the beam into the actuated position. Peak stresses then develop on the top and bottom surface of the structure's hinges in proportion to the amount of displacement of the tips. It is believed that peak stress is the key figure of merit, as yielding will occur at points of highest stress.

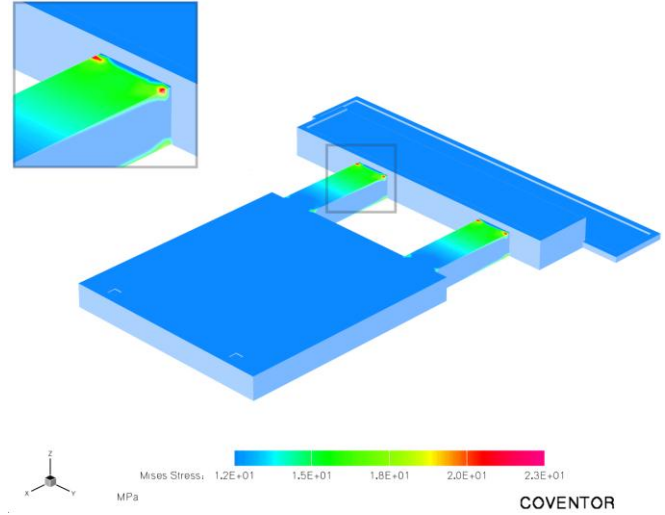


Figure 3: Simulated Stress Distribution of Actuated Switch with inset showing Peak Stress Points

The peak stresses taken from simulation are plotted in Figure 4. There is a direct proportionality between the tip displacement, and the amount of peak stress on the hinge, as expected from theory.

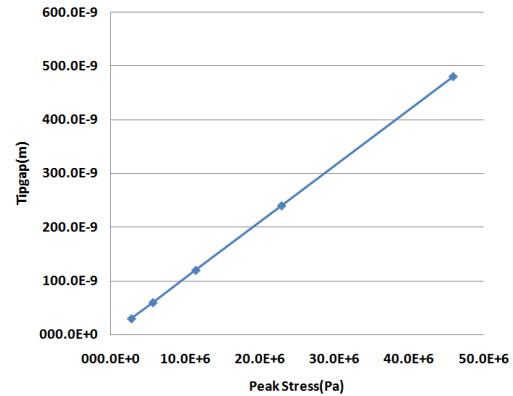


Figure 4: Tip-gap vs Peak stress and hinge stress

## III – Reliability Testing

### A. Hold-down test

The hold-down test, which is a key reliability measure for MEMS switches, tests the ability of the switch to withstand long term actuation. Under actuation, the beam and material's susceptibility to stresses caused by the closure are tested. A setup was assembled that allows long term holding down, or actuation of the switches. The setup can measure the actuation voltage at set intervals, allowing monitoring of the  $V_{pi}$  through-out the hold-down sequence. The voltage applied to the gate electrode during the hold-down phase, and the  $V_{pi}$  measure intervals are carefully chosen. An example of the resulting data is shown in Figure 5.

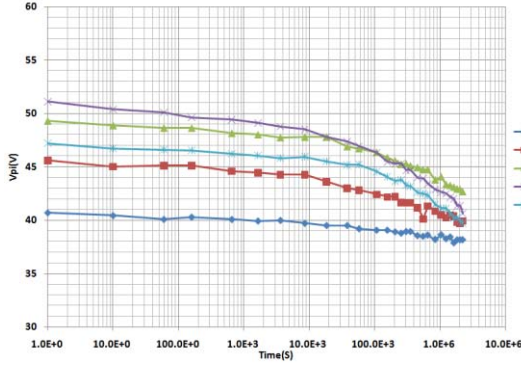


Figure 5:  $V_{pi}$  vs time data from a hold-down test carried out on 5 devices

As can be seen, the  $V_{pi}$  drop throughout the test, is larger for the higher  $V_{pi}$  devices. As  $V_{pi}$  correlates to tip-gap, this  $V_{pi}$  drop is believed to be due to the actuation stresses induced by the larger gaps. The correlation shown in Figure 6, shows this correlation in terms of initial  $V_{pi}$  and  $V_{pi}$  drop(delta).

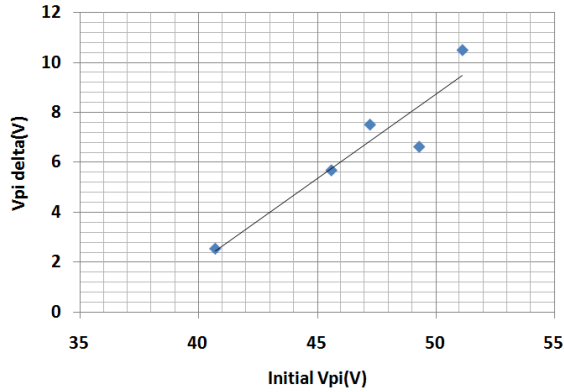


Figure 6: Initial  $V_{pi}$ , plotted vs  $V_{pi}$  change post 2M second hold-down test

Figure 7 plots tip-gap versus time, using equation (1) to complete the conversion. The larger gap, larger stress devices appear to have a larger gap change.

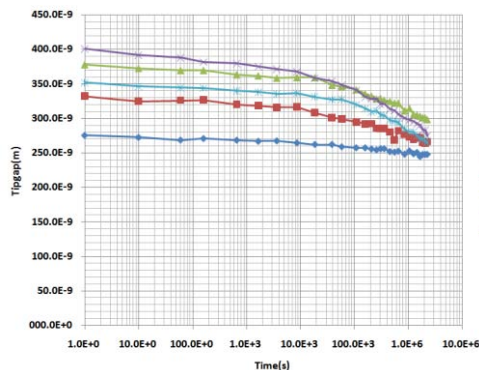


Figure 7: Tip-gap vs time data

### III – Reliability Model Development

#### A. Gap change data

To aid data interpretation, the gap data was converted to gap change data. Plotting this on a log-log

scale, Figure 8, shows strong time linearities, and stress to gap change correlations. This correlation indicates that a model could be used to predict these behaviors, both for stress dependence and time.

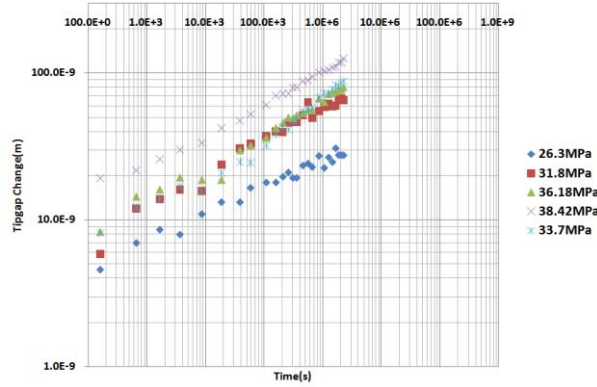


Figure 8: Tip-gap change vs time log-log

#### B. Fitting the model

The standard creep equation relates creep or  $\Delta L$  of a sample under test, to stress, time, and other factors such as temperature, material characteristics etc. [8]. The stress and time components of this equation can be used to develop a similar gap change equation for the situation discussed here. The thermal component which includes Boltzmann's constant, Temperature and Activation energy, is ignored for this analysis.

$$\epsilon_c = \text{creep strain} = A_0 \cdot \sigma^m \cdot t^n \cdot \exp\left(\frac{-Q}{RT}\right) \quad (2)$$

Curve fitting Equation(3) to measured data generates the equation parameters shown, where  $\sigma$  is stress in Pa,  $t$  is time in seconds, and  $A_0$  is a fitted gain constant.

$$\Delta \text{gap} = \sigma^m \cdot t^n \cdot A_0 \quad (3)$$

$(m = 4.01, n = 0.202, A_0 = 2.7e-39)$

The  $m$  in Equation (3) indicates the stress dependence, is very high at  $m=4$ , and suggests that small changes in the stress, will give large reductions in the gap change. The time coefficient  $n$ , at 0.202 suggests that with time, the gap change decelerates significantly, which is what is observed in the measured data.

#### C. Tip-gap drift with time

Plots were generated using Equation (3) and are overlaid on the measured data in Figure 9. The model is clearly overlaying the measured data both in terms of stress and time suggesting a good fit. The modeled data matches the measured data in the early time decades. These strong correlations with early data, suggest the model can be used to extrapolate to later life behavior. The extrapolation suggests the reduction in tip-gap of devices with higher actuation stress will exceed their



initial gap after 100M seconds, with the lower stress structures still open after 1Bn seconds.

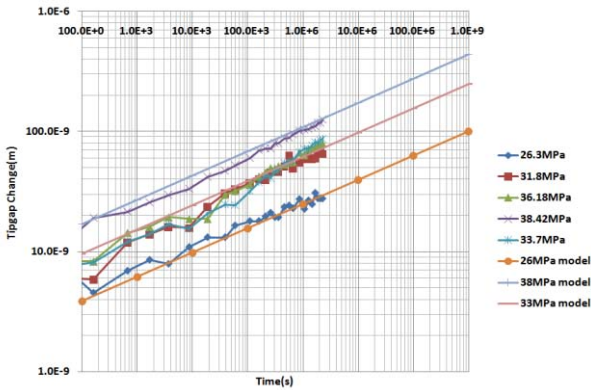


Figure 9: Tip-gap change vs time data and model

#### D. Modeling Actuation Stress

Figure 9 also illustrates the accuracy of the model. Both the low and high stress devices appear to be well modeled, which is expected as these were used to fit the model. The devices in the median also appear to be well modeled.

Equation (3) can be manipulated to make stress and gap change the dependent variable, fixing time, as in Equation (4).

$$\sigma = \left( \frac{\Delta gap}{t^n \cdot A_0} \right)^{\frac{1}{m}} \quad (4)$$

If a product specification dictates the lifetime of a device needs to be a given time, this time can be input to the model to generate a plot of expected gap change vs stress for that given time, as shown in Figure 10. The plot is then used to pick a maximum initial peak actuation stress for the design to achieve the desired lifetime.

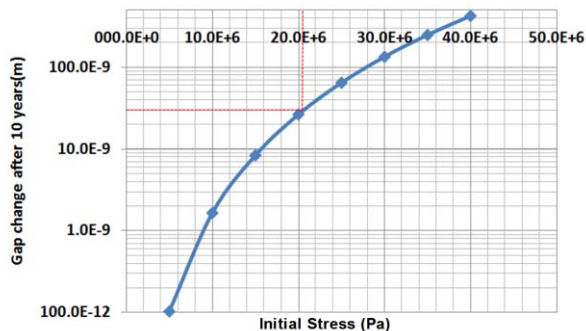


Figure 10: Tip-gap change after 10 years vs Initial Actuation Stress

A reasonable expected lifetime for a MEMS switch is 10 years, so stress is varied given 315M seconds in time. This predicts that for less than 30nm (10%) gap change, the peak stress of the MEMS cantilever device, must be less than 20MPa.

#### IV – Conclusion

A method has been proposed to predict the peak stress allowable for a particular gold cantilever design. A similar method could be applied to different structures and materials. The method involves measurement of pull-in voltage decrease during a hold-down test, for devices with a distribution of process induced gap variations. Pull-in voltage decreases faster in devices with the highest gaps. This is attributed to the increase in maximum stress in the device tethers where this stress may exceed the yield limit. From this data a model relating device stress to the change over time in the beam tip-gap has been developed and verified. The model was able to conclude that a peak stress less than 20MPa is required for a 10 year lifetime switch.

#### References

- [1] Gabriel M. Rebeiz, RF MEMS Theory, Design and Technology, John Wiley and Sons, 2003
- [2] Stephen D. Senturia, Microsystem design, Klower Academic Publishers, 2001
- [3] W.M. van Spengen, MEMS reliability from a failure mechanisms perspective, Microelectronics Reliability, vol. 43, no. 7, pp. 1049-1060, 2003
- [4] Warren C. Young, Richard G. Budynas, Roark's formula's for Stress and Strain, 7<sup>th</sup> edition
- [5] <http://www.coventor.com>
- [6] A. Karimi, K. Niayesh, A simple evaluation method of the thermal interruption limit of power circuit breakers, Electrical Engineering Journal, Springerlink, Vol. 90/Number 8/Feb 2009, p523-528
- [7] E.M. Yeatman, Design and performance analysis of thermally actuated MEMS circuit breakers, 2005 J. Micromech. Microeng. 15 S109
- [8] Martin J. Dropik, David H Johnson, David E. Roth, Penn state-Erie, Erie, PA, USA, Developing an ANSYS Creep Model for Polypropylene from Experimental Data, <http://www.ansys.com>
- [9] J.H. FabianK. Niayesh, L. Niemeyer, Matrix combination of elementary switches: general considerations and application to MEMS relays, Electrical Engineering Journal Springerlink, Vol. 90/Number 1/Nov 2007, p19-31
- [10] P.M. Zavracky, S. Majumder, N.E. McGruer, "Micromechanical Switches Fabricated Using Nickel Surface Micromachining", J. Microelectromech. Syst., vol. 6, pp. 3-9, 1997.

## Register

- A.A.A. Aarts 165  
L. Abelmann 193, 24, 52, 277, 257, 261  
M. Ádám 309  
S. Ahmed 108  
A. Albrecht 76  
B. Albrecht 153  
A. Alshehri 269  
F. Alves 132  
O. Ambacher 76  
A. Amini 136  
P. Ancey 301  
J. Arcamone 301  
K. Asada 48  
J.J. Atherton 112  
H. Aubert 250  
S. Azimi 136  
A. Backes 80  
S. Barabash 140  
I. Bársony 309  
G. Battistig 36, 201, 309  
J.G. Beekman 193  
A.J. Been 193  
R. Beernaert 44  
E. Berenschot 120, 24  
A. van den Berg 32, 293, 124, 220  
A. Bittner 80  
A. Blake 224  
C. Bleses 144  
S. Boden 88  
H. de Boer 193  
M.J. de Boer 120, 297  
J.G. Bommer 124  
S. Bouaziz 250  
A. Boukabache 235  
K. Brinkfeldt 140  
R.A. Brookhuis 297  
D.M. Brouwer 52  
K. Burlage 208  
A. Burr 144  
P. Calmon 235  
C.J. Camargo 181  
H. Campanella 181  
E.T. Carlen 220, 124, 32, 293  
J.P. Carmo 243  
J.F. Carpentier 301  
G. Carroll 197  
F. Casset 301  
J.-P. Celis 44  
F. Ceyssens 239, 231, 157  
S.M. Chakkalakkal Abdulla 120  
B.P. Chaudhri 239  
S. Chen 216, 32, 293  
V. Cherman 60  
Z. Chew 317  
A. Cismaru 281  
Y. Civet 301  
S. Clara 40  
J. Cleary 197  
J.H. Correia 116, 253, 243  
J. de Coster 44  
E. Cretu 96  
R. Cuperus 189  
A. De 32  
M. Deckert 144  
A. Delahunty 100  
D. Diamond 197  
N.S. Dias 243  
J.W. van Dijk 52  
M. Dijkstra 120, 297  
H. Droogendijk 149  
M. Držík 56  
F.F.C. Duval 60  
A. Ebrahimi 177  
I. El Gmati 235  
M. Elwenspoek 153, 277, 313, 257, 261  
A. Emadi 185, 104, 169  
M. Emanuelsson 140  
J.B.C. Engelen 193, 52  
P. Enoksson 108, 140  
M.A. Erismis 227  
J. Esteve 181  
F. Fachin 92  
L. Fangzhou 44  
Z. Fekete 36  
P. Fitzgerald 321  
J. Flokstra 189  
F.F. Flokstra 189  
G.A. Folkertsma 193  
L. Fortgens 193  
S. Franssila 64, 161  
P.J. French 96, 20  
B. Front 140  
R. Fulcran 235  
P. Fürjes 36  
P. Gardonio 269  
J. Geerlings 24  
T. Geiling 76  
C. Gerhardy 208  
P. Gijsenbergh 84  
L.M. Gonçalves 243, 116, 253  
K.V. Gothelf 19  
D. de Graaf 193  
G. de Graaf 216, 104, 185, 173, 20, 169  
L. Grand 201  
C. Grinde 28  
D. Gubán 36  
T. Haas 80  
S. Hascik 72, 56  
L. Haspeslagh 212  
D.S. Hautzinger 153  
J. Healy 197  
W.K. Hensinger 305  
J. Hesselbarth 204  
C. Hierold 204  
W. Hilber 40  
M. Hill 321, 265, 128  
M. Hoffmann 76, 289  
R.P. Hogervorst 52  
C. Van Hoof 165, 239  
I. Hotovy 72  
B. Jakoby 40  
O. Jakovlev 289  
H.V. Jansen 313  
R. Jansen 60  
M. Jin 220, 124  
S. Johnstone 112  
A. Kallala 235  
T. Kallio 161  
P. Kanninen 161  
G. Karmos 201  
L.J. Kauppine 120  
M. Kayyalha 177  
R.A. Ketola 64  
G. Keulemans 231  
H. Kizil 273  
F. Knöbber 76  
W.W. Koelmans 277  
G. Konstantinidis 281  
J.G. Korvink 153  
I. Kostic 56  
M. Kraft 269, 68, 305  
G.J.M. Krijnen 120  
B. Krijnen 52, 149  
M. Krüger 153  
Y. Kubarappa 128  
M. Kübler 144  
M. Kubota 48  
S. Kuhn 144  
S. Kühne 204  
A.A. Kuijpers 297  
M.A. Lantz 17  
T. Lalinský 56, 72  
R. Lameiro 116  
S. Lanceros-Mendez 116  
T. Lederer 40  
M.T. de Leon 68  
S. Leopold 76  
L. Li 317  
Y. Li 204  
D. van Lierop 297  
W.-Y. Lin 44  
E. Lorent 301  
J. Love 265  
A. Müller 281  
K.M. Müller 153  
D. Maher 197  
K.A.A. Makinwa 20  
A. Manz 261  
E. Markweg 289  
G. Márton 201  
F. Marty 48  
M.N. Masood 293  
F. Mazaleyrat 132  
M. Mehdi Jatlaoui 250

M. Mehran 136  
P.M. Mendes 116, 243  
D. Mingli 250  
K. Minoglou 227  
Y. Mita 48  
H. Mizuta 88  
B. Mogulkoc 313  
T. Mohácsy 309  
S. Mohajerzadeh 177, 136, 247  
V.R.S.S. Mokkapatni 104  
Z. Moktadir 88  
J. Montserrat 181  
P. de Moor 227, 239  
A. Moreira 92  
I. Mori 48  
S. Morishita 48  
J. Moulin 132  
K. de Munck 227  
J. Naghsh Nilchi 177, 136  
H. Nazeer 257  
D. Neculoiu 281  
H.P. Neves 165  
A. Niel 301  
J. van Nieuwkastele 32  
T. Nissilä 64  
J. O'Brien 224  
R. van 't Oever  
P. Ohlckers 28  
E. Ollier 301  
C. O'Mahony 128, 265, 224  
C. Otto 220  
A. Ozbey 273  
D. Pätz 76  
T. Peters 277  
L. Petricca 28  
N.P. Pham 60  
W.T. Pike 100  
S. Pinon 235  
T. Polster 76  
A. Pongrácz 36, 201  
P. Pons 250, 235  
A.J. Pontes 92  
D. Psychogiou 204  
R. Puers 165, 239, 231, 157, 212, 84  
V. Pullu 220  
V. Rajaraman 96, 20  
P. Ramachandra Rao 227  
H. Rattanasonti 305  
V. Rehacek 72  
P. Renaux 301  
T. Retkes 309  
J.F. Ribeiro 243, 253  
R.M. de Ridder 120  
P. Robert 301  
L.A. Rocha 92  
F.J.O. Rodrigues 116  
M.C. Rosamond 112  
C. Rusu 108  
M.V. Rusu 108  
H. Rutt 88  
I. Rýger 56  
V. Saarela 64  
I. Sabageh 96  
L. Sainiemi 64  
Z. Sanaee 247  
E. Sarajlic 24  
U. Schmid 80  
W.K. Schomburg 208  
G. Scotti 161  
J. Scully 224  
J.W. Seo 231  
A.T. Sepúlveda 92  
I. Shahosseini 132  
L. Shui 124  
M.H. Siekman 24  
M.M. Silva 253  
A.F. Silva 243  
J.M. Silva 92  
M.F. Silva 253, 243  
S. Sinzinger 76  
O. Solgaard 18 W. Sparreboom 32  
W.M. van Spengen 285  
P. Srinivasan 305  
O. Srivannavit 165  
A. Stavrinidis 281  
A. Stefanescu 281  
R.C. Sterling 305  
P. Taatizadeh 68  
N.R. Tas 24  
D. Tengeri 72  
H.J.M. ter Brake 313  
D.S. Tezcan 60, 227  
H.A.C. Tilmans 60  
L. Trabzon 273  
I. Ulbert 201  
A. Vali 136  
M. Vallo 56  
G. Vanko 56  
K. Vanstreels 84  
É. Vázsonyi 201, 36  
J. Verstraete 157  
J.C. Viana 92  
S. Vocke 193  
B. Volckaerts 157  
M. de Volder 231  
J. de Vos 227  
J. de Vries 261  
B.L. Wardle 92  
T. Weidisch 309  
S. Weinberger 289  
L. Wen 212  
S. Wiebe 201  
R.J. Wiegerink 297, 189  
M. Wieser 140  
C.H. Winkelmann 289  
K.D. Wise 165  
A. Witvrouw 212  
L.A. Woldering 193, 257  
I. de Wolf 44  
R. Wolffenbuttel 169, 216, 185, 104, 173  
K. Wouters 212 84  
H. Wu 216, 185, 104, 173, 169  
M. Yilmaz 273  
L. Yobas 273  
E. Yoon 165  
C. Zeilmann 80  
D.A. Zeze 112